

**INTERACTIONS OF NATIVE PEPTIDES
AND SMALL MOLECULES WITH THE
PDZ DOMAINS OF PSD-95 AND SAP97**

Thesis submitted in accordance with the
requirements of the

University of Liverpool

for the degree of

Doctor in Philosophy

by

LIAM ANTHONY DORR

July 2013

ABSTRACT

A PDZ domain is a small, ~ 90 amino acid residue region of a protein that acts as a protein-protein interaction module. There are currently 267 known PDZ domain-containing proteins in the human genome, with the predominant function of a PDZ domain being the recognition and binding of C-terminal motifs in partner proteins. Examples of well-studied multi PDZ domain-containing proteins are the postsynaptic density-95 protein (PSD-95) and the synapse-associated protein 97 (SAP97); different PSD-95 and SAP97 PDZ domain-mediated interactions have been implicated in a variety of pathological conditions. The interaction of the PSD-95 PDZ domains with the 5-hydroxytryptamine receptor 2a (5-HT_{2a}) & 2c (5-HT_{2c}) variants is known to be important in inducing hyperalgesia in neuropathic pain; the PDZ-mediated interaction of SAP97 with the human papillomavirus type 18 (HPV18) E6 protein is an important event in a p53-independent pathway of cervical carcinogenesis.

As PDZ domains have been shown to bind small organic molecules and that the majority of free energy contributions of the PDZ domain interaction interface to binding, are due to a select few 'hotspot' regions; the development of novel, reversible small molecule inhibitors of the PSD-95 and SAP97 PDZ domains was deemed a viable research target. This was the overriding aim of the research programme detailed in this thesis and encompassed biophysical techniques such as: protein production, NMR spectroscopy, isothermal titration calorimetry (ITC), restraint-driven docking and structure determination methodologies.

The PDZ-mediated interactions of 5-HT_{2a} and 5-HT_{2c} with the PSD-95 and SAP97 PDZ1 & PDZ2 were confirmed using NMR spectroscopy and then, quantified by ITC. The structure of the physiologically relevant complex formed between PSD-95

PDZ1 and 5-HT_{2c} was determined using NMR solution state spectroscopic determination methods; this is the first example of a PSD-95 PDZ – 5-HT_{2x} complex structure.

A systematic investigation into the interaction between the SAP97 PDZ2 domain and the HPV18 E6 protein was carried out by ITC; this process involved binding experiments utilising commercially acquired peptides of varying lengths and sequences, containing natural and non-natural amino acids.

A variety of small organic molecules that bind to the PSD-95 PDZ1 domain have been developed by an NMR screening process. The PSD-95 PDZ1 binding affinity of two of the small molecules was determined by NMR spectroscopy and their inhibitory effect on the native PSD-95 PDZ1 – 5-HT_{2c} interaction was quantified using ITC. The structure of the individual PSD-95 PDZ1 – small molecule complexes formed were determined by NMR restraint-driven docking, using the **high-ambiguity driven docking** (HADDOCK) programme; this is the first instance of HADDOCK being utilised to determine a PDZ domain – small molecule complex structure.

The research detailed in this thesis alludes to the possibility that PSD-95 and SAP97 PDZ domain-mediated interaction inhibition by a small molecule compound may not be a feasible research aim and that future PDZ domain inhibition research may need to be focus on other inhibitor structures i.e. β -strand peptidomimetics.

Abstract	i
Table of Contents	iii
Publications	viii
Acknowledgements	ix
Abbreviations	x
1. Introduction	1
1.1 Protein-Protein Interactions.....	2
1.2 Synapses	4
1.3 Postsynaptic Density Membrane-Associated Guanylate Kinases	5
1.4 PDZ Domains	6
1.5 PDZ Proteins: PSD-95 and SAP97.....	9
1.5.1 PDZ Domain Comparison	9
1.5.2 Postsynaptic Density-95 Protein (PSD-95)	10
1.5.1 General Overview	10
1.5.2 PSD-95 PDZ Domain-Mediated Interactions.....	11
1.5.3 Synapse-Associated Protein 97 (SAP97).....	14
1.5.1 General Overview	14
1.5.2 SAP97 PDZ Domain-Mediated Interactions	14
1.5.4 Roles of PSD-95 and SAP97 in LTD, LTP and Synaptic Plasticity	17
1.5.5 Summary.....	21
1.6 Previous PDZ Domain Inhibition Research	21
1.6.1 Peptides.....	21
1.6.2 Peptidomimetics	26
1.6.3 Small Molecule Inhibitors	30
1.6.3.1 Rational Design	30
1.6.3.2 Virtual Library Screening/NMR Spectroscopy	32
1.6.3.3 High-Throughput Screening	34
1.6.3.4 Re-Purposing of Existing Drugs.....	35
1.6.4 Summary of Previous PDZ Domain Inhibition Research.....	36
1.7 Conclusion.....	37
1.8 Research Aims.....	38
2. Introduction to Biophysical Techniques	41
2.1 General	42
2.2 Protein Nuclear Magnetic Resonance (NMR) Spectroscopy	42
2.2.1 Introduction to NMR Spectroscopy.....	42
2.2.2 Classical NMR Spectroscopy	42
2.2.3 Experimental Aspects of NMR Spectroscopy	52

2.2.4 Applications of NMR Spectroscopy	64
2.2.4.1 Protein Structure Determination	64
2.2.4.2 Characterisation of Intermolecular Interactions	64
2.3 Isothermal Titration Calorimetry (ITC).....	65
2.3.1 Introduction to ITC	65
2.3.2 Advantages of ITC.....	66
2.3.3 Instrumentation and Experimental Overview	67
2.3.4 Analysis of Experimental Data	69
2.3.5 Applications of ITC	71
3. Materials and Methods	72
3.1 Materials	73
3.1.1 Water.....	73
3.1.2 General Solvents	73
3.1.3 General Reagents	73
3.1.4 General Equipment	73
3.1.5 General Experimental Considerations	74
3.1.6 Expression Vectors	74
3.1.7 Bacterial Strains.....	74
3.1.8 Proteases	76
3.1.9 Media Recipes	76
3.2 Methods	80
3.2.1 Molecular Biology Methods	80
3.2.1.1 Site-Directed Ligase-Independent Mutagenesis (SLIM).....	80
3.2.1.1.1 Primer Design	80
3.2.1.1.2 Polymerase Chain Reaction (PCR).....	81
3.2.1.1.3 DpnI Digest of PCR Products.....	81
3.2.1.1.4 Agarose Gel Electrophoresis	83
3.2.1.1.5 Plasmid Preparation	84
3.2.1.2 Preparation of Chemically Competent Cells	84
3.2.1.3 Transformation of Chemically Competent <i>E.coli</i>	85
3.2.2 Protein Expression Methods	85
3.2.2.1 Expression in LB Medium.....	85
3.2.2.2 Expression in Minimal Medium	86
3.2.3 Protein Purification Methods.....	87
3.2.3.1 Cell Lysis	87

3.2.3.2 Ni ²⁺ Affinity Chromatography	87
3.2.3.3 Concentration of Protein Sample.....	88
3.2.3.4 Buffer Exchanging of Protein Sample.....	88
3.2.3.5 Hexahistidine-Tag Removal Using TEV Protease	89
3.2.3.6 SUMO-Tag Removal Using SUMO Protease	89
3.2.3.7 Size Exclusion Chromatography	89
3.2.3.8 PDZ Domain Construct	90
3.2.4 Analytical Methods.....	91
3.2.4.1 Protein Concentration Determination	91
3.2.4.2 SDS-PAGE Gel Electrophoresis.....	91
3.2.4.3 Coomassie Brilliant Blue Staining	92
3.2.4.4 Gel Imaging	92
3.3 NMR Spectroscopy	92
3.3.1 General.....	92
3.3.2 Unbound PDZ Domain Sample Preparation.....	93
3.3.3 PDZ Domain – Ligand Complex Sample Preparation	93
3.3.4 Ligand Binding Screening by NMR Spectroscopy	93
3.3.5 Binding Affinity Determination by NMR Spectroscopy.....	94
3.4 Isothermal Titration Calorimetry (ITC).....	96
3.4.1 Basic Set-Up of an ITC Experiment.....	96
3.4.2 Native Protein – Ligand Interaction Experiment.....	97
3.4.3 Competition Experiment.....	97
3.5 Protein – Ligand Structure Determination	98
3.5.1 Collection of a Suite of NMR Experiments.....	98
3.5.2 Assignment of ¹ H, ¹³ C and ¹⁵ N Resonances of a PDZ Domain	99
3.5.3 Assignment of NOESY's and Preliminary Structure Determination	105
3.5.4 Structure Determination and Water Refinement Using CNS	107
3.5.4.1 PSD-95 PDZ1 – 5-HT _{2c} Structure Refinement.....	107
3.5.5 Rigid Body Semi-Flexible Restraint-Driven Docking	109
4. The Biophysical Characterisation of PDZ Interactions Involving the 5-Hydroxytryptamine Receptor 2a and 2c Variants.....	116
4.1 Introduction	117
4.2 Purification of PSD-95 and SAP97 PDZ1 and PDZ2 Domains.....	118
4.3 Characterisation of PDZ Domains by NMR Spectroscopy	120
4.4 PDZ Domain Binding Screening of 5-HT _{2x} by NMR Spectroscopy	127
4.4.1 General.....	127

4.4.2 PDZ Domain-Mediated Interactions of 5-HT _{2a}	127
4.4.3 PDZ Domain-Mediated Interactions of 5-HT _{2c}	127
4.4.4 Discussion.....	137
4.5 Binding Affinity Determination by ITC.....	138
4.5.1 General.....	138
4.5.2 Quantification of PDZ Domain Binding Strength of 5-HT _{2a}	139
4.5.3 Quantification of PDZ Domain Binding Strength of 5-HT _{2c}	141
4.5.4 Comparison of 5-HT _{2a/c} PDZ Domain Binding.....	151
4.6 PSD-95 PDZ1 – 5-HT _{2c} NMR Solution State Structure Determination	153
4.6.1 Overview.....	153
4.6.2 Assignment of NMR Spectra.....	154
4.6.2.1 Bound Protein Backbone and Side-Chain Assignment	154
4.6.2.2 Bound Peptide Assignment.....	155
4.6.2.2.1 Introduction.....	155
4.6.2.2.2 NMR Titration	157
4.6.2.3 NOESY Assignment.....	170
4.6.3 Structure Calculation	171
4.6.3.1 <i>In Vacuo</i>	171
4.6.3.2 Water-Refinement.....	171
4.6.4 Characterisation and Validation of Water-Refined NMR Solution State Structure of the PSD-95 PDZ1 – 5-HT _{2c} Complex	172
4.7 Conclusion.....	183
5. The Biophysical Investigation into the Interaction Between the SAP97 PDZ2 Domain and the Human Papillomavirus Type 16/18 E6 Proteins.....	185
5.1 Introduction	186
5.2 Purification of SAP97 PDZ2 Mutants	189
5.3 Characterisation of SAP97 PDZ2 Mutants by NMR Spectroscopy.....	191
5.4 SAP97 PDZ2 – HPV E6 Interaction Binding Investigation.....	197
5.4.1 General.....	197
5.4.2 pH Investigation.....	197
5.4.3 Peptide Length Investigation	202
5.4.4 Hydrophobic Interaction Investigation	209
5.4.5 Hydrophobic Interaction Investigation Summary	211
5.4.6 Electrostatic Interaction Investigation	218
5.4.6.1 Ligand Perspective	218
5.4.6.2 PDZ Domain Perspective	225

5.4.7 Electrostatic Interaction Investigation Summary.....	226
5.5 General Discussion.....	232
6. The Development of Novel Small Molecule Inhibitors of the PSD-95 and SAP97 PDZ Domains by Biophysical Techniques.....	234
6.1 Introduction.....	235
6.2 Ligand Binding Screening by NMR Spectroscopy.....	237
6.2.1 General.....	237
6.2.2 First Generation Compounds.....	240
6.2.3 Second Generation Compounds.....	244
6.2.4 Third Generation Compounds.....	248
6.2.5 Fourth Generation Compounds.....	253
6.2.6 Fifth Generation Compounds.....	257
6.2.7 Summary of Ligand Binding Screening by NMR Spectroscopy.....	260
6.3 Binding Affinity Determination by NMR Spectroscopy.....	263
6.3.1 General.....	263
6.3.2 PSD-95 PDZ1 – 3c K_D Determination.....	263
6.3.3 PSD-95 PDZ1 – 4c K_D Determination.....	267
6.3.4 Discussion.....	271
6.4 Binding Affinity Determination by ITC.....	271
6.4.1 General.....	271
6.4.2 Competition Experiments with 3c	272
6.4.3 Competition Experiments with 4c	272
6.5 Comparison of K_D and K_i	273
6.6 PDZ Domain – Small Molecule Complex Structure Determination by NMR Restraint-Driven Docking.....	275
6.6.1 General.....	275
6.6.2 PSD-95 PDZ1 – 3c Structure Determination.....	276
6.6.3 PSD-95 PDZ1 – 4c Structure Determination.....	281
6.6.4 HADDOCK Structure Comparison.....	286
6.7 Conclusion.....	289
7. General Discussion and Future Research.....	291
7.1 Conclusions.....	292
7.2 Future PDZ Domain Inhibition Research.....	294
7.2.1 New Small Molecule Scaffold.....	295
7.2.2 B-Strand Peptidomimetics.....	295
8. References.....	297
Appendix.....	313

PUBLICATIONS

The research subsequently described in this thesis has led to the preparation of the following manuscripts:

- Bouzidi, N., Deokar, H., Vogrig, A., Boucherle, B., Ripoché, I., Abrunhosa-Thomas, I., Dorr, L., Wattiez, A.-S., Lian, L.-Y., Marin, P., Courteix, C. & Ducki, S. 2013. Identification of PDZ ligands by docking-based virtual screening for the development of novel analgesic agents. *Bioorganic & Medicinal Chemistry Letters*, 23, 2624-2627.
- Dorr, L., Vogrig, A., Bouzidi, N., Boucherle, B., Wattiez, A.-S., Cassier, E., Vallon, G., Ripoché, I., Abrunhosa-Thomas, I., Marin, P., Nauton, L., They, V., Courteix, C., Lian, L.-Y. & Ducki, S. 2013. Structure-based design of PDZ ligands as inhibitors of 5-HT_{2a}/PSD-95 PDZ1 interaction possessing anti-hyperalgesic activity. *ACS Chemical Biology*, 8, 2209-2216.
- Dorr, L & Lian, L.-Y. 2013. Chapter 4 research (Manuscript in preparation).
- Dorr, L., Phelan, M.M. & Lian, L.-Y. 2013. Chapter 5 research (Manuscript in preparation).
- Dorr, L & Lian, L.-Y. 2013. PSD-95 PDZ2 – nNOS interaction research (Data not shown in this thesis, manuscript in preparation).

ACKNOWLEDGEMENTS

First and foremost, I would like to thank my supervisor, Professor Lu-Yun Lian; not only for thinking of such an interested and varied research project for me to be a part of, but also for her continuous support, guidance and patience over the past four years. I can safely say I am not going to miss the 1am e-mails off her though! I would also like to thank the BBSRC and GE Healthcare for funding my research project and my secondary supervisor Dr Andrew Carnell, who was extremely helpful in the initial stages of the project.

I feel privileged to have been a researcher in Lab C and as it would take too much time to name everyone, I would simply like to thank all the Lab C members, past and present, for their friendship, help and advice. Although, I'm not too sure that they will miss listening to my terrible taste in music!

I'd like to give a special mention to a few colleagues, without whom I would not have made it to this point: Dr Mark Tully and Dr Rob Gibson for having the time and patience in the initial project stages to train a cowboy chemist in the joys of molecular biology! Dr Marie Phelan has been an absolute saint and in truth, deserves her own acknowledgement page for the sheer amount and variety of help she has given me over the course of four years; ranging from staying late to run NMR samples with me, to proof reading this thesis, a simple thank you does not seem enough! Thanks also to Professor Alexandre Bonvin, Dr Wayne Boucher and Dr Luminita Damian for providing excellent technical assistance when required.

My family, most notably my mum and sister, Hannah, deserve a huge thank you for all their love, belief, support and for generally putting up with the hassle that comes with living with a PhD student; I can only imagine how many night sleep of theirs I have disrupted by coming home late from the lab at night or leaving early for it in the morning! My only sadness is that my Dad and Nan are not here to see me reach this stage and it is in their memory I dedicate this thesis.

Last and definitely by all means least, I suppose I better thank all the uglies, young(ish) → (very) old, I have had the misfortune of calling my mates, some for far too long! They have always been there when I have needed a welcome distraction from the stresses and strains of research, whether it was a pint in the village or a game of footie, their continued friendship has helped enormously. Nice one la's!

Nil Satis Nisi Optimum.

ABBREVIATIONS

1-D	One-dimensional
2-D	Two-dimensional
3-D	Three-dimensional
5-HT	5-Hydroxytryptamine (aka serotonin)
5-HT _x	5-Hydroxytryptamine receptor
5-HT _{2x}	5-Hydroxytryptamine receptor 2a/b or c variant
5-HT _{2a}	5-Hydroxytryptamine receptor 2a variant
5-HT _{2c}	5-Hydroxytryptamine receptor 2c variant
AA	Amino acid
ADC	Analogue to digital converter
AJ	Adherens junction
AKAP79	A-kinase anchoring protein 79
AMPA(R)	α -amino-3-hydroxy-5-methyl-4-isoxazolepropionic acid (receptors)
APC	Adenomatous polyposis coli
ATFV	Average target function value
β_1 -AR	Beta-1-adrenergic receptor
Br1	Bridged macrocycle 1
BP1	Bridged peptide 1
BSA	Buried surface area
CAL	CFTR-associated ligand
CAMKII	Ca ²⁺ /calmodulin-dependent protein kinases II
CAPRI	Critical assessment of predicted interactions
CCPN	Collaborative computing project for NMR
CFTR	Cystic fibrosis transmembrane conductance regulator
CNS	Crystallography and NMR system
CP1	Chemically modified peptide 1
CRIP1	Cysteine-rich PDZ-binding protein
^c Pe	Cyclopentyl
DNA	Deoxyribonucleic acid
Dvl	Dishevelled
E6AP	E6-associated protein
EGFR	Epidermal growth factor
ES	Excitation sculpting
Et	Ethyl
FID	Free-induction decay
Fz	Frizzled
GIPC	GAIP-interacting protein, C terminus
HADDOCK	High ambiguity-driven docking
HPV	Human papillomavirus
HPV16	Human papillomavirus type 16
HPV18	Human papillomavirus type 18
HSQC	Heteronuclear single quantum coherence
HTLV1	Human T-cell leukaemia virus-1
HTS	High-throughput screening

HTS1	High-throughput screening molecule 1
IGF-IR	Insulin-like growth factor receptor-1
INEPT	Insensitive nuclei enhance by polarisation transfer
ITC	Isothermal titration calorimetry
K _{ir}	Inwardly rectifying potassium channel
K _v	Voltage-gated potassium channel
LARG	Leukaemia-associated RhoGEF
LB	Lysogeny broth
LTD	Long term depression
LTP	Long term potentiation
MAGI-1	Membrane-associated guanylate kinase-1
MD	Molecular dynamics
Me	Methyl
MP1	Metallopeptide 1
mtf	molecular topology file
MUPP1	Multiple PDZ domain-containing protein 1
NHERF	Na ⁺ /H ⁺ exchanger regulatory factor
NMR	Nuclear magnetic resonance
NMDA(R)	N-methyl-D-aspartate (receptors)
nNOS	neuronal Nitric oxide synthase
NOE	Nuclear Overhauser effect
NOESY	Nuclear Overhauser effect spectroscopy
ORF	Open reading frame
OCH ₂ Ph	Benzyloxy
O ^{cy} Pe	Cyclopentoxo
OEt	Ethoxy
OH	Hydroxyl
OMe	Methoxy
PCR	Polymerase chain reaction
PDB	Protein databank
Ph	Phenyl
PICK1	Protein interacting protein kinase C 1
PPI	Protein-protein interaction
ppm	parts per million
PSD	Postsynaptic density
PSD-95	Postsynaptic density-95 protein
PSD-MAGUKs	Postsynaptic density membrane-associated guanylate kinases
PTEN	Phosphatase and tensin homolog
RF	Radiofrequency
RhoGEF	Rho guanine nucleotide exchange factor
RMSD	Root mean square deviation
SAP97	Synapse-associate protein 97
Sc1	Scaffold 1
SDS-PAGE	SDS-polyacrylamide gel electrophoresis
SLIM	Site-directed ligase-independent mutagenesis
SM1	Small molecule 1

TACE	Tumour necrosis factor alpha-convertase
TAD	Torsion angle dynamics
SOC	Super-optimal medium with catabolite repression
SSTR	Somastatin receptor
STD	Saturation transfer difference
SUMO	Small ubiquitin-like modifier
TAE	Tris-acetate
TEV	Tobacco etch virus
TOCSY	Total correlation spectroscopy
VEGF	Vascular endothelial growth factor
VLS	Virtual library screening
WT	Wild-type

Chapter 1
INTRODUCTION

1. INTRODUCTION

1.1 Protein-Protein Interactions

The specific interaction between two proteins is a critical event in almost all biological processes (Sharma et al., 2002, Arkin and Wells, 2004); the key cellular operations of an individual protein are usually exerted through a protein-protein complex form, rather than in isolation (Berg, 2003). As a result of the vital role of protein-protein interactions (PPIs) in a wide-range of cellular processes, the formation of abnormal or undesirable PPIs has been implicated in a variety of pathological conditions (Arkin, 2005); thus, PPIs represent a large and attractive class of targets for human therapeutics (Gadek and Nicholas, 2003). The potential to interfere with PPIs is of the utmost importance, not just in the development of novel disease treatments but also in terms of developing our understanding of cell physiology; inhibition of a particular PPI and analysing the resultant cellular effect can elucidate the role of a specific protein or PPI (Cochran, 2001, Ockey and Gadek, 2002).

The vast majority of PPI inhibition research to-date has centred on the use of therapeutic antibodies, which are specific for their target and stable in human serum. An indication of the previous excitement in this therapeutic strategy is exhibited by the fact that over \$5 billion was spent on antibody-based antagonists in the US in 2005 (Arkin and Wells, 2004). However, there are a number of problems associated with the use of antibodies to inhibit PPIs; antibodies are not orally bioavailable, there are difficulties in their manufacture and they are not cell-permeable, so, intracellular PPI inhibition has been limited to antisense therapies (Arkin and Wells, 2004).

On the other hand, if suitably designed, small 'drug-like' organic molecules can be administered orally and are able to cross the blood-brain barrier c.f. therapeutic

antibodies which are not capable of brain penetration. Thus, the disruption of PPI by a small organic molecule is currently of great therapeutic interest and importance (Toogood, 2002, Fry, 2006); however, the characteristics of the PPI interface mean that achieving this target presents a huge challenge, as the PPI interface is:

- Usually vast, between 750 and 1500Å² for each protein involved in the interaction (Wells and McClendon, 2007).
- Generally flat and often lacks the grooves/pockets of typical proteins that bind small molecules (Wells and McClendon, 2007).
- The binding regions are often non-contiguous and cannot be mimicked by a simple synthetic molecule (Wells and McClendon, 2007).

Fortunately, however, it has been previously shown that it is often a subset of residues in the PPI interface that contribute most of the free energy to binding affinity (Clackson and Wells, 1995); this region of the interface is usually referred to as the 'hotspot' (Figure 1.1) and these 'hotspots' have been found to bind to both short peptide sequences and small organic molecules (Moreira et al., 2007). Therefore, the actual interface targeted in the drug discovery process by the small molecule is greatly reduced and so, disruption of PPI by small molecules has become a viable research target (Yin and Hamilton, 2005).

Synapses of the central nervous system (CNS) are an example of a region in living organisms where the interaction between proteins is of vital importance to normal function; the synaptic system is discussed next.

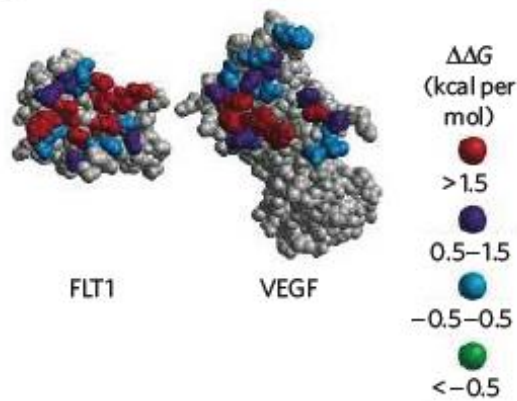


Figure 1.1: The protein-protein interface between FLT1 and the vascular endothelial growth factor (VEGF). Alanine-scanning mutational analysis was performed and the figure shows the resultant change in binding free energy ($\Delta\Delta G$) compared to the wild-type protein. It can be seen that most of the free energy is contributed by a small number of residues (red); these residues of the respective protein are known as the 'hotspots.' Image taken and adapted from (Wells and McClendon, 2007).

1.2 Synapses

Synapses are functional connections between two excitable cells (or neurons) in the mammalian central nervous and circulatory systems; they allow information to be passed from one cell to the other with precision and speed (Cowan et al., 2001). Transmission of a signal at a synapse can occur via direct propagation of an electrical stimulant (electrical synapse) or via a chemical intermediate known as a neurotransmitter (chemical synapse). The subsequent description relating to synapses will refer mainly to a chemical synapse, referred to as synapse(s) for simplicity from now on (Cowan et al., 2001).

Synapses are specialised junctions that consist of a pre-synaptic membrane with a post-synaptic membrane opposite, separated by a synaptic cleft (Figure 1.2) (Montgomery et al., 2004). Immediately behind the postsynaptic membrane is a protein dense region known as the postsynaptic density (PSD) (Ziff, 1997); this region contains numerous interlinking scaffold proteins, neurotransmitter receptors/ion channels and signalling molecules (Figure 1.2) (Montgomery et al., 2004, Cowan et al., 2001). The strength of a synapse is dependent on the number of ion channels/receptors present, with previous research indicating that the number of

synaptic components present can vary according to synaptic activity/demands (Ziff, 1997).

The localisation and transport of neurotransmitter receptors and ion channels to/from the synapse occurs via PPIs involving a family of scaffold proteins called the postsynaptic density membrane-associated guanylate kinases (PSD-MAGUKs) (Kennedy, 1997, Chen et al., 2007a).

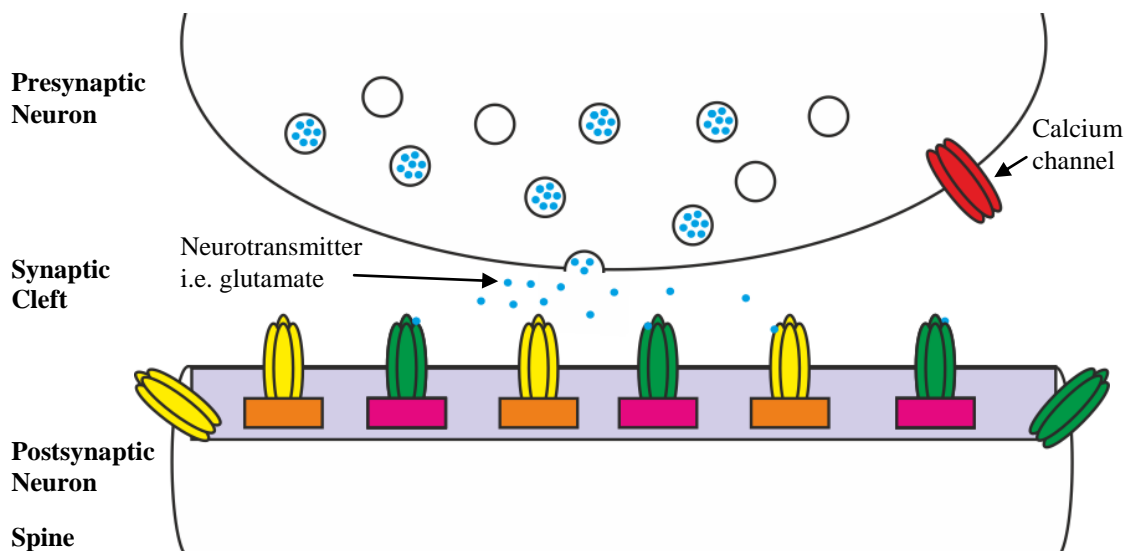


Figure 1.2: A simplified version of the structure of a chemical synapse based on a figure in (Genoux and Montgomery, 2007). The figure shows how the synapse consists of presynaptic and postsynaptic neurons separated by the synaptic cleft; the protein rich postsynaptic density region (PSD, purple) of the postsynaptic neuron containing the neurotransmitter receptors (AMPA and NMDAR [1.5], yellow and green respectively) and scaffold proteins (PSD-95 and SAP97, magenta and orange respectively [1.5]) has been identified. The transfer of a signal across the chemical synapse shown here occurs via a neurotransmitter chemical intermediate, glutamate in this instance; after the vesicle containing the glutamate fuses with the presynaptic membrane, it travels across the synaptic cleft and interacts with the desired receptor.

1.3 Post-Synaptic Density Membrane-Associated Guanylate Kinases

Postsynaptic density membrane-associated guanylate kinases (PSD-MAGUKs) predominantly function as organisers of neurotransmitter receptors/receptor-associated signalling proteins at synapses; this organisation is achieved through the formation of PPIs (Gardoni et al., 2009). PSD-MAGUKs are usually localised to the PSD of synapses in the central nervous and circulatory systems; although they have been found in alternative locations (Cai et al., 2002, DeGiorgis et al., 2006). The

most extensively studied PSD-MAGUKs are a subset known as the DLG (*Drosophila* tumour suppressor gene) family.

The DLG subfamily of the PSD-MAGUKs are an example of a family of proteins that contain numerous different protein interaction domains (Figure 1.3); they comprise of three N-terminal PDZ domains, an L₂₇ domain, an src homology 3 (SH₃) domain and an inactive C-terminal guanylate kinase domain (GUK) (Cousins et al., 2008); all of which are possible sites of PPIs (Montgomery et al., 2004). Previous research has shown that the important DLG – receptor interaction in the receptor localisation/transfer processes is between one of the PDZ domains of the particular DLG protein and the extreme C-terminus of the specific binding partner protein (Cai et al., 2002, Blazer and Neubig, 2009).

PDZ domains are an example of a protein-protein interaction interface where research has shown that most of the free energy of binding is due to a selection of a few residues contained within PDZ domain i.e. they contain the ‘hotspot’ regions described in [1.1]; thus, PDZ domains and the interactions they mediate have been deemed a suitable target for therapeutic intervention.

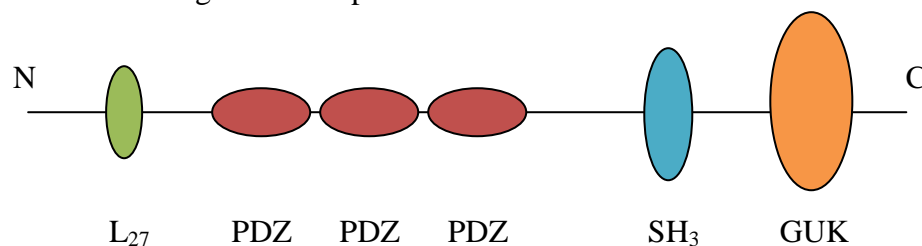


Figure 1.3: An overview of the generic structure of the DLG subfamily of postsynaptic density membrane-associated guanylate kinases (PSD-MAGUKs); the DLG family are an example of a family of proteins that contain numerous different protein-protein interaction domains. It can be seen that all proteins in the family contain three different PDZ domains, an L₂₇ domain, an src homology 3 (SH₃) domain and an inactive C-terminal guanylate kinase (GUK).

1.4 PDZ Domains

A PDZ domain is a small, ~ 90 amino acid residue region of a protein that acts as a protein-protein interaction module. The name ‘PDZ domain’ is an acronym of the first three proteins that were found to share the domain: PSD-95 (postsynaptic

density-95 protein), **Dlg** (*Drosophila* disc large tumour suppressor) and **ZO-1** (zona occludens-1). The predominant function of a PDZ domain is the recognition and binding of C-terminal motifs in partner proteins (Harris and Lim, 2001, Arkin and Wells, 2004).

A PDZ domain consists of six β -strands (β A- β F) and two α -helices (α A and α B), which fold into a six stranded β -sandwich (Figure 1.4a) (Garner et al., 2000). The binding region of PDZ domains consist of a hydrophobic pocket formed by the GLGF motif (red, Figure 1.4b) and hydrophobic residues (blue, Figure 1.4b) and an extended groove between the β B strand and α B helix. PDZ ligands bind to the PDZ domain via a mechanism known as β -strand addition, with the PDZ ligand effectively forming an extra anti-parallel β -strand (Figure 1.4c) (Dev, 2004).

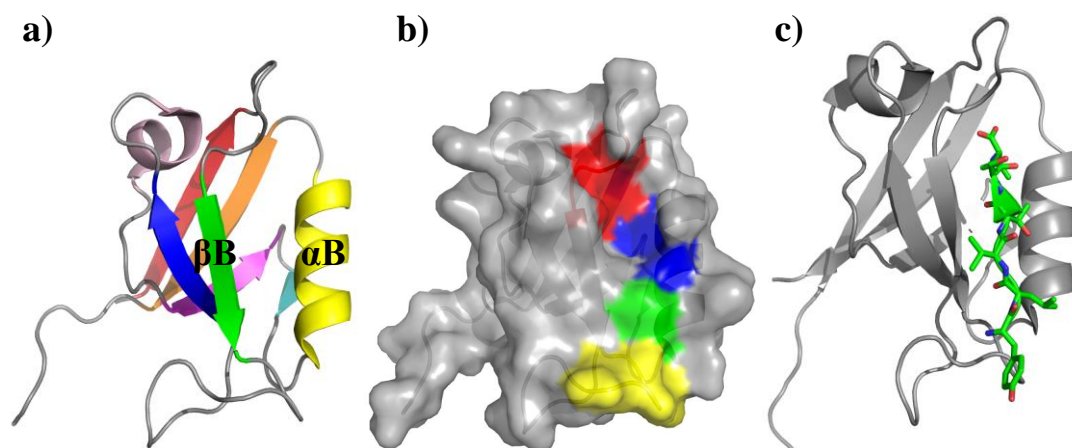


Figure 1.4: a & b) The crystal structure of the Scrib1 PDZ1 domain (PDB ID = 2W4F). a) The protein in a cartoon representation; the six β -strands and two α -helices that comprise a conventional PDZ domain structure can be seen. b) A surface representation of the protein that highlights the hydrophobic pocket and extended groove of the PDZ domain binding region; the GLGF motif (red), hydrophobic pocket (blue), conserved His (green) and β B – β C loop (yellow) residues have been highlighted. c) The crystal structure of the SAP97 PDZ2 – APC complex (PDB ID = 4G69) with the PDZ domain in a cartoon representation and the PDZ ligand represented as both sticks and a cartoon; the PDZ ligand is shown to bind in the typical manner between the β B strand and α B helix and effectively forms an extra anti-parallel β -strand.

The key PDZ binding motif is thought to rely on the three or four C-terminal residues, where the C-terminus residue of a PDZ domain ligand is conventionally labelled '0' and the adjacent residues then labelled with increasingly negative values as the distance from the C-terminus increases (Kurakin et al., 2007). PDZ domains

are conventionally divided into one of three different classes depending on the specific C-terminal sequence of their target partner protein(s); there are a few PDZ domains that do not fall into any of these classes and so, remain unclassified, i.e. the Dishevelled PDZ domain (Lee et al., 2009b). Class I PDZ domains recognise the extreme four C-terminal residue sequence X-S/T-X- Φ * (where X = any amino acid, Φ = hydrophobic amino acid and * represents the C-terminus). The S/T residue forms an important hydrogen bond to the His residue (green, Figure 1.4b) contained within the α B helix of the PDZ domain (Ponting et al., 1997, Cai et al., 2002); this interaction is known to be important, as if the S/T site becomes phosphorylated, then binding of the ligand to the PDZ domain does not occur in some examples (Cai et al., 2002). Class II PDZ domains associate with ligands with the C-terminal sequence X- Φ -X- Φ * and class III domains interact with the sequence X-X-C* (Harris and Lim, 2001).

The -1 and -3 residues of the PDZ domain ligand are thought to be involved in determining the particular PDZ domain binding specificity of the respective protein (Fujii et al., 2003); although recent research has indicated that residues further 'downstream' of the conventional four C-terminal residues may contribute towards affinity and specificity (yellow, Figure 1.4b) (Zhang et al., 2007).

There are currently 267 PDZ domain-containing proteins that have been identified in the human genome (Bouzidi et al., 2013); arguably the two most well-studied and important PDZ proteins are members of the previously described DLG subfamily of the PSD-MAGUKs: the postsynaptic density-95 protein (PSD-95) and the synapse-associated protein-97 (SAP97) (Tao and Raja, 2004, Schlueter et al., 2006).

1.5 PDZ Proteins: PSD-95 and SAP97

1.5.1 PDZ Domain Comparison

As PSD-95 and SAP97 are both members of the DLG subfamily of PSD-MAGUKs they both contain three different PDZ domains, with the overall sequence similarity of the six PDZ in total domains being 27.59% (Figure 1.5a); the sequence similarity of the respective PSD-95 and SAP97 PDZ1, PDZ2 and PDZ3 domains was found to be 90.81%, 88.51% and 86.42% respectively. Phylogenetic analysis of the different PDZ domains of the PSD-95 and SAP97 gives an insight into the evolutionary relationship of the individual PDZ domains. From the phylogenetic tree, it can be seen that the PDZ3 domains of PSD-95 and SAP97 do not share the same common ancestor as the PDZ1 & 2 domains. The tree also indicates that the respective PDZ1 domains were the last of the three different pairs of PDZ domains to diverge in their evolutionary history; this would account for the fact that they are the respective PDZ domain pair that showed the greatest sequence similarity (Figure 1.5b).

There has been a wide range of research performed on the PDZ domains of the PSD-95/SAP97 proteins and the interactions that they mediate; this has yielded some important and interesting information about the PDZ proteins PSD-95 and SAP97.



Figure 1.5: a) The sequence alignment (produced using www.uniprot.org) of the three different PDZ domains of the PSD-95 and SAP97 proteins. The overall sequence similarity of the six PDZ domains was 27.59%, with the sequence similarity of the respective PDZ1, PDZ2 and PDZ3 domains found to be 90.81%, 88.51% and 86.42% respectively. b) The phylogenetic tree (produced using www.uniprot.org) of the six different PDZ domains indicated that the PSD-95 and SAP97 PDZ3 domains do not share the same common ancestor as the PDZ1 & 2 domains. The tree also indicates that the order of evolutionary divergence of the respective PDZ domain pairs (from earliest to the latest) was PDZ3, PDZ2, PDZ1; this explains the trend in sequence similarity between the respective PDZ domains observed.

1.5.2 PSD-95

1.5.2.1 General Overview

PSD-95 was originally identified as a protein with a molecular weight of 90 – 95kDa that was highly homologous to the product of the *Drosophila* discs-large tumour suppressor gene (Dlg), during studies to identify synaptic components (Cho et al., 1992, Kistner et al., 1993). As a result, PSD-95 can also be found referred to in the literature as synapse-associated protein-90 (SAP90) and discs-large homolog-4 (Dlg4) (Hata and Takai, 1999); PSD-95 is almost exclusively found localised to the PSD of neuron synapses. Solution state NMR spectroscopy and X-ray crystallography have been utilised independently to determine the structure of the individual PSD-95 PDZ1 (Piserchio et al., 2002, Long et al., 2003), PDZ2 (Tochio et al., 2000) and PDZ3 domains (Doyle et al., 1996, Camara-Artigas et al., 2010); the

structure of the PSD-95 PDZ1 & 2 tandem domain has also been produced by these methods (Sainlos et al., 2011, Bach et al., 2012).

The role of the PSD-95 PDZ domain-mediated interactions in glutamate receptor localisation and trafficking is discussed further in [1.5.4]; however, a number of other important PSD-95 PDZ-mediated interactions have been identified by previous research studies.

1.5.2.2 PSD-95 PDZ-Mediated Interactions

There have been a variety of different proteins found to interact with at least one of the PDZ domains of PSD-95; the majority of these proteins are summarised (Table 1.1), with the respective PSD-95 PDZ domain(s) they interact with indicated. A PSD-95 PDZ domain-mediated interaction that is of particular relevance to the research described in this thesis is the PSD-95 PDZ – 5-hydroxytryptamine receptor interaction.

5-Hydroxytryptamine (5-HT, Figure 1.6a), also known in the literature as serotonin, and its corresponding 5-hydroxytryptamine receptors (5-HT_x) are found to have biological relevance in virtually all major organ systems (Berger et al., 2009). The 5-HT/5-HT_x system has been shown to have a role in essentially every major central nervous system (CNS) function (Roth, 1994); the system is also responsible for regulating a large number of diverse physiological processes such as platelet aggregation and gastrointestinal motility (Berger et al., 2009, Roth, 2011).

There are currently 15 distinct 5-HT_x identified in humans and these are divided into seven families (5-HT₁₋₇) (Gavarini et al., 2004); all the 5-HT_x are members of the G-protein coupled receptor super-family with the exception of 5-HT₃, which is a ligand-gated channel (Bockaert et al., 2006). A number of the interactions of the 5-HT_x have been studied previously (Figure 1.6b) (Marin et al., 2012, Wacker et al.,

2013) and it has been shown that there are physiologically relevant interactions between members of the 5-HT_{2x} family and the PSD-95 PDZ domains (Backstrom et al., 2000, Becamel et al., 2002, Xia et al., 2003, Becamel et al., 2004, Bockaert et al., 2006, Allen et al., 2008, Abbas et al., 2009, Pichon et al., 2010, Anastasio et al., 2010); the 5-HT_{2x} family interact with the PSD-95 PDZ domains via a conserved class I C-terminal PDZ binding motif.

Table 1.1: The different proteins that exhibit PSD-95 PDZ domain-mediated binding; the specific PSD-95 PDZ domain – protein interactions are indicated by a Y (= Yes), along with the corresponding reference.

Protein	PDZ1	PDZ2	PDZ1&2	PDZ3	Reference(s)
5-HT _{2a}			Y		(Xia et al., 2003)
5-HT _{2c}			Y		(Becamel et al., 2002)
β ₁ -AR			Y		(Kreienkamp, 2002)
Citron		Y		Y	(Lim et al., 2002)
CRIP1				Y	(Niethammer et al., 1998)
Cypin			Y		(Firestein et al., 1999)
DHHC5				Y	(Li et al., 2010)
Fz1,2,4&7	Y	Y	Y		(Hering and Sheng, 2002)
K _{ir} 2.1/2.3		Y	Y		(Cohen et al., 1996, Pegan et al., 2007)
Kv1.4	Y	Y	Y		(Imamura et al., 2002)
nNOS		Y	Y		(Brenman et al., 1996)
NR2A-D	Y	Y	Y		(Hata and Takai, 1999)
Sema4c/f					(Burkhardt et al., 2005)
Slo2	Y				(Uchino et al., 2003)
SSTR1&4	Y	Y			(Christenn et al., 2007)

There are three members of the 5-HT_{2x} family; 5-HT_{2a}, 5-HT_{2b} and 5-HT_{2c} with 5-HT_{2a} and 5-HT_{2c} being widely distributed in the CNS, whereas 5-HT_{2b} localisation in the CNS is sparse (Bockaert et al., 2006). 5-HT_{2a} and 5-HT_{2c} share about 50% sequence similarity, with 5-HT_{2a} being predominantly found in brain regions such as the hippocampus, cerebral cortex and spinal cord. 5-HT_{2a} can also be expressed in several peripheral tissues i.e. smooth and skeletal muscle, kidney, liver and platelets; 5-HT_{2c} are exclusively located in the brain regions such as the cerebral cortex and striatum (Marin et al., 2012). 5-HT_{2a} and 5-HT_{2c} have been shown to interact with

the PSD-95 PDZ domains (Becamel et al., 2004), whereas 5-HT_{2b} has been found to bind to MUPP1 PDZ10 domain (Becamel et al., 2001).

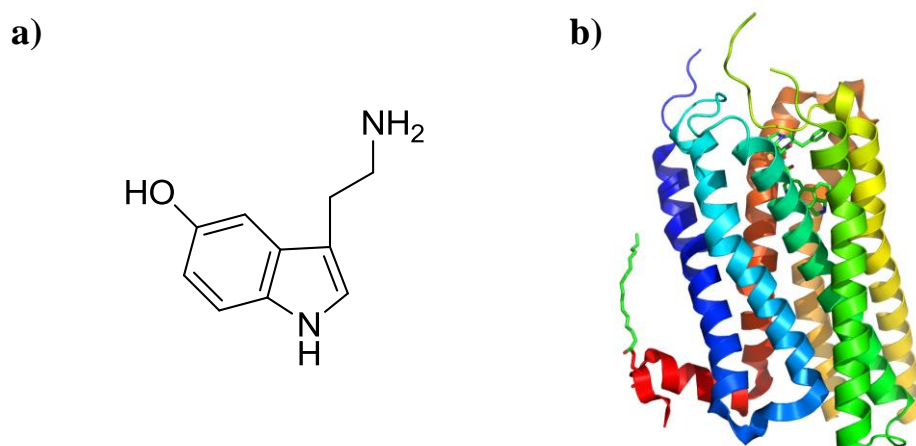


Figure 1.6: a) The chemical structure of the neurotransmitter 5-hydroxytryptamine (serotonin), the agonist of the 5-hydroxytryptamine receptor family. b) The crystal structure of the complex formed between the 5-HT_{2b} receptor (shown in a cartoon representation) and the alkaloid, ergotamine (represented as sticks); this is an example of previous research into the interactions of 5-hydroxytryptamine receptor family (PDB ID = 4IB4 (Wacker et al., 2013)).

The interaction between the PSD-95 PDZ domains and 5-HT_{2a} enhances 5-HT_{2a} receptor-mediated signal transduction by inhibition of agonist-induced receptor internalisation (Xia et al., 2003); the interaction has also been shown to be essential for somatodendritic targeting of 5-HT_{2a} *in vitro* and *in vivo* (Xia et al., 2003, Abbas et al., 2009). However, the PDZ domain-mediated interaction between PSD-95 and 5-HT_{2a} has been shown to contribute to induced analgesia in painful diabetic neuropathy (Roth, 2011); this is because inhibition of the interaction resulted in reduced hyperalgesia in neuropathic pain (Pichon et al., 2010).

The interaction between the PSD-95 PDZ domains and 5-HT_{2c} is important in the regulation, expression, synaptic localisation and organisation of 5-HT_{2c} (Becamel et al., 2002, Anastasio et al., 2010). The PSD-95 PDZ – 5-HT_{2c} interaction has also been found to increase desensitisation of the 5-HT_{2c} receptor Ca²⁺ response, as well as constitutive and agonist-induced receptor internalisation (Backstrom et al., 2000, Gavarini et al., 2006).

1.5.3 SAP97

1.5.3.1 General Overview

SAP97 was identified as the human homologue of the *Drosophila* discs-large tumour suppressor protein, with a molecular weight of 97kDa; this has resulted in SAP97 being referred to in the literature as humanDlg (hDlg) (Lue et al., 1994, Muller et al., 1995). Unlike PSD-95, SAP97 is ubiquitously expressed and has been isolated from the synapses and axons of the CNS, as well as the basal lateral membrane of epithelial cells and the cytoplasmic surface between adjacent cells in cultured T84 cells (Muller et al., 1995). As with PSD-95, solution state NMR spectroscopy and X-ray crystallography have been utilised independently to determine the structure of the individual SAP97 PDZ1 (Wang et al., 2005), PDZ2 (von Ossowski et al., 2006, Haq et al., 2010) and PDZ3 domains (Cabral et al., 1996).

The role of the SAP97 PDZ domain-mediated interactions in glutamate receptor localisation and trafficking is discussed further in [1.5.4]; however, a number of other important SAP97 PDZ-mediated interactions have been identified by previous research studies.

1.5.3.2 SAP97 PDZ-Mediated Interactions

There have been a variety of different proteins found to interact with at least one of the PDZ domains of SAP97; almost all of these proteins have been summarised (Table 1.2), with the respective PDZ domain(s) they interact with indicated. A SAP97 PDZ domain-mediated interaction that is of particular relevance to the research described in this thesis is the SAP97 PDZ – human papillomavirus E6 protein interaction.

The human papillomavirus (HPV) is a virus from the papillomavirus family that is capable of infecting humans; papillomaviruses are small, double stranded DNA

viruses that can induce hyperproliferative lesions in both mucosal and cutaneous epithelial tissue (Liu et al., 2007, Zhang et al., 2007). HPVs have been strongly associated with the development of both benign and malignant lesions; they have been found to promote cervical cancer in over 95% of cases (Munoz et al., 2003). There are over 60 different HPVs and these are commonly divided into two distinct groups depending on their clinical associations (Werness et al., 1990, Scheffner et al., 1990); HPVs are classified as either 'low risk' or 'high risk.'

Low risk HPV types, such as HPV6 and HPV11, are generally associated with benign proliferative lesions that infrequently progress to malignancy; high risk HPV types such as HPV16 and HPV18 are associated with malignant lesions (Chi et al., 2011). The oncogenic potential of high risk HPV types such as HPV16 and HPV18 (HPV16/18) is due to their ability to encode two oncoproteins, E6 and E7 (Kiyono et al., 1997). Research has shown that the open reading frames (ORFs) of the E6 and E7 proteins produced by high risk HPVs have been found intact and actively transcribed in cervical carcinomas and derived cell lines (Schwarz et al., 1985); this is further evidence of the causal factor of high risk HPVs in associated cancers. The HPV E6 protein has previously been shown to play an active role in the development and pathogenesis of several types of cancer such as cervical, head and neck (Syrjanen, 2005, Marur et al., 2010).

Extensive studies have indicated that this pathogenesis of high risk HPVs is achieved via the E6-mediated degradation of p53 tumour-suppressor protein, which prevents the cell apoptosis associated with viral infection and leads to uncontrolled cell growth. However, research has also shown evidence of p53-independent functions of E6 that are important and necessary for transformation; one such example is the binding of E6 to PDZ domain-containing tumour suppressor proteins such as SAP97,

hScrib, MUPP1 and MAGI, via a conserved C-terminal binding motif (Zhang et al., 2007). In epithelial cells of vertebrates, SAP97 is associated with the adherens junction (AJ), which is responsible for cell-cell contacts; the PDZ domain-mediated interaction of E6 targets SAP97 for degradation (as with p53), which decreases the phosphorylation of E-cadherin by protein kinase CK2 and this induced down-regulation is a common event in carcinogenesis. Interestingly, research has shown E6 mutants that are incapable of SAP97 PDZ domain binding are no longer able to induce E6-dependent transformation of rodent cells; this indicates that the SAP97 PDZ – HPV E6 interaction is an underlying mechanism in the development of cancers (Figure 1.7) (Kiyono et al., 1997).

The HPV16 and HPV 18 E6 oncoproteins have been shown to bind to all three PDZ domains of SAP97 (Chi et al., 2011); with the NMR solution state structures of the SAP97 PDZ2 – HPV18 E6 (Liu et al., 2007, Zhang et al., 2007) and SAP97 PDZ3 – HPV18 E6 (Zhang et al., 2007) being determined previously.

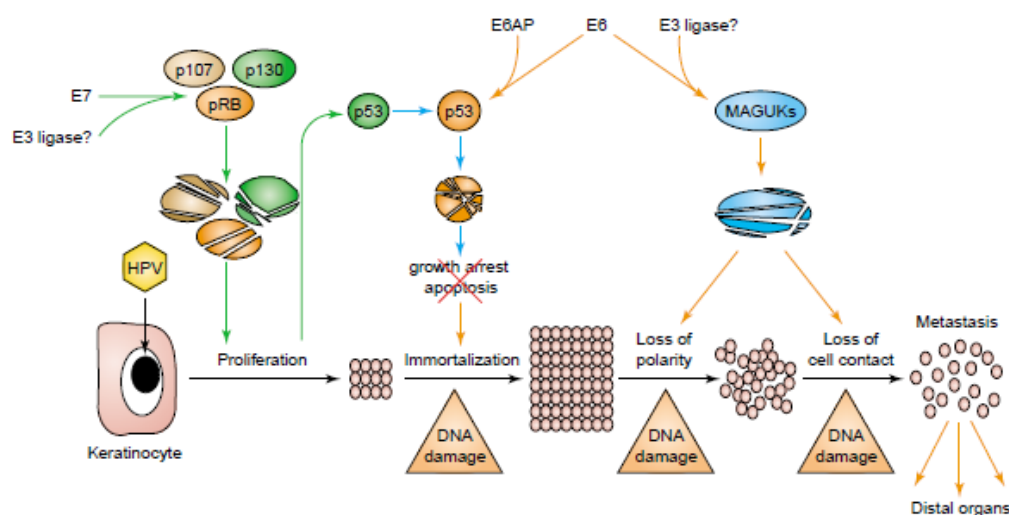


Figure 1.7: The effect of the two oncoproteins (E6 & E7) produced by high risk human papillomavirus (HPV) types on the malignant transformation of cells is characterised by targeting of substrates for degradation. The HPV infects keratinocytes that have exited the cell cycle, E7 interacts with proteasome machinery which results in cell proliferation; this proliferation results in a p53-mediated response that is targeted by the E6-E6AP (E6 associated protein) complex. The p53-independent process of MAGUK degradation (i.e. SAP97) occurs late on in the malignancy, which contributes to the subsequent metastasis. Image taken from (Banks et al., 2003).

Table 1.2: The different proteins that exhibit binding to the SAP97 PDZ domains; the specific SAP97 PDZ domain – protein interactions are indicated by a Y (= Yes), along with the corresponding reference.

Protein	PDZ1	PDZ2	PDZ3	ND^a	Reference(s)
AKAP79				Y	(Gardner et al., 2007)
APC	Y	Y			(Zhang et al., 2011b)
β 1-AR				Y	(Gardner et al., 2007)
Fz4&7	Y	Y			(Hering and Sheng, 2002)
GluR1		Y			(von Ossowski et al., 2006)
HPV16 E6	Y	Y	Y		(Chi et al., 2011)
HPV18 E6	Y	Y	Y		(Liu et al., 2007)
HTLV1 Tax				Y	(Lee et al., 1997)
Kv1.5				Y	(Godreau et al., 2003)
K _{ir} 2.1	Y	Y			(Pegan et al., 2007, Goult et al., 2007)
K _{ir} 2.2		Y			(Leonoudakis et al., 2001)
NR2A/B	Y	Y			(Gardoni et al., 2003, Wang et al., 2005)
TACE				Y	(Peiretti et al., 2003)

^a ND = Not determined.

1.5.4 Roles of PSD-95 and SAP97 in LTD, LTP and Synaptic Plasticity

As discussed previously [1.2-4], PSD-95 and SAP97 are PSD-MAGUKs and therefore, are involved in the functional localisation and trafficking of receptors in the PSD, via PDZ domain-mediated interactions. PSD-95 has been shown to predominantly interact with the N-methyl-D-aspartate receptors (NMDARs) (El-Hussein et al., 2000, Cui et al., 2007), whereas the most prominent PDZ domain-mediated receptor interaction of SAP97 is with the α -amino-3-hydroxy-5-methyl-4-isoxazolepropionic acid receptors (AMPA) (Waites et al., 2009a, Howard et al., 2010); research has shown the presence of PSD-95 – AMPAR and SAP97 – NMDAR interactions also (Xu et al., 2008, Li et al., 2011, Marcello et al., 2012, Opazo et al., 2012).

NMDARs/AMPA receptors belong to the glutamate subset of the ionotropic neurotransmitter receptor family and so, share some structural similarities. NMDARs are glutamate- and glycine-gated cation channels that are formed by the heterotetrameric assembly of subunits belonging to three classes: NR1, NR2A-D and

NR3A/B (Figure 1.8) (Gottschalk et al., 2009). Two NR1 subunits are a compulsory component of NMDARs, along with two of the other subunits; NR2A and NR2B are the primary other subunits in most central neurons. The NR1 subunit has been found to bind glycine, whereas the NR2 subunit binds glutamate; the NR2 subunit also contains a C-terminal class I PDZ domain binding motif and so, it is this subunit that participates in the PDZ domain-mediated interactions with PSD-95/SAP97 (Sheng and Sala, 2001).

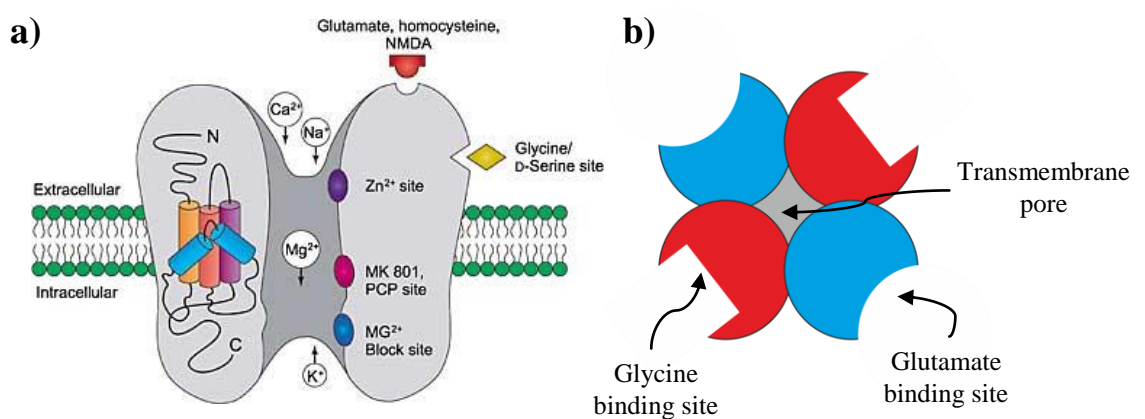


Figure 1.8: A simplistic overview of the structure of the N-methyl-D-aspartate receptors (NMDARs). a) A front-on perspective showing an individual NRX subunit, along with the different binding sites of various ions/chemicals and the different ions the NMDAR is responsible for transporting. b) A plan view illustrating the tetrameric structure forming a transmembrane pore; the NR1 (red) glycine and NR2 (blue) glutamate binding sites are shown. Image a) taken from <http://sunburst.usd.edu/>.

AMPA receptors (AMPAARs) comprise of four closely related subunits GluR1-4, each of which consists of four transmembrane domains (Figure 1.9a) and these subunits combine in different stoichiometries to form a tetramer ion channel (Figure 1.9b); these tetrameric channels usually consist of a pair of subunit dimers (Shepherd and Huganir, 2007). The GluR1 subunit contains a C-terminal class I PDZ domain binding motif and so, it is this subunit that participates in the PDZ domain-mediated interactions with PSD-95/SAP97 (Sheng and Sala, 2001).

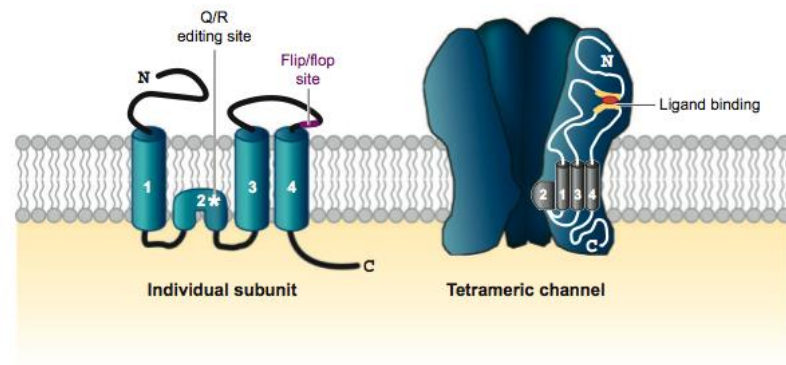


Figure 1.9: A simplistic overview of the structure of the α -amino-3-hydroxy-5-methyl-4-isoxazolepropionic acid receptors (AMPA receptors). a) A front-on perspective showing an individual GluRX subunit. b) A front-on perspective illustrating how the tetrameric structure of individual subunits forms a transmembrane pore. Image taken from (Shepherd and Huganir, 2007).

Research has shown that the PDZ domain-mediated association of PSD-95 and SAP97 with the C-termini of the NMDARs/AMPA receptors occurs via the PDZ1 and PDZ2 domains of the PDZ proteins (Wang et al., 2005, Marcello et al., 2012); the solution state NMR structures of SAP97 PDZ2 bound independently to NR2B (Wang et al., 2005) and GluR1 (von Ossowski et al., 2006) have been previously determined. The PDZ domain mediated-interaction between PSD-95/SAP97 and the NMDARs/AMPA receptors are vital in facilitating the role of PSD-95/SAP97 in the localisation of the NMDARs/AMPA receptors at the postsynaptic membrane and their transport to/from the membrane; therefore, PSD-95 and SAP97 are believed to have an important role in synaptic plasticity (Craven and Brecht, 1998).

Synaptic plasticity is defined as the ability of a synapse to change in strength and it is the most important foundation in learning and memory storage within the brain (Montgomery et al., 2004). Two of the key processes underlying synaptic plasticity are long-term potentiation (LTP) and long-term depression (LTD) (Shepherd and Huganir, 2007); these processes act by causing changes in the efficacy of synaptic connections via the addition or removal of receptors to/from the postsynaptic membrane (Montgomery et al., 2004).

LTP is an activity-dependent enhancement in synaptic transmission, this is usually induced by brief high frequency stimulation and is long lasting (more than 1 hour) (Shepherd and Huganirl, 2007); LTP is widely believed to be a key cellular mechanism in learning and long-term memory (Waites et al., 2009b). NMDARs are postulated to function as a cellular trigger for the phosphorylation of the AMPAR GluR1 subunit by CAMKII (Lau and Zukin, 2007); this facilitates AMPAR insertion into the PSD or directly at the synapse, this process is known as exocytosis (Figure 1.10a).

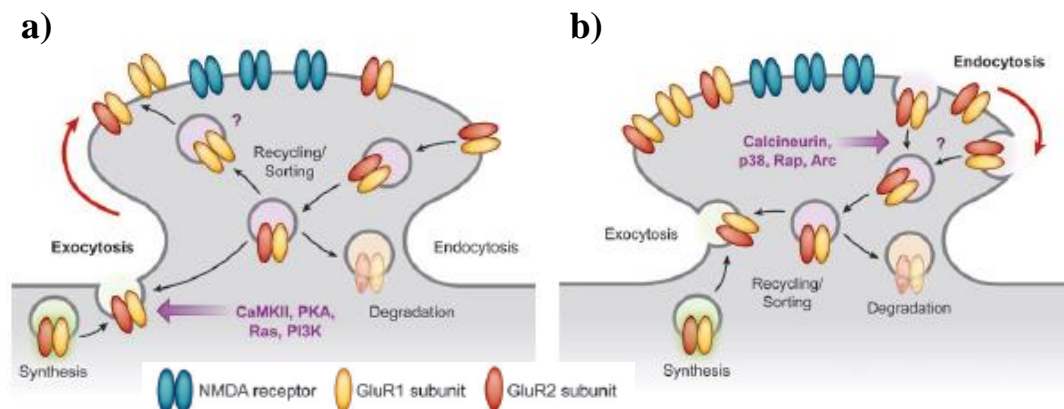


Figure 1.10: Two of the key processes underlying synaptic plasticity: long-term potentiation (LTP) and long-term depression (LTD). a) An overview of the exocytosis on-going during LTP; AMPAR insertion due to phosphorylation by NMDAR-mediated CaMKII activity occurs either directly at the synapse or at extrasynaptic sites and subsequent diffusion into the synapse (red arrow). b) An overview of the endocytosis occurring during LTD; AMPARs are either recycled or degraded. Image taken from (Shepherd and Huganirl, 2007).

LTD is a long-lasting suppression of synaptic strength and is typically dependent on NMDAR-activated dephosphorylation of the GluR1 AMPAR subunit (Xu et al., 2008); this allows retrieval of the AMPARs from synaptic sites and causes the AMPARs to diffuse out of the PSD, via endocytosis (Figure 1.10b) (Shepherd and Huganirl, 2007, Lau and Zukin, 2007). LTD is widely believed to be an important means of information storage in the brain and is implicated in the process of removing old memories.

The research to-date on the interaction between the PSD-MAGUKs PSD-95/SAP97 and the glutamate receptors NMDAR/AMPA suggests that this is an important and

beneficial set of PDZ domain-mediated interactions. However, there is evidence to suggest that the PDZ domain-mediated interaction between PSD-95 and NMDAR is a potential therapeutic target in the treatment of stroke (Aarts et al., 2002, Cook et al., 2012) and chronic pain (Florio et al., 2009, LeBlanc et al., 2010); this is discussed further in [1.6].

1.5.5 Summary

The brief summary of the PSD-95/SAP97 PDZ-mediated interaction research detailed in sections [1.5.1 – 1.5.4], along with other examples found in the literature, indicates that inhibition of PSD-95 and/or SAP97 PDZ domain-mediated interactions are valid therapeutic research topics. This would be also be a novel way of elucidating the exact role of the PDZ proteins in different cellular processes and hence, controlling signal cascades in complex diseases (Dev, 2004).

1.6 Previous PDZ Domain Inhibition Research

The PDZ domain/PDZ domain-mediated interaction inhibitor research to-date has produced different chemical classes of inhibitor, with varying strategies employed in the development process. A comprehensive collection of PDZ domain inhibition research-to-date is given in this section; this has been subdivided into depending on the chemical nature of the particular PDZ domain inhibitor.

1.6.1 Peptides

The use of PDZ domain inhibitory peptides derived from the C-terminus of the respective native PDZ domain ligand has been applied to different PDZ-mediated interactions; one such example is the three successive investigations by Tymianski's research group. This process involved the attempted inhibition of the interaction between the PSD-95 PDZ1/2 domains and the NMDA receptor subunit 2B (NR2B), by a peptide. The researchers believed that by inhibiting PSD-95 and hence,

uncoupling PSD-95 from neurotoxic signalling pathways, it was possible to treat, minimise or even prevent stroke damage without blocking synaptic activity or calcium influx.

The investigations utilised a 20 residue cell permeable peptide (Tat–NR2B9c) that consisted of the nine C-terminal residues of the NR2B subunit (KLSSIESDV) was fused to the 11-mer HIV-1 Tat protein (YGRKKRRQRRR). The effects of Tat–NR2B9c on stroke damage was assessed in rat brain (Aarts et al., 2002, Sun et al., 2008) and subsequently in gyrencephalic primate brain (Cook et al., 2012). In both mammals, it was established that stroke damage can be prevented by administration of a peptide inhibitor of the PSD-95 PDZ domain after stroke onset; efforts are now being made to translate these findings to humans.

Inhibition of Wnt signalling by a peptide inhibitor of the Dishevelled (Dvl) PDZ domain has been achieved (Zhang et al., 2009); this is favourable as Dvl regulates Wnt signalling pathways, many of which have been implicated in cancer progression. The inhibitory peptide development procedure involved a combination of peptide-phage display and shotgun alanine scanning; this process resulted in four peptides with low micromolar affinity. The inhibitory peptide developed (pen-N3, $K_D = 4.6\mu\text{M}$) consisted of an internal peptide (EIVLWSDIP), with an antennapedia sequence and a 5-carboxyfluorescein fluorophore fused to the N-terminus; this enabled internalisation and visualisation in cells respectively (Derossi et al., 1998). The results obtained demonstrated that pen-N3 inhibited Wnt/ β -catenin signalling in a specific and dose-dependent manner, upstream of β -catenin; thus, Dvl PDZ domain inhibition may be a viable therapeutic target for Wnt signalling in cancers that are dependent on Dvl function. In related research, a tripeptide (VWV) developed by a combination of NMR spectroscopy and computational methods has been shown to

bind to the Dvl PDZ domain with low micromolar affinity ($K_D = 2\mu\text{M}$) (Lee et al., 2009a); the effects of the tripeptide on Wnt were, however, not explored *in vivo*.

There are a number of other examples of peptides being utilised to inhibit PDZ domain-mediated interactions in the literature, these involve peptide inhibitors of the PSD-95 (Sharma et al., 2009), GIPC (Muders et al., 2009) and CAL PDZ-mediated interactions (Roberts et al., 2012).

A related area of PDZ domain inhibition research by peptides is the development of bivalent peptides, which are peptides that have been designed bind to two PDZ domains at the same time; these can either be adjacent to each other on the same protein or target the same PDZ domain on two separate protein molecules. The binding of bivalent peptides to PDZ domains has reported an increase in binding affinity of up to 1000-fold compared with the corresponding monomeric ligand (Bach et al., 2012).

An important example of this PDZ domain inhibition research area is the high affinity, dimeric inhibitor of the PSD-95 PDZ1/2 domains (Bach et al., 2012); the reasons for targeting the PSD-95 PDZ1/2 - NMDAR interaction for inhibition have been previously discussed. The dimeric inhibitor (Tat-N-dimer, Figure 1.11a) of the PSD-95 PDZ1/2 domains was developed from the group's previous monomeric and dimeric inhibitor research (Bach et al., 2008, Bach et al., 2009). The Tat-N-dimer bivalent peptide consisted of two pentapeptides (IETDV) linked by a chemically modified PEG-based linker (NPEG4); a Tat peptide [1.6.1] was attached to the linker nitrogen to improve cell permeability. Tat-N-dimer was found to bind the tandem PSD-95 PDZ1/2 with an unprecedented high affinity of 4.6nM; it was also found to have improved blood plasma stability compared to the related monomeric peptide version, Tat-NR2B9c. The obtained results illustrated that the Tat-N-dimer was a

highly efficacious neuroprotective agent and so, has therapeutic potential in stroke treatment.

The interaction of bivalent peptides with the PSD-95 PDZ3 domain has been investigated (Klosi et al., 2007); the bivalent peptides were derived from the protein CRIPT as it had previously shown good affinity for the PSD-95 PDZ3 domain ($K_D = 0.8\mu\text{M}$) (Klosi et al., 2007). Five bivalent peptides ranging from five to nine residues in length were produced, with diacid succinate used as the N-termini linker (BP1, Figure 1.11b); all five bivalent peptides were found to bind bivalently and showed low to moderate micromolar binding affinity to PSD-95 PDZ3 ($K_D = 4.3\mu\text{M} - 23.2\mu\text{M}$). A bivalent PDZ domain ligand of the PDZ-RhoGEF and LARG PDZ domains has also been reported in the literature (Paduch et al., 2007); however, no details of any PDZ domain-mediated interaction inhibition effects of the bivalent peptide detailed in the previous two studies were given.

Cyclic peptides that have an inhibitory effect on PSD-95 PDZ domain-mediated interactions have been developed (LeBlanc et al., 2010); the researchers hypothesised that inhibiting the PSD-95 PDZ domains would interfere with the physiological phenomena in the spinal cord related to central sensitisation. The design and synthesis of the nine residue cyclic peptide (CN2097, Figure 1.11c) was based on the previous cyclic peptide work performed by the research group (Piserchio et al., 2004); the cyclic peptide contained a poly-Arg tag to promote cell permeability of the peptide. The cyclic nature of the peptide was created by linking the -1 and -3 residue side-chains and this cyclic structure was found to impart stability to the peptide. The results obtained indicated that the cyclic peptide selectively bound to the PSD-95 PDZ domains; this PDZ domain inhibitory effect of the cyclic peptide was found to block central sensitisation and attenuated thermal

hyperalgesia. Cyclic peptide ligands of the MUPP1 PDZ10 domain have also been reported (Sharma et al., 2007).

The research into cyclic peptides has also led to the development of ‘bridged peptide macrocycles’ that have been found to bind to the PSD-95 PDZ3 domain with reasonable micromolar affinities (Br1, $K_D = 3.76\mu\text{M}$, Figure 1.11d) (Udugamasooriya et al., 2005); no inhibitory effects of these ‘bridged peptide macrocycles’ were detailed however.

The final form of peptides that have been investigated in previous PDZ domain inhibition research is that of chemically modified peptides, such as the chemically modified peptide designed to target the GIPC PDZ domain (Patra et al., 2012). GIPC was seen as a suitable target for such intervention as the abnormal activation of GIPC PDZ-mediated interactions has been implicated in breast and pancreatic cancers. A series of chemically modified and unmodified PDZ domain targeting peptides were produced, using previous research as the basis for design (Udugamasooriya et al., 2008). The most active modified peptide (CR1166) consisted of septapeptide (SNSKSKA) with a N-terminal myristate to allow cell permeability; the Lys -1 and -3 side-chains were modified by adding halogenated organic modifications CR1166 was found to target the GIPC PDZ domain both *in vitro* and *in vivo*, with pronounced down-regulation of EGFR/IGF-IR expression; thus, CR1166 was found to exhibit significant activity against breast and pancreatic cancer in both cellular and animal models.

Research into chemically modified peptide inhibitors of the PSD-95 PDZ – NMDAR interaction has also been performed (Bach et al., 2008); the implications of this PDZ-mediated interaction have been discussed previously in this section. In this study, the effect of N-methylation of the different residues of an NR2B C-terminal-related

tetrapeptide on its binding affinity to PSD-95 PDZ1 or PDZ2 was investigated, with N-methylation of the -3 residue being the only modification shown to improve PSD-95 PDZ binding affinity. The effect of different N-alkyl chemical groups on the N-terminal residue (-3) was then probed and yielded a potent tetrapeptide inhibitor of the PSD-95 PDZ – NMDAR interaction (CP1, Figure 1.11e) ($K_i = 0.94\mu\text{M}$ for PDZ1, $0.48\mu\text{M}$ for PDZ2 and $11\mu\text{M}$ for PDZ3).

One final example of the development of a chemically modified peptide in PDZ domain inhibition research is the hybrid organic-inorganic (metallopeptide) inhibitor of the CAL PDZ – CFTR interaction (Kundu et al., 2012). The interaction between the CAL PDZ domain and CFTR has been shown to lead to CAL-mediated CFTR degradation, this is an important process in cystic fibrosis; thus, the inhibition of this interaction was a desired therapeutic target for cystic fibrosis treatment. The metallopeptide (MP1, Figure 1.11f) consisted of a Rh(II) centre tetracarboxylate attached at the -6 residue of septapeptide ($\text{E}^{\text{Rh}}\text{VQSTRL}$) identified by inverted peptide array screens. The inhibitory effects of the produced metallopeptide was investigated with a CFTR C-terminal peptide; the results showed that the metallopeptide was the first reported inhibitor with submicromolar affinity for the CAL PDZ domain ($K_i = 0.56\mu\text{M}$).

1.6.2 Peptidomimetics

The use of peptides has been shown to extremely advantageous in PDZ domain inhibition research to-date but the common problems of peptide use as drugs still persist i.e. lack of oral bioavailability. Therefore, research into peptide mimics (peptidomimetics) for PDZ domain inhibition has been performed. Peptidomimetics usually involves an attempt to retain the desirable properties of a particular peptide but increase the oral bioavailability, cell permeability etc by use of a suitable

chemical scaffold. There has been evidence of a rational design approach to develop β -strand peptidomimetic PDZ domain interaction inhibitors; this is due to the knowledge that PDZ domain ligands/peptides effectively form an anti-parallel β -strand upon PDZ domain binding. Thus, the development of effective β -strand peptidomimetic scaffolds may represent an important area of PDZ domain inhibition research.

Bartlett *et al* undertook a developmental procedure to develop β -strand peptidomimetics. The initial stage of the process involved the incorporation of amino acid surrogate '@-unit' in an oligopeptide to give a β -strand peptidomimetics known as '@-tides' (Phillips *et al.*, 2005); this resulted in the oligopeptide showing a high propensity for the extended β -strand conformation. The '@-tides' amino acid surrogates were then developed further, this involved the incorporation of an 'aza-@-unit' into an oligopeptide instead of an '@-unit' (Hammond *et al.*, 2006); this retained the conformational advantages of the '@-unit' but enabled facile incorporation of precursor amino acid side-chains. The developed peptidomimetic contained an acyl amidine linkage to stabilise the compound sufficiently to permit its use in biological applications and consisted of a peptide sequence (Ac-K@^ESLV, Figure 1.11g) derived from a known ligand of the α 1-syntrophin PDZ domain (Schultz *et al.*, 1998); this PDZ domain was chosen to test the PDZ binding ability of the peptidomimetic as it was well-known to bind to short peptides with micromolar affinity.

Results of the α 1-syntrophin PDZ binding studies showed that the developed peptide bound to the α 1-syntrophin PDZ domain with submicromolar affinity ($K_D = 0.32\mu\text{M}$); this was 20-fold stronger binding than the parent KESLV peptide and is even stronger than one of the native α 1-syntrophin PDZ ligands, nNOS ($K_D =$

0.61 μ M). Although no evidence of *in vitro* or *in vivo* PDZ domain-mediated interaction inhibition was detailed, this research indicates that @-tide oligomers may hold considerable promise in future PDZ domain inhibition research.

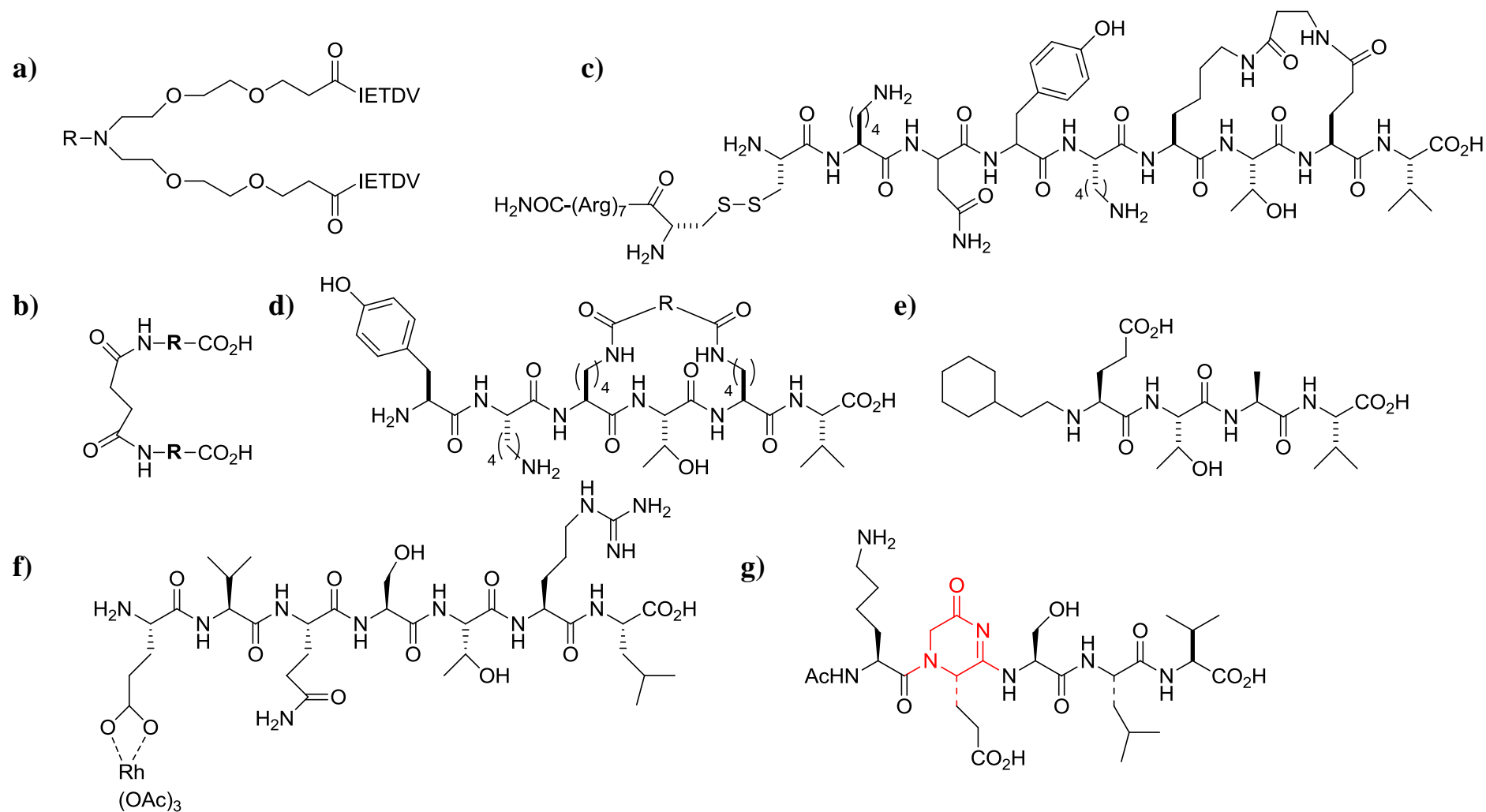


Fig 1.11: The chemical structures of a selection of the peptide and peptidomimetic compounds designed to inhibit PDZ domain/PDZ domain-mediated interactions. a) Tat-N-dimer (Bach et al., 2012). b) Bridged peptide 1 (BP1), where R = GKNYKQTSV (Klosi et al., 2007). c) CN2097 (LeBlanc et al., 2010). d) Bridged macrocycle 1 (Br1) (Udugamasooriya et al., 2005). e) Chemical peptide 1 (CP1) (Bach et al., 2008). f) Metallopeptide 1 (MP1) (Kundu et al., 2012). g) Ac-K@^ESLV (Hammond et al., 2006).

1.6.3 Small Molecule Inhibitors

The development of a specific, reversible small molecule PDZ domain/PDZ domain-mediated interaction inhibitor is an attractive therapeutic target in PDZ domain inhibition research. This is because small molecule inhibitor drugs are orally bioavailable unlike peptide drugs and the processes used to identify possible small molecule lead-drug candidates are much better established than peptidomimetic drug scaffolds. A wide range of structurally diverse small molecule compounds have been produced in PDZ domain inhibitor research to-date; this section has been sub-divided depending on the methodology utilised to obtain the particular small molecule inhibitor of the respective PDZ domain/PDZ domain-mediated interaction.

1.6.3.1 Rational Design

There are numerous examples of small molecule PDZ domain inhibitors that have been developed through a rational design procedure; this process is usually completed by attempting to mimic the interaction of the native PDZ ligand with the PDZ domain by a novel organic compound. The first ever published small molecule PDZ domain inhibitor was produced by a rational design methodology and this was a selective, irreversible inhibitor of the MAGI3 PDZ2 – PTEN interaction (SM1, Figure 1.12a) (Fujii et al., 2003); the small molecule was based on an indole chemical scaffold. MAGI3 is a member of the MAGI family, a subfamily of MAGUKs and binds to PTEN, a lipid/protein phosphatase via the MAGI3 PDZ2 domain; the role of this interaction is controversial and so, inhibition of this interaction by a small molecule inhibitor was seen as a novel method of elucidating the cellular role of the interaction. The small molecule inhibitor was found to inhibit the binding of PTEN to the MAGI3 PDZ2 domain; however, the inhibition of this

PDZ-mediated interaction was shown to be irreversible, which was obviously undesirable.

In an effort to develop this compound into a reversible inhibitor, computational experiments were performed and the structure of the irreversible inhibitor was modified accordingly (Fujii et al., 2007a); the resultant small molecule (SM2, Figure 1.12b) was shown to cause no covalent modification of the MAGI3 PDZ2 domain and so, was proven to be a reversible inhibitor of the MAGI3 PDZ2 – PTEN interaction. This research led to the production of a general chemical scaffold for developing reversible PDZ domain inhibitors, based on the indole aromatic ring (Sc1, Figure 1.12c); where different chemical groups can be placed around the indole structure to effectively mimic the side-chain structures of the native PDZ domain ligand. This general PDZ domain inhibitor scaffold has since been utilised to produce inhibitors of Dvl (Fujii et al., 2007c, Mahindroo et al., 2008), NHERF1 (Mayasundari et al., 2008) and NHERF2 (Zhang et al., 2011a) PDZ domain-mediated interactions. The indole scaffold has also formed the basis of a class I PDZ domain selective chemical probe developed by the same research group (Fujii et al., 2007b); this indicated how biotinylated probes could be used to differentially visualise the cellular proteome and identify PDZ proteins (P1, Figure 1.12d).

A small molecule inhibitor of the PSD-95 PDZ2 – nNOS interaction has been developed using a rational design process (Zhou et al., 2011); the PSD-95 PDZ2-nNOS interaction is known to be ischaemia-induced and thus, may be a strategy to treat stroke, which prevents ischemic damage without directly blocking NMDAR function or inhibiting nNOS activity. The small molecule design process focused on the mechanism of nNOS-PSD-95 PDZ2 dimer formation; a key intramolecular salt-bridge between the residues of the nNOS PDZ domain β -finger was identified as

structurally necessary for the nNOS β -finger to interact with the PSD-95 PDZ2 domain.

This is a rare example of a PDZ domain-mediated interaction inhibition design process where the focus of inhibitor design was targeted at the PDZ domain ligand, not the PDZ domain. A range of small molecule compounds were designed and synthesised in an attempt to disrupt the intramolecular nNOS salt bridge. The most potent compound (ZL006, $IC_{50} = 82\text{nM}$, Figure 1.12e) was shown to selectively inhibit the ischemia-induced PSD-95 PDZ2 – nNOS interaction, had potent neuroprotective activity and reduced ischemic brain damage; ZL006 also had no effect on NMDAR function and nNOS activity.

1.6.3.2 Virtual Library Screening/NMR Spectroscopy

A combination of virtual library screening (VLS) and NMR spectroscopy has proved effective in research on PDZ domain/PDZ domain-mediated interaction inhibition by a small molecule; Zheng's research group have developed a variety of different small molecule inhibitors of the Dvl – Frizzled receptor (Fz) interaction. The rationale for targeting the Dvl PDZ domain has been previously discussed [1.6.1].

A process of structure-based virtual ligand screening followed by NMR spectroscopy yielded the compound NSC668036 (Figure 1.12f) (Shan et al., 2005); this small molecule was identified to specifically bind to the Dvl PDZ domain with high micromolar affinity ($K_D = 237\mu\text{M}$). NSC668036 was shown to inhibit the Wnt signalling pathway at Wnt3A not at β -catenin, which is downstream of Dvl and so, indicates that the NSC668036 was exhibiting the desired inhibitory effect.

NSC668036 was then used as the basis for a pharmacophore model along with two other non-binding organic compounds in a ligand similarity screening (Shan and Zheng, 2009); this identified 15 structures that bound to the Dvl PDZ. By expanding

the chemical space used in their *in silico* search, the researchers were able to obtain nine more Dvl PDZ binding compounds; to give 24 small molecule structures in total and all 24 were based on one of two scaffolds (Sc2&3, Figure 1.12g) (Shan et al., 2012). Dvl PDZ domain binding affinities in the low micromolar range were reported by the researchers, however, the methodology implemented to determine the affinity values does not seem extremely accurate or reliable; hence, the K_D values quoted in their research may not be reliable and so, have not been detailed here. This is because the binding affinity determination utilised an NMR titration, where the values obtained were normalised based on the discrepancy in the Dvl PDZ binding affinity of NSC668036 obtained by both fluorescence and NMR spectroscopy techniques.

The VLS and NMR spectroscopy methodology has also been utilised by the same research group to develop the compound 3289-6825 (Figure 1.12h) (Grandy et al., 2009); this was found to bind to the Dvl PDZ domain with low micromolar affinity ($K_D = 10.6\mu\text{M}$) and exerted an inhibitory effect on the native Dvl PDZ - Dapper interaction ($K_i = 4.9\mu\text{M}$). The group have recently published their overall VLS and NMR spectroscopy methodology to small molecule PDZ domain inhibitor development (Shan and Zheng, 2012).

A related VLS, NMR screening and chemical synthesis approach has also been utilised to develop small molecule ligand of the ALL-1 fusion partner on chromosome 6 (AF6) PDZ domain (SM3, Figure 1.12i) (Joshi et al., 2006). Research detailed in this thesis has also implemented a VLS, NMR screening and chemical synthesis approach to development of small molecule inhibitors of PDZ domain-mediated interactions (Bouzidi et al., 2013).

1.6.3.3 High-Throughput Screening

High-throughput screening (HTS) drug discovery methodologies have been applied to PDZ domain/PDZ domain-mediated interaction research; the development of a small molecule inhibitor of the PICK1 PDZ domain is an example of this (Thorsen et al., 2010). PICK1 is known to bind to the AMPA receptors (AMPA receptors) through its PDZ domain; this interaction has recently been recognised as a putative target in neuropathic pain (Garry et al., 2003), excitotoxicity (Bell et al., 2009) and cocaine addiction (Bellone and Luscher, 2006) and so, inhibition of this PDZ domain-mediated interaction could have important therapeutic potential.

A high-throughput fluorescence polarisation assay screening of 44,000 small molecules in the Neurosearch A/S chemical library resulted in compound FSC231 (Figure 1.12j); FSC231 was found to bind specifically to the PICK PDZ1 domain with low micromolar affinity ($K_i = 10.1\mu\text{M}$). The small molecule was shown to inhibit the PICK1 PDZ – AMPAR interaction and that this inhibition affected AMPAR trafficking; FSC231 was also shown to inhibit synaptic plasticity in hippocampal CA1 neurons. The structure-activity relationship of the PDZ domain binding of FSC231 was subsequently investigated (Bach et al., 2010); this has produced an analogue with improved PICK1 PDZ binding affinity ($K_i = 7.2\mu\text{M}$) c.f. FSC231.

A small molecule inhibitor of the PSD-95 PDZ – nNOS interaction has also been developed using HTS methods (Florio et al., 2009); the therapeutic rationale behind targeting this interaction has been discussed previously [1.6.1]. A high-throughput *in vitro* assay screening of 150,000 small molecules in the ICOS chemical library yielded several PDZ interaction inhibitors; the most potent compound from the HTS was modified to improve stability to give IC87201 ($\text{IC}_{50} = 31\mu\text{M}$, Figure 1.12k).

IC87201 was found to inhibit *in vitro* binding of nNOS to PSD-95 without affecting nNOS catalytic activity; it was also shown to reverse mechanical allodynia by chronic constriction of the sciatic nerve. However, subsequent work in our laboratory showed that there was no interaction between IC87201 and either PSD-95 PDZ1, PDZ2 or nNOS PDZ observed by NMR spectroscopy; there was also no indication of any PDZ domain-mediated interaction inhibition by IC87201 observed by NMR spectroscopy or ITC (L Dorr, unpublished data).

High-throughput screening has also been used to develop small molecule inhibitors of Mint1 (HTS1, Figure 1.12l) (Chen et al., 2007b) and Shank3 (HTS2, Figure 1.12m) (Saupe et al., 2011) PDZ mediated–interactions.

1.6.3.4 Re-purposing of Existing Drugs

A common difficulty in the development of small molecule inhibitors is determining a rational starting point for drug design and therefore, there is a current effort to find ‘new purposes for old drugs.’ This is a potentially useful strategy for PDZ domain-related drug discovery as they can provide possible templates for future inhibitor design; an example of this is Sulindac (Lee et al., 2009b).

Sulindac (Figure 1.12n) is from a class of drugs known as non-steroidal anti-inflammatory drugs (NSAIDs); previous research had indicated that Sulindac could exhibit chemopreventive effects, possibly by targeting the Wnt signalling pathway (Han et al., 2008). Both Sulindac and its metabolite Sulindac sulfone (Figure 1.12o) were shown to specifically bind to the Dvl PDZ and inhibit Wnt signalling by disrupting the Dvl PDZ - Fz7 receptor interaction; this inhibition was revealed to be the Dvl PDZ-mediated not β -catenin-mediated Wnt signalling, which as previously discussed is desired.

1.6.4 Summary of Previous PDZ Domain Inhibition Research

The PDZ domain inhibition research to-date detailed in [1.6] has shown that there have been a wide range of different types of chemical compound produced in an effort to develop PDZ domain-mediated interaction inhibitors; the different development methodologies implemented to produce these compounds are just as numerous. Each of the three different types of inhibitor: peptides, peptidomimetics and small molecules, have exhibited good efficacy in PDZ domain interaction inhibition, mainly through *in vitro* analyses and there is even a large degree of differentiation between compounds in the same inhibitor type sub-category.

The highest affinity PDZ domain inhibitor developed at the time of writing is the bivalent peptide inhibitor of PSD-95 PDZ1/2 domains in tandem (Tat-N-dimer, $K_D = 4\text{nM}$) (Bach et al., 2012). However, this is still a peptide-based drug and although the tandem inhibition of two PDZ domains has been shown to increase binding affinity significantly, if the second PDZ domain has no role in the targeted interaction the inhibitor may also affect unrelated PDZ domain-mediated interactions and have adverse effects. Arguably, the ‘dream’ PDZ domain-mediated inhibitor would be a high affinity and highly inhibiting small molecule; with research to-date producing a low micromolar affinity small molecule inhibitor of the PICK1 PDZ domain ($K_i = 7.2\mu\text{M}$) (Bach et al., 2010), this dream may become a reality in the not too distant future.

However, it has been detailed that some examples of reported PDZ domain binding and/or inhibition reported in the literature may be erroneous (Florio et al., 2009) or unreliable (Shan and Zheng, 2009, Shan et al., 2012); this highlights the importance of critically evaluating the binding affinity determination methodology utilised when assessing the reliability of the information reported. Such flaws in PDZ domain

binding affinity determination methodologies could suggest why there has been little success in translating *in vivo* results into potential drugs for PDZ domain-mediated interactions to-date.

Thus, it would appear that determining the specific type of PDZ domain inhibitor and the methodology to implement to produce the inhibitor is a combination of different considerations such as: preferred drug administration method, desired length of development process, technology and expertise available, previous research and accuracy of *in vitro/in vivo* assays amongst other considerations.

1.7 Conclusion

The research detailed in this chapter has highlighted that the PDZ domain mediated interactions of the PSD-MAGUKs PSD-95 and SAP97 are valid research targets; there are a number of instances where inhibition PSD-95 and/or SAP97 PDZ domain-mediated interactions would be of therapeutic benefit. Although there has been a reasonably substantial amount of research on the PSD-95/SAP97 PDZ domains and the interactions they mediate up to the present, a lot of this work has been cell-based; with a disproportionately low amount of structural research performed to-date and so, little information on the exact nature of the PDZ domain-mediated interactions is available. The previous PDZ domain inhibition research has shown that there are a wide range of suitable types of compounds and methodologies to utilise; the design of a potentially potent inhibitor could be determined with structural knowledge of the target PDZ domain-mediated interaction. Thus, a research project that combines PDZ domain binding investigation with PDZ domain inhibitor development could be potentially effective.

1.8 Research Aims

The overriding goal of the research programme in the laboratory was to develop small molecule inhibitors against the PSD-95 and SAP97 PDZ domains. The specific aims of the research described in this thesis can be divided into three categories:

- Investigate the binding of the 5-HT_{2a/c} receptors to the PSD-95/SAP97 PDZ1&2 domains and determine the structure of a PDZ – 5-HT_{2x} complex (Chapter 4).
- Investigate the specific interactions in the binding regions of the SAP97 PDZ1&2 domains using biophysical techniques (Chapter 5).
- Through a developmental process, develop small molecule inhibitors of the PSD-95/SAP97 PDZ1&2 domains and determine the resultant PDZ – small molecule inhibitor complex(es) (Chapter 6).

The techniques required to satisfy these research aims were:

1. Protein production – to produce the various unlabelled and (¹³C,) ¹⁵N-isotopically labelled PDZ domains required for use in NMR spectroscopy and ITC. Site-directed ligase-independent mutagenesis was implemented to produce PDZ domain mutants.
2. NMR spectroscopy – utilised to determine if the produced PDZ domains were folded, to see if there was any interaction of an individual PDZ domain with a native peptide/small molecule and for binding affinity and structure determination purposes also.
3. Isothermal titration calorimetry (ITC) – to determine if any PDZ domain – peptide interaction occurred and if so, the resultant thermodynamic parameters, in the absence/presence of small molecule compounds.
4. NMR solution state structure determination methods:

- a. CYANA – for automated assignment of PDZ domain – peptide complex NOE NMR spectra.
 - b. CNS – to determine the *in vacuo* and water-refined structures of a PDZ domain – peptide complex.
5. NMR restraint-driven docking method, **High ambiguity-driven docking** (HADDOCK) – to determine the structure of PDZ domain – small molecule complexes, using inter- and intramolecular distance restraints determined by NMR spectroscopy.

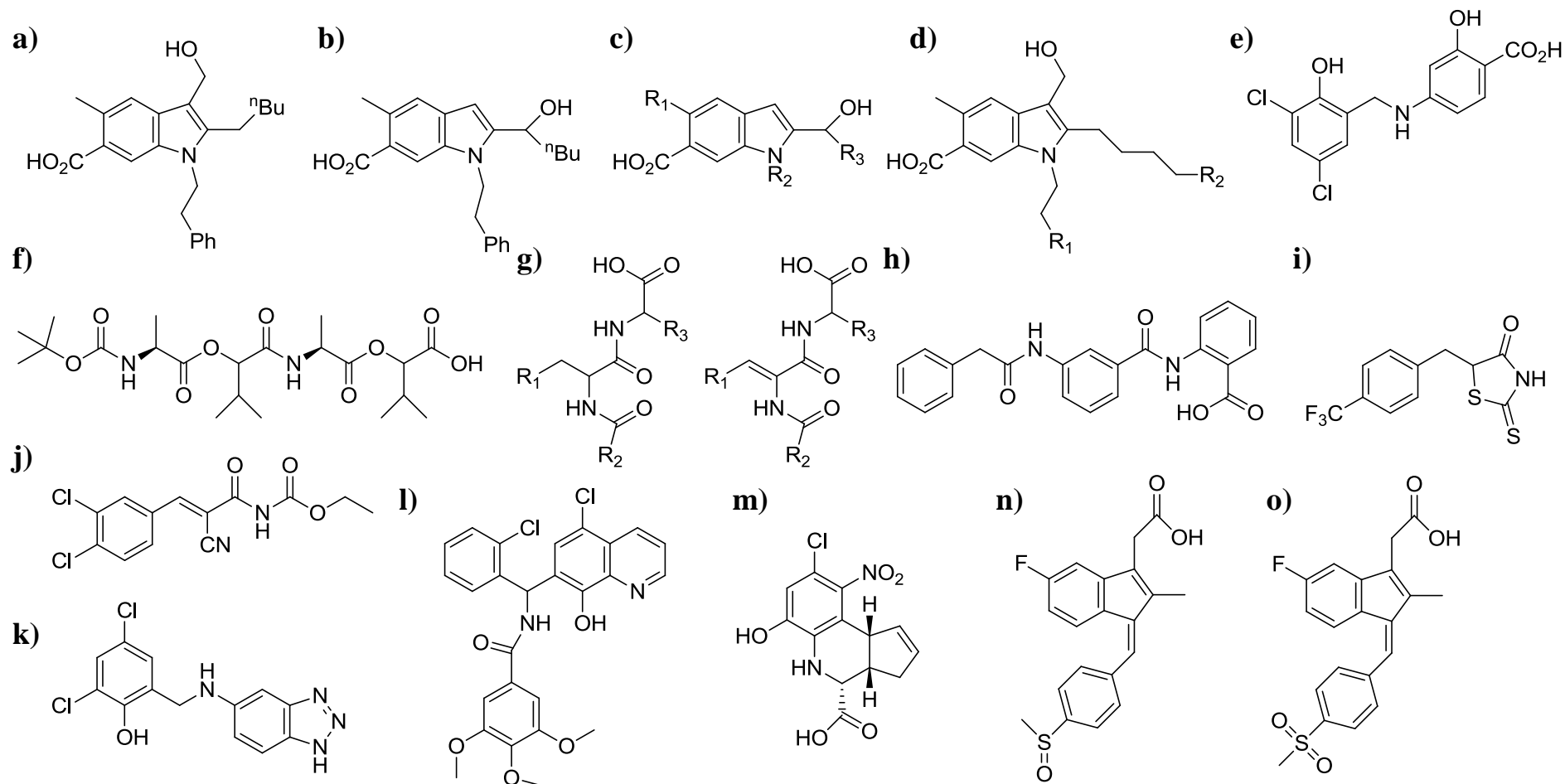


Fig 1.12: Chemical structures of a selection of the small molecule compounds designed to inhibit PDZ domain/PDZ domain-mediated interactions. a) Small molecule 1 (SM1) (Fujii et al., 2003). b) SM2 (Fujii et al., 2007a). c) Scaffold 1 (Sc1) (Fujii et al., 2007a). d) Probe 1 (Pr1) (Fujii et al., 2007b). e) ZL006 (Zhou et al., 2011). f) NSC668036 (Shan et al., 2005). g) Sc2&3 (Shan et al., 2012). h) 3289-6825 (Grandy et al., 2009). i) SM3 (Joshi et al., 2006). j) FSC231 (Thorsen et al., 2010). k) IC87201 (Florio et al., 2009). l) High-throughput screening 1 (HTS1) (Chen et al., 2007b). m) HTS2 (Saupe et al., 2011). n) Sulindac (Lee et al., 2009b). o) Sulindac sulfone (Lee et al., 2009b).

Chapter 2
INTRODUCTION TO
BIOPHYSICAL TECHNIQUES

2. INTRODUCTION TO BIOPHYSICAL TECHNIQUES

2.1 General

In the process of carrying out the research required to produce this thesis, there were two biophysical techniques employed; protein nuclear magnetic resonance (NMR) spectroscopy and isothermal titration calorimetry (ITC). An introduction to the theory, instruments, practical considerations and applications of these well-known techniques is detailed in this chapter.

2.2 Protein Nuclear Magnetic Resonance (NMR) Spectroscopy

(Keeler, 2005, Cavanagh, 2007, Levitt, 2008, Lian and Roberts, 2011)

2.2.1 Introduction to NMR Spectroscopy

The NMR spectroscopic methodology is one of the principal techniques used to obtain physical, chemical, electronic and three-dimensional (3-D) information about molecules in solution; these range from small molecules and nucleic acids to carbohydrates and proteins. NMR exploits the natural phenomenon that, when exposed to a very strong magnetic field (2 - 21.1 Tesla), certain atomic nuclei align to this field.

The first published NMR spectrum of a biological macromolecule was the 40MHz ^1H spectrum produced of pancreatic ribonuclease in 1957. Since this initial experiment, continuous development in the NMR spectrometer hardware/pulse sequence/data analysis/structure determination, molecular biology and NMR sample preparation fields has occurred. This has led to protein NMR spectroscopy becoming a mainstream biophysical technique and particularly useful in structural biology.

2.2.2 Classical NMR Spectroscopy

All forms of matter consist of atoms, which in turn are made up of nuclei and electrons. Each atomic nucleus has four important physical properties; mass, electric

charge, magnetism and spin. Nuclear spin is an intrinsic property of the particle itself, not produced by its rotation and is a form of angular momentum. Nuclear spin angular momentum is a quantum mechanical property that does not have a classical analogue and is characterised by the nuclear spin quantum number, I . NMR spectroscopy is made possible due to this property of nuclei and thus, the theory behind NMR spectroscopy is concerned mainly with the quantum mechanics of nuclear spin angular momentum. This section introduces the semi-classical vector model to describe the behaviour of non-interacting spin-half nuclei in a static magnetic field, formulated by Bloch. This may seem futile to detail here but most of the language used in pulsed NMR is derived from the vector model and many of the features of the vector model have direct counterparts in the quantum mechanical explanation of NMR spectroscopy theory.

To be NMR active, I must be a non-zero value. Nuclei with $I > 1/2$ possess quadrupole moments arising from non-spherical nuclear charge distribution and this results in the lifetime for these nuclei in solution being much shorter c.f. $I = 1/2$. The NMR resonance lines for quadrupolar nuclei are also more broad and difficult to study than the corresponding lines for $I = 1/2$. Therefore, for use in protein NMR spectroscopy, the most important nuclei are the $I = 1/2$ nuclei of ^1H , ^{13}C and ^{15}N and the important properties of these nuclei have been detailed (Table 2.1). The $I = 1$ nucleus of ^2H is also frequently utilised in protein NMR spectroscopy and so, its properties have been included in the table too.

Table 2.1: The properties of the nuclei of interest in protein NMR spectroscopy, where I is the nuclear spin angular momentum quantum number and γ is the gyromagnetic ratio – a characteristic constant for the corresponding nuclei. The natural isotopic abundance for each nuclei is also given.

Nuclei	Natural Abundance (%)	I	γ (T s) ⁻¹
^1H	99.99	1/2	2.6752×10^8
^2H	0.012	1	4.107×10^7
^{13}C	1.07	1/2	6.728×10^7
^{15}N	0.37	1/2	-2.713×10^7

Nuclear spin angular momentum is a vector quantity, where the z-component (I_z for axis notation, Figure 2.1) is specified by convention and this z-component has a discrete set of values as Equation 2.1 illustrates. As I_z has a discrete set of values and a constant magnitude, its orientation in space is quantised. In the absence of an external field, the spin angle vector does not have a preferred orientation. Nuclei where $I \neq 0$ also possess nuclear magnetic moments, where the nuclear magnetic moment, μ , is collinear with I and is defined by Equations 2.2 & 2.3.

$$I_z = \hbar m \quad \text{Equation [2.1]}$$

where, $m =$ magnetic quantum number i.e. $(-I \dots +I)$, $\hbar = \frac{h}{2\pi}$ and $h =$ Planck's constant

$$\mu = \gamma I_z \quad \text{Equation [2.2]}$$

$$\mu = \gamma \hbar m \quad \text{Equation [2.3]}$$

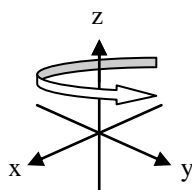


Figure 2.1: The right-handed set of axis that will be used throughout this chapter. The axis is described as right-handed as if the z-axis were grasped with the right hand, with the thumb pointing along +z, then the fingers curl from x to y; this is a positive rotation and has been shown in the figure. Image based on a figure in (Keeler, 2005).

When the nucleus is placed in a magnetic field (B_0), there is an interaction between the nuclear magnetic moment and the applied field, with the energy of the interaction depending on the angle between the two properties (Figure 2.2a). There is an energetic preference for the individual magnetic moments to align with the field (i.e. $\theta = 0$) but this is opposed by the random thermal motion of molecules; as a result, there is no magnetisation when the field is first applied. However, after a sufficient time, the orientations of magnetic moments aligned with the field become more populated. When this is summed over the sample, the net (or bulk) magnetisation is parallel to the field direction and it is said that equilibrium magnetisation has built up (Figure 2.2b).

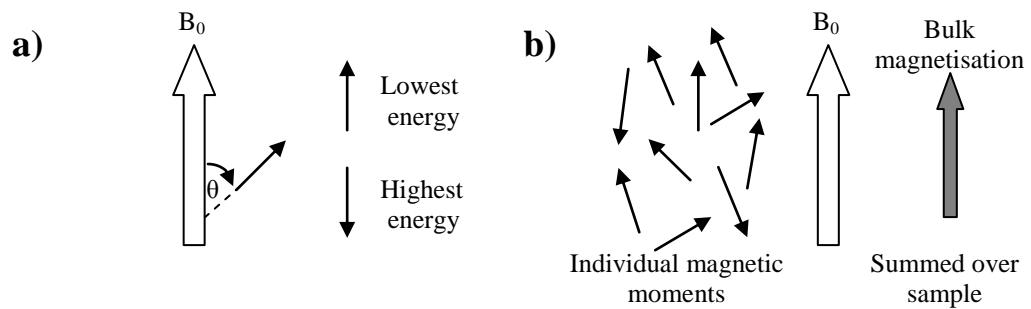


Figure 2.2: a) The energy of the interaction between a magnetic moment (small arrow) and an applied magnetic field (B_0) depends on the angle between the two components; the lowest energy arrangement is found when the magnetic moment is parallel to the field i.e. $\theta = 0$. Conversely, the highest energy arrangement is when the moment is opposite the field i.e. $\theta = \pi$. b) After a sufficient time in the magnetic field, the magnetic moments aligned with the field become more populated; when averaged over the sample, this gives rise to a bulk magnetisation parallel to the field. This is termed equilibrium magnetisation and can be represented as a vector. Image based on a figure in (Keeler, 2005).

Once formed, the equilibrium magnetisation vector is fixed in size and direction, does not vary over time and precesses about the main static field axis (z-axis, Figure 2.3a). The precession frequency is exactly the same as the frequency at which an allowed transition between two energy levels (Larmor frequency) occurs and hence, the precession of magnetisation about the field is sometimes termed Larmor precession. For those nuclei with a positive gyromagnetic ratio, the Larmor frequency (ω_0) is negative which corresponds to a negative rotation about the z-axis (Figure 2.3b); the opposite is true for those nuclei with a negative gyromagnetic ratio.

The precession of the magnetic moment about the static magnetic field constitutes a time-varying magnetic field and hence, according to Faraday's law of induction, should induce an electromotive force in a coil in close proximity. However, at thermal equilibrium, the bulk magnetisation vector is collinear with the static field and therefore, no signal is produced in the coil. To produce an NMR signal, the magnetisation has to be rotated away from its equilibrium position along the z-axis to the xy-plane and this precession in the transverse plane generates a detectable signal in the coil. It is impossible to switch the main magnetic field suddenly in this way as it is supplied by a powerful, superconducting magnet and so, this result is achieved

by the idea of resonance.

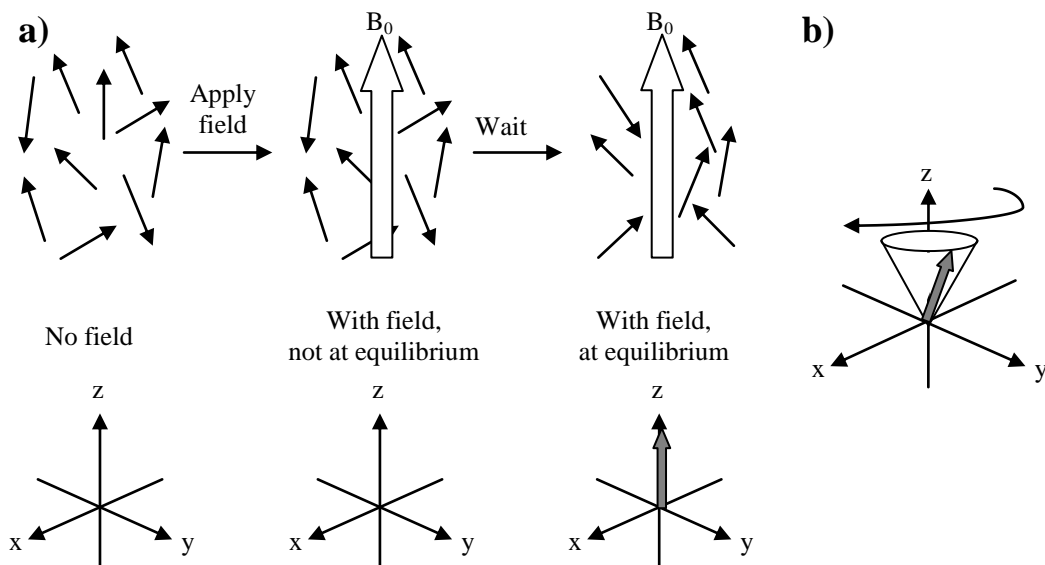


Figure 2.3: a) An illustration of how the equilibrium magnetisation vector described in Figure 2b builds up. When there is no magnetic field, the magnetic moments are in random orientations and so, there is no net magnetisation. It takes time for orientations aligned with the field to become populated and so, when the magnetic field is first applied along the +z-axis, there is still no net magnetisation. However, after a sufficient time period, those populations aligned with the field are populated enough to produce net magnetisation along the field direction axis. b) The precession of the magnetisation vector occurs by rotation about the field direction at a constant angle to the z-axis, this is called precession. The precession direction shown in the figure is for a nucleus with a positive gyromagnetic ratio and hence, a negative Larmor frequency. Image based on a figure in (Keeler, 2005).

The coil used to detect the precessing magnetisation can also be used to generate an oscillating magnetic field at or near the Larmor frequency by supplying radiofrequency (RF) electromagnetic radiation to the coil; this is termed the transmitter frequency (ω_{tx}). To understand how a weak RF field can overcome B_0 even though B_0 is much greater in size, it is easier to think of the oscillating field as two counter rotating fields about the z-axis (Figure 2.4).

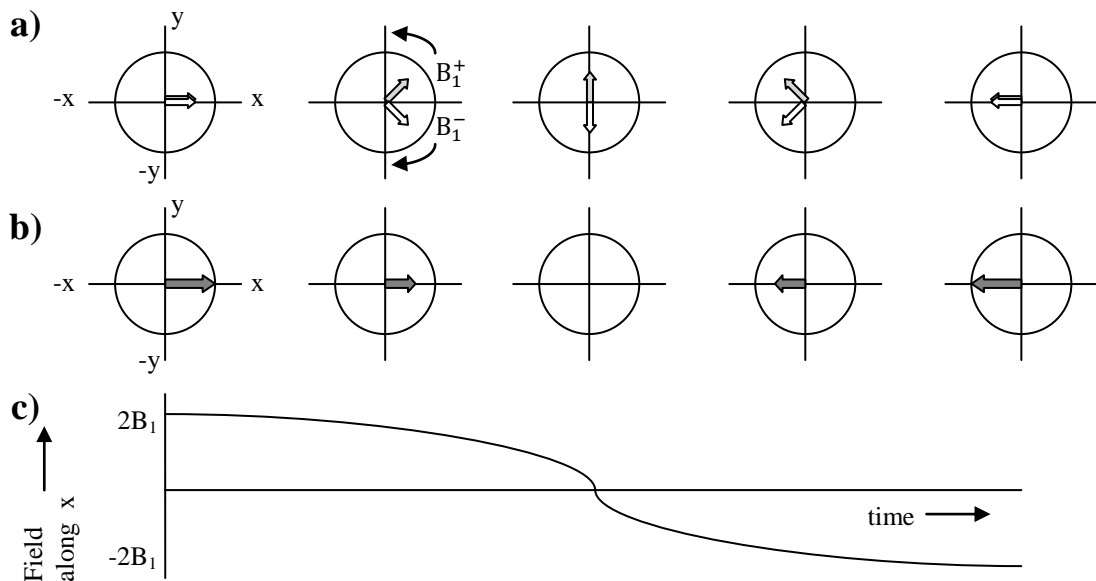


Figure 2.4: An examination of how two counter-rotating fields (B_1^+ and B_1^-) shown in a) add together to give a field that oscillates along the x-axis in b). The graph in c) indicates how the field along the x-axis varies over time. Image based on a figure in (Keeler, 2005).

Only the field rotating in the same sense as the magnetic moment interacts significantly with the magnetic moment (Figures 2.4 & 2.5); in this example, a nucleus with a positive gyromagnetic ratio i.e. negative rotation about the z-axis is considered and hence, it is the B_1^- field that interacts with the magnetic moment. The field rotating in the opposite sense to the magnetic moment (B_1^+) has no significant interaction with the magnetisation and thus, can be ignored.

A co-ordinate system is then employed where the field is rotated about the z-axis at the same rate and in the same direction as B_1 i.e. at $-\omega_{Lx}$; this is termed the rotating frame, as opposed to it being a static field (laboratory frame) (Figure 2.5). The rotating frame removes the time-dependence of the RF (or B_1) field and thus, makes it easier to determine the effect the field has on the magnetisation. If the rotating frame rotates at the same frequency and in the same sense as the Larmor precession, then the apparent magnetic field (or reduced field, ΔB) in the rotating frame will be zero (this can be seen by following Equations 2.4 – 2.6). This allows the conclusion that if the rotating frame is at the Larmor frequency, the apparent field is zero and thus, B_1 can exert an influence on the motion of magnetisation even though it is

much smaller than the applied field, B_0 .

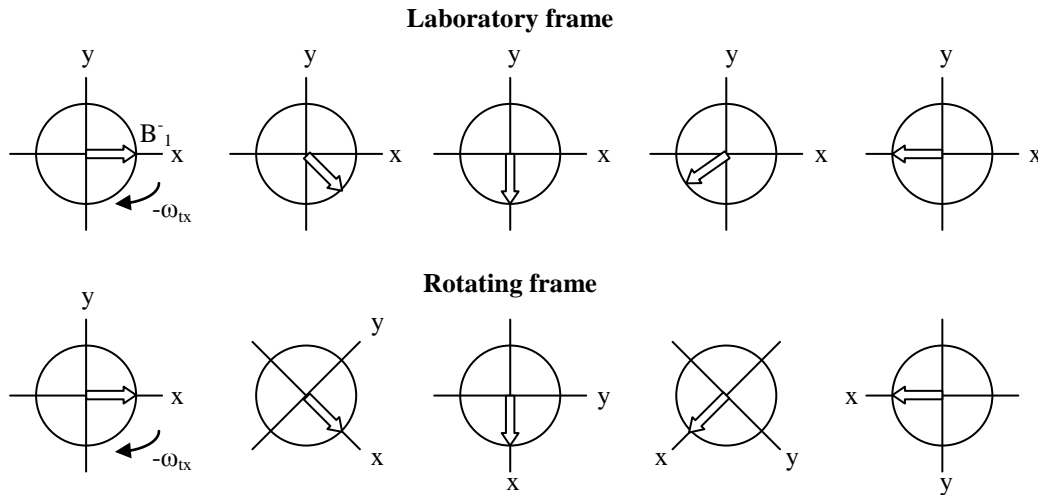


Figure 2.5: The laboratory frame (top) illustrates the motion of the field B_1^- when viewed in a fixed axis system; the field is rotating at $-\omega_{tx}$ i.e. in the negative sense (this is clockwise in this figure). The rotating frame is also shown (bottom), this is the same B_1^- field but this time viewed in an axis system that is rotating at $-\omega_{tx}$ about the z-axis and hence, shows how the B_1^- field appears to be static. Image based on a figure in (Keeler, 2005).

$$\Omega = \omega_0 - \omega_{rot.frame} \quad \text{Equation [2.4]}$$

where, Ω = the apparent precession frequency in the rotating frame

$$\omega = \gamma B \quad \text{Equation [2.5]}$$

$$\Delta B = -\frac{\Omega}{\gamma} \quad \text{Equation [2.6]}$$

This can be seen more clearly if the concept of the effective field (B_{eff}) is introduced, taking into account the two magnetic fields in the rotating frame; the RF field (where $\omega_{rot.frame} = -\omega_{tx}$ and thus, gives a static field along the x-axis) and the reduced field (ΔB , along the z-axis). In the rotating frame, the reduced field and the B_1 field add vectorially to give an effective field B_{eff} , with the tilt angle (θ) defined as the angle between B_{eff} and ΔB (Figure 2.6a). As the offset is small, the effective field will lie close to the x-axis and the equilibrium magnetisation will be rotated away from the z-axis as desired. In practical terms, it is more convenient to think of the construction of the effective field in terms of precession frequencies rather than magnetic fields (Figure 2.6b); the principle outcomes are the same regardless.

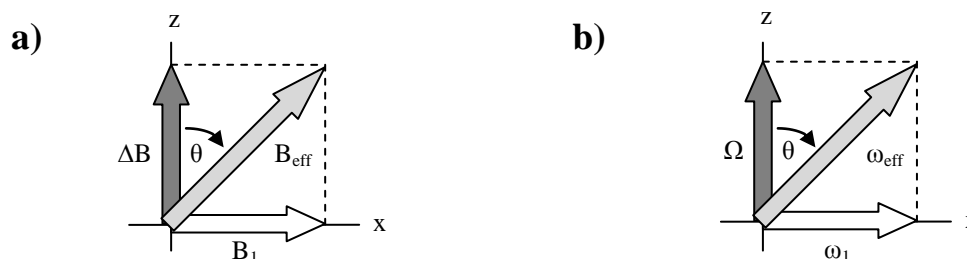


Figure 2.6: a) In the previously described rotating frame, the effective field B_{eff} is the vector sum of the reduced field ΔB and the B_1 field, with the angle between B_{eff} and ΔB labelled the tilt angle, θ . The effective field (B_{eff}) can also be defined in terms of frequencies instead of fields i.e. a). Image based on a figure in (Keeler, 2005).

The experimental aspects of the NMR spectrometer and the various processes that are performed during protein NMR spectroscopy to obtain the desired spectra are described in [2.2.3]. However, at this stage, the final spectrum output from a simple ^1H protein NMR spectroscopy experiment will be discussed here to introduce a few key aspects of NMR spectra (Figure 2.7).

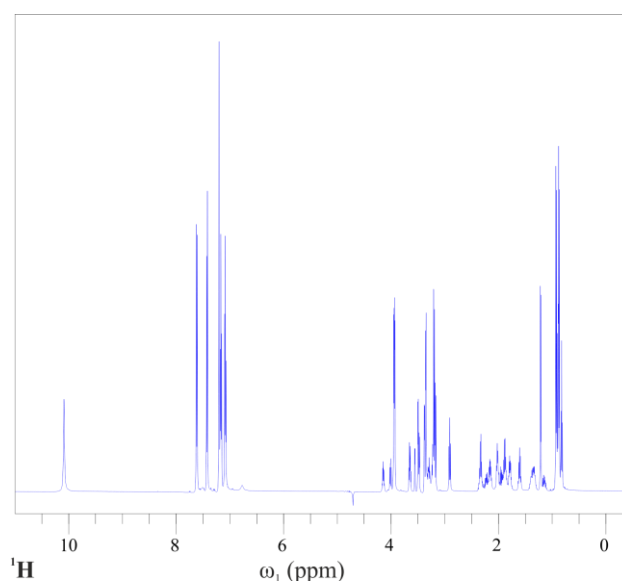


Figure 2.7: A ^1H NMR experiment of a seven-residue peptide acquired at 600MHz, at 298K. There are a number of lines (peaks) in the spectrum and these correspond to different proton environments present in the peptide, with the scale measuring these peaks given as parts per million (ppm) not Hz (s^{-1}); this is due to the magnetic field strength dependence of the frequencies of NMR lines.

Like all forms of spectroscopy, an NMR spectrum is a plot of the intensity of absorption (or emission) on the vertical axis against frequency on the horizontal axis. However, if the spectrum in Figure 2.7 is analysed, it is clear that the scale on the horizontal axis is not in Hz (or s^{-1}); the horizontal axis scale is given in parts per million (ppm). This is because the frequencies of NMR lines are directly

proportional to magnetic field strength (Figure 2.8) and thus, this field dependence makes it difficult to compare absorption frequencies between spectrometers which operate at different field strengths. In order to specify the position of an NMR line independent of the applied field, the chemical shift scale is introduced to NMR spectroscopy. This is done by using a simple reference compound (TMS for ^1H and ^{13}C) to define zero on the chemical shift scale. The position of a peak in the spectrum is determined by measuring its frequency separation from the reference peak and then dividing by the reference peak frequency. As the ratio of two frequencies is being obtained, the field dependence is cancelled out and the ratio multiplied by 10^6 to make the numbers more manageable (Equation 2.7). This is where the term chemical shift (δ) originates to describe the peaks in NMR spectra and why the values are quoted in parts per million (ppm).

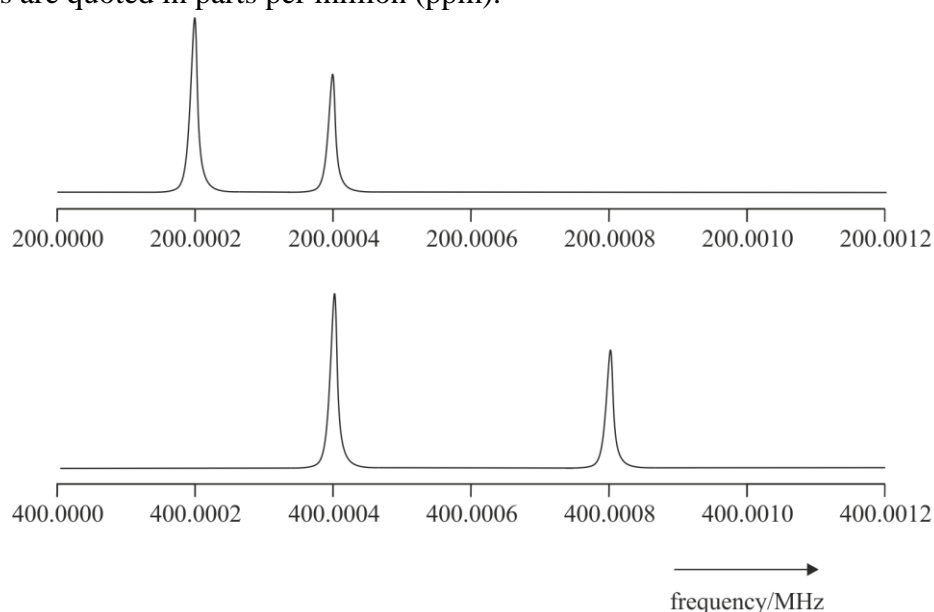


Figure 2.8: Two representative NMR spectra consisting of two peaks, to illustrate the magnetic field strength dependence of NMR lines. In a) the magnetic field is such that the two lines appear at 200.0002 and 200.0004MHz respectively; with a separation of 200Hz. However, in b) the magnetic field strength has been doubled, the frequency of each peak has doubled and thus, so has the separation between the two lines (400Hz). Image based on a figure in (Keeler, 2005).

$$\delta \text{ (ppm)} = 10^6 \frac{\nu - \nu_{ref}}{\nu_{ref}} \quad \text{Equation [2.7]}$$

The traditional chemical shift lineshape seen in simple NMR experiments is the

absorption mode lineshape (Figure 2.9a), this is a peak centred at ν_0 , height h and linewidth W (width measured at half the peak height, $h/2$). In ^1H NMR spectroscopy, the peak or multiplet integral i.e. the area under the respective peak is proportional to the number of hydrogen's that the peak represents (Figure 2.9b).

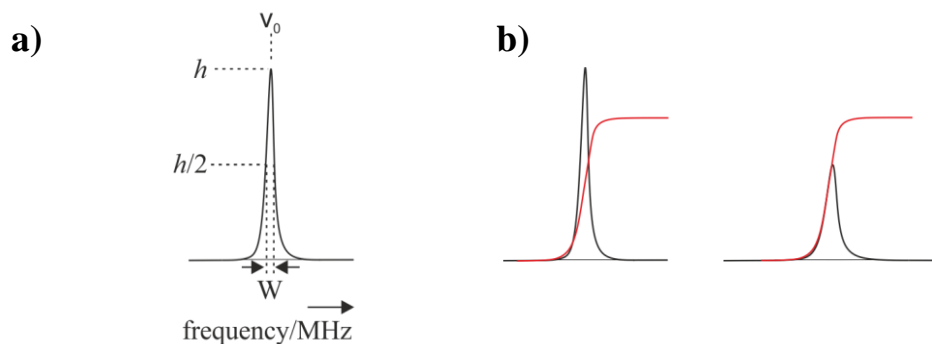


Figure 2.9: a) An example of an absorption mode lineshape seen in NMR experiments, where the peak is centred at ν_0 , with height h and linewidth W (measured at half the peak height i.e. $h/2$). b) An illustration of how the integral (area) of a peak that corresponds to a certain number of protons is fixed. The peak on the right hand side is twice as broad, but only half the height of the peak on the left hand side; thus, both peaks in the example contain the same number of protons, as shown by the integral (red). Image based on a figure in (Keeler, 2005).

The term ‘multiplet’ was used previously and this is an example of a peak in NMR spectra where the chemical shift has been split into two or more lines due to scalar (or J) coupling between nuclei and is mediated by chemical bonds. This property of NMR spectra is very useful in determining which nuclei are close to one another in the bonding framework; an example of two coupled spin-half nuclei can be seen (Figure 2.10).

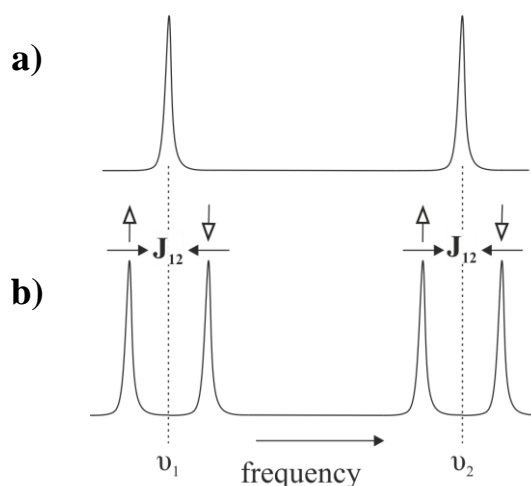


Figure 2.10: The spectrum shown in a) contains two lines at frequencies ν_1 and ν_2 corresponding to two different spins; if there is scalar (J) coupling between the two spins, each line splits symmetrically into two giving two ‘doublets.’ i.e. b). The splitting of the two lines is the coupling constant J_{12} and the two lines of the doublet can be thought of as either spin ‘up’ or ‘down’ states, indicated by the open headed arrows above the peaks. Image based on a figure in (Keeler, 2005).

2.2.3 Experimental Aspects of NMR Spectroscopy

The previous section [2.2.2] discussed the some of the theory and terminology of NMR spectroscopy; this section will now outline the essential aspects of NMR spectroscopic experiments using some of the terms introduced previously.

In the vast majority of protein NMR spectroscopy experiments, especially the more complex multi-dimensional experiments, an NMR sample of a protein with isotope labelling is required to enable ^{13}C and ^{15}N nuclei to be detected. This isotope labelling of proteins helps to circumvent the fundamental problems of protein NMR i.e. signal overlap and line broadening, as it allows more than just ^1H nuclei to be used; hence, increasing the number of dimensions that can be used to acquire the data. The methods for uniform or selective labelling of a protein with either ^2H , ^{13}C and/or ^{15}N isotopes have become well established in the past 20 years (Lian and Middleton, 2001).

An NMR spectrometer consists of a number of components (Figure 2.11a) and the roles and effects of a number of these constituents are now discussed in this section in more detail. The intense, stable and homogenous magnetic field discussed previously is produced by a superconducting magnet system (Figure 2.11b). The magnet consists of a superconducting coil immersed in liquid helium, in a dewar surrounded by a thermal radiation shield, a vacuum space and an outer dewar filled with liquid nitrogen. Obviously it is not desirable for the sample under investigation by NMR spectroscopy to be placed at liquid helium temperature and so, a room-temperature bore of the magnet is created; this is accessible to the outside world, centred on the z-axis of the coil and houses the room temperature shim coils and probe.

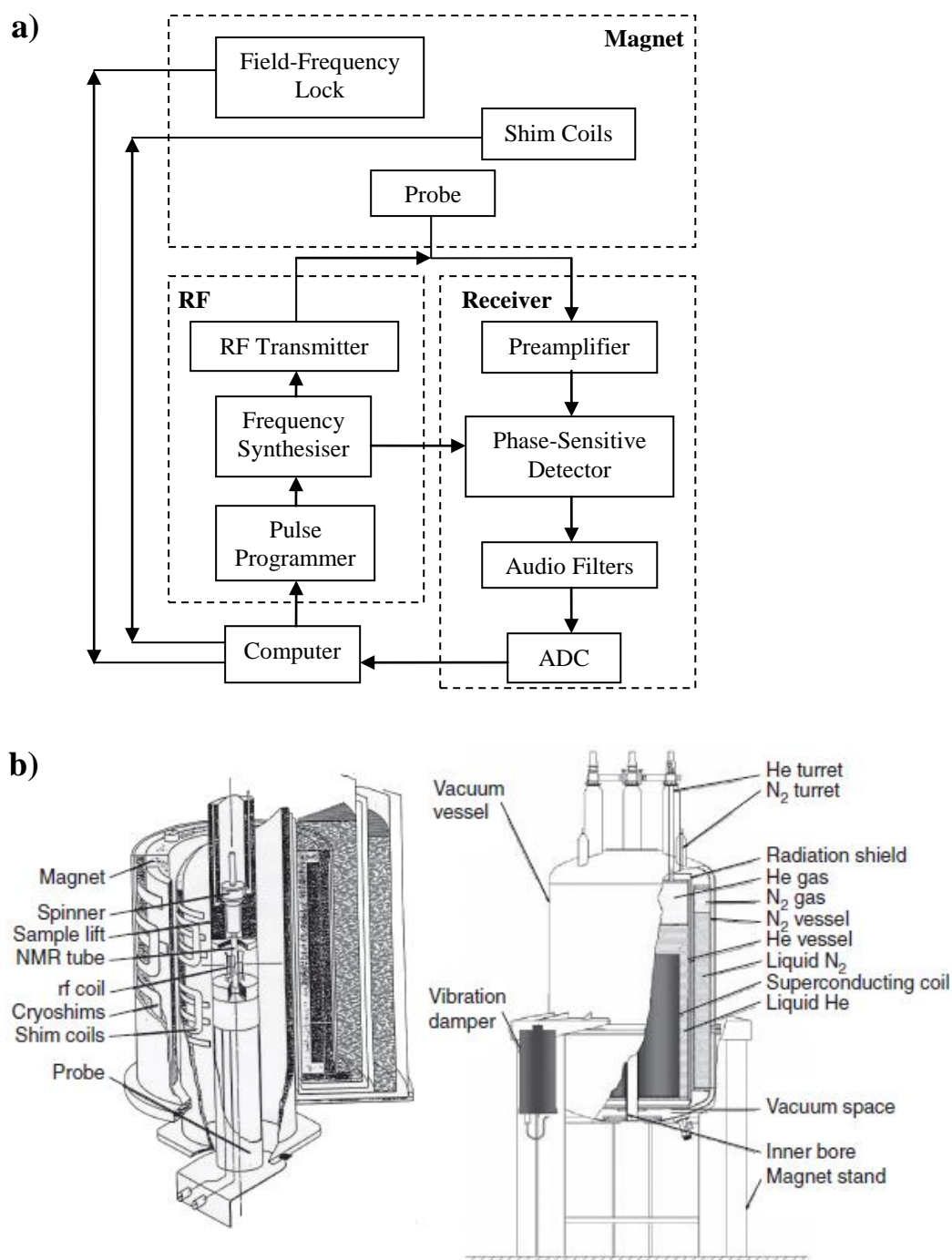


Figure 2.11: a) A block diagram of the NMR spectrometer, divided into four distinct components: the magnet, RF electronics, receiver and computer; the major subsystems of each component have been indicated. Image based on a figure in (Cavanagh, 2007). b) A cutaway diagram of a superconducting magnet illustrating how the probe, sample spinner and room-temperature shim coils are positioned coaxially in the room temperature bore of the magnet. The solenoid and cryoshim coils are immersed in liquid helium, with the helium dewar surrounded by a thermal radiation shield, vacuum space and liquid nitrogen dewar. Image taken from (Cavanagh, 2007), courtesy of Bruker Instruments, inc.

The field-frequency lock is a feedback system designed to keep the magnetic field at a steady value, by compensating for any small drift in magnetic field. The lock circuitry is essentially a specifically tuned (usually to the ^2H NMR signal in D_2O for

biological samples) NMR spectrometer that operates in parallel to the main spectrometer. The probe is a cylindrical metal tube that is inserted into the bore of the magnet, with the coil used to both excite and detect the NMR signal, held in proximity to where the NMR sample will be placed. The coil is connected in parallel with a capacitor to form a ‘tuned circuit’ and to ensure the best sensitivity possible, it is important that the tuned circuit is resonant at the Larmor frequency i.e. ‘tune the probe.’

The RF transmitter is the part of the spectrometer responsible for producing pulses of highly monochromatic RF electromagnetic radiation with defined phases and amplitudes (Figure 2.12). The pulse programmer executes the explicit pulse programme for the given NMR experiment by controlling the timing, duration, amplitudes and phases of the RF pulses produced by the RF transmitter.

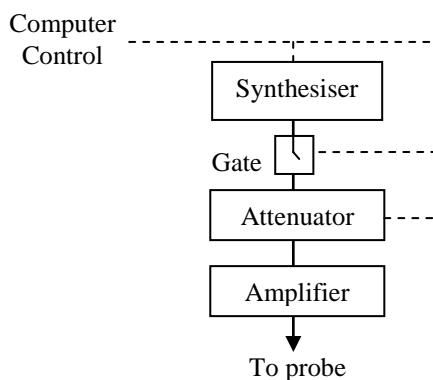


Figure 2.12: An overview of a typical arrangement of the RF transmitter where the source of the RF, the synthesiser produces a low level output that is fed to an attenuator and then onto a high-power amplifier, via a gate. The gate is used to switch on the RF power when required, with the attenuator used to vary the input to the amplifier and all the components of the RF transmitter are under computer control. Image based on a figure in (Keeler, 2005).

The NMR signal detected by the probe is very small and so, needs to be amplified with the minimum level of noise introduced; this process is performed by the pre-amplifier of the receiver. The phase-sensitive detector then performs quadrature detection of the signal (Figure 2.13) and reduces the amount of noise aliased into the spectrum using audio filters; quadrature detection is the generation of two orthogonal components from the NMR signal. An analogue to digital converter (ADC) then

converts the amplified analogue signal to a binary number, which is recorded and can be stored in computer memory. The digitisation process carried out by the ADC involves the sampling of the signal at regular intervals to give a good approximation of the smoothly varying signal (Figures 2.14a & b). The orthogonal components produced by quadrature detection are digitised separately and become the real and imaginary parts of the complex time-domain signal.

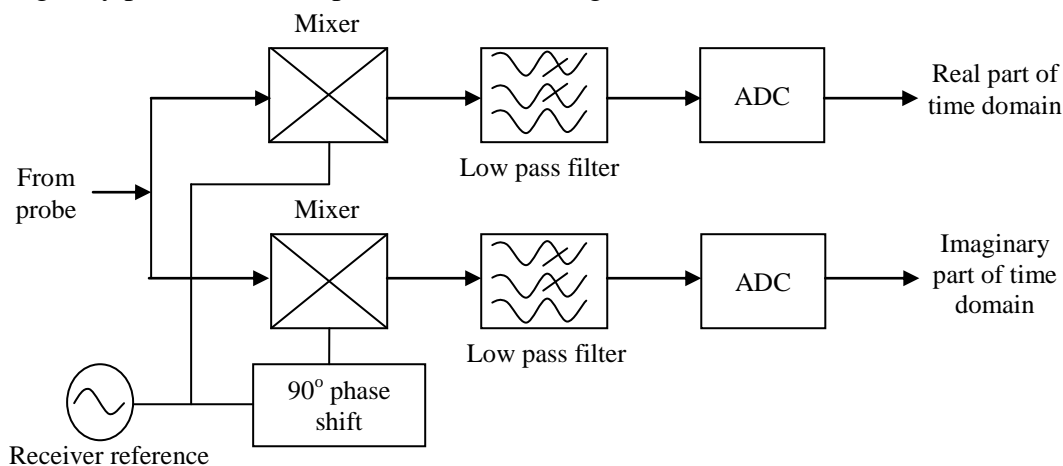


Figure 2.13: A schematic overview of the arrangement used in the quadrature detection process, where the receiver reference reaching one of the two mixers has been 90° phase shifted and results in orthogonal components of transverse magnetisation. The respective low-frequency difference signal from the post-mixer filter is digitised and can be stored in computer memory as real and imaginary parts of the time domain. Image based on a figure in (Keeler, 2005).

As the NMR signal is now represented as a discrete sampling sequence in digital form, powerful processing techniques can be applied to extract the information content of the signal. The most commonly used approach to convert from the time-domain signal to a frequency-domain signal is by applying a Fourier transform (Figure 2.14c).

The Fourier transform essentially works by multiplying the FID with a number of trial cosine functions of known frequency to give a product function. The NMR spectrum is then generated by plotting the area under the product function against the frequency of the corresponding trial cosine wave (Figure 2.15). Fourier transform of the exponentially decaying time-domain signal gives a complex frequency-domain signal, whose real and imaginary parts have absorption and desorption mode

Lorentzian lineshapes respectively (Figure 2.16).

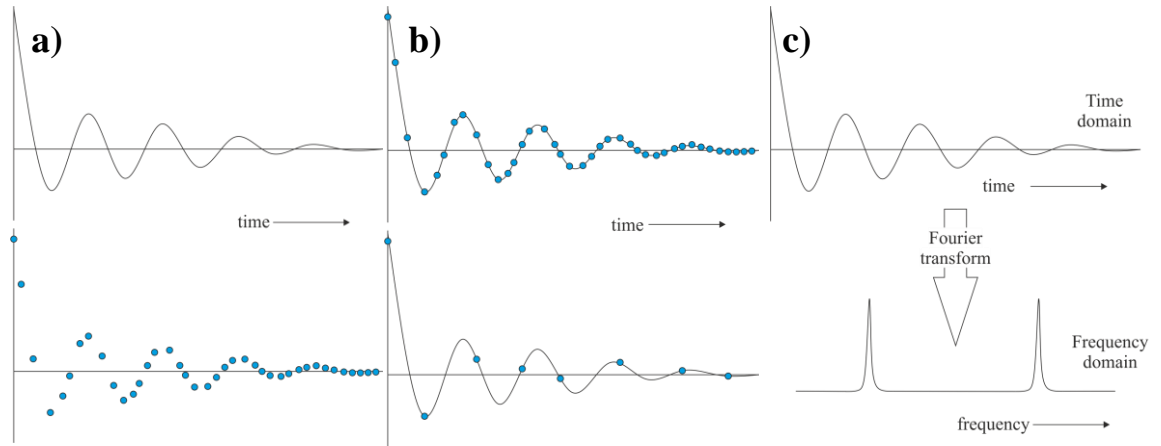


Figure 2.14: a) The amplitude of the free-induction decay (FID) varies smoothly as a function of time (top) and the subsequent digital version of the same FID (bottom). b) An illustration of the effect of the sampling rate on the representation of the FID; (top) the data points are a good representation of the signal (shown by the continuous line), whereas (bottom) the points are too widely separated and thus, are a poor representation of the signal. c) The conversion of a time-domain signal to a frequency-domain signal by the mathematical process of Fourier transformation, to give the familiar NMR spectrum. Images based on figures in (Keeler, 2005).

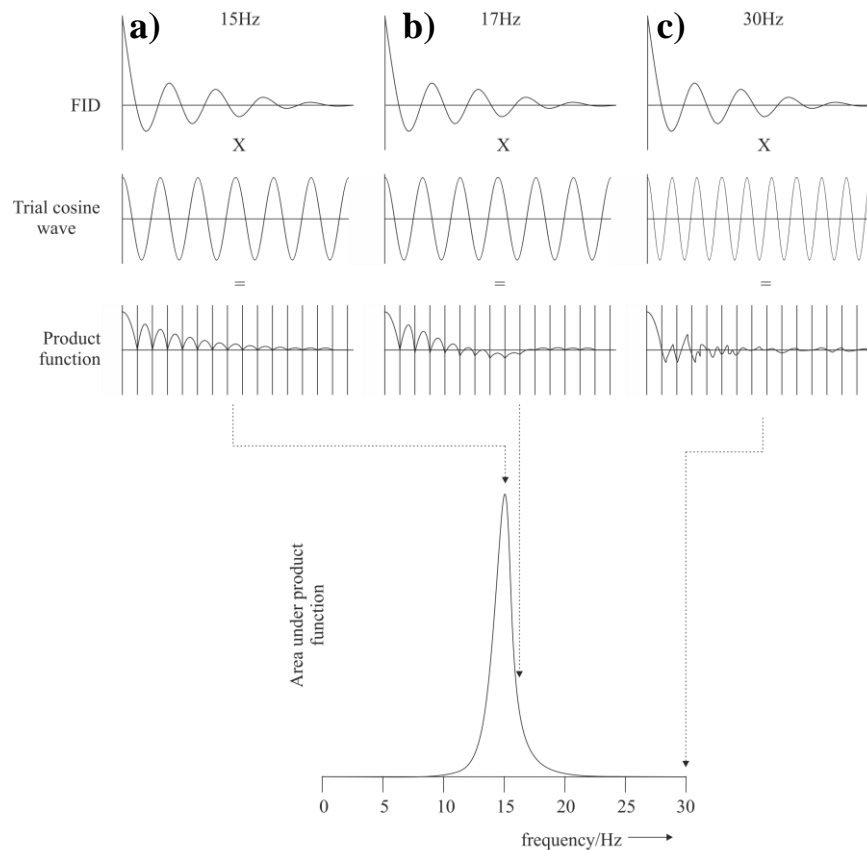


Figure 2.15: An overview of how the Fourier transformation process works. The FID is multiplied by trial cosine waves of known frequency to give a product function and the final spectrum is produced by plotting the area under the product function against the frequency of the corresponding trial cosine wave. In this example, the trial cosine wave of a) at 15 Hz matches the oscillations of the FID exactly, as a result the product function area is always positive and the area under this frequency is a maximum. b) at 17 Hz gives a positive area but not as large as a) due to negative excursions in its product function and c) at 30 Hz oscillates rapidly so the area under the product function and hence, the intensity in the spectrum is essentially zero. Image based on a figure in (Keeler, 2005).

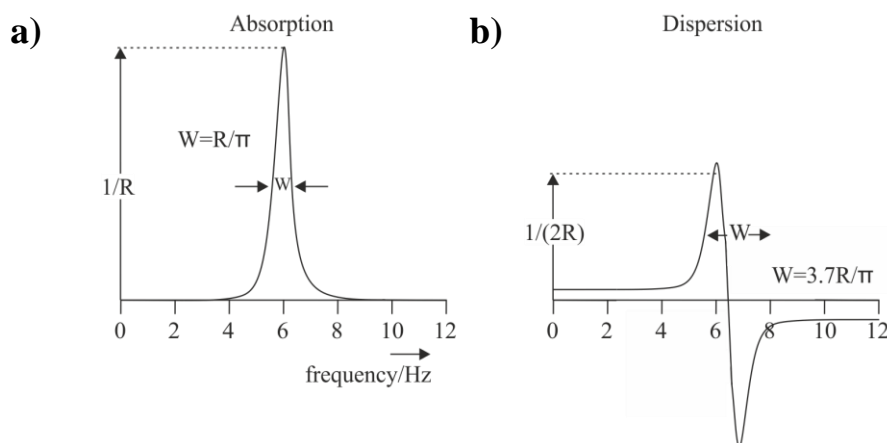


Figure 2.16: Fourier transformation of an exponentially decaying time-domain results in a complex frequency-domain signal, where the real and imaginary parts have adsorption (a) and desorption (b) lineshapes respectively; the width (W , at half height) has been indicated, where R is the decay constant. The dispersion lineshape is considerably broader (3.7 times) than the absorption lineshape and contains both positive and negative parts c.f. absorption lineshape which is always positive. Image based on a figure in (Keeler, 2005).

Prior to Fourier transform, it is possible to perform mathematical manipulations of the FID to enhance the signal-to-noise ratio. These manipulations include the application of weighting functions, zero filling and many others, however due to space constraints, these will not be discussed in any further detail. There also alternative methods for FID processing to Fourier transformation i.e. linear prediction but these will not be elaborated upon further in this chapter either.

A key experimental aspect of protein NMR spectroscopy is the different pulse techniques that can be employed and the specific ordering of the pulses (pulse sequence), to obtain the optimal results. A number of the basic pulse techniques are detailed in this section.

The simplest pulse to deal with is when the transmitter frequency (ω_{tx}) is the same as the Larmor frequency (ω_0) and thus, gives rise to the precession frequency about the B_1 field (ω_1); this is called an on-resonance pulse. When an on-resonance pulse is applied, rotation of equilibrium magnetisation occurs about a specified axis and the amount of rotation is called flip angle of the pulse (β); with an on-resonant pulse, the nuclei will respond ideally i.e. as described in [2.2.2]. The most commonly used flip

angles are 90° and 180° and different phases of pulse rotate the equilibrium magnetisation about different axis (x , $-x$, y or $-y$) (Figure 2.17).

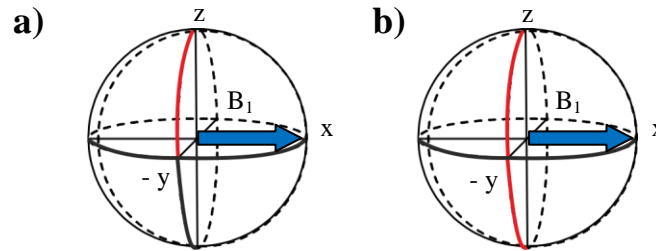


Figure 2.17: A three-dimensional representation of the motion of the magnetisation vector during an on-resonance pulse, the red line follows the tip of the vector from its assumed starting point on the $+z$ -axis. The effective field is the same as the B_1 field and lies along the x -axis with the magnetisation therefore precessing in the yz -plane. The rotation of magnetisation is in a positive sense about x and so the magnetisation ends up along a) the $-y$ -axis (90° pulse flip angle) or b) the $-z$ -axis (180° pulse flip angle). Image based on figure in (Keeler, 2005).

With several different resonances in the protein NMR sample, it is not possible to be on-resonance with all the lines in the spectrum. However, if a pulse is applied which allows $\omega_1 \gg \Omega$, the equilibrium magnetisation vector for a range of resonances will behave as if it were on-resonance; this type of pulse is called a hard pulse or non-selective pulse. A non-selective pulse is employed in the simple pulse-acquire experiment and if the pulse sequence for this experiment is analysed, it illustrates that all the key components of an NMR experiment are now known (Figure 2.18a). The most famous NMR experiment, the ‘spin echo,’ is composed of two hard pulses (90° (x) and 180° (x)) and is a component of a large number of much more complex protein NMR experiments (Figure 2.18b).

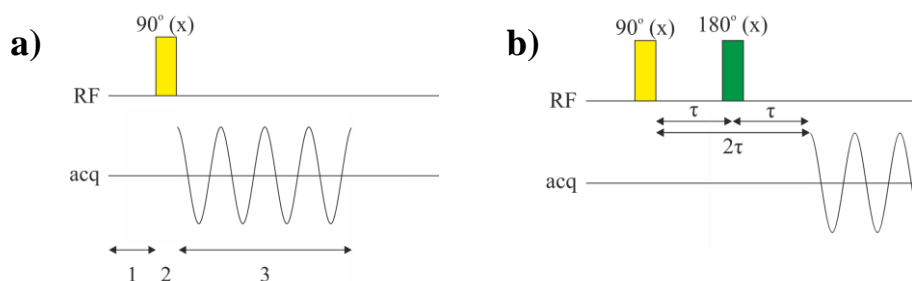


Figure 2.18: The timing diagram (pulse sequence) for the a) simple pulse-acquire NMR experiment and b) the ‘spin echo’ NMR experiment, where the line labelled ‘RF’ shows the location of the radiofrequency pulses and ‘acq’ shows when the signal is recorded (acquired). The different 90° and 180° pulses are indicated by yellow and green rectangles respectively. The pulse-acquire experiment can be divided into three sections, with the 180° pulse in the spin echo experiment in the centre of a 2τ delay between the 90° pulse and acquisition. Images based on figures in (Keeler, 2005).

An example of an NMR experiment based on the 'spin echo' experiment is the insensitive nuclei enhanced by polarisation transfer (INEPT) NMR experiment (Figure 2.19a); this experiment enhances signals observed from a low gyromagnetic ratio nucleus by transferring it to the larger equilibrium magnetisation of a high gyromagnetic ratio nucleus. Typically, the high gyromagnetic ratio nucleus is hydrogen and this magnetisation is transferred to nuclei, such as ^{13}C or ^{15}N ; thus, the INEPT experiment forms the basis of heteronuclear correlation experiments such as the heteronuclear single-quantum correlation (HSQC) experiment (Figure 2.19b). The HSQC is widely used for recording one-bond correlation spectra between ^1H and ^{15}N or ^{13}C , it is arguably the most useful experiment in protein NMR spectroscopy and its pulse sequence is the building block on which numerous three-dimensional experiments are derived; the described NMR experiments will not be discussed in any more detail here however.

To obtain the maximum intensity in NMR experiments, it is necessary to perform a preliminary pulse calibration; this process involves using a version of the simple pulse-acquire experiment i.e. contains a hard pulse (Figure 2.20). In this experiment, the flip angle (β) of the pulse is augmented by increasing the pulse length until it reaches zero; this flip angle is then 180° and thus, a 90° pulse is half the length of the 180° pulse.

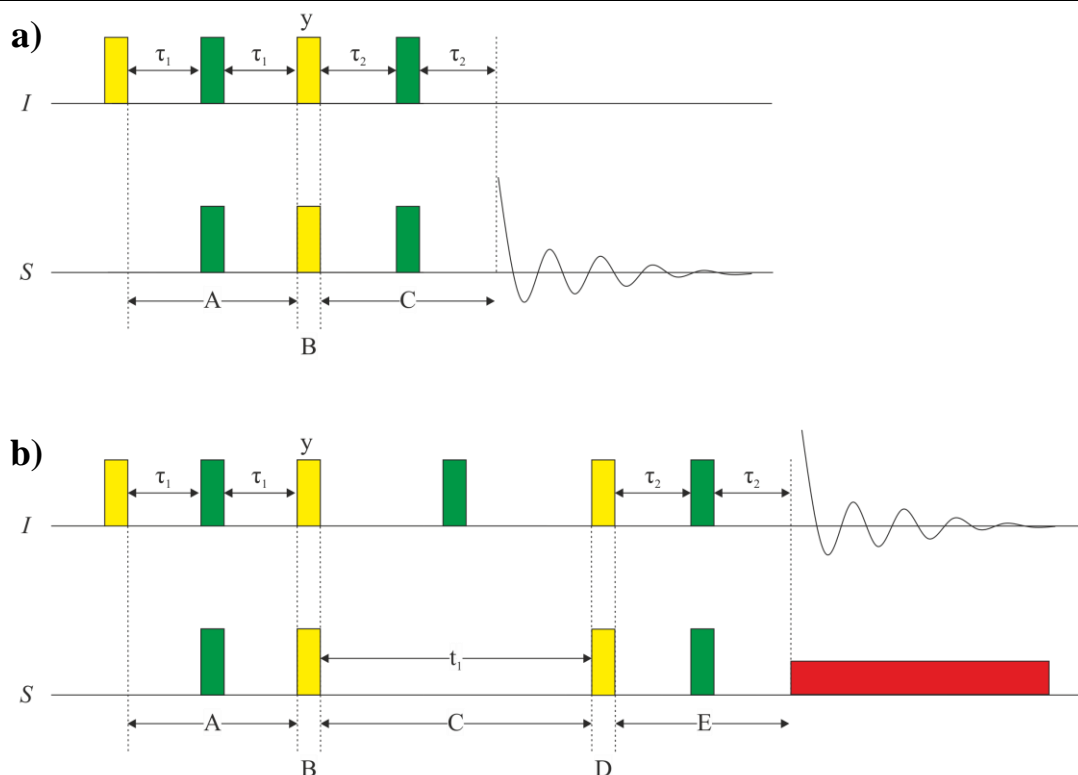


Figure 2.19: a) and b) The pulse sequences of the INEPT and HSQC NMR experiments, where the 90° and 180° pulses are denoted as yellow and green rectangles respectively; I and S denote the two different spins of the proton and heteronucleus i.e. ^{15}N respectively. a) The INEPT experiment results in an observable signal on the S spin, with the size of this signal depending on the equilibrium magnetisation of the I spin. By choosing, the I spin to have a higher gyromagnetic ratio than the S spin, the signal observed on the S spin is larger than it would be for a simple pulse-acquire experiment on the same spin. In the experiment, an anti-phase state is generated on the I spin during period **A**, this is transferred to S during period **B** and during period **C**, the anti-phase state evolves into an in-phase state and is then observed. b) The HSQC starts with an INEPT-like sequence during periods **A** and **B** and then the S spin magnetisation evolves for t_1 , with the centrally placed I spin 180° pulse refocusing the evolution of the coupling. The magnetisation is transferred back to the I spin, a spin echo period **E** allows the anti-phase signals to become in-phase and observed using broadband S spin decoupling (red rectangle). Images based on figures in (Keeler, 2005).

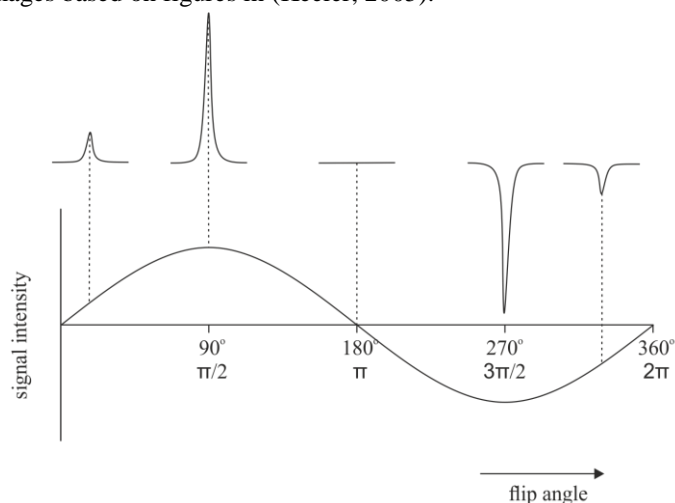


Figure 2.20: A depiction of how pulse calibration is achieved by varying the flip angle of the pulse, β ; as shown by the graph, the signal intensity in this experiment is proportional to $\sin\beta$. Above the graph are the expected signal intensities at various different flip angles, where a maximum is reached at a flip angle of 90° and null at 180° or 360° . Pulse calibration is achieved by increasing the duration of the pulse until the signal goes to a null i.e. 180° or 360° and dividing the resultant pulse length by two or four to give the 90° pulse length i.e. the maximum. Image based on a figure in (Keeler, 2005).

The pulses described in this chapter so far have either been on-resonance or the RF field strength is large compared to the offset. However, there are cases in NMR spectroscopy where i.e. off-resonance effects occur i.e. when $\omega_0 \neq \omega_{tx}$ and the offset (Ω) becomes comparable in size to the RF field strength (ω_1); this can both be a problem and advantageously exploited in protein NMR spectroscopy. This is problematic in NMR spectroscopy because as the offset becomes comparable with RF field strength, the effective field moves up from the x-axis towards the z-axis (assuming the offset is positive (Figure 2.21)). The result of these off-resonance effects is that the observed signal in the experiment is much weaker as less transverse magnetisation is generated and because x-magnetisation is generated, spectra with phase errors are produced.

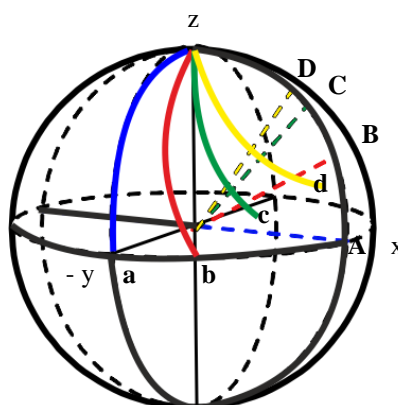


Figure 2.21: A three-dimensional representation of the path followed during an x pulse for various different resonance offsets. The different colour lines show the path followed by the tip of the magnetisation vector starting from +z-axis, with the duration chosen to give an on-resonance flip angle of 90° . Path a is the on-resonance case and b – d are for when the offset is 0.5 (i.e. $\Omega = \omega_1/2$), 1 and 1.5 times the RF field strength; the resultant effective field directions are indicated by the dashed line. Image based on a figure in (Keeler, 2005).

However, this effect also leads to the development of a pulse designed to excite just a small portion of the spectrum, such pulses are termed selective pulse or soft pulses (Figure 2.22). This is achieved by making the transmitter on-resonance with the line (or middle of the multiplet) and then reducing the RF field strength until the degree of excitation of the rest of the spectrum is sufficiently small. A selective inversion pulse follows the same principle as a selective pulse but with the pulse lengthened to

ensure the flip angle is maintained. There are many other important pulse techniques i.e. adiabatic, shaped, phase-modulated and composite, however these will not be discussed in this chapter.

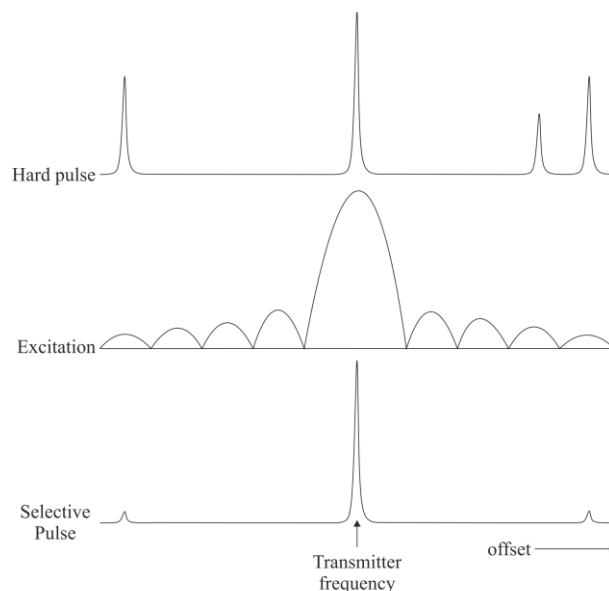


Figure 2.22: The selective excitation of just one line in an NMR spectrum using a selective or soft pulse. The top spectrum is the spectrum that would be expected from a hard pulse, however, if the transmitter is placed on-resonance with the desired line/region of spectrum (in this example, the central line), then the excitation pattern shown in the middle will result. This causes the other peaks to be attenuated and thus, the bottom spectrum will be obtained; the extent to which the off-resonance peaks are excited is dependent on the strength and duration of the pulse. Image based on a figure in (Keeler, 2005).

As the majority of studies of biological macromolecules by high-resolution protein NMR spectroscopy take place in aqueous solutions, the ^1H nuclei in water are in extreme excess to the macromolecules ($\sim 110\text{M}$ c.f. $0.1 - 2\text{mM}$). Thus, detection of the macromolecule signal in the presence of the solvent signal is a difficult problem but one that can be overcome by water suppression techniques or by using D_2O as the solvent. The incorporation of a water suppression technique in an NMR experiment is important to obtaining high quality spectra in protein NMR spectroscopy but the different techniques for this will not be discussed in this thesis.

A final experimental aspect of NMR spectroscopy is the phenomenon of relaxation; this is the process of the bulk magnetisation returning to its equilibrium position over time. Relaxation is unusually slow ($\mu\text{s} - \text{s}$) in NMR spectroscopy, compared to other

energy levels and this rate is determined by molecular properties such as shape and motion. This slow relaxation can be advantageous as it allows the transverse magnetisation to survive for long enough to be observed and it means that the FID persists for long enough to obtain high resolution spectra i.e. narrow linewidths. The disadvantage of slow relaxation is that it sets a lower limit on the repetition rate of a pulse, as equilibrium magnetisation needs to be re-established between pulses. The effects of relaxation are reasonably straightforward but understanding its origins and motion-dependence is a lot more complicated; neither of these relaxation topics will be discussed further but the important application of relaxation phenomena in the nuclear Overhauser effect (NOE) is included.

The NOE is due to a dipolar interaction between two spins in close proximity which causes relaxation-induced energy level transitions to occur, these transition leads to dipolar relaxation between the two spins and this effect is termed cross-relaxation. The differential equation of the rate of change of z-magnetisation (Equation 2.8) states that if the z-magnetisation of spin 1 is being affected by the z-magnetisation of spin 2, the cross-relaxation constant (σ_{12}) will have a non-zero value and thus, cross-relaxation must be occurring. As σ_{12} is proportional to b^2 (Equation 2.9), the distance-dependence of the cross-relaxation rate goes as $1/r^6$ and hence, the distance between two spins must be $<6\text{\AA}$ to be observed experimentally. The NOE is used in protein nuclear Overhauser effect spectroscopy (NOESY) NMR experiments to determine protons that are close in space; these could be intra-protein, intra-ligand or intermolecular between protein and ligand.

$$\frac{dI_z}{dt} = -R_z^{(1)}(I_{1z} - I_{1z}^0) - \sigma_{12}(I_{2z} - I_{2z}^0) \quad \text{Equation [2.8]}$$

$$\sigma_{12} = b^2 \frac{3}{10} j(2\omega_0) - b^2 \frac{1}{20} j(0) \quad \text{Equation [2.9]}$$

where, $b = \frac{\mu_0 \gamma_1 \gamma_2 \hbar}{4\pi r^3}$

2.2.4 Applications of NMR Spectroscopy

Protein NMR spectroscopy has many useful standard applications in structural biology ranging from determining if a particular protein is folded to deducing if there is an interaction between a protein and ligand. Two of the most important applications of protein NMR spectroscopy in structural biology are discussed briefly in this section.

2.2.4.1 Protein Structure Determination

Protein NMR spectroscopy is used to deduce the structure of an unbound protein or a bound protein-ligand complex by determining the individual protein residue resonance assignments and the corresponding structural distance restraints i.e. NOE, hydrogen bond etc. These are determined by performing 2-D and 3-D NMR experiments to give the desired spectra and then, using a spectral analysis software programme to assign the obtained spectra. The resultant assignments and restraints are then exported to a structure calculation programme to determine the structure. This whole process is discussed in more detail in chapters 3 & 4.

2.2.4.2 Characterisation of Intermolecular Interactions

Protein NMR spectroscopy can be used to obtain important information about the interaction between a protein and a ligand, where this information is not limited to simply whether a ligand binds to a protein or not. The exact residues that the ligand interacts with in the protein sequence can be deduced and hence, the ligand binding can be classified as specific or non-specific, if the binding site is known. More importantly, the specific binding site of a ligand to a protein can be determined by

protein NMR spectroscopy, as well as the binding affinity (K_D) of the ligand to the protein. As previously, the applications of protein NMR spectroscopy to the characterisation of intermolecular interactions are elaborated upon further in chapters 3 – 6.

2.3 Isothermal Titration Calorimetry (ITC)

(Freyer and Lewis, 2008, Jelesarov and Bosshard, 1999, Ladbury and Chowdhry, 1996, Leavitt and Freire, 2001, Sigurskjold, 2000)

2.3.1 Introduction to ITC

Calorimetry is the measurement of the heat change associated with a physical process i.e. chemical reaction, physical change. The instrument used to measure the heat change in this technique, the calorimeter, was one of the first scientific instruments reported in early literature. Black measured the heat capacity and latent heat of water in the 1760's (Black, 1803) and Lavoisier designed and employed an ice calorimeter to measure the metabolic heat produced by a guinea pig in the 1780's (Lavoisier and Laplace, 1780). It is interesting to note that the first calorimetric experiment performed was a biologically relevant measurement.

Titration calorimetry was first described as a method for the simultaneous determination of the equilibrium constant (K_{eq}) and enthalpy change (ΔH) for a reaction in the mid 1960's (Christen.Jj et al., 1968, Hansen et al., 1965). This method was originally applied to weak acid-base equilibria and metal ion complexation reactions; it wasn't until the late 1970's that titration calorimetry was used to study biological equilibria and until the late 1980's that the first commercially-available titration calorimeter for biological systems was developed (by MicroCal in 1989).

Isothermal titration calorimetry (ITC) employs a calorimeter where the temperature of both the sample of interest and the reference sample is kept at the same constant

value and hence, isothermal. ITC is a routinely used technique to directly characterise the thermodynamic and kinetic properties of a biological system; only the determination of thermodynamic parameters of binding between a protein (titrand) and ligand (titrant) is of relevance to this thesis and so, the introduction to ITC is tailored as such.

2.3.2 Advantages of ITC

ITC allows the direct measurement of the binding affinity and thermodynamic parameters i.e. enthalpy (ΔH) and entropy (ΔS) of a biological system. This is a label-free technique so spectroscopically silent materials, such as those with no chromophore/fluorophore/isotopic-labelling can still be utilised. ITC also facilitates the study of opaque/turbid solutions i.e. cell suspensions and can be carried out at a range of biologically relevant conditions i.e. different temperatures, pH values and salt concentrations. ITC is particularly advantageous over other spectroscopic techniques and equilibrium studies, where parameter values are indirectly obtained from the van't Hoff relationship; they are also expensive in both time and material terms. A single ITC experiment is used to determine the binding parameters for an interaction including ΔG and K_D and by repeating this same experiment at different temperatures it is possible to obtain the change in heat capacity of the binding (ΔC_p) for that interaction.

ITC can be used as a stand-alone biophysical technique or in conjunction with other biophysical techniques i.e. NMR spectroscopy, surface plasmon resonance (SPR) spectroscopy or analytical ultra-centrifugation (AUC), as a guide to binding affinity or as a comparison of reliability. ITC also has the possibility to validate structure-based computational predictions of binding by analysing the theoretical enthalpic and entropic contributions to the experimentally-determined values [2.3.4].

A historic problem associated with ITC was that, ITC experiments have upper/lower limits of binding affinity of $\sim 10\text{nM}$ and $\sim 1\text{mM}$ respectively. However, the development of competition (or ligand displacement) ITC experiments has led to binding parameter determination for very strong (or weak) binders. Complex systems involving multiple interacting or non-equivalent binding sites initially presented a problem; this was overcome by statistical thermodynamic treatment of obtained data and now deconvolution of isotherms of complex systems is becoming standard.

2.3.3 Instrumentation and Experimental Overview

There are a wide range of ITC calorimeters commercially available and each of these employ different temperature change detection and/or mixing techniques in the ITC experiment. An iTC200 Microcalorimeter (GE Healthcare, Figure 2.23a) was the only calorimeter used in this thesis and so, for the purposes of this brief overview it will be the only calorimeter discussed. The simplistic representation of the calorimeter (Figure 2.23b) shows that it consists of two cells; a reference cell containing water or buffer and a sample cell containing the titrand, into which the titrant is added. The titrant is added to the sample cell in a series of injections by a precision syringe driven by a computer-controlled motor; this means that the solution is constantly stirred to ensure thorough and rapid mixing of titrand and titrant throughout the experiment. There is a specified time delay between sequential injections, which is manipulated to a sufficient length of time that it allows the incidental heat change of each injection to return to baseline before the next injection. The shown calorimeter is a power-compensation calorimeter, this means that it measures the amount of power required to be applied (or removed) to maintain the same temperature in the sample cell as that in the reference cell at each injection point.

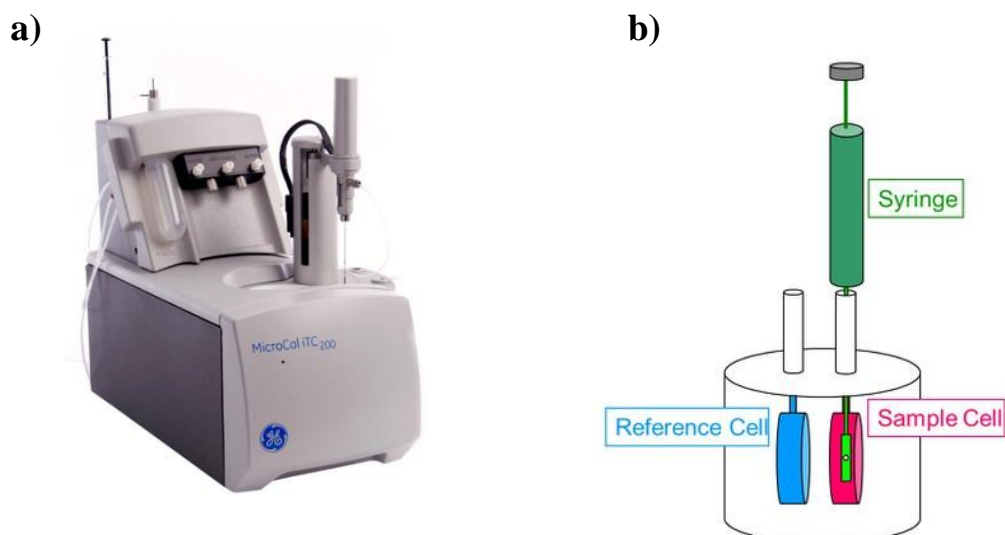


Figure 2.23: a) The iTC200 Microcalorimeter (GE Healthcare) that all ITC related-research described in this thesis was performed on. Image courtesy of GE Healthcare. b) A simplistic overview of an isothermal titration calorimeter; this instrument consists of three parts: a reference cell containing buffer or water, a sample cell containing the titrand and into which the titrant is added. The final component is the computer-controlled syringe containing the titrant; the syringe titrates the titrand in a series of sequential injections with stirring throughout, to ensure good mixing. The calorimeter shown here is a power-compensation calorimeter, this means that it measures the amount of power required to be applied (or removed) to maintain the same temperature in the sample cell as that in the reference cell, at each injection point. Image taken from <http://www.huck.psu.edu/>.

When planning an ITC experiment it is important to determine the optimum conditions in which to carry out the experiment, with possibly the most rational being the desired starting titrand and titrant concentrations. These concentrations must result in a heat change that is both measurable and that varies for subsequent injections, to produce a curved isotherm (Figure 2.24). The first condition is an obvious requirement but the second is more problematic and involves the calculation of Brandt's parameter, c (Equation 2.10).

$$c = [M] \times K \quad \text{Equation [2.10]}$$

where, $[M]$ is the starting titrand concentration and K is the equilibrium constant.

This relationship shows that some prior knowledge or an estimation of the possible equilibrium constant value is required when planning the ITC experiment; c should be between 10 and 100 to obtain accurate binding affinity (K_D) values. The starting concentrations of the samples used in planning the ITC experiment is not the only consideration prior to performing an ITC experiment that should be taken into

account; there are also the effects that pH, temperature, buffer and salt concentration could have on the interaction being investigated. Finally, both starting samples should be thoroughly buffer exchanged and degassed prior to use to avoid artefact heat changes, such as mixing or dilution effects.

2.3.4 Analysis of Experimental Data

At the conclusion of an ITC experiment, raw data is obtained (top, Figure 2.24) and this data may need to be corrected because after saturation, some small non-specific effects may be seen i.e. ligand dilution, solute mismatch. However, if the initial samples are well dialysed, these effects are virtually negligible and can often be omitted. The raw data is then analysed using a curve fitting process in which a non-linear regression procedure is used to fit a model to the data in an iterative process; the model is a mathematical description of the particular process (biological, chemical or physical) being studied. In terms of the protein-ligand binding experiments detailed in this thesis, the model is formed from equilibrium constant and mass balance equations. The output of this analysis is an isotherm (bottom, Figure 2.24) along with the 'best-fit' values of the binding parameters i.e. n , K_D , ΔH and ΔS . The (derivation of and the actual) mathematical equations used in this data analysis methodology will not be discussed here but can be found elsewhere (Freyer and Lewis, 2008, Jelesarov and Bosshard, 1999); however, the implications of the obtained parameter values on the binding process will be discussed.

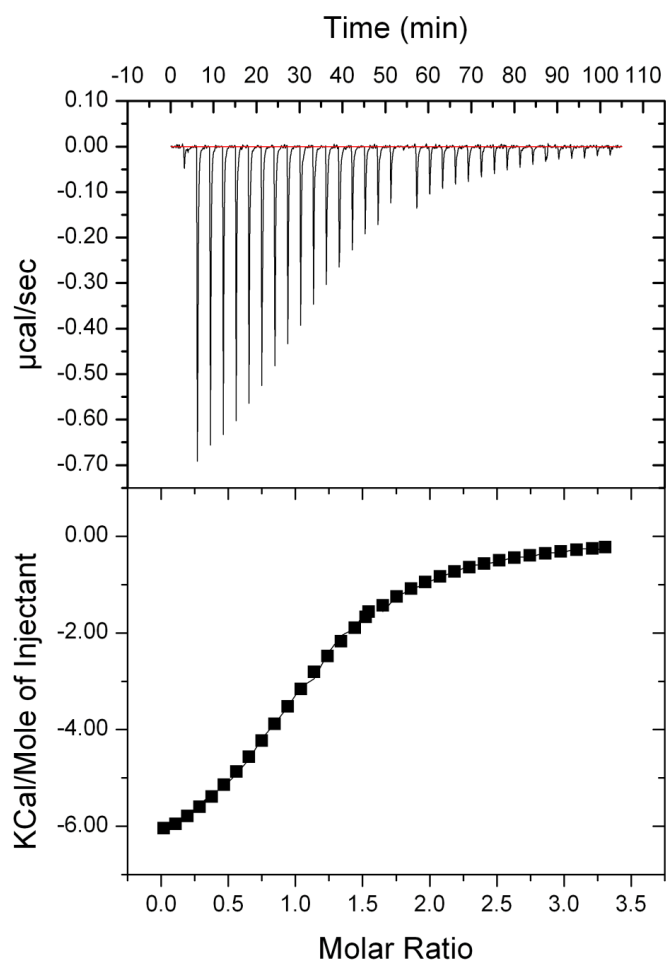


Figure 2.24: An example of the final ITC figure produced from the binding interaction between a protein (titrand) and a peptide (titrant) in 20mM phosphate, pH6.3, on an iTC₂₀₀ Microcalorimeter (MicroCal) at 298K. The isotherm produced by the ITC binding experiment can be seen (top), this data was then fitted to a single set of sites curve-fitting model, using Origin7 to give the curve shown (bottom). It is from this curve that all the thermodynamic parameters of the binding interaction can be determined i.e. stoichiometry, affinity, change in enthalpy/entropy and Gibbs free energy.

The values obtained from an individual ITC experiment of n and K_D give quantitative information about a binding process but not much qualitative information. By analysing the values of the thermodynamic parameters (ΔH and ΔS), it is possible to gain a more in-depth understanding of the processes that are on-going and hence, important to binding affinity of a particular interaction.

ΔH and ΔS are the enthalpy and entropy changes, respectively, between the free and bound forms of titrand and titrant. The formation or destruction of intermolecular interactions/bonds during binding is an important contribution to ΔH ; ΔH is more

negative and hence, more favourable for an interaction as the ratio of interactions formed : interactions broken increases. On the other hand, the addition or removal of water from an apolar surface is a significant contributor to the ΔS value; ΔS is more positive and hence, more favourable for an interaction as the amount of water molecules displaced increases or when conformational entropy is lost upon binding. Solute-solute dispersion interactions (Homans, 2007) and changes in internal dynamics (Tzeng and Kalodimos, 2012) upon ligand binding are also important contributors to any change in enthalpy and/or entropy observed, especially if the binding pocket is suboptimally hydrated. The binding between a titrand and a titrant can be classified as enthalpically- or entropically-driven depending on the magnitude of the values obtained from the ITC experiment. The knowledge of whether a particular interaction is enthalpically- or entropically-driven is extremely important for a variety of reasons i.e. it can be used to guide inhibitor design.

2.3.5 Applications of ITC

ITC has been used in a wide variety of biological investigations ranging from determining the stability, stoichiometry and specificity of biological systems, to elucidating the effects of co-solvents and denaturants on biological systems. As a result, ITC is becoming extremely useful in the drug design process and as the sensitivity of the instrument increases further then ITC will become even more important. ITC has been used in fragment-based drug discovery approaches where lead compounds have been developed from ITC fragment-based binding screening experiments. ITC has also been employed to determine the effect of protonisation on binding, which has led to different ionisable groups being developed to increase bioavailability of drug compounds.

Chapter 3
MATERIALS AND METHODS

3. MATERIALS AND METHODS

3.1 Materials

3.1.1 Water

The methods described in this chapter required at least de-ionised, distilled quality water; this was provided by the Institute of Integrative Biology, University of Liverpool and is be termed as RO water in this chapter. For the molecular biology methods detailed in this chapter, ultra-pure quality water was required and this was obtained by use of a Synergy Water Purification System (Millipore) fitted with a SynergyPak®1 cartridge and a MilliPak-20 Express system; this water is termed as MilliQ in the methods discussed subsequently.

3.1.2 General Solvents

Ethanol: The Department of Chemistry Solvent Service, University of Liverpool

Methanol: Fisher Scientific

3.1.3 General Reagents

Unless otherwise stated, all reagents used in the methods detailed in this were of laboratory grade and supplied by Sigma-Aldrich.

3.1.4 General Equipment

The experimental methods in this chapter describe specific volumes of liquids but do not detail the corresponding tubes or flasks or tubes that contained these liquids to avoid repetition; Table 3.1 is a guide to the typical size of tube/flask that was used for a given volume of liquid:

Table 3.1: The particular vessel chosen for a given volume of liquid in the experimental methods described in this chapter.

Volume (mL)	Tube/Flask
<1.5	1.5mL Eppendorf®
$1.5 \leq x \leq 10$	30mL Sterilin®
$10 \leq x \leq 60$	250mL conical flask
$60 \leq x \leq 250$	1L conical flask
$250 \leq x \leq 500$	2L conical flask

3.1.5 General Experimental Considerations

A number of the methods subsequently detailed involve the use of substances that are potentially harmful to health but these hazards are not discussed or elaborated upon in the actual method; precaution needs to be taken in the handling of:

- Ethidium bromide – it is extremely mutagenic and carcinogenic and so, gloves and labcoat must be worn and used on/over an absorbent surface to capture any spills.
- Liquid nitrogen – this can cause cryogenic burns and is an asphyxiant and so, thick gloves and labcoat must be worn; liquid nitrogen must not be used in a small, confined space with no outside ventilation.
- Sodium azide – it is extremely toxic and so, gloves and labcoat must be worn.
- Acrylamide – it is extremely toxic and so, gloves and labcoat must be worn and used on/over an absorbent surface to capture any spills.
- Strong acids and bases – these can be very corrosive and give off noxious fumes and so, gloves and labcoat must be worn and work with strong acid or base must be conducted in a fume cupboard.
- Antibiotics – these can be very toxic depending on the particular antibiotic and so, gloves and labcoat must be worn.

3.1.6 Expression Vectors

There were two different expression vectors used in the protein production process, pETM-11 and pOPINS and these are detailed in Figure 3.1.

3.1.7 Bacterial Strains

The two different strains of *E.coli* used in the protein production process were:

- XL1 Blue Competent Cells (Agilent Technologies)
- BL21 (DE3) Competent Cells (Novagen®)

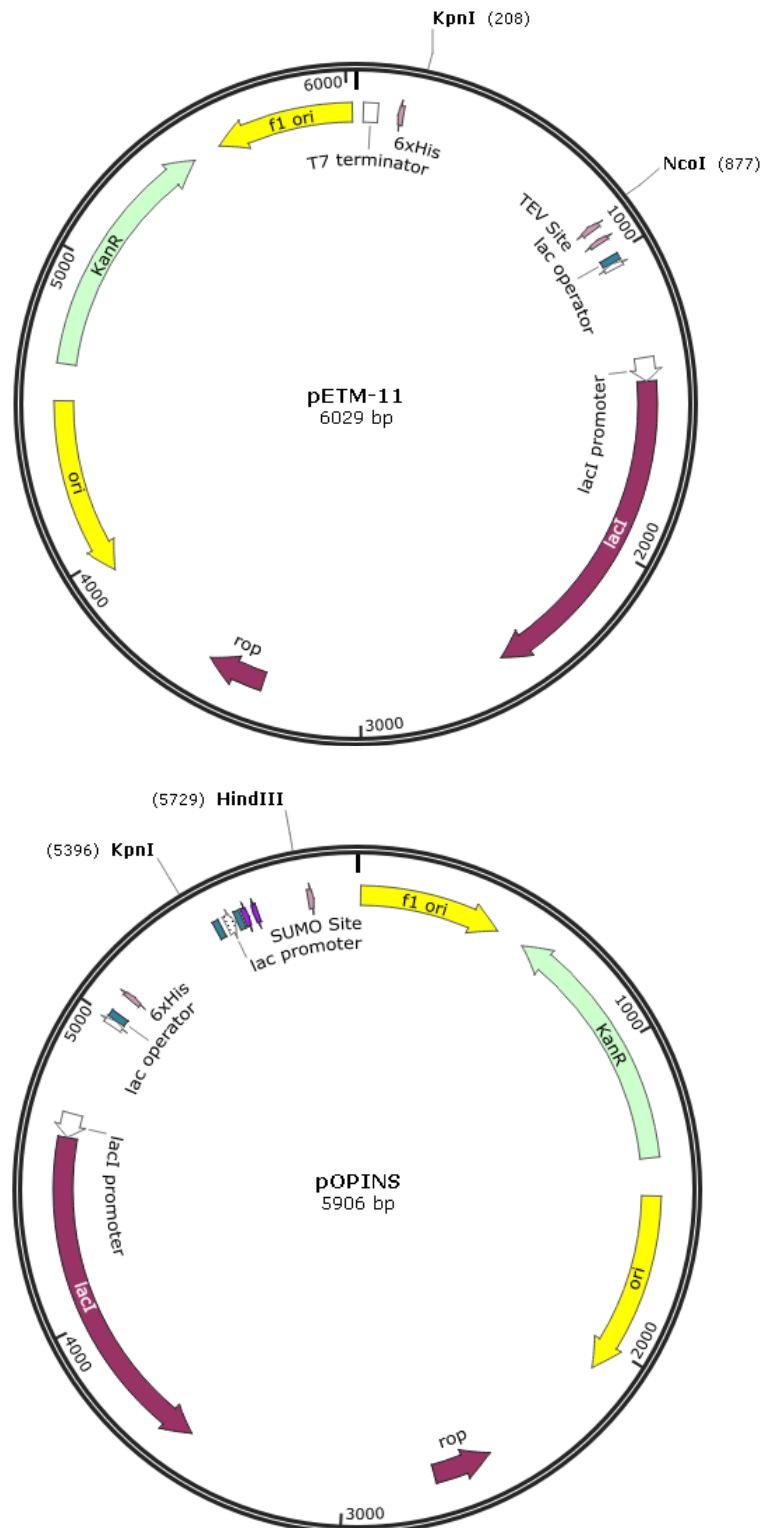


Figure 3.1: The maps of the two different expression vectors used in the protein production process, created with SnapGene® Viewer from the respective sequences – Top = pETM-11, Bottom = pOPINS. The restriction enzymes used in the preparation of the PDZ domain constructs utilised in the research in this thesis have been indicated, along with the positions of the respective vector they will cut at; the cleavage sites of the TEV and SUMO proteases used in the preparation of proteins from the pETM-11 and pOPINS vectors respectively have also been detailed; the T7 terminator feature of the pOPINS vector (5834-5881bp) has been hidden from the pOPINS vector map for this purpose. It can be seen that both the pETM-11 and pOPINS vectors are resistant to the antibiotic kanamycin.

3.1.8 Proteases

There were two different proteases used to cleave the hexahistidine Ni²⁺ affinity tag depending on the vector used, these were:

- Tobacco-etch virus (TEV) protease for proteins expressed in the pETM-11 vector
- Small ubiquitin-like modifier (SUMO) protease for proteins expressed in the pOPINS vector

3.1.9 Media Recipes

The recipes for the different growth media utilised in the methods in this chapter are:

Super Optimal Broth with Catabolite Repression (SOC) Medium

- Tryptone (20g, Fluka)
- Yeast extract (5g, Fluka)
- NaCl (10mM, Fisher Scientific)
- KCl (25mM, ProLabo)
- MgCl₂·6H₂O (10mM, BDH)
- pH to 7.0 in total volume of 200mL of RO water, autoclave and then add glucose (20mM, BDH)

Lysogeny Broth (LB)

- 25g of LB broth 'Miller' (Merck) per 1L of RO water

LB Agar

- 37g of LB agar 'Miller' (Merck) per 1L of RO water

Kanamycin-Selective LB

- LB containing kanamycin (32µg/mL, Melford)

Kanamycin-Selective LB Agar

- LB agar containing kanamycin (32µg/mL)

Minimal Medium Solution A (MM A)

- Na_2HPO_4 (88mM, ProLabo)
- KH_2PO_4 (55mM, Fisher Scientific)
- pH to 7.2 in total volume of 1L of RO water and autoclave

Minimal Medium Solution B (MM B)

- Thiamine.HCl (30 μ M, Duchefa Biochemie)
- $\text{CaCl}_2 \cdot 2\text{H}_2\text{O}$ (135 μ M)
- $\text{MgSO}_4 \cdot 7\text{H}_2\text{O}$ (1mM, Acros Organics)
- $^{15}\text{NH}_4\text{Cl}$ (20mM)
- (^{13}C) Glucose (20mM)
- In 10mL of MilliQ and syringe-filtered through a 0.22 μ M Millex® HA filter unit

Kanamycin-selective M9 Medium

- MM A
- MM B
- Kanamycin (32 μ g/mL)

3.1.10 Buffer Solutions

The components of the various different buffers included in the methods of this chapter are:

D-Buffer

- $\text{MgCl}_2 \cdot 6\text{H}_2\text{O}$ (20mM, BDH)
- Tris/HCl (20mM, Melford)
- DTT (5mM, Melford)
- pH 8.0

H-Buffer

- NaCl (150mM)
- Tris/HCl (25mM)
- EDTA (10mM)
- pH 8.0

50x TAE Buffer

- Tris base (2M, Fisher Scientific)
- Glacial acetic acid (5.71% (v/v))
- EDTA (5mM) at pH 8.0

4x Loading Buffer

- Tris/HCl (200mM)
- DTT (400mM)
- SDS (8% (w/v), Fisher Scientific)
- Bromophenol blue (0.4% (w/v))
- Glycerol (40% (v/v), Fisher Scientific)
- pH 6.8

His-Trap Buffer A

- Tris/HCl (50mM)
- NaCl (500mM)
- pH 7.5

His-Trap Buffer B

- Tris/HCl (50mM)
- NaCl (500mM)
- Imidazole (500mM, Fluka)
- pH 7.5

Gel Filtration Buffer

- Tris/HCl (50mM)
- NaCl (150mM)
- DTT (2mM)
- pH 7.4

15% Resolving Gel

- 30% Acrylamide (5mL)
- MilliQ (2.4mL)
- 1.5M Tris/HCl pH 8.8 (2.5mL)
- 10% (w/v) SDS (100 μ L)
- 10% (w/v) APS (75 μ L, BDH)
- TEMED (7.5 μ L)

4% Stacking Gel

- 30% Acrylamide (1.3mL)
- MilliQ (6.1mL)
- 0.5M Tris/HCl pH 6.8 (2.5mL)
- 10% (w/v) SDS (100 μ L)
- 10% (w/v) APS (75 μ L, BDH)
- TEMED (7.5 μ L)

2x Sample Buffer

- Tris/HCl (0.12mM)
- Glycerol (20% (v/v))
- SDS (4% (w/v))
- β -mercaptoethanol (10% (w/v))
- Bromophenol blue (0.004% (w/v)) and pH to 6.8

10x SDS-PAGE Running Buffer

- Tris/HCl (250mM)
- Glycine (1.92M, Fisher Scientific)
- SDS (1% (w/v))

Coomassie G250 Stain Solution

- Coomassie blue G250 (0.1% (w/v))
- MeOH (45% (v/v))
- MilliQ (44.9% (v/v))
- Acetic Acid (10% (v/v))

De-stain Solution

- MeOH (45% (v/v))
- MilliQ (45% (v/v))
- Acetic Acid (10% (v/v))

3.2 Methods

3.2.1 Molecular Biology Methods

3.2.1.1 Site-Directed Ligand Independent Mutagenesis (SLIM) of SAP97 PDZ2 WT to SAP97 PDZ2 H73G/T

3.2.1.1.1 Primer Design

SLIM is a novel PCR-mediated mutagenesis approach that utilised an inverse PCR amplification of the SAP97 PDZ2 template by two tailed long primers and two short primers in a single reaction (Figure 3.2) (Chiu et al., 2004). The tailed primers were designed to contain the desired mutation on complementary overhangs at the terminus of PCR products (Figure 3.3 & Table 3.2). The most naturally abundant 3-base code for the desired His to Gly and Thr mutations were determined using the Codon Usage Database (<http://www.kazusa.or.jp/codon/>); the primers were designed,

the suitability of their properties ensured by using the Promega BioMath Calculator (<http://www.promega.com/techserv/tools/biomath/calc11.htm>) and then ordered (Sigma-Aldrich).

3.2.1.1.2 Polymerase Chain Reaction (PCR)

A single PCR was performed for each SAP97 PDZ2 modification (including the wild type control) and consisted of the subsequent components in a PCR tube: 2.5 μ L of 10x Phusion[®] Reaction buffer (with 7.5mM MgCl₂, New England Biolabs), 200 μ M dNTP, 100mM betaine, 200nM of each of the primers, 0.5 μ L of the pETM-11 plasmid containing SAP97 PDZ2 WT template (final concentration of 1ng/ μ L), 2.5U of Phusion[®] Hot Start II High Fidelity DNA polymerase (New England Biolabs). The mixture was made up to a final volume of 25 μ L with MilliQ and the PCR tube transferred to a Mastercycler Personal (Eppendorf) for the PCR. The reactions were hot-started by heating to 95 $^{\circ}$ C for two minutes and then subjected to a further 29 cycles of 95 $^{\circ}$ C for 25s, 55 $^{\circ}$ C for 20s and 70 $^{\circ}$ C for 1 minute, with a 3.5 minute step on the last cycle at 68 $^{\circ}$ C for extension (Figure 3.2) (Chiu et al., 2004).

3.2.1.1.3 DpnI Digest of PCR Products

The PCR mixture was then subjected to a PCR clean up step using a GenElute[™] PCR Clean-Up kit (Sigma-Aldrich) to remove the excess primers, nucleotides, DNA polymerase, salts etc from the PCR amplification products; this yielded 50 μ L of the mixture in elution buffer. This was diluted with 5 μ L of D-buffer [3.1.10] plus 0.5 μ L DpnI (New England Biolabs) and this mixture was incubated at 37 $^{\circ}$ C for one hour. The DpnI digestion was terminated by the addition of 5 μ L of H-buffer [3.1.10]. The mixture was then denatured for three minutes at 99 $^{\circ}$ C and hybridisation was performed using two cycles of 65 $^{\circ}$ C for five minutes and 30 $^{\circ}$ C for 15 minutes. To

ensure that the SLIM procedure had been successful, agarose gel electrophoresis was carried out to visualise that the intact plasmid was at the correct molecular weight.

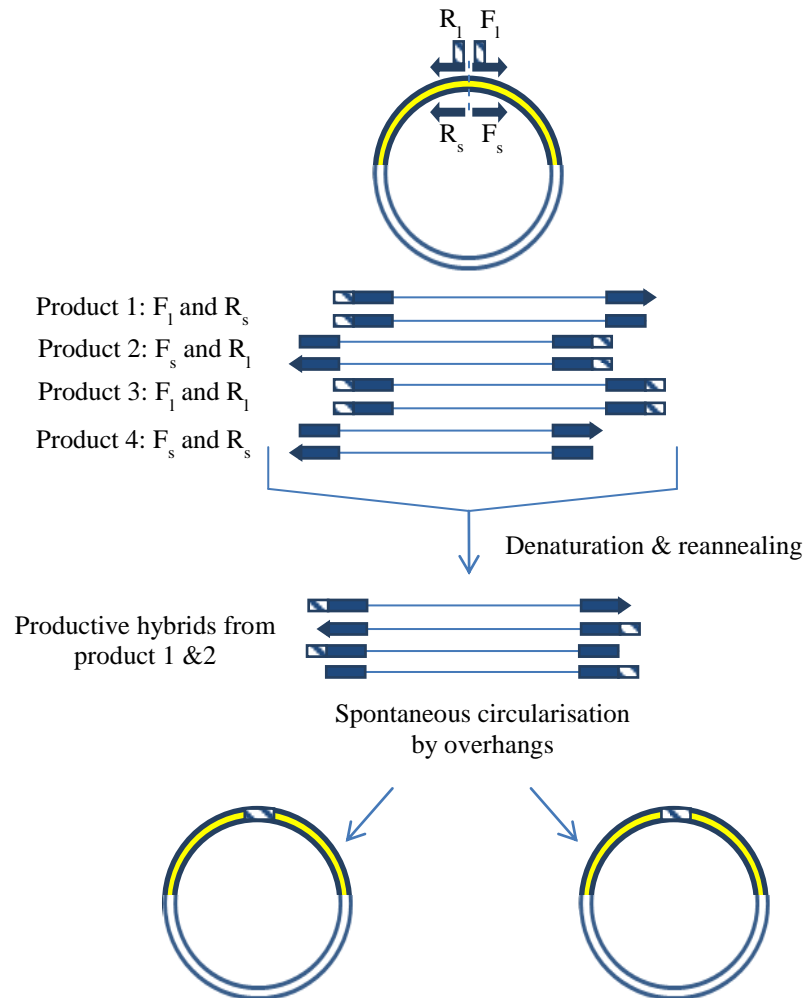


Figure 3.2: An overview of the SLIM procedure, where the specific designed primers are denoted by: F_1 = forward long, F_s = forward short, R_1 = reverse long and R_s = reverse short; the forward and reverse long contain the intended mutation. The designed primers used in the PCR reaction result in four different products possible and the subsequent denaturation and reannealing of these products forms hybrids of products 1 & 2 with complementary overhangs. These overhangs cause spontaneous circularisation to occur which results in the plasmid containing the desired mutation (blue and white stripes).

```

atagtgcgattatatgtgaaaaggcggaaagccagcctcagaaaaaatcatggaataaaa
I V R L Y V K R R K P A S E K I M E I K
cttattaaaggccctaaaggtccttgggttcagcattgctggagggtgttgaaaccagcac
L I K G P K G L G F S I A G G V G N Q H
attcctggggataaacagcatctatgtaacccaaaataattgaaggagggtgcagcacacaag
I P G D N S I Y V T K I I E G G A A H K
gacggcaaaacttcagattggagacaagcttctagcagtgaacagtgctctgtttagaagaa
D G K L Q I G D K L L A V N S V C L E E
gttactcatgaagaagcagtgactgccttaaagaatacatctgattttgtttatttgaaa
V T H E E A V T A L K N T S D F V Y L K
gtggcaaaaccaacaagtatgtatataaatgatggctatgcaccaccggacatcactaat
V A K P T S M Y I N D G Y A P P D I T N

```

Figure 3.3: The Ile201 – Asn320 section of the DNA base/residue sequence of full-length SAP97 with the residues of the SAP97 PDZ2 domain, Met217 – Ser306 highlighted (red). The desired His73 residue to be mutated to Gly and Thr residues is indicated (blue).

Table 3.2: The designed primers (two forward and two reverse) required for the SLIM methodology are detailed, with the DNA bases corresponding to the H73G/T mutations highlighted (blue). The G : C content and annealing temperatures for each individual primer are included in the table also.

SAP97 PDZ2 H73X Mutant	Primer	5' → 3' Sequence	G : C Content (%)	Annealing Temp (°C)
H73G	Forward long	gaagttact ggt gaagaagcagtgactg ccttaaagaatac	41.5	66
H73G	Forward short	gtgactgccttaaagaatacatctg	40	54
H73G	Reverse long	tgcttctt acc agtaacttcttctaaaca gacactgttcactgc	42.2	67
H73G	Reverse short	ttctaaacagacactgttcactgc	41.7	54
H73T	Forward long	gaagttact act gaagaagcagtgactg ccttaaagaatac	39.0	65
H73T	Forward short	gtgactgccttaaagaatacatctg	40	54
H73T	Reverse long	tgcttctt agt agtaacttcttctaaacag acactgttcactgc	40	66
H73T	Reverse short	ttctaaacagacactgttcactgc	41.7	54

3.2.1.1.4 Agarose Gel Electrophoresis

Preparation of the gels for agarose gel electrophoresis (0.8% (w/v) for 0.6 – 8.5kb separation) requires 60mL of 1x TAE buffer; 0.48g of powdered agarose (Bioline) was added to this and the mixture was gradually heated with periodic swirling to ensure the agarose dissolved. The solution was allowed to cool to <35°C and the cast for the subsequent gel was created by sealing the ends of the agarose gel plate; 5µL of ethidium bromide (final concentration = 0.1µg/mL) was then added to the solution. The mixture was poured into the cast, with a sample well comb inserted and allowed to set. 5µL of each of the individual SLIM products were added to 5µL of loading buffer and the full volume was pipetted into individual wells. 1kb standard DNA marker (New England Biolabs) was loaded in a separate well and the gel subjected to an 80V gradient using a BioRad PowerPac 3000 for ~ 40 minutes. The gel was then viewed under trans UV light to determine if the SLIM procedure had been successful (Appendices, A.1a).

3.2.1.1.5 Plasmid Preparation

2 μ L of each SLIM product was added to 50 μ L of XL1 Blue competent *E.coli* cells, mixed and then incubated on ice for 30 minutes. The cells were incubated at 42°C for 45 seconds before incubating at 0°C for a further five minutes. 200 μ L of GS96 medium (Fisher Scientific) was then added and this mixture was incubated at 37°C for an hour, with shaking at 180 rpm. 200 μ L of the transformed cells were then pipetted onto a kanamycin-selective LB agar plate, spread evenly and left at 20 - 25°C room temperature for 30 minutes. The agar plate was then incubated at 37°C for 14 – 18 hours without shaking.

7mL of kanamycin-selective LB was inoculated with a single colony from the respective transformed plate and incubated at 37°C for 14 – 18 hours, with shaking at 180rpm. 1mL of each of the resultant cultures was added to 500 μ L of autoclaved glycerol (Fisher Scientific) and 500 μ L of MilliQ to produce a glycerol stock of the plasmid in XL1 Blue cells and this was immediately stored at -80°C. 1mL of the individual culture was aliquoted for sequencing analysis (outsourced to Source Bioscience) [3.2.3.8]; a further 3mL was pelleted by centrifugation, in order to extract the plasmid DNA using a QIAprep Spin Miniprep kit (QIAGEN), to yield a 50 μ L stock of the plasmid; at concentrations of 10 – 100 ng/ μ L.

3.2.1.2 Preparation of Chemically Competent Cells

Commercial glycerol stocks of the BL21 (DE3) and XL1 Blue *E. coli* competent cells, were used to streak out an LB agar plate containing kanamycin (for BL21 (DE3) cells) or tetracycline (for XL1 Blue cells). 200mL of SOC medium (+ tetracycline for XL1 Blue cells) was inoculated with a single colony from the desired plate. This culture was incubated at 37°C with shaking at 180rpm until the optical density at 600nm (OD₆₀₀) measured between 0.3 – 0.4, using a Cary 300 Bio UV/Vis

photospectrometer. The culture was then centrifuged at 3,000g for 10 minutes at 4°C and the resultant pellet was gently resuspended in 60mL of CCMB80 buffer. This was then incubated at 0°C for 30 – 60 minutes before being centrifuged at 3,000g for 10 minutes at 4°C and resuspended in 6mL of CCMB80. The OD₆₀₀ of a 50µL cell resuspension diluted to 250µL with SOC medium was measured and the cell resuspension diluted with CCMB80 buffer until a final OD₆₀₀ of between 1 – 1.5 was obtained. The cells were then incubated on ice for a further 30 minutes before being aliquoted into 50µL quantities in 1.5mL eppendorfs (these were autoclaved and pre-chilled at -20°C before use). Finally, the cells were flash frozen using liquid Nitrogen and stored at -80°C for up to three years.

3.2.1.3 Transformation of Chemically Competent E.coli

2µL of the desired plasmid containing the specific PDZ domain prepared via the SLIM methodology or from existing stocks was added to 50µL of BL21 (DE3) competent cells, mixed well and incubated at 0°C for 30 minutes. The cells were then incubated at 42°C for 45 seconds before being incubated at 0°C for a further five minutes. 200µL of SOC medium was then added and this was incubated at 37°C for one hour with shaking at 180rpm. 200µL of the transformed cells was pipetted onto a kanamycin containing agar plate, spread evenly and left at 20 - 25°C for 30 minutes. The agar plate was then left to incubate at 37°C overnight, without shaking, after which it was removed and incubated at 20 - 25°C for a further 30 minutes. Finally, the agar plate was sealed with Parafilm® and stored at 4°C for up to two weeks.

3.2.2 Protein Expression Methods

3.2.2.1 PSD-95 PDZ1&2, SAP97 PDZ1, PDZ2 WT_{1&2}, PDZ2 H73G, PDZ2 H73T, & Expression in LB Medium

50mL of kanamycin selective LB was inoculated with a single colony from the

desired transformed plate and incubated at 37°C with shaking at 180rpm for 14 – 18 hours. The cells were centrifuged at 3,000g for 14 minutes at 4°C and the resultant pellet was resuspended in 5mL of kanamycin-selective LB. This cell suspension was then added to 1L of kanamycin-selective LB and the OD₆₀₀ measured (normally a value of between 0.05 - 0.1). The cells were incubated at 37°C with shaking at 180rpm until the OD₆₀₀ of the solution measured between 0.7 – 1 (approximately 2 – 3 hours); the cells were then induced with IPTG (Apollo Scientific), to a final concentration of 1mM and incubated at 18°C for 14 – 18 hours, with shaking at 180rpm. The induced cells were then pelleted by centrifugation at 3,000g for 20 minutes at 4°C, with the resultant supernatant decanted and discarded. The pellet was resuspended in HisTrap A buffer and a cComplete EDTA-free cocktail protease inhibitor tablet (Roche) dissolved in 1mL of HisTrap A buffer was added. The resuspended cell pellets were stored left at -80°C until purification (for up to 3 months).

3.2.2.2 PSD-95 PDZ1&2, SAP97 PDZ1, PDZ2 WT, PDZ2 H73G, PDZ2 H73T, & PDZ2 KI Expression in Minimal Medium

1mL of kanamycin-selective LB was inoculated with a single colony from the transformed plate and incubated at 37°C with shaking at 180rpm, for seven hours. 100µL of the resultant cells was added to 10mL of kanamycin-selective M9 medium and incubated overnight at 37°C, with shaking at 180rpm. This cell suspension was then added to the 1L of kanamycin-selective M9 medium and the OD₆₀₀ measured (normally a value of between 0.03 - 0.07). The cells were incubated at 37°C until the OD₆₀₀ measured between 0.8 – 1 (usually 5 – 6 hours), then induced with 1mM final concentration of IPTG and incubated at 18°C for 14 – 18 hours, with shaking at 180rpm. The induced cells were pelleted by centrifugation at 1,300g for 20 minutes

at 4°C and the subsequent supernatant was discarded. The cell pellet was resuspended in HisTrap buffer A, a cOmplete EDTA-free cocktail protease inhibitor tablet (Roche) dissolved in 1mL of HisTrap A buffer was then added and the mixture was stored at -80°C until purification.

3.2.3 Protein Purification Methods

3.2.3.1 Cell Lysis

The cell solutions stored at -80°C were gently thawed at 20 - 25 °C, with DNaseI from bovine pancreas then added to a final concentration of 12.5µg/mL (Sigma-Aldrich) and incubated at 0°C for 10 minutes. The cells were then mechanically lysed using a Stansted 'Pressure Cell' Homogeniser (SFP Ltd), at 1000 PSI. The cell debris in the crude cell lysate was pelleted by centrifugation at 37,000g for 30 minutes at 4°C; the resultant supernatant contained the desired protein. The supernatant was decanted and sterile filtered through a 0.45µm Millex® HA syringe-driven filter unit in preparation for purification by chromatographic techniques.

3.2.3.2 Ni²⁺ Affinity Chromatography

A 5mL HisTrap Fast Flow (FF) column (GE Healthcare) was used on an ÄKTApurifier10 FPLC system (GE Healthcare), with the column initially washed with MilliQ and then equilibrated with HisTrap A and B buffers, at 2.5mL/min. The filtered cell supernatant was then loaded onto the column at a flow rate of 2.5mL/min. The bound contents of the column were then eluted with a gradient of increasing imidazole concentrations at 2.5mL/min and fractionated into 5mL fractions. The fractions were analysed by UV absorbance at 280nm (A_{280}) and those fractions that showed absorption levels above the baseline were analysed using SDS polyacrylamide gel electrophoresis (SDS-PAGE) [3.2.4.2]. The fractions that yielded the desired gel retardation band were combined, ready to be concentrated.

3.2.3.3 Concentration of Protein Sample

Concentration of the combined protein fractions from the Ni²⁺ affinity chromatography was carried out using Amicon Ultra Centrifugal Filter units with a 3kDa molecular weight cutoff and volume capacity of 15mL (Millipore). The concentration unit membrane was equilibrated by centrifugation at 3,500g with MilliQ then HisTrap A buffer. The protein was then applied to the unit and centrifuged at 3,500g until the desired final volume of sample was achieved. The solution that passed through the membrane (flow through) was analysed by SDS-PAGE to ensure that there was no membrane failure and hence, that none of the protein of interest had passed through. After use, the concentration units were centrifuged at 3,500g with MilliQ, then 20% (v/v) EtOH and left at 20 - 25°C in 20% (v/v) EtOH for reuse (up to two months).

3.2.3.4 Buffer Exchange of Protein Sample

The concentrated fractions from the Ni²⁺ affinity chromatography were then buffer exchanged to remove any imidazole present using a Sephadex G-25 Medium Gravity-Flow PD-10 Column (GE Healthcare) and HisTrap A buffer. The PD-10 column was initially washed with 25mL of MilliQ and then 25mL of HisTrap A buffer to equilibrate the column. 2.5mL of the protein sample was applied to the column, with the flow through discarded; the sample was eluted by addition of 3.5mL of HisTrap A buffer. As the maximum volume of protein that can be loaded onto the PD-10 column was 2.5mL; the equilibration, sample addition and sample elution sequence was repeated as necessary. The PD-10 column was then washed with 25mL of MilliQ then 25mL of 20% (v/v) EtOH and stored at room temperature in 20% (v/v) EtOH until required again.

3.2.3.5 Hexahistidine-Tag Removal Using Tobacco Etch Virus (TEV) Protease for PSD-95 PDZ1, SAP97 PDZ1, PDZ2 WT, PDZ2 H73G, PDZ2 H73T & PDZ2 KI

TEV protease was added to the buffer exchanged protein in a ratio of PDZ domain : TEV protease = 20:1 (protein concentration determined as detailed in [3.2.4.1]) and the solution incubated at 20 – 25°C for 14 – 18 hours, without shaking. The cleavage solution was then loaded back through the Ni²⁺ affinity column at 2mL/min and the flow through containing successfully cleaved protein collected. Any uncleaved protein, cleaved tags and tagged protease in the cleavage solution all bound to the column and so, were eluted off using 100% HisTrap B buffer i.e. 500mM imidazole.

3.2.3.6 SUMO-Tag Cleavage Using SUMO Protease for PSD-95 PDZ2

The protocol detailed in [3.2.3.5] was followed for the SUMO-tag cleavage of PSD-95 PDZ2, except that SUMO protease was added to the buffer exchanged protein in a ratio of PDZ domain : SUMO protease = 100:1 (protein concentration determined as detailed in [3.2.4.1]), instead of TEV protease.

3.2.3.7 Size Exclusion Chromatography

A HiLoad 26/60 Superdex 75 column was connected on an ÄKTApurifier10 FPLC system, with the column initially washed with MilliQ and then equilibrated with gel filtration buffer. The affinity tag-cleaved protein was concentrated to less than 5mL [3.2.3.3], manually injected into a 10mL injection loop connected to the FPLC system and loaded onto the size exclusion column at a flow rate of 3mL/min. The protein was then eluted with increasing volume of gel filtration buffer; the fractions that showed A₂₈₀ levels above the baseline were analysed using SDS PAGE. The fractions that showed the desired molecular weight of protein were pooled, concentrated [3.2.3.3] and buffer exchanged into the desired buffer for NMR spectroscopy or ITC [3.2.3.4]. The final protein solution was flash frozen with liquid

Nitrogen and stored at -80°C.

3.2.3.8 PDZ Domain Construct Sequences

The amino acid sequence of the different PDZ domain proteins produced for the research described in this thesis have been detailed in this sub-section. It can be seen that two different SAP97 PDZ2 WT constructs were produced and utilised (WT₁ & WT₂), with the only difference between the two SAP97 PDZ2 constructs being the presence of an extra two amino acids (KI, blue) at the N-terminus of SAP97 PDZ2 WT₁; this increased the theoretical isoelectric point (pI) from 7.09 to 8.05. This resulted in the protein production being more productive as no protein was lost by precipitation incurred to crossing the pI. Mutagenesis of the SAP97 PDZ2 domain was performed on the SAP97 PDZ2 WT₂ construct and the residues mutated have been highlighted in red on the respective sequence:

PSD95 PDZ1

G A M E M E Y E E I T L E R G N S G L G F S I A G G T D N P H I G D D P S I F
I T K I I P G G A A A Q D G R L R V N D S I L F V N E V D V R E V T H S A A
V E A L K E A G S I V R L Y V M R R K P P A

PSD95 PDZ2

M K V M E I K L I K G P K G L G F S I A G G V G N Q H I P G D N S I Y V T K
I I E G G A A H K D G R L Q I G D K I L A V S S V G L E D V M H E D A V A
A L K N T Y D V V Y L K V A K P S N A

SAP97 PDZ1

G A M A D Y E Y E E I T L E R G N S G L G F S I A G G T D N P H I G D D S S
I F I T K I I T G G A A A Q D G R L R V N D C I L R V N E A D V R D V T H S
K A V E A L K E A G S I V R L Y V K R R K P A S

SAP97 PDZ2 WT₁

G A M G **K I** M E I K L I K G P K G L G F S I A G G V G N Q H I P G D N S I Y
V T K I I E G G A A H K D G K L Q I G D K L L A V N S V C L E E V T H E E A
V T A L K N T S D F V Y L K V A K P T S

SAP97 PDZ2 WT₂

G A M E I K L I K G P K G L G F S I A G G V G N Q H I P G D N S I Y V T K I I
 E G G A A H K D G K L Q I G D K L L A V N S V C L E E V T **H** E E A V T A L
 K N T S D F V Y L K V A K P T S

SAP97 PDZ2 H73G

G A M E I K L I K G P K G L G F S I A G G V G N Q H I P G D N S I Y V T K I I
 E G G A A H K D G K L Q I G D K L L A V N S V C L E E V T **G** E E A V T A L
 K N T S D F V Y L K V A K P T S

SAP97 PDZ2 H73T

G A M E I K L I K G P K G L G F S I A G G V G N Q H I P G D N S I Y V T K I I
 E G G A A H K D G K L Q I G D K L L A V N S V C L E E V T **T** E E A V T A L
 K N T S D F V Y L K V A K P T S

3.2.4 Analytical Methods

3.2.4.1 Protein Concentration Determination

All protein concentrations (c) were determined using Beers law ($A = \epsilon cl$), where the absorbance at 280nm (A_{280}) was obtained using an ND-1000 Spectrophotometer (NanoDrop®); with a standard path length (l) = 10mm and the extinction coefficient of the particular protein calculated from the protein sequence using the ProtParam tool on the ExPASy bioinformatics resource portal (web.expasy.org/protparam/).

3.2.4.2 SDS-PAGE Gel Electrophoresis

To prepare the gels required for SDS-PAGE gel electrophoresis, 10mL of 15% resolving gel was prepared, gently mixed and pipetted into a 0.75mm glass cast; with between 250 – 500µL of butan-2-ol added after to create a level surface. 10mL of 15% resolving gel is sufficient for two gels and the gels were left to polymerise for 15 minutes at 20 – 25°C; the butan-2-ol was then decanted off. 10mL of a 4% stacking gel was prepared, gently mixed and pipetted on top of the polymerised resolving gel in the cast; a sample well comb was then inserted. 10mL of 4% stacking gel is sufficient for four gels and the gels were left to polymerise for 20

minutes at 20 - 25°C.

To prepare the individual samples to run in the SDS-PAGE, protein samples were diluted up to 20µL with MilliQ, followed by addition of 20µL of 2x sample buffer; to give a final protein concentration in the range of 0.5 - 1mg/mL [3.2.4.1]. The samples were denatured at 100°C for five minutes before 7.5µL of each sample was loaded using a Hamilton syringe into an individual gel lane, excepting one lane per gel which was loaded with with 5µL of low-range molecular marker (Sigma-Aldrich). The gels were packed into a Protean II rack (BioRad), situated in a tank containing 1x gel running buffer and a gradient of 200V passed through the solution for ~ 45 minutes.

3.2.4.3 Coomassie Brilliant Blue Staining

The gels from the SDS-PAGE were carefully removed from the cast and washed with RO water, prior to staining for 10 minutes in a solution of Coomassie G250 with gentle rocking at 20 – 25°C. The Coomassie G250 stain solution was decanted off; the gels were washed with RO water and then destained by incubation for 14 – 18 hours at 20 – 25°C in destain solution, with gentle rocking.

3.2.4.4 Gel Imaging

All destained gels were visualised within 12 hours of destaining using an ImageScanner III machine (GE Healthcare).

3.3 NMR Spectroscopy

3.3.1 General

Samples to be examined by NMR spectroscopy of volumes 550µL or greater were pipetted into Wilmad 5mm 7” 800MHz Precision Pyrex Glass NMR Tubes (Goss Scientific). Samples of limited volume were pipetted into Shigemi Advanced NMR Microtube Assembly – Matched with D₂O, bottom L 8mm tubes (Sigma-Aldrich).

The NMR spectra were acquired at 25°C on either a Bruker AVANCE II+ 600MHz Ultrashield or 800MHz US² spectrometer, equipped with triple resonance cryoprobes. The Bruker TopSpin programme version 3.1 was used to process the resultant NMR spectra and the Collaborative Computational Project for NMR (CCPN) Analysis software programme was used for interactive spectral analysis and assignment.

3.3.2 Unbound PDZ Domain Sample Preparation

A 0.5mM uniformly ¹³C, ¹⁵N-doubly-labelled sample of the required PDZ domain was prepared in 20mM phosphate, 0.1mM EDTA, 1mM DTT, 0.01% (w/v) NaN₃, pH 6.3 buffer [3.2].

3.3.3 PDZ Domain – Ligand Complex Sample Preparation

A 0.5mM uniformly ¹³C, ¹⁵N-doubly-labelled sample of the required PDZ domain was prepared in 20mM phosphate, 0.1mM EDTA, 1mM DTT, 0.01% (w/v) NaN₃, pH 6.3 buffer [3.2] with the required ligand stock added to yield a final PDZ domain : ligand ratio of 1:5.

3.3.4 Ligand Binding Screening by NMR Spectroscopy

A 450mM stock of the potential PDZ domain binder was prepared by dissolving the appropriate mass of the organic compound/peptide in the necessary amount of hexadeuterodimethyl sulfoxide (DMSO-d₆). ¹H 1-D and 2-D ¹H-¹⁵N HSQC NMR experiments (Bodenhausen and Ruben, 1980) were performed using 0.1 - 0.2mM ¹⁵N-labelled PDZ domain in 20mM phosphate buffered to pH 6.3. The NMR sample contained the required volume of either organic compound stock solution added to give a protein : potential binder ratio of 1:10 or the equivalent volume of DMSO-d₆ (reference spectrum). This ensured that all solutions (reference and ligand present) contained the same DMSO-d₆ concentration and thus, any observed perturbations

were not due to the effects of DMSO-d₆. The concentration of DMSO-d₆ in the NMR sample never exceeded 0.44% (v/v) throughout the course of the ligand binding screening by NMR spectroscopy investigation.

The resultant spectra were then assigned by transfer of the previously determined unbound backbone assignments of each PDZ domain [3.5.2] and analysed to identify which residue(s) of the PDZ domain had been perturbed. The chemical shift sum perturbation value (Δd_{ppm}) for each residue was then calculated (Equation 3.1, (Tochio et al., 2000, Piserchio et al., 2002)):

$$\Delta d_{\text{ppm}} = \sqrt{((\Delta\delta_{\text{HN}})^2 + (\Delta\delta_{\text{N}} * \alpha_{\text{N}})^2)} \quad \text{Equation [3.1]}$$

where, α_{N} = Scaling Factor of 0.17

3.3.5 Binding Affinity Determination by NMR Spectroscopy

To determine the binding affinity (K_{D}) of the small molecule binders to the particular PDZ domain by NMR spectroscopy, a series of ¹H 1-D and ¹H-¹⁵N 2-D HSQC NMR experiments were performed.

The NMR experiments were carried out using ¹⁵N-labelled PDZ domain in 20mM phosphate buffered at pH 6.3 and the previously described stock of the potential small molecule inhibitors [3.3.4]. Two different ¹⁵N PDZ domain NMR samples were prepared (Table 3.3), with NMR experiments first carried out on these samples to give a reference (no inhibitor i.e. 100% solution A) and potential endpoint (20-fold excess of inhibitor i.e. 100% solution B). The same volume of sample was removed from solutions A and B, with the sample of solution A placed into solution B and vice-versa; the subsequent step-wise dilution of one solution with the other then allowed the formation of a number of intermediate points in the small molecule concentration titration series (Table 3.4).

Table 3.3: The composition of the initial two 550 μ L samples prepared for determination of dissociation constants using NMR spectroscopy. Concentrations of sample constituents are denoted by [] and are given in μ M or volume/volume percentages. Both solutions contained a PDZ:DTT ratio of 1:2 and solution B contained the small molecule inhibitor in 20-fold excess to the protein. As the small molecule binders are dissolved in DMSO-d₆, the same final percentage of DMSO was added to solution A as was present in solution B.

Constituent	Solution A	Solution B
PDZ Domain	[182]	[182]
Small Molecule	/	[3640] i.e.0.81% DMSO-d ₆
DMSO-d ₆	0.81%	/
DTT	[364]	[364]
D ₂ O	8.25%	8.25%

Table 3.4: The detailed series of sequential dilutions starting from solutions A and B and finishing with solution A^{VII}B^{VII} for the binding affinity determination titration to create a total of nine titration points ranging from PDZ domain : ligand 1:0 – 1:20.

Solution Number	PDZ:Ligand Ratio	Volume of B Added to A (μ L)	Volume of A Added to B (μ L)	Ligand Concentration (μ M)
A	1:0	0	/	0
A ^I	10:1	2.75	/	18.2
A ^{II}	5:1	2.75	/	36.4
A ^{III}	2:1	8.25	/	91
A ^{IV}	1:1	13.75	/	182
A ^V	1:2	27.5	/	364
A ^{VI}	1:5	82.5	/	910
A ^{VII} B ^{VII}	1:10	137.5	137.5	1820
B ^{VI}		/	82.5	
B ^V		/	27.5	
B ^{IV}		/	13.75	
B ^{III}		/	8.25	
B ^{II}		/	2.75	
B ^I	↓	/	2.75	↓
B	1:20	/	0	3640

To ensure that the complex reached saturation, additional small molecule stock was added to the A^{VII}B^{VII} solution to achieve a protein : ligand ratio of 1:30 (5.46mM ligand). One final titration point of 1:25 (4.55mM ligand) was obtained by dilution of the 5.46mM ligand sample with protein, with the highest DMSO-d₆ concentration achieved during the titration experiment being 1.21% (v/v).

The resultant spectra were then assigned by transfer of the previously determined assignments [3.5.2], the individual residue chemical shifts were tracked in sequential spectra and fitted (using Equation 3.2, (Morton et al., 1996)):

$$y = A((B + x) - \sqrt{((B + x)^2 - 4x)}) \quad \text{Equation [3.2]}$$

where, $x = \frac{[L]}{[P]}$, $y = \Delta\delta$, $A = \frac{1}{2}\Delta\delta_{max}$ and $B = 1 + \left(\frac{K_D}{[P]}\right)$

The K_D of the particular PDZ – small molecule interaction under investigation was determined by averaging the K_D value given by the 10 residues that fitted the function the best (Figure 3.4).

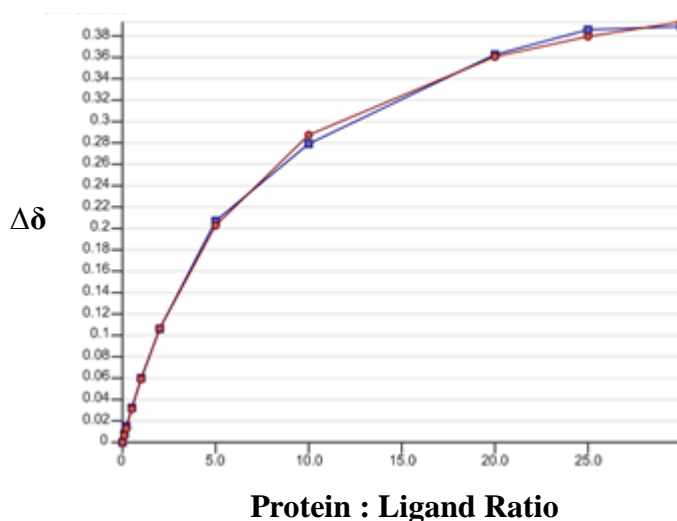


Figure 3.4: An example of a fit curve produced for an individual residue over the course of a small molecule concentration titration (blue) and the corresponding fitting function (magenta). This particular residue shows very good agreement between the experimental and fitting function values and would hence, be used in the K_D value determination process.

3.4 Isothermal Titration Calorimetry (ITC)

3.4.1 Basic Set-up of an ITC Experiment

All isothermal titration calorimetry experiments were carried out at 25°C on an iTC₂₀₀ Microcalorimeter (GE Healthcare) with a 200μL cell capacity and 40μL syringe volume. For each experiment, the PDZ domain in 20mM phosphate buffer, pH 6.3, was in the cell and a synthetic peptide derived from the C-terminus of the native PDZ ligand (GenicBio, China) was in the syringe. The lyophilised peptide was

directly resuspended into the identical buffer as the PDZ domain and minimal pH adjustments were made if required. All ITC titration experiments were carried out with 100 μ M PDZ domain and 750 μ M peptide concentrations and consisted of an initial injection of 0.5 μ L followed by fifteen 2.39 μ L injections and a final injection of 1.89 μ L. The ITC titration data collected was analysed using the Origin®7 software programme.

3.4.2 Native Protein – Ligand Interaction Experiment

Before the native protein – peptide ITC experiments were carried out, control experiments were performed whereby the peptide was titrated into buffer and buffer titrated into protein. In both cases no heat exchange was detected, confirming that there was appropriate match of buffer conditions with no evidence of dilution effects. As successful control experiments had been performed, the ITC titration experiments with protein and peptide were carried out as described in [3.4.1].

3.4.3 Competition Experiment

The ITC competition experiments were carried out in a similar manner to the direct binding experiments in [3.4.2]. In these experiments, both protein and peptide solutions contained the potential small molecule inhibitor obtained from the same stock of small molecule dissolved in DMSO-d₆ described in [3.3.4]. In each experiment, the protein (in the cell) and peptide (in the syringe) contained the same concentration of small molecule ligand and hence, the same DMSO-d₆ concentration. Control experiments were performed whereby the peptide (with ligand) was titrated into buffer containing the same DMSO-d₆ concentration and conversely, buffer containing the same DMSO-d₆ concentration titrated into protein (with ligand). Both of these control experiments exhibited undetectable heat exchange, confirming that there was appropriate match of DMSO-d₆/buffer conditions with no evidence of

dilution effects.

A control experiment was also carried out that involved a peptide-protein titration, where the protein and peptide were both in a buffer that contained 5% (v/v) DMSO-d₆ (Appendices, A.3). This showed that the presence of such a high level of DMSO-d₆ had no effect on the resultant K_D value obtained from the protein-peptide binding experiment; although it is possible that the presence of DMSO-d₆ may have had an effect on the ΔH and ΔS thermodynamic binding parameters obtained. Thus, this control experiment showed that any inhibitory effect observed in the competition experiments was due to the inhibition of the native interaction by the small molecule ligand and not caused by the presence of a small amount of DMSO-d₆. The highest concentration of DMSO-d₆ used in the competitive inhibition experiments was 1.34% (v/v), with the various competition experiments having slightly different % (v/v) DMSO-d₆ concentrations; as a result, only the K_D binding parameter values of the respective competition experiments were compared.

The competition experiments were performed at several concentrations of each potential small molecule inhibitor to obtain a range of K_D^{app} values. The K_i value of the ligand was determined using Equation 3.3 (Bodenreider et al., 2009):

$$K_D^{app} = K_D + \frac{K_D}{K_i} [L] \quad \text{Equation [3.3]}$$

where, K_D^{app} is the measured K_D in the presence of inhibitor, K_D the dissociation constant for the peptide (in the absence of inhibitor) and [L] is the concentration of the potential inhibitor present. The value of K_i is estimated from the K_D^{app} determined at various [L].

3.5 Protein : Ligand Structure Determination

3.5.1 Collection of a Suite of NMR Experiments

NMR samples were prepared as described in [3.3.1], [3.3.2] and [3.3.3]; these

samples were then used to perform several NMR spectroscopic experiments (Table 3.5). The aim of these experiments was either to determine the backbone NH assignment of an unbound PDZ domain or obtain the structure of the PDZ domain in complex with a peptide/small molecule.

3.5.2 Assignment of ^1H , ^{13}C and ^{15}N Resonances of a PDZ Domain

To assign the ^1H , ^{13}C and ^{15}N resonances of the desired PDZ domain (- ligand complex), the particular combination of 1-D, 2-D and 3-D NMR experiments shown in Table 3.5 were performed. 2-dimensional NMR experiments are based on the NMR theory described for the simple pulse-acquire experiment in chapter 2 (Figure 3.5); however, the magnetisation is transferred from a hydrogen to another nuclei either covalently connected in the amino acid sequence or close in space. The magnetisation is usually evolved on this atom and then transferred back to the hydrogen for detection. 3-dimensional NMR experiments are generally based upon 2-D experiments and so can be thought of as a 2-D experiment extended into a third dimension i.e. ^1H , ^{13}C or ^{15}N (Figure 3.5).

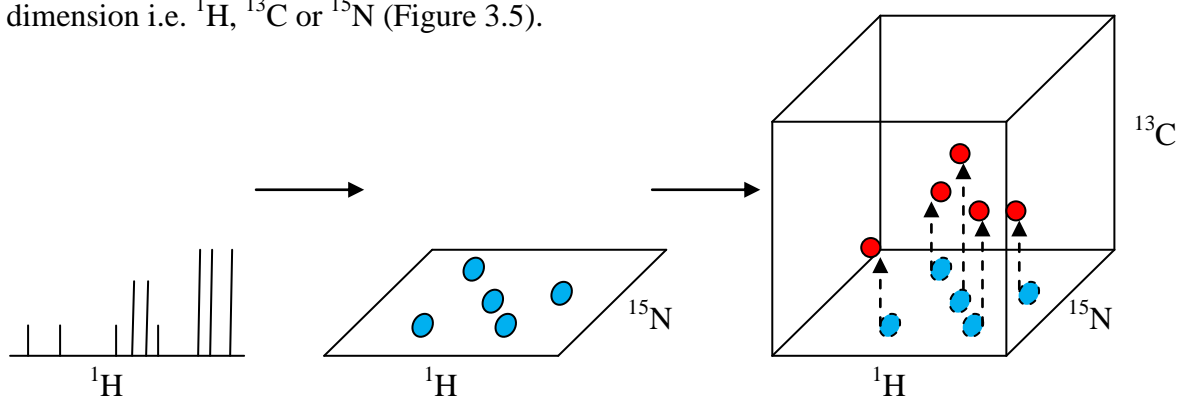


Figure 3.5: An overview of the relationship between one-dimensional (1-D), two-dimensional (2-D) and three-dimensional (3-D) NMR spectroscopic experiments. 2-D NMR experiments are based on 1-D NMR experiments (the theory for a simple pulse-acquire 1-D NMR experiment is detailed in chapter 2), however, the magnetisation is transferred from the hydrogen to another nuclei (^{15}N in the example given) either covalently connected in the amino acid sequence or close in space; the magnetisation is evolved on this nuclei and then usually transferred back to the hydrogen for detection. 3-D NMR experiments can be thought of as a 2-D experiment extended into a third-dimension; ^{13}C in the example given.

The resonance assignment process of the PDZ domain began with the backbone resonance determination, using a sequential assignment methodology with

complementary pairs of NMR spectra i.e. CBCACONH and HNCACB. The HNCACB experiment correlated each NH group in the protein with its own $^{13}\text{C}_\alpha$ and $^{13}\text{C}_\beta$ chemical shifts and the respective $^{13}\text{C}_{\alpha/\beta}$ chemical shifts of the preceding residue; the CBCACONH correlated a particular NH group in the protein with the $^{13}\text{C}_\alpha$ and $^{13}\text{C}_\beta$ chemical shifts of the preceding residue (Figure 3.6a). The correlation observed in this complementary set of spectra allowed the sequential linking of one NH group to the next (Figure 3.6b). This process was repeated with other related spectra, to allow the assignment of the PDZ domain ^{13}C (carbonyl) and $^1\text{H}_{\alpha/\beta}$ chemical shifts; thus, definitive sequence-specific backbone assignment achieved.

To assign the ^1H - ^{15}N HSQC of the individual PDZ domains, the previously described procedure was sufficient since only the backbone resonances need to be specifically assigned. However, to determine the structure of a PDZ domain – ligand complex, the residue side-chain assignment of the PDZ domain was also required; this was so that the precise intra- and intermolecular interactions occurring in the complex could be definitively assigned.

The residue side-chain assignment was accomplished using aromatic and aliphatic HCCH-TOCSY NMR experiments. By navigating to the $^1\text{H}_{\alpha/\beta}$ chemical shifts previously determined for a given residue, it is possible to observe the accompanying $\text{H}_{\gamma/\delta}$ chemical shifts and hence, determine the $\text{C}_{\gamma/\delta/\epsilon}$ residue chemical shifts (if present in the amino acid structure, Figure 3.7).

The intra- and intermolecular interactions present in a particular complex were detected by carrying out standard and intra-protein isotope filtered 3-D ^{13}C (aliphatic and aromatic) and ^{15}N NOESY experiments; the principles behind the NOE experiment are discussed in [2.2.3]. In the NMR solution state structure determination of the PSD-95 PDZ1 – 5-HT_{2c} complex, the peaks present in the

NOESY spectra were manually picked and then assigned by an automated procedure using a software programme, CYANA [3.5.3]. The assignment of the NOE spectra in the HADDOCK structure determination of a PDZ domain – small molecule complex is described in [3.5.5].

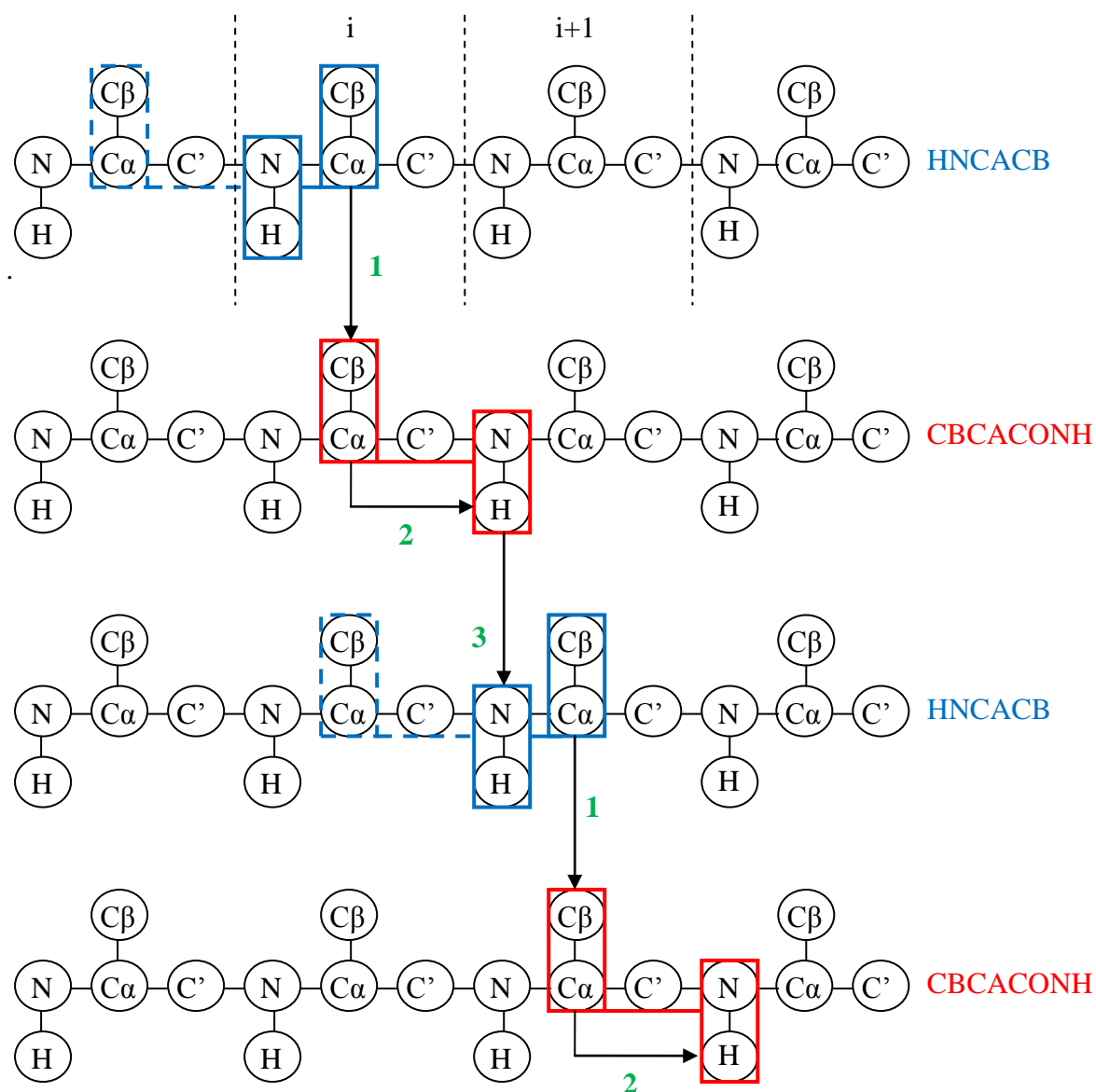


Figure 3.6a: The sequential assignment methodology implemented to complete the assignment of the PDZ domain backbone resonances using a complementary pair of 3-D NMR spectroscopic experiments (CBCACONH/HNCACB). The C_α/C_β peaks for a particular residue in the HNCACB spectrum were correlated to their respective peaks in the CBCACONH spectrum (1); this identified the residue in front of the residue in the amino acid sequence i.e. $i+1$. The C_α/C_β peaks of the $i+1$ residue were used to determine the corresponding NH group in the CBCACONH experiment (2); this assignment was transferred to the HNCACB experiment, which enabled the C_α/C_β peaks for the $i+1$ residue to be determined (3). The process was then repeated to determine the peaks corresponding to the $i+2$, $i+3$ residues etc.

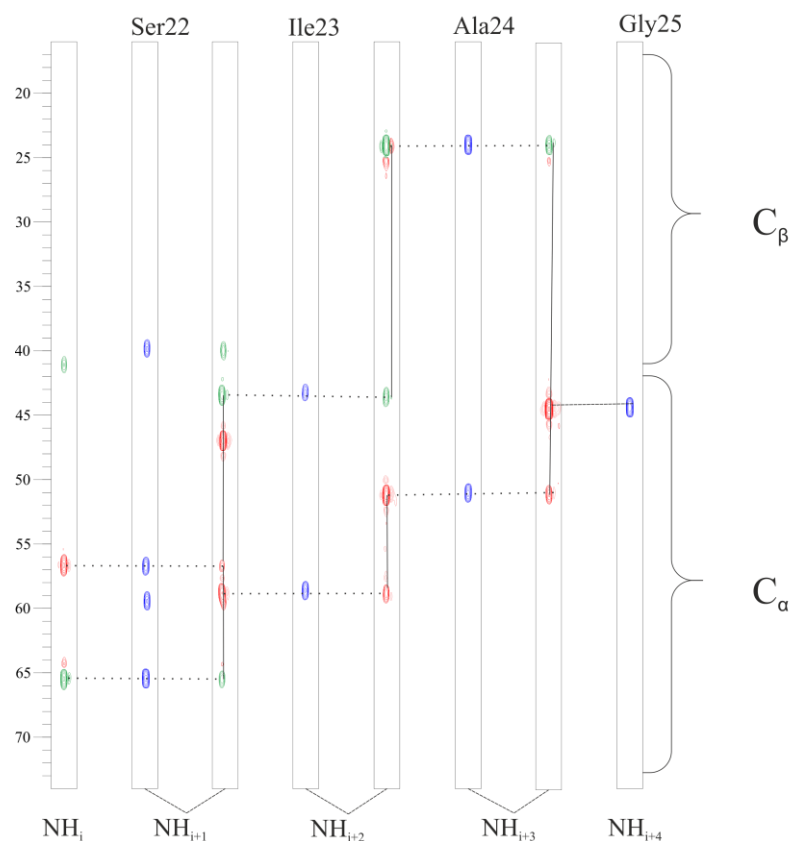


Figure 3.6b: An example of the residue backbone assignment performed on PSD-95 PDZ1 by sequential assignment; the C_α/C_β peaks of the CBCACONH spectrum are shown in blue, with the C_α/C_β peaks of the HNCACB spectrum are shown in red and green respectively. It can be seen how the Ser22 – Gly25 length of the PSD-95 PDZ1 domain sequence could be assigned from the complementary pair of NMR experiments. The figure also indicates how most C_α are found between 40 – 70ppm, whereas, the majority of C_β peaks are have chemical shifts of 10 – 40ppm; this is not true for Ser/Thr C_β peaks however (60 – 75ppm).

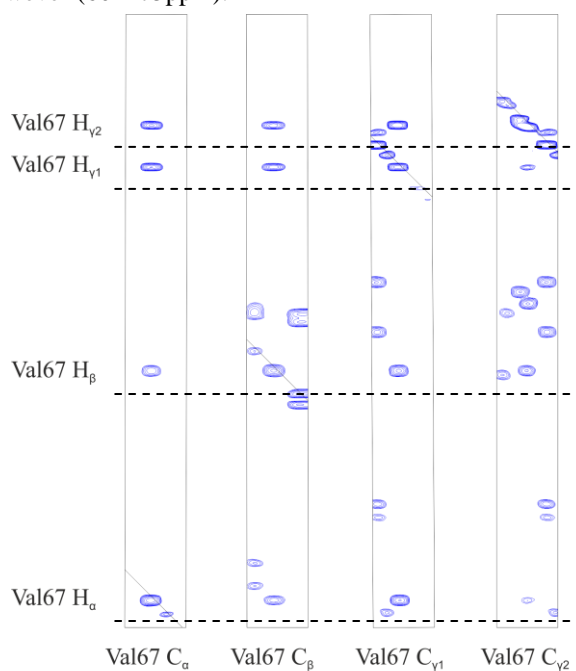


Figure 3.7: An example of the completed side-chain assignment of the Val67 residue of the PSD-95 PDZ1 domain using a 3-D HCCH-TOCSY NMR experiment. The four different Carbon and hydrogen environments of the Val67 residue can be seen in each respective slice of the NMR experiment.

Table 3.5 (continues onto page 33): The different NMR spectroscopic experiments that have been performed in the process of carrying out the research described in this thesis. The table indicates the different areas of NMR spectroscopy-related research that the particular experiment was used in; selected NMR experiment acquisition parameter values (number of scans and FID resolution) is detailed for each individual experiment. For all experiments with different proteins, typical offset values (ppm) were ^{13}C (aliphatic) = 27 – 45, ^{13}C (aromatic) = 124 – 126, ^{13}C carbonyl = 176 and ^{15}N = 117 - 119; for the NOESY and TOCSY experiments, the mixing times were 300ms and 45ms respectively. For a selection of the NMR experiments, the references for the pulse sequences implemented are given.

NMR Experiment	For PDZ Backbone Assignment	For NMR Structure Determination	For HADDOCK Structure Determination	No. of Scans	FID Resolution (Hz)		
					F1	F2	F3
1-D $^1\text{H}^a$	Yes	Yes	Yes	32	1.761	/	/
^{13}C ^{15}N -filtered 1-D ^1H	No	Yes	Yes	32	1.612	/	/
1-D Excitation Sculpting	No	Yes	No	32	0.587	/	/
1-D Saturation-Transfer Difference	No	Yes	No	32	1200.266	0.587	/
2-D ^1H - ^{15}N HSQC ^b	Yes	Yes	Yes	4	22.807	8.174	/
2-D ^1H - ^{12}C HSQC (Aliphatic)	No	Yes	No	32	82.528	10.016	/
2-D ^1H - ^{13}C HSQC (Aliphatic) ^c	Yes	Yes	Yes	4	84.424	10.016	/
2-D ^1H - ^{13}C HSQC (Aromatic)	Yes	Yes	Yes	4	75.843	13.951	/
2-D ^1H - ^{13}C HSQC ($\text{H}_\beta\text{C}_\beta\text{C}_\gamma\text{C}_\delta\text{H}_\delta$) ^d	Yes	Yes	No	96	75.483	12.520	/
2-D ^{13}C TROSY ^e	Yes	Yes	Yes	4	115.006	18.780	/
^{13}C , ^{15}N F1-filtered 2-D NOESY-HSQC	No	Yes	Yes	64	37.508	11.161	/
^{13}C , ^{15}N F1-filtered 2-D TOCSY	No	Yes	No	64	37.578	14.085	/
3-D HNCOf ^f	Yes	Yes	No	4	58.704	81.103	10.899
3-D HNCACOG ^g	Yes	Yes	No	8	100.636	133.482	10.899
3-D CBCACONH ^h	Yes	Yes	Yes	8	272.519	81.103	10.899

NMR Experiment	Apo PDZ Backbone Assignment	NMR Structure Determination	HADDOCK Structure Determination	No. of Scans	FID Resolution (Hz)		
					F1	F2	F3
3-D HNCACB ⁱ	Yes	Yes	Yes	8	272.519	81.103	10.899
3-D HBHACONH ^j	Yes	Yes	No	4	100.038	81.103	10.899
3-D HBHANH ^j	Yes	Yes	No	4	64.024	81.103	10.899
3-D HCCH-TOCSY (Aliphatic) ^k	No	Yes	No	8	48.010	97.853	8.22
3-D HCCH-TOCSY (Aromatic) ^k	No	Yes	No	4	75.028	180.295	21.798
3-D ¹³ C NOESY-HSQC (Aliphatic)	No	Yes	No	4	64.024	156.520	18.780
3-D ¹³ C NOESY-HSQC (Aromatic)	No	Yes	No	8	99.776	180.295	9.354
3-D ¹⁵ N NOESY-HSQC ^l	No	Yes	No	4	64.024	87.862	16.711
¹³ C, ¹⁵ N F1-filtered ¹³ C F3-edited 3-D NOESY-HSQC (Aliphatic)	No	Yes	No	16	102.166	204.386	12.019
¹³ C, ¹⁵ N F1-filtered ¹³ C F3-edited 3-D NOESY-HSQC (Aromatic)	No	Yes	Yes	8	100.038	180.295	16.711
¹³ C, ¹⁵ N F1-filtered ¹⁵ N F3-edited Filtered 3-D NOESY-HSQC	No	Yes	No	8	64.024	87.862	15.964

^a (Piotto et al., 1992, Sklenar et al., 1993) ^b (Bodenhausen and Ruben, 1980, Piotto et al., 1992, Sklenar et al., 1993) ^c (Vuister and Bax, 1992) ^d (Yamazaki et al., 1993) ^e (Meissner and Sorensen, 1999) ^f (Grzesiek and Bax, 1992c, Schleucher et al., 1993, Kay et al., 1994) ^g (Clubb et al., 1992, Kay et al., 1994) ^h (Grzesiek and Bax, 1992a, Grzesiek and Bax, 1993, Muhandiram and Kay, 1994) ⁱ (Grzesiek and Bax, 1992b, Wittekind and Mueller, 1993) ^j (Grzesiek and Bax, 1993, Muhandiram and Kay, 1994) ^k (Bax et al., 1990, Kay et al., 1993) ^l (Sklenar et al., 1993).

3.5.3 Assignment of NOESY's and Preliminary Structure Determination Using CYANA

The initial stage of the automated NMR solution state structure determination of the PSD-95 PDZ1 – 5-HT_{2c} complex structure involved the use of the CYANA version 2.1 programme (Guntert, 2004). Automated NOESY assignment with CYANA has been found to be as effective as the conventional, interactive ‘manual’ approach but is a lot faster and more objective. The amino acid (AA) sequences, sequence-specific assignments and NOESY cross-peak positions and volumes previously determined [3.5.2] were used as inputs for in CYANA (Figure 3.8); the individual PSD-95 PDZ1 and 5-HT_{2c} component parts of the complex were treated as one single protein in CYANA, separated by a 50 Gly residue linker.

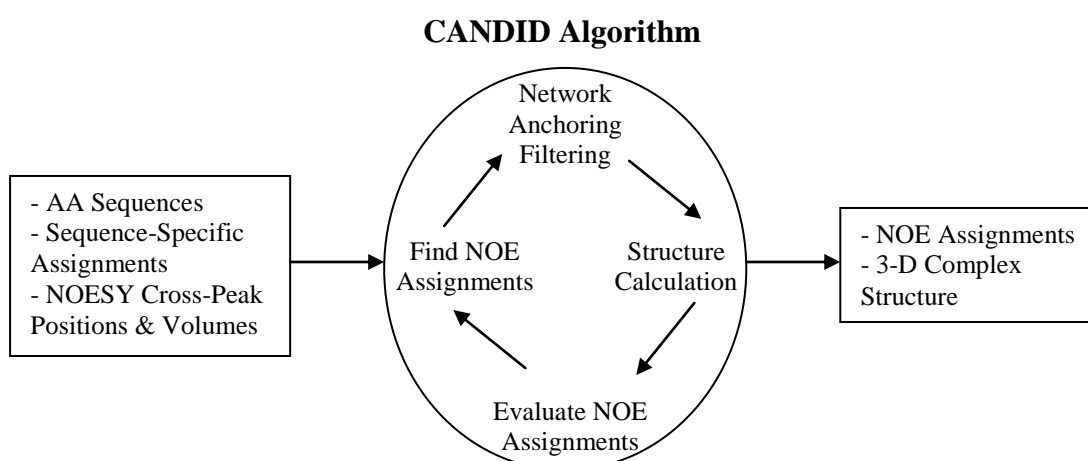


Figure 3.8: An overview of the automated combined NOESY assignment and structure calculation carried out by CYANA. The experimental input data (sequences, assignments and NOESY cross-peaks) is read as part of the CANDID algorithm which is a cycle of seven stages, at the end of which an ensemble of 3-D complex structures is produced and the cycle starts again with the previous structural information taken into account. At the end of seven cycles, the outputs from the CYANA methodology (NOESY assignments and final 3-D complex ensemble) are obtained.

In CYANA, the automated NOESY assignment is performed by the CANDID algorithm (Herrmann et al., 2002) and proceeds in seven iterative cycles of NOE assignment and subsequent structure calculation using torsion angle dynamics (TAD, Figure 3.9). The TAD algorithm uses a ‘geometric’ force field consisting of the short-range repulsive potential of non-bonded interactions and replaces the Lennard-

Jones and electrostatic interactions.

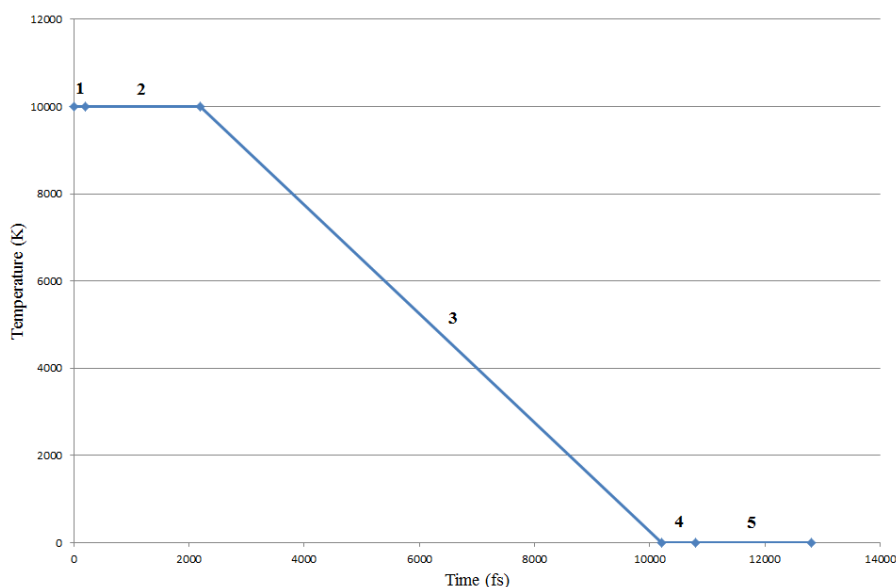


Figure 3.9: A plot at the five stages of the torsion angle dynamics (TAD) algorithm that forms the structure calculation part of the CANDID algorithm in CYANA (Figure 6); where, 1 = Initial minimisation (100 conjugate gradient minimisation steps), 2 = High temperature phase (10,000K, 1/5 of TAD steps, 2fs), 3= Slow cooling (close to 0K, 4/5 of TAD steps), 4 = Low temperature phase (0K, 100 conjugate gradient minimisation steps then 200 TAD steps) and 5 = Final minimisation (1000 conjugate gradient minimisation steps). The total number of TAD steps used in the CYANA process was 10,000; therefore 2,000 and 8,000 TAD steps were used at stages two and four respectively.

The structure calculation starts from a conformation with all torsion angles treated as independent, uniformly distributed random variables. In the first cycle, the structure-independent NOE self-consistency check (network anchoring) has a dominant impact because structure-based criteria cannot be applied yet. The second and subsequent cycles use the 3-D structures obtained from the previous cycle to guide NOESY assignment. In a single cycle, only cross-peaks with at least one assignment and a network anchoring score above a user-defined threshold are retained; a conventional distance restraint is created for those cross-peaks with a single assignment, with ambiguous distance restraints created for cross-peaks with multiple assignments. The final cycle has an additional filtering step to ensure that all NOE's have either a unique assignment to a single H-H interaction or are eliminated; those NOESY cross-peaks with ambiguous distance constraints are treated as a superposition of degenerate signals in this filtering step and so, the cross-peak is divided into fractions

based on the resultant structures generated.

The CYANA input file (CALC.cya) was amended so that the structure calculation contained 10,000 TAD steps, structural restraints (distance, hydrogen bond (determined by D₂O exchange NMR experiments, Appendices, A.4) and dihedral restraints (predicted by DANGLE in CCPN Analysis) [4.6.2.3]) and to ensure that the assigned intermolecular NOE's were kept throughout the structure determination process [4.6.2.3]. The output of the automated NMR solution state structure determination of the PSD-95 PDZ1 – 5-HT_{2c} complex by CYANA consists of 3-D structure as an ensemble of the 20 lowest energy complexes as well as lists of cross-peak assignments and potential artefacts/mis-assigned peaks. A value termed the 'average target function value' is also given for each cycle of the structure calculation; this would be zero if all experimental distance and torsion angle constraints are fulfilled and hence, should be as close to zero as possible.

3.5.4 Structure Determination & Water Refinement Using CNS

3.5.4.1 PSD-95 PDZ1 - 5-HT_{2c} Structure Refinement

The structure of the PSD-95 PDZ1 – 5-HT_{2c} complex determined by CYANA [3.5.3] was refined using CNS version 1.2, first in vacuo and then water-refined (Brunger, 2007). The list of cross-peak assignments outputted from CYANA was imported into the previous CCPN Analysis project [3.5.3] and exported as NOE-distance restraints in CNS format (Appendices, A.5). The template Protein DataBank (PDB) files for each component of the complex (PSD-95 PDZ1, segment ID A and 5-HT_{2c}, segment ID B) were generated from their sequence. The individual PDZ domain and ligand PDB's were used to create PDB and molecular topology files (mtf) of the complex and used as inputs in CNS. The hydrogen bond restraints used in CYANA were converted into CNS format (Appendices, A.6) and used as restraint inputs along with

the NOE-distance restraints in the CNS refinement methodology (Figure 3.10).

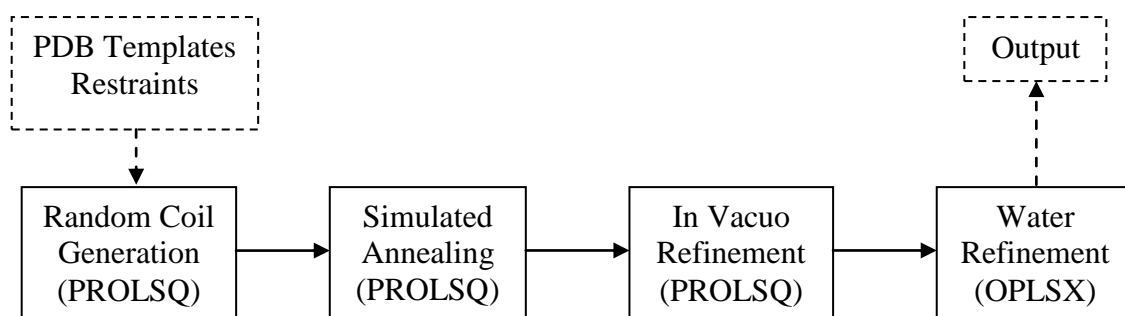


Figure 3.10: An overview of the CNS refinement protocol of the PSD-95 PDZ1 – 5-HT_{2c} structure determined by CYANA. The different non-bonded parameter force-field used in the different stages of the protocol is given in brackets. The input data (NOE-distance and hydrogen bond restraints and individual PDB's of the bound conformations of PSD-95 PDZ1 and 5-HT_{2c}) are used in 4 different Cartesian space molecular dynamics (MD) experiments – random coil generation followed by simulated annealing and in vacuo refinement and final explicit solvent refinement in water. The output from the CNS refinement methodology is an ensemble of the 20 lowest energy water-refined PSD-95 PDZ1 – 5-HT_{2c} complex structures.

The initial CNS in vacuo refinement protocol began with the generation of 100 random coil structures which were then subjected to two Cartesian space molecular dynamics (MD) simulated annealing stages: (i) a high-temperature phase in at 2,000K (4000 steps of 3fs integration time steps), (ii) cooling from 2000K to 100K in 50K temperature steps with 750 MD steps of 3s per temperature. At the end of the simulated annealing stage there was a final energy minimisation (400 steps).

The 100 structures were then refined in vacuo using a Cartesian space MD protocol consisting of: (i) a high temperature phase at 2,000K (20,000 steps of 5fs), (ii) Cartesian cooling phase from 2000K to 1000K (30,000 steps of 1fs) and (iii) Cartesian cooling phase from 1000K to 100K (12,000 steps of 1fs). At the end of the *in vacuo* refinement there was a final energy minimisation (500 steps).

The 20 lowest energy structures of the 100 obtained were water-refined using the final explicit solvent refinement protocol of the recalculated co-ordinate (RECOORD) database (Nederveen et al., 2005). This process involved: (i) immersion in a 7Å shell of water and energy minimisation, (ii) slow heating from 100K to 500K in 100K temperature steps with 200 MD steps of 3fs at each

temperature step, (iii) refinement at 500K with 2,000 MD steps of 4fs, (iv) slow cooling from 500K to 25K in 25K temperature steps with 200 MD steps of 4fs per temperature step and (v) final energy minimisation (200 steps). The output of this process was 20 water-refined structures of the PSD-95 PDZ1 – 5-HT_{2c} complex.

3.5.5 Rigid Body Semi-Flexible Restraint Driven Docking using HADDOCK

The HADDOCK webserver on the e-NMR GRID (<http://haddock.science.uu.nl/enmr/services/HADDOCK/haddock.php>) was utilised to determine the structure of the particular bound PDZ domain - small molecule complex. The HADDOCK webserver uses version 2.0 of HADDOCK, which is a docking method driven by experimental knowledge of the interface region between the molecular components. Unlike other docking programmes, HADDOCK allows for conformational change of the backbone and side chains of the molecules involved during complex formation. HADDOCK makes use of CNS version 1.2 as its ‘structure calculation engine’ but this is modified to use an optimised potential for liquid simulation **X** (OPLSX) force field and allow definition of additional docking restraints.

The HADDOCK webserver implements the full set of parameters supported by the HADDOCK programme and has access to the resources of the e-NMR GRID infrastructure (*). As a result, a typical docking run takes only a couple of minutes to prepare and a few hours to complete (Figure 3.11).

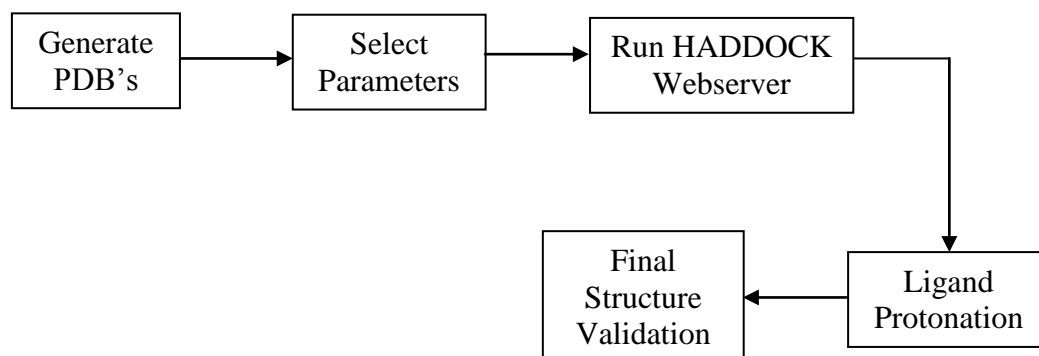


Figure 3.11: An overview of the different aspects of the HADDOCK webserver methodology used to determine the structure of the PDZ domain - small molecule inhibitor complexes. The PDB's of the protein and ligand were generated and inputted into the webserver. The most suitable parameters (including the NOE distance restraints) were selected and the HADDOCK webserver docking run started. The output from the webserver had the non-polar ligand protons added using CNS and the final structure quality validated by scoring energies and validation software including PROCHECK.

The HADDOCK webserver required both the initial protein and ligand information to be submitted as individual PDB files. The first PDZ domain component of the PSD-95 PDZ1&2 double domain crystal structure (PDB accession code: 3GSL, (Sainlos et al., 2011)) was used as the input for the PSD-95 PDZ1 domain. The lowest energy conformation structure of the small molecules were generated using ChemBio3D Ultra 12.0, saved as PDB files and used as the ligand input in the respective docking experiments.

On the HADDOCK webserver, there are a number of different possible interface selections, each of increasing complexity and allows greater user control over the docking procedure, on the HADDOCK webserver; for all docking runs the 'guru' interface was the chosen interface. This level of interface allows full control over most of the aspects of the docking procedure and supports a wide-range of experimental restraints including distance restraints determined by NMR spectroscopy.

The intermolecular and intra-ligand distance restraints were obtained as described in [3.5.1]; the protein side-chain atoms responsible for the NOE interactions observed were assigned by transfer of residue side-chain assignments from unbound assignments to the bound spectra. The specific atoms of the small molecule

inhibitors that showed NOE interactions to the particular PDZ domain were assigned by transfer of atom assignments from the unbound ^1H spectrum to the bound ^{13}C , ^{15}N F1-filtered ^1H spectrum. The cross-peak heights in the 2-D ^{13}C , ^{15}N F1-filtered NOESY experiment were used to calculate the distance restraints between atoms in the PDZ domain – small molecule inhibitor complex (Appendices, A.7 & A.8); the calculations were based on the proportional relationship between NOE intensity and interatomic distance described in chapter 2.

The HADDOCK docking process proceeds via several stages (Figures 3.12a & 3.12b); the initial step is the generation of CNS topologies of the molecules to be docked from the input PDB files. The actual docking protocol consists of three stages, with the first stage being a two temperature-step rigid body minimisation stage. The docked interface is then subjected to a two temperature-step semi-flexible simulated annealing stage, which minimizes clashing contacts. The final docking stage is a three temperature-step explicit solvent refinement process, where the presence of water in the molecular dynamics simulation provides a more realistic docked complex, both in side-chain orientation and surface polarity terms. The output structures from the HADDOCK webserver are subjected to clustering analysis and scored based on energy terms.

There are a number of different docking parameters that can be enabled or disabled in the docking procedure; the effect of each of these parameters on the output of the docking process was systematically investigated and the most suitable combination of these parameters for PDZ domain – small molecule complex determination was deduced (Table 3.6). It is possible to select PDZ domain residues that were thought to be involved in the small molecule binding to artificially direct the docking process i.e. the GLGF motif and conserved His residue; this would be biasing the docking

process based on no experimental evidence, which is obviously not ideal and so, this parameter was not used in the final docking conditions. Incorporating the intermolecular distance restraints determined by NMR spectroscopy as unambiguous restraints (where all NOE restraints are retained) rather than ambiguous restraints, (where 50% of NOE restraints are randomly discarded) gave less NOE violations and lower energy structures; thus, the NOE distance restraints were included as unambiguous restraints in the final docking parameter set. The structures obtained from docking runs where solvated docking was performed and all non-polar protons were kept, gave more realistic complex structures and so were included in the final docking conditions. The most suitable RMSD clustering cut-off was determined to be 1Å, as this gave the best balance between cluster size and overall structural similarity of the cluster. A range of various hydrogen bond restraints between the different residues of the GLGF motif and the 6-CO₂H group were investigated and, interestingly, were found to have little effect on the structure produced; this was also biasing the docking process with no experimental evidence to corroborate and so, hydrogen bond restraints were omitted from the final docking conditions used on the HADDOCK webserver.

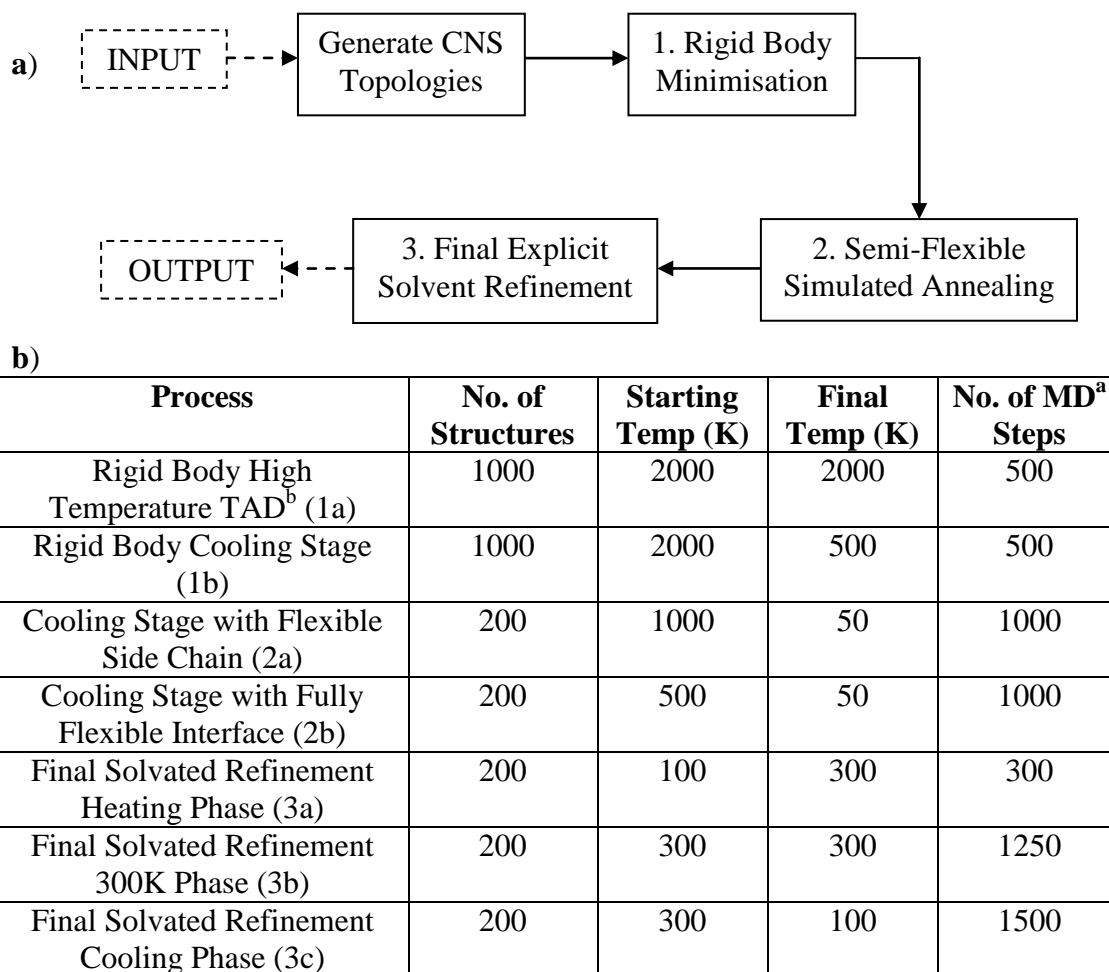


Figure 3.12: a) An overview of the different stages in the docking process carried out by the HADDOCK webserver. The HADDOCK webserver automatically generates the topology and energy parameters for the inputted PDZ domain and small molecule to be docked from the GlycoBioChem PRODRG2 server (<http://davapc1.bioch.dundee.ac.uk/prodrg/>). The docking protocol then consists of a rigid body minimization, followed by a semi-flexible refinement in torsion angle space and a final explicit solvent refinement in water. The docked complexes are then outputted as PDB files. b) ^a MD = Molecular dynamics The key parameters i.e. number of structures, starting and final temperature and the number of MD steps at the various different stages of the HADDOCK docking protocol.

Table 3.6: The various different parameters available to the user of the ‘guru level’ interface of the HADDOCK webserver. Each of these were trialled in order to obtain the best possible of the PDZ domain - inhibitor complexes. Active residues are residues of the PDZ domain that were selected as they were thought to be involved in small molecule binding and so, artificially direct the docking process. The distance restraints determined by NMR could either be included in the docking process as ‘ambiguous restraints’ (50% randomly removed) or ‘unambiguous restraints’ (all retained). The non-polar proton removal option removes non-polar protons at the beginning of the docking protocol and does not replace them. Solvated docking allows for the presence of water molecules in all the docking stages, not solely the final refinement stage in non-solvated docking. The RMSD clustering cut-off refers to the maximum allowed distance deviation in corresponding complex structures to be clustered together in the analysis stage of the HADDOCK webserver process. Similarly to the active residues option, hydrogen bonds that were believed to occur in the complex could be specified. The highlighted row at the bottom of the table indicates the optimal conditions used for all PDZ domain – inhibitor complexes.

Active Residues	Ambiguous Restraints	Unambiguous Restraints	Non-Polar Proton Removal	Solvated Docking	RMSD Clustering Cut-Off	Hydrogen Bonds
¹⁸ GLGF ²¹ , 74H	No	No	Yes	No	No	No
¹⁸ GLGF ²¹ , 74H	Yes	No	Yes	No	No	No
No	Yes	No	Yes	No	No	No
No	Yes	Yes	Yes	No	No	No
No	No	Yes	Yes	No	No	No
No	No	Yes	Yes	No	3Å	No
No	No	Yes	Yes	No	1Å	No
No	No	Yes	Yes	No	0.5Å	No
No	No	Yes	Yes	No	1Å	19L or 20G
No	No	Yes	Yes	No	1Å	20G or 21F
No	No	Yes	Yes	No	1Å	19L or 20G or 21F
No	No	Yes	Yes	Yes	1Å	No
No	No	Yes	No	Yes	1Å	No

As the desired docking parameter set for the HADDOCK webserver ‘guru’ interface had been established, the restraint-driven docking process was then initiated; the output of the docking procedure is ranked based on a fully flexible scoring system termed the ‘HADDOCK score.’ This is a weighted sum of all the different energy terms calculated during the run; the individual weighting for an energy term can be manually altered if required. The cluster with the lowest average sum of energy terms (HADDOCK score) is ranked first and hence, it is the lowest energy cluster obtained from the docking run. The 20 lowest energy structures of the lowest energy cluster were selected and analysed externally of the HADDOCK webserver, using the WHAT IF web interface (Vriend, 1990); this was to ensure that all the structures obtained were viable. The structures obtained from the HADDOCK webserver had all the protein protons present but only the polar protons present on the small molecule inhibitors. Thus, the process of re-protonation and geometry optimisation was performed outside the HADDOCK webserver using CNS version 1.2; this process was conducted on the lowest energy structure in the lowest energy cluster i.e. the representative structure.

To complete the protonation of the complex, the PDB file of the representative structure was split into its individual components and saved as two separate PDB files (PDZ domain and small molecule). The individual PDZ domain and ligand PDB’s were used to create PDB and molecular topology files (mtf) of the complex [3.5.4] using the standard CNS generate hydrogen’s protocol (Appendices, A.1b); the resultant PDB file of the complex was fully protonated. Finally, the quality of the final PDZ domain – small molecule complex structure was verified externally of HADDOCK or CNS, using PROCHECK (Laskowski et al., 1993).

Chapter 4

**THE BIOPHYSICAL CHARACTERISATION OF PDZ
INTERACTIONS INVOLVING THE 5-HYDROXYTRYPTAMINE
RECEPTOR 2A AND 2C VARIANTS**

4. THE BIOPHYSICAL CHARACTERISATION OF PDZ INTERACTIONS INVOLVING THE 5-HYDROXYTRYPTAMINE RECEPTOR 2A AND 2C VARIANTS

4.1 Introduction

As detailed in [1.5.2.2], the 5-hydroxytryptamine receptor 2a and 2c variants (5-HT_{2a} and 5-HT_{2c} respectively) are known to interact with the PSD-95 PDZ domains; the 5-HT_{2a/c} receptors are able to interact with the PSD-95 PDZ domains via their C-terminal class I PDZ domain binding motif i.e. X-S/T-X-Ω (VSCV and ISSV respectively).

The PSD-95 PDZ 5-HT_{2a} interaction has been found to enhance 5-HT_{2a} receptor-mediated signal transduction (Xia et al., 2003) and to be essential for somatodendritic targeting of 5-HT_{2a}, both *in vitro* and *in vivo* (Xia et al., 2003, Abbas et al., 2009). The PSD-95 PDZ domain-mediated interaction with 5-HT_{2c} is extremely important in the regulation, expression, synaptic localisation and organisation of 5-HT_{2c} (Becamel et al., 2002, Anastasio et al., 2010). However, the PDZ domain-mediated interactions between PSD-95 and 5-HT_{2a/c} have recently been implicated in a variety of pathological conditions, such as induced analgesia in painful diabetic neuropathy (Roth, 2011); this is because inhibition of the interaction resulted in reduced hyperalgesia in neuropathic pain (Pichon et al., 2010). This has led to the conclusion that disruption of the PDZ domain-mediated interaction between the 5-HT_{2a/c} receptors and PSD-95, as well as the related PSD-MAGUK protein SAP97, are valid therapeutic targets.

However, there have been no studies to date that have used a combination of NMR spectroscopy and ITC to qualitatively and quantitatively characterise the binding of 5-HT_{2a/c} to the PSD-95 and SAP97 PDZ domains. Furthermore, there are no

structures of the complex formed between a PSD-95/SAP97 PDZ domain and 5-HT_{2a/c} currently available in the PDB; these are the aims of the research discussed in this chapter.

The results of the transformation, expression and purification of the PSD-95 and SAP97 PDZ1 & PDZ2 domains are summarised in this chapter. NMR spectroscopy was used to determine the individual residue chemical shift assignments of three of the four (¹³C, ¹⁵N)-isotopically labelled PDZ domains. NMR spectroscopy was also employed to determine if there was any binding observed between a particular PDZ domain and a C-terminal nonapeptide of the 5-HT_{2a} or 5-HT_{2c} receptors; the binding observed was then quantified using ITC. Finally, the NMR spectroscopy solution state structure of the complex formed between the PSD-95 PDZ1 domain and the C-terminal peptide of 5-HT_{2c} was determined.

4.2 Purification of the PSD-95 and SAP97 PDZ1 & PDZ2 Domains

The transformation, expression and purification of unlabelled and (¹³C, ¹⁵N)-isotopically labelled PSD-95 and SAP97 PDZ1 & PDZ2 domains were carried out as detailed in [3.2.1.3], [3.2.2] and [3.2.3] respectively.

The chromatograms produced from size exclusion chromatography, the final purification stage of the four different PDZ domains, can be seen as a chromatogram overlay (Figure 4.1a). The size exclusion column had been previously calibrated (Appendices A.2) and so, the respective PDZ domain elution volumes in the size exclusion chromatography indicate the oligomeric states of the four different PDZ domains. As an elution volume of ~ 220mL was determined to correspond to a molecular weight of ~10kDa, all four PDZ domains were deduced to be monomeric. Samples of each of the four PDZ domains obtained at the end of the protein purification process were analysed by SDS-PAGE gel electrophoresis to ensure their

purity (Figure 4.1b); the SDS-PAGE gel showed each of the four different PDZ domains to be pure.

NMR spectroscopy was then utilised to ensure that the four PDZ domains were folded and then subsequently, in an attempt to determine the individual backbone residue chemical shift assignments of each individual PDZ domain.

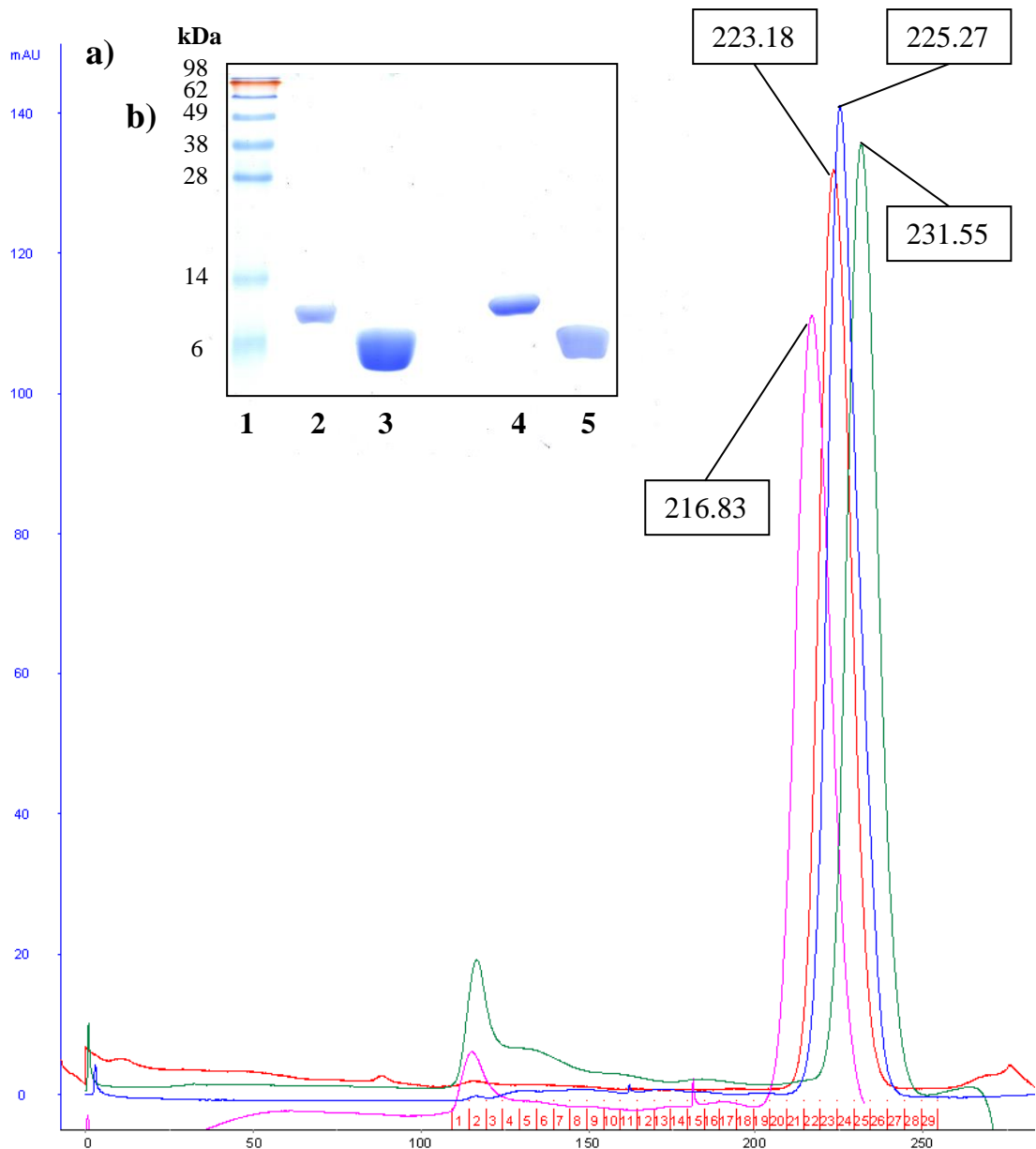


Figure 4.1: The chromatograms obtained from size exclusion chromatography using a HiLoad 26/60 Superdex 75 in 50mM Tris/HCl, 150mM NaCl, 2mM DTT buffer, pH 7.4; this was the final stage of the PDZ domain purification process. The size exclusion chromatograms for PSD-95 PDZ1 (pink), PSD-95 PDZ2 (green), SAP97 PDZ1 (blue) and SAP97 PDZ2 (red) are shown. The elution volume for each of the four PDZ domain chromatograms has been detailed; the column equilibration (Appendices, A.2) indicated that an elution volume of ~220mL corresponds to ~10kDa protein and thus, all four PDZ domains are shown to be within acceptable limit values for monomeric proteins. The corresponding SDS-PAGE gel (inset) of the obtained proteins shown that each final PDZ domain samples obtained was pure; 1 = marker, 2 = PSD-95 PDZ1, 3 = PSD-95 PDZ2, 4 = SAP97 PDZ1, 5 = SAP97 PDZ2.

4.3 Characterisation of the PDZ Domains by NMR Spectroscopy

Unlabelled and ^{15}N -labelled PDZ domain samples were prepared as described in [3.3.1] and both 1-D ^1H and 2-D $^1\text{H} - ^{15}\text{N}$ HSQC NMR spectroscopic experiments were performed. The resultant NMR spectra showed that all four PDZ domains were

definitely folded (Figure 4.2 – 4.6); this is shown by the well-defined and dispersed peaks present in the obtained NMR spectra for each PDZ individual domain. The assignment of the residue backbone NH chemical shifts present in the $^1\text{H} - ^{15}\text{N}$ HSQC spectra of the four different PDZ domains was then attempted. To do this, ^{13}C , ^{15}N -doubly labelled PDZ domain NMR samples were prepared [3.3.1 & 3.3.2], a suite of NMR spectroscopic experiments collected [3.5.1] and assigned using the methodology described in [3.5.2].

This process resulted in the complete residue backbone NH assignments for PSD-95 PDZ1, SAP97 PDZ1 & PDZ2 (Figures 4.3, 4.5 & 4.6 respectively). Unfortunately it was not possible to collect sufficient quality NMR spectra to facilitate a full assignment of the PSD-95 PDZ2; this was due to the limited stability of the protein. However, a limited assignment of the PSD-95 PDZ2 residue backbone NH chemical shifts was achieved by a combination of NMR spectroscopy and sequence comparison with PSD-95 PDZ1 (Figure 4.4).

As the four PDZ domains were shown to be folded, monomeric and the backbone NH chemical shifts assigned, NMR spectroscopy was then utilised to determine if there were any observable interactions between the four individual PDZ domains and the different 5-HT_{2a/c} nonapeptides; the residue assignments could be used to determine if any binding observed was specific or not.

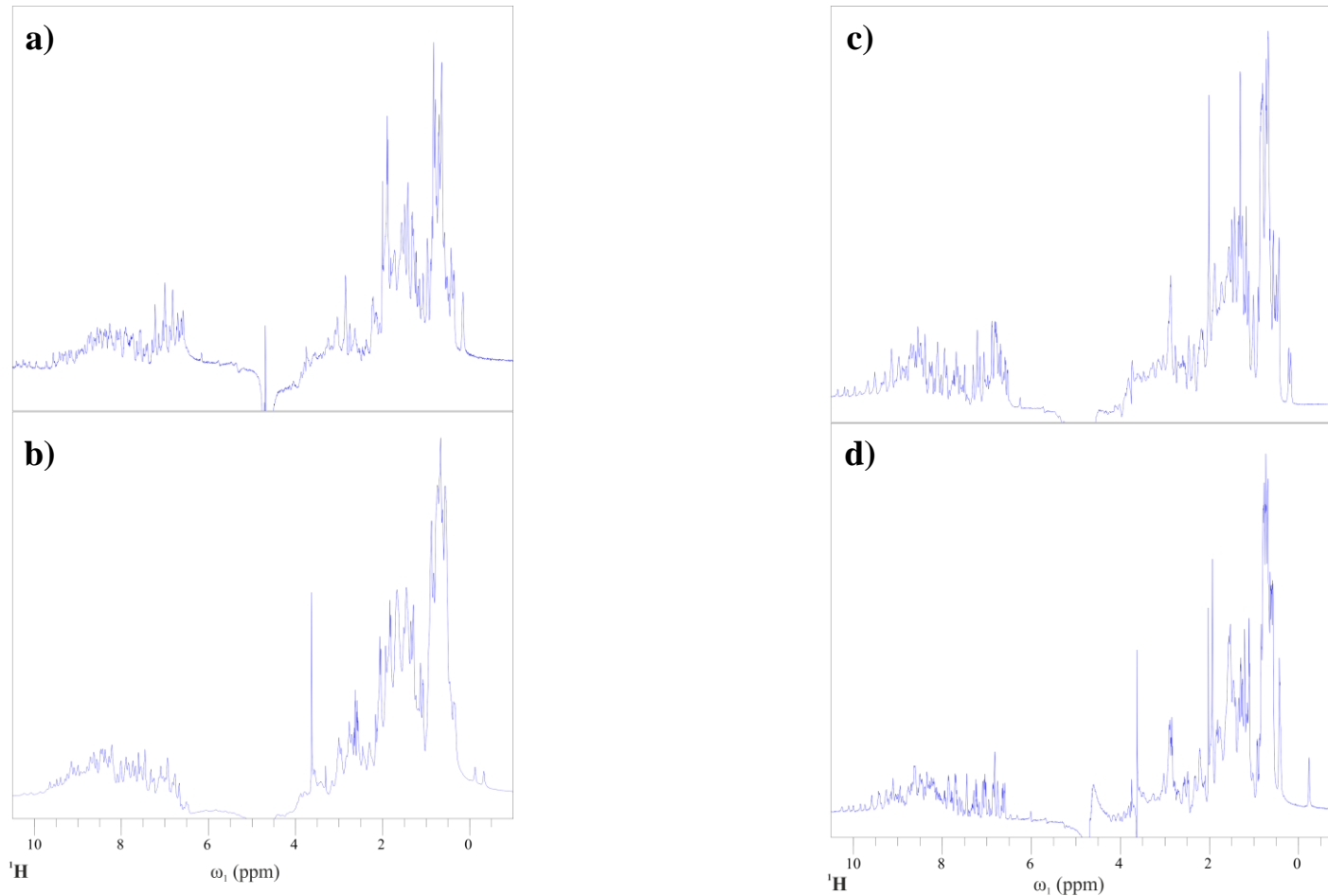


Figure 4.2: The 1-D ^1H NMR spectra of the PSD-95 and SAP97 PDZ1&2 domains acquired at 298K, with a field strength of 600MHz, in 20mM phosphate buffer, pH6.3. a) PSD-95 PDZ1. b) PSD-95 PDZ2. c) SAP97 PDZ1. d) SAP97 PDZ2 (red, bottom). All four NMR spectra shown indicate that the four PDZ domains produced were folded as the peaks are well defined and there is evidence of peak dispersion around the extreme upfield methyl (0ppm) region.

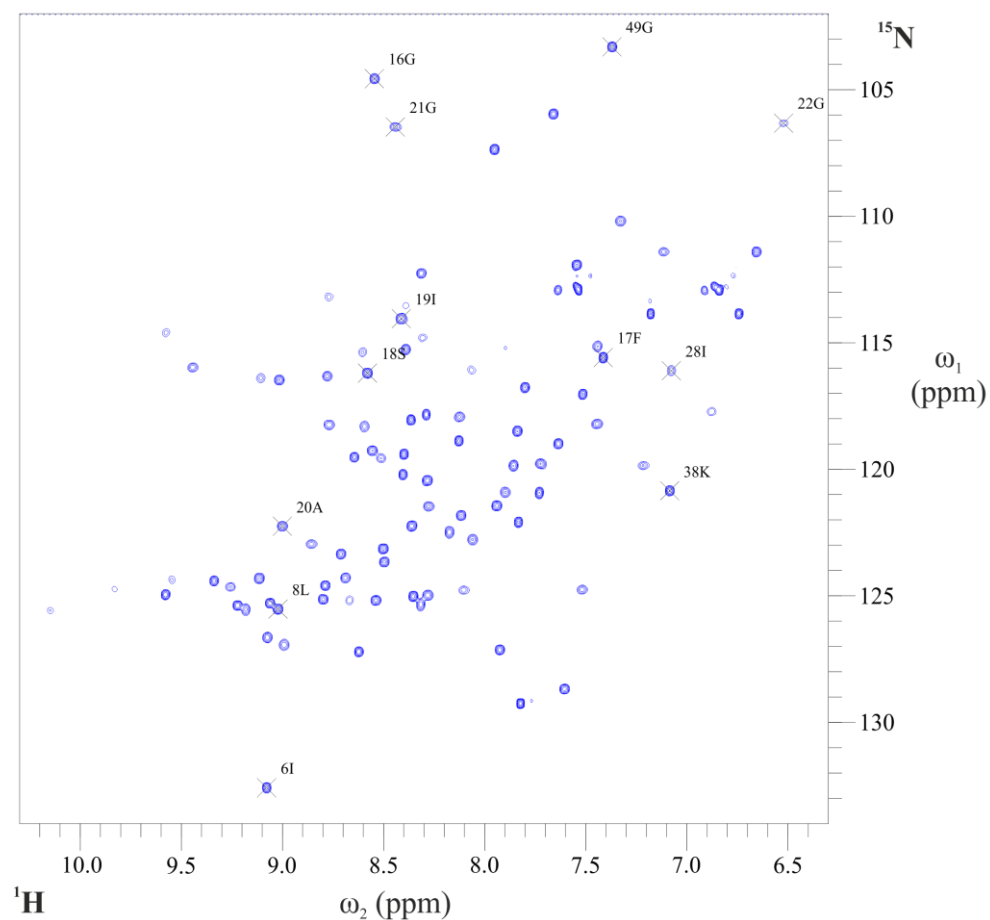


Figure 4.4: The 2-D $^1\text{H} - ^{15}\text{N}$ HSQC spectrum of PSD-95 PDZ2 acquired at 298K, with a field strength of 600MHz, in 20mM phosphate buffer, pH6.3; the individual residue chemical shift assignments for the PSD-95 PDZ2 domain construct were attempted by collecting a suite of NMR experiments [3.5.1], on a prepared NMR sample [3.3.1 & 3.3.2] and then, following the assignment methodology described in [3.5.2]. The given spectrum shows that the PSD-95 PDZ2 domain is folded, as the peaks are well dispersed; however, the PSD-95 PDZ2 NMR sample proved unsuitable for full NMR data collection, possibly due to aggregation and so, a complete backbone NH assignment was not possible. A partial assignment of the PSD-95 PDZ2 $^1\text{H} - ^{15}\text{N}$ HSQC spectrum has been performed using the NMR data that was successfully obtained and sequence similarity comparison with the PSD-95 PDZ1 domain.

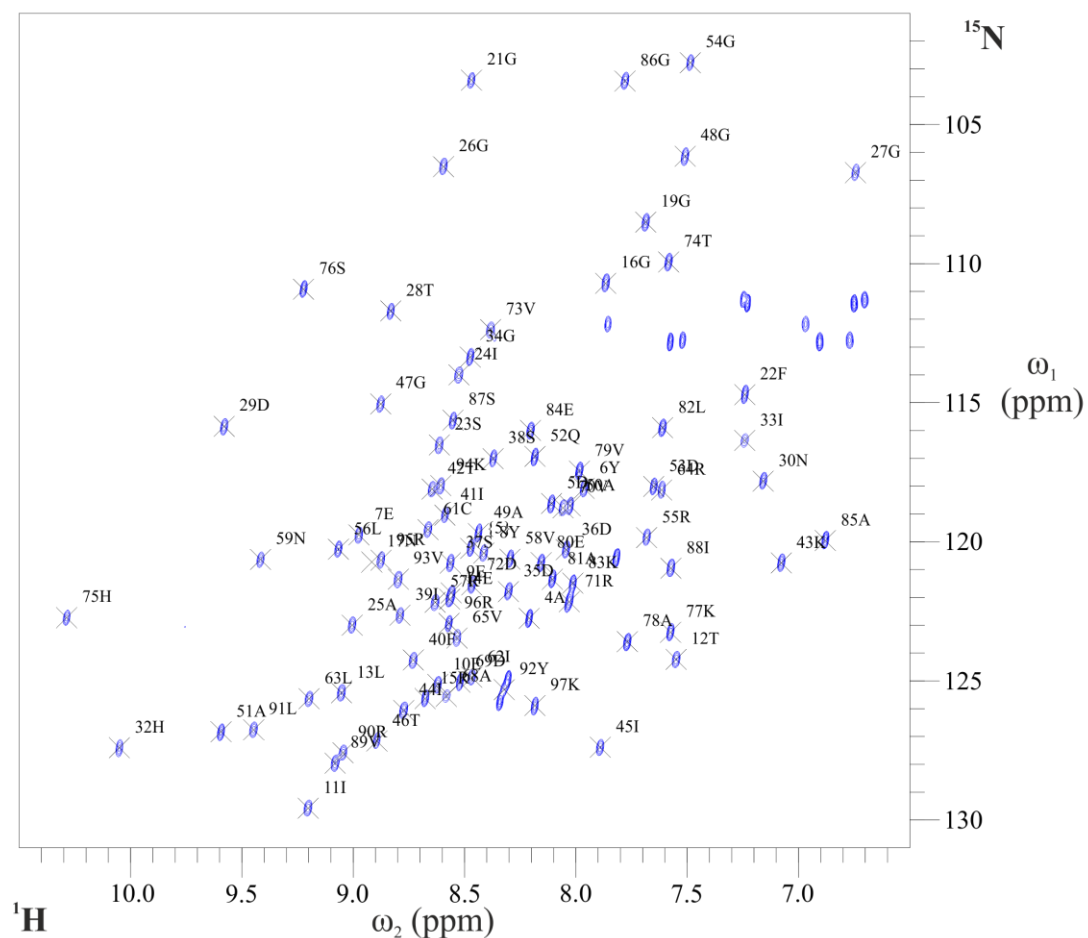


Figure 4.5: The 2-D $^1\text{H} - ^{15}\text{N}$ HSQC spectrum of SAP97 PDZ1 acquired at 298K, with a field strength of 600MHz, in 20mM phosphate buffer, pH6.3; the individual residue chemical shift assignments for the SAP97 PDZ1 domain construct were completed using a suite of NMR experiments [3.5.1], on a prepared NMR sample [3.3.1 & 3.3.2] and then, following the assignment methodology described in [3.5.2]. The given spectrum shows that the SAP97 PDZ1 domain is folded, as the peaks are well dispersed and that almost all of the peaks present were able to be definitively assigned.

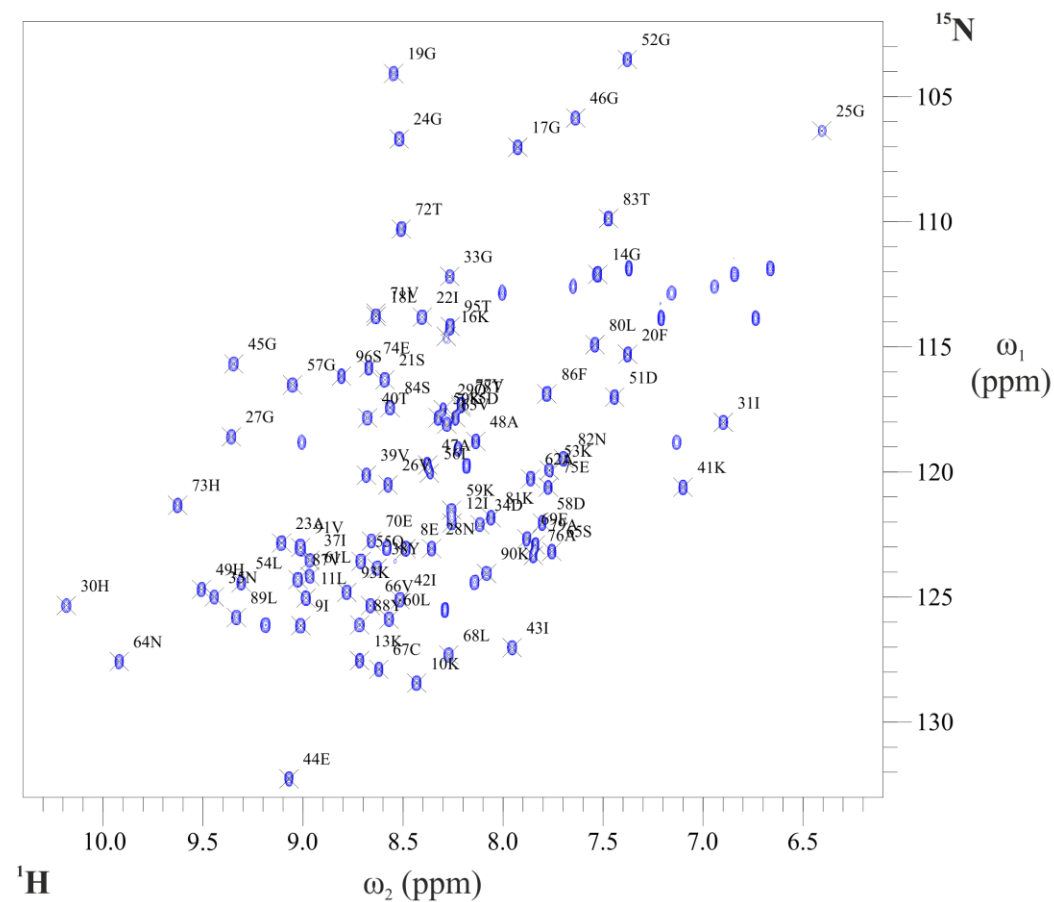


Figure 4.6: The 2-D $^1\text{H} - ^{15}\text{N}$ HSQC spectrum of SAP97 PDZ2 acquired at 298K, with a field strength of 600MHz, in 20mM phosphate buffer, pH6.3; the individual residue chemical shift assignments for the SAP97 PDZ2 domain construct were completed using a suite of NMR experiments [3.5.1], on a prepared NMR sample [3.3.1 & 3.3.2] and then, following the assignment methodology described in [3.5.2]. The given spectrum shows that the SAP97 PDZ2 domain is folded, as the peaks are well dispersed and that almost all of the peaks present were able to be definitively assigned.

4.4 PDZ Domain Binding Screening of 5-HT_{2x} Receptors by NMR Spectroscopy

4.4.1 General

The sample preparation and experimental conditions employed in the binding screening of the 5-HT_{2a/c} peptides to the four different PDZ domains, by NMR spectroscopy, are described in [3.3.1 & 3.3.4]. The nine residue C-terminal peptides of 5-HT_{2a} (GVNEKVSCV) and 5-HT_{2c} (VVSERISSV) were purchased from Innobiochips, France and GenicBio, China respectively.

4.4.2 PDZ Domain-Mediated Interactions of 5-HT_{2a}

The binding of a 5-HT_{2a} nonapeptide to the four different PDZ domains was investigated by NMR spectroscopy (Figures 4.7 – 4.10); this process indicated that the 5-HT_{2a} nonapeptide bound to all four of the PDZ domains. This conclusion was made as a result of the large number and/or magnitude of the residue chemical shift perturbations observed in the ¹H – ¹⁵N HSQC spectra in the presence of the peptide c.f. the free PDZ domain spectra. The binding of the 5-HT_{2a} nonapeptide to each individual PDZ domain was determined to be specific as the residues perturbed in each experiment were those of the respective PDZ domain ligand binding region that showed perturbations i.e. GLGF motif, hydrophobic binding pocket, conserved His residue, βB – βC loop etc.

4.4.3 PDZ Domain-Mediated Interactions of 5-HT_{2c}

The binding of the 5-HT_{2c} nonapeptide to the four different PDZ domains was investigated by NMR spectroscopy (Figures 4.11 – 4.14); this process indicated that the 5-HT_{2c} nonapeptide bound to all four of the PDZ domains with reasonable affinity. This conclusion was made as a result of the large number and/or magnitude of the residue chemical shift perturbations observed in the ¹H – ¹⁵N HSQC spectra in the presence of the peptide c.f. the free PDZ domain spectra. The binding of the 5-

HT_{2c} nonapeptide to each individual PDZ domain was determined to be specific as it was the residues of the respective PDZ domain binding region that showed perturbations i.e. GLGF motif, hydrophobic binding pocket, conserved His residue, β B – β C loop etc.

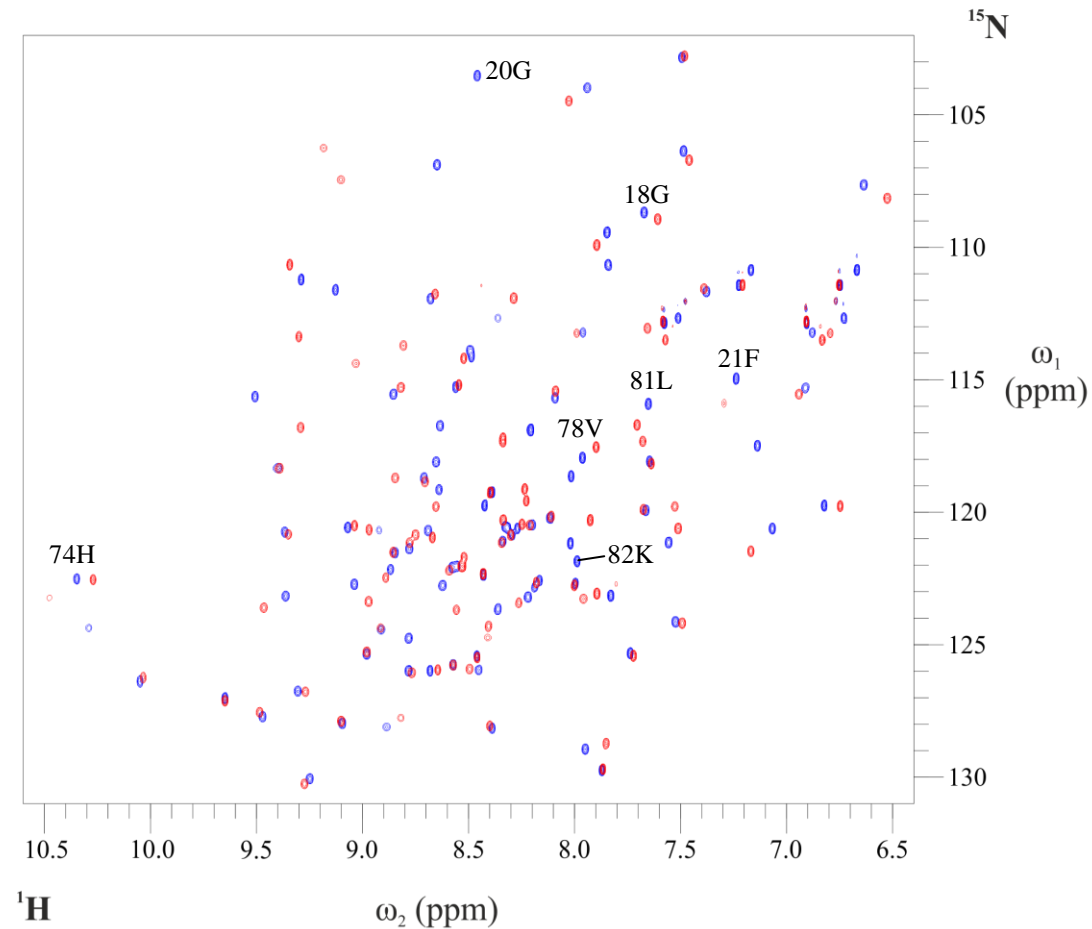


Figure 4.7: A 2-D overlay of the $^1\text{H} - ^{15}\text{N}$ HSQC spectra produced of PSD-95 PDZ1 in the free form (blue) and in the presence of 5-HT_{2a} nonapeptide (P:L = 1:10, red), acquired at 298K, with a field strength of 600MHz, in 20mM phosphate buffer, pH6.3; a number of the key peaks from residues in the GLGF motif, hydrophobic pocket and the conserved His have been labelled. It can be clearly seen that these peaks and many other peaks present in the apo PSD-95 PDZ1 spectrum shift in the presence of 5-HT_{2a}; this indicates that there is specific binding occurring between the PSD-95 PDZ1 domain and 5-HT_{2a} nonapeptide and that this binding is of reasonable affinity.

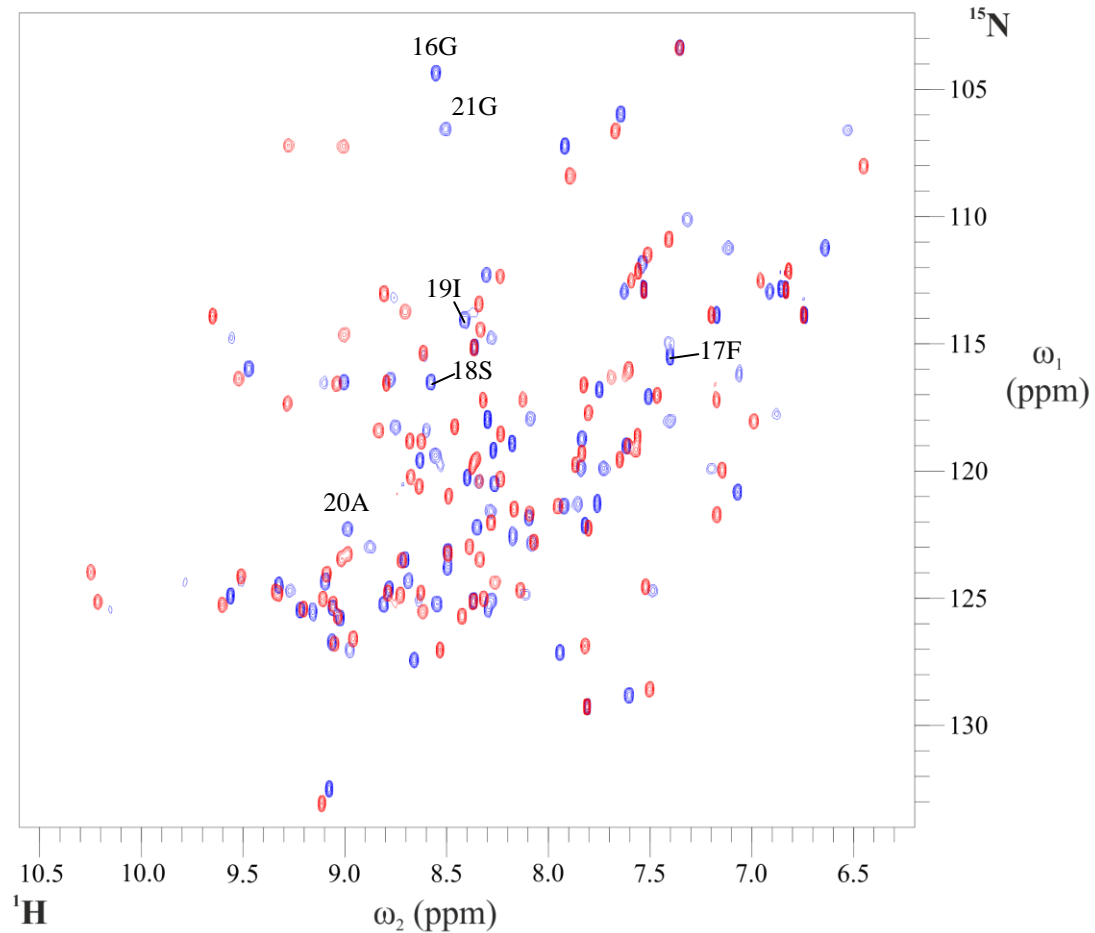


Figure 4.8: A 2-D overlay of the $^1\text{H} - ^{15}\text{N}$ HSQC spectra produced of PSD-95 PDZ2 in the free form (blue) and in the presence of 5-HT_{2a} nonapeptide (P:L = 1:10, red), acquired at 298K, with a field strength of 600MHz, in 20mM phosphate buffer, pH6.3; a number of the key peaks from residues in the GLGF motif and surrounding binding region have been labelled. It can be clearly seen that these peaks and many other peaks present in the apo PSD-95 PDZ2 spectrum shift in the presence of 5-HT_{2a}; this indicates that there is specific binding occurring between the PSD-95 PDZ2 domain and 5-HT_{2a} nonapeptide and that this binding is of reasonable affinity.

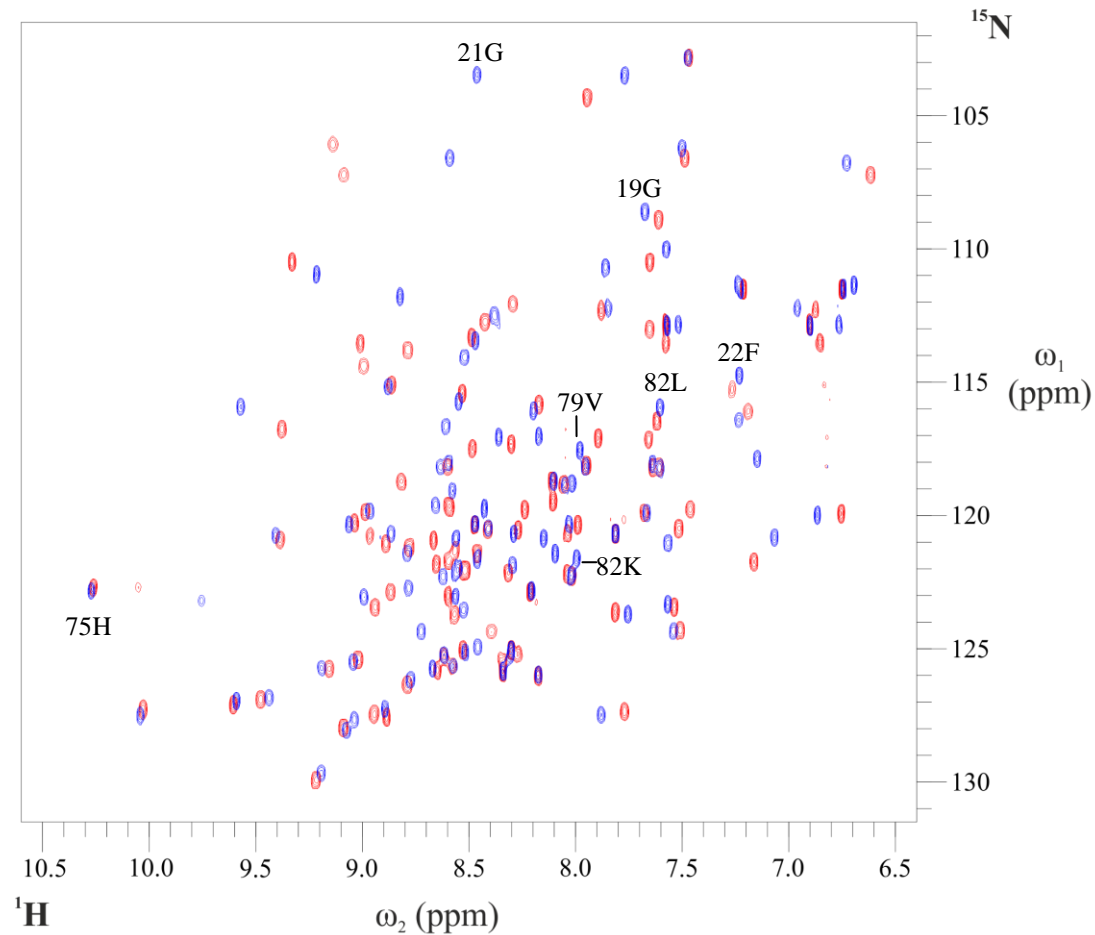


Figure 4.9: A 2-D overlay of the $^1\text{H} - ^{15}\text{N}$ HSQC spectra produced of SAP97 PDZ1 in the free form (blue) and in the presence of 5-HT_{2a} nonapeptide (P:L = 1:10, red), acquired at 298K, with a field strength of 600MHz, in 20mM phosphate buffer, pH6.3; a number of the key peaks from residues in the GLGF motif, hydrophobic pocket and the conserved His have been labelled. It can be clearly seen that these peaks and many other peaks present in the apo SAP97 PDZ1 spectrum shift in the presence of 5-HT_{2a}; this indicates that there is specific binding occurring between the SAP97 PDZ1 domain and 5-HT_{2a} nonapeptide and that this binding is of reasonable affinity.

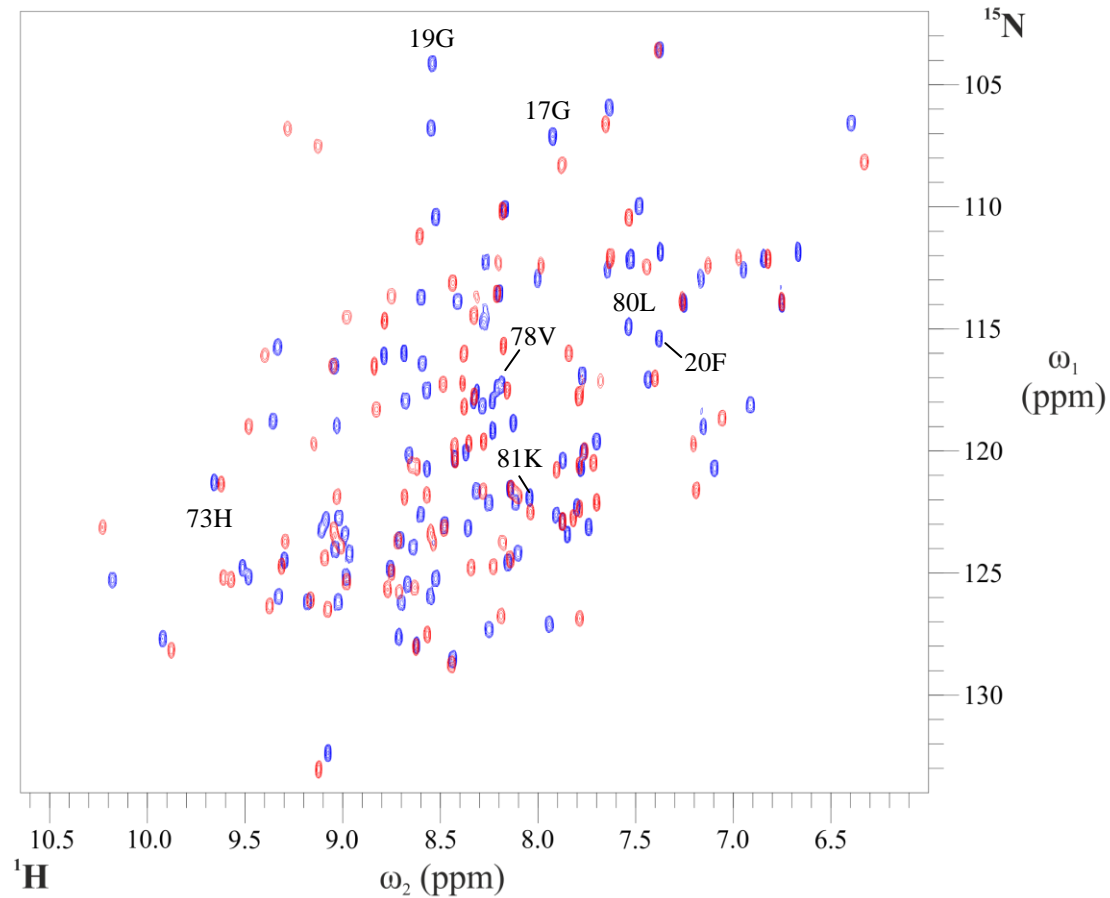


Figure 4.10: A 2-D overlay of the $^1\text{H} - ^{15}\text{N}$ HSQC spectra produced of SAP97 PDZ2 in the free form (blue) and in the presence of 5-HT_{2a} nonapeptide (P:L = 1:10, red), acquired at 298K, with a field strength of 600MHz, in 20mM phosphate buffer, pH6.3; a number of the key peaks from residues in the GLGF motif, hydrophobic pocket and the conserved His have been labelled. It can be clearly seen that these peaks and many other peaks present in the apo SAP97 PDZ2 spectrum shift in the presence of 5-HT_{2a}; this indicates that there is specific binding occurring between the SAP97 PDZ2 domain and 5-HT_{2a} nonapeptide and that this binding is of reasonable affinity.

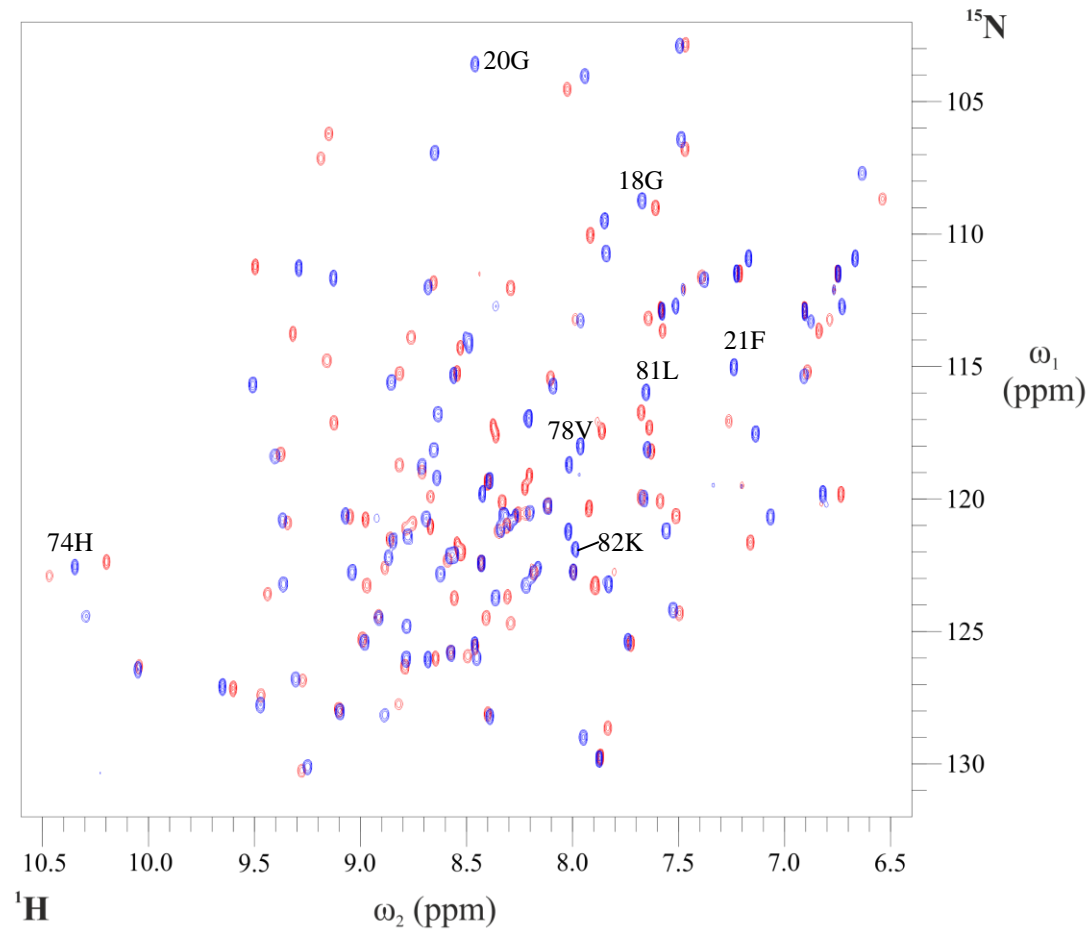


Figure 4.11: A 2-D overlay of the $^1\text{H} - ^{15}\text{N}$ HSQC spectra produced of PSD-95 PDZ1 in the free form (blue) and in the presence of 5-HT_{2c} nonapeptide (P:L = 1:10, red), acquired at 298K, with a field strength of 600MHz, in 20mM phosphate buffer, pH6.3; a number of the key peaks from residues in the GLGF motif, hydrophobic pocket and the conserved His have been labelled. It can be clearly seen that these peaks and many other peaks present in the apo PSD-95 PDZ1 spectrum shift in the presence of 5-HT_{2c}; this indicates that there is specific binding occurring between the PSD-95 PDZ1 domain and 5-HT_{2c} nonapeptide and that this binding is of reasonable affinity.

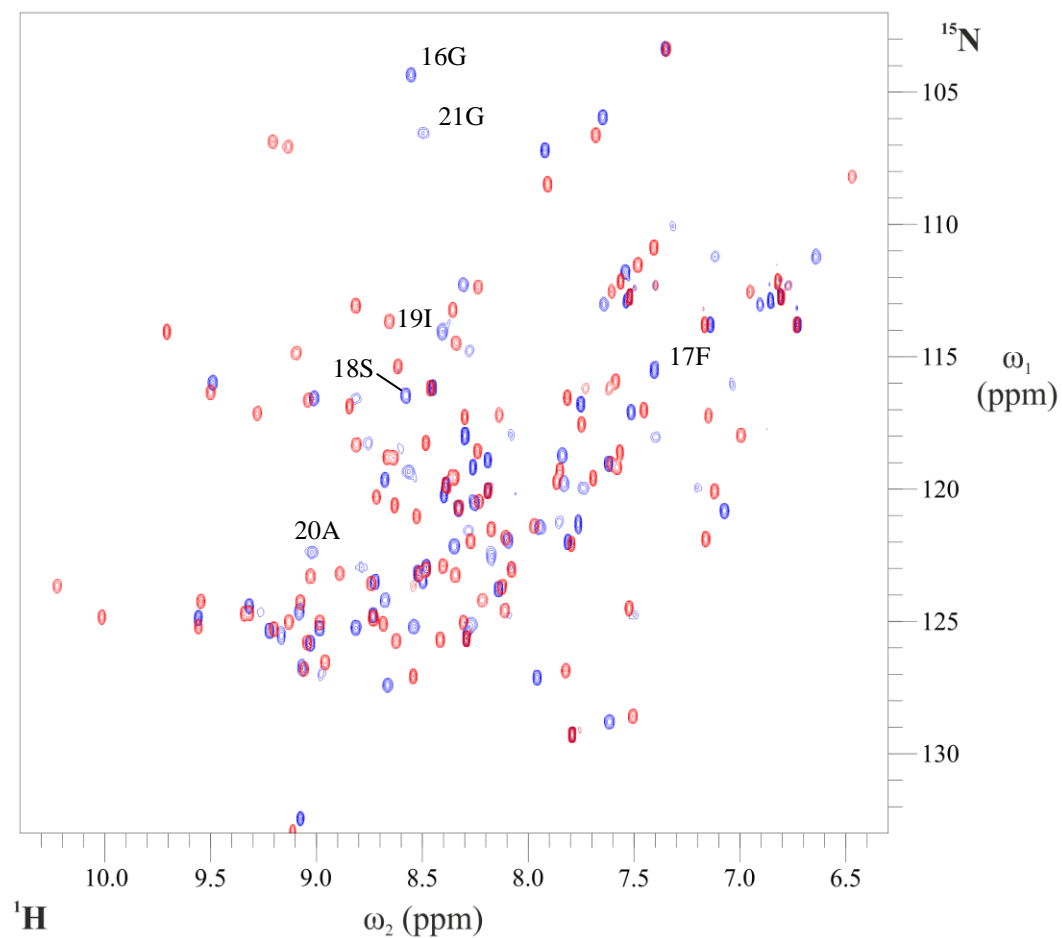


Figure 4.12: A 2-D overlay of the $^1\text{H} - ^{15}\text{N}$ HSQC spectra produced of PSD-95 PDZ2 in the free form (blue) and in the presence of 5-HT_{2c} nonapeptide (P:L = 1:10, red), acquired at 298K, with a field strength of 600MHz, in 20mM phosphate buffer, pH6.3; a number of the key peaks from residues in the GLGF motif and surrounding binding region have been labelled. It can be clearly seen that these peaks and many other peaks present in the apo PSD-95 PDZ2 spectrum shift in the presence of 5-HT_{2c}; this indicates that there is specific binding occurring between the PSD-95 PDZ2 domain and 5-HT_{2c} nonapeptide and that this binding is of reasonable affinity.

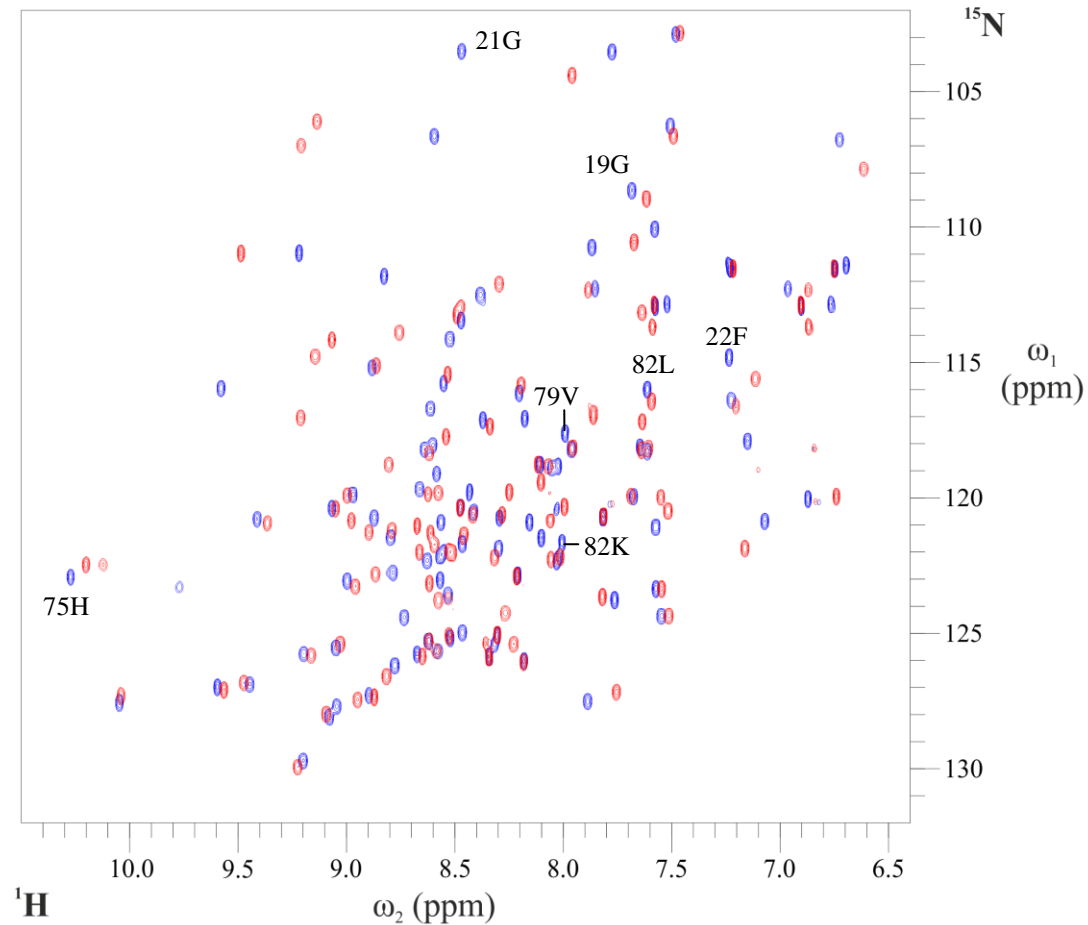


Figure 4.13: A 2-D overlay of the $^1\text{H} - ^{15}\text{N}$ HSQC spectra produced of SAP97 PDZ1 in the free form (blue) and in the presence of 5-HT_{2c} nonapeptide (P:L = 1:10, red), acquired at 298K, with a field strength of 600MHz, in 20mM phosphate buffer, pH6.3; a number of the key peaks from residues in the GLGF motif, hydrophobic pocket and the conserved His have been labelled. It can be clearly seen that these peaks and many other peaks present in the apo SAP97 PDZ1 spectrum shift in the presence of 5-HT_{2c}; this indicates that there is specific binding occurring between the SAP97 PDZ1 domain and 5-HT_{2c} nonapeptide and that this binding is of reasonable affinity.

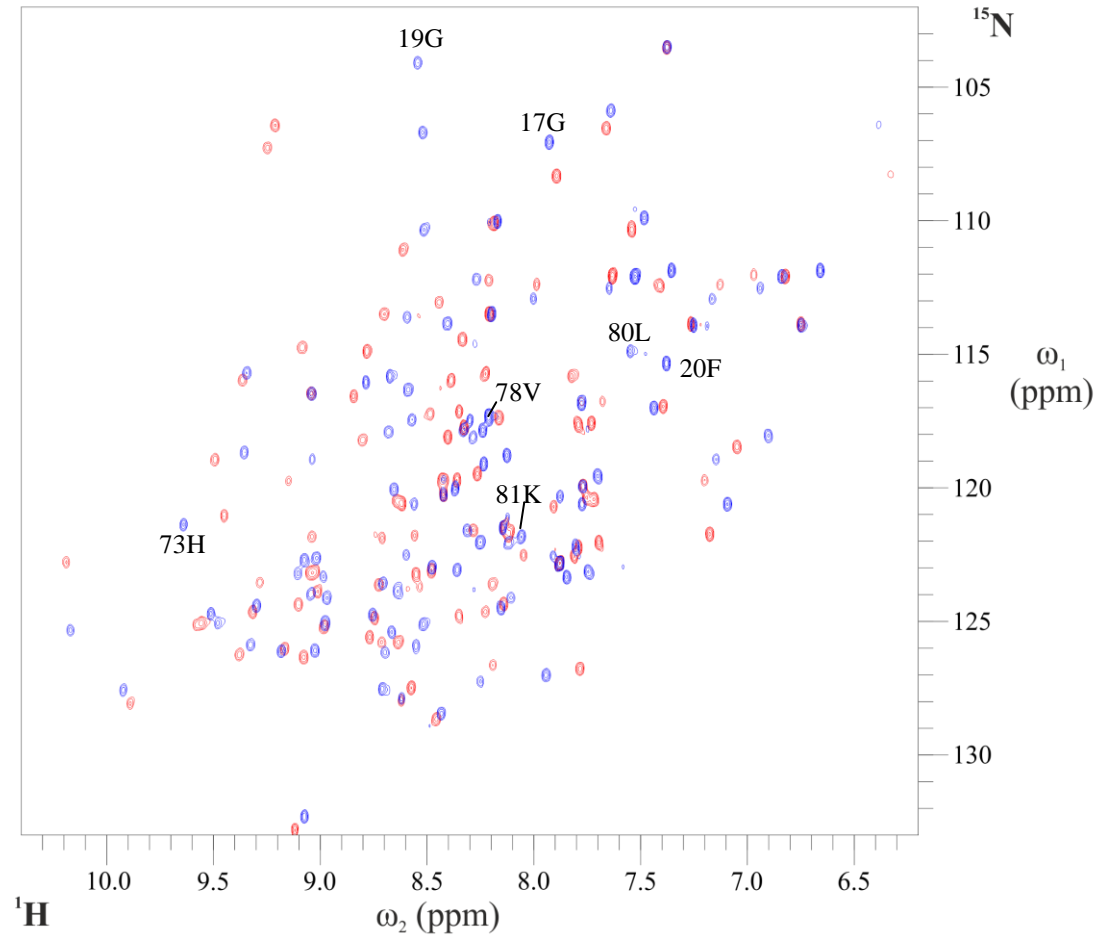


Figure 4.14: A 2-D overlay of the $^1\text{H} - ^{15}\text{N}$ HSQC spectra produced of SAP97 PDZ2 in the free form (blue) and in the presence of 5-HT_{2c} nonapeptide (P:L = 1:10, red), acquired at 298K, with a field strength of 600MHz, in 20mM phosphate buffer, pH6.3; a number of the key peaks from residues in the GLGF motif, hydrophobic pocket and the conserved His have been labelled. It can be clearly seen that these peaks and many other peaks present in the apo SAP97 PDZ2 spectrum shift in the presence of 5-HT_{2c}; this indicates that there is specific binding occurring between the SAP97 PDZ2 domain and 5-HT_{2c} nonapeptide and that this binding is of reasonable affinity.

4.4.4 Discussion

The binding screening utilising NMR spectroscopy showed that both the 5-HT_{2a} and 5-HT_{2c} nonapeptides bound specifically to all four of the PDZ domains investigated. The screening indicated that regardless of the particular peptide or PDZ domain involved, the pattern and strength of perturbations shown in the subsequent spectra were reasonably similar.

The binding of the 5-HT_{2a/c} nonapeptides to the four different PDZ domains was determined to be specific as the residues perturbed from the respective free spectra upon binding, were those of the known PDZ domain binding regions. The residue chemical shift perturbations induced in the PSD-95 PDZ1 domain upon binding of the 5-HT_{2c} nonapeptide were then quantified. This was achieved by performing an NMR titration, where the ligand concentration was varied [3.3.5]; related examples of this titration methodology are given in [6.3] and so, the resultant spectra will not be given here. The individual residue chemical shifts were tracked from P:L = 1:0 to 1:10 (i.e. the ligand binding screening ratio) to allow the assignment of the 5-HT_{2c} bound PSD-95 PDZ1 spectrum; the assigned NMR spectra of the PSD-95 PDZ1 – 5-HT_{2c} complex are given in [4.6.2] and so, will not be shown here. The difference in the individual residue chemical shifts between the nonapeptide free and the binding screening PSD-95 PDZ1 bound forms was then calculated [3.3.4] and plotted (Figure 4.15). The histogram indicates that the residues most significantly perturbed in the PSD-95 PDZ1 domain upon binding of the 5-HT_{2c} nonapeptide are those of the expected PDZ binding region and the surrounding flexible regions i.e. the GLGF motif (red), hydrophobic pocket (dark blue), conserved His (green) and the BB-BC loop (yellow); this definitively confirmed the binding was specific.

As the NMR binding experiments of 5-HT_{2a/c} to the four different PDZ domains had shown that interactions were present in all experiments, ITC was then used to quantify the actual strength of the individual PDZ domain – 5-HT_{2a/c} binding interactions.

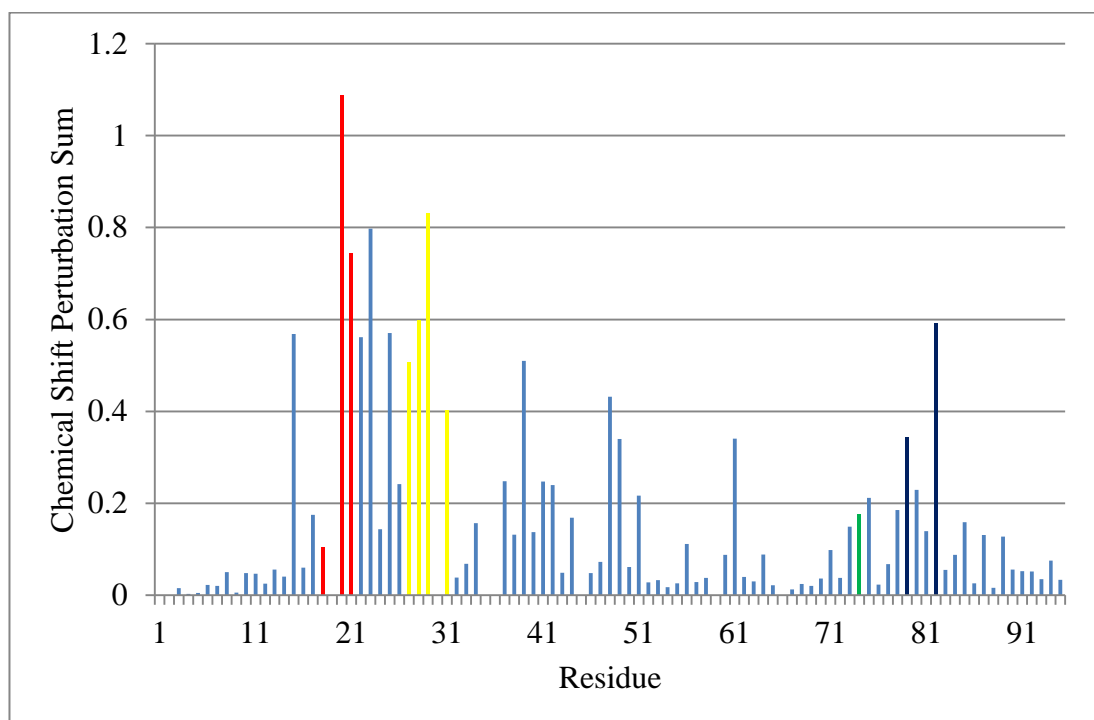


Figure 4.15: A plot of the chemical shift perturbation sum differences between free PSD-95 PDZ1 and bound to a C-terminal peptide of the 5-HT_{2c} receptor (VVSERISSV, P:L = 1:10), using the equation $\Delta d_{ppm} = \sqrt{((\Delta\delta_{HN})^2 + (\Delta\delta_N * \alpha_N)^2)}$ where, α_N = Scaling Factor of 0.17. The different areas of the PSD-95 PDZ1 domain thought to be important in determining binding affinity indicated: GLGF motif (red), hydrophobic pocket (dark blue), conserved His (green) and β B- β C loop (yellow). The histogram shows that the 5-HT_{2c} nonapeptide binds to the PSD-95 PDZ1 domain, as the number and strength of individual residue chemical shifts perturbed in PSD-95 PDZ1 is considerable. This binding can be defined as specific as those residues significantly perturbed are the residues of the PSD-95 PDZ1 domain binding region and the surrounding flexible regions i.e. the residues highlighted in the graph.

4.5 Binding Affinity Determination by ITC

4.5.1 General

The experimental conditions and procedure employed in each of the ITC binding experiments conducted in this section are described in [3.4.1] and [3.4.2]. The nonapeptides utilised were the same as those described in [4.4] and the initial protein and peptide concentrations were kept constant throughout to avoid any concentration effects biasing one experiment over another. As discussed in [2.3], ITC allows the

determination of the thermodynamic parameters, ΔH and ΔS for a particular binding interaction; ΔH and ΔS . These thermodynamic parameters can be used to calculate the Gibbs free energy (ΔG) for a particular interaction between two macromolecules (Equation 4.1), where a negative value indicates that non-covalent association is occurring. ΔG can then be used to determine the binding affinity of an interaction (Equation 4.2); hence, ITC is an extremely useful biophysical technique for determination and comparison of the interactions of 5-HT_{2a/c} nonapeptides with the four different PDZ domains.

$$\Delta G = \Delta H - T\Delta S \quad \text{Equation [4.1]}$$

$$\Delta G = -RT\ln K_D \quad \text{Equation [4.2]}$$

4.5.2 Quantification of PDZ Domain Binding Strength of 5-HT_{2a}

The binding between the 5-HT_{2a} nonapeptide and the four different PDZ domains was investigated using ITC; the individual isotherms can be seen (Figures 4.18 – 4.21) and the resultant data obtained has been summarised together (Table 4.1 and Figure 4.16).

The obtained data shows that the 5-HT_{2a} nonapeptide bound to the SAP97 PDZ2 domain most strongly of the four PDZ domains investigated, with the SAP97 PDZ1 – 5-HT_{2a} interaction being the weakest observed; analysis of the thermodynamic parameters obtained from the PDZ domain – 5-HT_{2a} ITC binding experiments is discussed in [4.5.4].

The ITC curve obtained for the PSD-95 PDZ1 – 5-HT_{2a} interaction (Figure 4.18), can be described as a ‘shallow ITC curve,’ as it does not exactly resemble the ‘typical ITC curve;’ this is due to the reasonably low affinity binding interaction being observed. The resultant errors in the binding parameters (K_D , ΔH , ΔS and ΔG) obtained from ‘shallow ITC curves’ such as Figure 4.18 are typically slightly larger

than those obtained from ITC experiments that result in ‘perfect ITC curves;’ to improve this ‘shallow curve’ a higher concentration of both titrand and titrant could have been employed. However, it was a balance between achieving the best possible quality data and protein and/or ligand availability/solubility; as the PSD-95 PDZ1 – 5-HT_{2a} interaction was performed in triplicate and gave concordant results, it was decided that the detailed conditions were suitably sufficient to yield accurate data.

Table 4.1: The different PDZ domains used in the 5-HT_{2a} binding experiment by ITC and the respective binding parameters obtained. The errors in the binding parameters were calculated from a PSD-95 PDZ1 – 5-HT_{2a} binding experiment that was performed in triplicate, with the standard deviation in calculated K_D and ΔG values used to determine the errors for the K_D and thermodynamic parameter values respectively in the binding experiments shown in the table.

PDZ Domain	K_D (μM)	ΔH (kcal mol^{-1})	$-T\Delta S$ (kcal mol^{-1})	ΔG (kcal mol^{-1})
PSD-95 PDZ1	94.34 ± 10.87	-5.371 ± 0.200	0.238 ± 0.009	-5.133 ± 0.191
PSD-95 PDZ2	30.03 ± 3.46	-9.617 ± 0.358	3.457 ± 0.128	-6.160 ± 0.229
SAP97 PDZ1	112.11 ± 12.92	-5.269 ± 0.196	-0.123 ± 0.005	-5.392 ± 0.201
SAP97 PDZ2	12.38 ± 1.43	-8.551 ± 0.318	1.857 ± 0.069	-6.694 ± 0.249

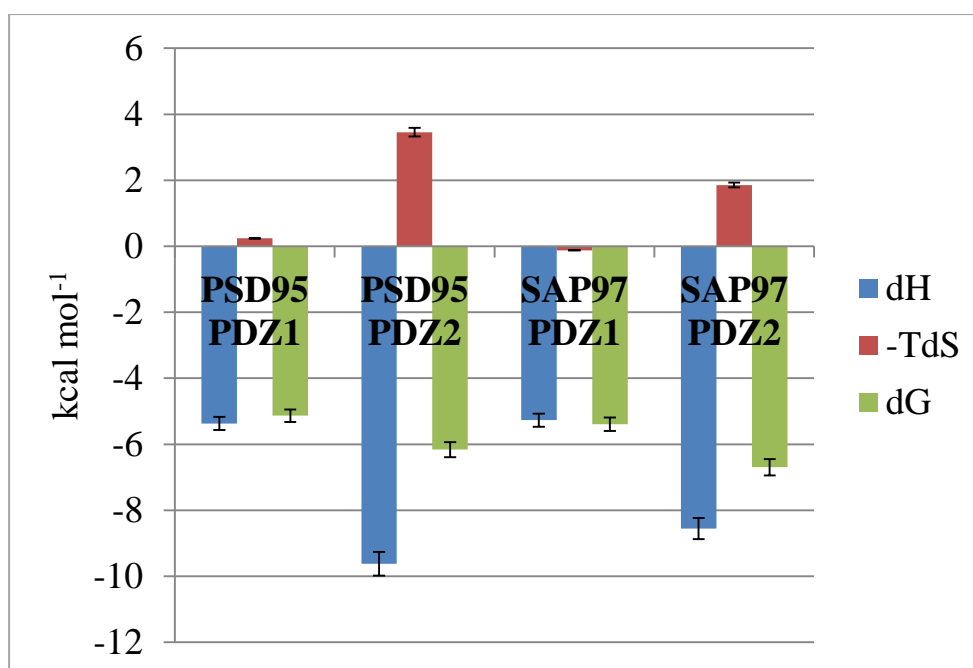


Figure 4.16: The thermodynamic parameters ($dH = \Delta H$ (blue), $-TdS = -T\Delta S$ (red) and $dG = \Delta G$ (green)) obtained from the binding interaction between the 5-HT_{2a} nonapeptide and each of the four different PDZ domains. ΔH is the dominant thermodynamic parameter in ΔG determination and hence, binding affinity; this is because ΔH is a moderate to large negative value in each ITC binding experiment, with $-T\Delta S$ being a small negative or positive value and so, contributes much less significantly to ΔG .

4.5.3 Quantification of PDZ Domain Binding Strength of 5-HT_{2c}

The binding between the 5-HT_{2c} nonapeptide and the four different PDZ domains was investigated using ITC; the individual isotherms can be seen (Figures 4.22 – 4.25) and the resultant data obtained has been summarised together (Table 4.2 and Figure 17).

The obtained data shows that the 5-HT_{2c} nonapeptide bound to the PSD-95 and SAP97 PDZ2 domains most strongly of the four PDZ domains investigated, with the SAP97 PDZ1 – 5-HT_{2c} interaction being the weakest observed; analysis of the thermodynamic parameters obtained from the PDZ domain – 5-HT_{2c} ITC binding experiments is located in [4.5.4].

Table 4.2: The different PDZ domains used in the 5-HT_{2c} binding experiment by ITC and the respective binding parameters obtained. The errors in the binding parameters were calculated from a PSD-95 PDZ1 – 5-HT_{2a} binding experiment that was performed in triplicate, with the standard deviation in calculated K_D and ΔG values used to determine the errors for the K_D and thermodynamic parameter values respectively in the binding experiments shown in the table.

PDZ Domain	K _D (μM)	ΔH (kcal mol ⁻¹)	-TΔS (kcal mol ⁻¹)	ΔG (kcal mol ⁻¹)
PSD-95 PDZ1	19.65 ± 2.26	-7.089 ± 0.264	0.668 ± 0.025	-6.421 ± 0.239
PSD-95 PDZ2	10.01 ± 1.15	-8.121 ± 0.302	1.299 ± 0.048	-6.822 ± 0.254
SAP97 PDZ1	43.86 ± 5.05	-6.687 ± 0.249	0.739 ± 0.027	-5.948 ± 0.221
SAP97 PDZ2	10.49 ± 1.21	-9.64 ± 0.359	2.843 ± 0.106	-6.797 ± 0.253

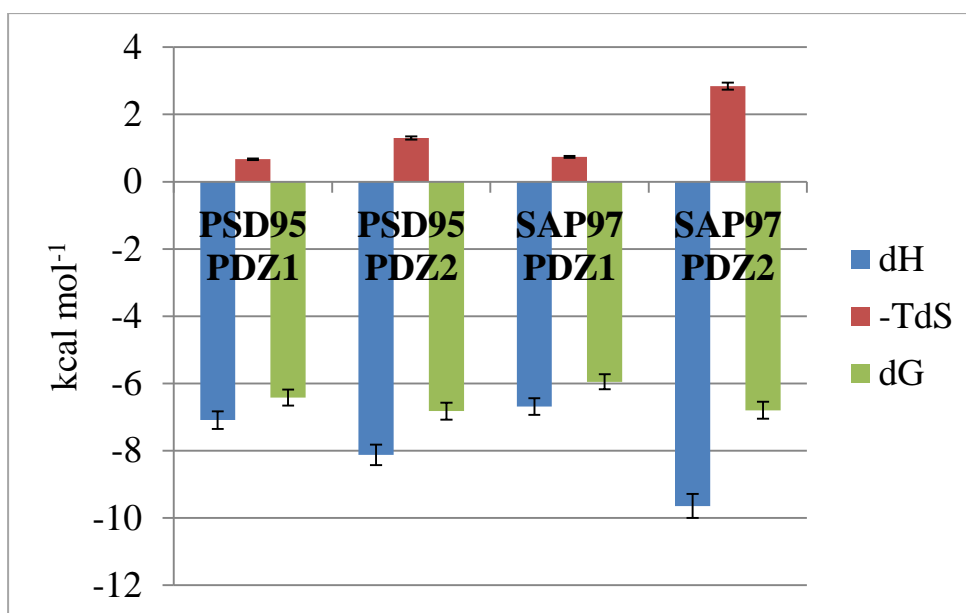


Figure 4.17: The thermodynamic parameters ($dH = \Delta H$ (blue), $-TdS = -T\Delta S$ (red) and $dG = \Delta G$ (green)) obtained from the binding interaction between the 5-HT_{2c} nonapeptide and each of the four different PDZ domains. ΔH is the dominant thermodynamic parameter in ΔG determination and hence, binding affinity; this is because ΔH is a moderate to large negative value in each ITC binding experiment, with $-T\Delta S$ being a small negative or positive value and so, contributes much less significantly to ΔG .

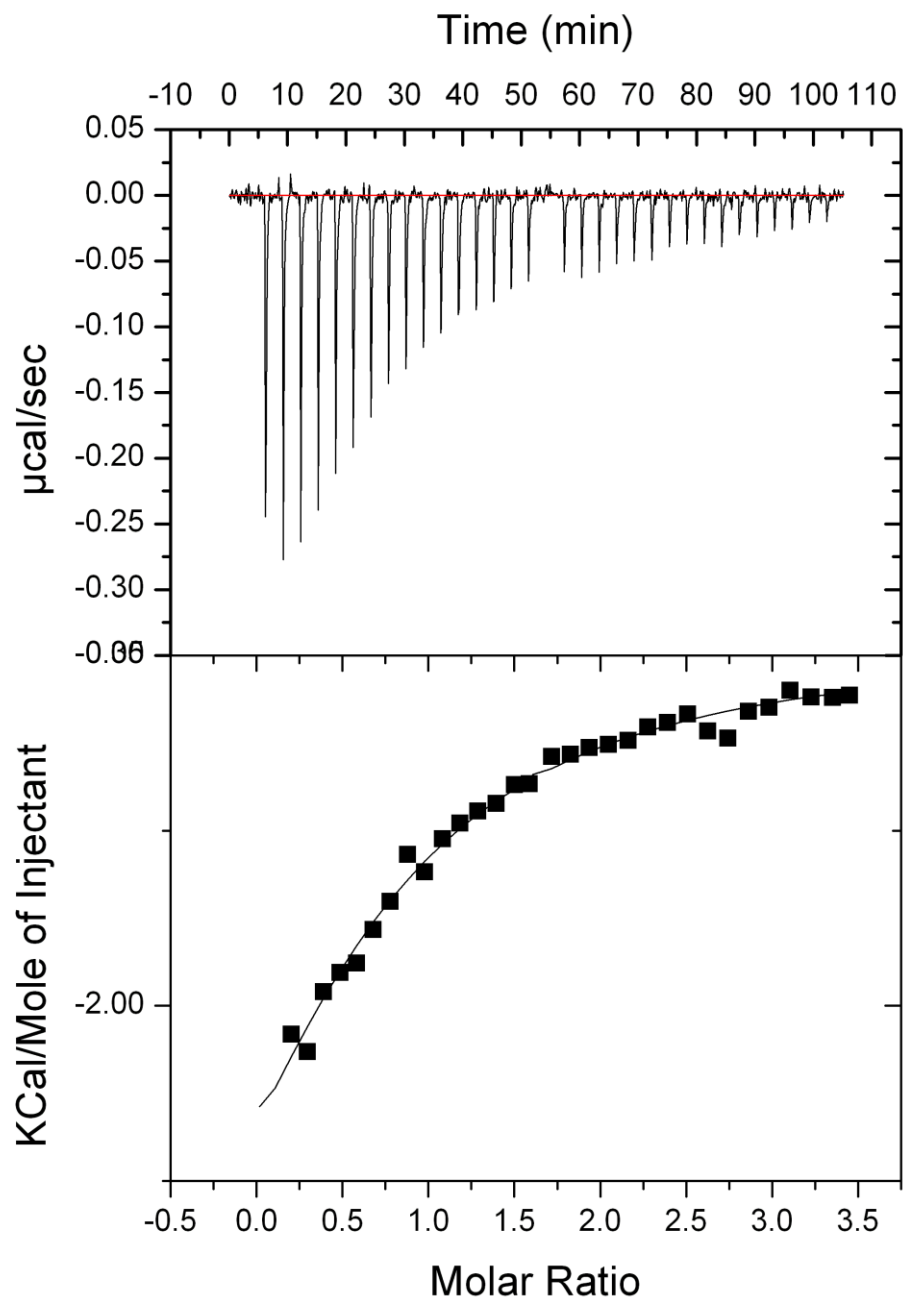


Figure 4.18: The ITC isotherm (top) and resultant curve (bottom) produced by the ITC binding experiment between $100\mu\text{M}$ PSD-95 PDZ1 (cell) and $750\mu\text{M}$ 5-HT_{2a} nonapeptide (syringe) in 20mM phosphate, pH6.3, on an iTC₂₀₀ Microcalorimeter (MicroCal) at 298K. Fitting of the curve produced by the ITC experiment to a single set of sites curve-fitting model, using Origin7, resulted in a binding affinity (K_D) of $94.34\mu\text{M}$ for 5-HT_{2a} to the PSD-95 PDZ1 domain.

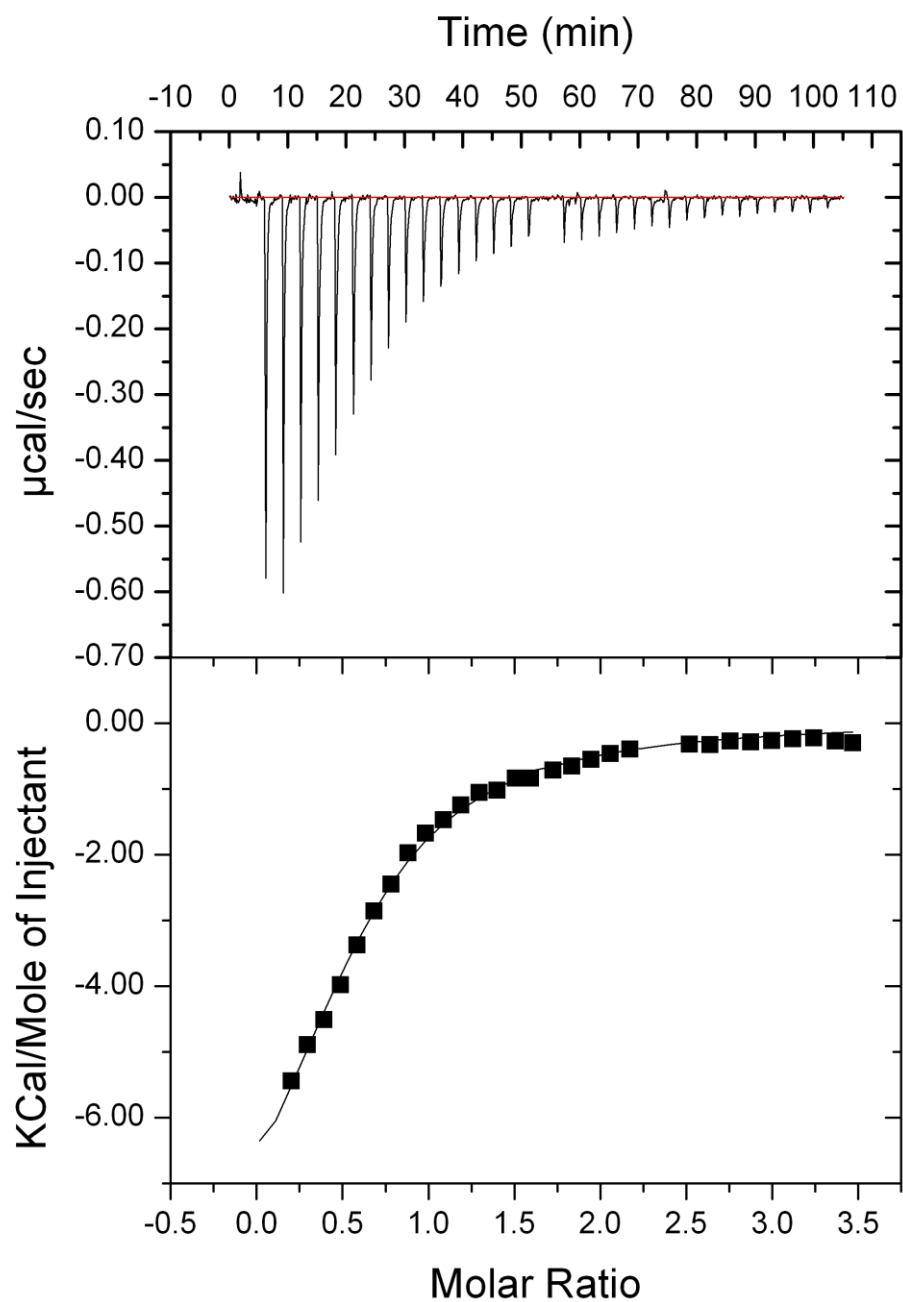


Figure 4.19: The ITC isotherm (top) and resultant curve (bottom) produced by the ITC binding experiment between $100\mu\text{M}$ PSD-95 PDZ2 (cell) and $750\mu\text{M}$ 5-HT_{2a} nonapeptide (syringe) in 20mM phosphate, pH6.3, on an iTC₂₀₀ Microcalorimeter (MicroCal) at 298K. Fitting of the curve produced by the ITC experiment to a single set of sites curve-fitting model, using Origin7, resulted in a binding affinity (K_D) of $30.03\mu\text{M}$ for 5-HT_{2a} to the PSD-95 PDZ2 domain.

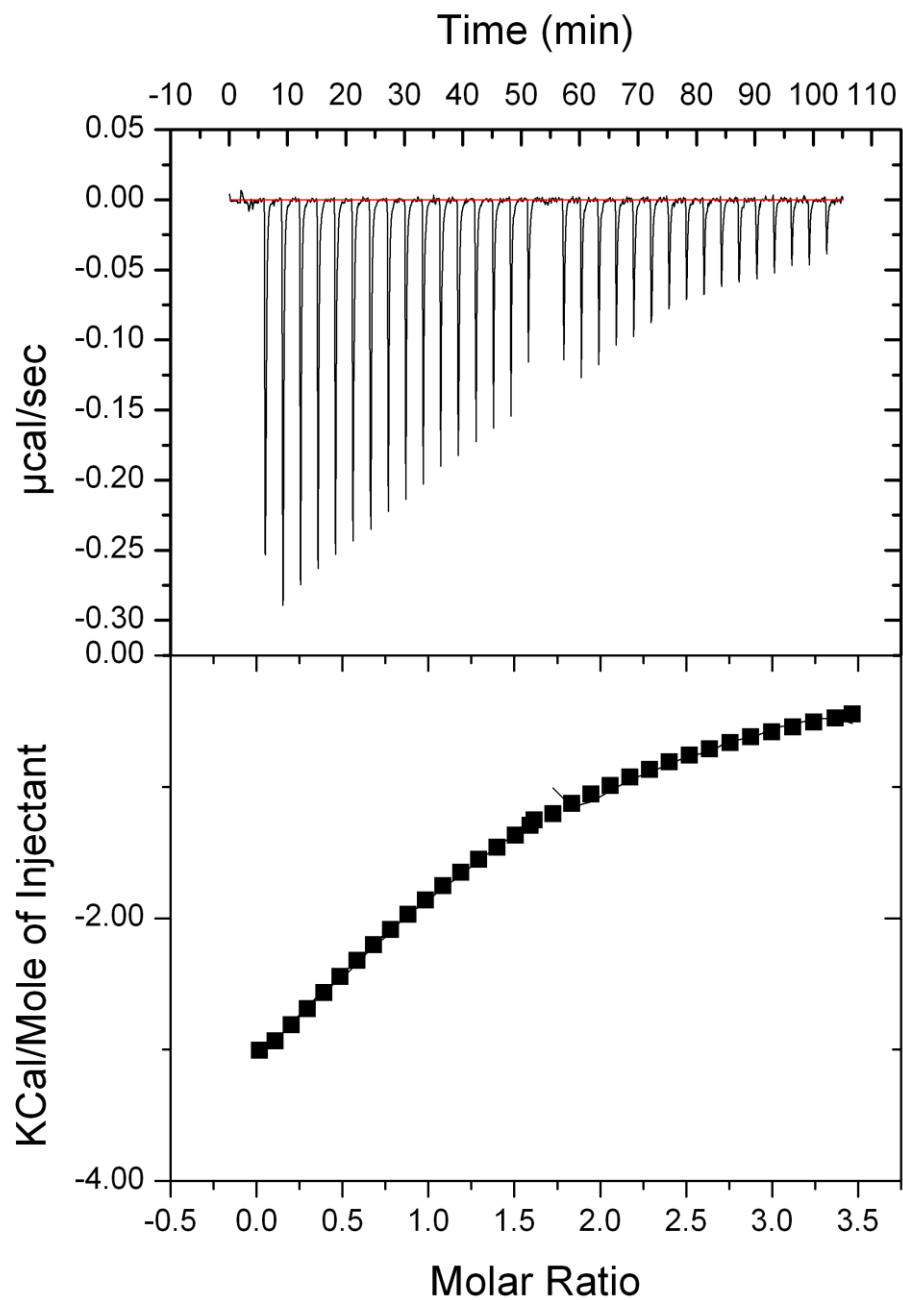


Figure 4.20: The ITC isotherm (top) and resultant curve (bottom) produced by the ITC binding experiment between $100\mu\text{M}$ SAP97 PDZ1 (cell) and $750\mu\text{M}$ 5-HT_{2a} nonapeptide (syringe) in 20mM phosphate, pH6.3, on an iTC₂₀₀ Microcalorimeter (MicroCal) at 298K. Fitting of the curve produced by the ITC experiment to a single set of sites curve-fitting model, using Origin7, resulted in a binding affinity (K_D) of $112.11\mu\text{M}$ for 5-HT_{2a} to the SAP97 PDZ1 domain.

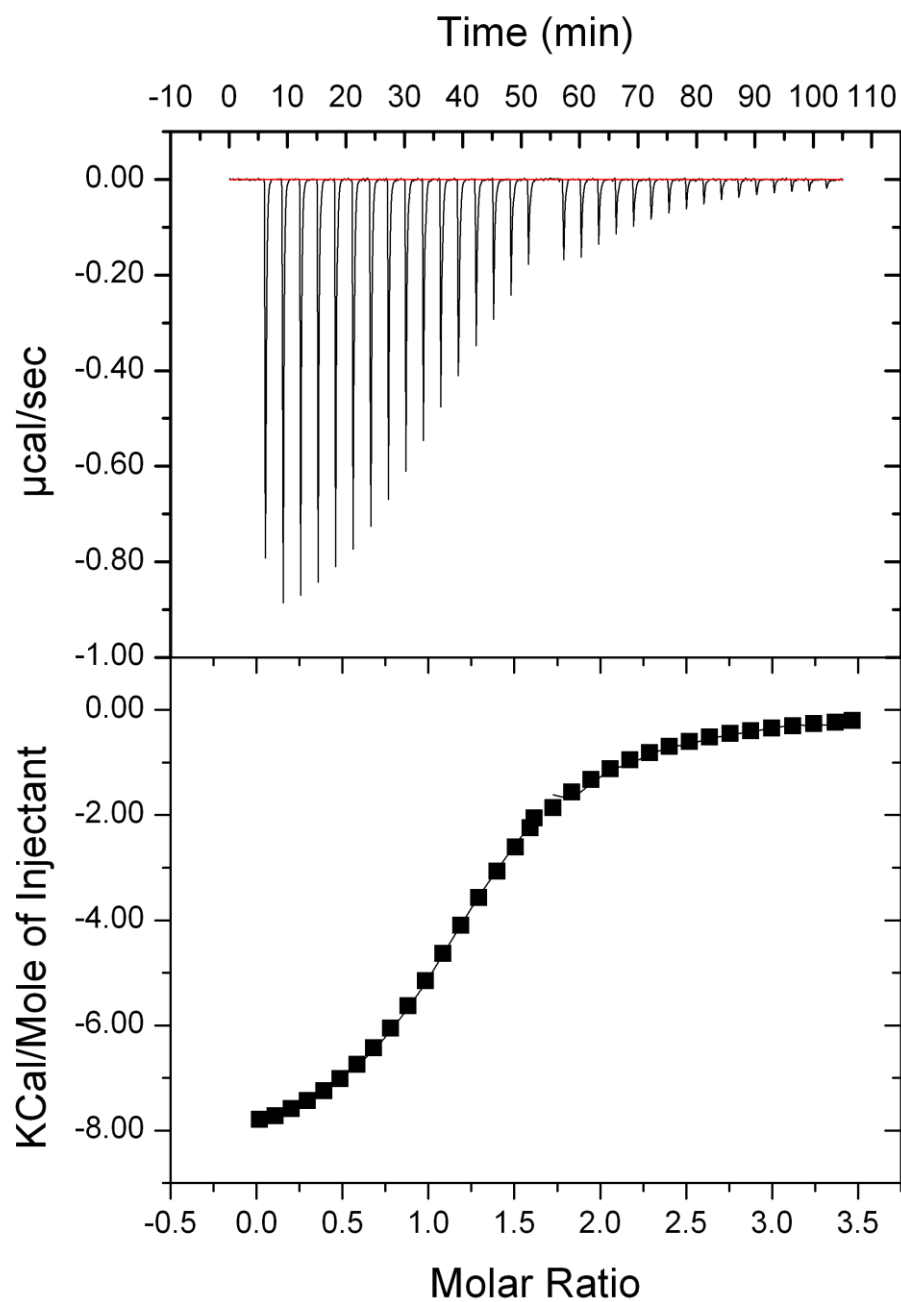


Figure 4.21: The ITC isotherm (top) and resultant curve (bottom) produced by the ITC binding experiment between $100\mu\text{M}$ SAP97 PDZ2 (cell) and $750\mu\text{M}$ 5-HT_{2a} nonapeptide (syringe) in 20mM phosphate, pH6.3, on an iTC₂₀₀ Microcalorimeter (MicroCal) at 298K. Fitting of the curve produced by the ITC experiment to a single set of sites curve-fitting model, using Origin7, resulted in a binding affinity (K_D) of $12.38\mu\text{M}$ for 5-HT_{2a} to the SAP97 PDZ2 domain.

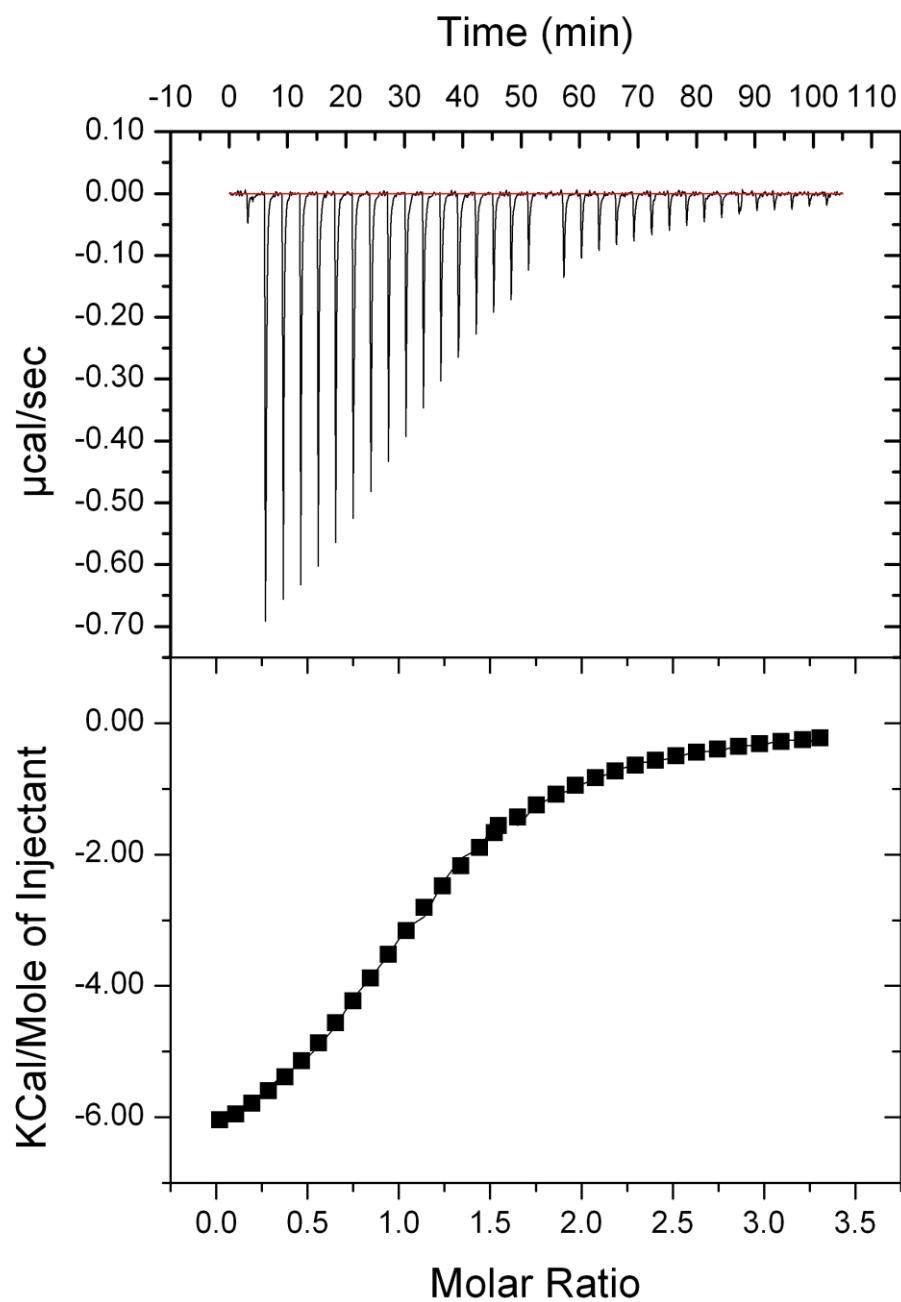


Figure 4.22: The ITC isotherm (top) and resultant curve (bottom) produced by the ITC binding experiment between $100\mu\text{M}$ PSD-95 PDZ1 (cell) and $750\mu\text{M}$ 5-HT_{2c} nonapeptide (syringe) in 20mM phosphate, pH6.3, on an iTC₂₀₀ Microcalorimeter (MicroCal) at 298K. Fitting of the curve produced by the ITC experiment to a single set of sites curve-fitting model, using Origin7, resulted in a binding affinity (K_D) of $19.65\mu\text{M}$ for 5-HT_{2c} to the PSD-95 PDZ1 domain.

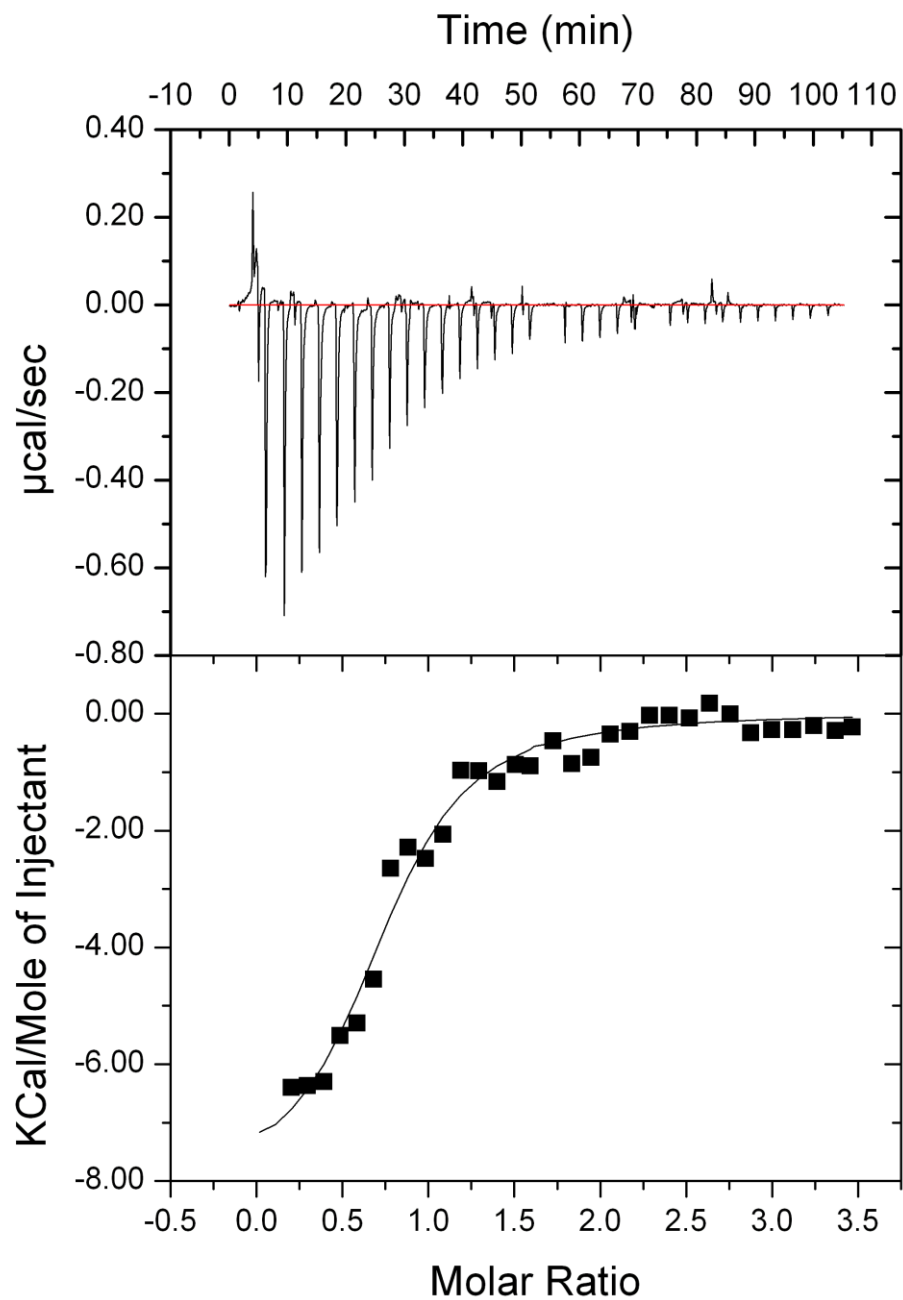


Figure 4.23: The ITC isotherm (top) and resultant curve (bottom) produced by the ITC binding experiment between $100\mu\text{M}$ PSD-95 PDZ2 (cell) and $750\mu\text{M}$ 5-HT_{2c} nonapeptide (syringe) in 20mM phosphate, pH6.3, on an iTC₂₀₀ Microcalorimeter (MicroCal) at 298K. Fitting of the curve produced by the ITC experiment to a single set of sites curve-fitting model, using Origin7, resulted in a binding affinity (K_D) of $10.01\mu\text{M}$ for 5-HT_{2c} to the PSD-95 PDZ2 domain.

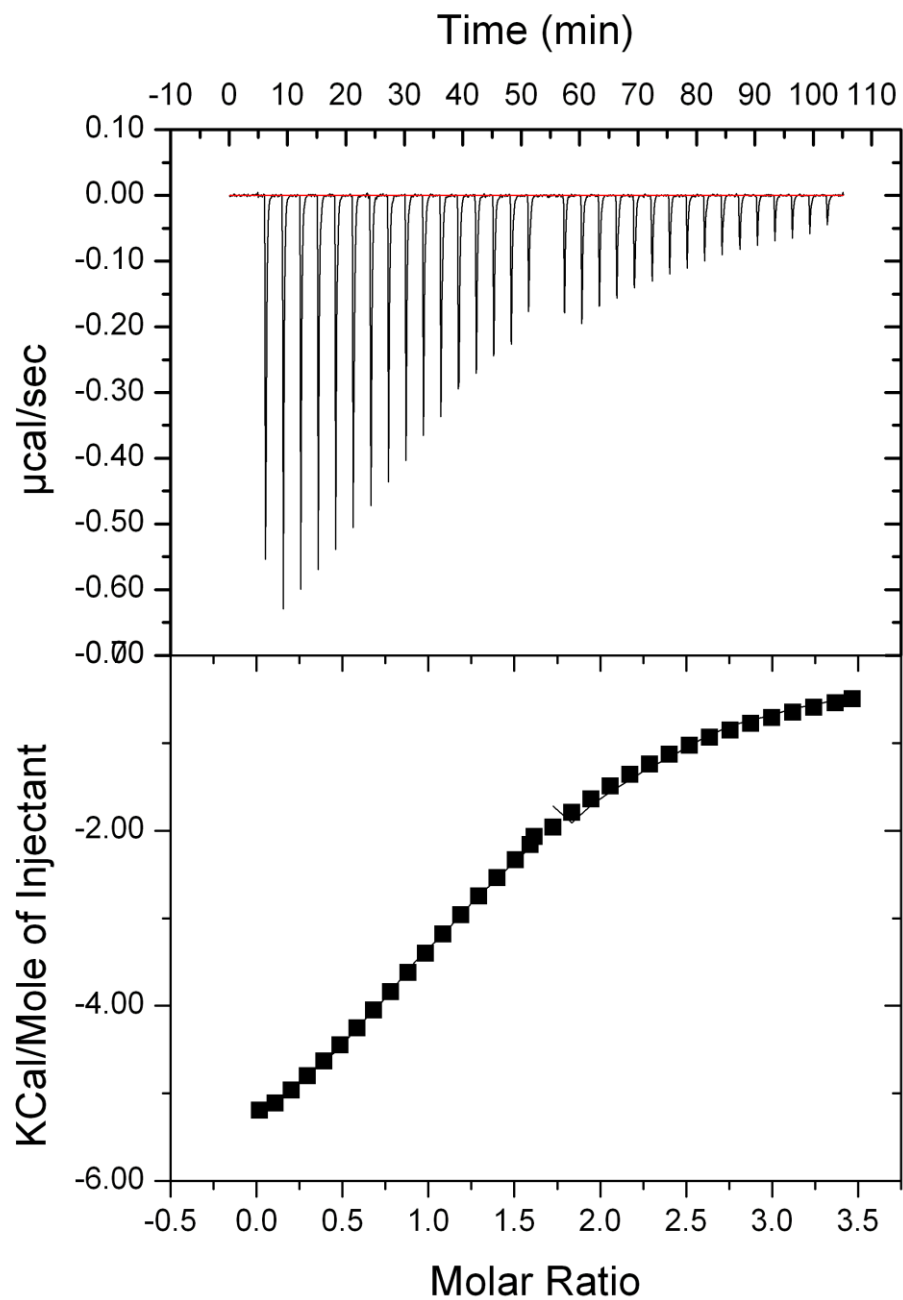


Figure 4.24: The ITC isotherm (top) and resultant curve (bottom) produced by the ITC binding experiment between $100\mu\text{M}$ SAP97 PDZ1 (cell) and $750\mu\text{M}$ 5-HT_{2c} nonapeptide (syringe) in 20mM phosphate, pH6.3, on an iTC₂₀₀ Microcalorimeter (MicroCal) at 298K. Fitting of the curve produced by the ITC experiment to a single set of sites curve-fitting model, using Origin7, resulted in a binding affinity (K_D) of $43.86\mu\text{M}$ for 5-HT_{2c} to the SAP97 PDZ1 domain.

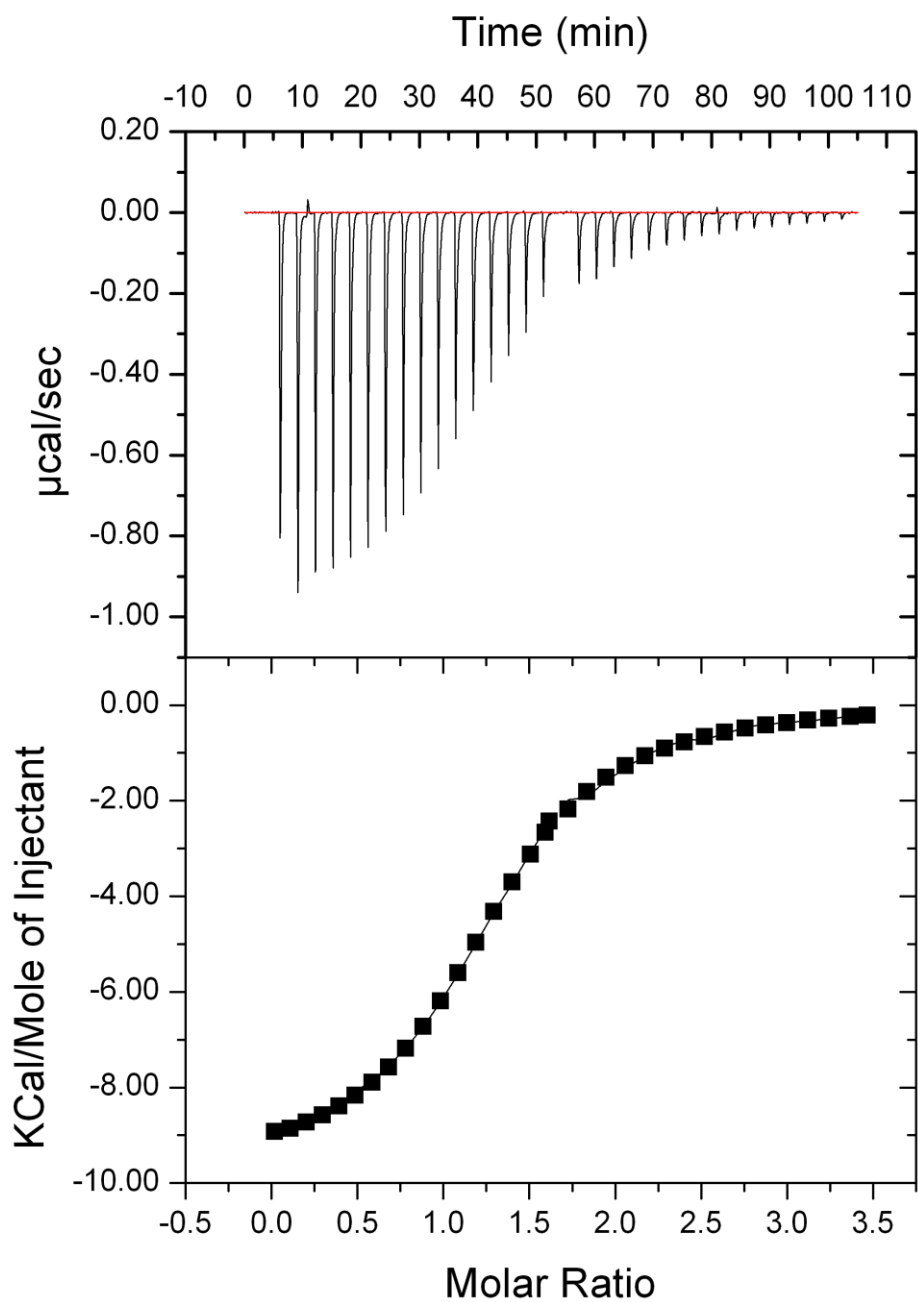


Figure 4.25: The ITC isotherm (top) and resultant curve (bottom) produced by the ITC binding experiment between $100\mu\text{M}$ SAP97 PDZ2 (cell) and $750\mu\text{M}$ 5-HT_{2c} nonapeptide (syringe) in 20mM phosphate, pH6.3, on an iTC₂₀₀ Microcalorimeter (MicroCal) at 298K. Fitting of the curve produced by the ITC experiment to a single set of sites curve-fitting model, using Origin7, resulted in a binding affinity (K_D) of $10.49\mu\text{M}$ for 5-HT_{2c} to the SAP97 PDZ2 domain.

4.5.4 Comparison of 5-HT_{2a/c} PDZ Domain Binding

If the binding of the 5-HT_{2a} and 5-HT_{2c} to the four different PDZ domains is analysed there are a number of similarities. In all experiments, the enthalpy change upon PDZ domain binding of the nonapeptide was the dominant contribution to the binding affinity; this is evident because ΔH was a moderate to large negative value, whereas, $-T\Delta S$ was a small positive or negative value and so, could be considered insignificant. As discussed in [2.3.4], ΔH is dependent on the strength and number of interactions formed/broken upon binding, whereas, $-T\Delta S$ is a measure of the amount of water displaced from buried surfaces and loss of conformational entropy by the act of binding. This observation therefore corresponds well with previously reported PDZ domain-mediated interactions with peptides (Liu et al., 2007). The observation that both nonapeptides exhibited stronger binding to the PSD-95 and SAP97 PDZ2 domains than the PDZ1 domains can be rationalised to the decrease in enthalpic change upon PDZ1 domain binding of the nonapeptides. However, this is a somewhat simplistic view of the binding interactions being observed and presumes that all the PDZ binding pockets are optimally hydrated. The vast number of residue chemical shift perturbations observed upon PDZ domain binding of the nonapeptides in the NMR binding screening experiments (Figures 4.7 – 4.14), indicates that there may be another important consideration to take into account; this is the change in entropic distribution of the particular PDZ domain from the unbound state to the peptide-bound state. It is possible that the PSD-95 and SAP97 PDZ2 domains are less affected by the change in internal dynamics upon binding of the nonapeptides than the PDZ1 domains and hence, account for the stronger nonapeptide binding observed for the PSD-95 and SAP97 PDZ2 domains c.f. PDZ1. It is possible to investigate if there was any change in rigidity/flexibility of the individual PDZ

domains upon nonapeptide binding, by utilising NMR spectroscopy relaxation experiments; however, this falls outside the scope of this particular investigation and thus, was will not be elaborated upon further.

All four PDZ domains exhibited stronger binding with the 5-HT_{2c} nonapeptide than the 5-HT_{2a} nonapeptide; with PSD-95 PDZ1 there was as much as a 4.5-fold stronger binding affinity for 5-HT_{2c} than 5-HT_{2a}. This was again due to a decrease in enthalpic change upon binding of the 5-HT_{2a} nonapeptide c.f. 5-HT_{2c}; this finding was interesting as, by convention, the 0 and -2 residues of a PDZ domain ligand are considered the most important in facilitating PDZ domain binding. Given that both 5-HT_{2a} (GVNEKVSCV) and 5-HT_{2c} (VVSERISSV) nonapeptides share the same 0 and -2 residues (Val and Ser respectively), the results obtained in this section suggest that other residues of the 5-HT_{2x} ligand are affecting the PDZ domain binding ability. This could be due to residues of 5-HT_{2a}, such as Val6 or Cys8, forming more unfavourable steric or electrostatic interactions with the PDZ domains than the corresponding 5-HT_{2c} residues of Ile6 or Ser8

A more likely conclusion for the observed difference in PDZ domain binding ability between the 5-HT_{2a} and 5-HT_{2c} nonapeptides is that residues outside of the conventional four C-terminal sequence are important to PDZ domain binding affinity. The 5-HT_{2c} (VVSERISSV) Arg5 or Ile6 residues may be able to form favourable hydrophobic or electrostatic interactions with residues of the PDZ domains more effectively than the 5-HT_{2a} (GVNEKVSCV) Lys5 or Val6 residues; this will increase the PDZ domain binding ability of 5-HT_{2c} c.f. 5-HT_{2a}.

As the binding between the 5-HT_{2a} and 5-HT_{2c} nonapeptides and the four different PDZ domains had been proven to be specific by NMR spectroscopy and quantified using ITC, the logical final step in the investigation into the interactions of the 5-

HT_{2x} receptors was to determine the structure of one of the PDZ – peptide complexes. The determination of the structure of the complex formed between a PDZ domain and a 5-HT_{2x} receptor was believed to be an extremely important achievement as it would highlight the important interactions for PDZ binding; this knowledge would then be able to be used to guide drug design for future therapeutic applications. The chosen interaction was the PSD-95 PDZ1 – 5-HT_{2c} complex as this had been shown to be physiologically relevant, there had been shown to be therapeutic requirements, there was no previously existing structure and ITC had shown that the affinity of the interaction would be suitable for structure determination. The chosen method for the structure determination process was solution state NMR spectroscopy, as this would give an atomic resolution PSD-95 PDZ1 – 5-HT_{2c} complex structure; attempts were made in parallel to produce a crystal structure of the complex by a colleague but these proved unsuccessful.

4.6 PSD-95 PDZ1 – 5-HT_{2c} NMR Solution State Structure Determination

4.6.1 Overview

An overview of the process implemented in the NMR solution state structure determination of the PSD-95 PDZ1 – 5-HT_{2c} complex has been detailed (Figure 4.26). The initial stage of the process was the preparation of an NMR sample of the PSD-95 PDZ1 – 5-HT_{2c} complex [3.3.1 & 3.3.3] and collection of a suite of NMR experiments [3.5.1].

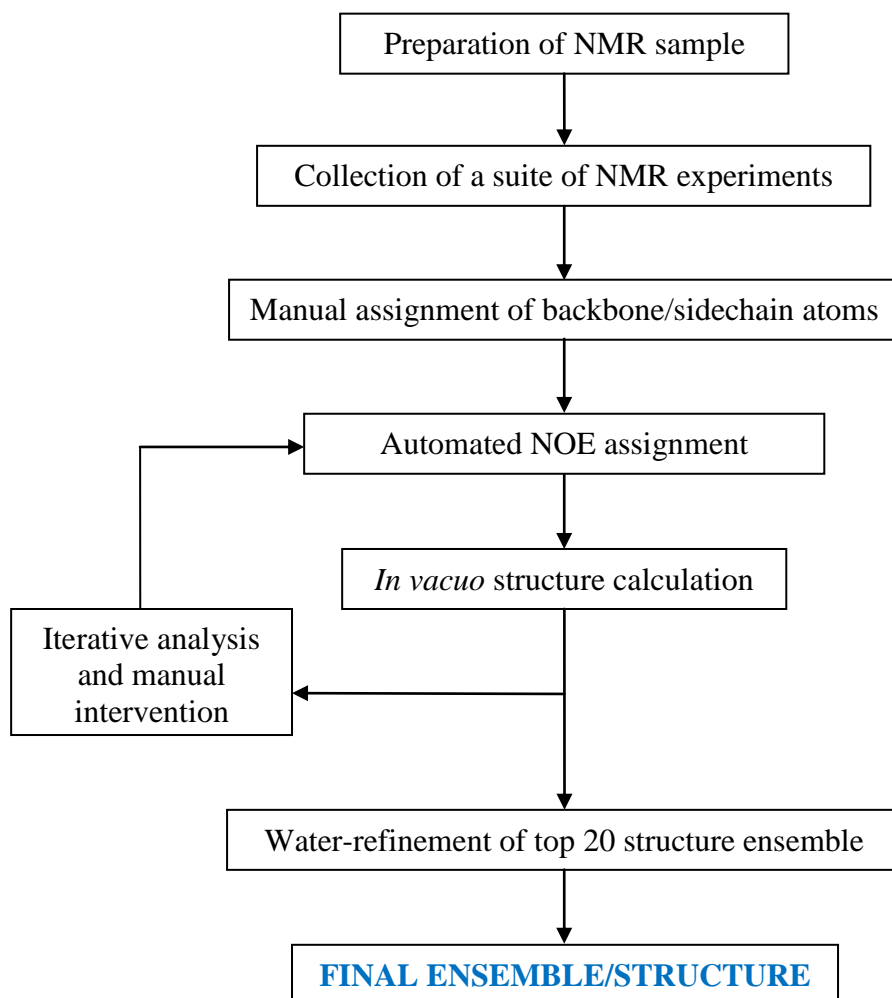


Figure 4.26: An overview of the different stages of the process performed to determine the NMR solution state structure of the PSD-95 PDZ1 – 5-HT_{2c} complex. The initial stages of the procedure were the preparation of the NMR sample [3.3.1 & 3.3.3], followed by the collection of the NMR experiments [3.5.1]. The backbone and side-chain atoms were assigned manually [3.5.2], with the observed NOE's assigned in an automated manner using CYANA [3.5.3]. The resultant assignments were then utilised in an *in vacuo* structure calculation [3.5.4] and the subsequent structures produced analysed for any errors/erroneous assignments; with the necessary adjustments made manually and the *in vacuo* structure calculation performed again in an iterative process. When no errors remained following the *in vacuo* structure calculation, the top 20 structures obtained were then water-refined [3.5.4] to give the final PSD-95 PDZ1 – 5-HT_{2c} NMR solution state structural ensemble.

4.6.2 Assignment of NMR Spectra

4.6.2.1 Bound Protein Backbone and Side-Chain Assignment

The collected NMR spectra corresponding to the backbone and side-chain atoms of the PSD-95 PDZ1 domain in the 5-HT_{2c} bound complex form were assigned as described in [3.5.2]. This process resulted in 97.3% backbone atom assignment and 85.59% side-chain assignment to give an overall assignment value of 91.54%; the missing resonance assignments have been mapped onto the PSD-95 PDZ1 sequence

(Figure 4.27). It can be seen that the vast majority of the residues with incomplete backbone or side-chain assignments are in highly flexible, surface exposed regions of the PDZ domain and/or are the extreme side-chain atoms of residues with long and/or flexible side-chains; the assignment of these type of protein residues is often problematic. The final assigned versions of the 2-D HSQC spectra are also shown (Figures 4.28 & 4.29).

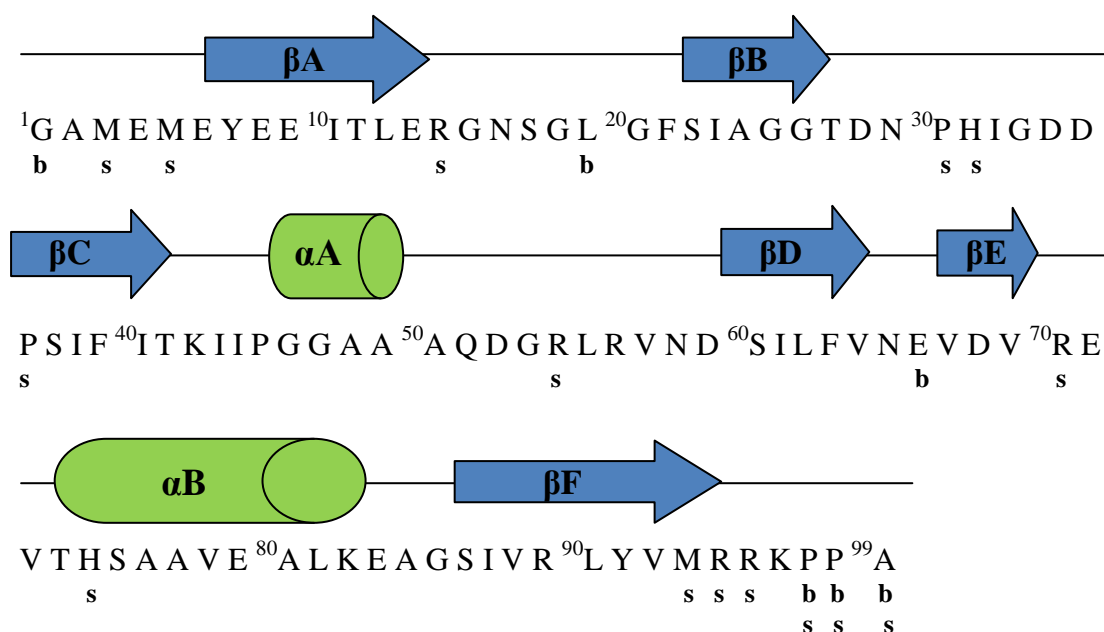


Figure 4.27: The sequence of the PSD-95 PDZ1 domain present in the PSD-95 PDZ1 – 5-HT_{2c} complex sample, with the secondary structure given above. Below the sequence, residues for which a full backbone (b) or side-chain (s) assignment has not been possible have been indicated; the majority of these residues are in highly flexible regions of the protein and/or have long flexible side-chains that make assignment more difficult.

4.6.2.2 Bound Peptide Assignment

4.6.2.2.1 Introduction

In the free form, it was possible to definitively assign the Ser3 – Val9 residues of the 5-HT_{2c} nonapeptide (Figure 4.30). ¹³C, ¹⁵N-filtered NMR experiments were carried out on the PSD-95 PDZ1 – 5-HT_{2c} complex sample so that the peptide could be assigned in the bound form; however, these NMR experiments indicated that the peptide was in intermediate-exchange between the unbound and bound complex forms (Figures 4.31 & 4.32). This phenomenon can be seen by analysing the overlaid

unbound (and bound ^{13}C , ^{15}N filtered-) 1-D ^1H and 2-D TOCSY NMR spectra (Figures 4.31 & 4.32 respectively); there is an obvious reduction in the number, intensity and form of the peaks present in the bound complex spectra c.f. unbound spectra, which is indicative of an intermediate-exchange process occurring. Of particular importance is the NMR spectra overlays of the extreme upfield methyl region (Figure 4.31d), which corresponds to the three different Val H_γ and Ile residue H_δ . The figure shows how, in the bound form of 5-HT_{2c}, one of the residue peaks is attenuated completely and the intensity and form of the peak of another is severely affected by intermediate-exchange.

As the 5-HT_{2c} nonapeptide was shown to be in intermediate-exchange between free and bound states, the process of definitively assigning the bound peptide was much more difficult; thus, only a few residues could be definitively assigned (Figures 4.32b and d), with no peaks assigned for the Ile6 and Val9 residues. However, there were two peaks present in the filtered-TOCSY spectrum of the PSD-95 PDZ1 – 5-HT_{2c} complex filtered-TOCSY spectra that could have corresponded to either/or both of the residues (circled in red, Figure 32d). It was important to conclusively assign peaks corresponding to Ile6 and/or Val9 before the NOE assignment and structure calculation processes were initiated as they were believed to be important residues in the binding of 5-HT_{2c}. It was also imperative that all assignments could be validated so the obtained complex structures were reliable and representative of the data. Therefore, an NMR titration of ^{13}C , ^{15}N PSD-95 PDZ1 into 5-HT_{2c} was performed; the aim of this experiment set was to track each individual peak from the free 5-HT_{2c} form to the bound complex form, in an attempt to conclusively assign peaks corresponding to Ile6 and/or Val9.

4.6.2.2.2 NMR Titration

An initial NMR sample of free 5-HT_{2c} nonapeptide (909 μM) was prepared, with 1-D ¹H, excitation sculpting (ES) and saturation transfer difference (STD) and 2-D NOESY and TOCSY NMR experiments carried out on the sample. A series of 1-D ¹H, ES and STD, ¹³C, ¹⁵N-filtered-1-D ¹H, ¹³C, ¹⁵N-filtered 2-D NOESY and TOCSY NMR experiments were then performed at different 5-HT_{2c} : PSD-95 PDZ1 ratios; this NMR titration series was achieved by adding an appropriate amount of ¹³C, ¹⁵N-labelled PSD-95 PDZ1 (1mM) to the sample to give the desired peptide:protein ratio. A range of different peptide:protein ratios were investigated so that individual peaks could be tracked from unbound to the bound complex positions (Table 4.3).

Table 4.3: The concentrations of the 5-HT_{2c} nonapeptide and ¹³C,¹⁵N-labelled PSD-95 PDZ1 present in the respective sample of the NMR titration series.

[5-HT _{2c}] (μM)	[PSD-95 PDZ1] (μM)	5-HT _{2c} : PSD-95 PDZ1
909	/	1:0
889	18	50:1
851	43	20:1
825	55	15:1
800	80	10:1
727	145	5:1
667	267	2.5:1

By performing the NMR titration and tracking the movement of each signal (Figure 4.33), it was possible to definitively show that the peak in the bound TOCSY spectrum at 4 ppm (ω1), 2 ppm (ω2) (circled in red, Figure 4.33c) corresponded to the Val9 H_β atom; in addition, several other atoms could be assigned and the previous assignments were validated (Figure 4.34). The confirmed assignments were then transferred onto the bound peptide (Figure 4.35) and complex NOESY spectra, in preparation for the subsequent automated NOESY assignment by CYANA process [4.6.2.3].

The NMR titration series also provided some useful information about the binding of the 5-HT_{2c} nonapeptide to the PSD-95 PDZ1 domain, by analysis of the different 1-D NMR experiments performed at each titration point (Figures 4.36 – 4.38). The ¹H 1-D spectra (Figure 4.36) show that there is evidence of free peptide signals at a ratio as low as peptide:protein = 2.5:1 (Figure 4.36a) and bound peptide signals can be observed up to peptide:protein = 15:1; this indicates the difficulty of intermediate-exchange that can be encountered when trying to determine a PDZ domain – peptide complex structure. The ES experiments exhibit how the free peptide signals decrease (Figure 4.37a) and the bound peptide signals increase (Figure 4.37b), as the concentration of PSD-95 PDZ1 in the NMR sample increases. The STD experiments (Figure 4.38) indicated the different protein – peptide interactions that occur at the various L:P ratios; this experiment seems more susceptible to interference from protein signal than the ES experiment and so, only the free 5-HT_{2c} (blue) and L:P = 50:1 (red) spectra have been shown for clarity. Figure 4.38 shows a prominent peak in the L:P = 50:1 spectrum; the figure highlights that this peak corresponds to an intermolecular interaction and is not due to interference from protein signal by comparison with the unbound PSD-95 PDZ1 spectrum (black). However, the specific residue chemical group of the 5-HT_{2c} nonapeptide that is responsible for the predominant interaction with PSD-95 PDZ1 can only be ambiguously assigned to either Ile6H_δ or Val9H_{γ1/2} by comparison with the free and bound spectra of 5-HT_{2c} (magenta and green respectively).

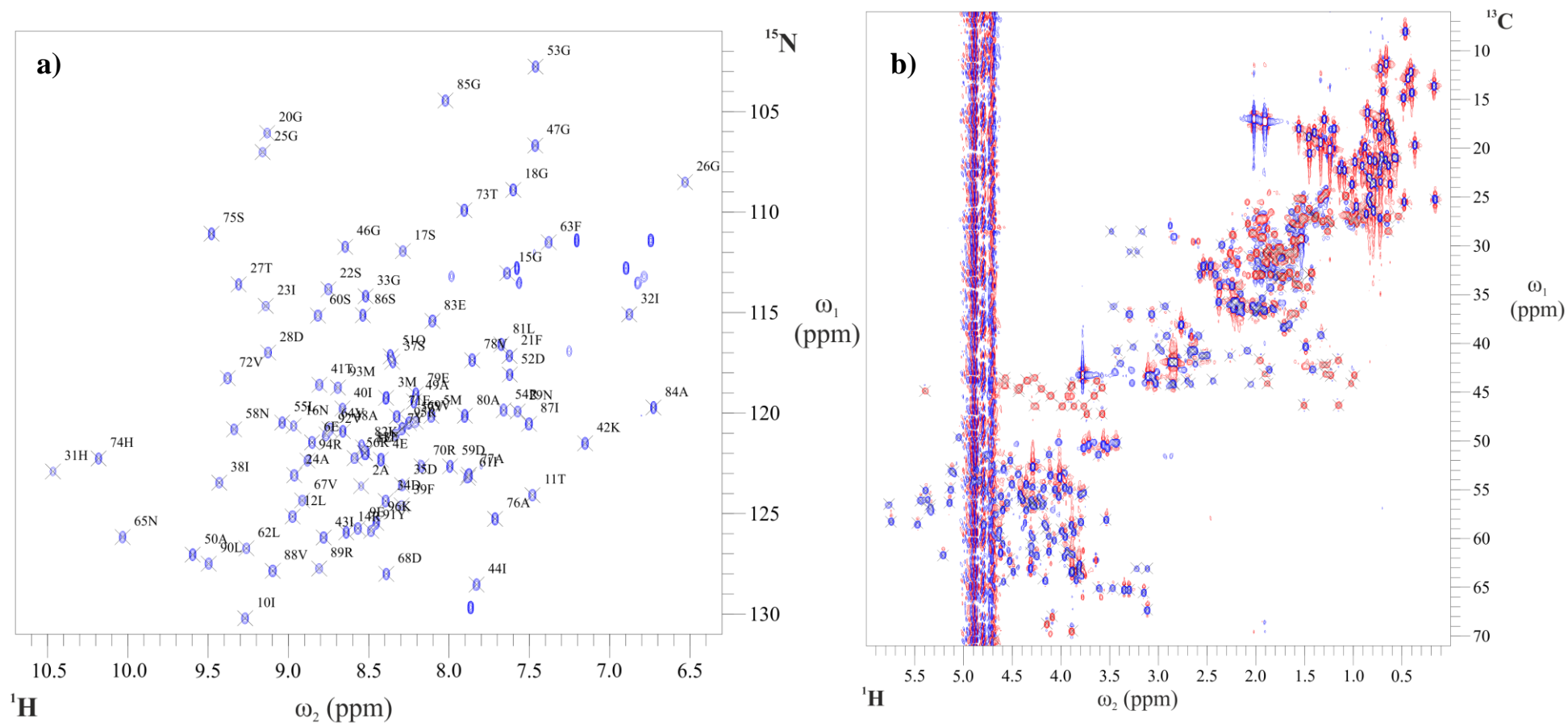


Figure 4.28: NMR spectra acquired at 298K, with a field strength of 600MHz, in 20mM phosphate 0.1mM EDTA buffer, pH6.3. a) The 2-D ¹H - ¹⁵N HSQC spectrum of the PSD-95 PDZ1 - 5-HT_{2c} complex (P:L = 1:5); the individual protein residue corresponding to the backbone NH peak present in the spectrum has been labelled (90 out of 94 possible, 95.7%). b) The 2-D ¹H - ¹³C aliphatic HSQC spectrum of the PSD-95 PDZ1 - 5-HT_{2c} complex (P:L = 1:5); with both positive (i.e. Thr C_α-H_α, blue) and negative (i.e. Thr C_β-H_β, red) levels shown every 'X' corresponds to a peak that has been assigned to an individual Carbon-bound H_x atom of PSD-95 PDZ1, the individual assignment has not shown on the spectrum for clarity, however.

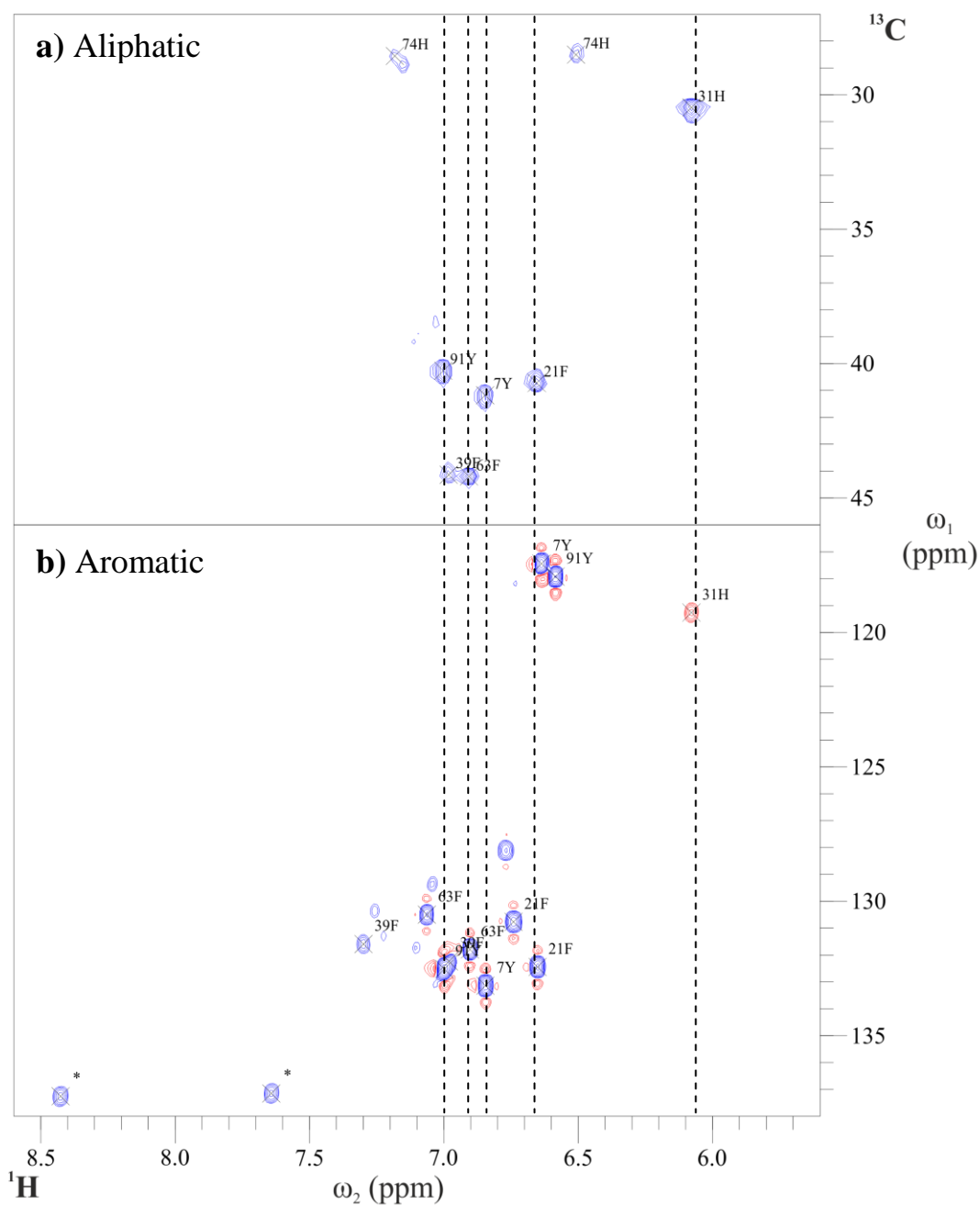


Figure 4.29: NMR spectra acquired at 298K, with a field strength of 600MHz, in 20mM phosphate 0.1mM EDTA buffer, pH6.3. a) The 2-D $^1\text{H} - ^{13}\text{C}$ $\text{H}_\beta\text{C}_\beta\text{C}_\gamma\text{C}_\delta\text{H}_\delta$ HSQC spectrum of the PSD-95 PDZ1 – 5-HT_{2c} complex (P:L = 1:5); the individual Carbon-bound H_x atom responsible for the specific peak present in the spectrum has been labelled. b) The 2-D $^1\text{H} - ^{13}\text{C}$ aromatic TROSY spectrum of the PSD-95 PDZ1 – 5-HT_{2c} complex (P:L = 1:5); the individual Carbon-bound H_x atom responsible for the specific peak present in the spectrum has been labelled.

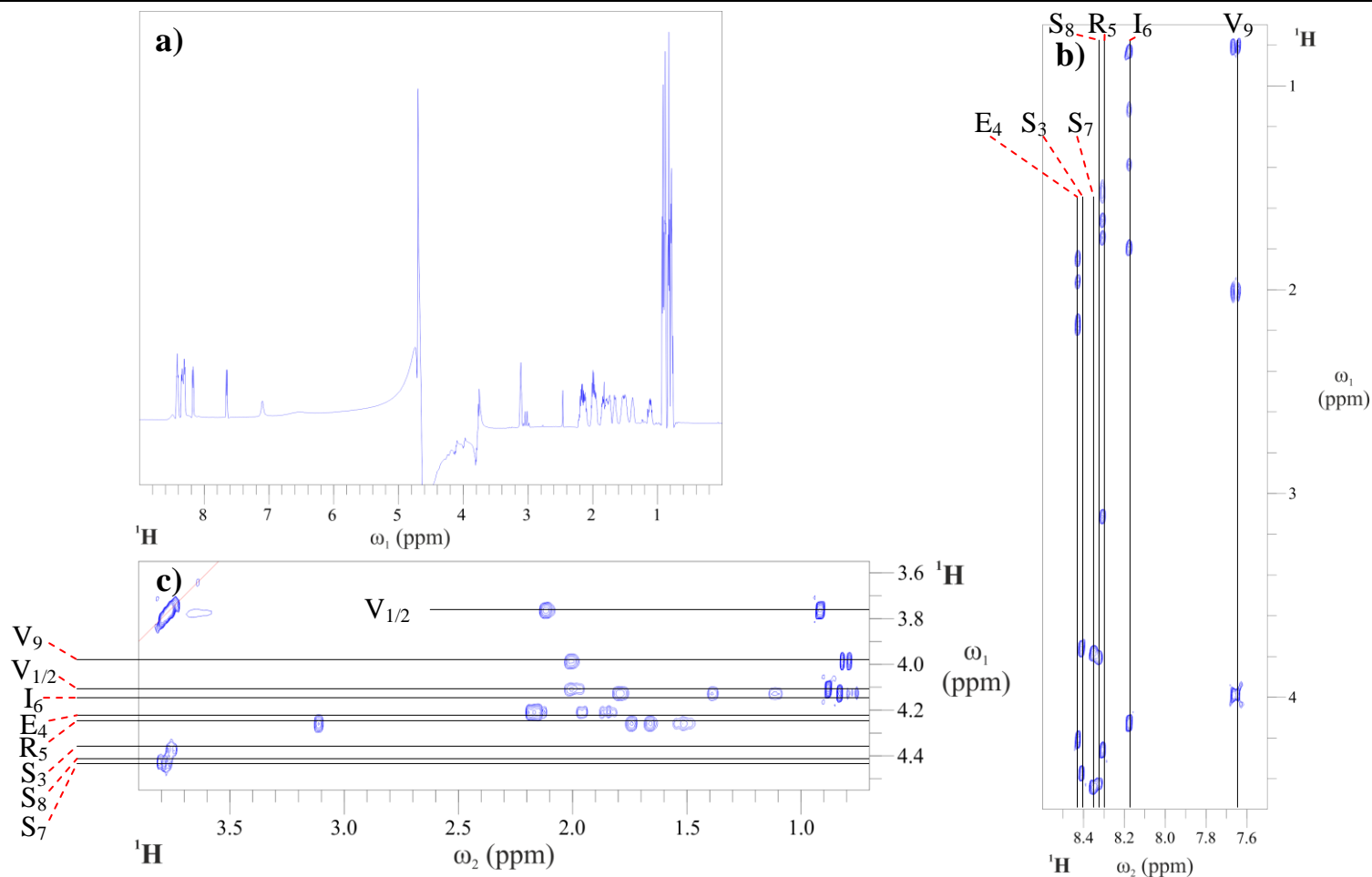


Figure 4.30: NMR spectra collected of free 5-HT_{2c} nonapeptide (VVSERISSV) acquired at 298K, with a field strength of 600MHz, in 20mM phosphate 0.1mM EDTA buffer, pH6.3; it can be seen that all spectra show numerous, well-defined peaks. a) The 1-D ¹H spectrum of free 5-HT_{2c}. b) The aliphatic-amide region (ω₁-ω₂) region of the 2-D TOCSY spectrum of free 5-HT_{2c} (mixing time = 100ms); the peaks corresponding to Ser3 – Val9 have been indicated, it was not possible to locate any peaks corresponding to Val1 or Val2 due to exchange with the solvent water. c) The aliphatic-aliphatic region (ω₁-ω₂) of the 2-D TOCSY spectrum of free 5-HT_{2c}; the peaks corresponding to Ser3 – Val9 have been indicated, it was not possible to definitively assign Val1 or Val2, although they could ambiguously identified as Val residues.

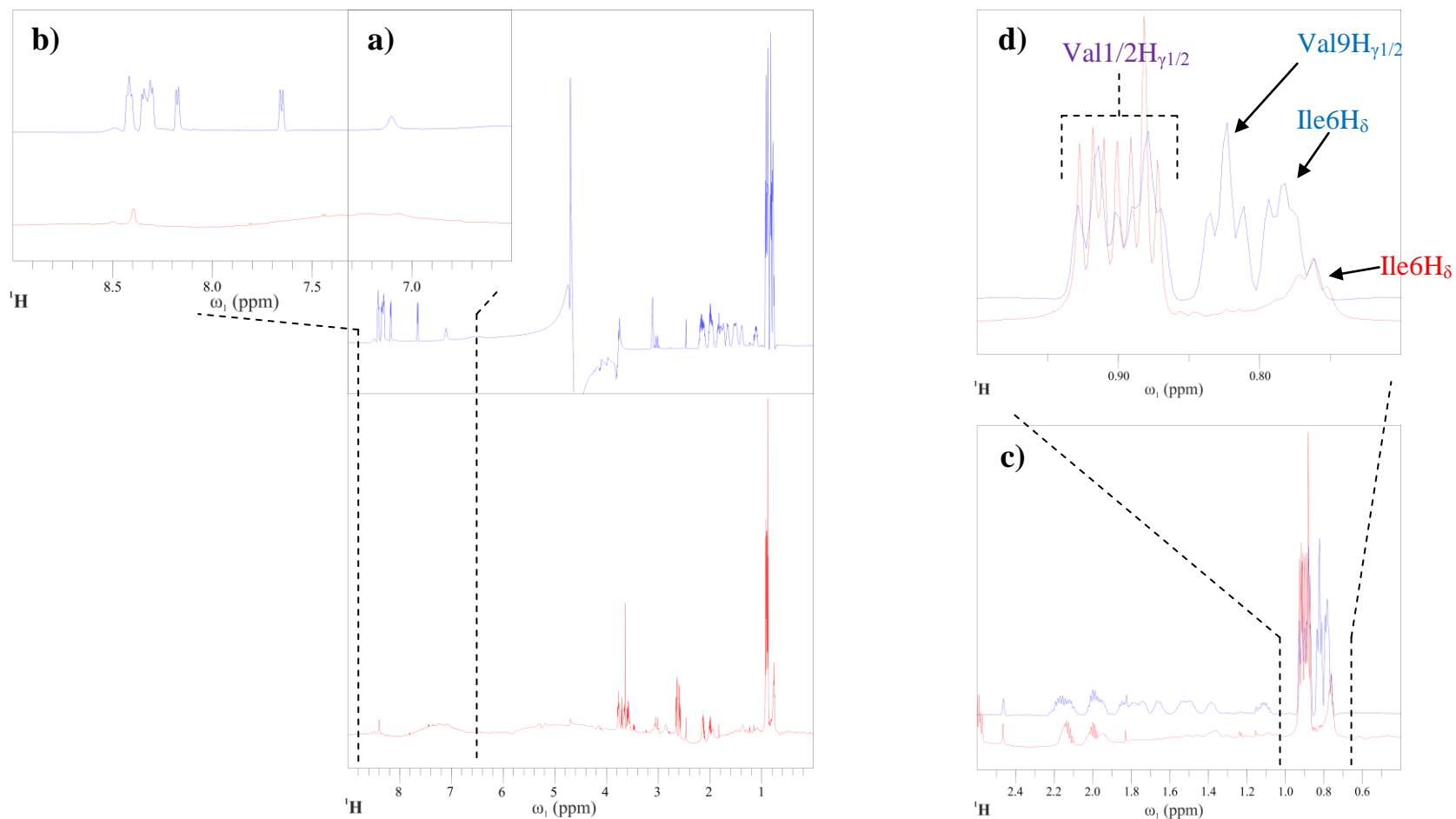


Figure 4.31: A selection of different views of the 1-D ^1H NMR spectrum of free 5-HT_{2c} (blue) overlaid with the 1-D ^1H spectrum of PSD-95 PDZ1 bound 5-HT_{2c} (red) acquired at 298K, with a field strength of 600MHz, in 20mM phosphate 0.1mM EDTA buffer, pH6.3. a) The full ^1H spectra. b) The amide region. c) An expansion of a section of the aliphatic region. d) The Val H_γ/Ile H_δ region of the ^1H spectra with the corresponding peaks in the respective spectra labelled in the spectrum colour; this indicates that the Ile6 and Val9 residues are in intermediate-exchange in the PSD-95 PDZ1 – 5-HT_{2c} complex. It is clear that there are a lot fewer and less well-defined peaks present in the spectrum of bound 5-HT_{2c}, due to intermediate-exchange between the free and bound 5-HT_{2c} forms occurring.

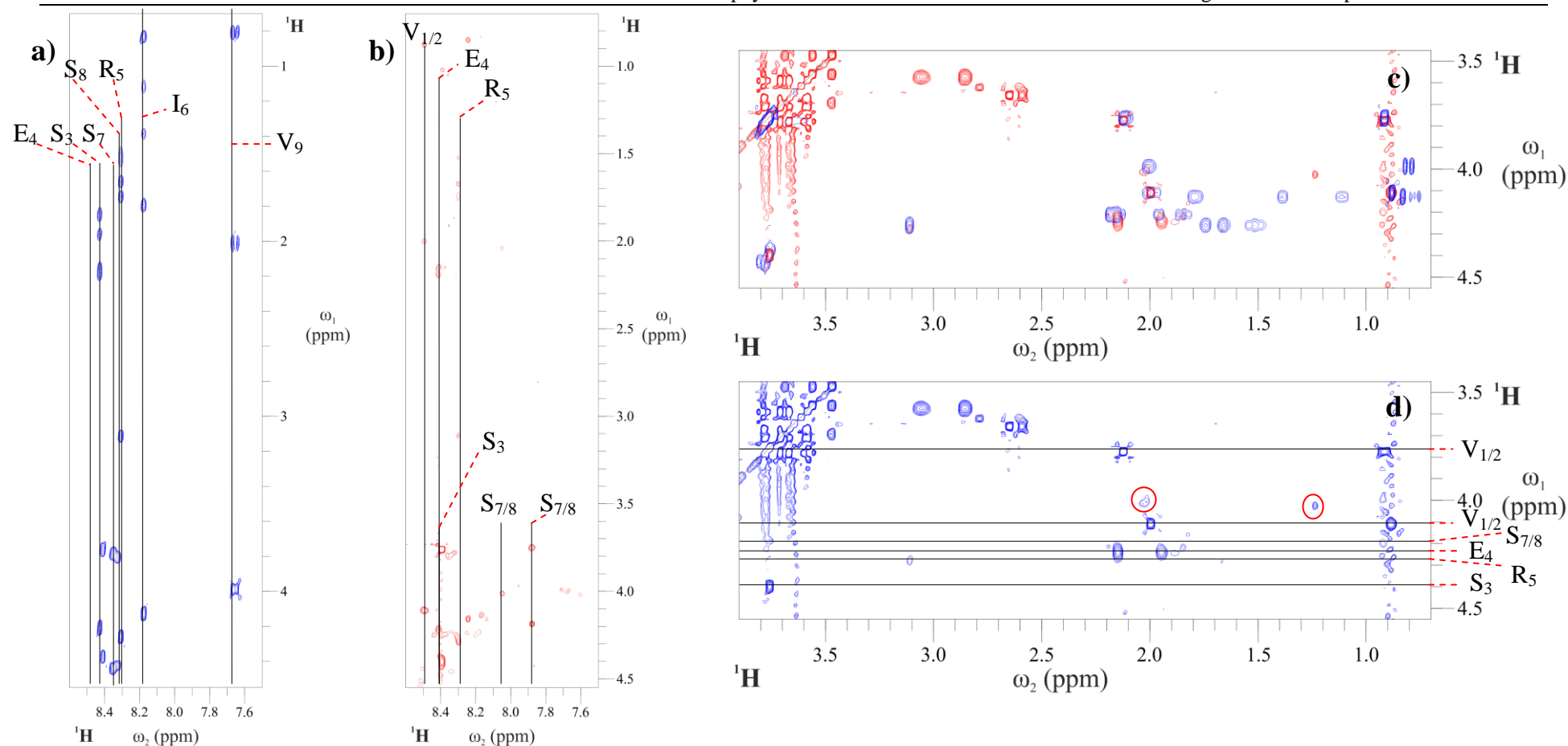


Figure 4.32: Expansions of the ^{13}C , ^{15}N -filtered 2-D TOCSY NMR spectra of free and PSD-95 PDZ1 bound 5-HT $_{2c}$ acquired at 298K, with a field strength of 600MHz, in 20mM phosphate 0.1mM EDTA buffer, pH6.3. a) The assigned aliphatic-amide region (ω_1 - ω_2) of free 5-HT $_{2c}$. b) The assigned aliphatic-amide (ω_1 - ω_2) region of PSD-95 PDZ1 bound 5-HT $_{2c}$. c) The overlaid aliphatic-aliphatic (ω_1 - ω_2) region of the free (blue) and PSD-95 PDZ1 bound (red) forms of 5-HT $_{2c}$. d) The assigned aliphatic-aliphatic region (ω_1 - ω_2) of PSD-95 PDZ1 bound 5-HT $_{2c}$. In b) & d), the peaks that were able to be definitively or ambiguously assigned prior to the NMR titration have been indicated, with the two possible peaks that could have corresponded to Ile6/Val9 circled in red. It is clear that there are a lot fewer and less well-defined peaks present in the spectrum of bound 5-HT $_{2c}$, this is due to intermediate-exchange between the free and bound 5-HT $_{2c}$ forms occurring.

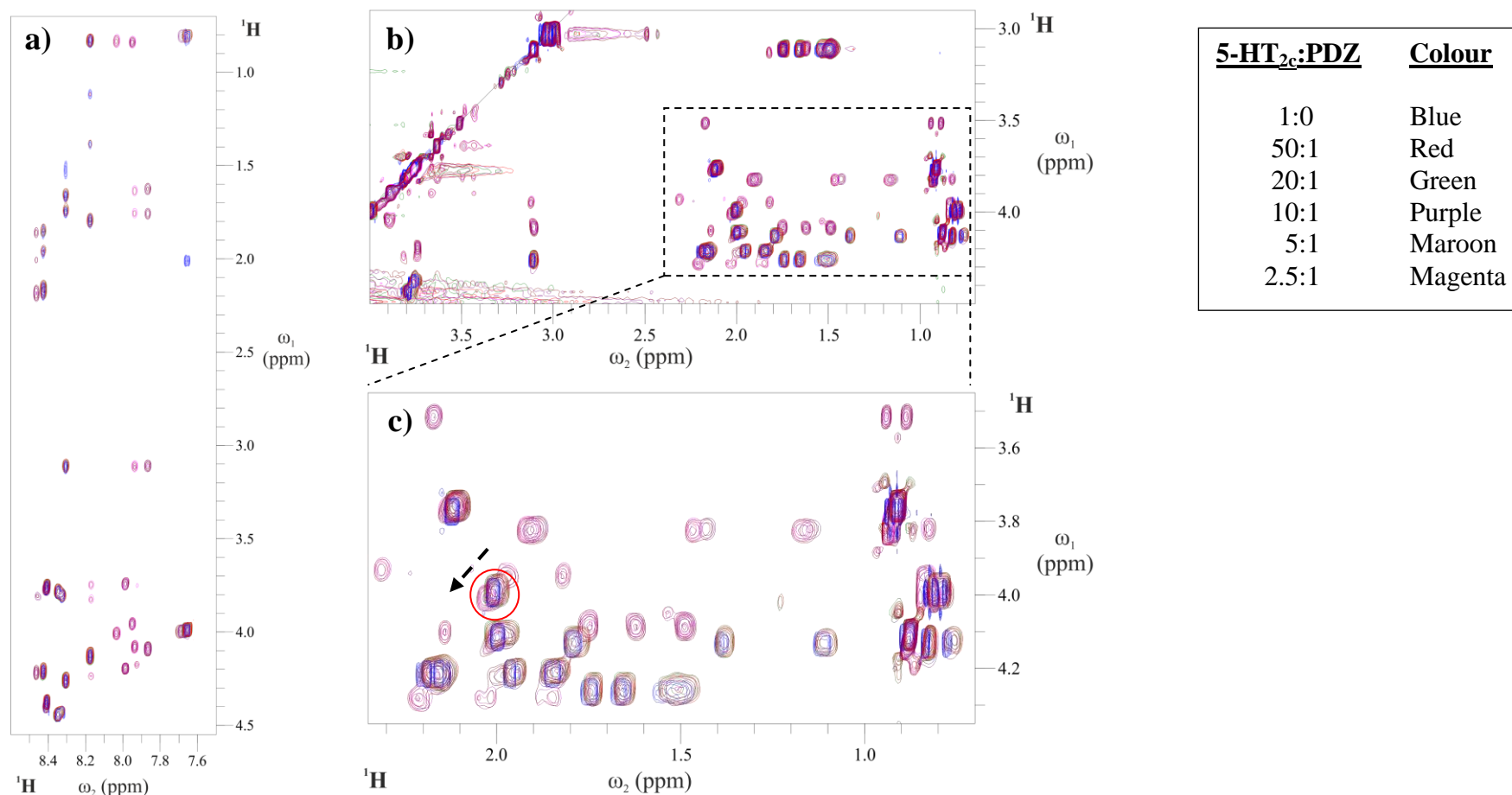


Figure 4.33: A selection of different regions of the overlaid ^{13}C , ^{15}N -filtered 2-D TOCSY spectra produced at the different 5-HT_{2c} : PSD-95 PDZ1 ratios during the NMR titration series, acquired at 298K, with a field strength of 600MHz, in 20mM phosphate 0.1mM EDTA buffer, pH6.3; a titration key is given on the right hand side. a) The aliphatic-amide region (ω_1 - ω_2); at lower peptide:protein ratios there are more peaks observed, these correspond to exchange peaks between free and PSD-95 PDZ1 bound forms of 5-HT_{2c}. b) The aliphatic-aliphatic region (ω_1 - ω_2). c) An expanded view of the methyl region of the aliphatic-aliphatic (ω_1 - ω_2) section of the spectrum highlighted by the dashed rectangle in b); the Val9 H β has been tracked from the free peptide form (dashed black arrow) and can be assigned to the peak at 2, 4ppm (circled in red), which is also shown in Figure 4.32d.

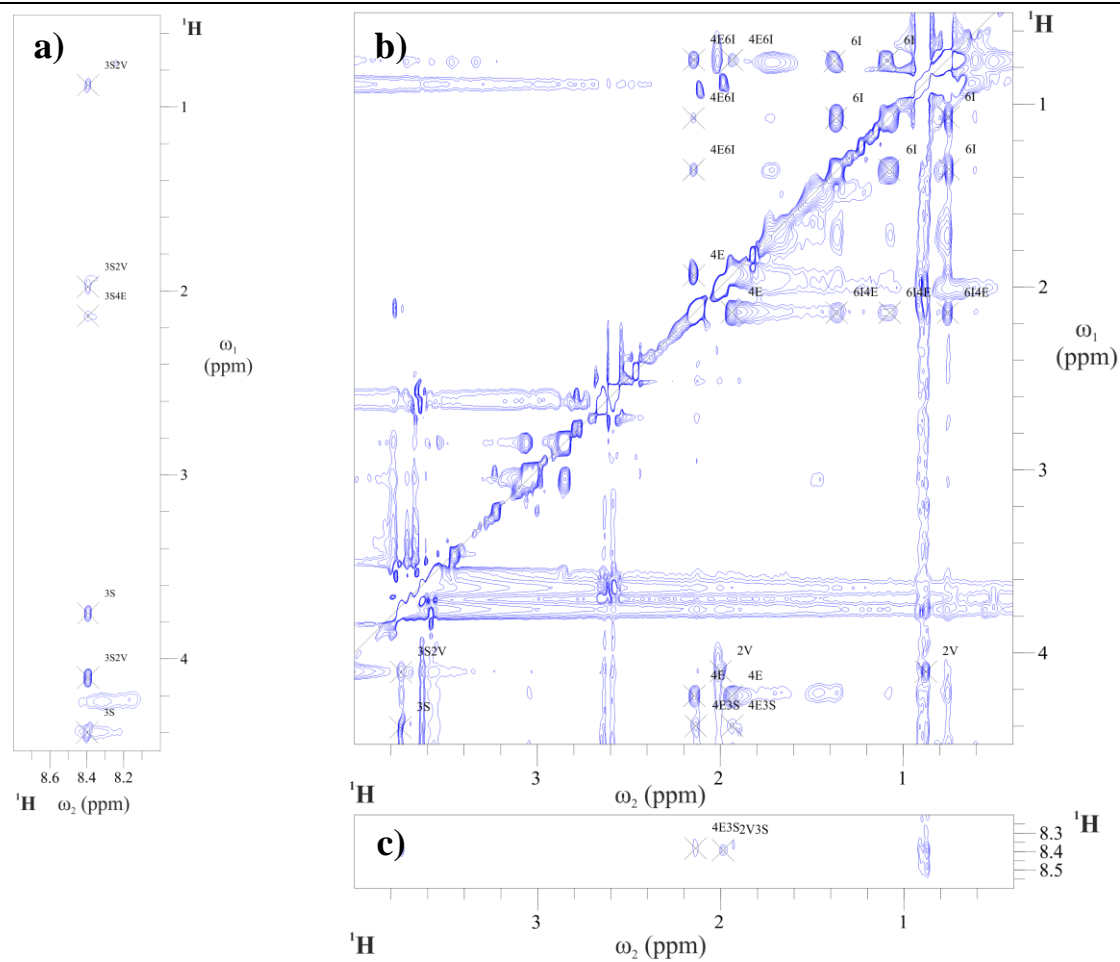


Figure 4.35: The final assignment of the 2-D ^{13}C , ^{15}N -filtered NOESY NMR spectrum of the ^{13}C , ^{15}N PSD-95 PDZ1 bound form of the 5-HT_{2c} peptide acquired at 298K, with a field strength of 600MHz, in 20mM phosphate 0.1mM EDTA buffer, pH6.3; the definitive assignments of the peaks in this spectrum had been possible due to the tracking of the peaks from the free peptide form in the NMR titration series previously described. The peaks corresponding to Val1/2 individually, have been assigned to a single Val residue in the spectra shown here but the resultant peak file produced was adapted to introduce the desired ambiguity to ensure no bias or inaccuracies in the structure calculation; the same is also true for the Ser7/8 residues.

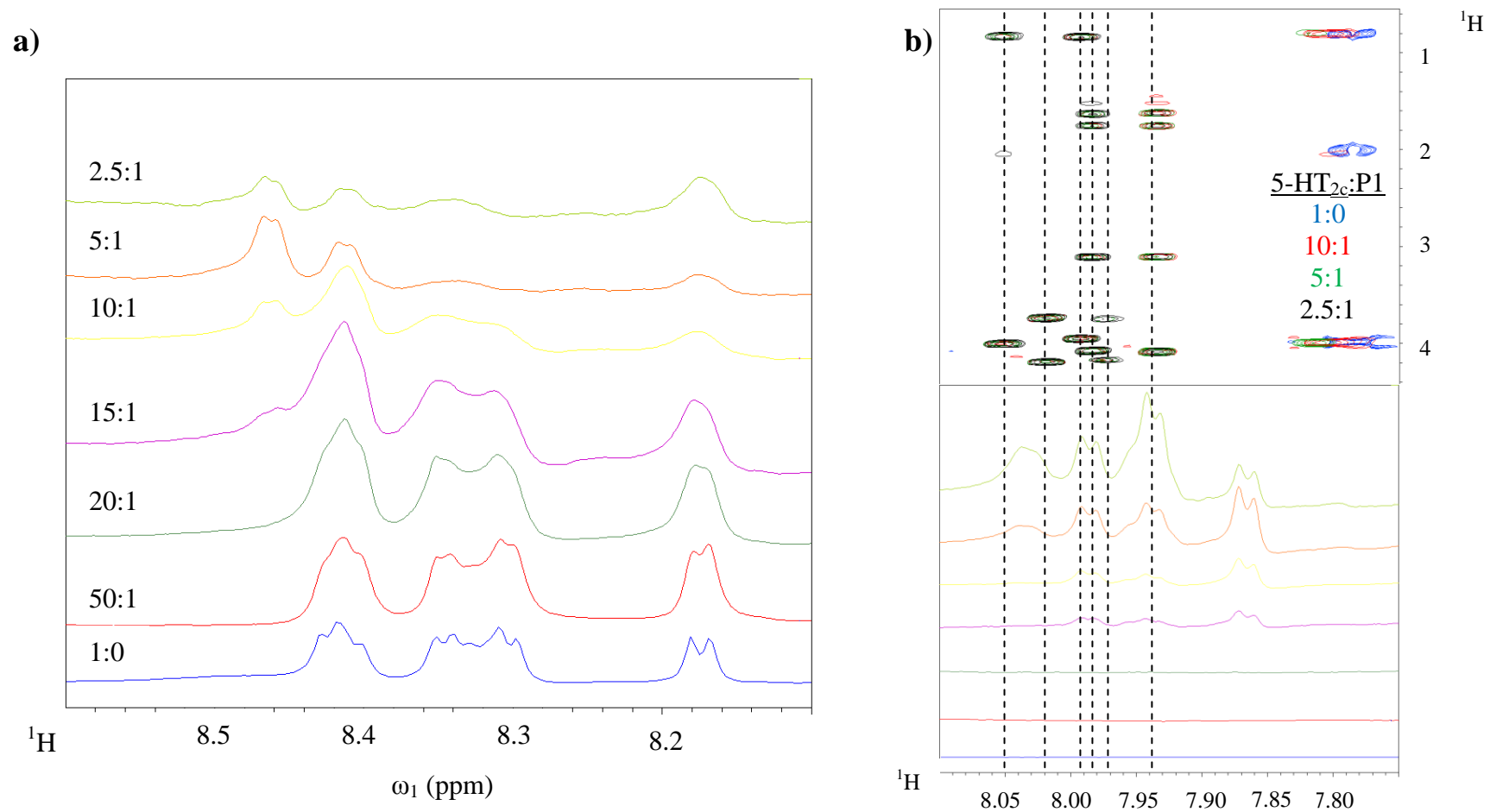


Figure 4.36: The spectra produced by the ^{13}C , ^{15}N -filtered 1-D NMR experiments performed throughout the course of the NMR titration of ^{13}C , ^{15}N PSD-95 PDZ1 into the 5-HT_{2c} nonapeptide, acquired at 298K, with a field strength of 600MHz, in 20mM phosphate 0.1mM EDTA buffer, pH6.3. a) An expansion of a section of the amide region; the peaks present in the spectrum of the free peptide lose definition and intensity as the P:L ratio increases, with free peptide signals still seen as low as L:P = 2.5:1. b) An expansion of a different section of the amide region; as the P:L ratio increases, the presence of bound 5-HT_{2c} forms can be seen up to L:P = 15:1. This spectrum has been aligned with a selection of the titration TOCSY spectra to highlight that these peaks correspond to bound peaks in the TOCSY spectra.

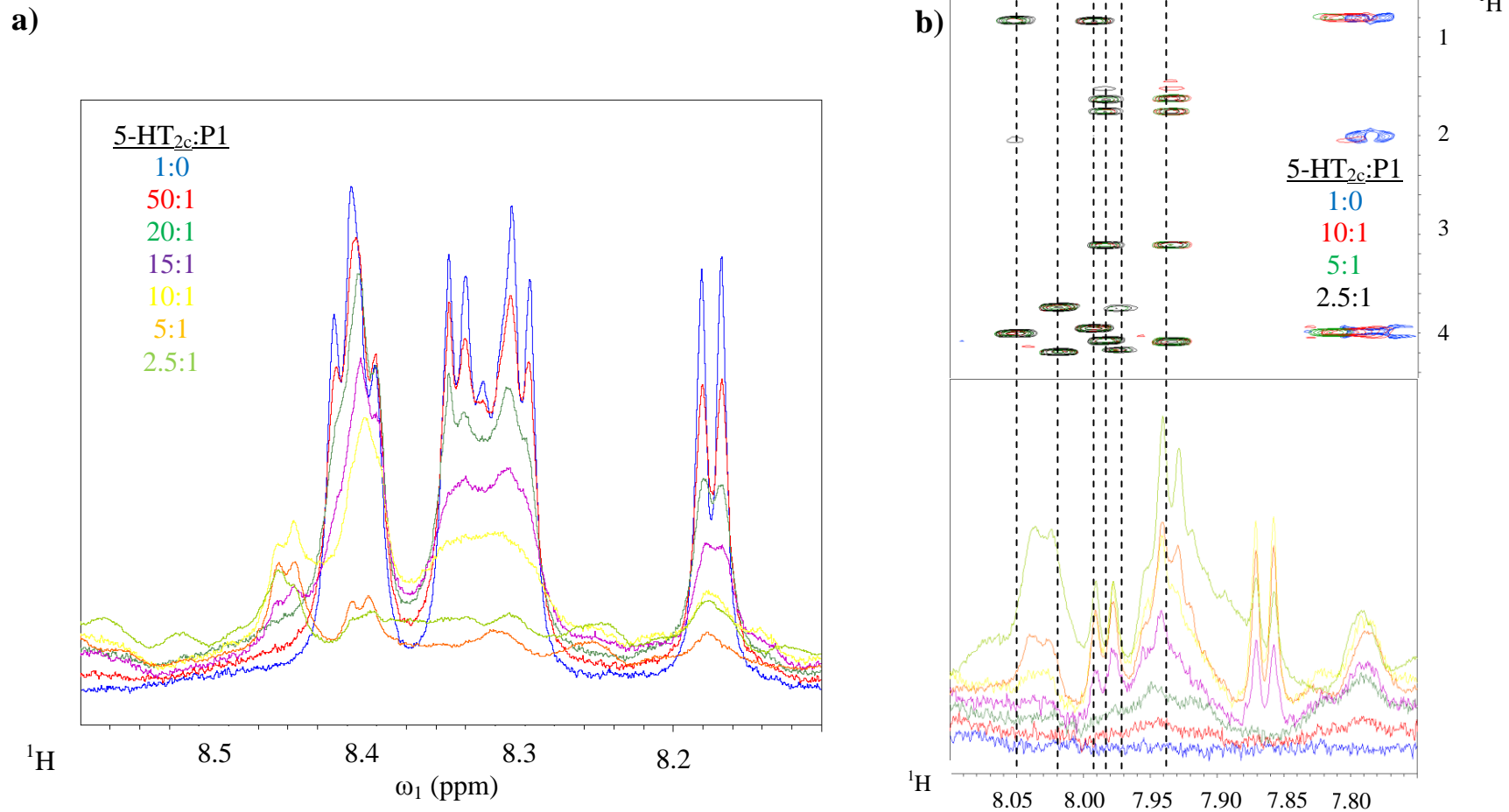


Figure 4.37: The spectra produced by the 1-D excitation sculpting (ES) NMR experiment throughout the course of the titration of ¹³C, ¹⁵N PSD-95 PDZ1 into the 5-HT_{2c} nonapeptide, acquired at 298K, with a field strength of 600MHz, in 20mM phosphate 0.1mM EDTA buffer, pH6.3. a) An expansion of a section of the amide region; this shows how the peaks present in the spectrum of the free peptide lose definition and intensity as the P:L ratio increases. b) An expansion of a different section of the amide region; this shows that as the P:L ratio increases, the presence of bound 5-HT_{2c} forms can be seen. This spectrum has been aligned with a selection of the titration TOCSY spectra to highlight that these peaks correspond to bound peaks in the TOCSY spectra.

Key:Blue = Free 5-HT_{2c} STD

Red = STD titration point (L:P = 50:1)

Green = Complex 5-HT_{2c}
filtered 1-D (L:P = 5:1)Purple = Free 5-HT_{2c} 1-D

Black = Unbound PSD-95 PDZ1 1-D

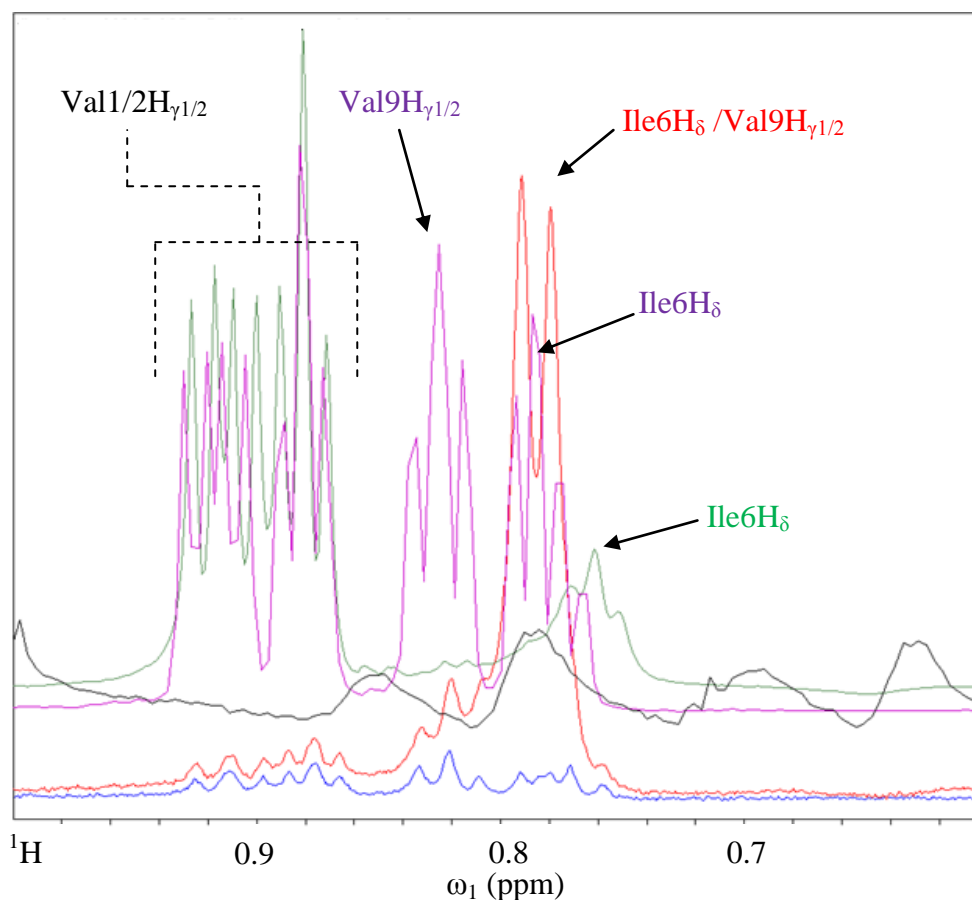


Figure 4.38: A 1-D saturation transfer difference (STD) NMR experiment was performed at each concentration titration point in attempt to evaluate the mode of binding of 5-HT_{2c} to the PSD-95 PDZ1 domain, acquired at 298K, with a field strength of 600MHz, in 20mM phosphate 0.1mM EDTA buffer, pH6.3. The figure shows an overlay of the STD experiments of free 5-HT_{2c} (blue) and 5-HT_{2c}:PSD-95 PDZ1 = 50:1 (red); it can be seen that there is a peak at ~0.78ppm. Interference from protein signal cannot account for this peak after comparison with the ¹H spectrum of the unbound PSD-95 PDZ1 (black) and the peak is due to the 5-HT_{2c} residue side-chain group that shows the most prominent interaction with PSD-95 PDZ1. The peaks in this spectral region of both the free (magenta) and PSD-95 PDZ1 bound (green) 5-HT_{2c} forms have been assigned (un)ambiguously but do not aid in the unambiguous assignment of the peak in the 50:1 (L:P) STD spectrum. Thus, it can be concluded that the 5-HT_{2c} residue chemical group participating in the most prominent intermolecular interaction with PSD-95 PDZ1 is either Ile6H_δ or Val9H_{γ1/2}.

4.6.2.3 NOESY Assignment

The assignment of the respective 3-D NOESY spectra [Table 3.5, 3.5.1] of the PSD-95 PDZ1 – 5-HT_{2c} complex was carried out in an automated manner using the CYANA programme as described in [3.5.3]; the results of the process are detailed (Table 4.4). The final cycle statistics of the automated NOE assignment process were deemed acceptable due to comparison with the documented validation criteria in the CYANA manual:

- There were nearly 1600 NOE distance restraints assigned; this represented on average over 16 NOE restraints per residue which is a reasonably large number of restraints and thus, should enable an accurate structure to be calculated.
- The backbone and heavy atom RMSD were below 0.5Å and 1Å respectively; which suggests that the NOE's assigned have produced structures with convergent structure and so, it is possible to have more confidence that the assignments are correct.
- The average target function value (ATFV) was a reasonably low value (11); as discussed in [3.5.3], this value should be as close to zero as possible but as a 50xGly linker was used to connect the protein and peptide chains, achieving an ATFV of lower than ~20 may, in this instance, be considered a desirable result.

Table 4.4: The statistics obtained from the different cycles of the CYANA programme during the automated NOE assignment process for the PSD-95 PDZ1 – 5-HT_{2c} complex spectra.

Cycle	1	2	3	4	5	6	7	Final
Peaks:								
Selected	2642	2642	2642	2642	2642	2642	2642	
Assigned	2505	2517	2478	2491	2468	2446	2432	
Unassigned	137	125	164	151	174	196	210	
Upper Distance Limits:								
Total	1698	1615	1548	1538	1491	1495	1495	1581
Short Range ((i-j) = 1)	1021	937	884	854	808	790	731	778
Medium Range (1 < (i-j) < 5)	516	397	230	233	227	212	239	250
Long Range ((i-j) > 5)	161	281	434	451	456	442	525	553
Ave Assignment / Constraint	4.61	2.43	1.53	1.49	1.39	1.32	1.00	1.00
Average Target Function Value	72.10	38.22	77.23	21.59	17.87	14.79	10.71	11.01
Average RMSD to mean (residues 20 – 80):								
Backbone	1.82	1.27	0.52	0.55	0.46	0.52	0.52	0.45
Heavy Atom	2.28	1.78	1.04	1.04	0.99	1.01	1.00	0.95

The NOE assignments obtained from the automated assignment process using CYANA were then converted into a CNS suitable format [3.5.3], in preparation for use in structure calculation using CNS.

4.6.3 Structure Calculation

4.6.3.1 *In Vacuo*

The initial *in vacuo* structure calculation of the PSD-95 PDZ1 – 5-HT_{2c} complex was conducted as detailed in [3.5.4]; the statistical details of the 20 lowest energy complex structures obtained from the *in vacuo* structure calculation process were analysed (Table 4.5). The 20 lowest energy structures did not violate any NOE restraints over 0.5Å; this was a good indication that the NOE's assigned were non-contradictory. The structures also had comparable overall energy values, which suggests that they were thermodynamically and hence, structurally similar to each other.

Table 4.5: The relevant statistics of the 20 lowest energy PSD-95 PDZ1 – 5-HT_{2c} complex ensemble obtained from the *in vacuo* structure calculation using CNS; the standard deviation from the average values of the 20 structure ensemble have been indicated by a \pm value.

NOE Violations	Bond Energy	Angle Energy	Improper Energy	Van der Waals Energy	NOE Energy	Dihedral Energy	Overall Energy
0	3.70 \pm 0.33	40.51 \pm 3.23	4.84 \pm 0.82	69.58 \pm 3.66	52.26 \pm 4.48	490.10 \pm 4.20	673.50 \pm 9.48

To give a more accurate and therefore, physiologically relevant NMR solution state structure of the PSD-95 PDZ1 – 5-HT_{2c} complex, the 20 lowest energy structures from the *in vacuo* structure calculation were subjected to an explicit water-refinement protocol in CNS.

4.6.3.2 *Water-Refinement*

The refinement of the top 20 PSD-95 PDZ1 – 5-HT_{2c} complex structures from the *in vacuo* structure calculation [4.6.3.1], in the presence of water, was performed using the procedure described in [3.5.4]. The relevant statistics for the structures obtained from the water-refinement protocol are given (Table 4.6), the structures had

comparable overall energy values, which again suggested that they were thermodynamically and hence, structurally similar to each other. The ensemble showed a small number of NOE restraint violations above the 0.5Å threshold, after the water refinement process (average of 2.45 NOE violations per structure); it was not possible to achieve a water-refined ensemble of the PSD-95 PDZ1 – 5-HT_{2c} complex with no NOE violations over the 0.5Å threshold. However, as those NOE violations observed were mostly small (less 0.7Å) and there were no consistent distance restraint violations in the ensemble, it was decided that this ensemble was sufficient to determine the representative structure of the PSD-95 PDZ1 – 5-HT_{2c} complex from.

Table 4.6: The relevant average value statistics of the top 20 lowest energy PSD-95 PDZ1 – 5-HT_{2c} complex ensemble obtained from the water refinement in CNS of the *in vacuo* structure calculation; the standard deviation from the average values of the 20 structure ensemble have been indicated by a ± value.

NOE Violations	Bond Energy	Angle Energy	Improper Energy	Van der Waals Energy	NOE Energy	Dihedral Energy	Overall Energy
2.45 ± 1.10	1139.11 ± 13.63	1070.04 ± 51.68	141.85 ± 13.52	2541.17 ± 23.22	10.08 ± 2.77	517.89 ± 6.46	5441.91 ± 84.77

4.6.4 Characterisation and Validation of Water-Refined NMR Solution State Structure of the PSD-95 PDZ1 – 5-HT_{2c} Complex

The ensemble of the PSD-95 PDZ1 – 5-HT_{2c} complex obtained from the NMR solution state structure determination process was characterised and validated using a number of different NMR structure analysis methodologies. These included the **structure identification** (Stride) web interface (Heinig and Frishman, 2004), PDBsum (<http://www.ebi.ac.uk/pdbsum/>), MultiProt (Shatsky et al., 2004), MOLMOL (Koradi et al., 1996) and the **interactive common interface for NMR structure generation** iCING (<http://nmr.cmbi.ru.nl/cing/iCing.html>) (Table 4.7). Stride showed that the ensemble of 20 complex structures exhibited the desired secondary structure of the PSD-95 PDZ1 domain, with six β-strands and two α-helices present in the bound complex form (Figures 4.36 & 4.37). MultiProt and

MOLMOL were used in tandem to determine the backbone and heavy atom root mean square deviation (RMSD) of the individual components and the overall PSD-95 PDZ1 – 5-HT_{2c} complex structure ensemble (Table 4.7): PSD-95 PDZ1 (residues 5 – 14 & 18 – 96, RMSD = 0.401Å and 1.181Å), 5-HT_{2c} (residues 4 – 9, RMSD = 0.348Å and 1.277Å) and PSD-95 – 5-HT_{2c} complex (RMSD = 0.439Å and 1.226Å). The RMSD values obtained for the ensemble suggests that the techniques used in the NOE assignment and structure calculation process were sufficient to result in consistent structures of the PSD-95 PDZ1 – 5-HT_{2c} complex.

iCING carried out a plethora of NMR structure validation processes including Ramachandran analysis on the complex structure ensemble (Table 4.7 & Appendices, A.9a) and indicated that over 80% of the residues of the ensemble are in favoured regions (80.4%), with less than 2% of residues in disallowed regions (1.6%). The majority of the 1.6% of residues of the 20 structures in disallowed regions corresponded to Leu19 and Asn65, which are both residues in highly flexible regions of the PSD-95 PDZ1 domain and so, could be forming non-favoured orientations as a result. Although these values are not as optimal as desired i.e. ideal values being >90% and <1% for residues in favoured and disallowed regions respectively, they compare well with the Ramachandran statistics of the only other ligand-bound PSD-95 PDZ1 bound NMR solution state structure in the protein database (PDB ID = 2KA9 (Wang et al., 2009), favoured = 70.2%, additionally allowed = 25.1%, generously allowed = 3.4% and disallowed 1.3%); Leu19 and Asn65 were again found to be prominent disallowed residues in this NMR solution state structure ensemble indicating that these residues are endemic of unfavourable orientations. The crystal structure of the tandem PSD-95 PDZ1 & PDZ2 domain (PDB ID = 3GSL), also shows 2.6% of residues in disallowed regions. This

information collated suggests that the less than optimal Ramachandran statistics obtained for the PSD-95 PDZ1 – 5-HT_{2c} complex ensemble could be due to the inherent differences in the bound structure of the PSD-95 PDZ1 domain, than that of those structures used as references in the Ramachandran analysis procedures.

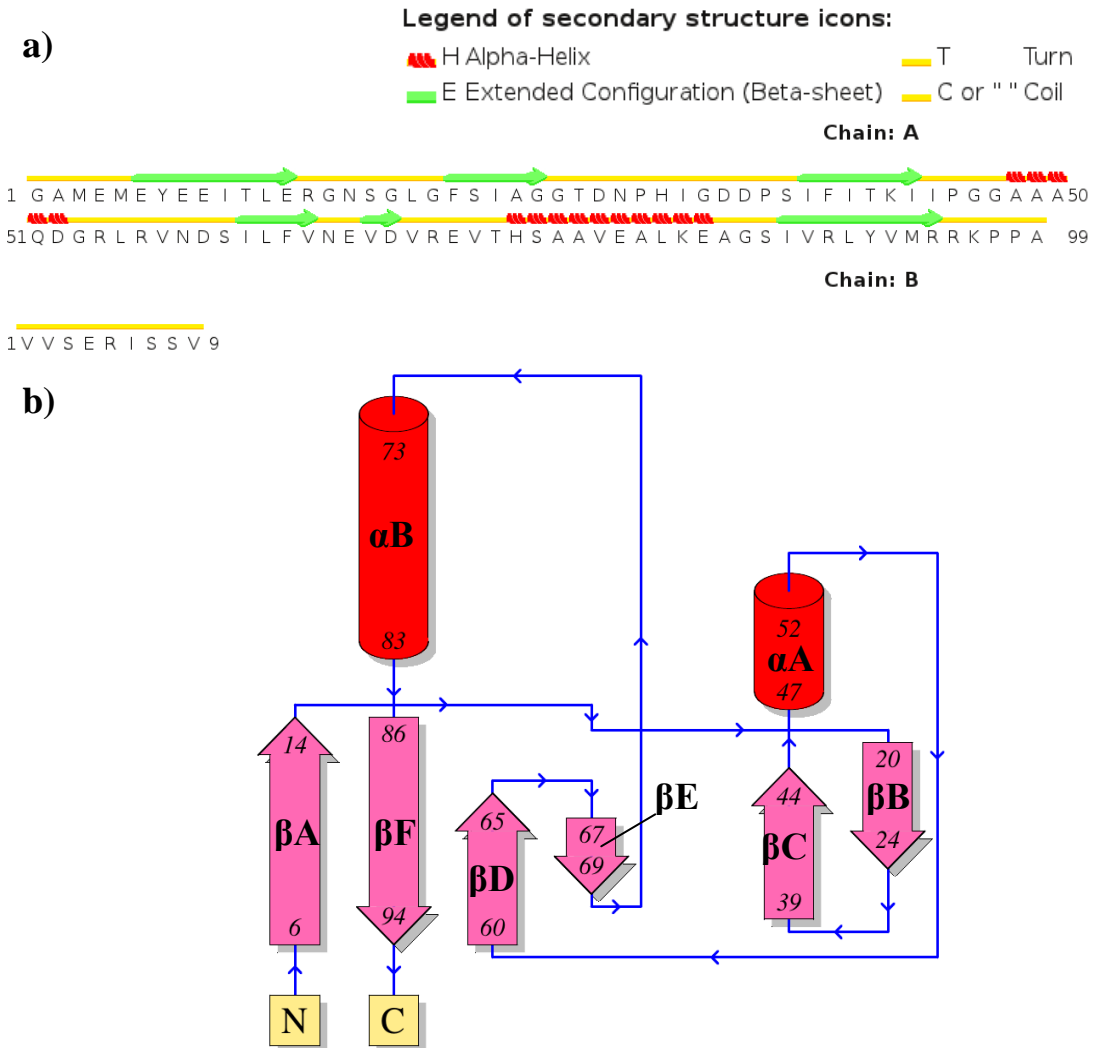


Figure 4.36: The secondary structure of PSD-95 PDZ1 – 5-HT_{2c} complex as predicted by: a) Stride (Heinig and Frishman, 2004) with a legend that details the different secondary structure icons given, b) PDBsum (<http://www.ebi.ac.uk/pdbsum/>) where β -strands are indicated by pink arrows, α -helices indicated by red cylinders and random coil regions denoted by blue connecting lines. The N and C termini have been labelled, with the numbers inside the secondary structure elements denoting the residue range for the particular feature. Both secondary structure prediction methodologies determine that the bound complex form of PSD-95 PDZ1 has the standard PDZ domain secondary structure with six β -strands and two α -helices. However, both Stride and PDBsum did not determine that the bound 5-HT_{2c} nonapeptide had any notable secondary structure.

Table 4.7: Summary of the structure calculation statistics and the relevant statistics for the resultant water-refined ensemble of 20 NMR solution state structures of the PSD-95 PDZ1 – 5-HT_{2c} complex.

Number of Structures	20
NOE Distance Restraints	
Total	1581
Short Range ((i-j) = 1)	778
Medium Range (1 < (i-j) < 5)	250
Long Range ((i-j) > 5)	553
Intermolecular	52
Hydrogen Bonds	20
Root Mean Square Deviation (RMSD, Å):	
Overall Complex Backbone	0.439
Overall Complex Heavy atom	1.226
PSD-95 PDZ1 (5 – 14, 18 – 96) ^a Backbone	0.401
PSD-95 PDZ1 (5 – 14, 18 – 96) ^a Heavy Atom	1.181
5-HT _{2c} (4 – 9) ^a Backbone	0.396
5-HT _{2c} (4 – 9) ^a Heavy Atom	1.277
Ramachandran Assessment ^b (%):	
Most Favoured	80.4
Additionally Allowed	12.8
Generously Allowed	5.2
Disallowed	1.6
Buried Surface Area (BSA, Å ²)	628

^a Residues 5-14 and 18-96 of PSD-95 PDZ1 and 4-9 of 5-HT_{2c} were defined as structured regions of the respective components of the complex from the NOE's observed using MultiProt (Shatsky et al., 2004). ^b Determined by using the PROCHECK (Laskowski et al., 1993) analysis function in iCING (<http://nmr.cmbi.ru.nl/cing/iCing.html>) to check structure viability.

The 20 water-refined complex structures were used to determine a representative NMR solution state structure of the PSD-95 PDZ1 – 5-HT_{2c} complex; this was done by creating an average co-ordinate structure for the ensemble using MOLMOL and selecting the PSD-95 PDZ1 – 5-HT_{2c} water-refined complex structure with the closest heavy atom RMSD to this average structure i.e. a closest-to-mean structure (Figures 4.38A & 4.39). The representative NMR solution state structure of the PSD-95 PDZ1 – 5-HT_{2c} complex shows that 5-HT_{2c} binds to PSD-95 PDZ1 in the classic PDZ domain ligand manner, in the hydrophobic pocket and extended groove between the βB strand and the αB helix. Both Stride and iCING were not able to

ascertain that any secondary structure was present in the 5-HT_{2c} nonapeptide when bound to PSD-95 PDZ1. This was not unexpected as it reflects the difficulties encountered in the peptide assignment process previously described and hence, demonstrates that the determined structure is fully representative of the data obtained. The use of a ¹³C, ¹⁵N-labelled 5-HT_{2c} peptide was considered and may have facilitated the determination of dihedral constraints to restrain the bound peptide further; however, there were obvious problems such as cost to acquire or cost/difficulty of recombinant production and time constraints.

Detailed analysis of the protein – peptide interaction interface of the representative PSD-95 PDZ1 – 5-HT_{2c} complex structure was performed utilising NACCESS (<http://www.bioinf.manchester.ac.uk/naccess/>), PDBsum, the protein interactions calculator (PIC, (Tina et al., 2007)) and PDB ePISA (http://www.ebi.ac.uk/msd-srv/prot_int/cgi-bin/piserver). Analysis of the interaction interface shows that 21 residues of PSD-95 PDZ1 (21.2%) and all 9 residues of the 5-HT_{2c} peptide (100%) participate in intermolecular interactions in the complex. The buried surface area (BSA, Å²) of the PSD-95 PDZ1 and 5-HT_{2c} interaction interfaces are 492.8 and 685.9 Å² respectively, which indicates that the interactions formed upon PSD-95 PDZ1 binding of 5-HT_{2c} occur over a relatively large area of the protein (6.4%). It was interesting to observe that Ramachandran analysis of the representative structure on its own showed 82% of residues were in favoured regions, 12.4% of residues in additionally regions, 5.6% in generously allowed regions and 0 residues in unfavoured regions; this suggests that the representative structure is an appropriate representation of the data (Appendices, A.9b).

The representative structure highlights the presence of a number of important intermolecular interactions which enable binding, stabilise the complex and account

for the moderate micromolar binding affinity. The subsequent described interactions of the Arg5 → Val9 residues of the 5-HT_{2c} nonapeptide were probed across the 20 complex structures and were found to be regular features in at least 90% of the ensemble.

The Ile6 and Val9 residues of the 5-HT_{2c} peptide are over 90% buried in the complex, forming hydrophobic interactions with the surrounding residues. The 5-HT_{2c} C-terminal Val9 side-chain forms hydrophobic interactions with the side-chains of residues that constitute the hydrophobic pocket of the PSD-95 PDZ1 domain binding region i.e. Leu19, Phe21, Val78 and Leu81 (Figure 4.39b); with Ile6 residue interacting with the side-chains of the residues in the βB strand i.e. Ser22 and Ala24 (Figure 4.39c). These hydrophobic interactions of Val9 and Ile6 are most likely the reason why the corresponding bound peaks were so difficult to detect in NMR experiments. The representative structure indicates the formation of the expected hydrogen bond between the 5-HT_{2c} C-terminal Val9 carboxyl group and PSD-95 PDZ1 Phe21 carbonyl in the obtained structure (Figure 4.39a).

The 5-HT_{2c} Ser8 residue is over 50% buried in the determined complex structure, interacting with the Phe21, Ser22, Ile23 and Val78 surrounding residues of the hydrophobic pocket (Figure 4.38b). As PSD-95 PDZ1 is a class I PDZ domain, it was expected that there would be evidence for a hydrogen bond formed between the PSD-95 PDZ1 His74 residue and the 5-HT_{2c} Ser7 (i.e. -2) residue; however, this was not observed in the representative structure nor any member of the ensemble, with the distance between the two atoms measuring between 5Å and 8Å across the ensemble. This is not surprising however, as all the previous examples of class I PDZ domain – ligand NMR solution state structures, where the ligand contains a Ser (-2) residue (PDB ID's = 2KA9 (Wang et al., 2009), 2PDZ (Schultz et al., 1998) and

2K2O) do not show this proposed hydrogen bond either. There are also examples of PDZ domain – peptide NMR solution state structures where the peptide contains a Thr (-2) and there is no evidence of an intermolecular hydrogen bond with the PDZ conserved His residue (PDB ID = 2OQS, (Liu et al., 2007)). This suggests that this electrostatic interaction between class I PDZ domains and the -2 residue of PDZ ligands in solution is more transient than previously thought and so is more difficult to model in NMR solution state structures than it is in compactly packed proteins in a crystal lattice. This over representation of an interaction by a crystal structure that is not observed in solution should serve as a cautionary note for future research.

The Arg5 residue side-chain methylene groups were found to interact with the PSD-95 PDZ1 His74 side-chain imidazole ring, with the Arg5 side-chain $N_{\eta}H_2$ groups forming a hydrogen bond with the Asn29 amide carbonyl (Figures 4.38b & 4.39d); the importance of Arg5 (-5) interactions in improving binding affinity has been alluded to previously in the literature (Zhang et al., 2007).

The four N-terminal residues of the 5-HT_{2c} peptide (Val1 → Glu4) exhibit a greater degree of flexibility in their bound conformation and so, display an array of different minor interactions with the residues of the $\beta B - \beta C$ loop across the ensemble of structures; this was to be expected as this region of the peptide was less constrained by intermolecular distance restraints. In the representative structure, the N-terminal residues show interactions with Pro30, His31 and Ile32 residues and so, this indicates the importance of residues further adjacent to the C-terminus to PSD-95 PDZ1 domain binding; rather than just the accepted canonical C-terminal sequence of X-S/T-X- Ω for class I PDZ domains only; this extended binding motif is investigated further in Chapter 5.

The representative structure/ensemble of structures of the PSD-95 PDZ1 – 5-HT_{2c}

complex could have important future uses in PDZ domain/PDZ domain-mediated interaction inhibition research and will be deposited into the PDB in the near future, if proven to be of sufficient quality. Furthermore, the over-reliance on crystal structures and their more rigid conformations in this case has led to what could be a mistaken belief that the PDZ His – PDZ ligand S/T hydrogen bond interaction is conserved in solution.

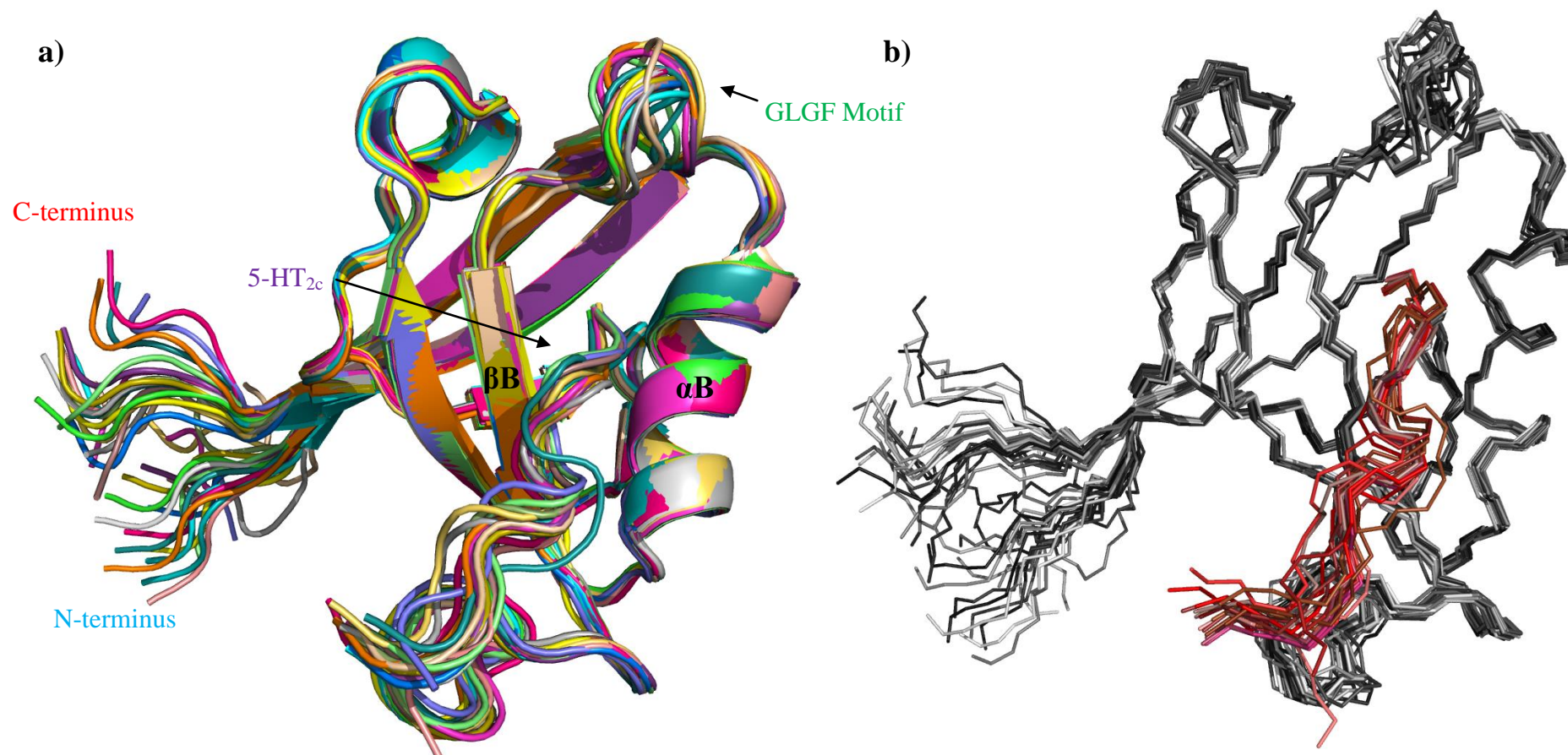


Figure 4.37: The final 20 water-refined NMR solution state structure ensemble of the PSD-95 PDZ1 – 5-HT_{2c} complex obtained from the structure calculation process with both PSD-95 PDZ1 and 5-HT_{2c}: a) in the cartoon representation, b) backbone atoms represented as sticks. The 20 aligned complex structures all show the expected secondary structure of the 5-HT_{2c} bound form of the PSD-95 PDZ1 domain of six β -strands and two α -helices, with high structural similarity (Overall complex backbone and heavy atom RMSD = 0.439Å and 1.226Å respectively), with only the highly flexible regions of PSD-95 PDZ1 i.e. N/C termini and GLGF motif showing any slight structural deviation (PSD-95 PDZ1 backbone and heavy atom RMSD = 0.401Å and 1.181Å respectively); there is little difference in the bound conformation of the 5-HT_{2c} peptide across the ensemble but no inherent secondary structure was identified by Stride (5-HT_{2c} nonapeptide backbone and heavy atom RMSD = 0.348Å and 1.277Å respectively).

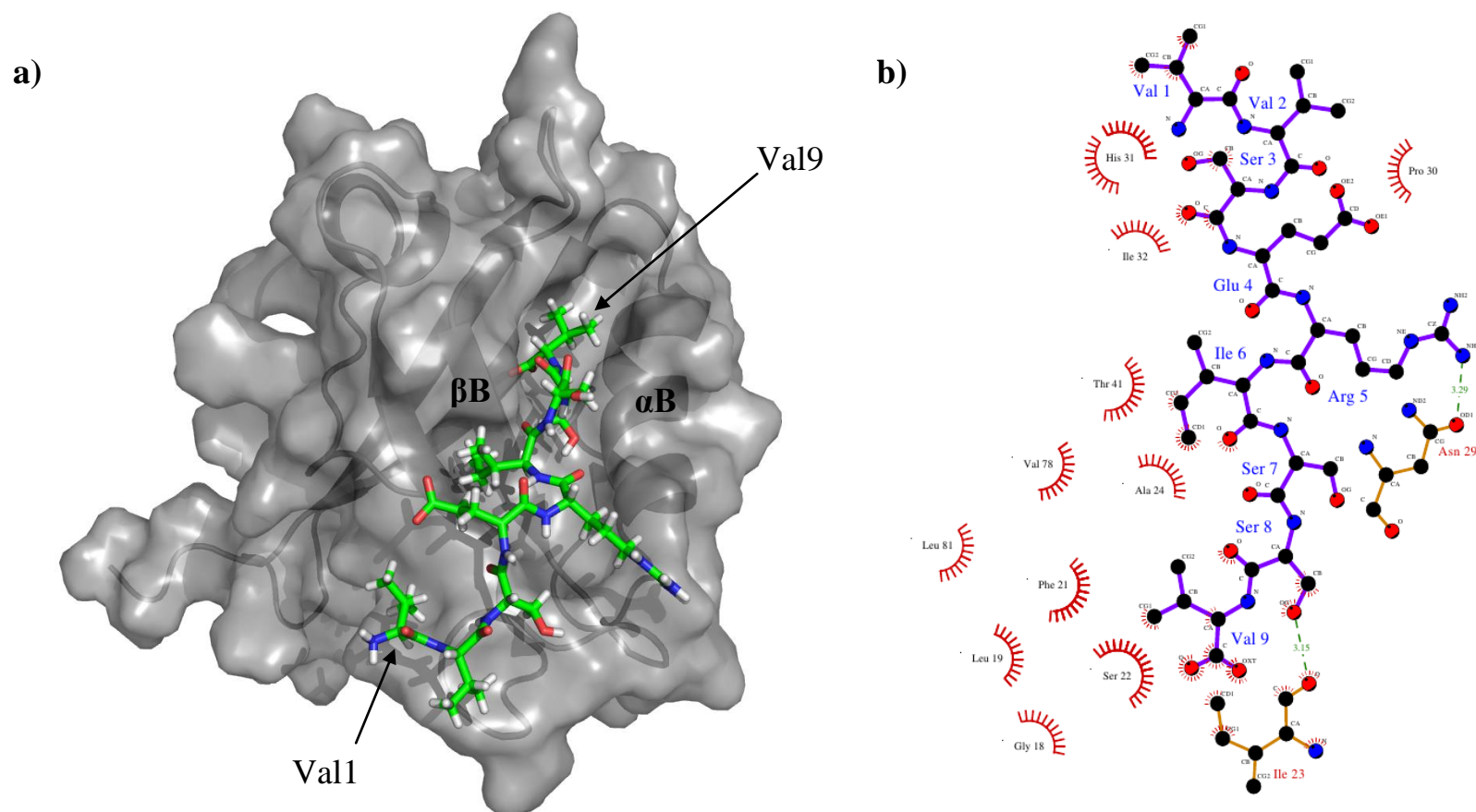


Figure 4.38: a) The representative structure of the PSD-95 PDZ1 – 5-HT_{2c} complex determined by NMR solution state spectroscopy, where PSD-95 PDZ1 is shown as a surface representation (grey) with the 5-HT_{2c} nonapeptide represented as sticks; the representative structure was obtained by creating an average co-ordinate structure of the 20 water-refined structure ensemble and selecting the ensemble structure with the lowest heavy atom RMSD to the average structure i.e. it is a closest to mean structure. The representative structure shows that 5-HT_{2c} binds to PSD-95 PDZ1 in the hydrophobic pocket and extended binding groove between the β B-strand and α B-helix i.e. the classical manner. b) A LigPlot representation created using PDBsum (<http://www.ebi.ac.uk/pdbsum/>) showing most of the important intermolecular interactions occurring in the representative structure of the PSD-95 PDZ1 – 5-HT_{2c} complex, such as hydrophobic interactions of Val9 with Leu19, Phe21 and Val78. The presence of interactions of ligand residues further away from the C-terminus i.e. Ile6 → Val1, suggests that residues further up from the C-terminus than the conventional X-S/T-X- Ω of a PDZ ligand may be important in PSD-95 PDZ1 binding.

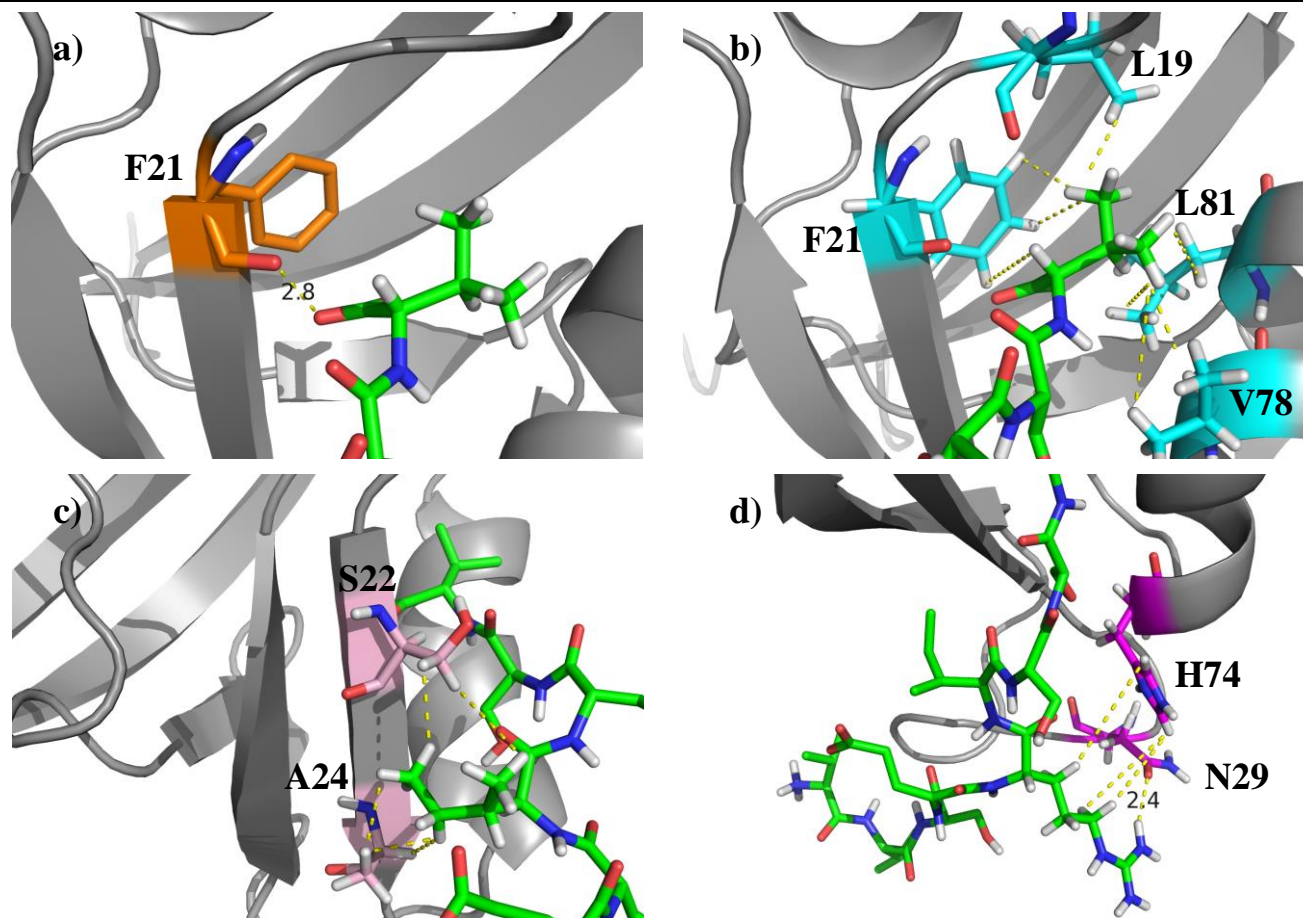


Figure 4.39: Expansions of different key areas of the interaction interface in the representative structure of the PSD-95 PDZ1 – 5-HT_{2c} complex, with the PSD-95 PDZ1 domain in cartoon representation (grey) with the residues involved in intermolecular interactions and the 5-HT_{2c} nonapeptide represented as sticks. All non-polar protons have been removed for clarity, except those involved in the intermolecular interactions; interactions have been indicated with yellow dashed lines, with hydrogen bonds differentiated from hydrophobic interactions by the addition of distance values (Å). a) The hydrogen bond formed between the C-terminal Val9 carboxyl group of 5-HT_{2c} and the backbone carbonyl of Phe21 of PSD-95 PDZ1 (orange). b) The 5-HT_{2c} Val9 interacts with residues of the PSD-95 PDZ1 hydrophobic pocket (cyan); these residues include Leu19, Phe21, Val78 and Leu81. c) The 5-HT_{2c} Ile6 residue with the Ser22 and Ala24 residues of the PSD-95 PDZ1 βB-strand (light pink). d) The 5-HT_{2c} Arg5 interacts with the His74 and Asn29 side-chains of PSD-95 PDZ1 (magenta).

4.7 Conclusion

Through a process that encompassed protein expression, purification, NMR spectroscopy and ITC, the binding of 5-HT_{2a} and 5-HT_{2c} nonapeptides to the PDZ1&2 domains of PSD-95 and SAP97 were investigated in detail. The PDZ binding affinity of 5-HT_{2c} was found to be stronger than that of 5-HT_{2a} for each PDZ domain, even though they share the same 0 and -2 residues; this suggests the importance in other residues of the PDZ ligand in determining PDZ domain binding affinity.

The most important aspect of the research detailed in this chapter is the determination of the NMR solution state structure ensemble of the PSD-95 PDZ1 – 5-HT_{2c} complex; this is a structure that has not been solved previously and is currently in the process of deposition into the protein databank (PDB). The representative structure showed that all the 5-HT_{2c} nonapeptide residues exhibited interactions with residues of the PSD-95 PDZ1 domain; this corroborated the finding by ITC that PDZ ligand residues other than the 0 and -2 residues form important interactions with the PSD-95 PDZ1 domain and contribute to binding affinity. There are few previous examples of PDZ domain – peptide complex structures determined by NMR solution state spectroscopy, only 39 out of a total of 367 PDZ domain/PDZ domain complex structures in the PDB. This comparison highlights that other researchers may have experienced similar problems to those described in this chapter i.e. ligand residues being in intermediate-exchange between unbound and bound forms. This assignment difficulty was overcome by performing an NMR titration series of doubly-labelled PSD-95 PDZ1 into free 5-HT_{2c}; the titration series also helped to further elucidate the PSD-95 PDZ1 binding mode of 5-HT_{2c} via ES and STD NMR experiments.

By close analysis of the structure of the determined PSD-95 PDZ1 – 5-HT_{2c} complex, it is possible to determine the key interactions required for developing potent and selective PSD-95 PDZ1 binders/inhibitors. Therefore, it is hoped that the NMR solution state ensemble of the PSD-95 PDZ1 – 5-HT_{2c} complex provides valuable insight and direction for not just future PSD-95 PDZ1 – 5-HT_{2c} inhibition research but for PSD-95 PDZ1-mediated interaction and PSD-95 PDZ1 domain inhibition research in general.

Chapter 5

**THE BIOPHYSICAL INVESTIGATION INTO THE
INTERACTION BETWEEN THE SAP97 PDZ2 DOMAIN AND THE
HUMAN PAPILLOMAVIRUS TYPE 16/18 E6 PROTEINS**

5. THE BIOPHYSICAL INVESTIGATION INTO THE INTERACTION BETWEEN THE SAP97 PDZ2 DOMAIN AND THE HUMAN PAPILLOMAVIRUS TYPE 16/18 E6 PROTEINS

5.1 Introduction

As discussed in [1.5.3.2], the SAP97 PDZ domains are known to interact with the human papillomavirus (HPV) E6 oncoprotein produced by ‘high-risk’ HPV types, such as HPV16 and HPV18 (Lee et al., 1997); this interaction occurs via PDZ domain binding motif at the C-terminus of the HPV16/18 E6 proteins (Chi et al., 2009). This PDZ domain-mediated interaction causes SAP97 to be targeted for degradation and leads to p53-independent HPV E6-induced pathogenesis (Kiyono et al., 1997, Mantovani and Banks, 2003, Latorre et al., 2005, Zhang et al., 2007). It has therefore been concluded that the PDZ domain-mediated interaction between SAP97 and the HPV16/18 E6 oncoproteins is a viable research/therapeutic target.

The binding affinity of the SAP97 PDZ2 - HPV16/18 E6 oncoproteins interaction has been previously determined using N-acetylated hexaresidue C-terminal peptides of the HPV16 (Ac-RRETQL) and HPV18 (Ac-RRETQV) E6 oncoproteins in ITC experiments (SAP97 PDZ2 – HPV16/18 E6 $K_D = 1.33\mu\text{M}$ and $6.49\mu\text{M}$ respectively) (Liu et al., 2007). The solution-state NMR and crystal structures of SAP97 PDZ2 in complex with a C-terminal peptide of the HPV18 E6 peptide have also been determined (Liu et al., 2007, Zhang et al., 2007); the structures obtained showed the presence of important interactions between the SAP97 PDZ2 domain and residues of the HPV18 E6 peptide further away from the C-terminus than was previously thought important. This observation was also confirmed when recombinant full-length HPV16 and HPV16_{L151V} mutant (a mimic of HPV18) E6 protein was produced and its binding to the three individual SAP97 PDZ domains quantified by

ITC (Chi et al., 2011); the determined binding affinity to SAP97 PDZ2 was higher than that given by the hexaresidue peptides (SAP97 PDZ2 – HPV16_{L151V} E6 $K_D = 0.34\mu\text{M}$).

The previous research into the interaction between the SAP97 PDZ domains and the HPV E6 oncoproteins has given useful information about the interaction, although the main factors that contribute to binding affinities have not been investigated in a systematic manner. There are a number of factors that are considered to contribute to the binding of the SAP97 PDZ – HPV E6 interaction, yet these have not been investigated in detail to determine the relative importance of each to the overall binding affinity (Figure 5.1). The contributing factors to binding are:

- The hydrogen bond interaction between the carboxyl group of the C-terminal amino acid and the amide backbone of the GLGF motif (Figure 5.1, red).
- The hydrophobic interaction between the side-chain of the C-terminal ligand residue (0) and the residues that form the hydrophobic pocket of the SAP97 PDZ domain (Figure 5.1a, blue).
- The hydrogen bond between the S/T (-2) ligand residue and the conserved His residue in the class I PDZ domains of SAP97 (Figure 5.1a, green).
- The interaction between residues further away from the C-terminus of the ligand than the conventional four C-terminal residues and the binding region of the SAP97 PDZ domains (Figure 5.1a, yellow).

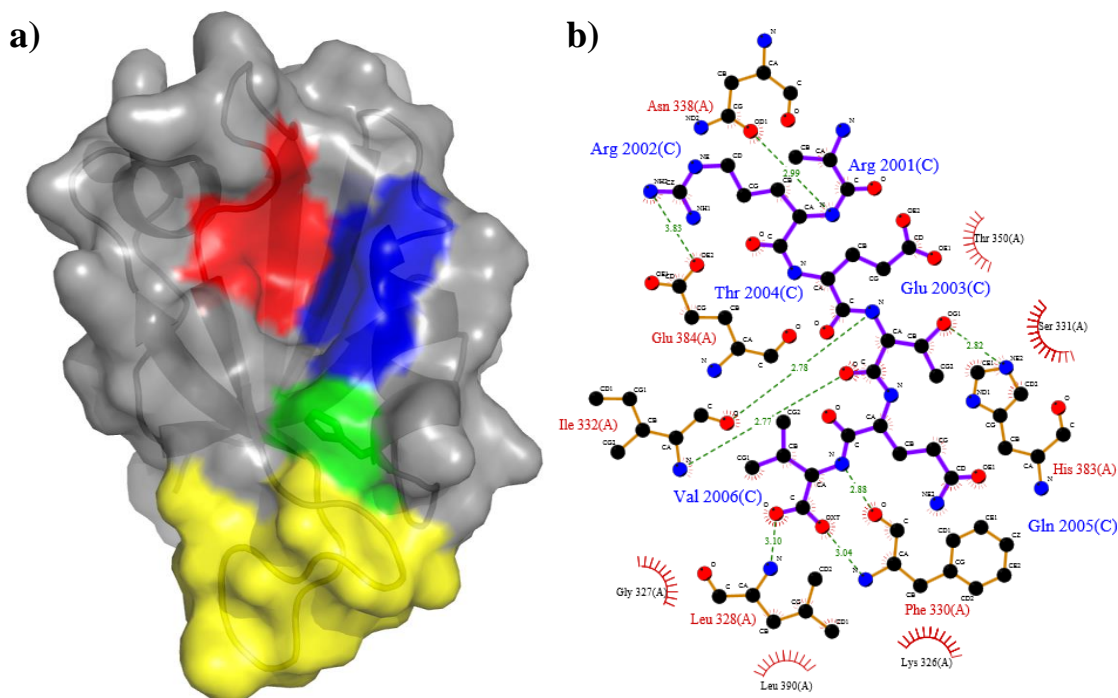


Figure 5.1: a) The crystal structure of the SAP97 PDZ2 domain in complex with a C-terminal peptide of HPV18 E6 (PDB ID = 2I0L, (Zhang et al., 2007)) in a cartoon and surface representation, with the peptide ligand removed. The different contributing factors to binding affinity highlighted; the GLGF motif (red), hydrophobic interactions of the binding pocket (blue), the electrostatic interaction involving the conserved His residue (green) and the further downfield interactions with the residues of the $\beta\text{B} - \beta\text{C}$ loop (yellow). b) A LIGPLOT representation of the hydrophobic and electrostatic interactions that occur in the SAP97 PDZ2 – HPV18 E6 crystal structure; it is evident that there are important intermolecular interactions between the C-terminal Val (0 or 2006 in this figure) to the Arg (-5 or 2001) of HPV18 E6 and the regions of the SAP97 PDZ2 domain highlighted in a): Val (0) – Leu328/Phe330 (GLGF motif, red), Val (0) – Leu390 (hydrophobic pocket, blue), Thr (-2) – His383 (conserved His, green) and Arg (-4/-5) – Asn338 (βB - βC loop, yellow).

Data that characterised the relative importance of each of the above contributions to SAP97 PDZ binding would be extremely useful in the design of potential inhibitors of the SAP97 PDZ domains. The investigation detailed in this chapter attempts to explore the contributions to SAP97 PDZ2 binding of the different factors.

The research described in this chapter is a systematic investigation into the interaction between the SAP97 PDZ2 domain and the HPV18 E6 protein. The methodology described in this chapter employs standard protein production procedure to produce wild-type SAP97 PDZ2, with site-directed ligase-independent mutagenesis (SLIM) employed to produce mutant forms of the SAP97 PDZ2 domain. ITC was utilised to detect the resultant binding (or lack thereof) between the particular SAP97 PDZ2 domain and commercially acquired peptides of the HPV18

E6 C-terminus (Table 6.1) and quantify the dissociation constants. The peptides investigated had varying lengths and amino acids at the 0/-2 ligand positions; a couple of peptides of the HPV16 E6 protein C-terminus were included in the investigation to see if there were any common binding trends between the two different E6 proteins (Table 6.1). ITC was the chosen biophysical technique for this investigation as not only is it able to quantify the binding affinity of the particular protein-peptide interaction, it is able to provide qualitative thermodynamic parameter information about the binding process; the change in enthalpy and entropy induced by binding is measured and this can be used to evaluate the interactions occurring during the binding process.

The investigation was also carried out on the SAP97 PDZ1 – HPV18 E6 interaction but will not be discussed here due to the space constraints of this thesis.

Table 6.1: The sequences of the different peptides (GenicBio, China) utilised in the SAP97 PDZ – HPV18 E6 binding investigation by ITC; the peptides corresponding to the HPV16 E6 sequence have been highlighted in red.

Tripeptide	Pentapeptide	Pentapeptide	Nonapeptide	Nonapeptide
TQV	RETQV	RETQ α^a	LQRRRETQV	LQRRREGQV
TQA	RETQL	RETQ β^b	SRTRRETQL	
	RETQI	RE γ QV ^c	LQRRRETQF	
	RETQG	RE δ QV ^d	LQRRRESQV	

^a α = norvaline. ^b β = norleucine. ^c γ = allothreonine. ^d δ = betahydroxynorvaline.

5.2 Purification of SAP97 PDZ2 Mutants

By mutating His73 of the SAP97 PDZ2 domain, it was possible to investigate the effect of removing the potential to form a hydrogen bond interaction between the PDZ domain and the ligand. The His73 residue was mutated to both Gly and Thr residues; Gly was chosen as this would definitely eliminate the ability to form a hydrogen bond between the mutant PDZ domain and peptide ligand and so the effect on binding affinity of the electrostatic interaction could be deduced. On the other hand, Thr was selected to determine if it was still possible to form an alternative hydrogen bond between the SAP97 PDZ2 mutant domain and the HPV18 E6

peptide. Both mutant forms enabled comparison of the resultant binding affinity to that of the wild-type domain, in the absence or possible presence of an electrostatic interaction. The mutation of the His73 residue of wild-type SAP97 PDZ2 to Gly and Thr was carried out using SLIM as detailed in [3.2.1.1] and was shown to be successful (Appendices, A.1a).

The subsequent transformation, expression and purification of unlabelled and ^{15}N -isotopically labelled SAP97 PDZ2 wild-type, H73G and H73T mutant domains was carried out as detailed in [3.2.1.3], [3.2.2] and [3.2.3] respectively. The chromatograms produced from size exclusion chromatography, the final purification stage of the three different SAP97 PDZ2 domains, can be seen as a chromatogram overlay (Figure 5.2a). As mentioned in [4.2], the size exclusion column had been previously calibrated and so, the three PDZ domains were deduced to be monomeric. Samples of each of the SAP97 PDZ2 domains obtained at the end of the protein purification process were analysed by SDS-PAGE gel electrophoresis to ensure their purity (Figure 5.2b); the SDS-PAGE gel showed each of the three different PDZ domains to be pure.

The three SAP97 PDZ2 domains were then characterised by NMR spectroscopy to determine if the mutant forms of the SAP97 PDZ2 domain were folded like the wild-type form and to ensure that the His73 residue had been mutated successfully.

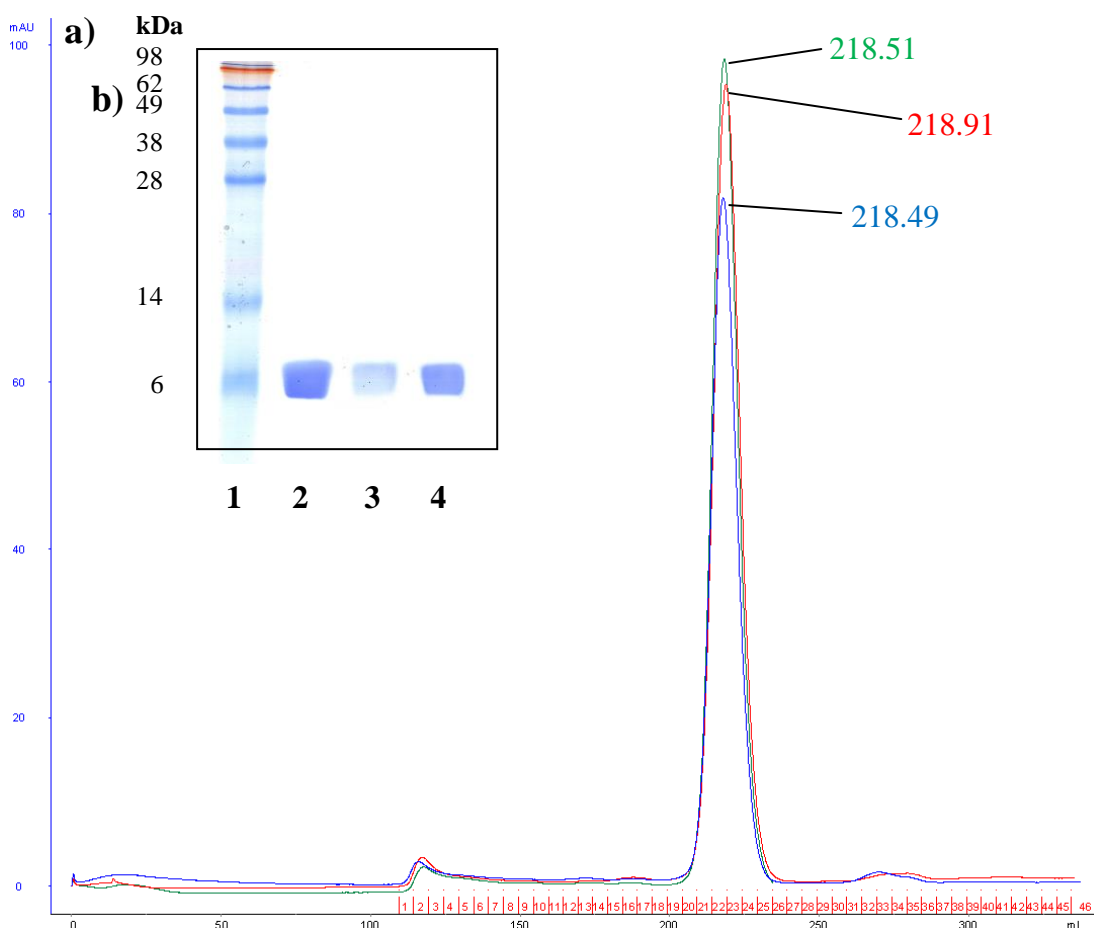


Figure 5.2: a) The chromatograms obtained from size exclusion chromatography using a HiLoad 26/60 Superdex 75 in a 50mM Tris/HCl, 150mM NaCl, 2mM DTT buffer, pH 7.4; this was the final stage of the PDZ domain purification process. The size exclusion chromatograms for SAP97 PDZ2 wild-type (blue) and the SAP97 PDZ2 H73G (red) and H73T mutants (green) are shown. The elution volume for each of the three PDZ domain chromatograms has been detailed; the column equilibration (Appendices, A.2) indicated that an elution volume of ~220mL corresponds to ~10kDa protein and thus, all three PDZ domains are shown to be within acceptable limit values for monomeric proteins. b) The corresponding SDS-PAGE gel of the obtained proteins shown that each final PDZ domain samples obtained was pure; 1 = marker, 2 = SAP97 PDZ2 wild-type, 3 = SAP97 PDZ2 H73G, 4 = SAP97 PDZ2 H73T.

5.3 Characterisation of SAP97 PDZ2 Mutants by NMR Spectroscopy

^{15}N -labelled SAP97 PDZ2 domain mutant samples were prepared [3.3.2] and ^1H 1-D and ^1H - ^{15}N 2-D HSQC NMR spectroscopic experiments were carried out. The resultant NMR spectra showed that all three forms of the SAP97 PDZ2 domain were folded and that the His73 residue of the wild-type SAP97 PDZ2 had been successfully mutated in both proteins (Figures 5.3 – 5.5). This was concluded as the peak corresponding to the His residue in the wild-type (circled red in Figure 5.3) was not present in either spectra of the mutant forms (Figures 5.4 & 5.5). There were also

extra peaks present in the spectra of the mutant SAP97 PDZ2 proteins corresponding to the Gly and Thr residue mutations; hence the mutagenesis was deemed successful. As expected, there are a number of peaks shifted in the mutant SA97 PDZ2 forms c.f. wild-type SAP97 PDZ2. A number of the residues in the binding region that have been shown to be shifted in the SAP97 PDZ2 mutant forms c.f. wild-type, have been mapped onto the SAP97 PDZ2 wild-type structure (solid rectangles, Figure 5.6). The residues of the SAP97 PDZ2 mutants shown to be affected by the His73 mutation are in structured or flexible regions close in space to the wild-type His73 residue; this suggests that the binding region of the SAP97 PDZ2 H73G/T mutants could be structurally different to that of the wild-type SAP97 PDZ2 domain.

As the SAP97 PDZ2 mutants were shown to be monomeric, pure and folded they were ready for use, along with the SAP97 PDZ2 wild-type domain, in the SAP97 PDZ2 – HPV18 E6 interaction binding investigation by ITC.

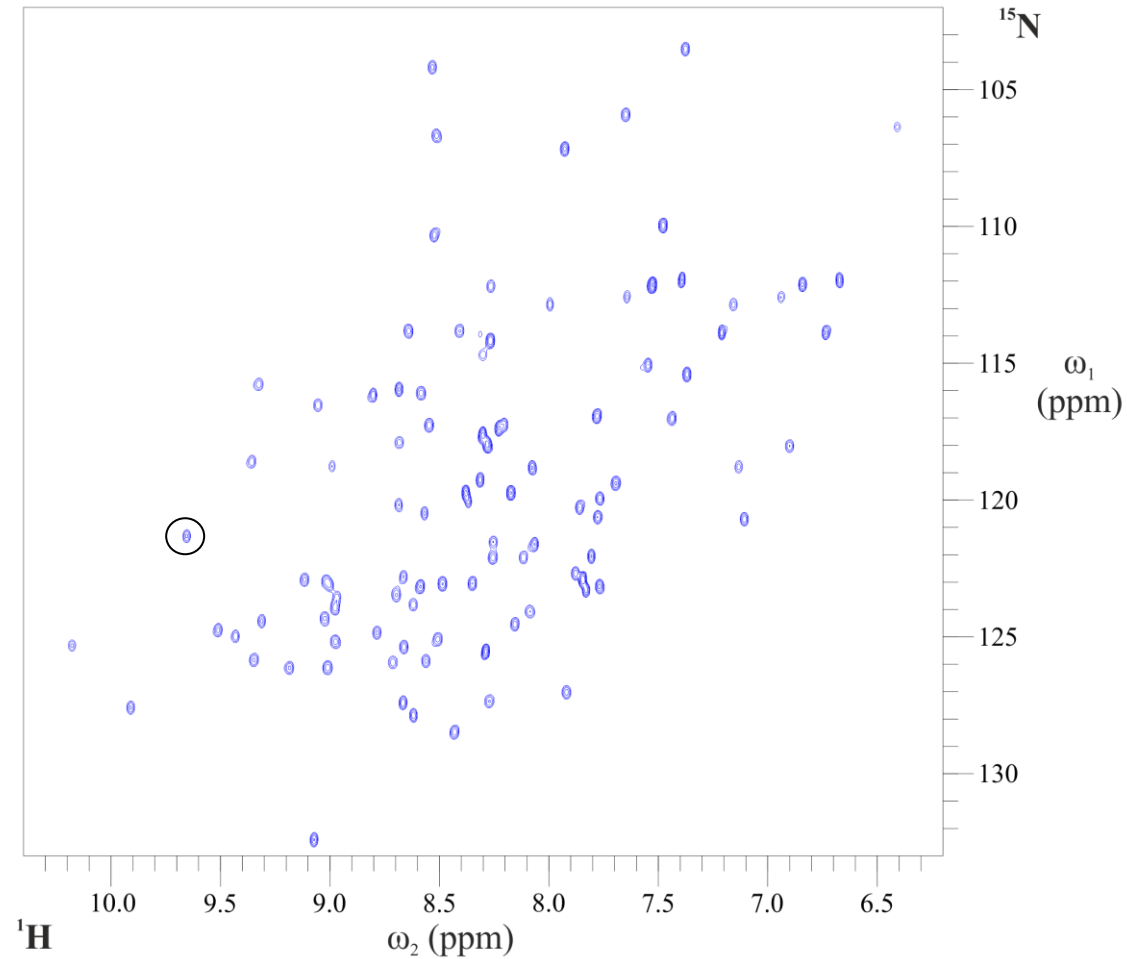


Figure 5.3: The 2-D ^1H - ^{15}N HSQC spectrum of SAP97 PDZ2 wild-type acquired at 298K, with a field strength of 600MHz, in 20mM phosphate buffer, pH6.3. The spectrum shows that the SAP97 PDZ2 wild-type domain is folded as the peaks are well dispersed and the conserved His73 residue that is mutated in the SAP97 PDZ2 mutants has been circled.

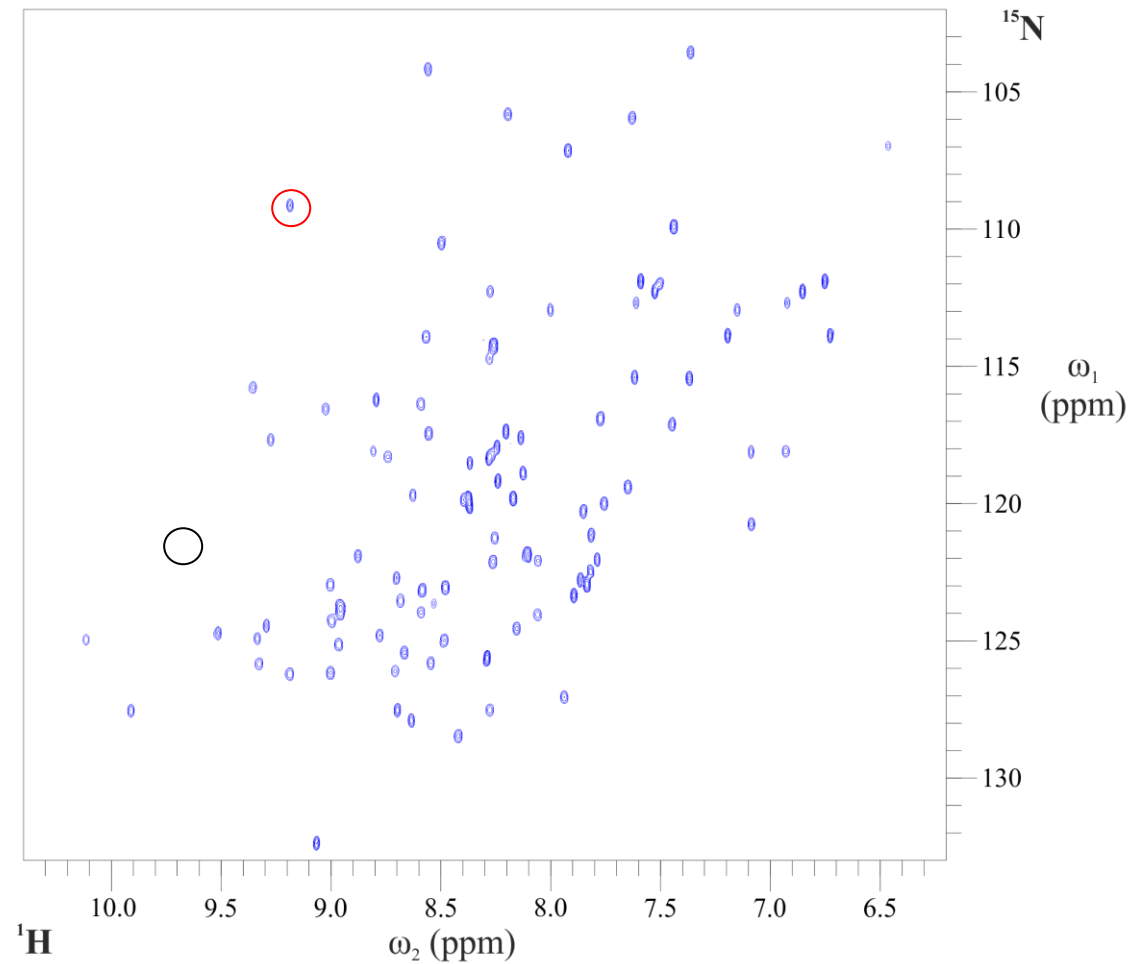


Figure 5.4: The 2-D ^1H - ^{15}N HSQC spectrum of the SAP97 PDZ2 H73G mutant acquired at 298K, with a field strength of 600MHz, in 20mM phosphate buffer, pH6.3. The spectrum shows that the SAP97 PDZ2 H73G mutant is folded as the peaks are well dispersed, with the region corresponding to the conserved His73 and mutant Gly73 residues circled in black and red respectively.

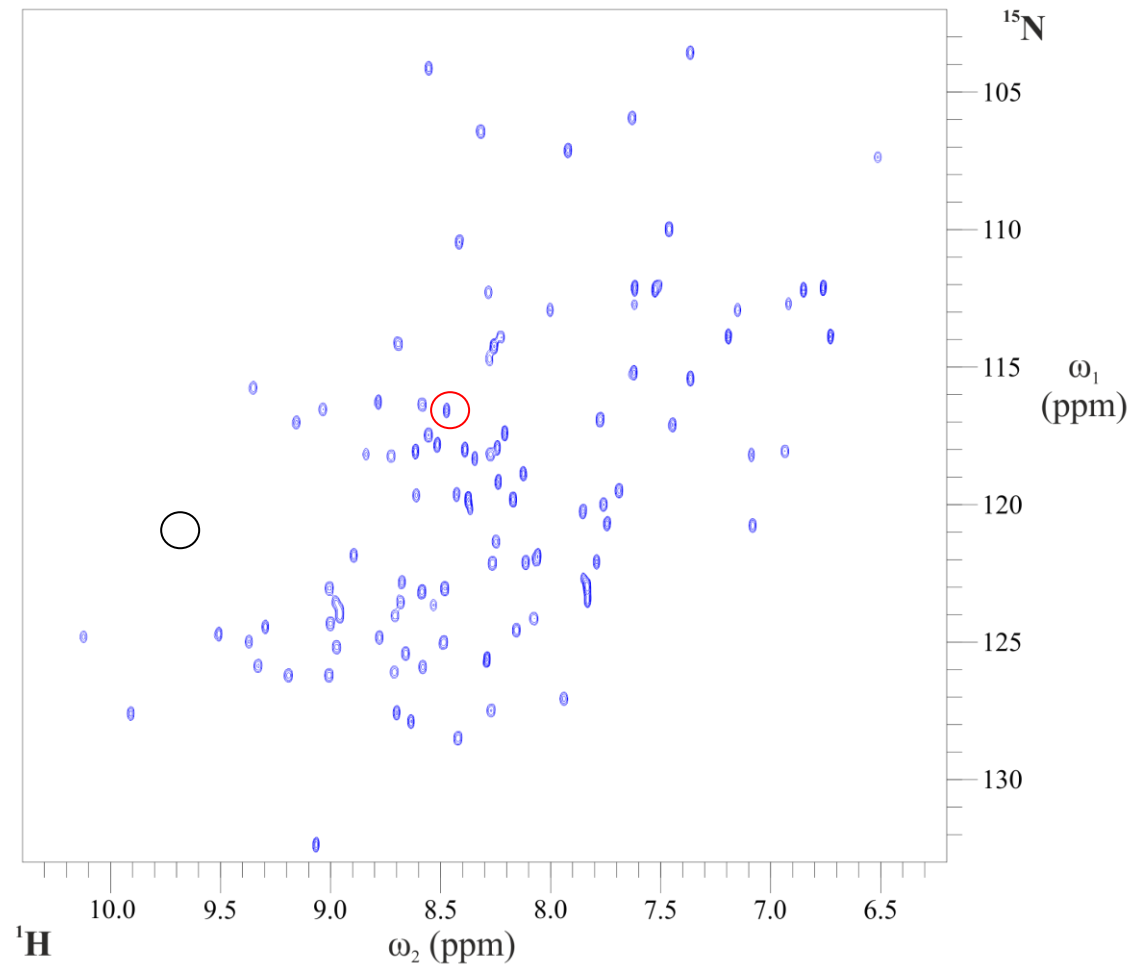


Figure 5.5: The 2-D ^1H – ^{15}N HSQC spectrum of the SAP97 PDZ2 H73T mutant acquired at 298K, with a field strength of 600MHz, in 20mM phosphate buffer, pH6.3. The spectrum shows that the SAP97 PDZ2 H73T mutant is folded as the peaks are well dispersed, with the region corresponding to the conserved His73 and mutant Thr73 residues circled in black and red respectively.

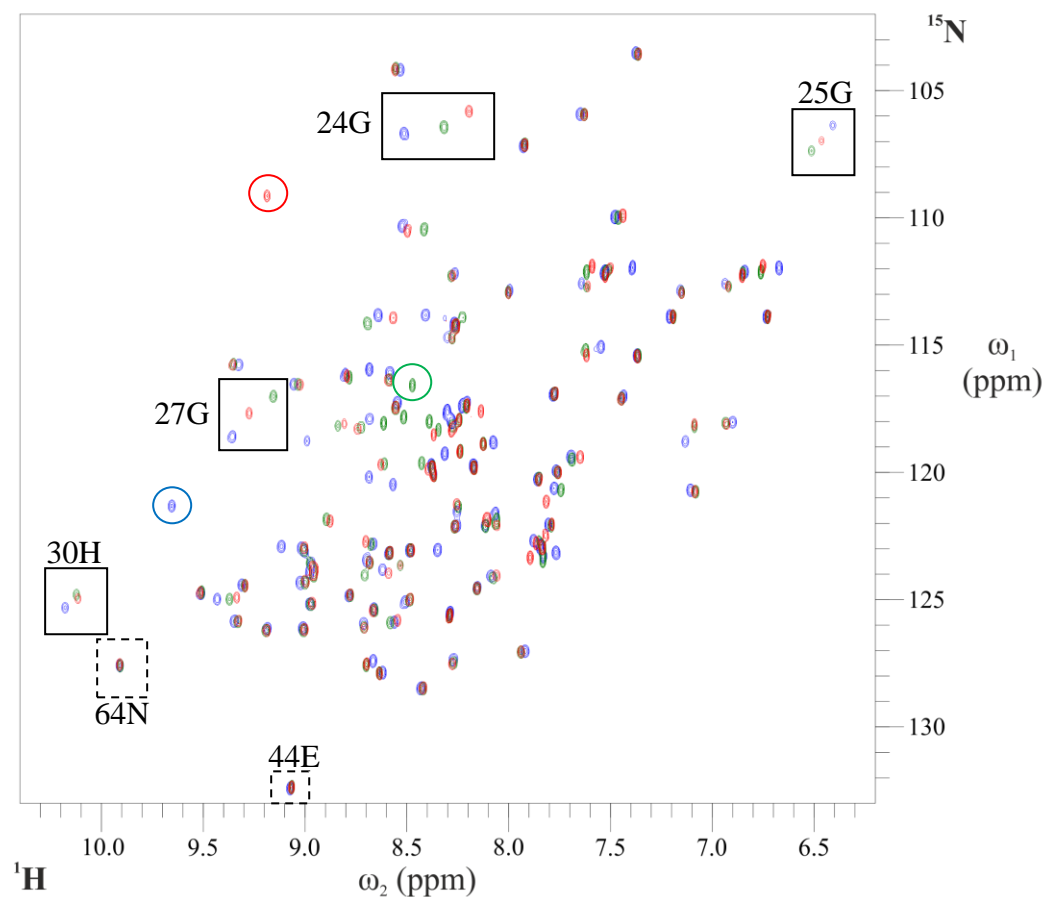


Figure 5.6: An overlay of the 2-D $^1\text{H} - ^{15}\text{N}$ HSQC NMR spectroscopic experiments of SAP97 PDZ2 WT (blue), SAP97 PDZ2 H73G (red) and SAP97 PDZ2 H73T (green) acquired at 298K, with a field strength of 600MHz, in 20mM phosphate buffer, pH6.3; the peaks corresponding to the His73, Gly73 and Thr73 residue residues in the respective spectra have been circled in blue, red and green respectively. The peaks corresponding to Glu44 and Asn64 (dashed rectangles) overlay perfectly in all three spectra and so, are not affected by the mutation of the wild-type His73 residue; this is not surprising as these residues are in structured regions of the SAP97 PDZ2 domain away from the mutagenesis site. However, Gly24, Gly25, His30 and Thr 72 (solid rectangle) are residues affected by the His73 mutation as they are in structured or flexible regions close to the His73 residue in the wild-type form and hence, suggests that that the binding region of the SAP97 PDZ2 H73G/T mutants might be could be affected.

5.4 SAP97 PDZ2 – HPV E6 Interaction Binding Investigation

5.4.1 General

The experimental conditions and procedure employed in each of the ITC experiments conducted in this chapter are described in [3.4.1] and [3.4.2]. In two of the experiments performed, the protein and peptide were in 20mM phosphate, pH 7.4 buffer, instead of pH 6.3; this was to compare the effect of pH on the binding affinity and thermodynamic parameters of the SAP97 PDZ2 – HPV18 E6 interaction. The initial protein and peptide concentrations in the cell and syringe respectively, were kept constant throughout to avoid any concentration effects biasing one experiment over another; therefore, the highest K_D values that could be obtained reliably under the experimental concentrations was $\sim 250\mu\text{M}$. The results of the binding investigation by ITC of the SAP97 PDZ2 – HPV18 E6 interaction has been divided into four areas; the investigation into the contribution to binding of pH, peptide length, the hydrophobic interaction and that of the electrostatic interaction.

5.4.2 pH Investigation

The effect of pH on SAP97 PDZ2 binding affinity was probed by performing two separate ITC binding experiments with the HPV18 E6 nonapeptide (LQRRRETQV), in the same buffer but at either pH 6.3 or 7.4 (Table 5.2 and Figures 5.7 – 5.9). The SAP97 PDZ2 – LQRRRETQV interaction was found to be stronger at pH 6.3, than the more physiologically relevant pH 7.4. The enthalpy change (ΔH) upon SAP97 PDZ2 binding was shown to be the driving force in both experiments, with the change in entropy (ΔS , $-T\Delta S$) due to binding unfavourable; the less negative ΔH value for SAP97 PDZ2 binding at pH 7.4 results in the weaker binding affinity observed. At pH 6.3 it is likely that the majority of populations of the conserved SAP97 PDZ2 His residue will be protonated, which increases the strength of the

intermolecular hydrogen bond formed between the His and Thr (-2), relative to pH 7.4. As ΔH is dependent on the strength/number of interactions formed/broken upon binding, this accounts for the more favourable ΔH value at pH 6.3 and hence, stronger binding affinity observed for the SAP97 PDZ2 – LQRRRETQV interaction, than at pH 7.4.

Table 5.2: The different pH values used in the SAP97 PDZ2 – LQRRRETQV binding experiment by ITC and the respective binding parameters obtained. The errors in the binding parameters were calculated from a PSD-95 PDZ1 – 5-HT_{2a} binding experiment that was performed in triplicate, with the standard deviation in calculated K_D and ΔG values used to determine the errors for the K_D and thermodynamic parameter values respectively in the binding experiments shown in the table.

pH	K_D (μM)	ΔH (kcal mol^{-1})	$-T\Delta S$ (kcal mol^{-1})	ΔG (kcal mol^{-1})
6.3	0.61 ± 0.07	-14.430 ± 0.537	5.960 ± 0.222	-8.470 ± 0.315
7.4	1.08 ± 0.12	-11.790 ± 0.439	3.636 ± 0.135	-8.154 ± 0.303

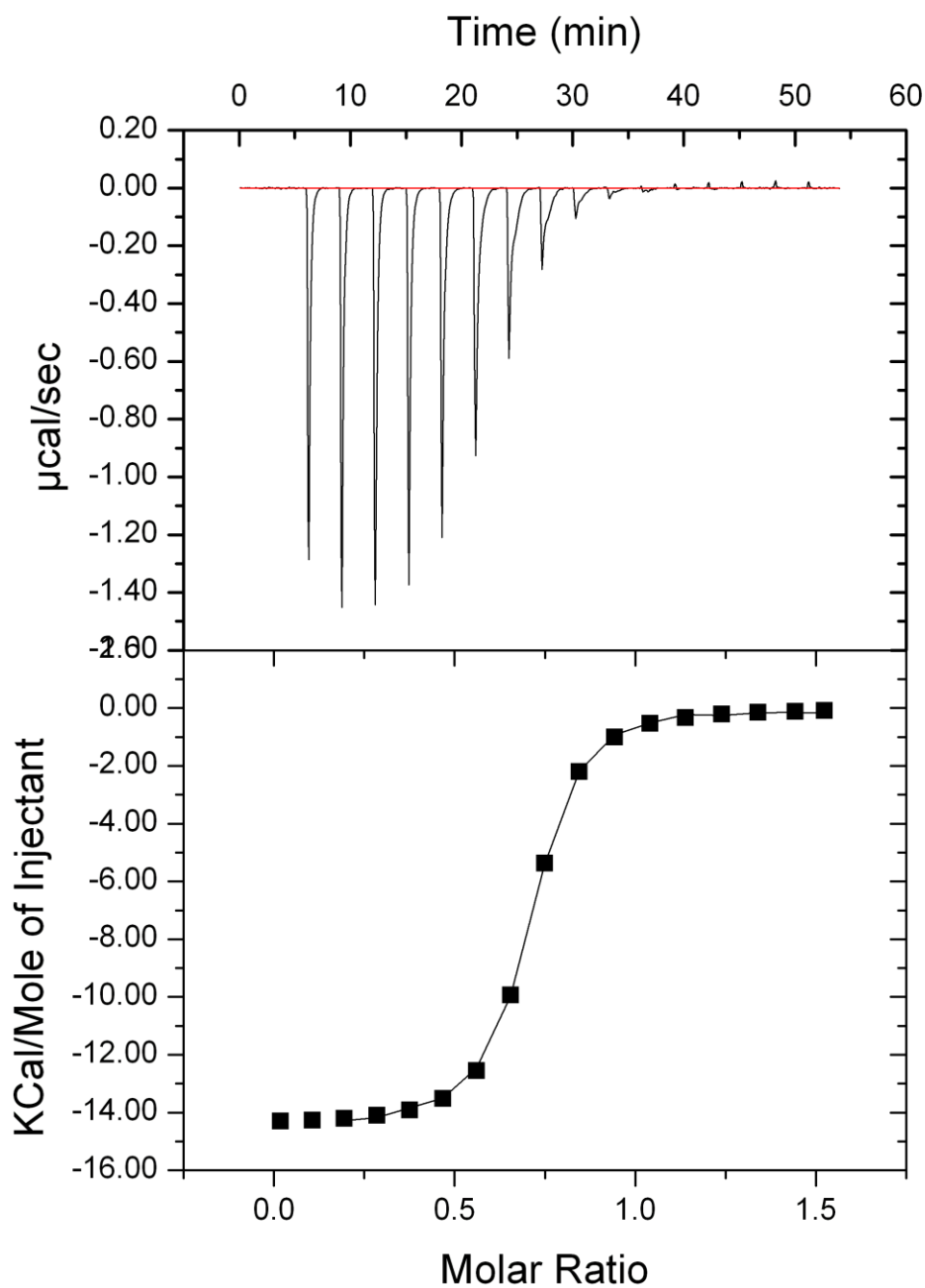


Figure 5.7: The ITC isotherm (top) and resultant curve (bottom) produced by the ITC binding experiment between $100\mu\text{M}$ SAP97 PDZ2 (cell) and $750\mu\text{M}$ LQRRRETQV (syringe) in 20mM phosphate, $\text{pH}6.3$, on an iTC_{200} Microcalorimeter (MicroCal) at 298K . Fitting of the curve produced by the ITC experiment to a single set of sites curve-fitting model, using Origin7, resulted in a binding affinity (K_D) of $0.61\mu\text{M}$ for LQRRRETQV to the SAP97 PDZ2 domain.

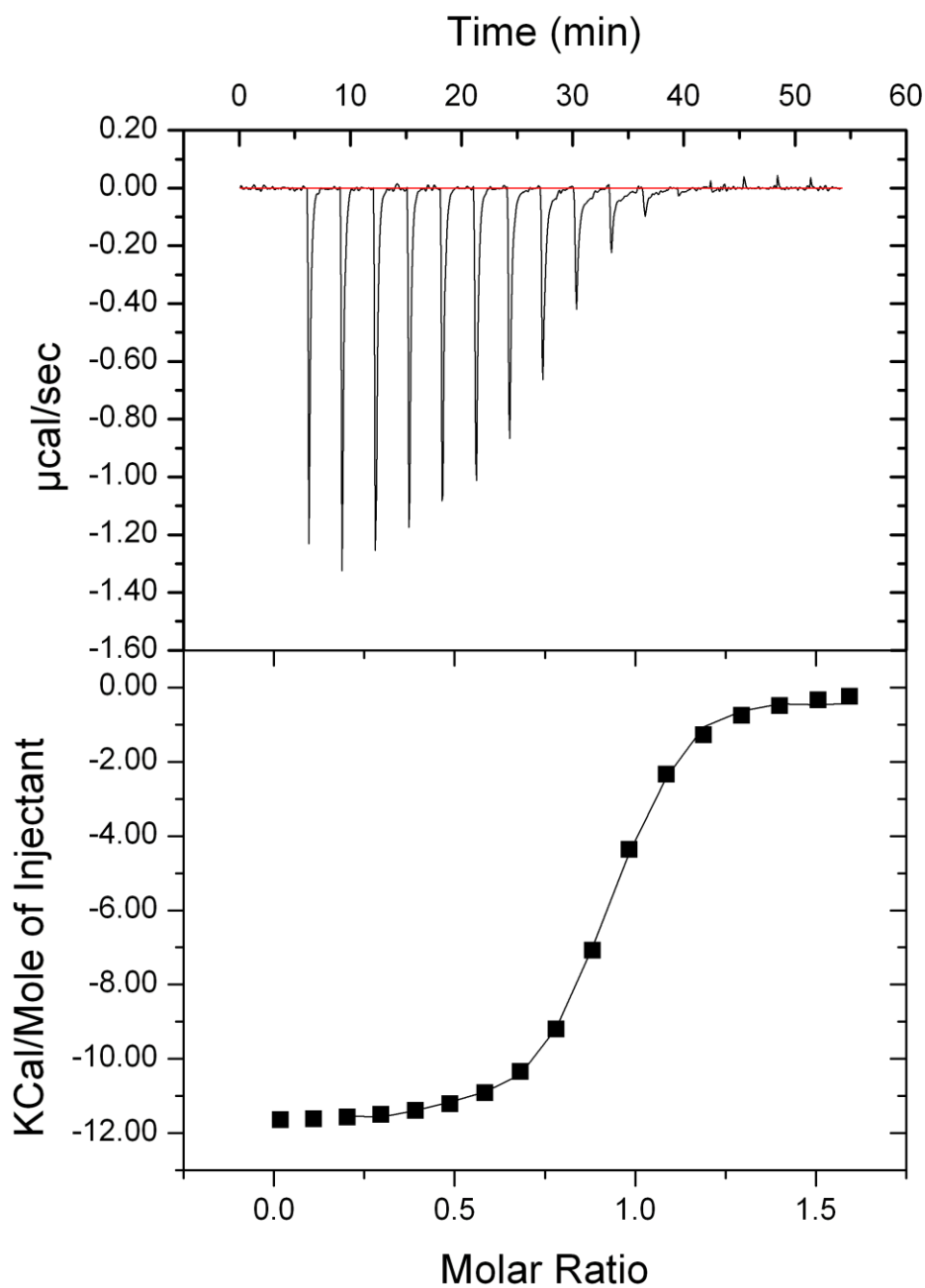


Figure 5.8: The ITC isotherm (top) and resultant curve (bottom) produced by the ITC binding experiment between $100\mu\text{M}$ SAP97 PDZ2 (cell) and $750\mu\text{M}$ LQRRRETQV (syringe) in 20mM phosphate, $\text{pH}7.4$, on an iTC_{200} Microcalorimeter (MicroCal) at 298K . Fitting of the curve produced by the ITC experiment to a single set of sites curve-fitting model, using Origin7, resulted in a binding affinity (K_D) of $1.08\mu\text{M}$ for LQRRRETQV to the SAP97 PDZ2 domain.

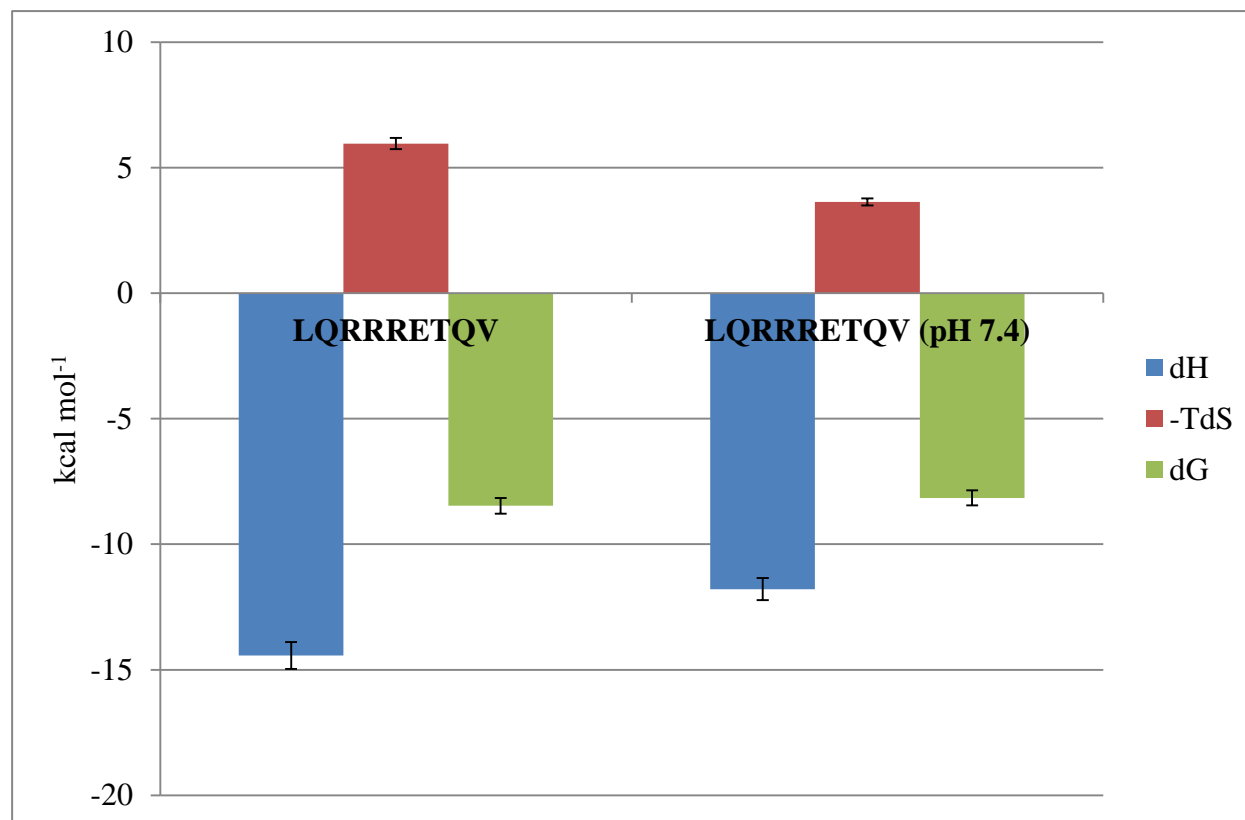


Figure 5.9: The thermodynamic parameters (ΔH = blue, $-T\Delta S$ = red and ΔG = green) obtained from the binding interaction between the HPV18 E6 nonapeptide (LQRRRETQV) and the SAP97 PDZ2 domain at both pH 6.3 and pH 7.4. ΔH is the dominant thermodynamic parameter in ΔG determination and hence, binding affinity; this is because ΔH is a moderate to large negative value in both ITC binding experiments, with $-T\Delta S$ being a small positive value in comparison and so, contributes much less significantly to ΔG . The ΔG value for the SAP97 PDZ2 – LQRRRETQV interaction at pH 6.3 is more favourable than at pH 7.4 i.e. more negative and hence, the interaction was shown to be stronger at the lower pH value. The difference in ΔG value between the two pH values is due to the less favourable ΔH value at pH 7.4 c.f. pH 6.3; this is due to a weaker intermolecular hydrogen bond formed between the SAP97 PDZ2 His and Thr (-2) at pH 7.4 as the populations of the His residue in the protonated state are much less than those at pH 6.3. The more favourable $-T\Delta S$ value at pH 7.4 is not sufficient to compensate for this decrease in enthalpy and hence, leads to weaker SAP97 PDZ2 binding of LQRRRETQV, than at pH 6.3.

5.4.3 Peptide Length Investigation

The effect of peptide length on SAP97 PDZ2 binding affinity was then investigated by performing ITC binding experiments with three, five and nine residue peptides of the C-terminus of HPV18 E6 (Table 5.3 and Figures 5.7, 5.10 – 12).

Table 5.3: The peptide ligands used in the SAP97 PDZ2 domain binding experiment by ITC and the respective binding parameters obtained. The errors in the binding parameters were calculated from a PSD-95 PDZ1 – 5-HT_{2a} binding experiment that was performed in triplicate, with the standard deviation in calculated K_D and ΔG values used to determine the errors for the K_D and thermodynamic parameter values respectively in the binding experiments shown in the table.

Ligand	K_D (μM)	ΔH (kcal mol^{-1})	$-T\Delta S$ (kcal mol^{-1})	ΔG (kcal mol^{-1})
TQV	57.14 ± 6.58	-5.623 ± 0.209	-0.163 ± 0.006	-5.786 ± 0.215
RETQV	1.08 ± 0.12	-5.077 ± 0.189	-3.069 ± 0.114	-8.146 ± 0.303
LQRRRETQV	0.61 ± 0.07	-14.430 ± 0.537	5.960 ± 0.222	-8.470 ± 0.315

Extension of the C-terminal HPV18 E6 peptide from three to five and five to nine residues was shown to increase binding affinity; with all three interactions shown to be enthalpy driven, as the entropy change upon binding is small in comparison. The tripeptide (TQV) was able to bind to SAP97 PDZ2 with moderate micromolar affinity, indicating that SAP97 PDZ2 domain binding is possible with a small organic molecule capable of forming effective hydrophobic and electrostatic interactions.

The difference in SAP97 PDZ2 binding affinity of the tri- and pentapeptide (RETQV) is due to the more favourable change in binding entropy of RETQV c.f. TQV; this indicates that the extension in peptide length increases the ability of the peptide to remove bound water molecules from the SAP97 PDZ2 binding region. This shows that the residues preceding the 0 and -2 ligand residues are important to SAP97 PDZ2 domain binding affinity; this corroborates previous research where Arg (-4) has been shown to form extended interactions with the SAP97 PDZ2 conserved His residue and residues of the $\beta\text{B} - \beta\text{C}$ loop (Liu et al., 2007, Zhang et al., 2007).

Extending the pentapeptide to a nonapeptide (LQRRRETQV) increased the ΔH value for SAP97 PDZ2 binding by over 9 kcal mol⁻¹ but decreased the $-T\Delta S$ value by almost the same amount. This is because the extension of the peptide length to nine residues extends the number of intermolecular interactions possible with the SAP97 PDZ2 domain; however, this also multiplies the loss of conformational entropy leading to the unfavourable $-T\Delta S$ and hence, only results in the modest increase in binding affinity by extension from five to nine residue peptide length observed. It is not possible to determine if the nonapeptide is the optimal length for SAP97 PDZ2 binding from the data obtained, as it is plausible that the intervening length peptides i.e. 6- to 8-mers may balance ΔH and $-T\Delta S$ binding factors more favourably and hence, produce stronger SAP97 PDZ2 binding. This is an area of important future research as knowledge of the optimal peptide length would be extremely useful in guiding future SAP97 PDZ2 domain inhibition research.

Penta- (RETQL) and nonapeptides (SRTRRETQL) of the C-terminus of the HPV16 E6 protein were also used in ITC experiments to determine the effect of peptide length on SAP97 PDZ2 binding affinity (Table 5.4).

Table 5.4: The peptide ligands used in the SAP97 PDZ2 domain binding experiment by ITC and the respective binding parameters obtained. The errors in the binding parameters were calculated from a PSD-95 PDZ1 – 5-HT_{2a} binding experiment that was performed in triplicate, with the standard deviation in calculated K_D and ΔG values used to determine the errors for the K_D and thermodynamic parameter values respectively in the binding experiments shown in the table.

Ligand	K_D (μM)	ΔH (kcal mol ⁻¹)	$-T\Delta S$ (kcal mol ⁻¹)	ΔG (kcal mol ⁻¹)
RETQL	24.94 ± 2.87	-3.109 ± 0.116	-3.159 ± 0.118	-6.268 ± 0.233
SRTRRETQL	9.35 ± 1.08	-5.444 ± 0.203	-1.416 ± 0.053	-6.860 ± 0.255

As with HPV18 E6, increasing the peptide length was shown to increase the SAP97 PDZ2 binding affinity of HPV16 E6. The SAP97 PDZ2 binding of RETQL is equally dependent on both enthalpy and entropy factors; by extending to the nonapeptide, the binding enthalpy becomes the determining factor and is able to

compensate for the less favourable entropy change and yield tighter binding. The relative binding affinities of the HPV16/18 E6 pentapeptides is discussed in the next section [5.4.4].

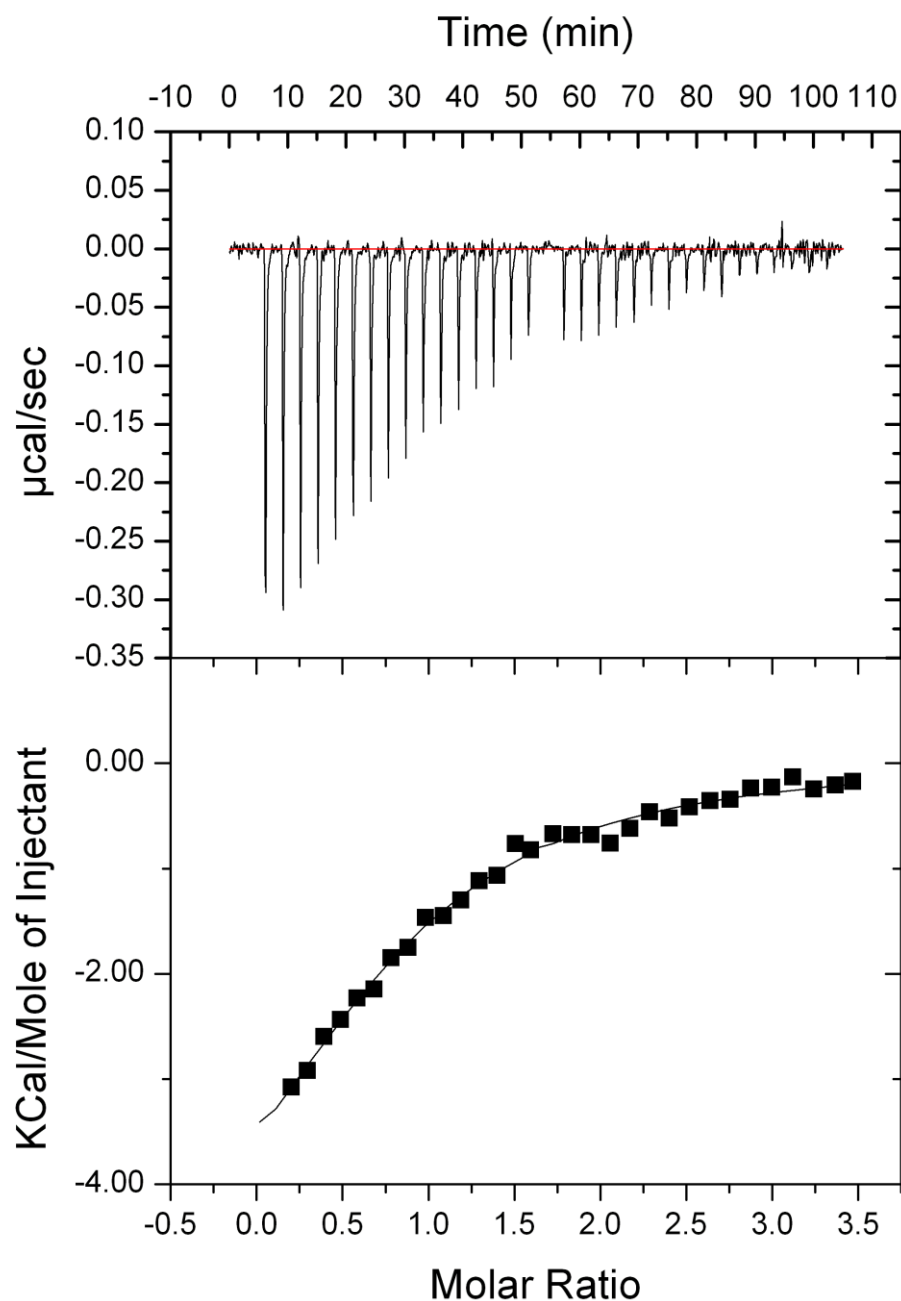


Figure 5.10: The ITC isotherm (top) and resultant curve (bottom) produced by the ITC binding experiment between $100\mu\text{M}$ SAP97 PDZ2 (cell) and $750\mu\text{M}$ TQV (syringe) in 20mM phosphate, $\text{pH}6.3$, on an iTC_{200} Microcalorimeter (MicroCal) at 298K . Fitting of the curve produced by the ITC experiment to a single set of sites curve-fitting model, using Origin7, resulted in a binding affinity (K_D) of $57.14\mu\text{M}$ for TQV to the SAP97 PDZ2 domain.

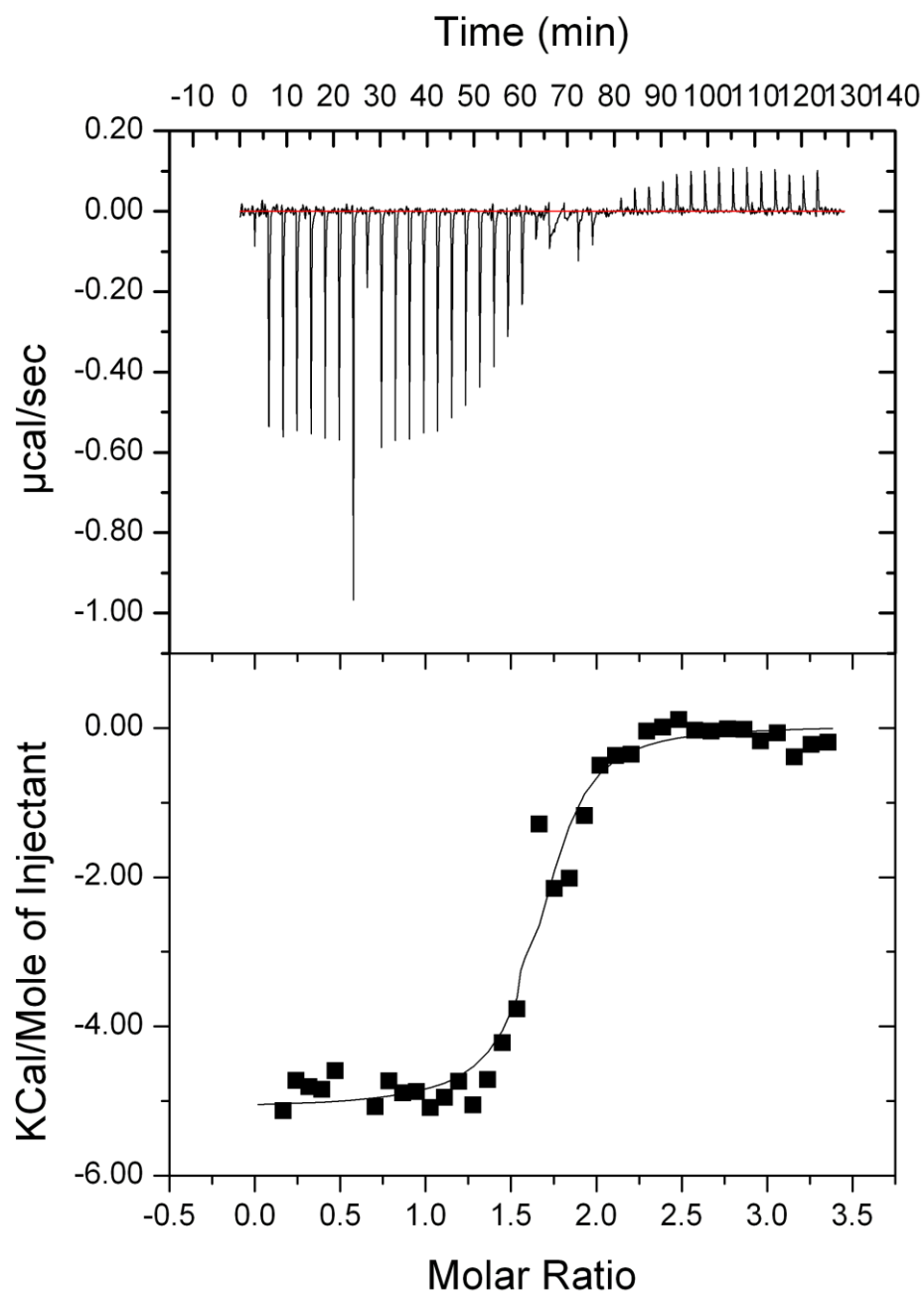


Figure 5.11: The ITC isotherm (top) and resultant curve (bottom) produced by the ITC binding experiment between $100\mu\text{M}$ SAP97 PDZ2 (cell) and $750\mu\text{M}$ RETQV (syringe) in 20mM phosphate, $\text{pH}6.3$, on an iTC_{200} Microcalorimeter (MicroCal) at 298K . Fitting of the curve produced by the ITC experiment to a single set of sites curve-fitting model, using Origin7, resulted in a binding affinity (K_D) of $1.08\mu\text{M}$ for RETQV to the SAP97 PDZ2 domain.

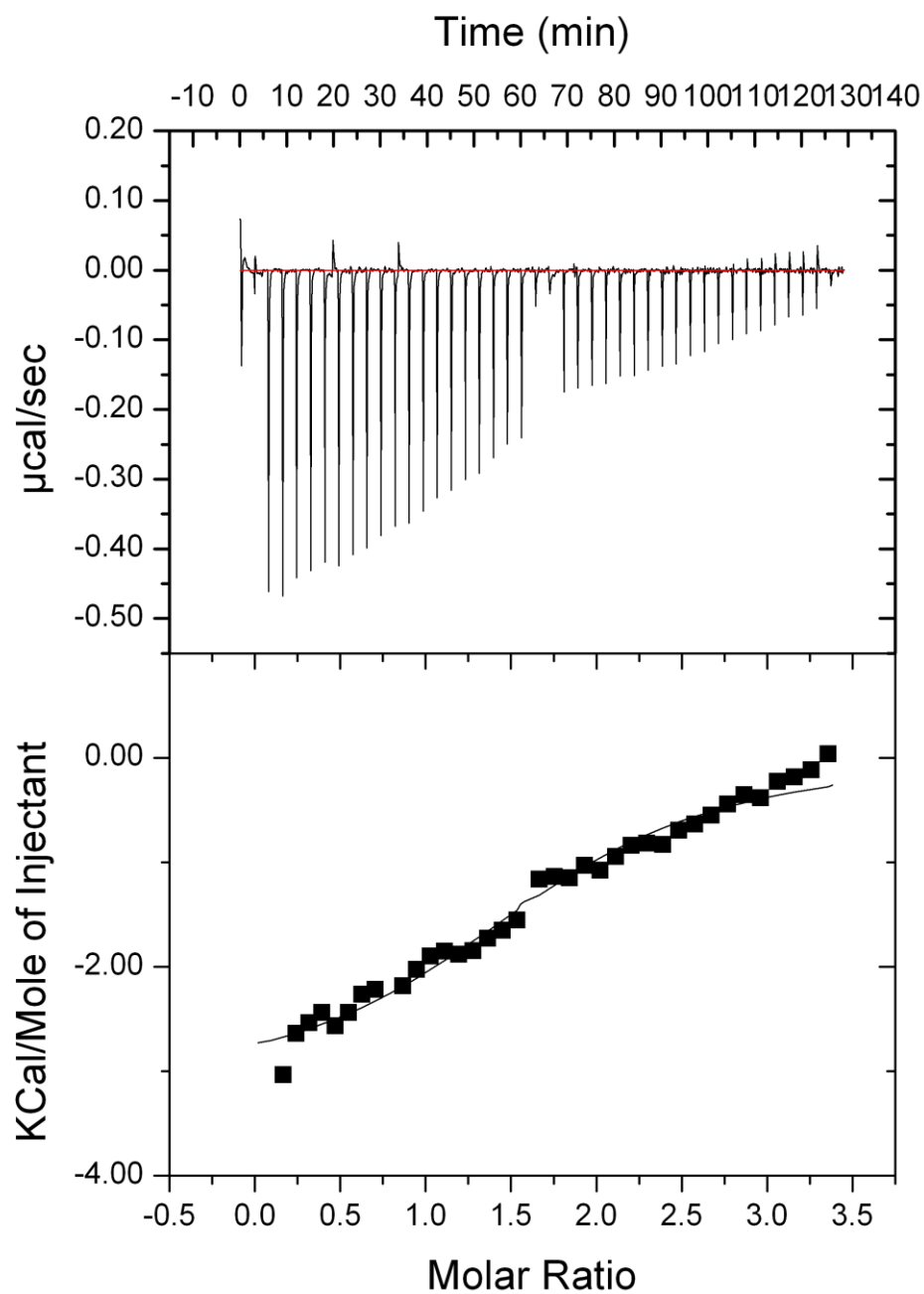


Figure 5.12: The ITC isotherm (top) and resultant curve (bottom) produced by the ITC binding experiment between $100\mu\text{M}$ SAP97 PDZ2 (cell) and $750\mu\text{M}$ RETQL (syringe) in 20mM phosphate, $\text{pH}6.3$, on an iTC_{200} Microcalorimeter (MicroCal) at 298K . Fitting of the curve produced by the ITC experiment to a single set of sites curve-fitting model, using Origin7, resulted in a binding affinity (K_D) of $24.94\mu\text{M}$ for RETQL to the SAP97 PDZ2 domain.

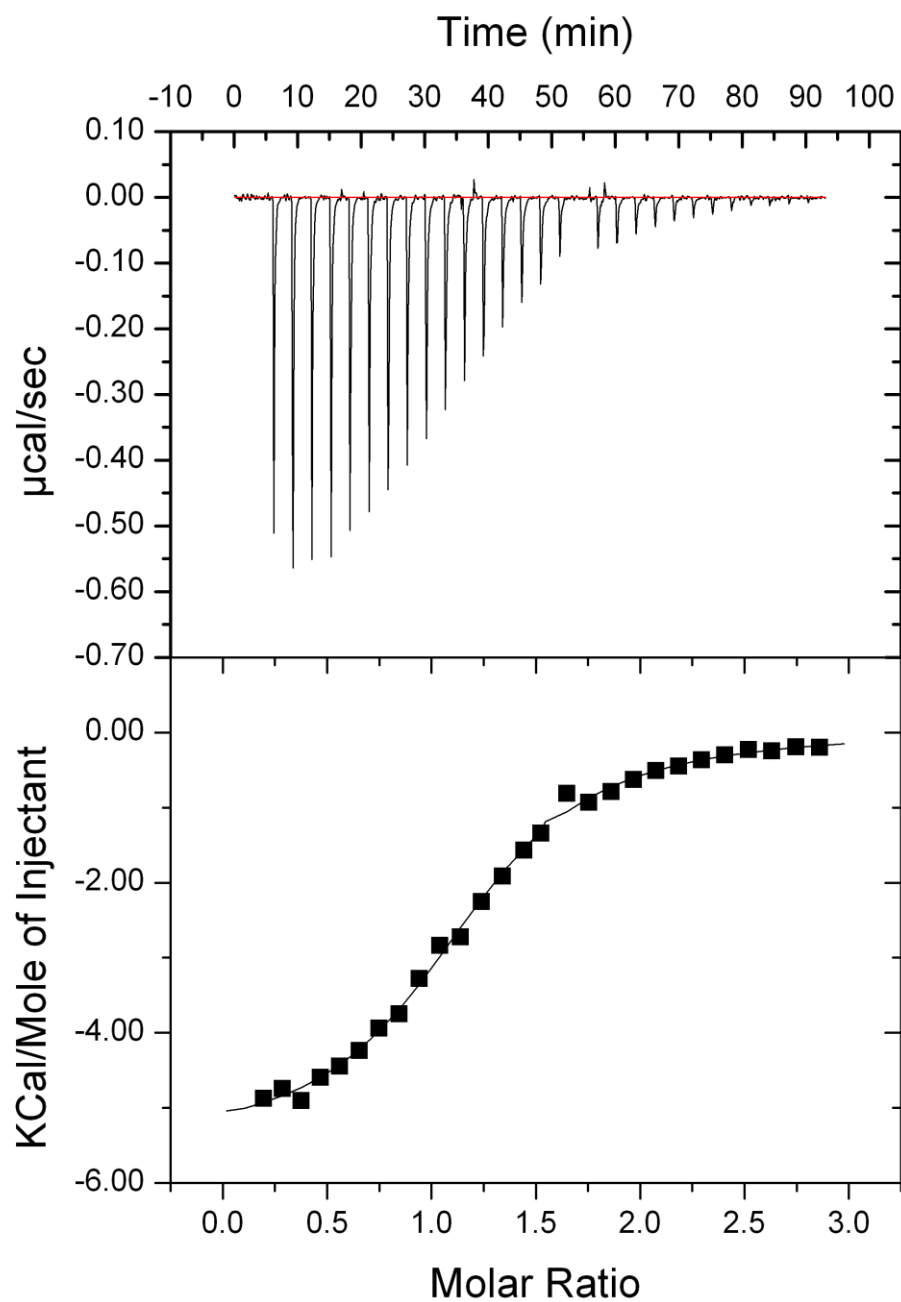


Figure 5.13: The ITC isotherm (top) and resultant curve (bottom) produced by the ITC binding experiment between $100\mu\text{M}$ SAP97 PDZ2 (cell) and $750\mu\text{M}$ SRTRRETQL (syringe) in 20mM phosphate, $\text{pH}6.3$, on an iTC_{200} Microcalorimeter (MicroCal) at 298K . Fitting of the curve produced by the ITC experiment to a single set of sites curve-fitting model, using Origin7, resulted in a binding affinity (K_D) of $9.35\mu\text{M}$ for SRTRRETQL to the SAP97 PDZ2 domain.

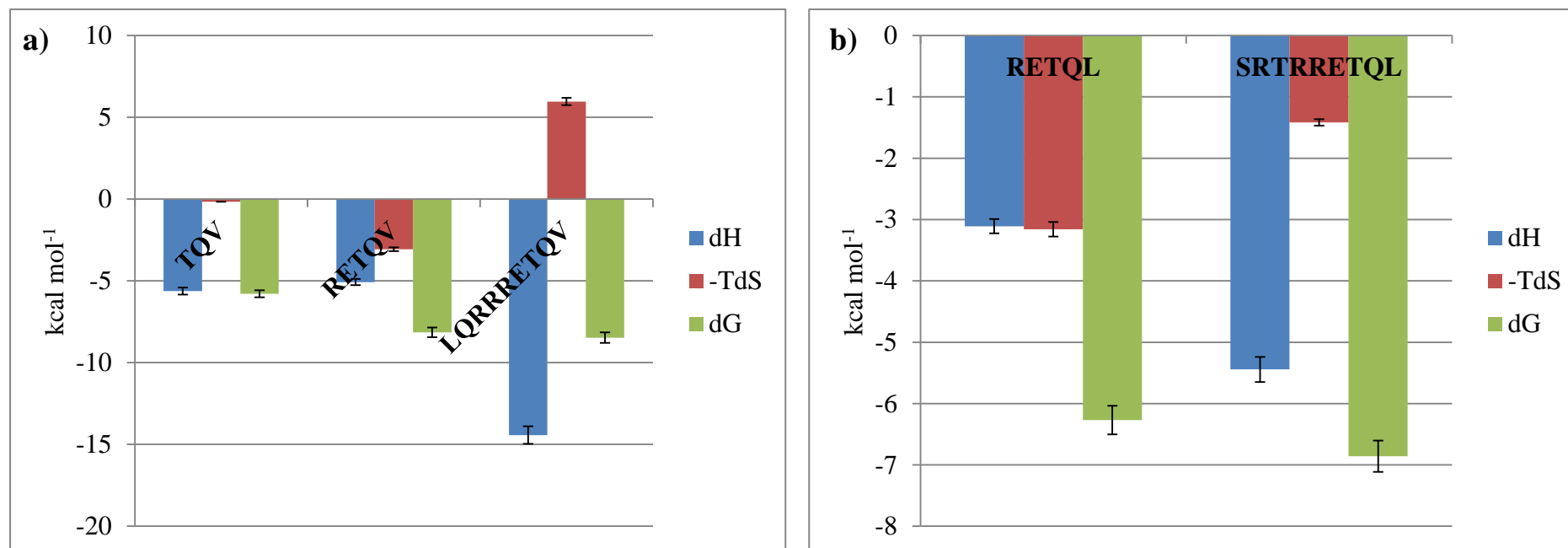


Figure 5.14: The thermodynamic parameters (ΔH = blue, $-T\Delta S$ = red and ΔG = green) obtained from the binding interaction between various length peptides of the a) HPV18 E6 and b) HPV16 E6 C-termini to the SAP97 PDZ2 domain, in the investigation of the effect of peptide length on SAP97 PDZ2 binding affinity. With the exception of RETQL, ΔH is the dominant thermodynamic parameter in ΔG determination and hence, binding affinity; this is because ΔH is a moderate to large negative value in all ITC binding experiments, with $-T\Delta S$ being a small to moderate negative/positive value in comparison and so contributes much less significantly to ΔG . The tripeptide (TQV) was able to bind to SAP97 PDZ2 with moderate micromolar affinity, indicating that SAP97 PDZ2 domain binding is possible with a small organic molecule capable of forming the hydrophobic and electrostatic interactions as effectively as the native ligand. The difference in SAP97 PDZ2 binding affinity of the tri- and pentapeptide (RETQV) is due to the more favourable change in binding entropy of RETQV c.f. TQV; this indicates that the extension in peptide length increases the ability of the peptide to remove bound water molecules from the SAP97 PDZ2 binding region. Extending the pentapeptide to a nonapeptide (LQRRRETQV) increased the ΔH value for SAP97 PDZ2 by over 9 kcal mol⁻¹ but decreased ΔS by almost the same value; this results in the modest increase in binding affinity shown. The extension of the peptide length to nine residues extends the number of intermolecular interactions possible with the SAP97 PDZ2 domain; however, this also multiplies the loss of conformational entropy by the act of PDZ domain leading to the unfavourable ΔS observed. As with HPV18 E6, increasing the peptide length was shown to increase the SAP97 PDZ2 binding affinity of HPV16 E6. The binding of RETQL is equally dependent on both enthalpy and entropy factors; by extending to the nonapeptide, the binding enthalpy becomes the determining factor and is able to compensate for the less favourable entropy change and yield tighter binding.

5.4.4 Hydrophobic Interaction Investigation

This section of the investigation involved the substitution of the C-terminal Val residue of HPV18 E6 peptides of various lengths, with a range of natural and non-natural amino acids (Tables 5.5 – 5.7, Figures 5.7, 5.10 – 5.12 and 5.15 – 5.21).

Table 5.5: The tripeptide ligands used in the SAP97 PDZ2 domain binding experiment by ITC and the respective binding parameters obtained. The errors in the binding parameters were calculated from a PSD-95 PDZ1 – 5-HT_{2a} binding experiment that was performed in triplicate, with the standard deviation in calculated K_D and ΔG values used to determine the errors for the K_D and thermodynamic parameter values respectively in the binding experiments shown in the table. ^a DNB = Did not bind.

Ligand	K _D (μM)	ΔH (kcal mol ⁻¹)	-TΔS (kcal mol ⁻¹)	ΔG (kcal mol ⁻¹)
TQV	57.14 ± 6.58	-5.623 ± 0.209	-0.163 ± 0.006	-5.786 ± 0.215
TQA	DNB ^a	DNB	DNB	DNB

Table 5.6: The pentapeptide ligands used in the SAP97 PDZ2 domain binding experiment by ITC and the respective binding parameters obtained. The errors in the binding parameters were calculated from a PSD-95 PDZ1 – 5-HT_{2a} binding experiment that was performed in triplicate, with the standard deviation in calculated K_D and ΔG values used to determine the errors for the K_D and thermodynamic parameter values respectively in the binding experiments shown in the table. ^a DNB = Did not bind, ^b α = Norvaline, ^c β = Norleucine.

Ligand	K _D (μM)	ΔH (kcal mol ⁻¹)	-TΔS (kcal mol ⁻¹)	ΔG (kcal mol ⁻¹)
RETQV	1.08 ± 0.12	-5.077 ± 0.189	-3.069 ± 0.114	-8.146 ± 0.303
RETQL	24.94 ± 2.87	-3.109 ± 0.116	-3.159 ± 0.118	-6.268 ± 0.233
RETQI	4.51 ± 0.52	-5.737 ± 0.213	-1.556 ± 0.058	-7.293 ± 0.271
RETQG	DNB ^a	DNB	DNB	DNB
RETQα ^b	2.58 ± 0.30	-7.129 ± 0.265	-0.498 ± 0.019	-7.627 ± 0.284
RETQβ ^c	5.92 ± 0.68	-6.468 ± 0.241	-0.665 ± 0.025	-7.133 ± 0.265

Table 5.7: The nonapeptide ligands used in the SAP97 PDZ2 domain binding experiment by ITC and the respective binding parameters obtained. The errors in the binding parameters were calculated from a PSD-95 PDZ1 – 5-HT_{2a} binding experiment that was performed in triplicate, with the standard deviation in calculated K_D and ΔG values used to determine the errors for the K_D and thermodynamic parameter values respectively in the binding experiments shown in the table.

Ligand	K _D (μM)	ΔH (kcal mol ⁻¹)	-TΔS (kcal mol ⁻¹)	ΔG (kcal mol ⁻¹)
LQRRRETQV	0.61 ± 0.07	-14.430 ± 0.537	5.960 ± 0.222	-8.470 ± 0.315
LQRRRETQF	20.37 ± 2.35	-9.824 ± 0.365	3.427 ± 0.127	-6.397 ± 0.238

With the exception of RETQL, the individual peptide binding interactions with the SAP97 PDZ2 were shown to be enthalpy driven, with the entropy change upon

binding shown to be a much smaller negative or positive values than that of ΔH . Removal of the ability of the C-terminal residue to form effective hydrophobic interactions with the SAP97 PDZ2 domain by substitution of Val with Ala or Gly eradicated binding completely (Table 5.5 & 5.6), indicating that the electrostatic interaction alone was not enough to facilitate binding of the peptides. Substitution of the C-terminal Val of HPV18 E6 led to a decrease in binding affinity in all cases (Tables 5.6 & 5.7); this was due to the less favourable entropy change of the interactions i.e. $-T\Delta S$ was less negative. The exception to this rule was RETQL, where the $-T\Delta S$ was comparable with RETQV but ΔH upon SAP97 PDZ2 binding of RETQL was reduced; the reduction in ΔH indicates that the Leu side-chain is not able to form as effective hydrophobic interactions with the hydrophobic pocket as Val and hence, ΔG and K_D values are reduced for the HPV16 c.f. HPV18 E6 protein. The obtained data corroborates the previously described disparity in SAP97 PDZ2 binding of the HPV16/18 E6 proteins (Liu et al., 2007).

As $-T\Delta S$ is dependent upon dynamic changes such as displacement of bound water molecules and conformational entropy loss by a binding interaction, this indicates that the Val side-chain is the optimal side-chain for the SAP97 PDZ2 domain, both in terms of size and rigidity. The peptides with C-terminal Ile and non-natural amino acids norvaline (NorV, isomeric with Val) and norleucine (NorL) show increased enthalpy change which indicates that their side-chains interact more effectively with SAP97 PDZ2 than the native HPV18 E6 Val; however, the reduction in ΔS upon binding is not sufficiently compensated by the increase in ΔH and so, the binding is comparable but still weaker than the native peptide.

The obtained data suggests that the side-chains of Leu and Phe are much less suitable for SAP97 PDZ2 domain binding than the other C-terminal residues investigated.

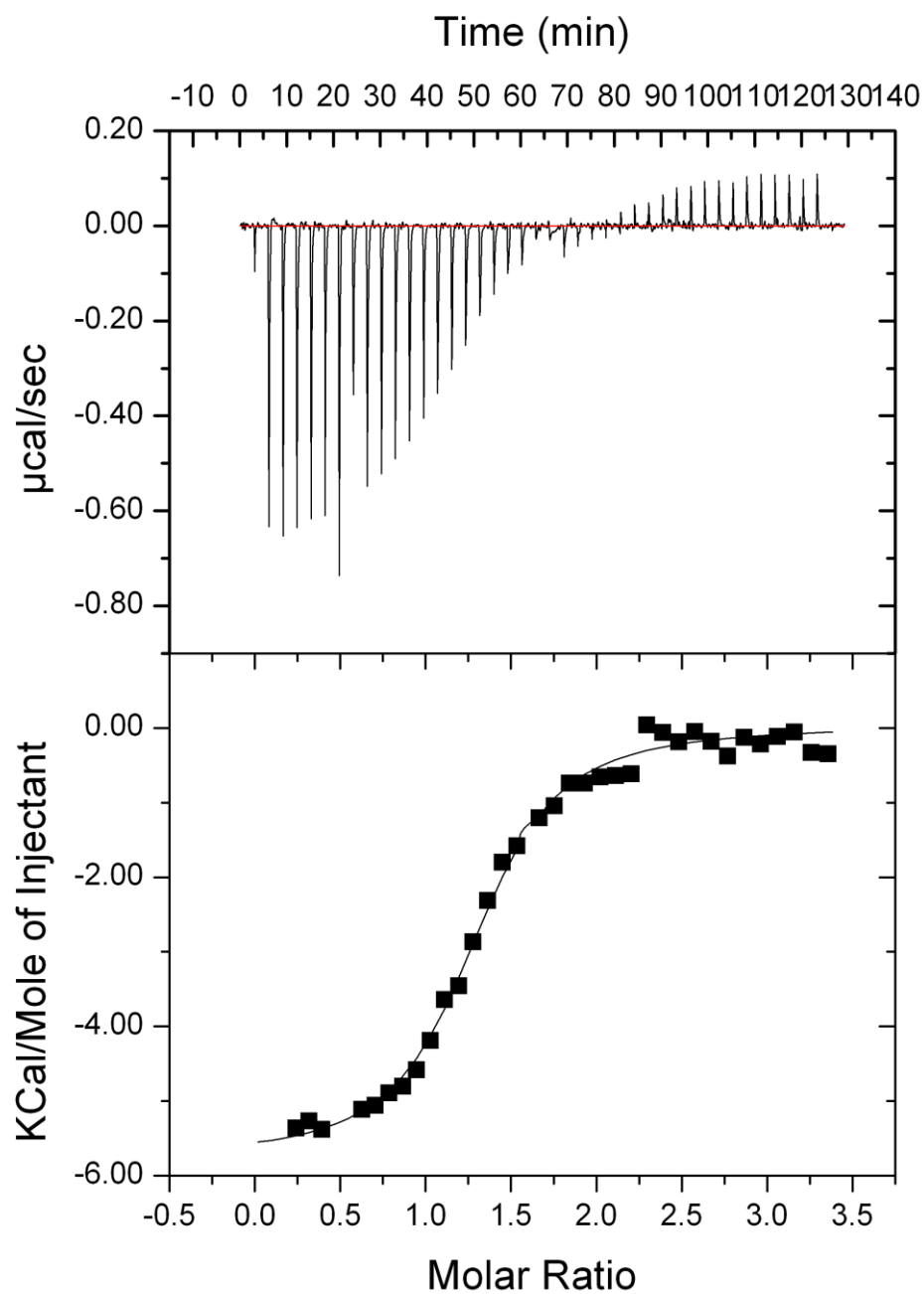


Figure 5.16: The ITC isotherm (top) and resultant curve (bottom) produced by the ITC binding experiment between $100\mu\text{M}$ SAP97 PDZ2 (cell) and $750\mu\text{M}$ RETQI (syringe) in 20mM phosphate, $\text{pH}6.3$, on an iTC_{200} Microcalorimeter (MicroCal) at 298K . Fitting of the curve produced by the ITC experiment to a single set of sites curve-fitting model, using Origin7, resulted in a binding affinity (K_D) of $4.51\mu\text{M}$ for RETQI to the SAP97 PDZ2 domain.

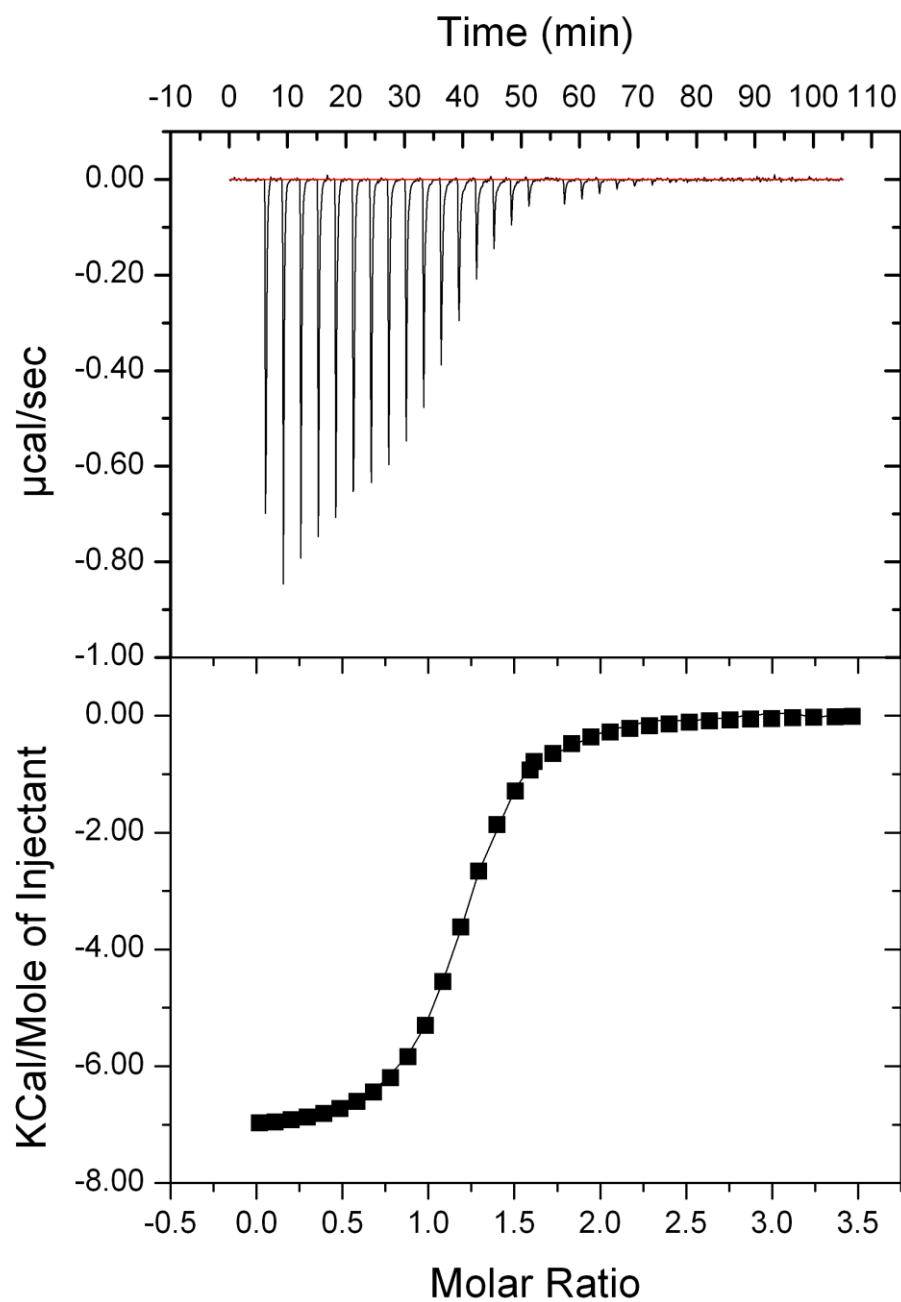


Figure 5.17: The ITC isotherm (top) and resultant curve (bottom) produced by the ITC binding experiment between $100\mu\text{M}$ SAP97 PDZ2 (cell) and $750\mu\text{M}$ RETQ α (syringe) in 20mM phosphate, $\text{pH}6.3$, on an iTC_{200} Microcalorimeter (MicroCal) at 298K . Fitting of the curve produced by the ITC experiment to a single set of sites curve-fitting model, using Origin7, resulted in a binding affinity (K_D) of $2.58\mu\text{M}$ for RETQ α to the SAP97 PDZ2 domain.

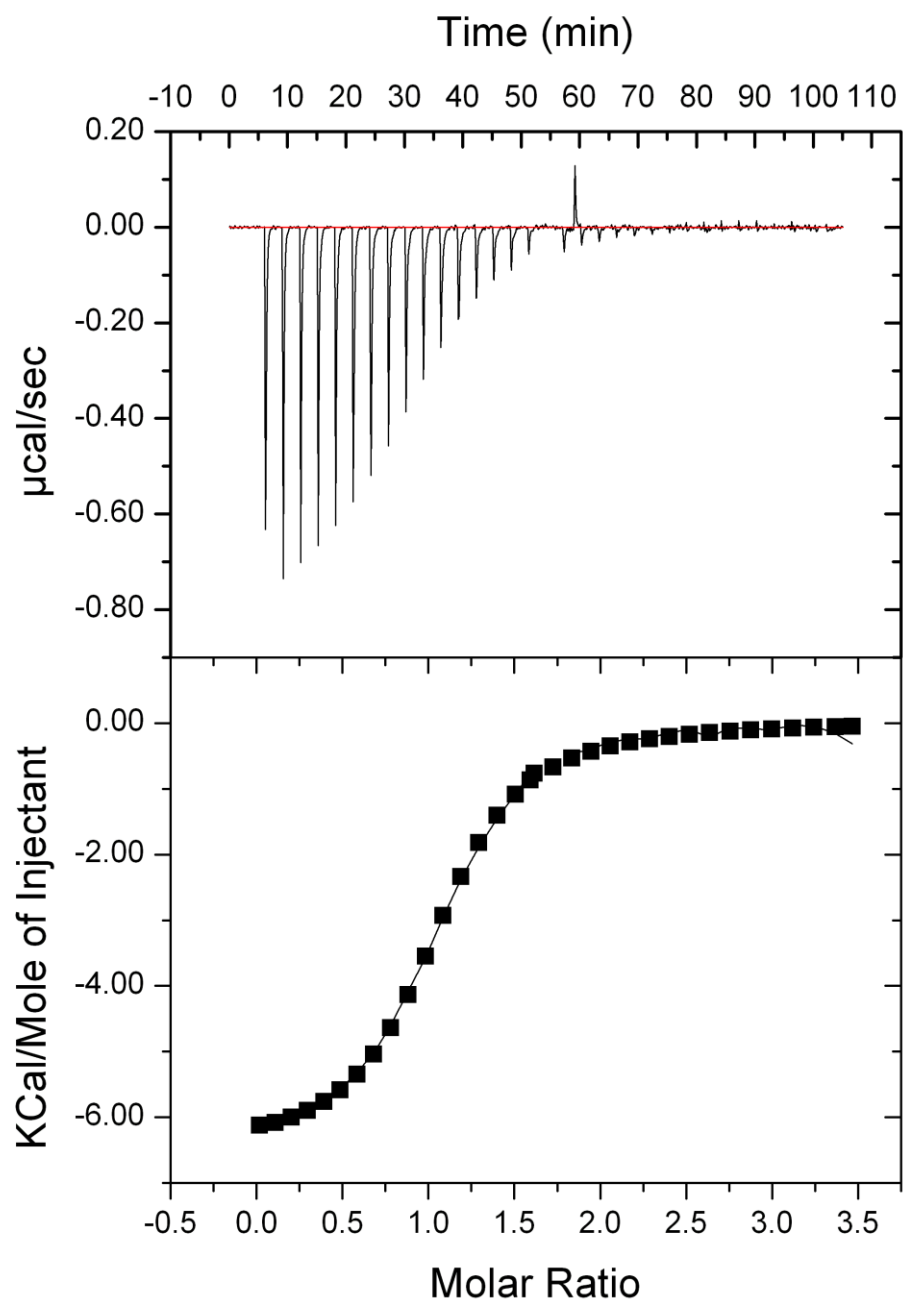


Figure 5.18: The ITC isotherm (top) and resultant curve (bottom) produced by the ITC binding experiment between $100\mu\text{M}$ SAP97 PDZ2 (cell) and $750\mu\text{M}$ RETQ β (syringe) in 20mM phosphate, pH6.3, on an iTC_{200} Microcalorimeter (MicroCal) at 298K . Fitting of the curve produced by the ITC experiment to a single set of sites curve-fitting model, using Origin7, resulted in a binding affinity (K_D) of $5.92\mu\text{M}$ for RETQ β to the SAP97 PDZ2 domain.

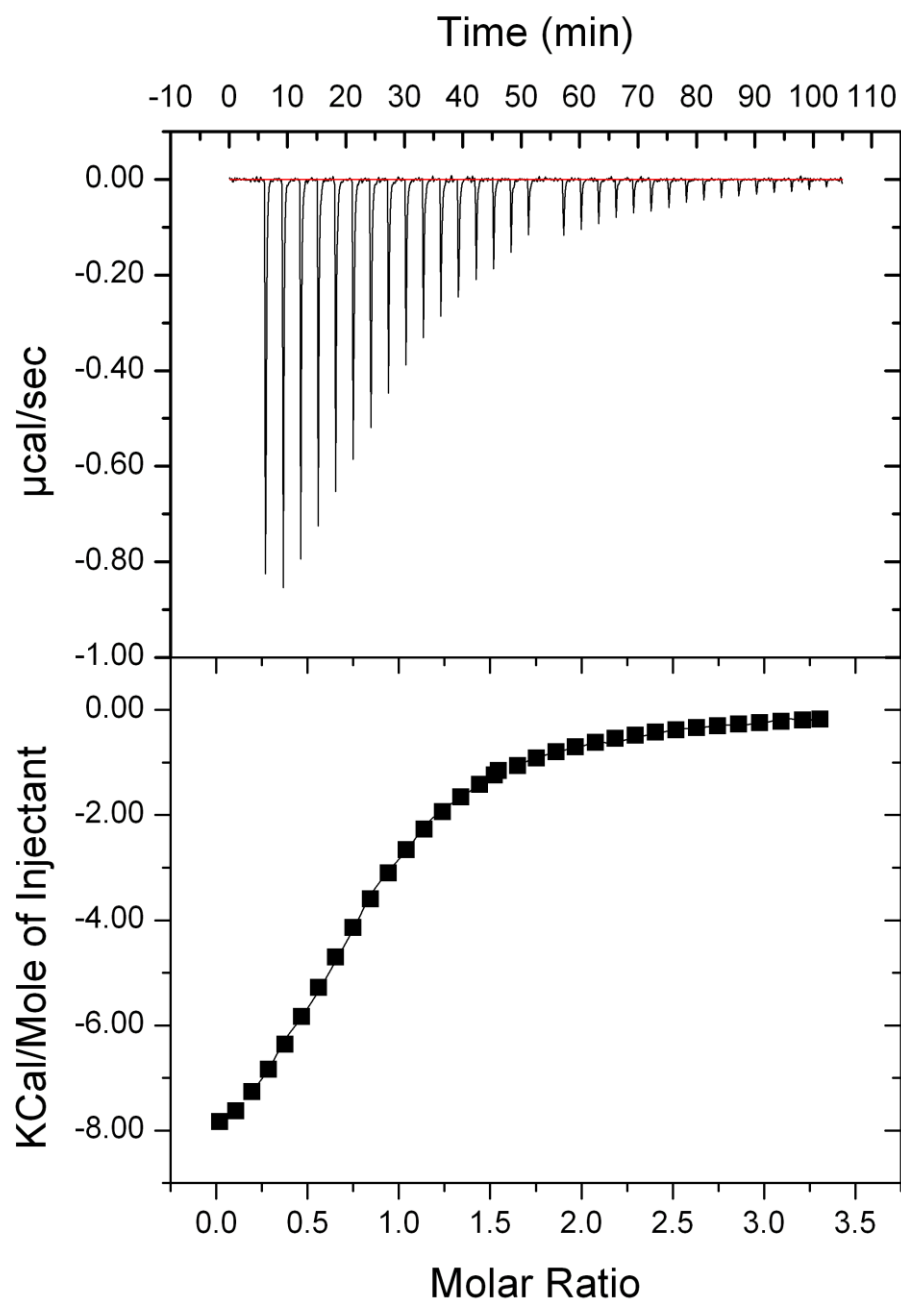


Figure 5.19: The ITC isotherm (top) and resultant curve (bottom) produced by the ITC binding experiment between 100 μ M SAP97 PDZ2 (cell) and 750 μ M LQRRRETQF (syringe) in 20mM phosphate, pH6.3, on an iTC₂₀₀ Microcalorimeter (MicroCal) at 298K. Fitting of the curve produced by the ITC experiment to a single set of sites curve-fitting model, using Origin7, resulted in a binding affinity (K_D) of 20.37 μ M for LQRRRETQF to the SAP97 PDZ2 domain.

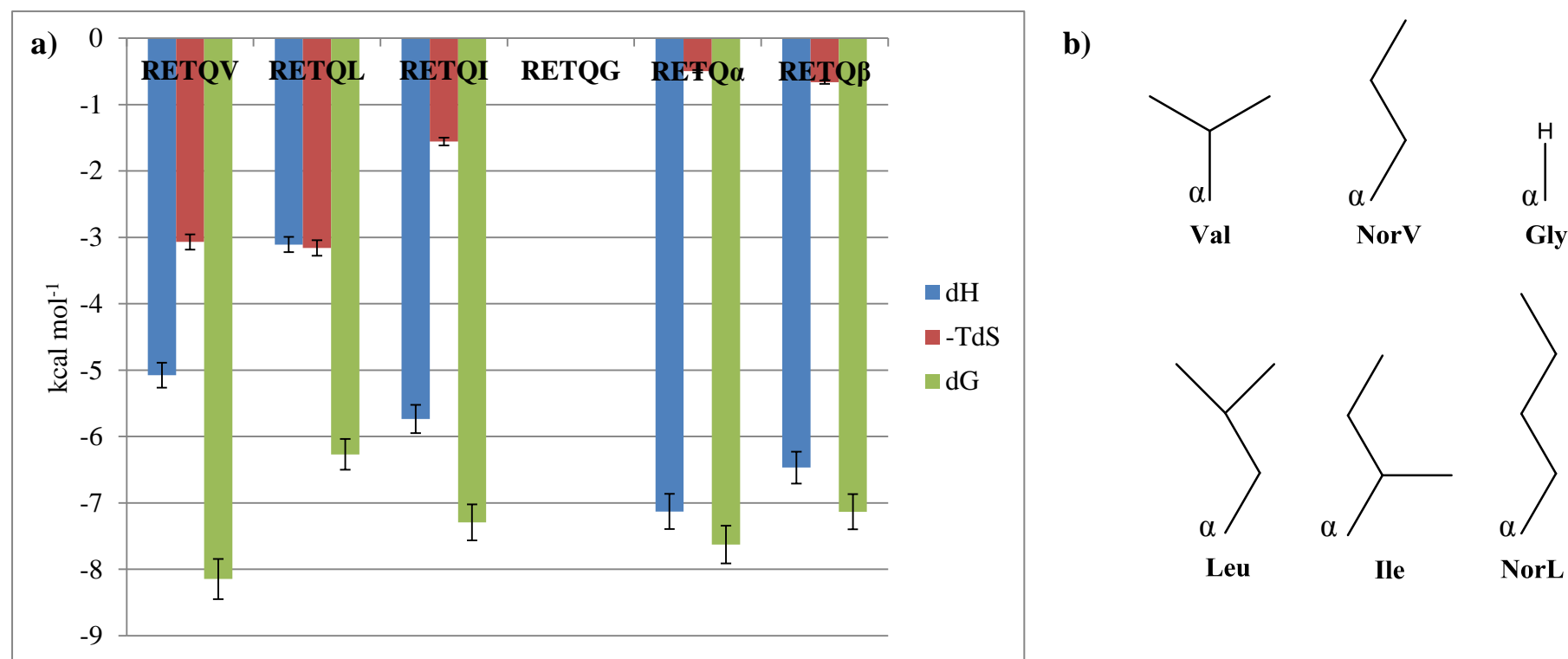


Figure 5.20: a) The thermodynamic parameters (ΔH = blue, $-T\Delta S$ = red and ΔG = green) obtained from the binding interaction between the HPV18 E6 pentapeptide (RETQV) and pentapeptides with substituted C-terminal residues to the SAP97 PDZ2 domain, in the investigation of the effect of the hydrophobic interaction on SAP97 PDZ2 binding affinity. With the exception of RETQL, ΔH is the dominant thermodynamic parameter in ΔG determination and hence, binding affinity; this is because ΔH is a moderate to large negative value in all ITC binding experiments, with $-T\Delta S$ being a small to moderate negative/positive value in comparison and so, contributes much less significantly to ΔG . The removal of the ability of the C-terminal residue to effectively form hydrophobic interactions with the SAP97 PDZ2 domain by substitution of Val with Gly eradicated binding completely; indicating that the electrostatic interaction alone was not enough to facilitate binding of the peptides. Substitution of the C-terminal Val of HPV18 E6 led to a decrease in binding affinity in all cases (Tables 5.6 & 5.7); this was due to the less favourable entropy change of the interactions i.e. $-T\Delta S$ was less negative. The exception to this rule was RETQL, where the $-T\Delta S$ values were comparable with RETQV but the enthalpy change upon SAP97 PDZ2 binding of RETQL was reduced, compared to RETQV. The data indicates that the Val side-chain is the optimal side-chain for the SAP97 PDZ2 domain of the residues investigated. b) The structure of the side-chains of the native C-terminal HPV18 E6 residue Val and the five other residues substituted in the hydrophobic interaction investigation; the Val side-chain was shown to be the optimal for SAP97 PDZ2 binding, with the Leu side-chain having most detrimental effect on SAP97 PDZ2 binding affinity of the six C-terminal residues.

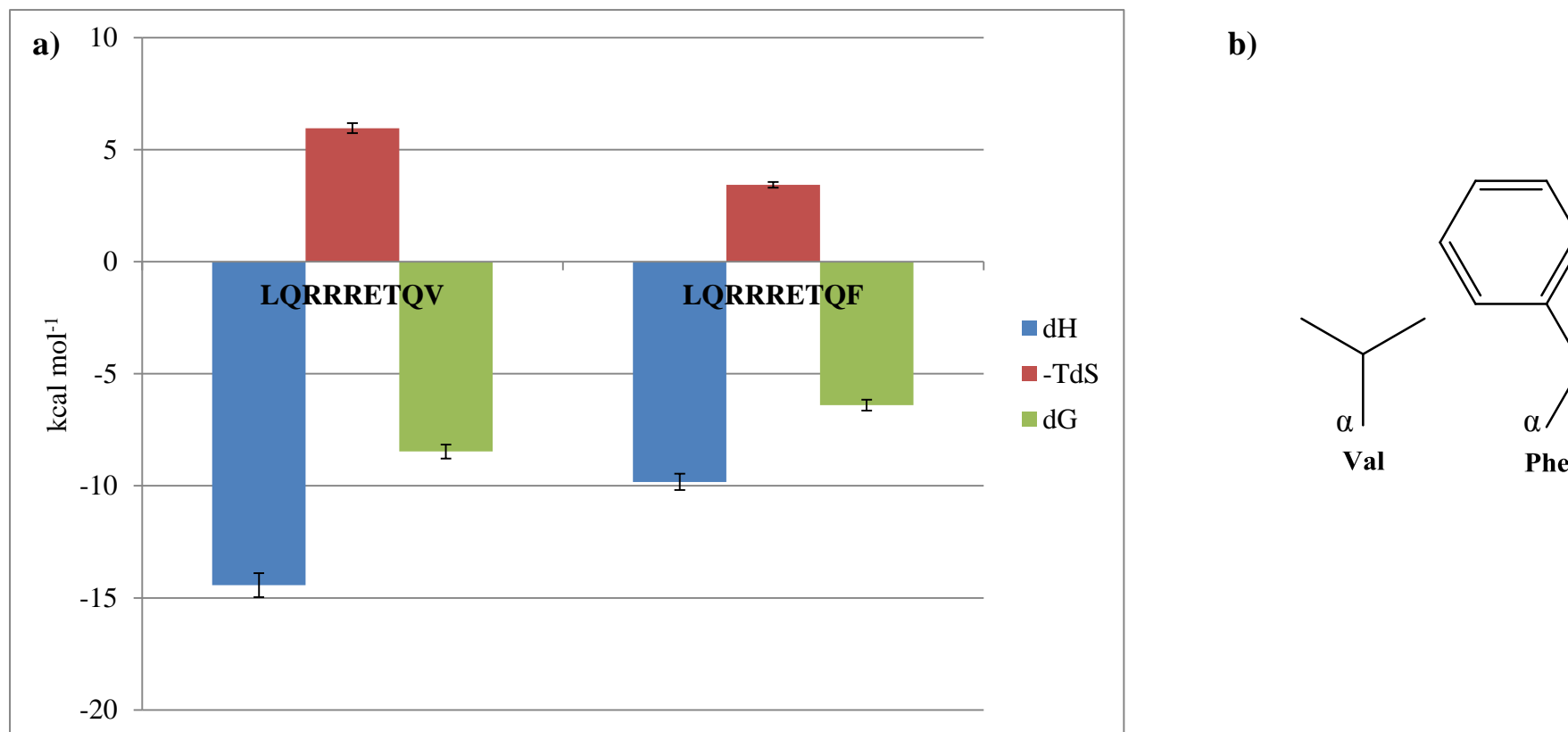


Figure 5.21: a) The thermodynamic parameters (ΔH = blue, $-T\Delta S$ = red and ΔG = green) obtained from the binding interaction between the HPV18 E6 nonapeptide (LQRRRETQV) and a nonapeptide with a Phe C-terminal residue to the SAP97 PDZ2 domain, in the investigation of the effect of the hydrophobic interaction on SAP97 PDZ2 binding affinity. ΔH is the dominant thermodynamic parameter in ΔG determination and hence, binding affinity; this is because ΔH is a large negative value in both ITC binding experiments, with $-T\Delta S$ being a small to moderate positive value in comparison and so, contributes much less significantly to ΔG . The substitution of the C-terminal Val of HPV18 E6 with Phe led to a decrease in binding affinity; this was due to the less favourable enthalpy change of the interaction i.e. ΔH was less negative, indicating that the bulk of the Phe side-chain prevents effective interaction with the SAP97 PDZ2 hydrophobic binding pocket. b) The structure of the side-chains of the native C-terminal HPV18 E6 residue Val and the Phe residues substituted in the hydrophobic interaction investigation; it can be seen that the side-chain of Phe is much bulkier than that of Val and hence, is not suitable to effectively interact with the SAP97 PDZ2 domain.

5.4.6 Electrostatic Interaction Investigation

This section investigates the contribution of the electrostatic interaction between the His residue of the SAP97 PDZ2 domain and the Thr (-2) residue of the HPV18 E6 protein. This is investigated from both the ligand (by substitution of the -2 Thr residue) and PDZ domain (by mutation of the His residue) perspectives.

5.4.6.1 Ligand Perspective

The contribution of the electrostatic interaction to binding affinity, from the ligand perspective, was examined by substitution of the Thr (-2) residue of HPV18 E6 peptides of differing lengths, with a variety of natural and non-natural amino acids (Tables 5.8 & 5.9, Figures 5.7, 5.10&11 and 5.22 – 5.25).

Table 5.8: The peptide ligands used in the SAP97 PDZ2 domain binding experiment by ITC and the respective binding parameters obtained. The errors in the binding parameters were calculated from a PSD-95 PDZ1 – 5-HT_{2a} binding experiment that was performed in triplicate, with the standard deviation in calculated K_D and ΔG values used to determine the errors for the K_D and thermodynamic parameter values respectively in the binding experiments shown in the table. ^a γ = Allothreonine, ^b DNB = Did not bind, ^c δ = Betahydroxynorvaline.

Ligand	K_D (μM)	ΔH (kcal mol^{-1})	$-T\Delta S$ (kcal mol^{-1})	ΔG (kcal mol^{-1})
RETQV	1.08 ± 0.12	-5.077 ± 0.189	-3.069 ± 0.114	-8.146 ± 0.303
RE γ QV ^a	DNB	DNB	DNB	DNB
RE δ QV ^c	13.04 ± 1.50	-3.671 ± 0.137	-2.980 ± 0.111	-6.651 ± 0.247

Table 5.9: The peptide ligands used in the SAP97 PDZ2 domain binding experiment by ITC and the respective binding parameters obtained. The errors in the binding parameters were calculated from a PSD-95 PDZ1 – 5-HT_{2a} binding experiment that was performed in triplicate, with the standard deviation in calculated K_D and ΔG values used to determine the errors for the K_D and thermodynamic parameter values respectively in the binding experiments shown in the table. ^a DNB = Did not bind.

Ligand	K_D (μM)	ΔH (kcal mol^{-1})	$-T\Delta S$ (kcal mol^{-1})	ΔG (kcal mol^{-1})
LQRRRETQV	0.61 ± 0.07	-14.430 ± 0.537	5.960 ± 0.222	-8.470 ± 0.315
LQRRREGQV	DNB	DNB	DNB	DNB
LQRRRESQV	4.02 ± 0.46	-8.240 ± 0.307	0.879 ± 0.033	-7.361 ± 0.274

As with the hydrophobic interaction investigation, the binding interactions are driven by enthalpic factors, although the SAP97 PDZ2 binding of RE δ QV is much more dependent on entropic factors, compared with the binding of the other peptides. Substitution of the -2 Thr of HPV18 E6 led to a decrease in binding affinity in all

cases, due to the less favourable enthalpy change of the non-native peptide interactions i.e. ΔH was less negative c.f. HPV18 E6. This indicates that the substituted residues have formed a weaker hydrogen bond with the SAP97 PDZ2 domain conserved His than the native Thr residue, as ΔH is dependent upon the number/strength of interactions formed/broken in the act of binding. Allothreonine (AThr) is a non-natural amino acid and diastereoisomer of Thr (Figure 5.24b), where the hydroxyl group is pointing in the opposite direction in space c.f. Thr and so, is too far away in space from the His residue. The removal of the ability to form the electrostatic interaction with the SAP97 PDZ2 His residue by substitution with AThr and Gly obliterated binding; suggesting that the hydrophobic interaction involving the hydrophobic C-terminal residue alone is not sufficient to facilitate SAP97 PDZ2 binding.

The substitution of Thr (-2) with the non-natural amino acid betahydroxynorvaline (BVal) or Ser indicated that the addition/removal of a methyl group from the Thr side-chain structure of Thr respectively, had a detrimental effect on binding affinity. The extra residue side-chain methylene of BVal leads to less favourable ΔH and $-T\Delta S$ parameters, suggesting that either the extra methylene group causes unfavourable side-chain steric clashes with the residues of the SAP97 PDZ2 binding region or that it places the methyl group in a less optimal position c.f. Thr side-chain; this will affect the ability of the methyl group to form hydrophobic interactions with the surrounding residues. The position of the methyl group of Thr in space has been shown to be important as it forms hydrophobic interactions with the surrounding residues of the SAP97 PDZ2 binding region and constrain the hydroxyl group orientation in space; the Ser side-chain does not have this methyl group present (Figure 5.25b). The less favourable ΔH value of LQRRRESQV binding to SAP97

PDZ2 can therefore be attributed to a weaker hydrogen bond formed in the absence of the methyl group and hence, results in weaker SAP97 PDZ2 binding, compared to LQRRRETQV.

The contribution of the electrostatic interaction to the binding affinity of the SAP97 PDZ2 – HPV18 E6 interaction was then investigated from the protein perspective.

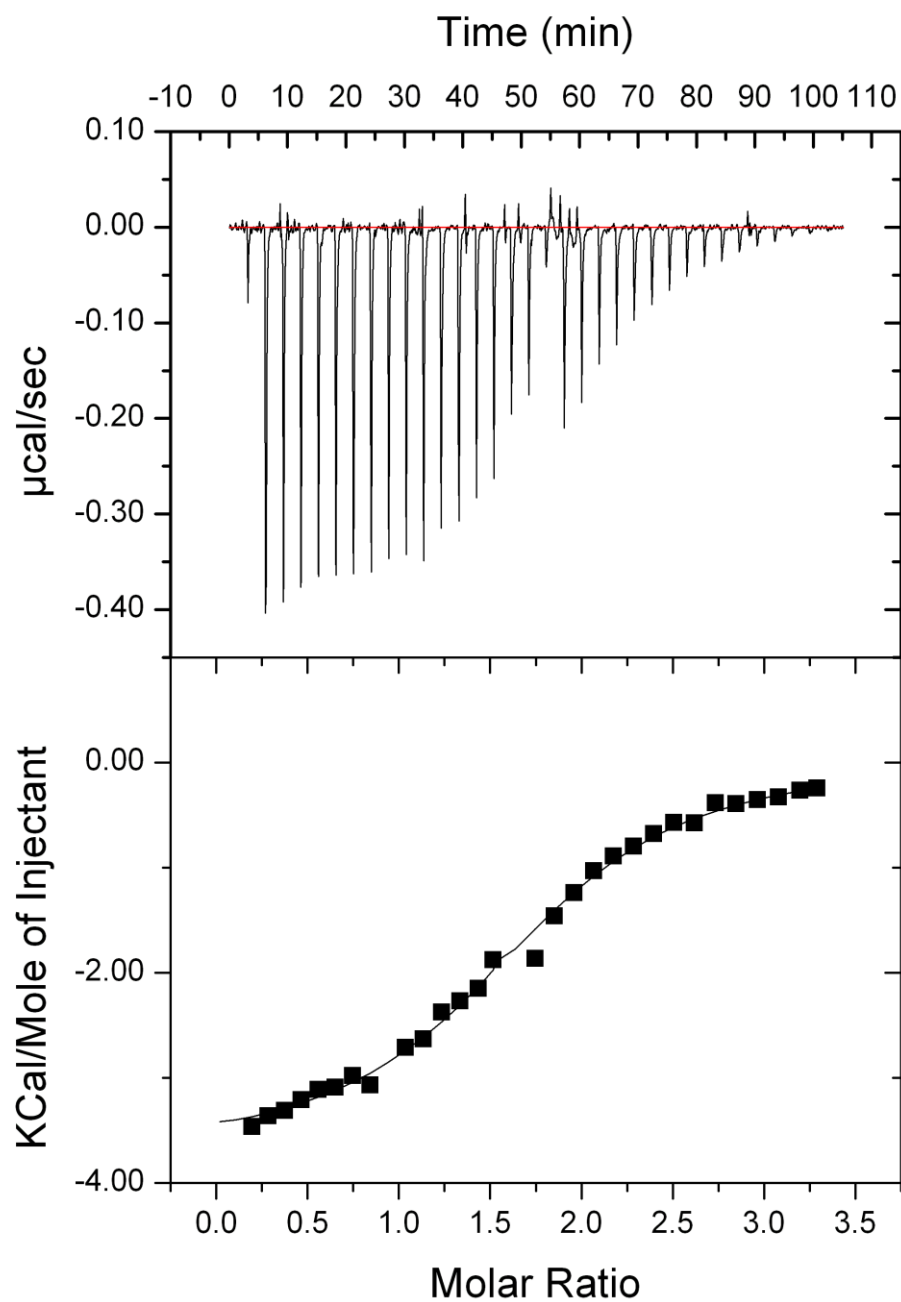


Figure 5.22: The ITC isotherm (top) and resultant curve (bottom) produced by the ITC binding experiment between $100\mu\text{M}$ SAP97 PDZ2 (cell) and $750\mu\text{M}$ RE δ QV (syringe) in 20mM phosphate, pH6.3, on an $i\text{TC}_{200}$ Microcalorimeter (MicroCal) at 298K . Fitting of the curve produced by the ITC experiment to a single set of sites curve-fitting model, using Origin7, resulted in a binding affinity (K_D) of $13.04\mu\text{M}$ for RE δ QV to the SAP97 PDZ2 domain.

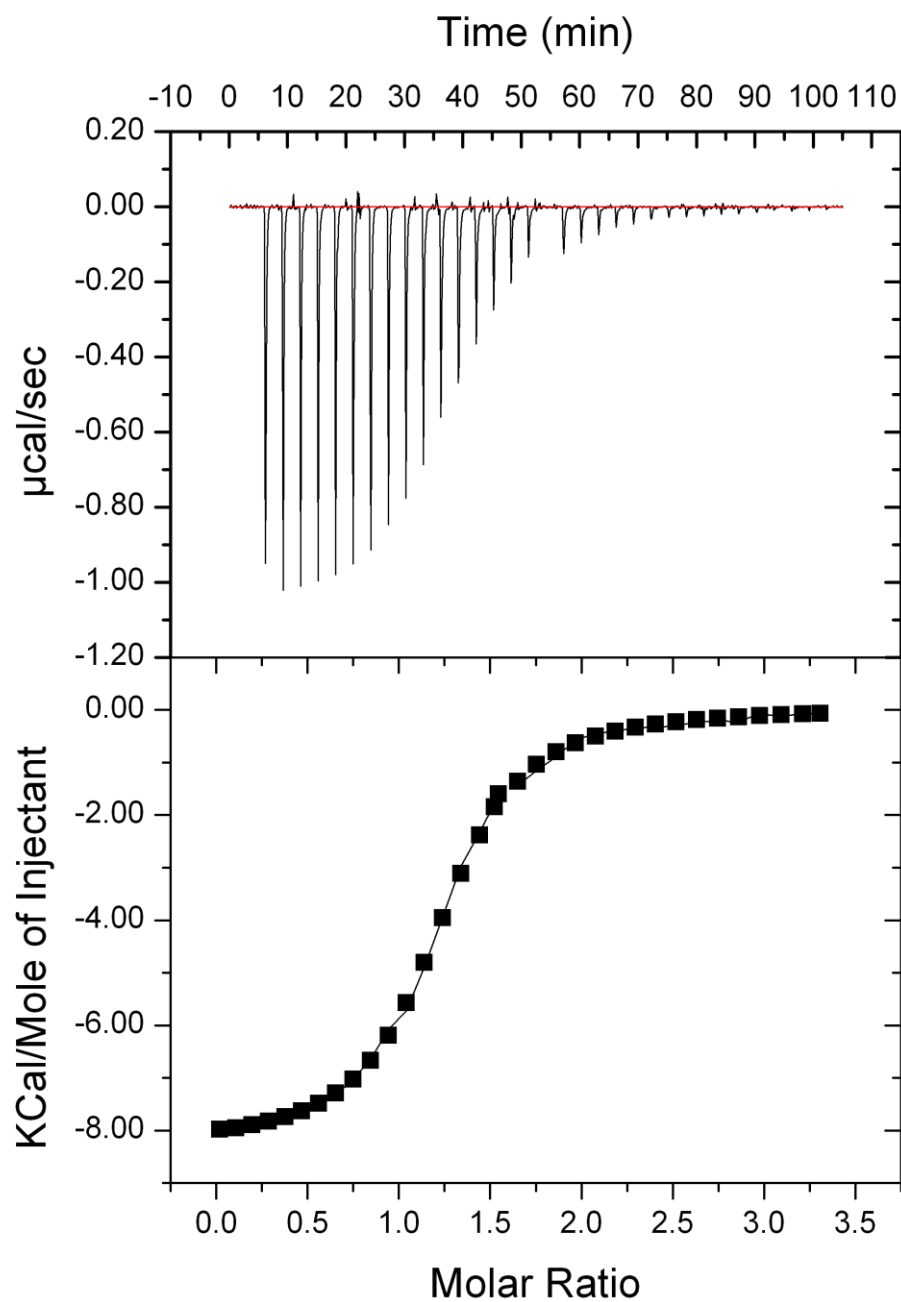


Figure 5.23: The ITC isotherm (top) and resultant curve (bottom) produced by the ITC binding experiment between $100\mu\text{M}$ SAP97 PDZ2 (cell) and $750\mu\text{M}$ LQRRRESQV (syringe) in 20mM phosphate, $\text{pH}6.3$, on an iTC_{200} Microcalorimeter (MicroCal) at 298K . Fitting of the curve produced by the ITC experiment to a single set of sites curve-fitting model, using Origin7, resulted in a binding affinity (K_D) of $4.02\mu\text{M}$ for LQRRRESQV to the SAP97 PDZ2 domain.

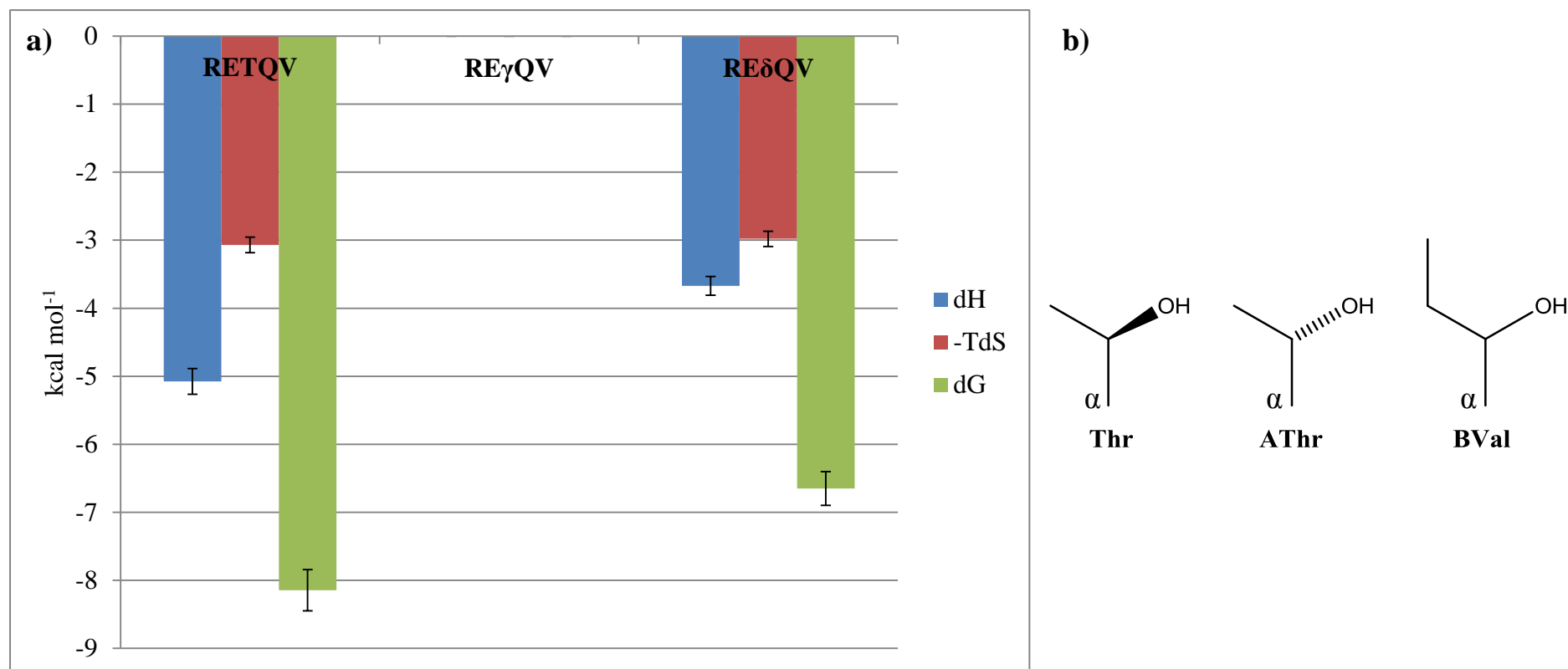


Figure 5.24: a) The thermodynamic parameters (ΔH = blue, $-T\Delta S$ = red and ΔG = green) obtained from the binding interaction between the HPV18 E6 pentapeptide (RETQV) and pentapeptides with substituted non-natural amino acid -2 residues to the SAP97 PDZ2 domain, in the investigation of the effect of the electrostatic interaction on SAP97 PDZ2 binding affinity. ΔH is the dominant thermodynamic parameter in ΔG determination and hence, binding affinity; this is because ΔH is a moderate to large negative value in both ITC binding experiments but $-T\Delta S$ is also a moderate negative value in comparison and so, contributes more significantly to ΔG than previous interactions. The removal of the peptides ability to form an electrostatic interaction with the SAP97 PDZ2 His by substitution of Thr with AThr eradicated binding completely; indicating that the hydrophobic interaction alone was not enough to facilitate peptide binding. Substitution of the -2 Thr of HPV18 E6 with BVal led to a decrease in binding affinity; this was due to the less favourable enthalpy change of the interaction i.e. $-\Delta H$ was less negative, due to a weaker hydrogen bond formed with the His. b) The side-chain structure of the native HPV18 E6 -2 residue Thr and the two non-natural amino acids substituted in the electrostatic interaction investigation; the Thr side-chain was shown to be the optimal side-chain for SAP97 PDZ2 domain binding as this was able to maximise the electrostatic interaction with the conserved His residue, as the hydroxyl group of AThr side-chain is oriented in the wrong direction in space and the absence of the methyl group in the Ser side-chain has a detrimental effect.

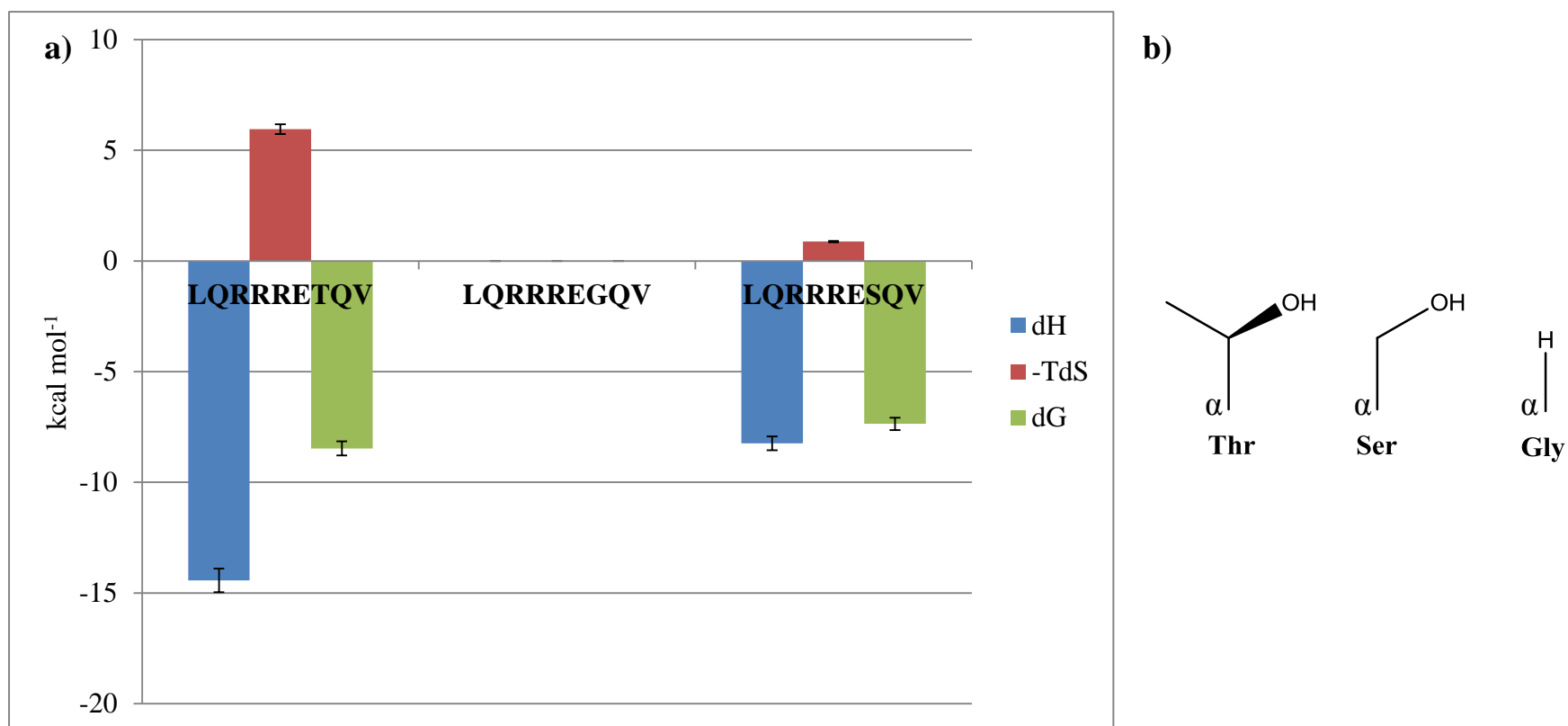


Figure 5.25: a) The thermodynamic parameters (ΔH = blue, $-T\Delta S$ = red and ΔG = green) obtained from the binding interaction between the HPV18 E6 nonapeptide (LQRRRETQV) and nonapeptides with substituted -2 residues to the SAP97 PDZ2 domain, in the investigation of the effect of the electrostatic interaction on SAP97 PDZ2 binding affinity. ΔH is the dominant thermodynamic parameter in ΔG determination and hence, binding affinity; this is because ΔH is a moderate to large negative value in the ITC binding experiments, with $-T\Delta S$ being a small to moderate positive value in comparison and so, contributes much less significantly to ΔG . The removal of the ability of the peptide to form an electrostatic interaction with the SAP97 PDZ2 domain His by substitution of Thr with Gly eradicated binding completely, as seen previously with ATr (Figure 5.24). Substitution of the -2 Thr of HPV18 E6 with Ser led to a decrease in binding; this was due to the less favourable enthalpy change of the interactions i.e. $-\Delta H$ was less negative, due to a weaker hydrogen bond formed with the SAP97 PDZ2 His caused the lack of a methyl group on the side-chain of Ser c.f. Thr (Figure 5.25b). b) The structure of the side-chains of the native HPV18 E6 -2 residue Thr and the two other residues substituted in the electrostatic interaction investigation; the Thr side-chain was shown to be the optimal side-chain for SAP97 PDZ2 domain binding as this was able to maximise the electrostatic interaction with the conserved His residue, substitution with Gly eradicated SAP97 PDZ2 binding and the absence of the methyl group in the Ser side-chain has a detrimental effect on the binding interaction and hence, affinity.

5.4.6.2 PDZ Domain Perspective

To investigate the contribution of the electrostatic interaction to the binding affinity of the SAP97 PDZ2 – HPV18 E6 interaction from the protein perspective, the SAP97 PDZ2 H73G/T mutants [5.2 & 5.3] were utilised in ITC binding experiments with the HPV 18 E6 (LQRRRETQV) and LQRRRESQV nonapeptides (Tables 5.11&12 and Figures 7 and 26 – 29).

Table 5.11: The different forms of the SAP97 PDZ domain used with the HPV18 E6 nonapeptide (LQRRRETQV) ligand in the binding experiment by ITC and the respective binding parameters obtained. The errors in the binding parameters were calculated from a PSD-95 PDZ1 – 5-HT_{2a} binding experiment that was performed in triplicate, with the standard deviation in calculated K_D and ΔG values used to determine the errors for the K_D and thermodynamic parameter values respectively in the binding experiments shown in the table.

Protein	K _D (μM)	ΔH (kcal mol ⁻¹)	-TΔS (kcal mol ⁻¹)	ΔG (kcal mol ⁻¹)
WT	0.61 ± 0.07	-14.430 ± 0.537	5.960 ± 0.222	-8.470 ± 0.315
H73G	62.11 ± 7.16	-7.788 ± 0.290	2.047 ± 0.076	-5.741 ± 0.214
H73T	79.37 ± 9.14	-10.070 ± 0.375	4.470 ± 0.166	-5.600 ± 0.208

Table 5.12: The different forms of the SAP97 PDZ domain used with the Ser nonapeptide (LQRRRESQV) ligand in the binding experiment by ITC and the respective binding parameters obtained. The errors in the binding parameters were calculated from a PSD-95 PDZ1 – 5-HT_{2a} binding experiment that was performed in triplicate, with the standard deviation in calculated K_D and ΔG values used to determine the errors for the K_D and thermodynamic parameter values respectively in the binding experiments shown in the table.

Protein	K _D (μM)	ΔH (kcal mol ⁻¹)	-TΔS (kcal mol ⁻¹)	ΔG (kcal mol ⁻¹)
WT	4.02 ± 0.46	-8.240 ± 0.307	0.879 ± 0.033	-7.361 ± 0.274
H73G	DNB	DNB	DNB	DNB
H73T	166.7 ± 19.20	-4.468 ± 0.166	-0.685 ± 0.025	-5.153 ± 0.192

The binding of the nonapeptides to the SAP97 PDZ2 H73G/T mutant forms was again shown to be dependent on enthalpic factors; with the decrease in binding affinity of the nonapeptides to the mutant SAP97 PDZ2 domains due to a decrease in enthalpy. This is in agreement with the related investigation into the effect of the electrostatic interaction from the ligand perspective in the previous section, where perturbation of the SAP97 PDZ2 – HPV18 E6 hydrogen bond decreased the ΔH parameter and hence, weakened binding. However, removal of the ability to form an

electrostatic interaction in [5.4.4.1] eradicated binding, whereas, the SAP97 PDZ2 mutants were both found to bind the HPV18 E6 nonapeptide. As the H73G mutant shows better affinity for LQRRRETQV than H73T, this cannot be rationalised by the formation of a hydrogen bond with the -2 Thr residue of the nonapeptide and thus, facilitate binding. It is possible that the single point mutation of the SAP97 PDZ2 His73 residue to Gly and Thr respectively has induced a structural change in the SAP97 PDZ2 mutants, relative to the wild-type structure; this was alluded to previously when comparing the HSQC spectra of the SAP97 PDZ2 wild-type and H73G/T domains (Figure 5.6). The binding region of the SAP97 PDZ2 H73G/T mutants may therefore be able to bind in an unconventional manner that is not accessible to the wild-type domain and hence, explain the unexpected observed binding of the HPV18 E6 nonapeptide to both SAP97 PDZ2 mutant forms (and LQRRRESQV to the H73T mutant).

5.4.7 Electrostatic Interaction Investigation Summary

The investigation into the electrostatic interaction contribution to the binding affinity of the SAP97 PDZ2 – HPV18 E6 interaction has led to the following deductions:

- The Thr side-chain is the amino acid side-chain structure that results in the strongest binding affinity out of the -2 residues investigated.
- When the electrostatic interaction is removed, the contribution of the electrostatic interaction to binding is not sufficient enough to facilitate binding, even in longer peptide forms.
- The binding of peptides containing non-natural amino acid isomers of natural amino acids at the ligand -2 position showed no binding or weaker binding than the natural amino acid peptide variants.

- PDZ domain mutant forms were still able to bind to the nonapeptides despite the reduced or lack of ability to form an electrostatic interaction; this could have been due to structural changes of the PDZ domain binding region induced by the residue mutation.

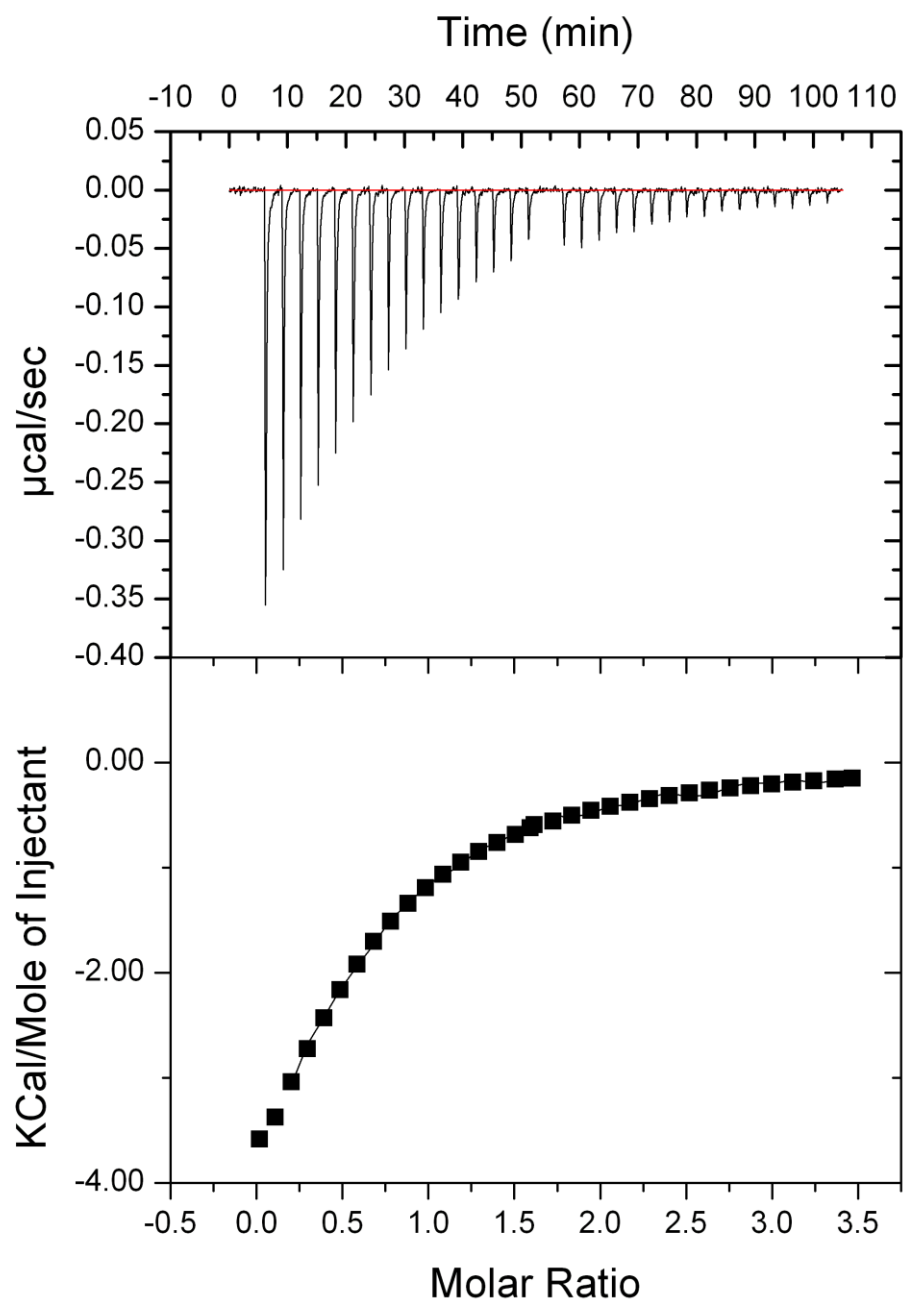


Figure 5.26: The ITC isotherm (top) and resultant curve (bottom) produced by the ITC binding experiment between $100\mu\text{M}$ SAP97 PDZ2 H73G (cell) and $750\mu\text{M}$ LQRRRETQV (syringe) in 20mM phosphate, $\text{pH}6.3$, on an iTC_{200} Microcalorimeter (MicroCal) at 298K . Fitting of the curve produced by the ITC experiment to a single set of sites curve-fitting model, using Origin7, resulted in a binding affinity (K_D) of $62.11\mu\text{M}$ for LQRRRETQV to the SAP97 PDZ2 H73G domain.

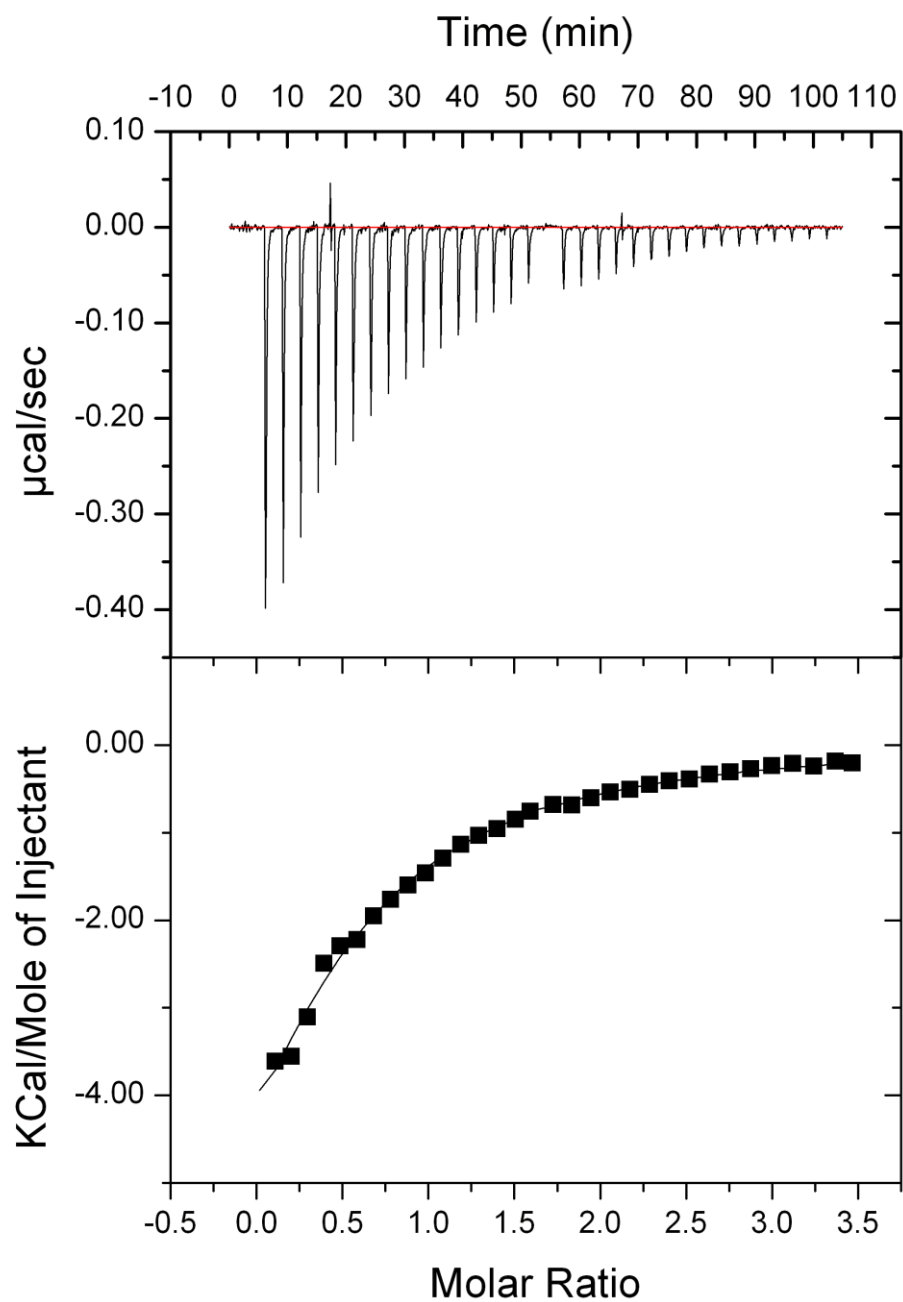


Figure 5.27: The ITC isotherm (top) and resultant curve (bottom) produced by the ITC binding experiment between $100\mu\text{M}$ SAP97 PDZ2 H73T (cell) and $750\mu\text{M}$ LQRRRETQV (syringe) in 20mM phosphate, $\text{pH}6.3$, on an iTC_{200} Microcalorimeter (MicroCal) at 298K . Fitting of the curve produced by the ITC experiment to a single set of sites curve-fitting model, using Origin7, resulted in a binding affinity (K_D) of $79.37\mu\text{M}$ for LQRRRETQV to the SAP97 PDZ2 H73T domain.

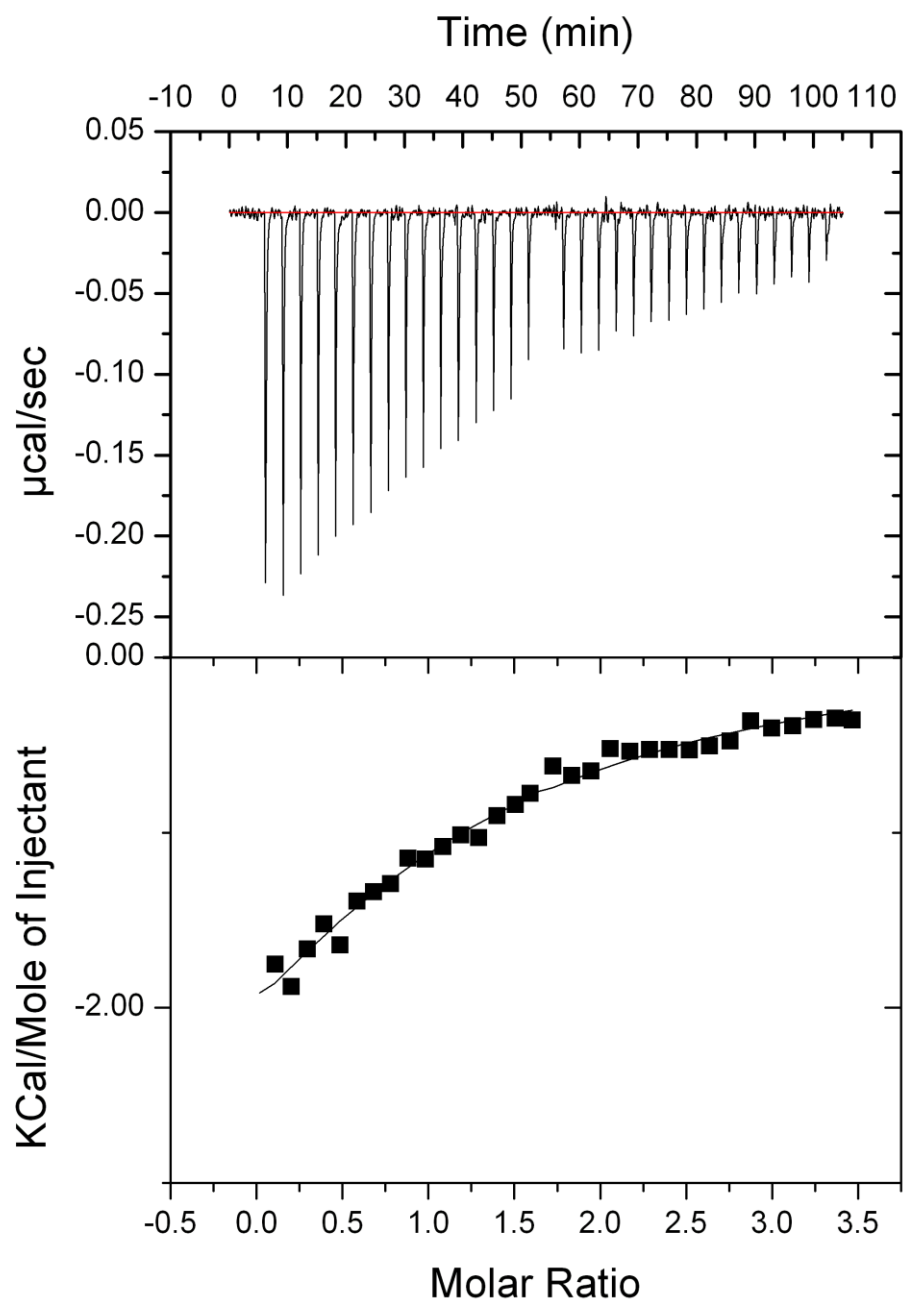


Figure 5.28: The ITC isotherm (top) and resultant curve (bottom) produced by the ITC binding experiment between $100\mu\text{M}$ SAP97 PDZ2 H73T (cell) and $750\mu\text{M}$ LQRRRESQV (syringe) in 20mM phosphate, $\text{pH}6.3$, on an iTC_{200} Microcalorimeter (MicroCal) at 298K . Fitting of the curve produced by the ITC experiment to a single set of sites curve-fitting model, using Origin7, resulted in a binding affinity (K_D) of $166.67\mu\text{M}$ for LQRRRESQV to the SAP97 PDZ2 H73T domain.

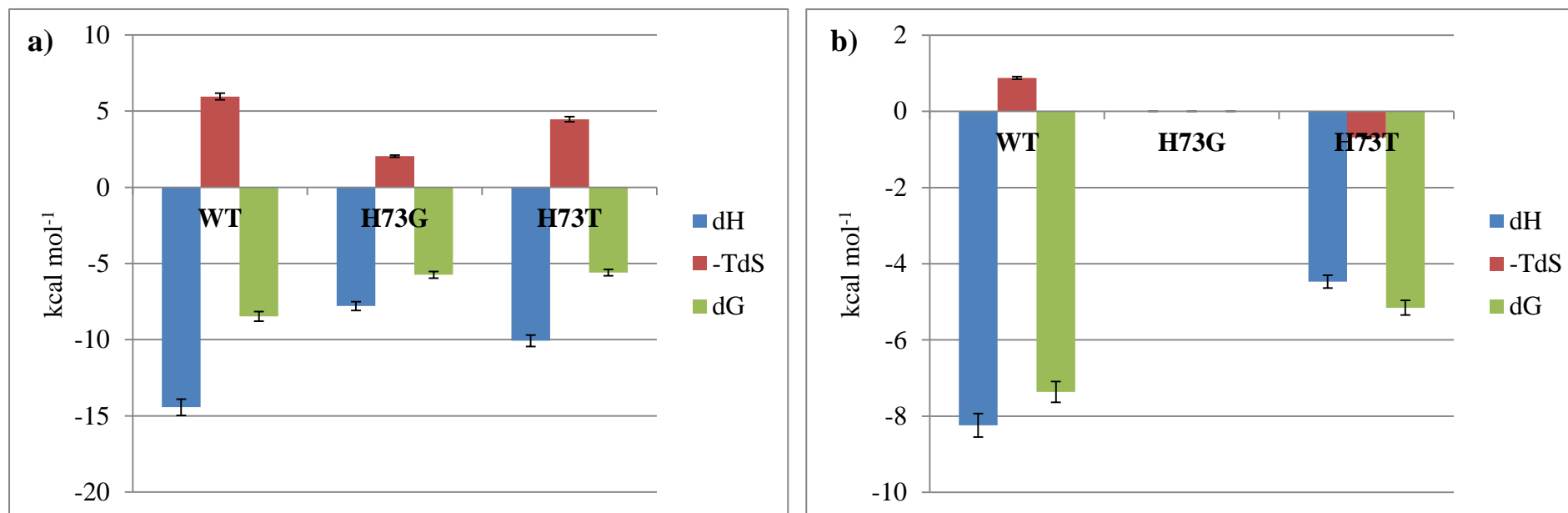


Figure 5.29: The thermodynamic parameters (ΔH = blue, $-T\Delta S$ = red and ΔG = green) obtained from the binding interaction between the SAP97 PDZ2 wild-type, H73G and H73T domains with a) HPV18 E6 nonapeptide (LQRRRETQV) and b) LQRRRESQV, in the investigation of the effect of the electrostatic interaction on SAP97 PDZ2 binding affinity, from the protein perspective. ΔH is the dominant thermodynamic parameter in ΔG determination and hence, binding affinity; this is because ΔH is a moderate to large negative value in both ITC binding experiments, with $-T\Delta S$ being a small to moderate negative/positive value in comparison and so, contributes much less significantly to ΔG . The decrease in binding affinity of the nonapeptides to the mutant SAP97 PDZ2 domains was due to a decrease in enthalpy. This is in agreement with the related investigation into the effect of the electrostatic interaction from the ligand perspective in the previous section, where perturbation of the SAP97 PDZ2 – HPV18 E6 hydrogen bond decreased the ΔH parameter and hence, weakened binding. However, removal of the ability to form an electrostatic interaction in [5.4.4.1] eradicated binding, whereas, the SAP97 PDZ2 mutants were both found to bind the HPV18 E6 nonapeptide. As the H73G mutant showing better affinity for LQRRRETQV than H73T, this cannot be rationalised by the formation of a hydrogen bond with the -2 Thr residue of the nonapeptide and thus, facilitate binding. It is possible that the single point mutation of the SAP97 PDZ2 His73 residue to Gly and Thr respectively has induced a structural change in the SAP97 PDZ2 mutants, relative to the wild-type structure; this was alluded to previously when comparing the HSQC spectra of the SAP97 PDZ2 wild-type and H73G/T domains (Figure 5.6). The binding region of the SAP97 PDZ2 H73G/T mutants may therefore be able to bind in an unconventional manner that is not accessible to the wild-type domain and hence, explain the unexpected observed binding of the HPV18 E6 nonapeptide to both SAP97 PDZ2 mutant forms (and LQRRRESQV to the H73T mutant).

5.5 General Discussion

The systematic investigation into the factors that determine SAP97 PDZ2 binding affinity has yielded a number of extremely important points that will guide future SAP97 PDZ2 domain inhibitor design consideration:

- The residue side-chain structure that interacts most effectively with the SAP97 PDZ2 hydrophobic binding pocket is the isopropyl group of Val.
- To maximise the electrostatic interaction with the conserved SAP97 PDZ2 His residue, the Thr side-chain is the optimal conformation and orientation of constituent chemical groups.
- To bind to the SAP97 PDZ2 domain with an affinity $< 250\mu\text{M}$, both hydrophobic and electrostatic interactions must be formed with the PDZ binding region.
- Formation of the minimal hydrophobic and electrostatic interactions will result in moderate micromolar affinity (K_D of TQV = $57.14\mu\text{M}$); the presence of a more extensive network of interactions with the SAP97 PDZ2 domain binding region is required to achieve low micromolar/high nanomolar affinity.
- The HPV18 E6 peptide length that maximises SAP97 PDZ2 binding was found to be greater than five residues, up to and including nine residues.

The knowledge obtained from the research detailed in this chapter will be invaluable in guiding an SAP97 PDZ2 domain inhibition research. Critical analysis of the resultant information obtained from this research could lead to the hypothesis that, given the expansive area and number of interactions required for effective SAP97 PDZ2 domain binding, the development of a high affinity small molecule inhibitor of the SAP97 PDZ2 domain may not be a feasible target. Therefore, the development of

native SAP97 PDZ2 ligand peptidomimetic scaffolds may be a more suitable starting point, from which to design reversible inhibitors of SAP97 PDZ2 domain-mediated interaction inhibitors.

Chapter 6

**THE DEVELOPMENT OF NOVEL SMALL MOLECULE INHIBITORS
OF THE PSD-95 AND SAP97 PDZ DOMAINS BY BIOPHYSICAL
TECHNIQUES**

6. THE DEVELOPMENT OF NOVEL SMALL MOLECULE INHIBITORS OF THE PSD-95 AND SAP97 PDZ DOMAINS BY BIOPHYSICAL TECHNIQUES

6.1 Introduction

As detailed in [1.6], there are a number of PDZ domain-mediated interactions where reversible inhibition of the interaction by a small organic molecule would be favourable for therapeutic reasons. As a result, there have been a variety of strategies employed by different research groups/organisations in an effort to develop inhibitors of PDZ domain-mediated interactions; with varying degrees of success [1.6]. As a brief summary, these strategies have either involved the use of peptides, rational non-peptide small molecule design, screening of virtual libraries, high-throughput screening or the ‘re-purposing of existing drugs.’

The two particular PDZ domain-containing proteins of interest to this thesis are PSD-95 and SAP97. There are no examples of any SAP97 PDZ domain inhibition research to-date and a reasonably limited amount of previous research into developing inhibitors of the PSD-95 PDZ domains; these research efforts have focussed almost exclusively on the development of inhibitory peptides (Piserchio et al., 2004, Pichon et al., 2010, Sainlos et al., 2011, Bach et al., 2012, Cook et al., 2012). There are also two examples of PSD-95 PDZ domain-mediated interaction by a small molecule compound, although this inhibitor targets the ligand protein rather than the PDZ domain itself. Thus, to date, there are no examples in the literature where an attempt has been made to develop a novel, reversible small molecule inhibitor of the PSD-95/SAP97 PDZ domains by a rational design and development procedure; this was the aim of the research detailed in this chapter.

This chapter describes the screening of potential small molecule inhibitors for binding to the PSD-95 PDZ1 domain by NMR spectroscopy and then investigates their effect on PSD-95 PDZ1 – 5-HT_{2c} receptor interaction; the investigation was carried out with all four PDZ domains of interest but was limited solely to the above described interaction due to the space constraints of the thesis.

The initial starting compounds in the binding screening were designed using computational docking by the group of our collaborators (Professor Sylvie Ducki *et al.*, Clermont Université), with a number of the compounds adapted from the previously described Fujii indole scaffold [1.6.3.1] (Figure 6.1) (Fujii *et al.*, 2007a) and were synthesised via well-known synthetic routes to PDZ domain ligands (Mayasundari *et al.*, 2008, Vogrig *et al.*, 2011). NMR samples of the particular PDZ domain under investigation, in the absence and presence of the potential inhibitor, were prepared and the resultant NMR spectra analysed. Specific binding was identified and binding efficacy quantified by comparison to the chemical shift perturbations induced by the binding of the native ligand of the respective PDZ domain. Designs for the possible structure of future compounds that were thought to enhance binding affinity were then relayed to our collaborators, in an iterative manner, to develop subsequent generations of compounds. The potential inhibitors initially started as relatively simple organic compounds and became progressively more substituted and complex as the inhibitor development process advanced.

Those compounds that showed the best PDZ domain binding (i.e. most numerous and/or largest chemical shift perturbations of the key residues in the binding pocket/extended groove) had their binding affinity (K_D) for the specific PDZ domain quantified by NMR spectroscopy. To see if these compounds then exhibited any inhibitory effects of the respective native PDZ domain – ligand interaction, ITC

competitive inhibition experiments were performed. This led to the determination of the quantitative inhibitory constant (K_i) of that small molecule compound for that specific interaction.

Finally, the structure of the bound complexes formed between a number of different PDZ domains and small molecule inhibitors were solved by a combination of NMR spectroscopy and NOE distance restraint-driven docking. These are the first examples of HADDOCK being used to determine the structure of PDZ domain – small molecule inhibitor complexes.

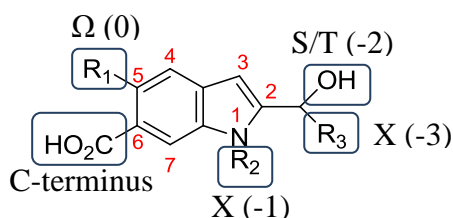


Figure 6.1: The structure of the indole chemical scaffold developed by Fujii *et al* to target class I PDZ domains such as PSD-95 PDZ1 (Fujii *et al.*, 2007a); the chemical numbering used conventionally to describe the different positions around the indole scaffold has been labelled. The scaffold was developed to mimic the interactions of the native PDZ domain ligand by substitution of appropriate chemical groups around the indole scaffold i.e. the 6-carboxyl group represents the C-terminus carboxylic acid group, which is known to form a hydrogen bond with the GLGF motif. This scaffold was modified by our collaborators using docking studies in an attempt to be specific for PSD-95 PDZ1.

6.2 Ligand Binding Screening by NMR Spectroscopy

6.2.1 General

The experimental conditions and the procedure employed to analyse the resultant data obtained from the binding screening of potential small molecule binders to the PSD-95 PDZ1 domain by NMR spectroscopy, discussed in this section are described in [3.3.1] and [3.3.4]. The chemical shift perturbations induced in the residues of the PSD-95 PDZ1 domain upon binding of a nine residue peptide of the C-terminus of the 5-HT_{2c} receptor (VVSERISSV) i.e. the native ligand, was used as a reference for the PSD-95 PDZ1 domain inhibitor development process (Figures 6.2a & 6.2b).

Those residues significantly perturbed in the PSD-95 PDZ1 domain, upon binding of the 5-HT_{2c} receptor (Table 6.1), were used to determine if any binding by potential

inhibitor was specific. A residue was considered significantly perturbed if it was known to be a key residue in the PSD-95 PDZ1 binding region and/or the shift sum value was greater than the average shift sum i.e. the shift sum threshold. The shifts perturbed above the threshold are therefore an indication of the binding mode of the ligand.

Table 6.1: The significant residue chemical shift perturbations induced by the binding of the nine residue C-terminal peptide of the 5-HT_{2c} receptor to different regions of the PSD-95 PDZ1 domain, along with the corresponding shift sum threshold value.

Ligand	Shift Sum Threshold ^a (ppm)	GLGF Motif & β_B Strand ^b	$\beta_B - \beta_C$ Loop ^b	αB Helix ^b	Others ^b
5-HT _{2c}	0.30	15G, 18G, 20G, 21F, 22S, 23I, 24A, 25G	26G, 27T, 31H	74H, 78V, 81L	43I, 44I, 49A, 50A, 88V, 90L

^a The equation used to determine the individual residue chemical shift perturbation sum value was $\Delta d_{ppm} = \sqrt{((\Delta\delta_{HN})^2 + (\Delta\delta_N * \alpha_N)^2)}$ where, α_N = Scaling Factor of 0.17. ^b Residues were considered significantly perturbed if they were known to be in PSD-95 PDZ1 binding region and/or the chemical perturbation shift sum value upon binding was greater than the shift sum threshold.

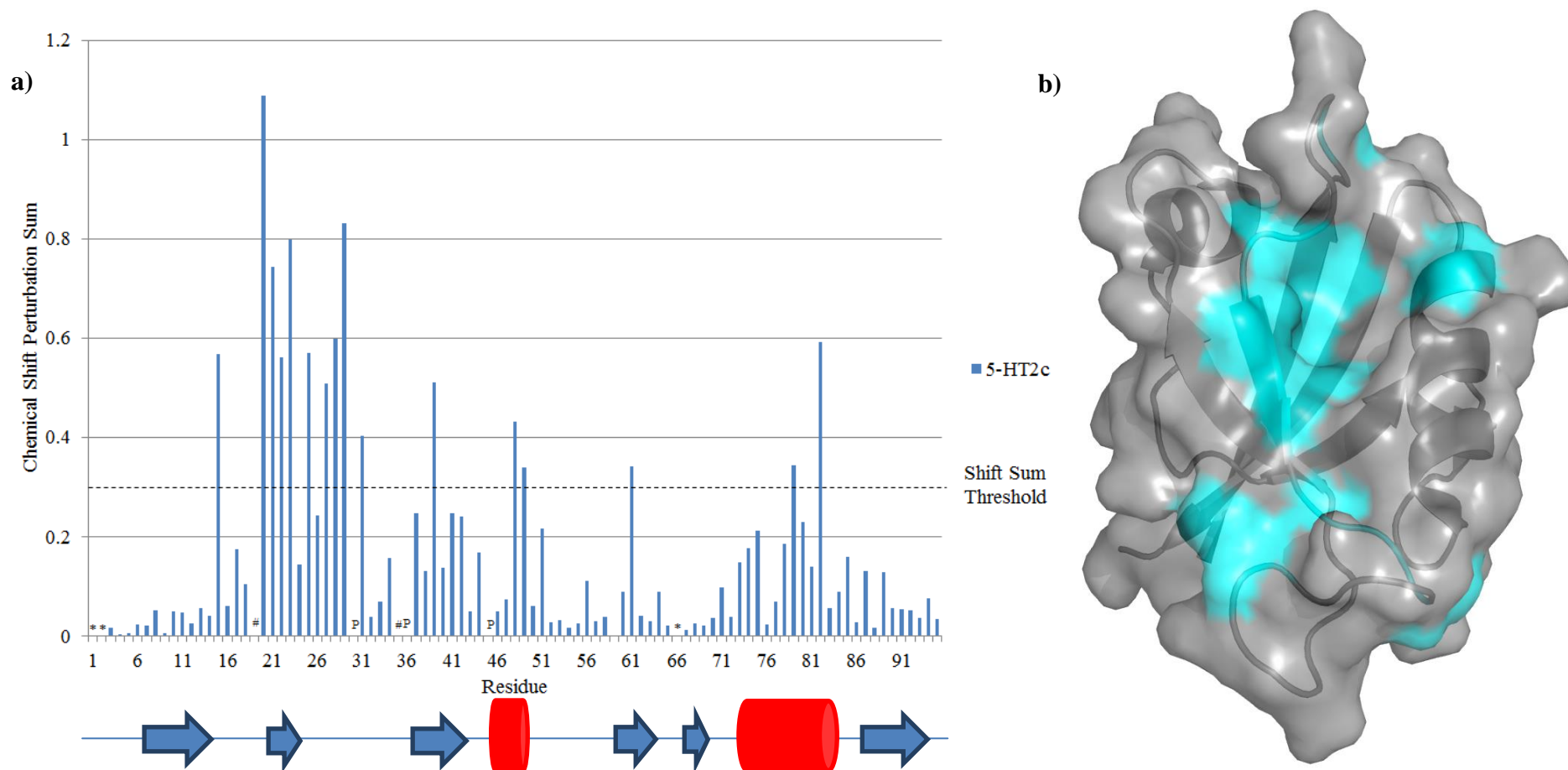


Figure 6.2: a) A plot of the chemical shift perturbation sum differences between free PSD-95 PDZ1 and bound to a C-terminal peptide of the 5-HT_{2c} receptor (VVSERISSV), with the shift sum threshold value indicated by the horizontal dashed line. The secondary structure of the PSD-95 PDZ1 domain (blue arrow = β -strand, red cylinder = α -helix) is given below the plot. (* = residue not able to assign in unbound PSD-95 PDZ1, # = residue not able to assign in bound PSD-95 PDZ1 and P = Proline; these residues are absent from the chemical shift perturbation sum graph here and subsequently) b) A surface representation (grey) of the PSD-95 PDZ1 domain structure (PDB ID: 3GSL (Sainlos et al., 2011)) with the residues that produced the most pronounced chemical shifts mapped onto the structure (cyan). Overall the figure shows how the residues of the GLGF motif and the β B strand (18 – 24) and those residues in flexible regions of the PDZ domain are the most affected by binding of the C-terminal 5-HT_{2c} receptor peptide.

6.2.2 First Generation Compounds

The first generation of potential PDZ domain binders consisted of four compounds (Figure 6.3), with three based on an indole chemical scaffold (compounds **1a-c**) and one based on a quinoline chemical scaffold (compound **1d**); the numbering used to describe the different positions around the indole scaffold in this chapter is also shown in the figure. As mentioned previously, these compounds were the result of preliminary computational docking attempts of small molecule structures into the PSD-95 PDZ1 domain by our collaborators.

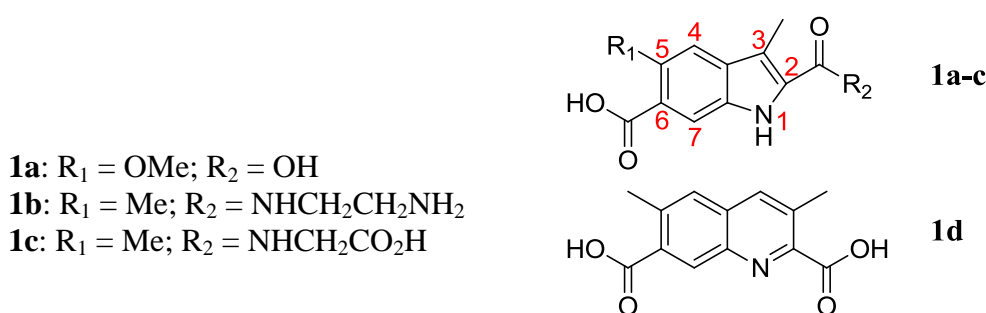


Figure 6.3: The structures of the first generation of potential PSD-95 PDZ1 domain binders, where **1a-c** are small molecule compounds based on the Fujii indole scaffold with chemical group variations at R₁ and R₂; **1d** is a more divergent potential binder based on a quinolone scaffold. (Me = methyl i.e. CH₃)

The NMR binding screening showed that three of the four first generation compounds exhibited binding to the PSD-95 PDZ1 domain, albeit quite weak, when compared to that of the native ligand (Table 6.2 & Figure 6.4).

Table 6.2: The significant residue chemical shift perturbations induced by the binding of the small molecule compounds **1a-d** to different regions of the PSD-95 PDZ1 domain, along with the corresponding shift sum threshold value.

Ligand	Shift Sum Threshold ^a (ppm)	GLGF Motif & β _C Strand	β _B - β _C Loop	αB Helix	Others	Binding Efficacy ^b
1a	0.03	20G, 21F, 22S	32I	74H, 78V	49A	Weak
1b	/	/	/	/	/	DNB ^c
1c	0.01	20G	/	/	/	VV Weak ^d
1d	0.02	20G	32I	74H	/	V Weak ^d

^a The equation used to determine the individual residue chemical shift perturbation sum value was $\Delta d_{\text{ppm}} = \sqrt{((\Delta\delta_{\text{HN}})^2 + (\Delta\delta_{\text{N}} * \alpha_{\text{N}})^2)}$ where, α_{N} = Scaling Factor of 0.17. ^b Binding efficacy was classified using the shift sum threshold value: <0.01 = DNB, 0.01 – 0.019 = VV Weak, 0.02 – 0.024 = V Weak, 0.025 – 0.039 = Weak, 0.04 – 0.044 = Weak – Moderate, 0.045 – 0.059 = Moderate, 0.06 – 0.074 = Moderate – Good, 0.075 – 0.139 = Good, 0.14 – 0.199 = Good – V Good, 0.2 – 0.299 = V Good, 0.30 < = Excellent. ^c DNB = Did Not Bind. ^d V = Very.

From Table 6.2 and Figure 6.3, it is apparent that **1a** binds better than **1c** and **1d**, with **1b** showing no detectable binding to the PSD-95 PDZ1 domain; this was concluded as **1a** showed the most numerous and substantial perturbations of the four first generation compounds. The binding was believed to be specific because those residues that showed chemical shift perturbations were the same as those affected by the binding of the native PSD-95 PDZ1 ligand, 5-HT_{2c}.

The reason why **1a** showed the most numerous and substantial perturbations of the four first generation compounds may have been due to the carboxylic acid group at the 6-position forming a hydrogen bond with the residues in the GLGF motif, with the alkyl chain of the 5-methoxy (5-OMe) group extending into the hydrophobic pocket to give tighter binding; as the indole chemical scaffold had been shown to previously (Figure 6.1) (Fujii et al., 2007a). There is also the possibility that this hydrogen bond could have been formed between the GLGF motif and the 2-carboxyl group; however, this would not explain why **1a** is shown to bind better to the PSD-95 PDZ1 domain than **1c**. The fact that no binding between **1b** and PSD-95 PDZ1 is observed (or any of the other PDZ domains investigated) could have been as a result of the group at the 2-position being too large in terms of length or bulk, resulting in an unfavourable steric clash; which would also explain the very weak binding of **1c** to the PSD-95 PDZ1 domain.

Interestingly, the quinoline-based inhibitor **1d** showed only very weak binding to the PSD-95 PDZ1 domain, whereas with the other three PDZ domains (PSD-95 PDZ2, SAP97 PDZ1&2), it showed reasonably good binding (Appendices, A.10 - A.12). This finding suggests that the actual binding pocket and extended groove of PSD-95 PDZ1 may have a different shape to that of the other PDZ domains and hence, not be a suitable fit for the quinoline chemical scaffold. The exhibited PDZ domain

specificity of the quinoline scaffold of **1d** may be useful for future research into novel, reversible, specific small molecule PDZ domain inhibitors.

It was decided that the most logical next step would be to design and synthesise a number of inhibitors that have a longer and/or bulkier alkyl chain at the indole 5-position. The rationale for this decision was to probe further into the hydrophobic pocket of the PSD-95 PDZ1 domain to see if this substitution has any effect on binding affinity. It was also believed that extension of the hydrophobic interactions between PSD-95 PDZ1 and the potential binders would ensure that the small molecule would bind in the desired orientation i.e. hydrogen bond formed between GLGF – 6-CO₂H rather than GLGF – 2-CO₂H. In addition to extending the alkyl chain at the 5-position, a couple of more novel and less rigid chemical scaffolds were designed; the aim was to investigate the suitability of other non-indole structure based scaffolds.

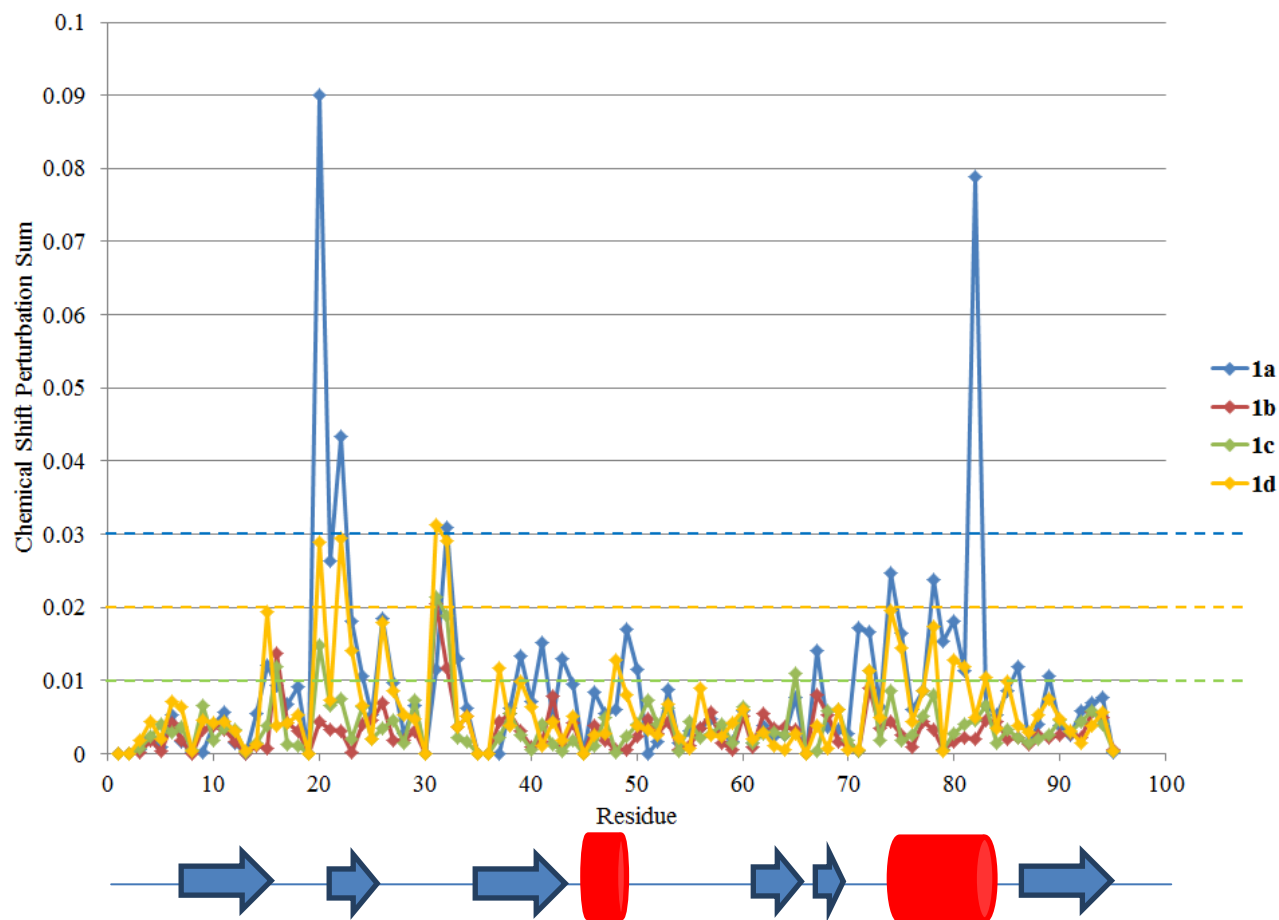


Figure 6.4: A plot of the chemical shift perturbation sum differences between free PSD-95 PDZ1 domain and in the presence of the respective first generation potential PDZ domain binders, with the shift sum threshold values for the individual potential binder has been indicated by a horizontal dashed line in the corresponding colour of the data in the plot. The secondary structure of the PSD-95 PDZ1 domain (blue arrow = β -strand and red cylinder = α -helix) is given below the plot. The plot shows that small molecules **1a**, **1c** and **1d** bound to the PSD-95 PDZ1 domain with **1a** being the potential PDZ binder that induced the strongest and most numerous chemical shift perturbations of the first generation compounds; **1b** did not produce any significant chemical shift perturbations and so, was concluded to not to bind to PSD-95 PDZ1.

6.2.3 Second Generation Compounds

Our collaborators synthesised a second generation of compounds (Figure 6.5), based on the analysis of the results from the first generation.

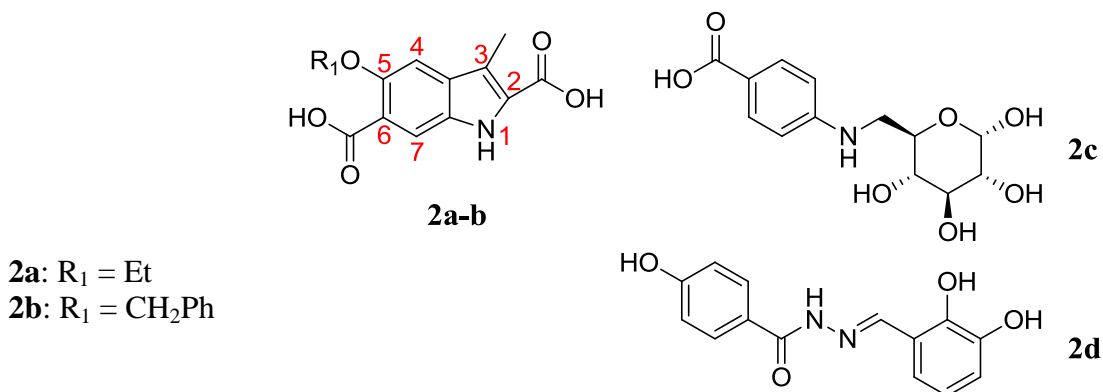


Figure 6.5: The structures of the second generation of potential PSD-95 PDZ1 domain binders, where **2a&b** are small molecule compounds based on the Fujii indole scaffold with chemical group variations at R_1 . The structure of compounds **2c** and **2d** are based on more novel and extended organic scaffolds. (Et = ethyl i.e. C_2H_5 and Ph = phenyl i.e. C_6H_5)

The binding screening of the second generation of compounds showed that two indole scaffold-based compounds (**2a** & **2b**) specifically bound to the PSD-95 PDZ1 domain (Table 6.3 & Figure 6.6). The binding of these two compounds was deemed to be better than the first generation as they perturbed a greater number of residues and with greater magnitude of chemical shift perturbations than those of the first generation. Whereas the remaining two compounds, with the more novel organic scaffolds (**2c** & **2d**), showed no evidence of binding to the PSD-95 PDZ1 domain whatsoever.

The only difference between first generation **1a** and second generation compounds **2a** & **2b** is the alkyl chain attached to the 5-O atom (OMe c.f. OEt and OCH_2Ph respectively). **2a** and **2b** were shown to induce greater and more substantial chemical shift perturbations in the PSD-95 PDZ1 domain than **1a**, this suggests that the previous hypothesis of adding a larger 5-alkyl chain would increase strength of binding may have been correct. This is most likely due to the ability of the small

molecule to interact more effectively with the hydrophobic pocket. The 5-ethoxy (5-OEt) group of **2a** has a small effect on increasing the chemical shift perturbations of the PSD-95 PDZ1 domain c.f. **1a** but this is only a minor improvement. This could be due to the ethyl chain not being long enough or orientated sufficiently well enough to interact effectively enough with the hydrophobic pocket.

Based on the number and magnitude of chemical shift perturbations, **2b** was shown to be the best PSD-95 PDZ1 domain binder of the second generation compounds and this is most likely due to the large phenyl (Ph) ring being able to form more extensive hydrophobic interactions with the hydrophobic pocket. The inherent rotation possible around the 5-benzyloxy (5-O-CH₂-Ph) side chain means that the phenyl ring is able to maximise the hydrophobic interaction with the pocket and yet still maintain the important 6-CO₂H – GLGF motif hydrogen bond.

It was disappointing that compounds **2c** and **2d** that contained the reasonably novel organic scaffolds, proved to be unsuccessful binders to the PSD-95 PDZ1 domain; **2d** did not show binding to any of the other three PDZ domains investigated either. **2c** showed some binding to the other three PDZ domains but the residues perturbed were far away from the canonical PDZ domain binding site and so the binding was believed to be non-specific (Appendices, A.13 – A.15). The size/length of **2c** and **2d** was probably too great to fit effectively in the PDZ binding region of the hydrophobic pocket and extended groove; this removed the potential for formation of favourable interactions and hence, resulted in no binding.

The second generation of NMR binding screening experiments led to the conclusion that the indole chemical scaffold was the most suitable scaffold upon which to develop a PDZ domain inhibitor. Therefore, efforts were made to develop more extensive interactions between the designed potential inhibitors and those residues in

the binding region. As a result, a number of potential binders with alternative groups placed at various positions around the indole chemical scaffold were designed in an attempt to determine the importance of these positions to PDZ domain binding affinity and specificity.

Table 6.3: The significant residue chemical shift perturbations induced by the binding of the small molecule compounds **2a-d** to different regions of the PSD-95 PDZ1 domain, along with the corresponding shift sum threshold value.

Ligand	Shift Sum Threshold ^a (ppm)	GLGF Motif & β_C Strand	$\beta_B - \beta_C$ Loop	α_B Helix	Others	Binding Efficacy ^b
2a	0.04	20G, 21F, 22S	32I,	78V	49A	Weak
2b	0.07	15G, 17S, 20G, 21F, 22S	32I	74H, 78V, 81L	44I, 49A	Moderate - Good
2c	/	/	/	/	/	DNB ^c
2d	/	/	/	/	/	DNB ^c

^a The equation used to determine the individual residue chemical shift perturbation sum value was $\Delta d_{ppm} = \sqrt{((\Delta\delta_{HN})^2 + (\Delta\delta_N * \alpha_N)^2)}$ where, α_N = Scaling Factor of 0.17. ^b Binding efficacy was classified using the shift sum threshold value: <0.01 = DNB, 0.01 – 0.019 = VV Weak, 0.02 – 0.024 = V Weak, 0.025 – 0.039 = Weak, 0.04 – 0.044 = Weak – Moderate, 0.045 – 0.059 = Moderate, 0.06 – 0.074 = Moderate – Good, 0.075 – 0.139 = Good, 0.14 – 0.199 = Good – V Good, 0.2 – 0.299 = V Good, 0.30 < = Excellent. ^c DNB = Did Not Bind.

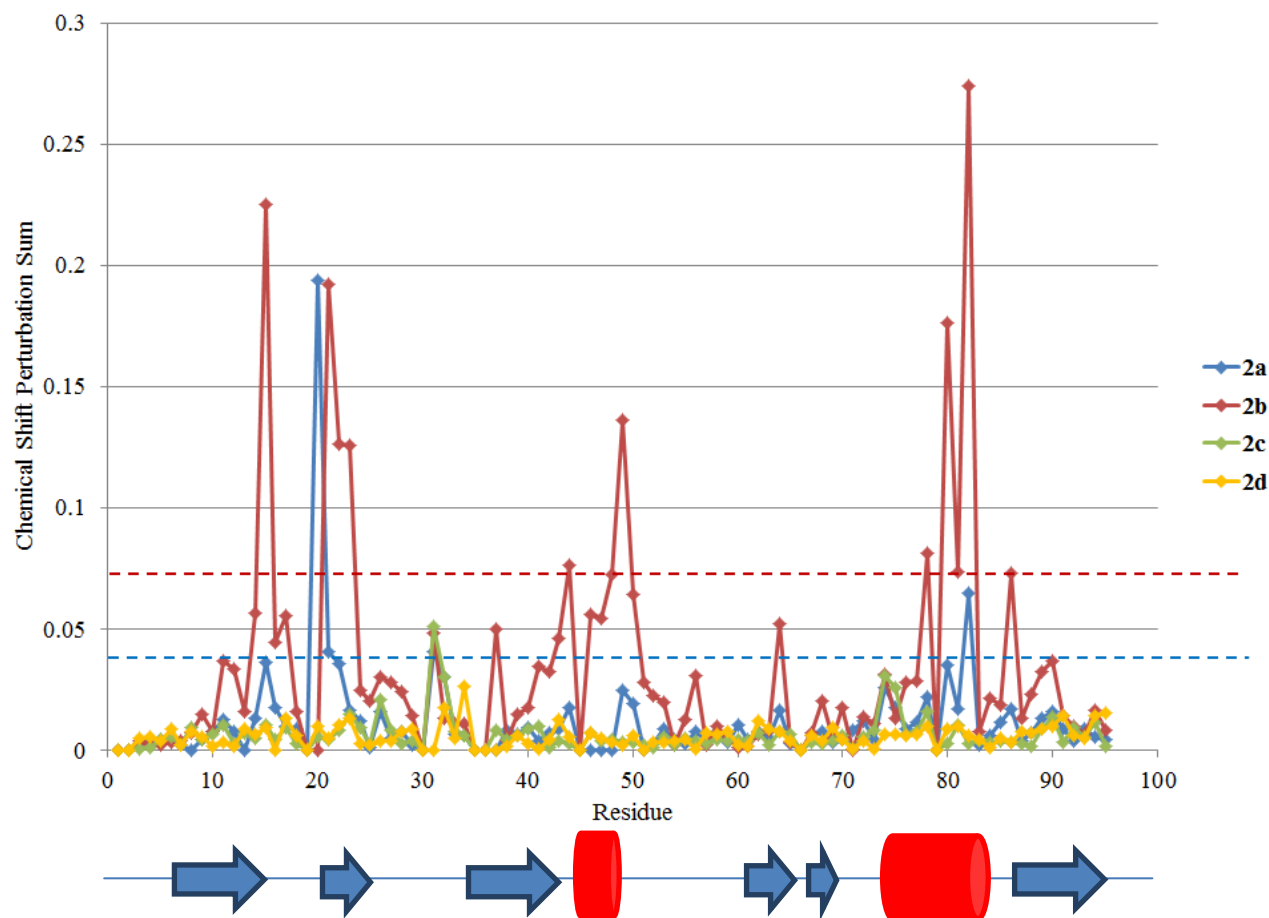


Figure 6.6: A plot of the chemical shift perturbation sum differences between free PSD-95 PDZ1 domain and in the presence of the respective second generation potential PDZ domain binders, with the shift sum threshold values for the individual potential binder has been indicated by a horizontal dashed line in the corresponding colour of the data in the plot. The secondary structure of the PSD-95 PDZ1 domain (blue arrow = β -strand and red cylinder = α -helix) is given below the plot. The plot shows that small molecules **2a** and **2b** bound to the PSD-95 PDZ1 domain with **2b** being the potential PDZ binder that induced the strongest and most numerous chemical shift perturbations of the second generation compounds; **2c** and **2d** did not produce any significant chemical shift perturbations and so, were concluded to not to bind to PSD-95 PDZ1.

6.2.4 Third Generation Compounds

The structures of the resultant five indole scaffold-based third generation potential PDZ domain binders synthesised are shown below (Figure 6.7):

- 3a:** R₁ = CH₂Ph; R₂ = NHCH₂CH₂NHCH₃; R₃ = H
3b: R₁ = CH₂Ph; R₂ = OH; R₃ = CH₂CH₂CO₂H
3c: R₁ = CH₂Ph; R₂ = OH; R₃ = CH₂CH₂CH₂CO₂H
3d: R₁ = OMe; R₂ = NHCH₂CH₂NH₂; R₃ = H
3e: R₁ = OH; R₂ = OH; R₃ = H

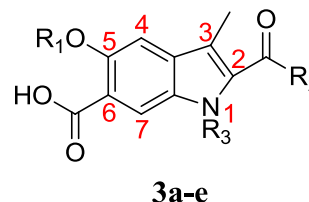


Figure 6.7: The structures of the third generation of potential PSD-95 PDZ1 domain binders, where **3a-e** are small molecule compounds based on the Fujii indole scaffold with chemical group variations of different length/bulk at R₁, R₂ and/or R₃. (Me = methyl i.e. CH₃ and Ph = phenyl i.e. C₆H₅)

The binding screening investigation showed that four of the five compounds bound to PSD-95 PDZ1 (**3a**, **3b**, **3c** and **3e**, Table 6.4), with **3d** being the only potential inhibitor not to bind to the PDZ domain under investigation (Figure 6.8).

Table 6.4: The significant residue chemical shift perturbations induced by the binding of the small molecule compounds **3a-e** to different regions of the PSD-95 PDZ1 domain, along with the corresponding shift sum threshold value.

Ligand	Shift Sum Threshold ^a (ppm)	GLGF Motif & β _C Strand	β _B - β _C Loop	αB Helix	Others	Binding Efficacy ^b
3a	0.06	15G, 20G, 21F	32I	/	44I, 47G, 50A, 90L	Moderate - Good
3b	0.075	15G, 17S, 18G, 20G, 21F, 22S	/	78V, 81L	44I, 46G, 47G, 49A, 50A, 90L	Good
3c	0.1	15G, 17S, 18G, 20G, 21F, 22S	/	78V, 81L	44I, 46G, 47G, 49A, 50A, 88V, 90L	Good
3d	/	/	/	/	/	DNB ^c
3e	0.1	20G, 21F, 22S	31H, 32I	74H, 78V, 81L	49A, 72V	Good

^a The equation used to determine the individual residue chemical shift perturbation sum value was $\Delta d_{\text{ppm}} = \sqrt{((\Delta\delta_{\text{HN}})^2 + (\Delta\delta_{\text{N}} * \alpha_{\text{N}})^2)}$ where, α_{N} = Scaling Factor of 0.17. ^b Binding efficacy was classified using the shift sum threshold value: <0.01 = DNB, 0.01 – 0.019 = VV Weak, 0.02 – 0.024 = V Weak, 0.025 – 0.039 = Weak, 0.04 – 0.044 = Weak – Moderate, 0.045 – 0.059 = Moderate, 0.06 – 0.074 = Moderate – Good, 0.075 – 0.139 = Good, 0.14 – 0.199 = Good – V Good, 0.2 – 0.299 = V Good, 0.30 < = Excellent. ^c DNB = Did Not Bind.

The four PSD-95 PDZ1 binders from the third generation all showed more significant and better defined chemical shift perturbations than the compounds

produced in the second generation. **3a-c** are, in structural terms, reasonably similar to each other with **3b** and **3c** differing only in the length of the alkyl chain prior to the carboxyl group at the 1-position; **3c** has an extra CH₂ c.f. **3b**. The screening by NMR showed that **3b** and **3c** perturbed more residues (and more strongly) upon binding to the PSD-95 PDZ1 domain than **3a**. **3a-c** are also structurally similar to **2b**; **3a** has an alternative group substituted at the 2-position c.f. **2b**; whereas, **3b** and **3c** have an alkylcarboxyl group at the 1-position c.f. **2b**. This shows that substitution of **2b** with a reasonably large amide side chain at the 2-position is not as effective as substitution with an alkylcarboxyl group at the 1-position; this can be concluded as **3b** and **3c** are found to perturb the chemical shifts of PSD-95 PDZ1 residues in greater number and magnitude than **3a**. These results may indicate that substitution at the 1-position of the indole scaffold enables different, potentially more favourable interactions to be formed with other residues in the binding area c.f. the 2-position. It is also possible that the 2-position is a suitable indole position to substitute at with various chemical groups but that the long amide-based side-chain (R₂) of **3a** forms undesirable interactions with surrounding residues; this will obviously reduce the binding potential of **3a** c.f. **3b** & **3c**.

The reason why **3b** has a closer shift sum threshold to **3a** than **3c** may be due to the synthetic route utilised in its production. Our collaborators found it difficult to completely separate the 1-N-unsubstituted form i.e. **2b** from the 1-N-substituted form i.e. **3b** when producing **3b** and so, some of the free NH form (**2b**) was detected in the **3b** sample; this will have meant that the actual PSD-95 PDZ1 : **3b** ratio in the NMR sample was lower than intended. This problem was not encountered in the synthesis of **3c** and so, is a possible explanation for the discrepancy in the chemical shift perturbations induced by **3b** and **3c** upon binding to PSD-95 PDZ1.

3d & **3e** are structurally much simpler than **3a-c**, with **3e** in particular having no large chains at any position of the indole scaffold. **3d**, in addition to no observable PSD-95 PDZ1 binding, also showed no binding to the SAP97 & PSD-95 PDZ2 domains and only weak binding to the SAP97 PDZ1 domain (Appendices, A.16 – A.18). **3d** is structurally similar to **1a**, with the exception that **3d** has an amide side chain at the 2-position, instead of the 2-carboxyl group of **1a**. The lack of observable binding of **3d** to three of the four PDZ domains is interesting as **1a** bound, albeit weakly, to all four of the PDZ domains under investigation. This suggests that the large amide substitution (R_2) has a detrimental effect on the binding of **3d** to PDZ domains, possibly due to steric clashes or unfavourable interactions.

The structure of **3d** is very similar to **3a** also, although **3d** has a 5-methoxy group rather than the 5-benzyloxy group of **3a**. As **3a** bound satisfactorily to all four PDZ domains, this highlights the importance of the 5-benzyloxy group in ‘anchoring’ the small molecule into the binding pocket; probably by the formation of extensive interactions with the hydrophobic residues of the PSD-95 PDZ1 domain. The 5-methoxy group is not able to form these hydrophobic interactions as successfully and hence, this combined with the bulky amine group at the 2-position possibly results in the inability of **3d** to bind to the PSD-95 PDZ1 domain.

3e was shown to exhibit good levels of chemical shift perturbations in the PSD-95 PDZ1 domain, which is reasonably surprising given its simplicity i.e. it is identical to **1a** except for a 5-hydroxy group present in **3e** (**1a** = 5-methoxy group). The observed levels of chemical shift perturbations could be due to **3e** binding to the PSD-95 PDZ1 domain in a number of different orientations in the high small molecule concentrations (10-fold excess) implemented in the binding screening by NMR process. This is a valid hypothesis as **3e** does not have an alkyl chain at the 5-

position and so, has no potential to form hydrophobic interactions with the hydrophobic pocket of the PDZ domain binding region to confer rigidity for a particular bound conformation; it also has four hydrogen bond acceptor/donor groups present (two carboxylic acid groups, one hydroxyl group and one amine group). A combination of these factors could possibly lead to **3e** binding in a number of different orientations and hence, explain the surprising levels of perturbations observed.

The 5- and 1-positions of the indole scaffold had been shown, by the effects of a range of substitutions in the binding screening by NMR of the third generation compounds, to be the regions of greatest impact to binding potential. Hence, the design of the next generation of potential binders focussed on substituting alternative groups at these positions.

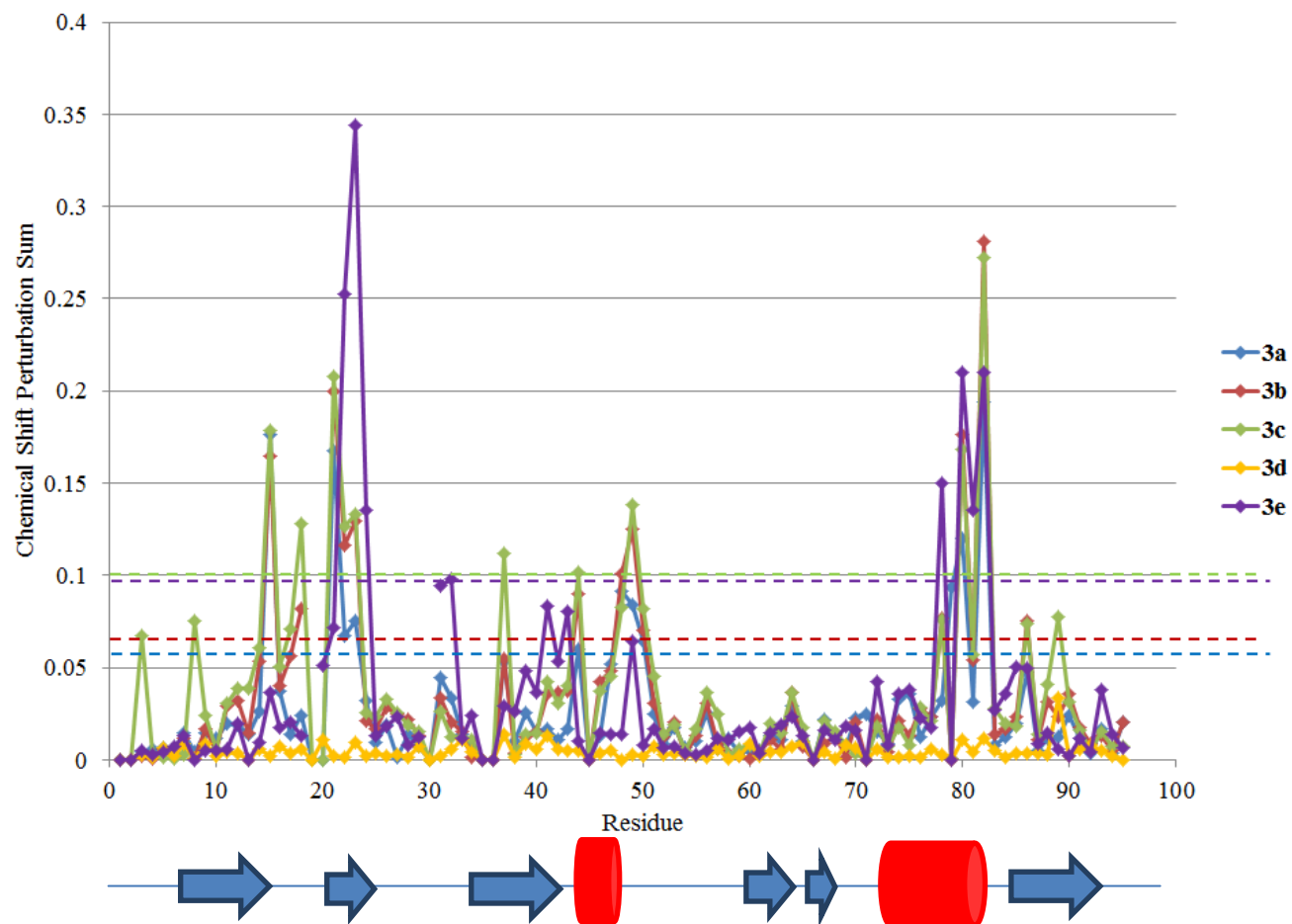


Figure 6.8: A plot of the chemical shift perturbation sum differences between free PSD-95 PDZ1 domain and in the presence of the respective third generation potential PDZ domain binders, with the shift sum threshold values for the individual potential binder has been indicated by a horizontal dashed line in the corresponding colour of the data in the plot. The secondary structure of the PSD-95 PDZ1 domain (blue arrow = β -strand and red cylinder = α -helix) is given below the plot. The plot shows that small molecules **3a-c** and **3e** bound to the PSD-95 PDZ1 domain with **3c** and **3e** being the potential PDZ binders that induced the strongest and most numerous chemical shift perturbations of the third generation compounds; **3d** did not produce any significant chemical shift perturbations and so, was concluded to not to bind to PSD-95 PDZ1.

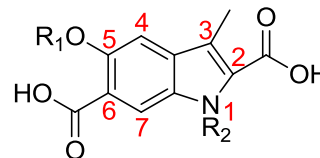
6.2.5 Fourth Generation Compounds

The PDZ domain inhibitor design process then led to the production of three more potential small molecule PDZ domain inhibitors (Figure 6.9).

4a: R₁ = CH₂Ph; R₂ = CH₂CH₂CH₂OH

4b: R₁ = ^{Cy}Pe; R₂ = CH₂CH₂CH₂CO₂H

4c: R₁ = OH; R₂ = CH₂CH₂CH₂CO₂H



4a-c

Figure 6.9: The structures of the fourth generation of potential PSD-95 PDZ1 domain binders, where **4a-c** are small molecule compounds based on the Fujii indole scaffold with chemical group variations of different length/bulk at R₁. (Ph = phenyl i.e. C₆H₅ and ^{Cy}Pe = cyclopentyl i.e. C₅H₉)

All three of the fourth generation compounds bound to the PSD-95 PDZ1 domain, with **4c** showing promising levels of residue chemical shift perturbations of the PDZ domain upon binding (Table 6.5 & Figure 6.10).

Table 6.5: The significant residue chemical shift perturbations induced by the binding of the small molecule compounds **4a-c** to different regions of the PSD-95 PDZ1 domain, along with the corresponding shift sum threshold value.

Ligand	Shift Sum Threshold ^a (ppm)	GLGF Motif & β _C Strand	β _B - β _C Loop	αB Helix	Others	Binding Efficacy ^b
4a	0.025	20G, 21F	/	/	/	Weak
4b	0.08	15G, 18G, 20G, 21F, 22S	26G, 31H	74H, 78V, 81L	43I, 44I, 49A, 50A, 90L	Good
4c	0.20	15G, 18G, 20G, 21F, 22S, 23I, 24A, 25G	26G, 27T, 31H	74H, 78V, 81L	43I, 44I, 49A, 50A, 88V, 90L	V Good ^c

^a The equation used to determine the individual residue chemical shift perturbation sum value was $\Delta d_{\text{ppm}} = \sqrt{((\Delta\delta_{\text{HN}})^2 + (\Delta\delta_{\text{N}} * \alpha_{\text{N}})^2)}$ where, α_{N} = Scaling Factor of 0.17. ^b Binding efficacy was classified using the shift sum threshold value: <0.01 = DNB, 0.01 – 0.019 = VV Weak, 0.02 – 0.024 = V Weak, 0.025 – 0.039 = Weak, 0.04 – 0.044 = Weak – Moderate, 0.045 – 0.059 = Moderate, 0.06 – 0.074 = Moderate – Good, 0.075 – 0.139 = Good, 0.14 – 0.199 = Good – V Good, 0.2 – 0.299 = V Good, 0.30 < = Excellent. ^c V = Very.

4a was designed to see if an 1-alkylhydroxyl group could form a better (or indeed any) interaction with the conserved His residue in the class I PDZ domain of PSD-95 PDZ1 c.f. a 1-alkylcarboxyl group in **3c**. However, this substitution made the compound extremely insoluble in aqueous buffer and sparingly soluble in DMSO-d₆;

the maximum solubility in the aqueous NMR sample in the presence of 0.44% (v/v) DMSO- d_6 was $\sim 100\mu\text{M}$. As a result, even though the binding screening showed that **4a** bound to the PSD-95 PDZ1 domain, the actual concentration of **4a** present in the NMR sample was not the desired 10-fold excess, instead PSD-95 PDZ1 was in slight excess. Thus, it is not possible to directly compare, based on chemical shift perturbations, how well **4a** binds to PSD-95 PDZ1 relative to the other ligands due to the solubility issue incurred. To investigate the effects of the 1-alkylhydroxyl group on PDZ domain binding, alterations would have to be made to the structure of **4a** or of **4a**-like compounds to make them more soluble in aqueous solutions.

4b and **4c** are structurally similar, differing only by the incorporation of 5-cyclopentoxy (5- O^{CyPe}) and 5-hydroxy (5-OH) groups respectively. Of the two compounds, **4c** appeared to bind better; the binding of **4c** to PSD-95 PDZ1 is reminiscent of the native ligand binding, as virtually every residue of the PSD-95 PDZ1 domain is perturbed upon binding (Figure 13). **4c** is an evolution of **3e** with a 1-alkylcarboxyl group added instead of an unsubstituted 1-NH group and the binding screening shows that this addition results in much more extensive chemical shift perturbations of the PSD-95 PDZ1 domain. This implies that substitution of an alkylcarboxyl group at the 1-position of the indole scaffold enables more interactions to be formed between the small molecule and PSD-95 PDZ1 and hence, more chemical shift perturbations produced upon binding. However, as with **3e**, it cannot be ruled out that the lack of an alkyl chain at the 5-position may allow **4c** to bind to the PSD-95 PDZ1 domain in a number of different orientations in the binding region. The multiple binding modes possible could therefore account for the extensive and native ligand-like chemical shift perturbations exhibited by **4c** upon binding to the PSD-95 PDZ1 domain.

4b shows that substitution of the 5-benzyloxy group in **3c** with 5-cyclopentoxy group results in slightly weaker binding to the PSD-95 PDZ1 domain compared to **3c**, suggesting that the cyclopentyl ring of **4b** is not able to form as numerous and/or as strong hydrophobic interactions with the PDZ domain binding pocket than the benzyl group. This could be because the cyclopentyl ring structure is a less suitable structure to fit in the hydrophobic pocket of PSD-95 PDZ1 than the phenyl ring and hence, does not maximise the possible interactions with the surrounding residues as effectively.

The final stage of the binding screening by NMR spectroscopy investigation was to determine the importance of the 6-carboxyl and 3-methyl groups to the binding of the PSD-95 PDZ1 domain; therefore a final generation of inhibitors was designed and synthesised accordingly.

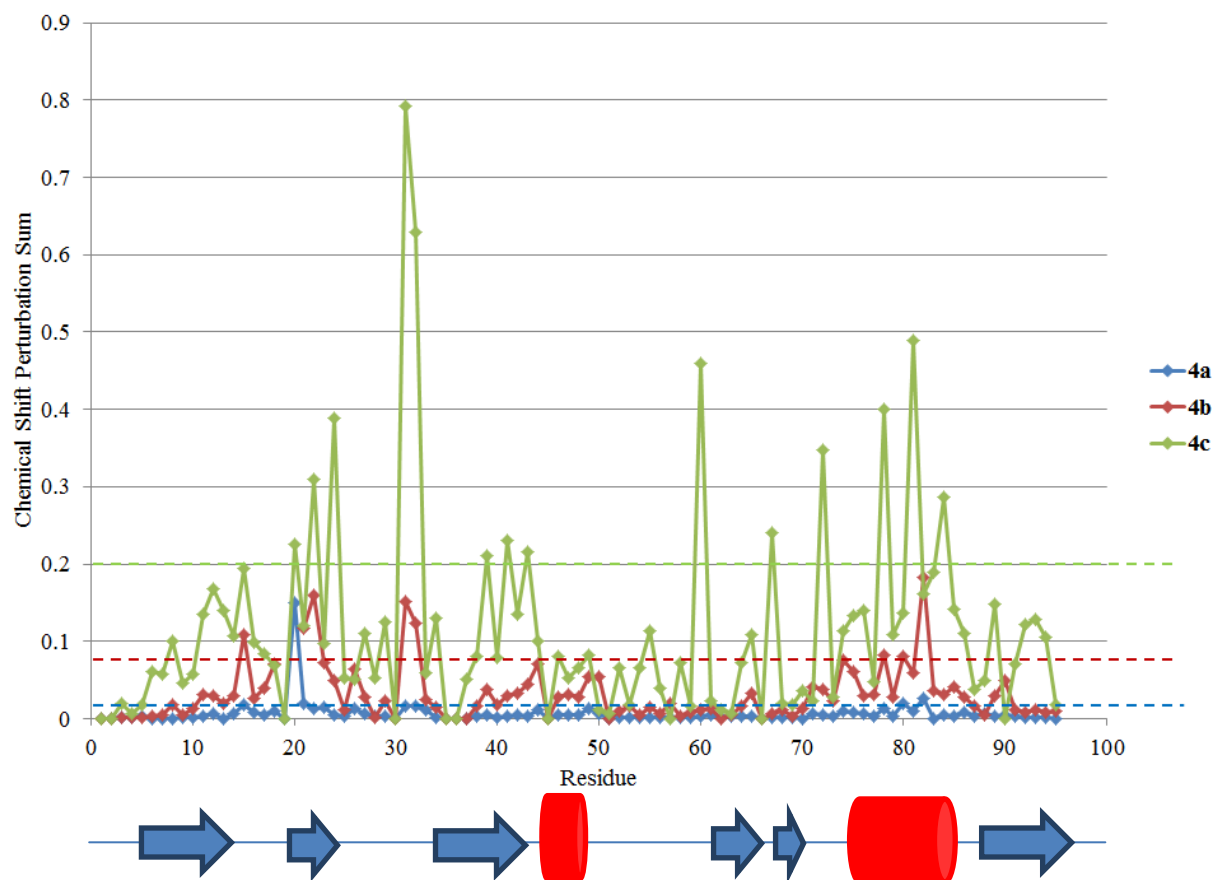


Figure 6.10: A plot of the chemical shift perturbation sum differences between free PSD-95 PDZ1 domain and in the presence of the respective fourth generation potential PDZ domain binders, with the shift sum threshold values for the individual potential binder has been indicated by a horizontal dashed line in the corresponding colour of the data in the plot. The secondary structure of the PSD-95 PDZ1 domain (blue arrow = β -strand and red cylinder = α -helix) is given below the plot. The plot shows that small molecules **4a-c** all bound to the PSD-95 PDZ1 domain with **4c** being the potential PDZ binders that induced the strongest and most numerous chemical shift perturbations of the fourth generation compounds. The limited solubility in aqueous buffer of **4a** meant that, although it was shown to bind to PSD-95 PDZ1, it was not an accurate indication of the actual strength of binding of **4a** relative to that of the other fourth generation compounds.

6.2.6 Fifth Generation Compounds

Three final potential small molecule PDZ domain inhibitors were designed, synthesised and screened for binding to the PSD-95 PDZ1 domain (Figure 6.11).

5a: R₁ = O CH₂Ph; R₂ = H; R₃ = CH₂CH₂CH₂CO₂H; R₄ = CO₂H

5b: R₁ = O CH₂Ph; R₂ = H; R₃ = CH₂CH₂CO₂H; R₄ = H

5c: R₁ = O CH₂Ph; R₂ = Me; R₃ = CH₂CH₂CH₂CO₂H; R₄ = H



5a-c

Figure 6.11: The structures of the fifth generation of potential PSD-95 PDZ1 domain binders, where **5a-c** are small molecule compounds based on the Fujii indole scaffold with chemical group variations of different length/bulk at R₂ and/or R₄. (Ph = phenyl i.e. C₆H₅)

The binding screening by NMR spectroscopy showed that all three compounds bound to the PSD-95 PDZ1 domain, although there was a marked difference between the perturbations induced upon binding of **5a** and those of **5b** & **5c** (Table 6.6 & Figure 6.12); where **5a** was found to bind to PSD-95 PDZ1 much better than **5b** and **5c**.

Table 6.6: The significant residue chemical shift perturbations induced by the binding of the small molecule compounds **5a-c** to different regions of the PSD-95 PDZ1 domain, along with the corresponding shift sum threshold value.

Ligand	Shift Sum Threshold ^a (ppm)	GLGF Motif & β _C Strand	β _B - β _C Loop	αB Helix	Others	Binding Efficacy ^b
5a	0.15	15G, 18G, 20G, 21F, 22S, 23I, 25G	26G, 27T, 31H	72V, 74H, 78V	42K, 44I, 49A, 88V, 90L	Good – V Good ^c
5b	0.04	/	31H, 32I	74H, 78V, 81L	90L	Weak - Moderate
5c	0.03	/	31H, 32I	74H	/	Weak

^a The equation used to determine the individual residue chemical shift perturbation sum value was $\Delta d_{ppm} = \sqrt{((\Delta\delta_{HN})^2 + (\Delta\delta_N * \alpha_N)^2)}$ where, α_N = Scaling Factor of 0.17. ^b Binding efficacy was classified using the shift sum threshold value: <0.01 = DNB, 0.01 – 0.019 = VV Weak, 0.02 – 0.024 = V Weak, 0.025 – 0.039 = Weak, 0.04 – 0.044 = Weak – Moderate, 0.045 – 0.059 = Moderate, 0.06 – 0.074 = Moderate – Good, 0.075 – 0.139 = Good, 0.14 – 0.199 = Good – V Good, 0.2 – 0.299 = V Good, 0.30 < = Excellent. ^c V = Very.

The structure of **5a** is very similar to **3c**, but with the 3-methyl group removed; this alteration indicates that removal is preferential for binding strength as **5a** showed

more extensive chemical shift perturbations than **3c**. Interestingly, this indicates that the presence of the 3-methyl group in **3c** either leads to slightly unfavourable steric clashes or prevents the molecule from interacting as effectively with neighbouring residues in the binding site.

5b has the same structure as **5a** but with the 6-carboxyl group removed. This has a pronounced effect on the residue chemical shift perturbations induced upon binding to the PSD-95 PDZ1 domain and hence, the binding affinity of **5b**; based on chemical shift perturbations, the PSD-95 PDZ1 binding of **5b** is much weaker **5a**. This was as expected because as the ability to form a 6-CO₂H – GLGF hydrogen bond has been removed and so, the binding of **5b** to the PSD-95 PDZ1 domain relies mainly upon the hydrophobic interactions between the 5-benzyloxy group and the residues of the binding pocket; thus, less PSD-95 PDZ1 residues will be perturbed. It is possible that the molecule could ‘flip’ its binding orientation and form a 2-CO₂H – GLGF hydrogen bond but this is likely to be more unfavourable due to steric clashes of the 1-alkylcarboxyl group with the surrounding residues of the PSD-95 PDZ1 domain.

5c is a variation on the structure of **5b** with an additional 3-methyl group and **5c** and was shown to bind to PSD-95 PDZ1 less effectively than **5b** as **5c** induced less chemical shift perturbations in the PSD-95 PDZ1 domain c.f. **5b**. This again suggests that the presence of a 3-methyl group has a detrimental effect on binding, which is consistent with the trend in binding affinity observed between **3c** and **5a**. This can again be attributed to the same reasons described previously.

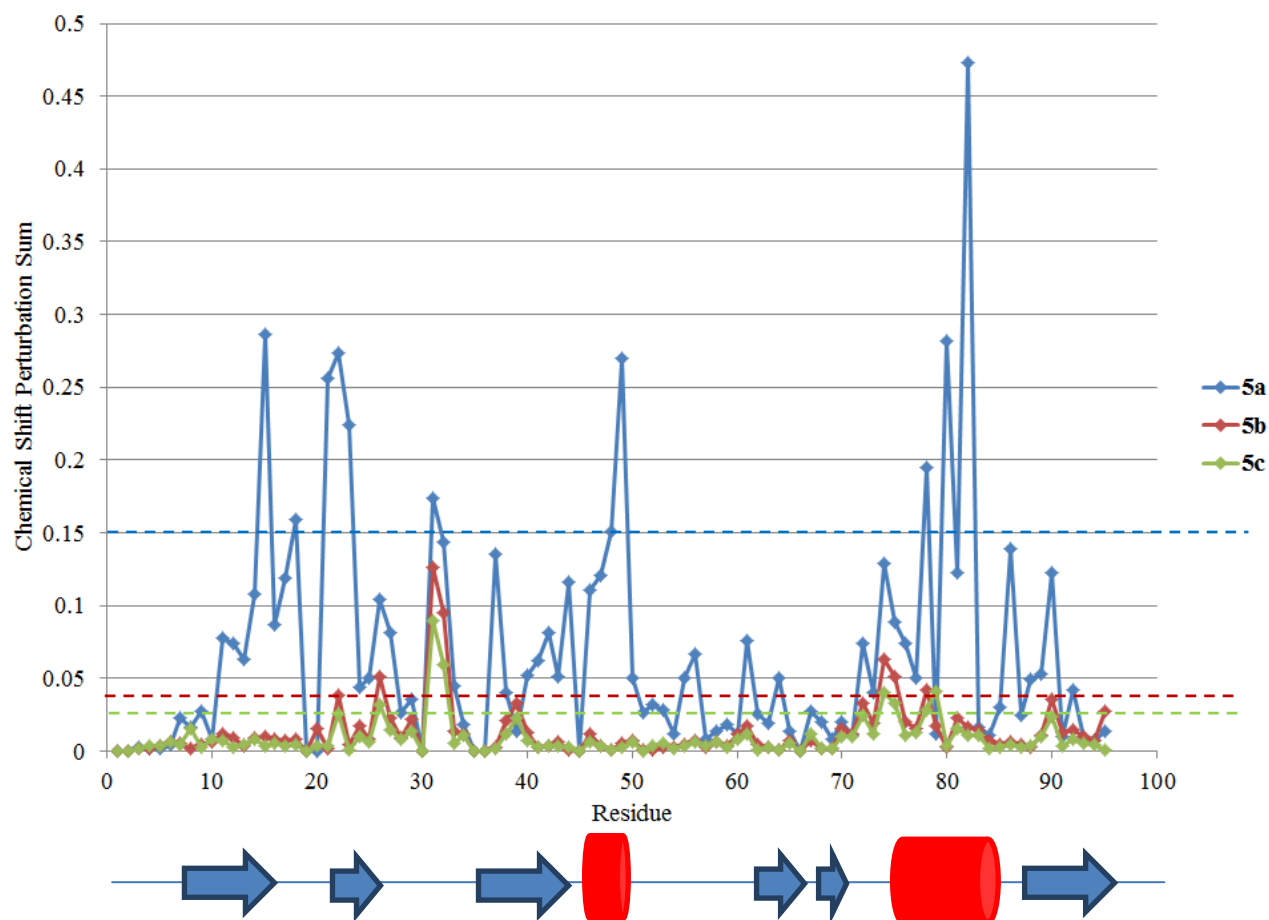


Figure 6.12: A plot of the chemical shift perturbation sum differences between free PSD-95 PDZ1 domain and in the presence of the respective fifth generation potential PDZ domain binders, with the shift sum threshold values for the individual potential binder has been indicated by a horizontal dashed line in the corresponding colour of the data in the plot. The secondary structure of the PSD-95 PDZ1 domain (blue arrow = β -strand and red cylinder = α -helix) is given below the plot. The plot shows that small molecules **5a-c** all bound to the PSD-95 PDZ1 domain with **5a** being the potential PDZ binders that induced the strongest and most numerous chemical shift perturbations of the fifth generation compounds. The reduced perturbations of **5b** and **5c** upon binding c.f.**5a** indicate the importance of the 6-CO₂H group to PSD-95 PDZ1 binding affinity.

6.2.7 Summary of Ligand Binding Screening by NMR Spectroscopy

A number of different small organic molecules have been designed and synthesised. These compounds started from relatively simple organic molecules and got increasingly more complex and substituted as the inhibitor development process progressed (Figure 6.13).

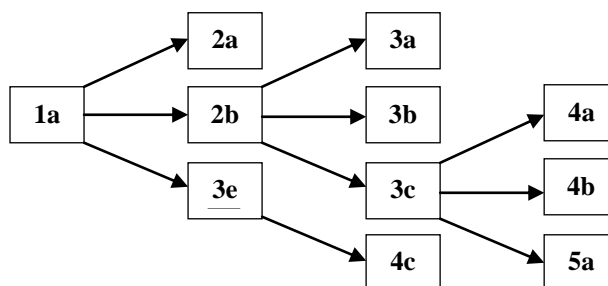


Figure 6.13: The figure shows the evolution of the potential PSD-95 PDZ1 domain binders from the initial lead compound from the first generation of compounds – **1a**. It can be seen that **2b** and **3c** were the structures in their respective binder design iteration that were used as templates for the subsequent generation of potential binders. It is interesting to note that the two strongest PSD-95 PDZ1 binders (**4c** and **5a**) do not share similar development processes and this is reflected in the relative complexity of their structures.

The binding affinity, as assessed by the number and magnitude of chemical shift perturbations induced, of the small molecule compounds to the PSD-95 PDZ1 domain was shown to increase substantially from the early to late development stages (Figure 6.14). A large number of the synthesised potential inhibitors showed binding to the PSD-95 PDZ1 domain, with **4c** and **5a** showing levels of residue chemical shift perturbations approaching that of the native PSD-95 PDZ1 ligand, the 5-HT_{2c} receptor.

There was a number of important PDZ domain inhibitor design points discovered during the ligand binding screening by NMR spectroscopy process:

- The most suitable organic scaffold to build a PDZ domain inhibitor upon was found to be an indole structure.
- An indole 6-carboxyl group is extremely important for binding.

- An extended alkyl chain at the indole 5-position helps to confine the small molecule inhibitor to bind in the desired orientation/conformation.
- The indole 1-position is a more effective position to substitute at than the indole 2-position to improve binding affinity.
- Any chemical group substitution at the indole 3-position other than a hydrogen may be detrimental to binding affinity.

The next stage in the development of novel small molecule inhibitors of the PSD-95 PDZ1 – 5-HT_{2c} interaction was to determine the actual strength of binding of a number of the small molecules to PSD-95 PDZ1. This was done using two different biophysical methods – NMR Spectroscopy and isothermal titration calorimetry (ITC).

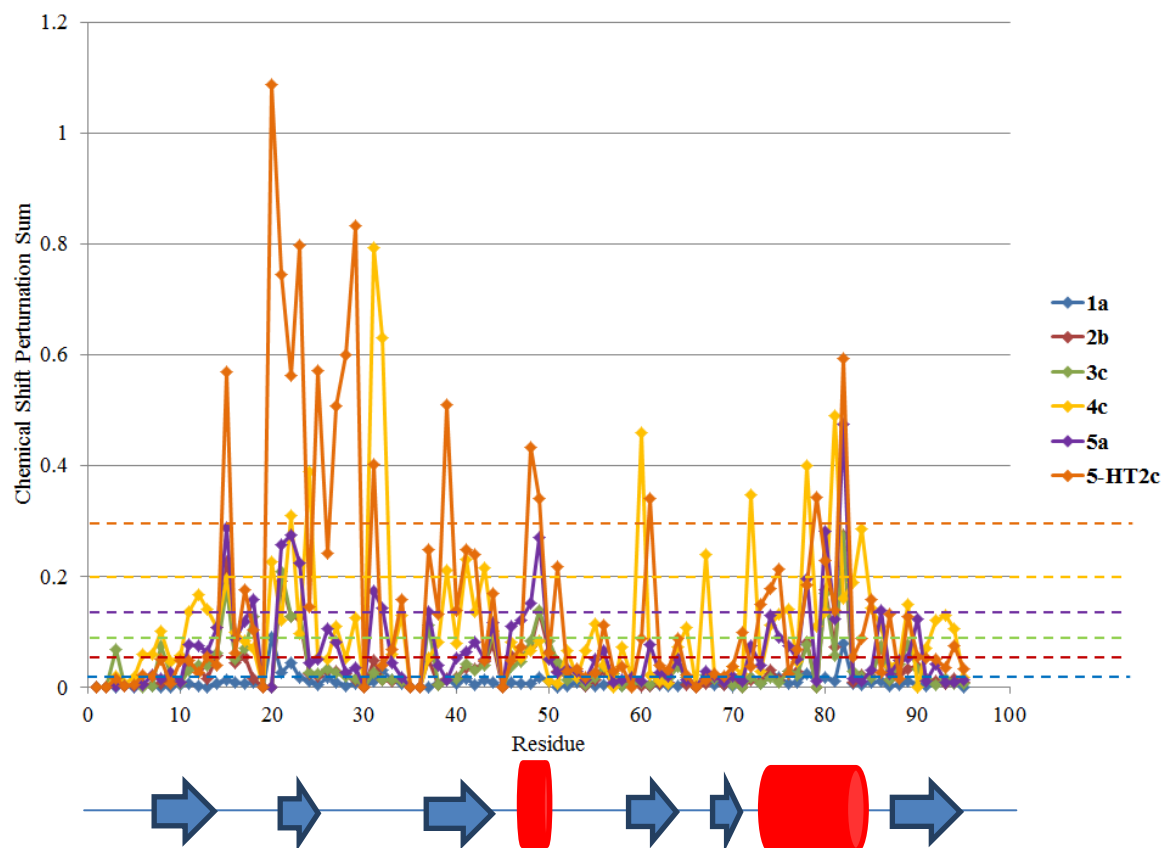


Figure 6.14: A plot of the chemical shift perturbation sum differences between free PSD-95 PDZ1 domain and in the presence of the best binder in each of the five generations of compounds tested in the PSD-95 PDZ1 domain inhibitor development process and the C-terminal peptide of the 5-HT_{2c} receptor, with the shift sum threshold values for the individual potential binder has been indicated by a horizontal dashed line in the corresponding colour of the data in the plot. The secondary structure of the PSD-95 PDZ1 domain (blue arrow = β -strand and red cylinder = α -helix) is given below the plot. The plot and the threshold values show how the binding affinity has progressed from the initial low values of the lead compound **1a** to the high levels of chemical shift perturbations produced by binders **4c** and **5a**. It can be seen that binding of the **4c** to the PSD-95 PDZ1 domain induces perturbations of practically all the PSD-95 PDZ1 domain residues in a similar manner that the 5-HT_{2c} peptide does and that **5a** binding shows a similar profile of individual residue perturbations to the native ligand, although to a lesser extent in terms of magnitude.

6.3 Binding Affinity Determination by NMR Spectroscopy

6.3.1 General

The experimental conditions and the procedure employed to analyse the resultant data from the binding affinity determination of **3c** and **4c** to the PSD-95 PDZ1 domain by NMR spectroscopy discussed in this chapter are described in [3.3.5].

6.3.2 PSD-95 PDZ1 – **3c** K_D Determination

The NMR experiments were first carried out on ^{15}N PSD-95 PDZ1 in the absence and presence of up-to 30-fold excess of **3c** (Figure 6.16); the data obtained was used to determine how strongly **3c** bound to the PSD-95 PDZ1 domain. Analysis of this data yielded a PSD-95 PDZ1 K_D of 2.355mM (Table 6.7 & Figure 6.15) and indicates that **3c** binds to the PSD-95 PDZ1 domain with an affinity of over two orders of magnitude weaker than the 5-HT_{2c} receptor (K_D (determined by ITC [4.5.3]) = 19.95 μM); the native PSD-95 PDZ1 ligand. This difference in the **3c** PSD-95 PDZ1 K_D value to the native ligand was not unexpected as the binding screening had indicated that compared to native ligand binding, the extent and magnitude of the chemical shift perturbations induced by **3c** in the PSD-95 PDZ1 domain were both fewer and of weaker magnitude.

As well as being able to calculate the binding affinity of **3c** to the PSD-95 PDZ1 domain using this NMR experimental methodology, it is also possible to gain an insight into how **3c** binds to the PDZ domain. This is achieved by analysing the residue chemical shifts perturbed at each concentration point compared to the reference spectrum and how strongly these residues are perturbed overall (Table 6.8).

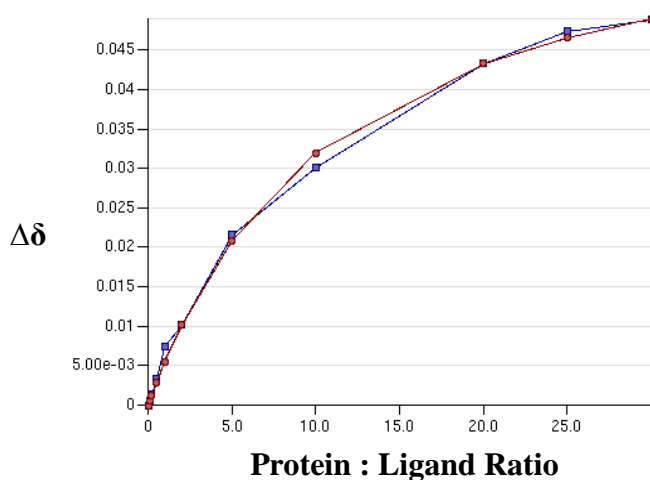


Figure 6.15: The fit curve produced for Val88 of PSD-95 PDZ1 over the course of the **3c** concentration titration (blue) and the corresponding fitting function (magenta). This particular residue shows very good agreement between the experimental and fitting function values and hence, was used in the K_D value determination process.

Table 6.7: The K_D measured for the ten residues of the PSD-95 PDZ1 domain that best fitted the fitting function during the NMR titration with **3c** and hence, were used in the determination of the binding affinity of **3c** to PSD-95 PDZ1.

Residue	K_D (mM)
15Gly	2.498
21Phe	2.38
49Ala	2.495
50Ala	2.712
53Gly	2.342
71Glu	2.899
80Ala	1.693
82Lys	2.497
86Ser	2.191
88Val	1.841
Average =	2.355mM

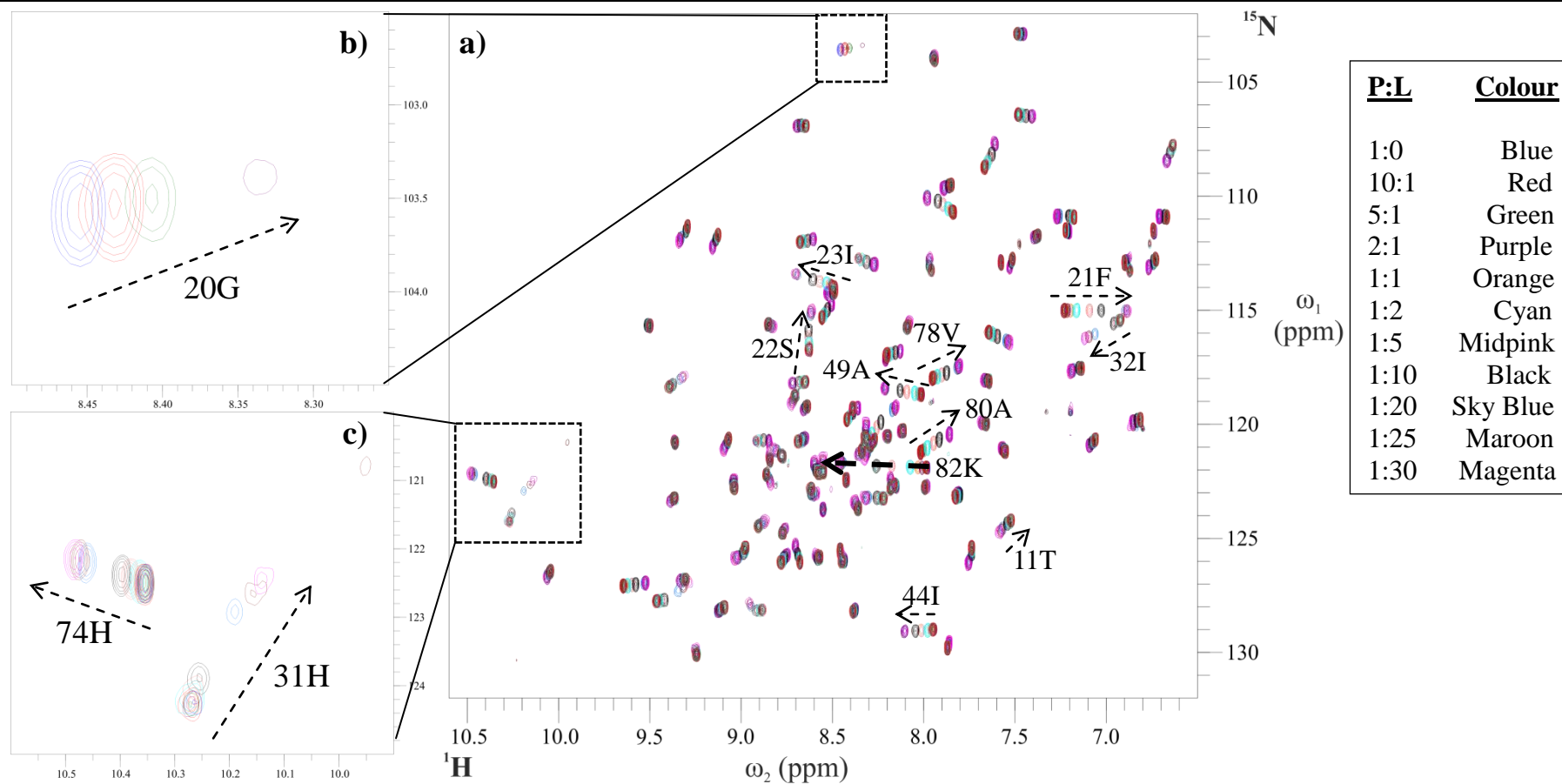


Figure 6.16: a) An overlay of the ^1H - ^{15}N HSQC experiments of ^{15}N PSD-95 PDZ1 in the presence of **3c** (P:L = 1:0-1:30, acquired at 298K, with a field strength of 600MHz, in 20mM phosphate 0.1mM EDTA buffer, pH6.3); where the colour of the spectrum corresponding to each titration point is given in the table to the right. A number of the important residues and/or largest perturbations have been labelled, along with the direction of the shift over the course of the titration. b) An enlarged view of the peak corresponding to Gly20 over the titration; it can be seen how the peak intensity shifts and decreases from P:L = 1:0 – 2:1 and then disappears from 1:1 onwards. c) An enlarged view of the peaks corresponding to the 31His and 74His in the titration.

Table 6.8: The individual residues of the PSD-95 PDZ1 domain that are perturbed at the different **3c** concentrations. Those residues highlighted in red are those that showed the most pronounced shift perturbations over the series of titrations.

PSD-95 PDZ1 – 3c Ratio	Residue(s) Perturbed
1:0	/
10:1	20G
5:1	/
2:1	21F, 49A, 80A, 82K
1:1	15G, 22S, 23I, 44I, 78V, 81L
1:2	18G, 46G, 47G, 71E, 86S
1:5	11T, 16N, 26G, 31H, 32I, 48A, 50A, 74H , 77A, 84A, 88V, 90L
1:10	24A, 25G, 27T, 41T, 61I, 64V, 75S, 89R, 92V, 94R
1:20	25G, 29N, 38I, 40I, 53G, 65N, 76A, 84A

The titration indicates that even at a 10-fold excess of protein, **3c** appears to target the GLGF motif (Gly20 indicated in bold) as desired and is able to show a perturbation in the chemical shift of Gly20. A number of residues in the binding region of the PSD-95 PDZ1 domain show perturbations at **3c** concentrations of equimolar or less; suggesting that the compound binds in a conformation and orientation to form numerous interactions with surrounding residues. The Gly20 peak disappears from the spectrum from equimolar concentrations onwards, which suggests the residue is in intermediate exchange between unbound and **3c** bound states; this has caused attenuation of the peak to occur. By 10-fold excess of **3c**, all the key residues in the binding domain showed perturbations and by 20-fold excess, over 50% of the PSD-95 PDZ1 domain residues showed perturbations. At 30-fold excess, the residue perturbations had ceased, suggesting that the PSD-95 PDZ1 domain had reached saturation level of **3c**.

6.3.3 PSD-95 PDZ1 – **4c** K_D Determination

A second series of NMR experiments were carried out on ^{15}N PSD-95 PDZ1 in the absence and presence of up-to 30-fold excess of **4c** (Figure 6.19). This data was used to determine how strongly **4c** bound to the PSD-95 PDZ1 domain and yielded a K_D of 1.177mM (Table 6.9 & Figure 6.17). Therefore, **4c** apparently binds to the PSD-95 PDZ1 domain with an affinity of under 1.5 orders of magnitude weaker than the 5-HT_{2c} receptor. Given that the NMR binding screening results displayed that **4c** showed similar residue chemical shift perturbations to 5-HT_{2c}, this K_D value is somewhat surprising. It is possible that **4c** binds heterogeneously to the PSD-95 PDZ1 domain, via a number of different orientations and conformations at higher **4c** concentrations or that determination of K_D by NMR spectroscopy may not be the most suitable or accurate method; this could be due to solubility effects or limited accessibility of the saturated state.

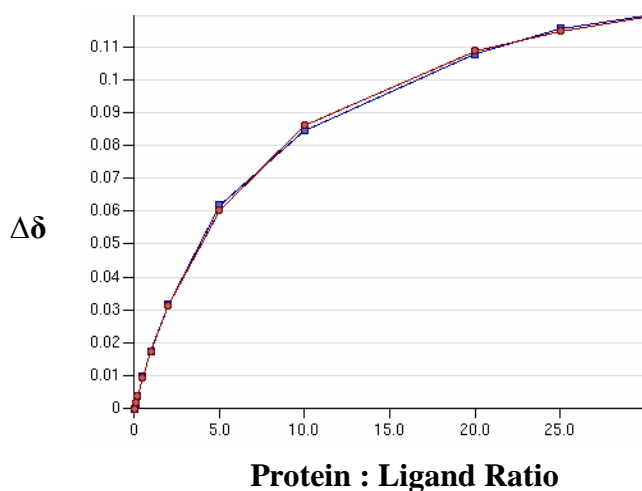


Figure 6.17: The fit curve produced for Gly85 of PSD-95 PDZ1 over the course of the **4c** concentration titration (blue) and the corresponding fitting function (magenta). This particular residue shows very good agreement between the experimental and fitting function values and hence, was used in the K_D value determination process.

4c was calculated to have a K_D of 348 μM to SAP97 PDZ1 (Figure 6.18) by the same NMR methodology and this appears to be a better approximation of the PDZ domain binding ability of **4c**, given the binding screening results. This result indicates a level

of PDZ domain specificity of **4c**, this had been initially indicated in the NMR binding screening as **4c** had shown more substantial chemical shift perturbations when binding to the SAP97 PDZ1 domain c.f. PSD-95 PDZ1 (Appendices, A.19).

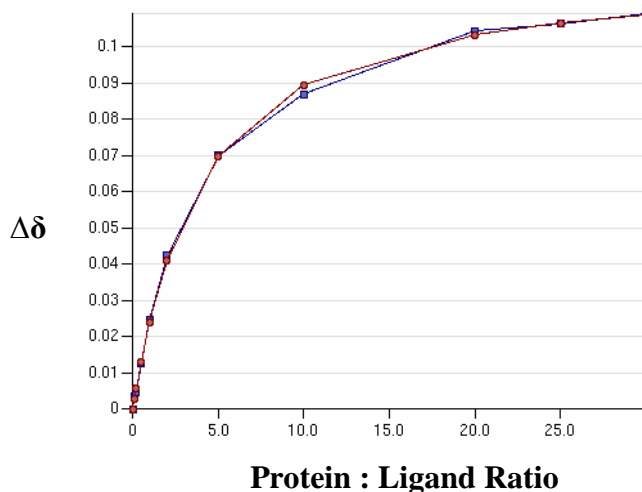


Figure 6.18: The fit curve produced for Lys43 of SAP97 PDZ1 over the course of the **4c** concentration titration (blue) and the corresponding fitting function (magenta). This particular residue shows very good agreement between the experimental and fitting function values and hence, was used in the K_D value determination process.

Table 6.9: The K_D of the 10 residues of the PSD-95 PDZ1 domain that best fitted the fitting function best during the NMR titration with **4c** and hence, were used in the determination of the binding affinity of **4c** to PSD-95 PDZ1.

Residue	K_D (mM)
20Gly	1.191
24Ala	1.341
42Lys	1.454
43Ile	1.129
46Gly	0.935
48Ala	0.846
49Ala	1.346
80Ala	1.124
85Gly	1.178
86Ser	1.222
Average =	1.177mM

Analysis of the residues perturbed at low concentration of **4c** i.e. 5-fold excess of PSD-95 PDZ1 indicates that **4c** binds in the binding region as desired (Table 6.10). However, unlike **3c**, it does not perturb residues of the GLGF motif until equimolar

concentrations and the Gly20 peak, although shifted, remains unattenuated throughout the titration. This means that 20Gly is not going into intermediate exchange upon binding to **4c** unlike **3c**, suggestive of a difference in the binding nature of the two molecules. By 5-fold of excess of **4c**, 50% of the PSD-95 PDZ1 domain residues showed perturbations and by 10-fold excess, there was uniform residue perturbation.

Table 6.10: The individual residues of the PSD-95 PDZ1 domain that are perturbed at the different **4c** concentrations. Those residues highlighted in red are those that showed the most pronounced shift perturbations over the series of titrations.

PSD-95 PDZ1 – 3c Ratio	Residue(s) Perturbed
1:0	/
10:1	/
5:1	22S, 23I, 80A, 81L, 82K
2:1	24A, 31H, 49A, 78V, 82K, 84A
1:1	15G, 16N, 20G, 32I, 84A
1:2	21F, 41T , 42K, 43I, 44I , 48A, 83E, 85G
1:5	12L, 14R, 18G, 27T, 38I, 39F, 40I, 46G, 47G, 61I, 64V, 72V, 74H, 75S, 76A, 88V, 89R, 90L
1:10	All other residues

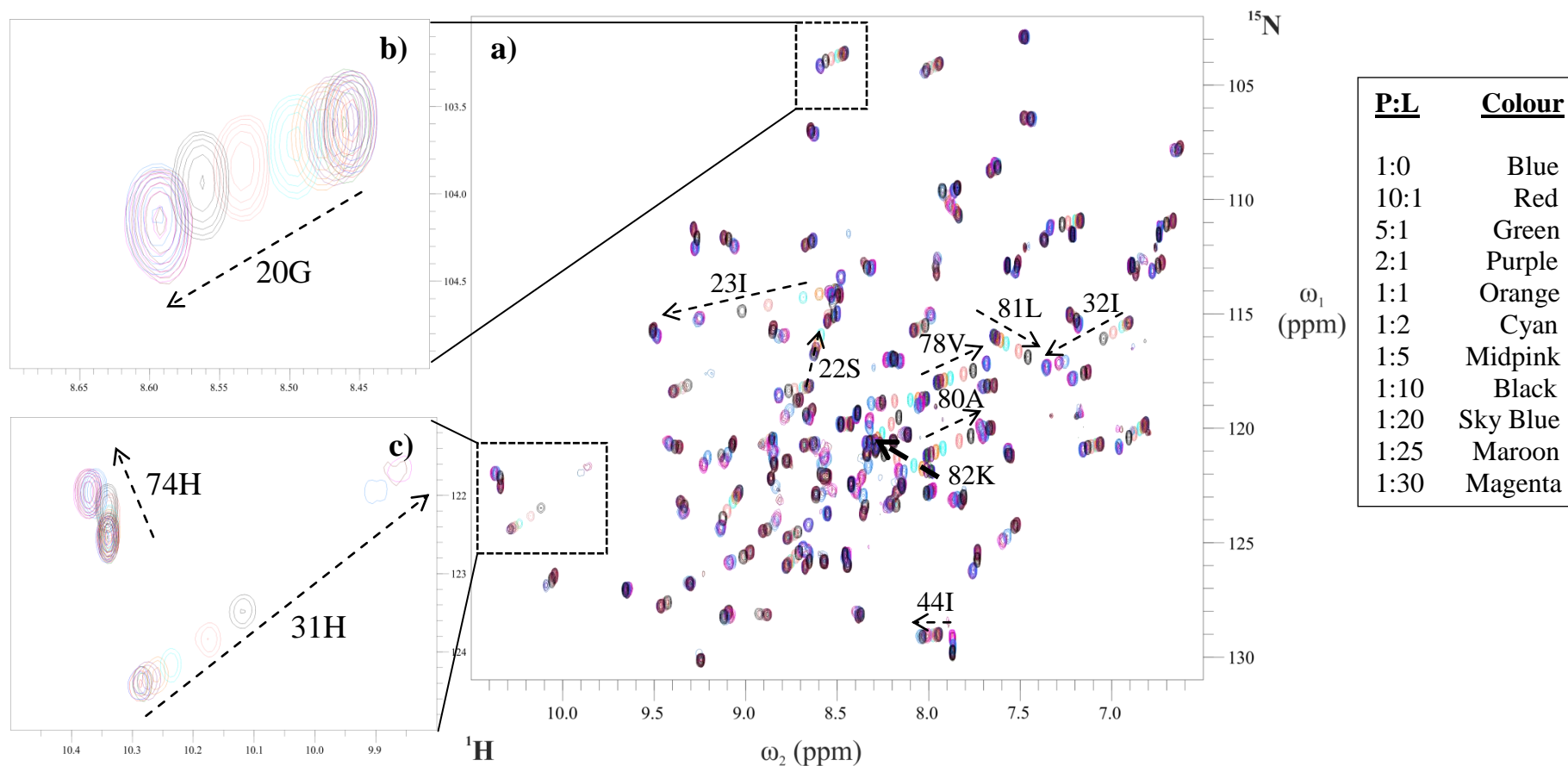


Figure 6.19: a) An overlay of the ^1H - ^{15}N HSQC experiments of ^{15}N PSD-95 PDZ1 in the presence of **4c** (P:L = 1:0 = 1:30, acquired at 298K, with a field strength of 600MHz, in 20mM phosphate 0.1mM EDTA buffer, pH6.3); where the colour of the spectrum corresponding to each titration point is given in the table to the right. A number of the important residues and/or largest perturbations have been labelled, along with the direction of the shift over the course of the titration. b) An enlarged view of the peak corresponding to Gly20 over the titration; it can be seen how the peak shifts across the course of the titration but in the opposite direction and does not disappear c.f. **3c** (Figure 6.16). c) An enlarged view of the peaks corresponding to the 31His and 74His in the titration.

6.3.4 Discussion

Determination of the binding affinity of **3c** and **4c** to the PSD-95 PDZ1 domain by NMR spectroscopy shows that **4c** binds the PDZ domain more strongly than **3c**, which is consistent with the initial NMR chemical shift perturbation data. The determined PSD-95 PDZ1 K_D values with the various small molecules were slightly weaker than expected, especially in the case of **4c**; this was based upon initial docking statistics and the levels of chemical shift perturbations induced in the NMR binding screening. Therefore, it was important to verify the binding constant of **3c** and **4c** to PSD-95 PDZ1 using another biophysical technique, such as isothermal titration calorimetry (ITC).

6.4 Binding Affinity Determination by Isothermal Titration Calorimetry

6.4.1 General

Determination of a direct binding affinity value (K_D) between the PSD-95 PDZ1 domain and either **3c** or **4c** by ITC was unsuccessful, due to the weak binding of the small molecule binders; therefore, an indirect measurement was used. This was done by determining the inhibitory constant value (K_i). To determine the K_i value for **3c** or **4c**, titrations of the native PSD-95 PDZ1 interaction were required in the absence and presence of (and thus, in competition with), the potential inhibitor under investigation. This process also indicated if (and to what extent) the PDZ domain binders were able to disrupt the native PSD-95 PDZ1 – 5-HT_{2c} interaction.

The experimental conditions and the procedure employed to analyse the resultant data obtained from the inhibitory constant determination of **3c** and **4c** for the PSD-95 PDZ1 - 5-HT_{2c} interaction by ITC discussed in this chapter are described in [3.4.1] and [3.4.3].

6.4.2 Competition Experiments with **3c**

Two ITC experiments were carried out between 100 μ M PSD-95 PDZ1 and 750 μ M 5-HT_{2c} with **3c** present in both samples at a protein : **3c** ratio of 1:10 and 1:25 (1mM or 2.5mM ligand respectively, Appendices, A.20). The resultant ITC curves were overlaid with the native interaction ITC curve (Figure 6.20a) and the resultant K_D^{app} , along with the native K_D , values were plotted against ligand concentration to determine K_i (Figure 6.20b).

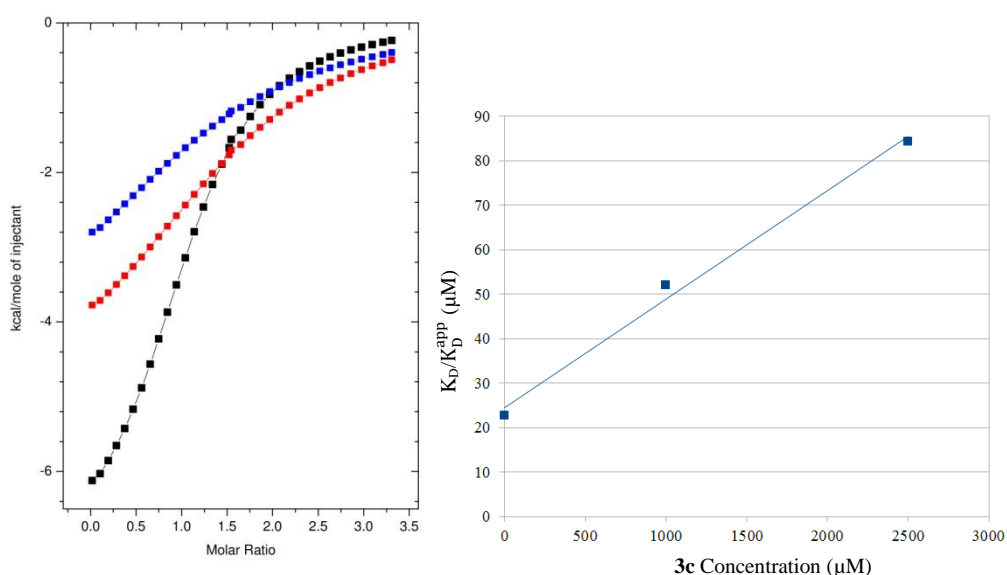


Figure 6.20: (a) Overlay of PSD-95 PDZ1 – 5HT_{2c} ITC titration curves in the absence (black) and presence of **3c** at PDZ : **3c** ratio of 1:10 (red) and 1:25 (blue). As the concentration of **3c** increases, the binding curve gradient becomes shallower indicating weaker binding i.e. an inhibitory effect. (b) The plot of resultant K_D/K_D^{app} values used in the equation $K_D^{app} = K_D + \frac{K_D}{K_i} [L]$, to give a K_i for **3c** of 932 μ M.

The competition experiments carried out by ITC with **3c** resulted in a K_i value of 932 μ M for the PSD-95 PDZ1 – 5-HT_{2c} interaction. This shows that **3c** is able to exert an inhibitory effect on the native interaction of the PSD-95 PDZ1 domain albeit reasonably weakly, by reversibly binding to PSD-95 PDZ1.

6.4.3 Competition Experiments with **4c**

Three ITC experiments were carried out between 100 μ M PSD-95 PDZ1 and 750 μ M 5-HT_{2c} with **4c** present in both samples at either a protein : **4c** ratio of 1:2.5, 1:5 or

1:7.5 (250 μ M, 500 μ M or 750 μ M ligand respectively, Appendices, A.21). The resultant ITC curves were overlaid with the native interaction ITC curve (Figure 6.21a) and the resultant K_D^{app} , along with the native K_D , values were plotted against ligand concentration to determine K_i (Figure 6.21b).

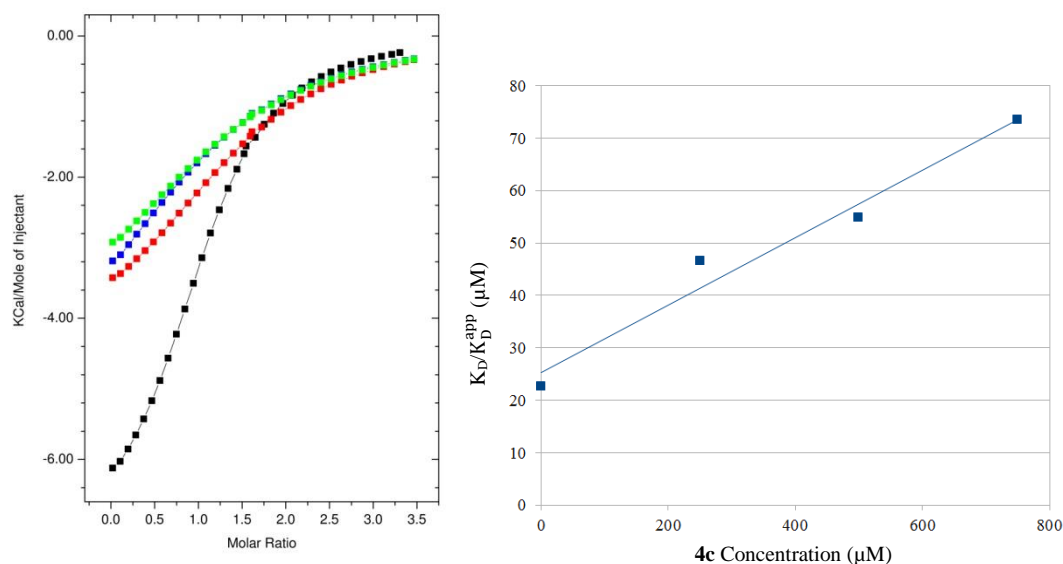


Figure 6.17: (a) Overlay of PSD-95 PDZ1 – 5HT_{2c} ITC titration curves in the absence (black) and presence of **4c** at PDZ : **4c** ratio of 1:2.5 (red), 1:5 (blue) and 1:7.5 (green). As the concentration of **4c** increases, the binding curve gradient becomes shallower indicating weaker binding i.e. an inhibitory effect. (b) The plot of resultant K_D/K_D^{app} values used in equation $K_D^{app} = K_D + \frac{K_D}{K_i} [L]$, to give a K_i for **4c** of 353 μ M.

The competition experiments carried out by ITC with **4c** resulted in an inhibitory constant value of 353 μ M for the PSD-95 PDZ1 – 5-HT_{2c} interaction. This shows that **4c**, like **3c**, is able to exert a reasonably satisfactory inhibitory effect on the native interaction of the PSD-95 PDZ1 domain, by reversibly binding to PSD-95 PDZ1. The lower K_i value for **4c** than **3c** indicates that **4c** has more of an inhibitory effect on the PSD-95 PDZ1 – 5-HT_{2c} interaction than **3c**; which is again consistent with the previous results of the NMR binding screening and K_D determination by NMR spectroscopy.

6.5 Comparison of K_D and K_i

Comparison of the K_D and K_i values for **3c** and **4c** shows that the two values differ, with K_i being consistently lower than K_D (Table 6.11); however, both methods

consistently indicate that **3c** binds more weakly to PSD-95 PDZ1 than **4c**. The reason for these observed differences could be due to the inherent differences in the two biophysical techniques.

Table 6.11: A comparison of the binding affinities of the small molecule binders **3c** and **4c** with the PSD-95 PDZ1 domain determined by NMR spectroscopy and ITC

Inhibitor	K_D	K_i
3c	2.355mM	930 μ M
4c	1.177mM	353 μ M

For the NMR titration to yield reliable K_D values, the system should be in a very fast exchange regime; deviation from this leads to errors in the determination of K_D values. Furthermore, the K_D value determined by NMR spectroscopy is specific for the PSD-95 PDZ1 domain itself regardless of the various different ligands that it may interact with naturally; it is a measure of how strongly **3c** or **4c** bind to the PDZ domain. Whereas, the K_i value is specific solely to the PSD-95 PDZ1 – 5-HT_{2c} interaction; it is a measure of how strongly **3c** or **4c** disrupts this particular interaction and hence, could vary reasonably significantly from one PSD-95 PDZ1 domain interaction to the next.

In terms of the respective experimental procedures, the determination of binding affinity by NMR uses higher protein and ligand concentrations than the ITC methodology. In addition, the process of tracking individual residue chemical shifts quantitatively and then using these in a fitting function has a number of sources of possible of error and inaccuracy. The ITC titrations themselves have been shown to be more precise; thus, a combination of the described technical differences could have led to the variation in constant values determined for **3c** and **4c**. It can be concluded that although, the constants K_D and K_i values are not directly comparable, they can be used in conjunction with each other to give an idea of the binding efficacy of small molecule inhibitor **3c** and **4c** to the PSD-95 PDZ1 domain.

It was important to determine the structure of the PSD-95 PDZ1 domain bound separately to both **3c** and **4c**, to get an accurate idea of the various intermolecular interactions that were occurring in each PDZ domain – small molecule complex. This information could then be used to direct future research in PSD-95 PDZ1 domain inhibition or even PDZ domain inhibition research in general.

6.6 PDZ Domain – Small Molecule Complex Structure Determination by NMR Restraint-Driven Docking

6.6.1 General

Due to the weak binding of the small molecules, it was not possible to obtain a structure of the PSD-95 PDZ1 domain bound to either **3c** or **4c** by crystallographic or NMR spectroscopy methods, the High Ambiguity Driven DOCKing program webserver (HADDOCK) (Dominguez et al., 2003, van Dijk et al., 2006, De Vries et al., 2010) on the e-NMR grid (*) was utilised. HADDOCK was the chosen docking methodology as it has performed extremely well in the critical assessment of predicted interactions (CAPRI) experiments (van Dijk et al., 2005, De Vries et al., 2007) and because this docking methodology allows the incorporation of experimentally-derived parameters, such as distance restraints determined by NMR spectroscopic experiments, to drive the docking protocol.

To determine the distance restraints for the particular PSD-95 PDZ1 – small molecule complex by NMR spectroscopy, the desired NMR sample was prepared and the experimental procedure carried out as described in [3.3.3] and [3.3.5] respectively. The HADDOCK methodology utilised for the restraint-driven docking of the PSD-95 PDZ1 domain in complex with the particular small molecule inhibitor is detailed in [3.5.5].

6.6.2 PSD-95 PDZ1 – **3c** Complex Structure Determination

The NMR experiments were performed on the prepared PSD-95 PDZ1 – **3c** complex sample and the resultant intra-ligand and intermolecular interactions obtained were assigned to the respective protein and ligand atoms, as previously described [3.5.5] (Figure 6.22 & Appendices, A.7).

The intra-ligand and intermolecular distance restraints were incorporated into the HADDOCK docking procedure, along with the docking options that were found to be the most suitable [Table 3.6, 3.5.5]. The output of the distance restraint-driven docking gave seven different possible clusters of structures of the PSD-95 PDZ1 domain in a bound complex with **3c** (Figure 6.23a & b). An ensemble of the 20 lowest HADDOCK scoring structures from the lowest HADDOCK scoring cluster was created (Figure 6.23c) and the structure with the lowest HADDOCK score of these was taken as the representative structure of the PSD-95 PDZ1 – **3c** complex (Figure 6.23d-f). It can be seen that the complexes from the top three clusters produced from the HADDOCK docking process are very similar structurally and these account for over 180 of the 200 final solvent refined structures. There is some deviation observed in the docked conformation of **3c** in the other four clusters c.f. the representative cluster; however these are of limited number and are a consequence of the cluster analysis method. The calculated structure of the complex formed between PSD-95 PDZ1 and **3c** highlights a number of important details that could explain:

- a) Why **3c** is able to bind to the PSD-95 PDZ1 domain
- b) Why **3c** is not able to bind with greater affinity to the PSD-95 PDZ1 domain

The obtained structure shows that the 6-carboxyl group of **3c** forms a hydrogen bond with the backbone NH of the 19L residue of the GLGF motif, as the native ligand does. Such is the power of the rigid body docking algorithm, that the HADDOCK

webservice was able to model this interaction even without any hydrogen bond restraints being placed in the docking parameter set. As mentioned in [3.5.5], when hydrogen bond restraints were added to the run parameters, there was very little difference in the resultant structures obtained; as there was no need to artificially bias the docking process, the hydrogen bond restraints were not included in the docking protocol. There are also hydrophobic interactions present in the representative structure between the 5-benzyloxy group and the residues that form the hydrophobic binding pocket including Val78 and Leu81. These hydrophobic interactions were thought to be crucial in allowing **3c** to bind to the PSD-95 PDZ1 domain in the NMR binding screening process and this has been corroborated by the representative structure obtained from the HADDOCK webservice.

Conversely, the bound complex structure indicates that the presence of a 3-methyl group on **3c** could be causing unfavourable steric clashes with the Gly20 and Phe21 residues in the GLGF motif of PSD-95 PDZ1; this indicates that the rationale behind the description as to why **5a** binds to the PSD-95 PDZ1 domain more tightly than **3c**, may have been correct. Also, from the representative structure, there is no evidence of the 1-alkylcarboxyl group forming any intermolecular interactions with the PSD-95 PDZ1 domain and so, may in fact, be detrimental to binding affinity by causing unfavourable steric clashes or electrostatic repulsion (Figure 6.23d-f).

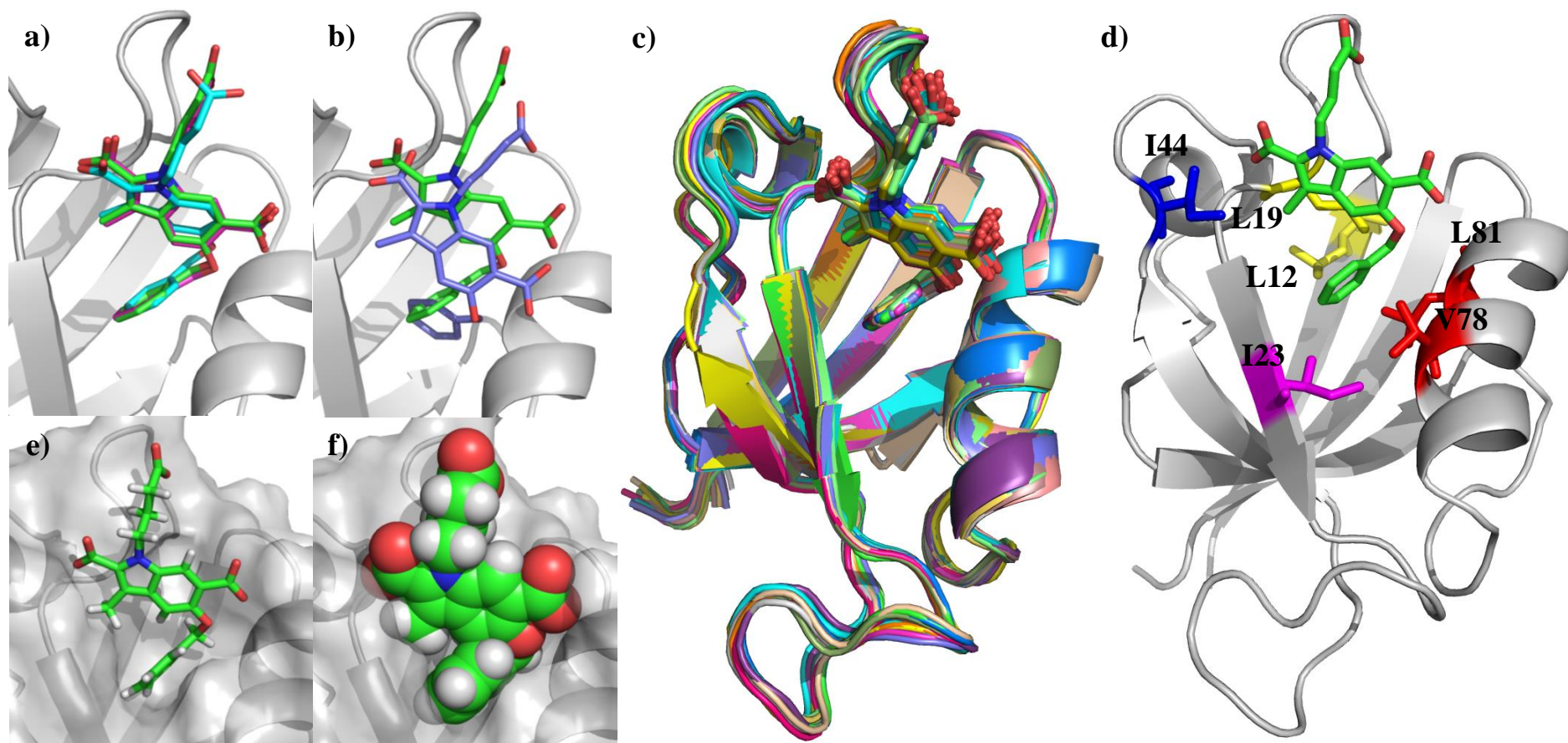


Figure 6.23: In this figure, PSD-95 PDZ1 is depicted as a cartoon representation (grey), with **3c** represented by sticks; for clarity the hydrogen's have been omitted from some structures. a) The representative structures of the first (green), second (blue) and third (magenta) lowest energy clusters of the seven total clusters. b) The representative structures of the lowest (green) and highest energy (purple) clusters. c) The top 20 lowest energy structures of the lowest energy cluster. d) The representative structure of the PSD-95 PDZ1 - **3c** complex, with the residues that showed intermolecular NOE'S highlighted. e) Enlarged view of the PSD-95 PDZ1 domain binding region with the protein surface shown. f) Enlarged view of the PSD-95 PDZ1 domain binding region with the protein surface shown and **3c** in a space-filling representation.

The relevant parameters, clustering and validation analysis for the restraint-driven docking process are displayed in Table 6.12. 34 distance restraints for the PSD-95 PDZ1 – **3c** complex were obtained from the NMR spectroscopic experiments and only two of these restraints were slightly violated in the obtained representative structures obtained. It would have been desirable to have produced a representative structure of the complex with no distance restraint violations but given the nature of the NOESY NMR experiment, it was possible to observe a range of NOE interactions. Therefore, distance restraints can be derived from minor populations of **3c** bound to PSD-95 PDZ1, as well as the major population; the two distance restraints violated may have been from a minor population of **3c** and hence, this could be why HADDOCK has not been able to satisfy them in the representative structure.

As mentioned in [3.5.5], the output of the HADDOCK docking procedure is given as a ‘HADDOCK score;’ this is a weighted sum of all the energy terms calculated during the docking process, with a more negative value indicating the more energetically favourable the subsequent complex is. The value of the root mean square deviation (RMSD) of the structures in the representative cluster is 0.479Å; this low value shows that the 105 structures in the representative cluster show little deviation in the overall bound structure.

As the HADDOCK score for the representative structure of the PSD-95 PDZ1 – **3c** complex is an extremely negative value of -76.04, this indicates that the representative structure obtained is energetically favourable. The average HADDOCK score of the 20 lowest energy structures is -58.51, which is also a large negative value; this demonstrates that the top 20 representative structures cluster are similarly energetically favoured. The average buried surface area (BSA) value of

570.44Å² is a quantification of the change in solvent accessible area from the free PSD-95 PDZ1 domain to the PSD-95 PDZ1 – **3c** complex; this shows the ability of **3c** to interact with a substantial surface area of the PSD-95 PDZ1 domain binding region.

Table 6.12: The statistical characteristics of the HADDOCK structural determination process for the complex between PSD-95 PDZ1 and **3c**.

Unambiguous restraints	
Intermolecular NOEs ^a	26
Intramolecular NOEs ^b	8
RMSD of lowest energy cluster (105 structures) (Å)	0.479
HADDOCK score of lowest energy structure	-76.04
Average HADDOCK score of 20 lowest energy structures in the lowest energy cluster	-58.51
Average buried surface area of 20 lowest energy structures in the lowest energy cluster (Å ²)	570.44
Number of unambiguous distance restraint violations	2
Number of bad contacts	0
Ramachandran plot (%) ^c	
Residues in most favoured regions	76.6
Residues in additional allowed regions	20.8
Residues in generously allowed regions	0
Residues in disallowed regions	2.6 ^d

^a Obtained from 3-D [¹³C, ¹⁵N]-filtered NOE Experiment (mixing time = 300 ms, 25°C, pH 6.3). ^b 2-Dimensional [¹³C, ¹⁵N]-filtered NOE Experiment (mixing time = 300 ms, 25°C, pH 6.3). ^c Determined by using PROCHECK (Laskowski et al., 1993) analysis to check structure viability. ^d Consistent with the residues in disallowed regions of the initial crystal structure used in the docking process (PDB ID = 3GSL (Sainlos et al., 2011)).

6.6.3 PSD-95 PDZ1 – **4c** Complex Structure Determination

As with **3c**, the NMR experiments were carried out on the prepared PSD-95 PDZ1 – **4c** complex (Figure 6.24), the resultant intra-ligand and intermolecular interactions were assigned (Appendices, A.8) and incorporated along with the other parameters highlighted in the experimental procedure in the HADDOCK docking method.

It is clear that **4c** showed less intra-ligand and intermolecular interactions with the PSD-95 PDZ1 domain than **3c**. This was not unexpected as the structure of **4c** is

much simpler and less-substituted; hence, it contains fewer atoms to form NOE's with the PSD-95 PDZ1 domain, than **3c**. The output of the distance restraint-driven docking gave four different possible structures of the PSD-95 PDZ1 domain in complex with **4c** (Figure 6.25a & b). An ensemble of the 20 lowest energy structures from the lowest energy cluster was created (Figure 6.25c) and the structure with the lowest energy of these was taken as the representative structure of the PSD-95 PDZ1 – **4c** complex structure (Figure 6.25d-f). It can be seen that the lowest energy complexes from the top three low energy clusters generated from the HADDOCK docking process are very similar structurally and these account for over 190 of the 200 final solvent refined structures. However, there is some deviation between the representative complex structure and the fourth cluster but this is due to the ability of the HADDOCK webserver to explore all local minima in the energy landscape. The structure shows that the 5-hydroxy group of **4c** forms a hydrogen bond with the backbone NH of Ile23 and this bound conformation is stabilised by polar interactions between the 1-alkylcarboxyl and 2-carboxyl groups of **4c** and the side chains of residues Lys82 and Arg14 respectively in the PSD-95 PDZ1 domain. The 3-methyl group shows hydrophobic interactions with those residues of the hydrophobic binding pocket including Leu81.

Given the simple and little-substituted nature of **4c**, the structure does not indicate any areas of the molecule that could be detrimental to its PSD-95 PDZ1 binding affinity. After careful analysis of the bound orientation, it may be possible to increase the binding affinity of **4c** by substitution with a 2-alkylhydroxyl group to interact with His74 or a larger alkyl group than 3-methyl to interact with the hydrophobic pocket more effectively of the PSD-95 PDZ1 domain.

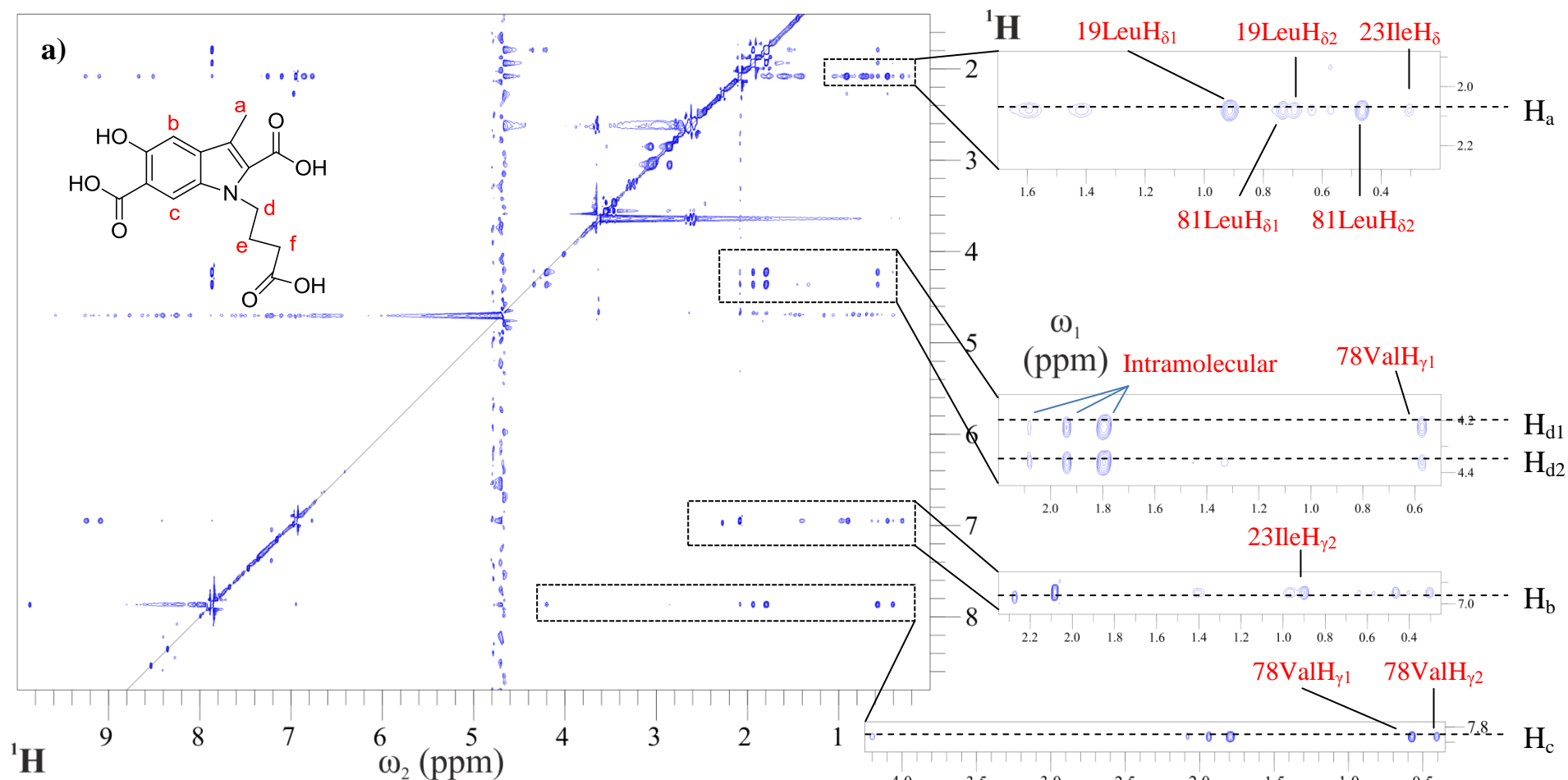


Figure 6.24: a) The obtained 2-D ^{13}C , ^{15}N -filtered NOESY spectrum of ^{13}C ^{15}N PSD-95 PDZ1 domain : **4c** complex (P:L = 1:5, acquired at 298K, with a field strength of 600MHz, in 20mM phosphate 0.1mM EDTA buffer, pH6.3 and with an NOE mixing time of 300ms); the structure of **4c** is inset into the spectrum with the different proton environments in the structure labelled. The peaks on the right-hand side of the diagonal correspond to intra-ligand and intermolecular interactions observed; the protein and ligand contributions to the interaction can be seen on the x- and y-axis respectively and a number of these inter/intramolecular interactions have been assigned.

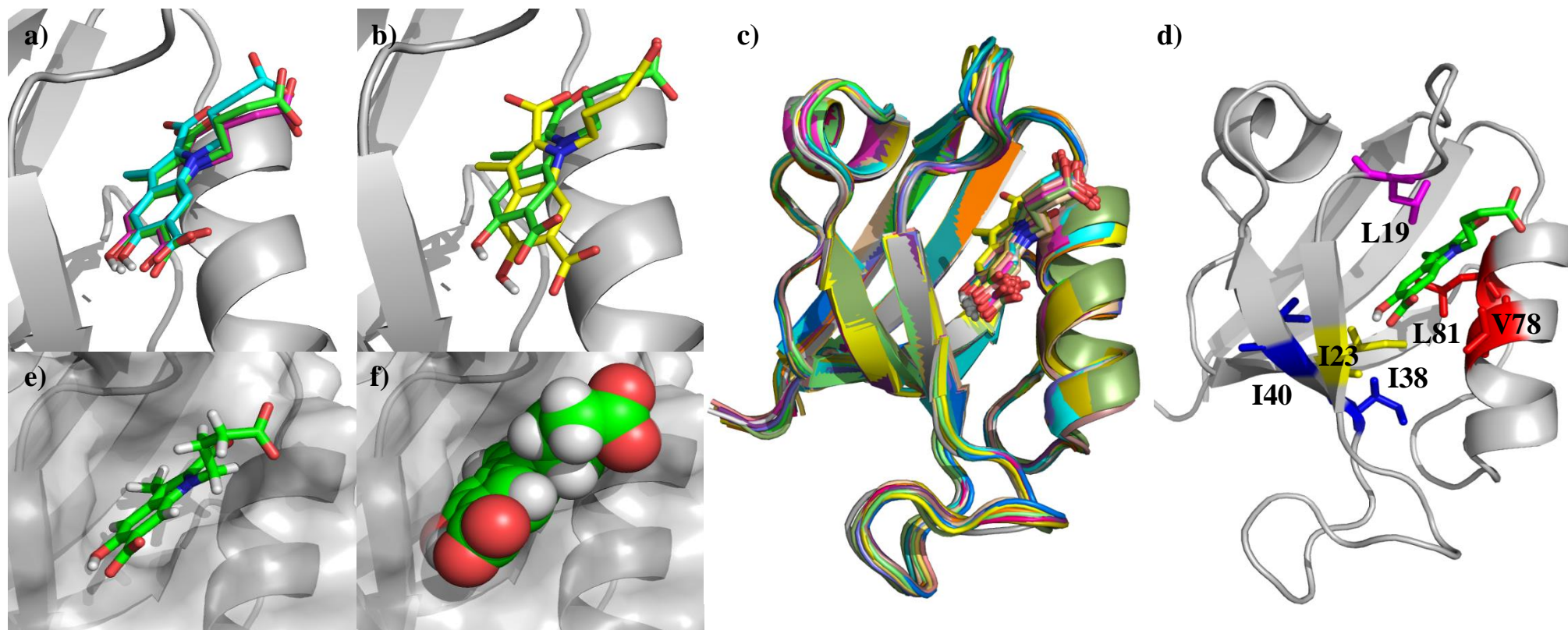


Figure 6.25: In this figure, PSD-95 PDZ1 is depicted as a cartoon representation (grey), with **4c** represented by sticks; for clarity the hydrogen's have been omitted from most structures. a) The representative structures of the first (green), second (blue) and third (magenta) lowest energy clusters of the four total clusters. b) The representative structures of the lowest (green) and highest energy (yellow) clusters. c) The top 20 lowest energy structures of the lowest energy cluster. d) The representative structure of the PSD-95 PDZ1 – **4c** complex, with the residues that showed intermolecular NOE'S highlighted. e) Enlarged view of the PSD-95 PDZ1 domain binding region with the protein surface shown. f) Enlarged view of the PSD-95 PDZ1 domain binding region with the protein surface shown and **4c** in a space-filling representation.

The relevant parameters, clustering and validation analysis for the restraint-driven docking process are displayed in Table 6.13. 25 distance restraints for the PSD-95 PDZ1 – **4c** complex were obtained from the NMR spectroscopic experiments and only one of these restraints was slightly violated in the obtained representative structure. As with the PSD-95 PDZ1 – **3c** complex, it would have been desirable to obtain a representative structure of the complex that had no distance restraint violations but the reasons as to possibly why this is not the case were discussed in [6.6.2]. As only one NOE is violated out of the 25 distance restraints, this would suggest that the NOE's assigned were either for one predominant bound orientation of **4c** or that the NOE's observed were an average of the different bound orientations at a 5-fold excess of **4c**. It is difficult to distinguish between these two possibilities but the HADDOCK process has produced the most likely structure of the PSD-95 PDZ1 – **4c** complex in solution, at the given concentration.

The RMSD value of the structures in the representative cluster is 0.448Å; this low value shows that the 167 structures in the cluster show little total deviation in the overall bound structure. As the HADDOCK score for the representative structure of the PSD-95 PDZ1 – **4c** complex is an extremely negative value of -77.88, and so, indicates that the representative structure obtained is energetically favourable. The average HADDOCK score of the 20 lowest energy structures is -64.78, which is also a very large negative value; this demonstrates that the top 20 representative structures cluster are similarly energetically favoured. As with the PSD-95 PDZ1 – **3c** structure, the average BSA value of 471.63Å² quantifies the change in solvent accessible area from the free PSD-95 PDZ1 domain to the PSD-95 PDZ1 – **4c** complex and again, shows the ability of **4c** to interact with a substantial surface area of the PSD-95 PDZ1 domain binding region.

Table 6.13: The statistical characteristics of the HADDOCK structural determination process for the complex between PSD-95 PDZ1 and **4c**.

Unambiguous restraints	
Intermolecular NOEs ^a	16
Intramolecular NOEs ^b	9
RMSD of lowest energy cluster (167 structures) (Å)	0.448
HADDOCK score of lowest energy structure	-77.88
Average HADDOCK score of 20 lowest energy structures in the lowest energy cluster	-64.78
Average buried surface area of 20 lowest energy structures in the lowest energy cluster (Å ²)	471.63
Number of unambiguous distance restraint violations	1
Number of bad contacts	0
Ramachandran plot (%) ^c	
Residues in most favoured regions	81.8
Residues in additional allowed regions	15.6
Residues in generously allowed regions	0
Residues in disallowed regions	2.6 ^d

^a Obtained from 3-D [¹³C, ¹⁵N]-filtered NOE Experiment (mixing time = 300 ms, 25°C, pH 6.3). ^b 2-Dimensional [¹³C, ¹⁵N]-filtered NOE Experiment (mixing time = 300 ms, 25°C, pH 6.3). ^c Determined by using PROCHECK (Laskowski et al., 1993) analysis to check structure viability. ^d Consistent with the residues in disallowed regions of the initial crystal structure used in the docking process (PDB ID = 3GSL (Sainlos et al., 2011)).

6.6.4 HADDOCK Structure Comparison

It is clear to see that the representative structures of small molecule inhibitors **3c** and **4c** bound to the PSD-95 PDZ1 domain indicates that the two inhibitors bind in completely different orientations. The indole scaffold of **3c** is orientated almost perpendicular to α B helix and the β B strand, whereas the indole scaffold of **4c** is in a more parallel orientation to α B helix and the β B strand (Figure 6.26). This shows the importance of the large alkyl group attached to the 5-O atom in ‘anchoring’ in the binding pocket and hence, restricting the bound orientation of the small molecule. As solvated docking is employed in the HADDOCK protocol, the docking methodology is able to account for the presence and influence of water molecules in the PSD-95 PDZ1 – **3c/4c** complexes; however, HADDOCK is not able to model the presence of

any key bridging water molecules in the resultant PSD-95 PDZ1 – small molecule complexes. As a result, it is not possible to interpret the relative enthalpic and entropic contributions of the **3c** and **4c** small molecules to PSD-95 PDZ1 binding from the HADDOCK structures, as it would be from a reasonable resolution crystal structure.

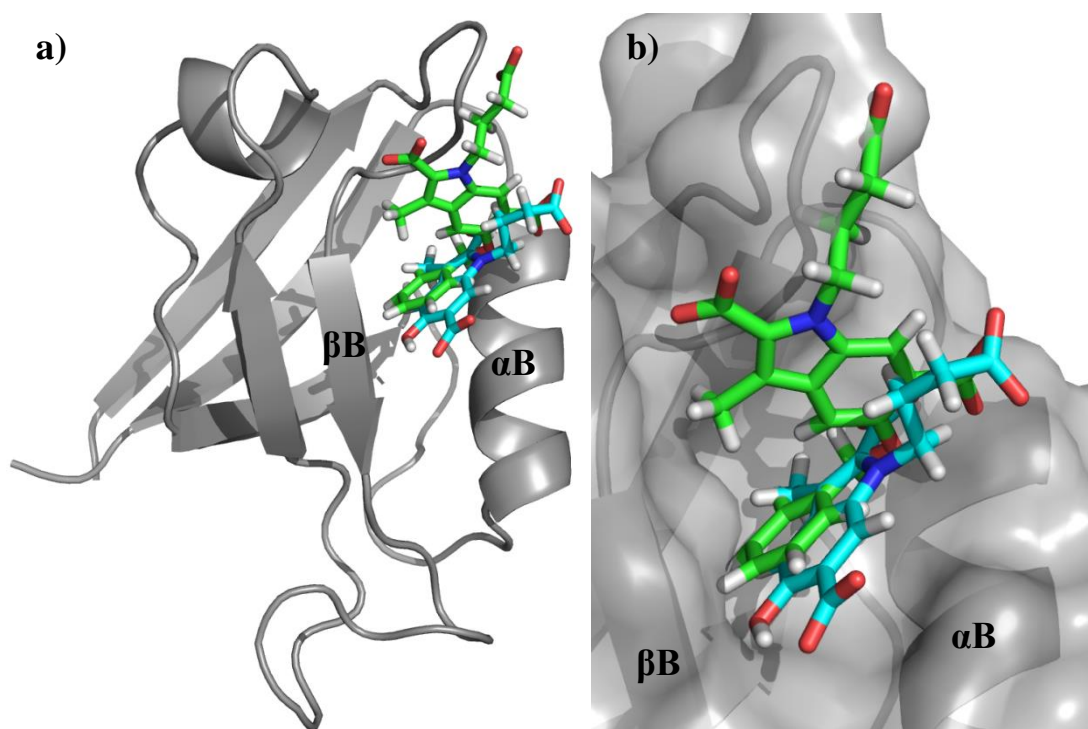


Figure 6.26: In this figure, the PSD-95 PDZ1 crystal structure (PDB ID = 3GSL (Sainlos et al., 2011)) is depicted as a cartoon representation (grey), with the representative structures of **3c** (green) and **4c** (blue) represented by sticks. a) A comparison of the different PSD-95 PDZ1 bound conformations of the two small molecule inhibitors; it can be seen that the indole scaffold of **3c** is oriented almost perpendicular to the α B helix, c.f. the indole scaffold of **4c** is almost parallel. b) A close-up view of the representative structures, this view shows more clearly how the 5-benzyloxy and 3-methyl groups of **3c** and **4c** respectively, interact with the binding pocket.

It is interesting to observe that the less-substituted compound **4c** forms fewer clusters (4) i.e. exists in fewer possible PSD-95 PDZ1 bound orientations, than **3c** (7) and that **4c** also has more structures in its representative cluster (167) than **3c** (105). These observations could either be due to the ability of the more-substituted structure of **3c** to explore more of the slight variations in the local minima in the energy landscape than the less-substituted **4c**. Alternatively, as alluded to in [6.6.3], it is possible that the assigned NOE's of the PSD-95 PDZ1 – **4c** complex may have been

due to either a sole, major population of **4c** bound to PSD-95 PDZ1 or an average of all the bound populations; either of these possibilities will result in more cluster analysis variation of **3c** c.f. **4c**.

Direct comparison of the HADDOCK scores obtained from the representative structures of the PSD-95 PDZ1 complexes with **3c** and **4c** is not possible as the HADDOCK score output is a relevant value only for the individual protein and ligand set in the docking process; it is not a comparable value. However, both HADDOCK scores for the representative structures of the PSD-95 PDZ1 – **3c/4c** complexes are large negative values; this suggests that the structures obtained are energetically favourable and thus, are an accurate representation of the actual bound orientations of the respective small molecule inhibitor.

The BSA of the representative PSD-95 PDZ1 – **3c/4c** structures indicates that upon binding, **3c** is able to induce the greater change in buried surface area than **4c**; this was to be expected as **3c** is a larger and more-substituted small molecule c.f. **4c** and so, is able to occupy more surface area of the PSD-95 PDZ1 domain binding region upon binding. The Ramachandran plot analysis performed by PROCHECK (Laskowski et al., 1993) shows that both the PSD-95 PDZ1 – small molecule inhibitor complexes have the majority of residues in favoured or additionally allowed regions; those residues that are in the disallowed regions are consistent with the initial PSD-95 PDZ1 crystal structure utilised (PDB ID = 3GSL (Sainlos et al., 2011)). As a result, both the obtained representative structures can be concluded to viable representations of the PSD-95 PDZ1 domain in complex with either small molecule inhibitor **3c** or **4c**.

Analysis of the bound structures and the subsequent clustering and validation analysis of both of the PSD-95 PDZ1 inhibitors have led to the identification of key

moieties of ligand binding to PSD-95 PDZ1, as well as how to reduce unwanted clashes/repulsions with the PSD-95 PDZ1 domain. As a result, the obtained PSD-95 PDZ1 – small molecule complex structures can provide an essential insight for use in future small molecule inhibitor development of the PSD-95 PDZ1 domain and possibly, even PDZ domains in general.

6.7 Conclusion

Through a developmental process encompassing a number of different biophysical techniques, a large number of novel, reversible small molecule binders of the PSD-95 PDZ1 domain have been rationally synthesised and tested for binding. The binding affinity to PSD-95 PDZ1 of two of these compounds has been determined and both of these compounds have been shown to have a reversible inhibitory effect on the native interaction. A selection of the small molecule binders developed by the research process detailed in this chapter have been shown to corroborate the *in vitro* results shown and have been found to exert PSD-95 PDZ domain inhibitory effects *in vivo* ((Bouzidi et al., 2013, Vogrig et al., 2013)). This may be seen as surprising as, in order to exert an observable effect in the rat models, the developed small organic molecules are required to cross the blood-brain barrier; molecules that achieve this are often quite hydrophobic. Given the presence of a number of carboxylic acid groups on the detailed organic molecules, these compounds are not particularly hydrophobic. Thus, this suggests that the small molecules are still able to pass the blood-brain barrier or that they are able to exert an inhibitory effect, via an alternate pathway, that does not require blood-brain barrier passage.

Arguably, the most important aspect of the research detailed in this chapter is the determination of the representative structure of the PSD-95 PDZ1 domain bound individually to small molecule inhibitors **3c** and **4c**, using the HADDOCK

webservice. These are the first examples of the HADDOCK webservice being utilised to determine a PDZ domain – small molecule inhibitor complex and has a wide-range of possible applications for future PDZ domain research. Given how well HADDOCK has performed in the CAPRI experiments; the reliability, validity and accuracy of the obtained PSD-95 PDZ1 – small molecule complexes can be substantiated. As a result, this illustrates how HADDOCK can be an extremely important tool for future PDZ domain research, by determining the structure of PDZ – small molecule inhibitor complexes when it is not possible to obtain a crystallographic or NMR structure. It is hoped that the research detailed in the latter part of this chapter illustrates how determination of PDZ – small molecule inhibitor structure by HADDOCK, can facilitate a much quicker and easier method to enhancing PDZ domain binding affinity; this technique should drive future PDZ domain inhibition by small molecules research forward at a more accelerated rate.

Chapter 7
GENERAL DISCUSSION AND
FUTURE RESEARCH

7. GENERAL DISCUSSION AND FUTURE RESEARCH

7.1 Conclusions

If the original aims of the research are reviewed, it can be seen that these have been satisfied:

- The interactions of the 5-HT_{2a/c} receptors with PSD-95/SAP97 PDZ1&2 have been proven by NMR spectroscopy and quantified by ITC; the structure of the PSD-95 PDZ1 – 5-HT_{2c} complex has been determined for the first time using NMR solution state spectroscopy and is in the process of being deposited onto the PDB.
- Using ITC, a thorough and systematic biophysical investigation of the SAP97 PDZ1&2 binding regions using peptides containing natural and non-natural amino acids has been performed; the effect of peptide length, 0 and -2 residue substitutions, pH and functional group orientation was probed.
- A variety of moderate to high micromolar affinity small molecule PSD-95/SAP97 PDZ1&2 binders have been developed through an NMR spectroscopy-based screening process; a number of these small molecules have shown PDZ domain-mediated inhibitory effects *in vitro* and *in vivo* (Bouzidi et al., 2013, Vogrig et al., 2013). PSD-95 PDZ1/SAP97 PDZ2 – small molecule complexes has been determined using NMR restraint-driven docking with HADDOCK; this is the first example of HADDOCK being used to determine a PDZ – small molecule complex.

After reviewing the research presented in this thesis and the accompanying appendices, it can be concluded that the production of indole scaffold-based small molecule inhibitors of the PSD-95/SAP97 PDZ domains may not be an achievable target; this may even be extended to PSD-95/SAP97 PDZ domain-mediated

interaction by small molecule compounds in general. This has been proposed for the following reasons:

- Although the presence of ‘hotspots’ within the PDZ domain had been identified by previous research, the research detailed in this thesis has shown the interactions that a small molecule needs to mimic, are spread out over a reasonably large area of over 490\AA^2 ; (area of the PSD-95 PDZ1 domain that interacts with the 5-HT_{2c} nonapeptide in the representative structure). This may mean that small molecule inhibition of the PSD-95/SAP97 PDZ domains is not feasible (Figure 7.1):
 - The PSD-95 PDZ1 – 5-HT_{2c} complex structure showed the presence of interactions of 5-HT_{2c} with the residues of the $\beta\text{B} - \beta\text{C}$ loop.
 - The biophysical characterisation of the SAP97 PDZ1/2 binding regions showed the importance of interactions outside the canonical class I C-terminal PDZ binding sequence (X-S/T-X- Ω).
- The produced indole scaffold-based binders of the PSD-95/SAP97 PDZ1&2 domains showed only a moderate to high micromolar binding affinity despite five stages of the development process.
- The examples of low micromolar/nanomolar affinity small molecule PSD-95 PDZ – nNOS interaction inhibitors *in vivo* were designed to bind target the PDZ domain ligand, nNOS, not the PSD-95 PDZ domain itself. Subsequent research in our laboratory has indicated that one of these small molecule compounds, IC87021, has no observable inhibitory effect on the PSD-95 PDZ – nNOS interaction by NMR spectroscopy and ITC; this possibly raises questions over the validity of other reported small molecule compounds as PDZ domain inhibitors.

Therefore, the future inhibition of PSD-95/SAP97 PDZ domain-mediated interactions research has a variety of different directions in which to progress.

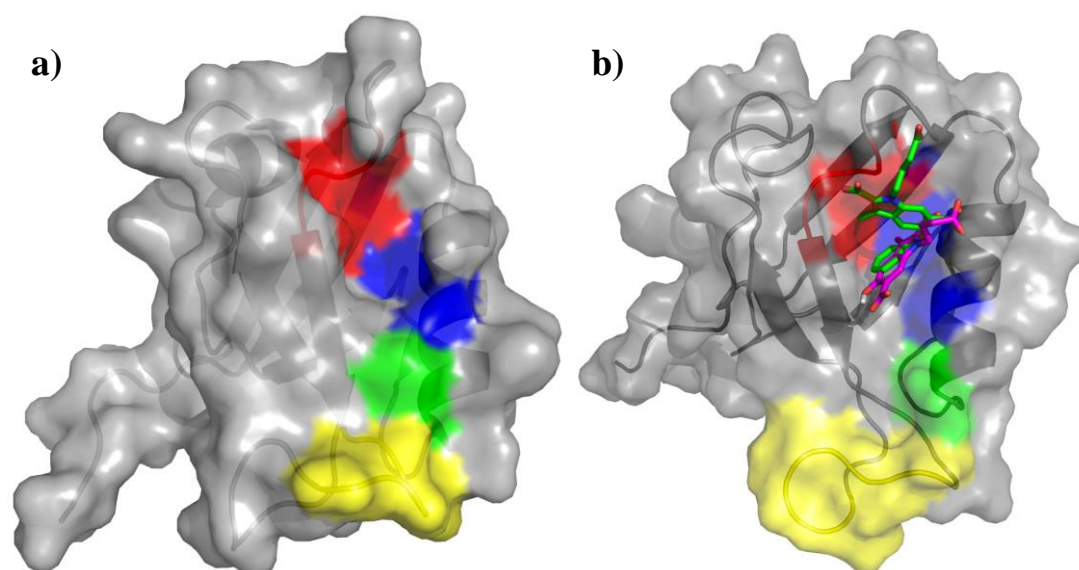


Figure 7.1: The ‘hotspot’ binding regions of typical PDZ domains in a surface representation: GLGF motif (red), hydrophobic pocket (blue), conserved His (green) and β B – β C loop (yellow). a) The crystal structure of the Scrib1 PDZ1 domain (PDB ID = 2W4F). b) The representative structure of the PSD-95 PDZ1 – 5-HT_{2c} complex structure determined by solution state NMR spectroscopy (grey) with the 5-HT_{2c} ligand removed; the PSD-95 PDZ1 bound conformations of small molecules **3c** (green) and **4c** (magenta) determined by restraint-driven docking using HADDOCK have been aligned with the representative structure, with the non-polar protons have been removed for clarity in the small molecule compounds. The figure shows how difficult it is to develop a small molecule inhibitor of the PSD-95 PDZ1 domain that is able to effectively interact with the four different hotspot regions indicated and hence, produce sufficient binding affinity; it is possible that this difficulty may apply to all PSD-95 PDZ1 inhibition by small molecule research, regardless of the chemical scaffold utilised.

7.2 Future PDZ Domain Inhibition Research

After analysing the previous PDZ domain inhibition research and the research detailed in this thesis, the future research into the development of inhibitors of PSD-95/SAP97 PDZ domain-mediated interactions can be divided into two different areas:

- Development of a more effective chemical scaffold on which to base a small molecule PDZ domain inhibitor.
- Production of a β -strand peptidomimetic as a PDZ domain inhibitor.

7.2.1 New Small Molecule Scaffold

The development of a new chemical scaffold for small molecule inhibition of PDZ domains could proceed in a variety of methodologies; one such example is a fragment-based screening approach. This drug discovery approach has been used for a variety of different protein targets (Congreve et al., 2008); this methodology would entail screening of PSD-95/SAP97 PDZ domain binding of fragments by a biophysical technique i.e. ITC or surface plasmon resonance (SPR), determining the PDZ – fragment bound structures by X-ray crystallography or NMR restraint-driven docking and finally, chemical knowledge or in-silico methods to produce a suitable chemical scaffold capable of positioning the fragments as desired (Figure 7.2) (Rees et al., 2004, Jhoti et al., 2007).

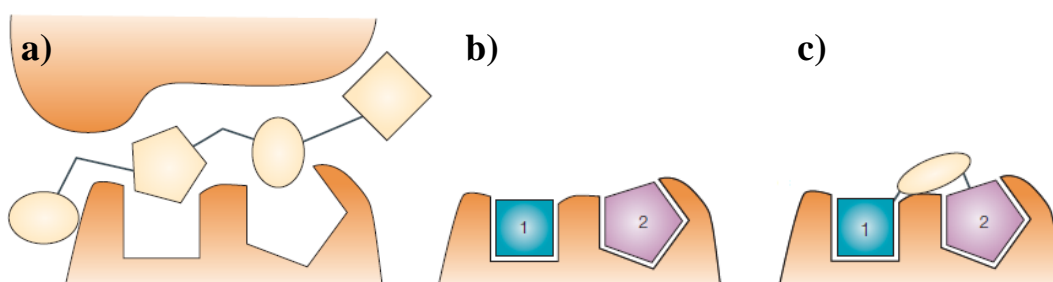


Figure 7.2: A comparison of the potential advantages of using a fragment-based screening rather than a high-throughput drug discovery methodology. a) A poor HTS hit of a molecule that contains four different functional fragments; two of these functional fragments have the potential to bind to the target well but are unable to in the molecule screened. b) & c) By adopting a fragment-based screening approach to drug discovery it is possible to identify the two fragments that bind to the target well and then connect these using a suitable chemical scaffold/linker to produce a potentially strong binder. Images taken and adapted from (Rees et al., 2004).

The design of an alternative small molecule chemical scaffold could also be achieved by implementing one of the previously described methodologies utilised in PDZ domain inhibition research [1.6]: virtual library screening (VLS), high-throughput screening (HTS) or the re-purposing of existing drugs.

7.2.2 β -strand Peptidomimetics

As discussed in [1.4 & 1.6], PDZ domain ligands form an antiparallel β -strand upon PDZ domain binding and so, a β -strand peptidomimetic could be an effective non-

peptidic PDZ domain inhibitor; a couple of β -strand peptidomimetic binders of PDZ domains have already been designed (Figure 7.3a) (Hammond et al., 2006). These compounds showed promising levels of α 1-syntrophin PDZ domain binding affinity ($K_D = 0.32\mu\text{M}$) and so, the fact that there have been no further examples of PDZ domain peptidomimetic inhibitor investigations is surprising; this could be as a result of unforeseen problems with the particular peptidomimetic design i.e. solubility, stability issues etc. Adaptation of this previous PDZ domain research to overcome such issues and result in the particular PSD-95/SAP97 PDZ domain specificity may yield a potent peptidomimetic inhibitor of a PDZ domain-mediated interaction.

There is also evidence in the literature of other examples of β -strand (peptido)mimetics developed for non-PDZ domain-containing protein targets (Figure 7.3b) (Smith et al., 1992, Smith et al., 1994, Kang et al., 2012, Sutherell et al., 2012); these could possibly be adapted for PSD-95/SAP97 PDZ domain-targeting and hence, be important in future PDZ domain inhibition research.

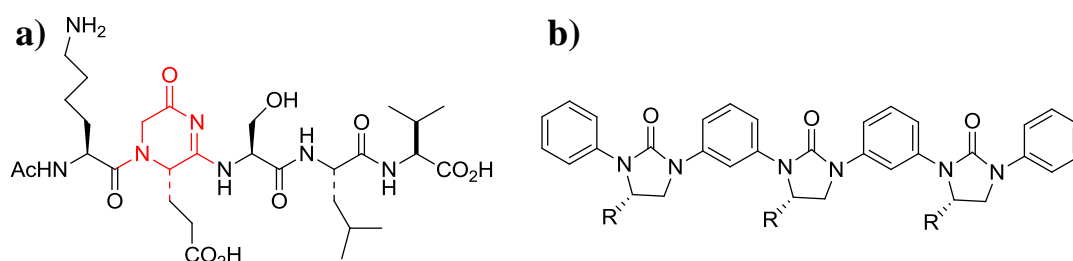


Figure 7.3: a) The structure of the β -strand peptidomimetic developed to bind to the α 1-syntrophin PDZ domain; the aza-@-unit has been highlighted (red) and this peptidomimetic showed low micromolar/high nanomolar PDZ domain ($K_D = 0.32\mu\text{M}$) (Hammond et al., 2006). b) The aryl-linked imidazolidin-2-one developed as a non-peptidic β -strand mimic; this and/or related compounds could have important applications in future PDZ domain inhibition research (Sutherell et al., 2012).

Chapter 8
REFERENCES

8. REFERENCES

- * = The eNMR project (European FP7 e-Infrastructure grant, contract no. 213010, www.enmr.eu), supported by the national GRID Initiatives of Italy, Germany and the Dutch BiG Grid project (Netherlands Organization for Scientific Research), is acknowledged for the use of web portals, computing and storage facilities.
- AARTS, M., LIU, Y. T., LIU, L. D., BESSHOH, S., ARUNDINE, M., GURD, J. W., WANG, Y. T., SALTER, M. W. & TYMIANSKI, M. 2002. Treatment of ischemic brain damage by perturbing NMDA receptor-PSD-95 protein interactions. *Science*, 298, 846-850.
- ABBAS, A. I., YADAV, P. N., YAO, W.-D., ARBUCKLE, M. I., GRANT, S. G. N., CARON, M. G. & ROTH, B. L. 2009. PSD-95 Is Essential for Hallucinogen and Atypical Antipsychotic Drug Actions at Serotonin Receptors. *Journal of Neuroscience*, 29, 7124-7136.
- ALLEN, J. A., YADAV, P. N. & ROTH, B. L. 2008. Insights into the regulation of 5-HT_{2A} serotonin receptors by scaffolding proteins and kinases. *Neuropharmacology*, 55, 961-968.
- ANASTASIO, N. C., LANFRANCO, M. F., BUBAR, M. J., SEITZ, P. K., STUTZ, S. J., MCGINNIS, A. G., WATSON, C. S. & CUNNINGHAM, K. A. 2010. Serotonin 5-HT_{2C} receptor protein expression is enriched in synaptosomal and post-synaptic compartments of rat cortex. *Journal of Neurochemistry*, 113, 1504-1515.
- ARKIN, M. 2005. Protein-protein interactions and cancer: small molecules going in for the kill. *Current Opinion in Chemical Biology*, 9, 317-324.
- ARKIN, M. R. & WELLS, J. A. 2004. Small-molecule inhibitors of protein-protein interactions: Progressing towards the dream. *Nature Reviews Drug Discovery*, 3, 301-317.
- BACH, A., CHI, C. N., OLSEN, T. B., PEDERSEN, S. W., RODER, M. U., PANG, G. F., CLAUSEN, R. P., JEMTH, P. & STROMGAARD, K. 2008. Modified Peptides as Potent Inhibitors of the Postsynaptic Density-95/N-Methyl-D-Aspartate Receptor Interaction. *Journal of Medicinal Chemistry*, 51, 6450-6459.
- BACH, A., CHI, C. N., PANG, G. F., OLSEN, L., KRISTENSEN, A. S., JEMTH, P. & STROMGAARD, K. 2009. Design and Synthesis of Highly Potent and Plasma-Stable Dimeric Inhibitors of the PSD-95-NMDA Receptor Interaction. *Angewandte Chemie-International Edition*, 48, 9685-9689.
- BACH, A., CLAUSEN, B. H., MOLLER, M., VESTERGAARD, B., CHI, C. N., ROUND, A., SORENSEN, P. L., NISSEN, K. B., KASTRUP, J. S., GAJHEDE, M., JEMTH, P., KRISTENSEN, A. S., LUNDSTROM, P., LAMBERTSEN, K. L. & STROMGAARD, K. 2012. A high-affinity, dimeric inhibitor of PSD-95 bivalently interacts with PDZ1-2 and protects against ischemic brain damage. *Proceedings of the National Academy of Sciences of the United States of America*, 109, 3317-3322.
- BACH, A., STUHR-HANSEN, N., THORSEN, T. S., BORK, N., MOREIRA, I. S., FRYDENVANG, K., PADRAH, S., CHRISTENSEN, S. B., MADSEN, K. L., WEINSTEIN, H., GETHER, U. & STROMGAARD, K. 2010. Structure-activity relationships of a small-molecule inhibitor of the PDZ domain of PICK1. *Organic & Biomolecular Chemistry*, 8, 4281-4288.
- BACKSTROM, J. R., PRICE, R. D., REASONER, D. T. & SANDERS-BUSH, E. 2000. Deletion of the serotonin 5-HT_{2C} receptor PDZ recognition motif prevents receptor phosphorylation and delays resensitization of receptor responses. *Journal of Biological Chemistry*, 275, 23620-23626.

- BANKS, L., PIM, D. & THOMAS, M. 2003. Viruses and the 26S proteasome: hacking into destruction. *Trends in Biochemical Sciences*, 28, 452-459.
- BAX, A., CLORE, G. M. & GRONENBORN, A. M. 1990. H-1-H-1 correlation via isotropic mixing of C-13 magnetisation, a new 3-dimensional approach for assigning H-1 and C-13 spectra of C-13-enriched proteins. *Journal of Magnetic Resonance*, 88, 425-431.
- BECAMEL, C., ALONSO, G., GELEOTTI, N., DEMEY, E., JOUIN, P., ULLMER, C., DUMUIS, A., BOCKAERT, J. & MARIN, P. 2002. Synaptic multiprotein complexes associated with 5-HT_{2C} receptors: a proteomic approach. *Embo Journal*, 21, 2332-2342.
- BECAMEL, C., FIGGE, A., POLIAK, S., DUMUIS, A., PELES, E., BOCKAERT, J., LUBBERT, H. & ULLMER, C. 2001. Interaction of serotonin 5-hydroxytryptamine type 2C receptors with PDZ10 of the multi-PDZ domain protein MUPP1. *Journal of Biological Chemistry*, 276, 12974-12982.
- BECAMEL, C., GAVARINI, S., CHANRION, B., ALONSO, G., GALEOTTI, N., DUMUIS, A., BOCKAERT, J. & MARIN, P. 2004. The serotonin 5-HT_{2A} and 5-HT_{2C} receptors interact with specific sets of PDZ proteins. *Journal of Biological Chemistry*, 279, 20257-20266.
- BELL, J. D., PARK, E., AI, J. & BAKER, A. J. 2009. PICK1-mediated GluR2 endocytosis contributes to cellular injury after neuronal trauma. *Cell Death and Differentiation*, 16, 1665-1680.
- BELLONE, C. & LUSCHER, C. 2006. Cocaine triggered AMPA receptor redistribution is reversed in vivo by mGluR-dependent long-term depression. *Nature Neuroscience*, 9, 636-641.
- BERG, T. 2003. Modulation of protein-protein interactions with small organic molecules. *Angewandte Chemie-International Edition*, 42, 2462-2481.
- BERGER, M., GRAY, J. A. & ROTH, B. L. 2009. The Expanded Biology of Serotonin. *Annual Review of Medicine*.
- BLAZER, L. L. & NEUBIG, R. R. 2009. Small Molecule Protein-Protein Interaction Inhibitors as CNS Therapeutic Agents: Current Progress and Future Hurdles. *Neuropsychopharmacology*, 34, 126-141.
- BOCKAERT, J., CLAEYSEN, S., BECAMEL, C., DUMUIS, A. & MARIN, P. 2006. Neuronal 5-HT metabotropic receptors: fine-tuning of their structure, signaling, and roles in synaptic modulation. *Cell and Tissue Research*, 326, 553-572.
- BODENHAUSEN, G. & RUBEN, D. J. 1980. Natural abundance N-15 NMR by enhanced heteronuclear spectroscopy. *Chemical Physics Letters*, 69, 185-189.
- BODENREIDER, C., BEER, D., KELLER, T. H., SONNTAG, S., WEN, D. Y., YAP, L. J., YAU, Y. H., SHOCHAT, S. G., HUANG, D. Z., ZHOU, T., CAFLISCH, A., SU, X. C., OZAWA, K., OTTING, G., VASUDEVAN, S. G., LESCAR, J. & LIM, S. P. 2009. A fluorescence quenching assay to discriminate between specific and nonspecific inhibitors of dengue virus protease. *Analytical Biochemistry*, 395, 195-204.
- BOUZIDI, N., DEOKAR, H., VOGRIG, A., BOUCHERLE, B., RIPOCHE, I., ABRUNHOSA-THOMAS, I., DORR, L., WATTIEZ, A.-S., LIAN, L.-Y., MARIN, P., COURTEIX, C. & DUCKI, S. 2013. Identification of PDZ ligands by docking-based virtual screening for the development of novel analgesic agents. *Bioorganic & Medicinal Chemistry Letters*, 23, 2624-2627.
- BRENMAN, J. E., CHAO, D. S., GEE, S. H., MCGEE, A. W., CRAVEN, S. E., SANTILLANO, D. R., WU, Z. Q., HUANG, F., XIA, H. H., PETERS, M. F., FROEHLNER, S. C. & BREDET, D. S. 1996. Interaction of nitric oxide synthase with

- the postsynaptic density protein PSD-95 and alpha 1-syntrophin mediated by PDZ domains. *Cell*, 84, 757-767.
- BRUNGER, A. T. 2007. Version 1.2 of the Crystallography and NMR system. *Nature Protocols*, 2, 2728-2733.
- BURKHARDT, C., MULLER, M., BADDE, A., GARNER, C. C., GUNDELFINGER, E. D. & PUSCHEL, A. W. 2005. Semaphorin 4B interacts with the post-synaptic density protein PSD-95/SAP90 and is recruited to synapses through a C-terminal PDZ-binding motif. *Febs Letters*, 579, 3821-3828.
- CABRAL, J. H. M., PETOSA, C., SUTCLIFFE, M. J., RAZA, S., BYRON, O., POY, F., MARFATIA, S. M., CHISHTI, A. H. & LIDDINGTON, R. C. 1996. Crystal structure of a PDZ domain. *Nature*, 382, 649-652.
- CAI, C., COLEMAN, S. K., NIEMI, K. & KEINANEN, K. 2002. Selective binding of synapse-associated protein 97 to GluR-A alpha-amino-5-hydroxy-3-methyl-4-isoxazole propionate receptor subunit is determined by a novel sequence motif. *Journal of Biological Chemistry*, 277, 31484-31490.
- CAMARA-ARTIGAS, A., MURCIANO-CALLES, J., GAVIRA, J. A., COBOS, E. S. & MARTINEZ, J. C. 2010. Novel conformational aspects of the third PDZ domain of the neuronal post-synaptic density-95 protein revealed from two 1.4 angstrom X-ray structures. *Journal of Structural Biology*, 170, 565-569.
- CAVANAGH, J. 2007. *Protein NMR spectroscopy [electronic book] : principles and practice / John Cavanagh ... [et al.]*, Amsterdam ; Academic Press, c2007. 2nd ed.
- CHEN, L., TRACY, T. & NAM, C. I. 2007a. Dynamics of postsynaptic glutamate receptor targeting. *Current Opinion in Neurobiology*, 17, 53-58.
- CHEN, X., LONGGOOD, J. C., MICHNOFF, C., WEI, S., FRANTZ, D. E. & BEZPROZVANNY, I. 2007b. High-throughput screen for small molecule inhibitors of Mint1-PDZ domains. *Assay and Drug Development Technologies*, 5, 769-783.
- CHI, C. N., BACH, A., ENGSTROM, A., STROMGAARD, K., LUNDSTROM, P., FERGUSON, N. & JEMTH, P. 2011. Biophysical Characterization of the Complex between Human Papillomavirus E6 Protein and Synapse-associated Protein 97. *Journal of Biological Chemistry*, 286, 3597-3606.
- CHI, C. N., BACH, A., ENGSTROM, A., WANG, H., STROMGAARD, K., GIANNI, S. & JEMTH, P. 2009. A Sequential Binding Mechanism in a PDZ Domain. *Biochemistry*, 48, 7089-7097.
- CHIU, J., MARCH, P. E., LEE, R. & TILLET, D. 2004. Site-directed, Ligase-Independent Mutagenesis (SLIM): a single-tube methodology approaching 100% efficiency in 4 h. *Nucleic Acids Research*, 32, e174.
- CHO, K. O., HUNT, C. A. & KENNEDY, M. B. 1992. The rat-brain postsynaptic density fraction contains a homolog of the Drosophila disks-large tumour suppressor protein. *Neuron*, 9, 929-942.
- CHRISTENJJ, WRATHALL, D. P., OSCARSON, J. O. & IZATT, R. M. 1968. Theoretical evaluation of entropy titration method for calorimetric determination of equilibrium constants in aqueous solution. *Analytical Chemistry*, 40, 1713-&.
- CHRISTENN, M., KINDLER, S., SCHULZ, S., BUCK, F., RICHTER, D. & KREIENKAMP, H.-J. 2007. Interaction of brain somatostatin receptors with the PDZ domains of PSD-95. *Febs Letters*, 581, 5173-5177.
- CLACKSON, T. & WELLS, J. A. 1995. A hot-spot of binding-energy in a hormone-receptor interface. *Science*, 267, 383-386.
- CLUBB, R. T., THANABAL, V. & WAGNER, G. 1992. A constant-time 3-dimensional triple resonance pulse scheme to correlate intrasidue H-1(N), N-15,

- AND C-13(′) chemical shifts in N-15-C-13-labelled proteins. *Journal of Magnetic Resonance*, 97, 213-217.
- COCHRAN, A. G. 2001. Protein-protein interfaces: mimics and inhibitors. *Current Opinion in Chemical Biology*, 5, 654-659.
- COHEN, N. A., BRENNAN, J. E., SNYDER, S. H. & BREDT, D. S. 1996. Binding of the inward rectifier K⁺ channel Kir 2.3 to PSD-95 is regulated by protein kinase A phosphorylation. *Neuron*, 17, 759-767.
- CONGREVE, M., CHESSARI, G., TISI, D. & WOODHEAD, A. J. 2008. Recent developments in fragment-based drug discovery. *Journal of Medicinal Chemistry*, 51, 3661-3680.
- COOK, D. J., TEVES, L. & TYMIANSKI, M. 2012. Treatment of stroke with a PSD-95 inhibitor in the gyrencephalic primate brain. *Nature*, 483, 213-U112.
- COUSINS, S. L., PAPADAKIS, M., RUTTER, A. R. & STEPHENSON, F. A. 2008. Differential interaction of NMDA receptor subtypes with the post-synaptic density-95 family of membrane associated guanylate kinase proteins. *Journal of Neurochemistry*, 104, 903-913.
- COWAN, M., SUDHOF, T. & STEVENS, C. 2001. Synapses. *In*: COWAN, M., SUDHOF, T. & STEVENS, C. (eds.) *Synapses*. 1 ed. Maryland: Howard Hughes Medical Institute.
- CRAVEN, S. E. & BREDT, D. S. 1998. PDZ proteins organize synaptic signaling pathways. *Cell*, 93, 495-498.
- CUI, H., HAYASHI, A., SUN, H.-S., BELMARES, M. P., COBEY, C., PHAN, T., SCHWEIZER, J., SALTER, M. W., WANG, Y. T., TASKER, R. A., GARMAN, D., RABINOWITZ, J., LU, P. S. & TYMIANSKI, M. 2007. PDZ protein interactions underlying NMDA receptor-mediated excitotoxicity and neuroprotection by PSD-95 inhibitors. *Journal of Neuroscience*, 27, 9901-9915.
- DE VRIES, S. J., VAN DIJK, A. D. J., KRZEMINSKI, M., VAN DIJK, M., THUREAU, A., HSU, V., WASSENAAR, T. & BONVIN, A. M. J. J. 2007. HADDOCK versus HADDOCK: New features and performance of HADDOCK2.0 on the CAPRI targets. *Proteins-Structure Function and Bioinformatics*, 69, 726-733.
- DE VRIES, S. J., VAN DIJK, M. & BONVIN, A. M. J. J. 2010. The HADDOCK web server for data-driven biomolecular docking. *Nature Protocols*, 5, 883-897.
- DEGIORGIS, J. A., GALBRAITH, J. A., DOSEMEDI, A., CHEN, X. & REESE, T. S. 2006. Distribution of the scaffolding proteins PSD-95, PSD-93, and SAP97 in isolated PSDs. *Brain Cell Biology*, 35, 239-250.
- DEROSI, D., CHASSAING, G. & PROCHIANTZ, A. 1998. Trojan peptides: the penetratin system for intracellular delivery. *Trends in Cell Biology*, 8, 84-87.
- DEV, K. K. 2004. Making protein interactions druggable: Targeting PDZ domains. *Nature Reviews Drug Discovery*, 3, 1047-1056.
- DOMINGUEZ, C., BOELEN, R. & BONVIN, A. 2003. HADDOCK: A protein-protein docking approach based on biochemical or biophysical information. *Journal of the American Chemical Society*, 125, 1731-1737.
- DOYLE, D. A., LEE, A., LEWIS, J., KIM, E., SHENG, M. & MACKINNON, R. 1996. Crystal structures of a complexed and peptide-free membrane protein-binding domain: Molecular basis of peptide recognition by PDZ. *Cell*, 85, 1067-1076.
- EL-HUSSEIN, A. E., SCHNELL, E., CHETKOVICH, D. M., NICOLL, R. A. & BREDT, D. S. 2000. PSD-95 involvement in maturation of excitatory synapses. *Science*, 290, 1364-1368.

- FIRESTEIN, B. L., BRENNAN, J. E., AOKI, C., SANCHEZ-PEREZ, A. M., EL-HUSSEINI, A. E. D. & BREDT, D. S. 1999. Cypin: A cytosolic regulator of PSD-95 postsynaptic targeting. *Neuron*, 24, 659-672.
- FLORIO, S. K., LOH, C., HUANG, S. M., IWAMAYE, A. E., KITTO, K. F., FOWLER, K. W., TREIBERG, J. A., HAYFLICK, J. S., WALKER, J. M., FAIRBANKS, C. A. & LAI, Y. 2009. Disruption of nNOS-PSD95 protein-protein interaction inhibits acute thermal hyperalgesia and chronic mechanical allodynia in rodents. *British Journal of Pharmacology*, 158, 494-506.
- FREYER, M. W. & LEWIS, E. A. 2008. Isothermal titration calorimetry: Experimental design, data analysis, and probing Macromolecule/Ligand binding and kinetic interactions. In: CORREIA, J. J. & DETRICH, H. W. (eds.) *Biophysical Tools for Biologists: Vol 1 in Vitro Techniques*. San Diego: Elsevier Academic Press Inc.
- FRY, D. C. 2006. Protein-protein interactions as targets for small molecule drug discovery. *Biopolymers*, 84, 535-552.
- FUJII, N., HARESCO, J. J., NOVAK, K. A. P., GAGE, R. M., PEDEMONTE, N., STOKOE, D., KUNTZ, I. D. & GUY, R. K. 2007a. Rational design of a nonpeptide general chemical scaffold for reversible inhibition of PDZ domain interactions. *Bioorganic & Medicinal Chemistry Letters*, 17, 549-552.
- FUJII, N., HARESCO, J. J., NOVAK, K. A. P., STOKOE, D., KUNTZ, I. D. & GUY, R. K. 2003. A selective irreversible inhibitor targeting a PDZ protein interaction domain. *Journal of the American Chemical Society*, 125, 12074-12075.
- FUJII, N., SHELAT, A., HALL, R. A. & GUY, R. K. 2007b. Design of a selective chemical probe for class IPDZ domains. *Bioorganic & Medicinal Chemistry Letters*, 17, 546-548.
- FUJII, N., YOU, L., XU, Z., UEMATSU, K., SHAN, J., HE, B., MIKAMI, I., EDMONDSON, L. R., NEALE, G., ZHENG, J., GUY, R. K. & JABLONS, D. M. 2007c. An antagonist of dishevelled protein-protein interaction suppresses beta-catenin-dependent tumor cell growth. *Cancer Research*, 67, 573-579.
- GADEK, T. R. & NICHOLAS, J. B. 2003. Small molecule antagonists of proteins. *Biochemical Pharmacology*, 65, 1-8.
- GARDNER, L. A., NAREN, A. P. & BAHOUTH, S. W. 2007. Assembly of an SAP97-AKAP79-cAMP-dependent protein kinase scaffold at the type 1 PSD-95/DLG/ZO1 motif of the human beta(1)-adrenergic receptor generates a receptosome involved in receptor recycling and networking. *Journal of Biological Chemistry*, 282, 5085-5099.
- GARDONI, F., MARCELLO, E. & DI LUCA, M. 2009. Postsynaptic density-membrane associated guanylate kinase proteins (PSD-MAGUKs) and their role in CNS disorders. *Neuroscience*, 158, 324-333.
- GARDONI, F., MAUCERI, D., FIORENTINI, C., BELLONE, C., MISSALE, C., CATTABENI, F. & DI LUCA, M. 2003. CaMKII-dependent phosphorylation regulates SAP97/NR2A interaction. *Journal of Biological Chemistry*, 278, 44745-44752.
- GARNER, C. C., NASH, J. & HUGANIR, R. L. 2000. PDZ domains in synapse assembly and signalling. *Trends in Cell Biology*, 10, 274-280.
- GARRY, E. M., MOSS, A., ROSIE, R., DELANEY, A., MITCHELL, R. & FLEETWOOD-WALKER, S. M. 2003. Specific involvement in neuropathic pain of AMPA receptors and adapter proteins for the GluR2 subunit. *Molecular and Cellular Neuroscience*, 24, 10-22.

- GAVARINI, S., BECAMEL, C., ALTIER, C., LORY, P., PONCET, J., WIJNHOLDS, J., BOCKAERT, J. & MARIN, P. 2006. Opposite effects of PSD-95 and MPP3 PDZ proteins on serotonin 5-hydroxytryptamine(2C) receptor desensitization and membrane stability. *Molecular Biology of the Cell*, 17, 4619-4631.
- GAVARINI, S., BECAMEL, C., CHANRION, B., BOCKAERT, J. & MARIN, P. 2004. Molecular and functional characterization of proteins interacting with the C-terminal domains of 5-HT₂ receptors: Emergence of 5-HT₂ "Receptosomes". *Biology of the Cell*, 96, 373-381.
- GENOUX, D. & MONTGOMERY, J. M. 2007. Glutamate receptor plasticity at excitatory synapses in the brain. *Clinical and Experimental Pharmacology and Physiology*, 34, 1058-1063.
- GODREAU, D., VRANCKX, R., MAGUY, A., GOYENVALLE, C. & HATEM, S. N. 2003. Different isoforms of synapse-associated protein, SAP97, are expressed in the heart and have distinct effects on the voltage-gated K⁺ channel Kv1.5. *Journal of Biological Chemistry*, 278, 47046-47052.
- GOTTSCHALK, M., BACH, A., HANSEN, J. L., KROGSGAARD-LARSEN, P., KRISTENSEN, A. S. & STROMGAARD, K. 2009. Detecting Protein-Protein Interactions in Living Cells: Development of a Bioluminescence Resonance Energy Transfer Assay to Evaluate the PSD-95/NMDA Receptor Interaction. *Neurochemical Research*, 34, 1729-1737.
- GOULT, B. T., RAPLEY, J. D., DART, C., KITMITTO, A., GROSSMANN, J. G., LEYLAND, M. L. & LIAN, L.-Y. 2007. Small-angle X-ray scattering and NMR studies of the conformation of the PDZ region of SAP97 and its interactions with Kir2.1. *Biochemistry*, 46, 14117-14128.
- GRANDY, D., SHAN, J., ZHANG, X., RAO, S., AKUNURU, S., LI, H., ZHANG, Y., ALPATOV, I., ZHANG, X. A., LANG, R. A., SHI, D.-L. & ZHENG, J. J. 2009. Discovery and Characterization of a Small Molecule Inhibitor of the PDZ Domain of Dishevelled. *Journal of Biological Chemistry*, 284, 16256-16263.
- GRZESIEK, S. & BAX, A. 1992a. Correlating backbone amide and side-chain resonances in larger proteins by multiple relayed triple resonance NMR. *Journal of the American Chemical Society*, 114, 6291-6293.
- GRZESIEK, S. & BAX, A. 1992b. An efficient experiment for sequential backbone assignment of medium-sized isotopically enriched proteins. *Journal of Magnetic Resonance*, 99, 201-207.
- GRZESIEK, S. & BAX, A. 1992c. Improved 3-D triple resonance NMR techniques applied to a 31-kDa protein. *Journal of Magnetic Resonance*, 96, 432-440.
- GRZESIEK, S. & BAX, A. 1993. Amino-acid type determination in the sequential assignment procedure of uniformly C-13/N-15-enriched proteins. *Journal of Biomolecular Nmr*, 3, 185-204.
- GUNTERT, P. 2004. Automated NMR structure calculation with CYANA. *Methods in molecular biology (Clifton, N.J.)*, 278, 353-78.
- HAMMOND, M. C., HARRIS, B. Z., LIM, W. A. & BARTLETT, P. A. 2006. beta strand peptidomimetics as potent PDZ domain ligands. *Chemistry & Biology*, 13, 1247-1251.
- HAN, A., SONG, Z., TONG, C., HU, D., BI, X., AUGENLICHT, L. H. & YANG, W. 2008. Sulindac suppresses beta-catenin expression in human cancer cells. *European Journal of Pharmacology*, 583, 26-31.

- HANSEN, L. D., CHRISTEN, J. J. & IZATT, R. M. 1965. ENTROPY TITRATION . A calorimetric method for determination of ΔG , ΔH and ΔS . *Chemical Communications*, 36-&.
- HAQ, S. R., JURGENS, M. C., CHI, C. N., KOH, C.-S., ELFSTROM, L., SELMER, M., GIANNI, S. & JEMTH, P. 2010. The Plastic Energy Landscape of Protein Folding: A triangular folding mechanism with an equilibrium intermediate for a small protein domain. *Journal of Biological Chemistry*, 285, 18051-18059.
- HARRIS, B. Z. & LIM, W. A. 2001. Mechanism and role of PDZ domains in signaling complex assembly. *Journal of Cell Science*, 114, 3219-3231.
- HATA, Y. & TAKAI, Y. 1999. Roles of postsynaptic density-95/synapse-associated protein 90 and its interacting proteins in the organization of synapses. *Cellular and Molecular Life Sciences*, 56, 461-472.
- HEINIG, M. & FRISHMAN, D. 2004. STRIDE: a web server for secondary structure assignment from known atomic coordinates of proteins. *Nucleic Acids Research*, 32, W500-W502.
- HERING, H. & SHENG, M. 2002. Direct interaction of Frizzled-1,-2,-4, and-7 with PDZ domains of PSD-95. *Febs Letters*, 521, 185-189.
- HERRMANN, T., GUNTERT, P. & WUTHRICH, K. 2002. Protein NMR structure determination with automated NOE assignment using the new software CANDID and the torsion angle dynamics algorithm DYANA. *Journal of Molecular Biology*, 319, 209-227.
- HOMANS, S. W. 2007. Water, water everywhere - except where it matters? *Drug Discovery Today*, 12, 534-539.
- HOWARD, M. A., ELIAS, G. M., ELIAS, L. A. B., SWAT, W. & NICOLL, R. A. 2010. The role of SAP97 in synaptic glutamate receptor dynamics. *Proceedings of the National Academy of Sciences of the United States of America*, 107, 3805-3810.
- IMAMURA, F., MAEDA, S., DOI, T. & FUJIYOSHI, Y. 2002. Ligand binding of the second PDZ domain regulates clustering of PSD-95 with the Kv1.4 potassium channel. *Journal of Biological Chemistry*, 277, 3640-3646.
- JELESAROV, I. & BOSSHARD, H. R. 1999. Isothermal titration calorimetry and differential scanning calorimetry as complementary tools to investigate the energetics of biomolecular recognition. *Journal of Molecular Recognition*, 12, 3-18.
- JHOTI, H., CLEASBY, A., VERDONK, M. & WILLIAMS, G. 2007. Fragment-based screening using X-ray crystallography and NMR spectroscopy. *Current Opinion in Chemical Biology*, 11, 485-493.
- JOSHI, M., VARGAS, C., BOISGUERIN, P., DIEHL, A., KRAUSE, G., SCHMIEDER, P., MOELLING, K., HAGEN, V., SCHADE, M. & OSCHKINAT, H. 2006. Discovery of low-molecular-weight ligands for the AF6 PDZ domain. *Angewandte Chemie-International Edition*, 45, 3790-3795.
- KANG, C. W., SUN, Y. & DEL VALLE, J. R. 2012. Substituted Imidazo 1,2-a pyridines as beta-Strand Peptidomimetics. *Organic Letters*, 14, 6162-6165.
- KAY, L. E., XU, G. Y., SINGER, A. U., MUHANDIRAM, D. R. & FORMANKAY, J. D. 1993. A gradient-enhanced HCCH TOCSY experiment for recording side-chain H-1 AND C-13 correlations in H2O samples of proteins. *Journal of Magnetic Resonance Series B*, 101, 333-337.
- KAY, L. E., XU, G. Y. & YAMAZAKI, T. 1994. Enhanced-sensitivity triple-resonance spectroscopy with minimal H2O saturation. *Journal of Magnetic Resonance Series A*, 109, 129-133.
- KEELER, J. 2005. *Understanding NMR spectroscopy / James Keeler*, Chichester : Wiley, 2005.

- KENNEDY, M. B. 1997. The postsynaptic density at glutamatergic synapses. *Trends in Neurosciences*, 20, 264-268.
- KISTNER, U., WENZEL, B. M., VEH, R. W., CASESLANGHOFF, C., GARNER, A. M., APPELTAUER, U., VOSS, B., GUNDELFINGER, E. D. & GARNER, C. C. 1993. SAP90, a rat presynaptic protein related to the product of the Drosophila tumour suppressor gene DLG-A. *Journal of Biological Chemistry*, 268, 4580-4583.
- KIYONO, T., HIRAIWA, A., FUJITA, M., HAYASHI, Y., AKIYAMA, T. & ISHIBASHI, M. 1997. Binding of high-risk human papillomavirus E6 oncoproteins to the human homologue of the Drosophila discs large tumor suppressor protein. *Proceedings of the National Academy of Sciences of the United States of America*, 94, 11612-11616.
- KLOSI, E., SARO, D. & SPALLER, M. R. 2007. Bivalent peptides as PDZ domain ligands. *Bioorganic & Medicinal Chemistry Letters*, 17, 6147-6150.
- KORADI, R., BILLETER, M. & WUTHRICH, K. 1996. MOLMOL: A program for display and analysis of macromolecular structures. *Journal of Molecular Graphics*, 14, 51-&.
- KREIENKAMP, H. J. 2002. Organisation of G-protein-coupled receptor signalling complexes by scaffolding proteins. *Current Opinion in Pharmacology*, 2, 581-586.
- KUNDU, R., CUSHING, P. R., POPP, B. V., ZHAO, Y., MADDEN, D. R. & BALL, Z. T. 2012. Hybrid Organic-Inorganic Inhibitors of a PDZ Interaction that Regulates the Endocytic Fate of CFTR. *Angewandte Chemie-International Edition*, 51, 7217-7220.
- KURAKIN, A., SWISTOWSKI, A., WU, S. C. & BREDESEN, D. E. 2007. The PDZ domain as a complex adaptive system. *PLoS One*, 2, e953.
- LADBURY, J. E. & CHOWDHRY, B. Z. 1996. Sensing the heat: The application of isothermal titration calorimetry to thermodynamic studies of biomolecular interactions. *Chemistry & Biology*, 3, 791-801.
- LASKOWSKI, R. A., MACARTHUR, M. W., MOSS, D. S. & THORNTON, J. M. 1993. PROCHECK - A program to check the stereochemical quality of protein structures. *Journal of Applied Crystallography*, 26, 283-291.
- LATORRE, I. J., ROH, M. H., FRESE, K. K., WEISS, R. S., MARGOLIS, B. & JAVIER, R. T. 2005. Viral oncoprotein-induced mislocalization of select PDZ proteins disrupts tight junctions and causes polarity defects in epithelial cells. *Journal of Cell Science*, 118, 4283-4293.
- LAU, C. G. & ZUKIN, R. S. 2007. NMDA receptor trafficking in synaptic plasticity and neuropsychiatric disorders. *Nature Reviews Neuroscience*, 8, 413-426.
- LEAVITT, S. & FREIRE, E. 2001. Direct measurement of protein binding energetics by isothermal titration calorimetry. *Current Opinion in Structural Biology*, 11, 560-566.
- LEBLANC, B. W., IWATA, M., MALLON, A. P., RUPASINGHE, C. N., GOEBEL, D. J., MARSHALL, J., SPALLER, M. R. & SAAB, C. Y. 2010. A cyclic peptide targeted against PSD-95 blocks central sensitisation and attenuates thermal hyperalgesia. *Neuroscience*, 167, 490-500.
- LEE, H.-J., WANG, N. X., SHAO, Y. & ZHENG, J. J. 2009a. Identification of tripeptides recognized by the PDZ domain of Dishevelled. *Bioorganic & Medicinal Chemistry*, 17, 1701-1708.
- LEE, H.-J., WANG, N. X., SHI, D.-L. & ZHENG, J. J. 2009b. Sulindac Inhibits Canonical Wnt Signaling by Blocking the PDZ Domain of the Protein Dishevelled. *Angewandte Chemie-International Edition*, 48, 6448-6452.

- LEE, S. S., WEISS, R. S. & JAVIER, R. T. 1997. Binding of human virus oncoproteins to hDIg/SAP97, a mammalian homolog of the *Drosophila* discs large tumor suppressor protein. *Proceedings of the National Academy of Sciences of the United States of America*, 94, 6670-6675.
- LEONOUDAKIS, D., MAILLIARD, W. S., WINGERD, K. L., CLEGG, D. O. & VANDENBERG, C. A. 2001. Inward rectifier potassium channel Kir2.2 is associated with synapse-associated protein SAP97. *Journal of Cell Science*, 114, 987-998.
- LEVITT, M. H. 2008. *Spin dynamics : basics of nuclear magnetic resonance / Malcolm H. Levitt*, Chichester : John Wiley & Sons, 2008. 2nd ed.
- LI, D., SPECHT, C. G., WAITES, C. L., BUTLER-MUNRO, C., LEAL-ORTIZ, S., FOOTE, J. W., GENOUX, D., GARNER, C. C. & MONTGOMERY, J. M. 2011. SAP97 directs NMDA receptor spine targeting and synaptic plasticity. *Journal of Physiology-London*, 589, 4491-4510.
- LI, Y., HU, J., HOEFER, K., WONG, A. M. S., COOPER, J. D., BIRNBAUM, S. G., HAMMER, R. E. & HOFMANN, S. L. 2010. DHHC5 Interacts with PDZ Domain 3 of Post-synaptic Density-95 (PSD-95) Protein and Plays a Role in Learning and Memory. *Journal of Biological Chemistry*, 285, 13022-13031.
- LIAN, L.-Y. & MIDDLETON, D. A. 2001. Labelling approaches for protein structural studies by solution-state and solid-state NMR. *Progress in Nuclear Magnetic Resonance Spectroscopy*, 39, 171-190.
- LIAN, L.-Y. & ROBERTS, G. C. K. 2011. *Protein NMR spectroscopy [electronic book] practical techniques and applications / edited by Lu-Yun Lian, Gordon Roberts*, Hoboken, N.J. : Wiley, 2011.
- LIM, I. A., HALL, D. D. & HELL, J. W. 2002. Selectivity and promiscuity of the first and second PDZ domains of PSD-95 and synapse-associated protein 102. *Journal of Biological Chemistry*, 277, 21697-21711.
- LIU, Y., HENRY, G. D., HEGDE, R. S. & BALEJA, J. D. 2007. Solution structure of the hDIg/SAP97 PDZ2 domain and its mechanism of interaction with HPV-18 Papillomavirus E6 protein. *Biochemistry*, 46, 10864-10874.
- LONG, J. F., TOCHIO, H., WANG, P., FAN, J. S., SALA, C., NIETHAMMER, M., SHENG, M. & ZHANG, M. J. 2003. Supramodular structure and synergistic target binding of the N-terminal tandem PDZ domains of PSD-95. *Journal of Molecular Biology*, 327, 203-214.
- LUE, R. A., MARFATIA, S. M., BRANTON, D. & CHISHTI, A. H. 1994. Cloning and characterisation of hDLG - the human homolog of the *Drosophila* disks large tumour-suppressor binds to protein-4.1. *Proceedings of the National Academy of Sciences of the United States of America*, 91, 9818-9822.
- MAHINDROO, N., PUNCHIHEWA, C., BAIL, A. M. & FUJII, N. 2008. Indole-2-amide based biochemical antagonist of Dishevelled PDZ domain interaction down-regulates Dishevelled-driven Tcf transcriptional activity. *Bioorganic & Medicinal Chemistry Letters*, 18, 946-949.
- MANTOVANI, F. & BANKS, L. 2003. Regulation of the discs large tumor suppressor by a phosphorylation-dependent interaction with the beta-TrCP ubiquitin ligase receptor. *Journal of Biological Chemistry*, 278, 42477-42486.
- MARCELLO, E., EPIS, R., SARACENO, C., GARDONI, F., BORRONI, B., CATTABENI, F., PADOVANI, A. & DI LUCA, M. 2012. SAP97-mediated local trafficking is altered in Alzheimer disease patients' hippocampus. *Neurobiology of Aging*, 33.

- MARIN, P., BECAMEL, C., DUMUIS, A. & BOCKAERT, J. 2012. 5-HT Receptor-Associated Protein Networks: New Targets for Drug Discovery in Psychiatric Disorders? *Current Drug Targets*, 13, 28-52.
- MARUR, S., D'SOUZA, G., WESTRA, W. H. & FORASTIERE, A. A. 2010. HPV-associated head and neck cancer: a virus-related cancer epidemic. *Lancet Oncology*, 11, 781-789.
- MAYASUNDARI, A., FERREIRA, A. M., HE, L., MAHINDROO, N., BASHFORD, D. & FUJII, N. 2008. Rational design of the first small-molecule antagonists of NHERF1/EBP50 PDZ domains. *Bioorganic & Medicinal Chemistry Letters*, 18, 942-945.
- MEISSNER, A. & SORENSEN, O. W. 1999. The role of coherence transfer efficiency in design of TROSY-type multidimensional NMR experiments. *Journal of Magnetic Resonance*, 139, 439-442.
- MONTGOMERY, J. M., ZAMORANO, P. L. & GARNER, C. C. 2004. MAGUKs in synapse assembly and function: an emerging view. *Cellular and Molecular Life Sciences*, 61, 911-929.
- MOREIRA, I. S., FERNANDES, P. A. & RAMOS, M. J. 2007. Hot spots-A review of the protein-protein interface determinant amino-acid residues. *Proteins-Structure Function and Bioinformatics*, 68, 803-812.
- MORTON, C. J., PUGH, D. J. R., BROWN, E. L. J., KAHMANN, J. D., RENZONI, D. A. C. & CAMPBELL, I. D. 1996. Solution structure and peptide binding of the SH3 domain from human Fyn. *Structure*, 4, 705-714.
- MUDERS, M. H., VOHRA, P. K., DUTTA, S. K., WANG, E., IKEDA, Y., WANG, L., UDUGAMASOORIYA, D. G., MEMIC, A., RUPASHINGHE, C. N., BARETTON, G. B., AUST, D. E., LANGER, S., DAM, K., SIMONS, M., SPALLER, M. R. & MUKHOPADHYAY, D. 2009. Targeting GIPC/Synectin in Pancreatic Cancer Inhibits Tumor Growth. *Clinical Cancer Research*, 15, 4095-4103.
- MUHANDIRAM, D. R. & KAY, L. E. 1994. Gradient-enhanced triple-resonance 3-dimensional NMR experiments with improved sensitivity. *Journal of Magnetic Resonance Series B*, 103, 203-216.
- MULLER, B. M., KISTNER, U., VEH, R. W., CASESLANGHOFF, C., BECKER, B., GUNDELFINGER, E. D. & GARNER, C. C. 1995. Molecular characterisation and spatial distribution of SAP97, a novel presynaptic protein homologous to SAP90 and the Drosophila disks-large tumour suppressor. *Journal of Neuroscience*, 15, 2354-2366.
- MUNOZ, N., BOSCH, F. X., DE SANJOSE, S., HERRERO, R., CASTELLSAGUE, X., SHAH, K. V., SNIJDERS, P. J. F., MEIJER, C. & INT AGCY RES CANC MULTICENTER, C. 2003. Epidemiologic classification of human papillomavirus types associated with cervical cancer. *New England Journal of Medicine*, 348, 518-527.
- NEDERVEEN, A. J., DORELEIJERS, J. F., VRANKEN, W., MILLER, Z., SPRONK, C., NABUURS, S. B., GUNTERT, P., LIVNY, M., MARKLEY, J. L., NILGES, M., ULRICH, E. L., KAPTEIN, R. & BONVIN, A. 2005. RECOORD: A recalculated coordinate database of 500+proteins from the PDB using restraints from the BioMagResBank. *Proteins-Structure Function and Bioinformatics*, 59, 662-672.
- NIETHAMMER, M., VALTSCHANOFF, J. G., KAPOOR, T. M., ALLISON, D. W., WEINBERG, R. J., CRAIG, A. M. & SHENG, M. 1998. CRIPT, a novel postsynaptic protein that binds to the third PDZ domain of PSD-95/SAP90. *Neuron*, 20, 693-707.

- OCKEY, D. A. & GADEK, T. R. 2002. Inhibitors of protein-protein interactions. *Expert Opinion on Therapeutic Patents*, 12, 393-400.
- OPAZO, P., SAINLOS, M. & CHOQUET, D. 2012. Regulation of AMPA receptor surface diffusion by PSD-95 slots. *Current Opinion in Neurobiology*, 22, 453-460.
- PADUCH, M., BIERNAT, M., STEFANOWICZ, P., DEREWENDA, Z. S., SZEWCZUK, Z. & OTLEWSKI, J. 2007. Bivalent peptides as models for multimeric targets of PDZ domains. *Chembiochem*, 8, 443-452.
- PATRA, C. R., RUPASINGHE, C. N., DUTTA, S. K., BHATTACHARYA, S., WANG, E., SPALLER, M. R. & MUKHOPADHYAY, D. 2012. Chemically Modified Peptides Targeting the PDZ Domain of GIPC as a Therapeutic Approach for Cancer. *Acs Chemical Biology*, 7, 770-779.
- PEGAN, S., TAN, J., HUANG, A., SLESINGER, P. A., RIEK, R. & CHOE, S. 2007. NMR studies of interactions between C-terminal tail of Kir2.1 channel and PDZ1,2 domains of PSD95. *Biochemistry*, 46, 5315-5322.
- PEIRETTI, F., DEPREZ-BEAUCLAIR, P., BONARDO, B., AUBERT, H., JUHAN-VAGUE, I. & NALBONE, G. 2003. Identification of SAP97 as an intracellular binding partner of TACE. *Journal of Cell Science*, 116, 1949-1957.
- PHILLIPS, S. T., BLASDEL, L. K. & BARTLETT, P. A. 2005. @-tides as reporters for molecular associations. *Journal of the American Chemical Society*, 127, 4193-4198.
- PICHON, X., WATTIEZ, A. S., BECAMEL, C., EHRLICH, I., BOCKAERT, J., ESCHALIER, A., MARIN, P. & COURTEIX, C. 2010. Disrupting 5-HT_{2A} Receptor/PDZ Protein Interactions Reduces Hyperalgesia and Enhances SSRI Efficacy in Neuropathic Pain. *Molecular Therapy*, 18, 1462-1470.
- PIOTTO, M., SAUDEK, V. & SKLENAR, V. 1992. GRADIENT-TAILORED EXCITATION FOR SINGLE-QUANTUM NMR-SPECTROSCOPY OF AQUEOUS-SOLUTIONS. *Journal of Biomolecular Nmr*, 2, 661-665.
- PISERCHIO, A., PELLEGRINI, M., MEHTA, S., BLACKMAN, S. M., GARCIA, E. P., MARSHALL, J. & MIERKE, D. F. 2002. The PDZ1 domain of SAP90 - Characterization of structure and binding. *Journal of Biological Chemistry*, 277, 6967-6973.
- PISERCHIO, A., SALINAS, G. D., LI, T., MARSHALL, J., SPALLER, M. R. & MIERKE, D. F. 2004. Targeting specific PDZ domains of PSD-95: Structural basis for enhanced affinity and enzymatic stability of a cyclic peptide. *Chemistry & Biology*, 11, 469-473.
- PONTING, C. P., PHILLIPS, C., DAVIES, K. E. & BLAKE, D. J. 1997. PDZ domains: Targeting signalling molecules to sub-membranous sites. *Bioessays*, 19, 469-479.
- REES, D. C., CONGREVE, M., MURRAY, C. W. & CARR, R. 2004. Fragment-based lead discovery. *Nature Reviews Drug Discovery*, 3, 660-672.
- ROBERTS, K. E., CUSHING, P. R., BOISGUERIN, P., MADDEN, D. R. & DONALD, B. R. 2012. Computational Design of a PDZ Domain Peptide Inhibitor that Rescues CFTR Activity. *Plos Computational Biology*, 8.
- ROTH, B. L. 1994. Multiple serotonin receptors: clinical and experimental aspects. *Annals of clinical psychiatry : official journal of the American Academy of Clinical Psychiatrists*, 6, 67-78.
- ROTH, B. L. 2011. Irving Page Lecture: 5-HT_{2A} serotonin receptor biology: Interacting proteins, kinases and paradoxical regulation. *Neuropharmacology*, 61, 348-354.

- SAINLOS, M., TIGARET, C., POUJOL, C., OLIVIER, N. B., BARD, L., BREILLAT, C., THIOLON, K., CHOQUET, D. & IMPERIALI, B. 2011. Biomimetic divalent ligands for the acute disruption of synaptic AMPAR stabilization. *Nature Chemical Biology*, 7, 81-91.
- SAUPE, J., ROSKE, Y., SCHILLINGER, C., KAMDEM, N., RADETZKI, S., DIEHL, A., OSCHKINAT, H., KRAUSE, G., HEINEMANN, U. & RADEMANN, J. 2011. Discovery, Structure-Activity Relationship Studies, and Crystal Structure of Nonpeptide Inhibitors Bound to the Shank3 PDZ Domain. *Chemmedchem*, 6, 1411-1422.
- SCHEFFNER, M., WERNESS, B. A., HUIBREGTSE, J. M., LEVINE, A. J. & HOWLEY, P. M. 1990. The E6 oncoprotein encoded by human papillomavirus type-16 and type-18 promotes the degradation of p53. *Cell*, 63, 1129-1136.
- SCHLEUCHER, J., SATTLER, M. & GRIESINGER, C. 1993. Coherence selection by gradients without signal attenuation - application to the 3-dimensional HNCO experiment. *Angewandte Chemie-International Edition in English*, 32, 1489-1491.
- SCHLUETER, O. M., XU, W. & MALENKA, R. C. 2006. Alternative N-terminal domains of PSD-95 and SAP97 govern activity-dependent regulation of synaptic AMPA receptor function. *Neuron*, 51, 99-111.
- SCHULTZ, J., HOFFMULLER, U., KRAUSE, G., ASHURST, J., MACIAS, M. J., SCHMIEDER, P., SCHNEIDER-MERGENER, J. & OSCHKINAT, H. 1998. Specific interactions between the syntrophin PDZ domain and voltage-gated sodium channels. *Nature Structural Biology*, 5, 19-24.
- SCHWARZ, E., FREESE, U. K., GISSMANN, L., MAYER, W., ROGGENBUCK, B., STREMLAU, A. & HAUSEN, H. Z. 1985. Structure and transcription of human papillomavirus sequences in cervical-carcinoma cells. *Nature*, 314, 111-114.
- SHAN, J., ZHANG, X., BAO, J., CASSELL, R. & ZHENG, J. J. 2012. Synthesis of Potent Dishevelled PDZ Domain Inhibitors Guided by Virtual Screening and NMR Studies. *Chemical Biology & Drug Design*, 79, 376-383.
- SHAN, J. & ZHENG, J. J. 2009. Optimizing Dvl PDZ domain inhibitor by exploring chemical space. *Journal of Computer-Aided Molecular Design*, 23, 37-47.
- SHAN, J. & ZHENG, J. J. 2012. Virtual ligand screening combined with NMR to identify Dvl PDZ domain inhibitors targeting the Wnt signaling. *Methods in molecular biology (Clifton, N.J.)*, 928, 17-28.
- SHAN, J. F., SHI, D. L., WANG, J. M. & ZHENG, J. 2005. Identification of a specific inhibitor of the dishevelled PDZ domain. *Biochemistry*, 44, 15495-15503.
- SHARMA, S. C., MEMIC, A. M., RUPASINGHE, C. N., DUC, A.-C. E. & SPALLER, M. R. 2009. T7 Phage Display as a Method of Peptide Ligand Discovery for PDZ Domain Proteins. *Biopolymers*, 92, 183-193.
- SHARMA, S. C., RUPASINGHE, C. N., PARISIEN, R. B. & SPALLER, M. R. 2007. Design, synthesis, and evaluation of linear and cyclic peptide Ligands for PDZ10 of the Multi-PDZ domain protein MUPP1. *Biochemistry*, 46, 12709-12720.
- SHARMA, S. K., RAMSEY, T. M. & BAIR, K. W. 2002. Protein-Protein interactions: Lessons learned. *Current Medicinal Chemistry - Anti-Cancer Agents*, 2, 311-330.
- SHATSKY, M., NUSSINOV, R. & WOLFSON, H. J. 2004. A method for simultaneous alignment of multiple protein structures. *Proteins-Structure Function and Bioinformatics*, 56, 143-156.
- SHENG, M. & SALA, C. 2001. PDZ domains and the organization of supramolecular complexes. *Annual Review of Neuroscience*, 24, 1-29.

- SHEPHERD, J. D. & HUGANIRL, R. L. 2007. The cell biology of synaptic plasticity: AMPA receptor trafficking. *Annual Review of Cell and Developmental Biology*.
- SIGURSKJOLD, B. W. 2000. Exact analysis of competition ligand binding by displacement isothermal titration calorimetry. *Analytical Biochemistry*, 277, 260-266.
- SKLENAR, V., PIOTTO, M., LEPIK, R. & SAUDEK, V. 1993. Gradient-tailored water suppression for H-1-N-15 HSQC experiments optimised to retain full sensitivity. *Journal of Magnetic Resonance Series A*, 102, 241-245.
- SMITH, A. B., GUZMAN, M. C., SPRENGELER, P. A., KEENAN, T. P., HOLCOMB, R. C., WOOD, J. L., CARROLL, P. J. & HIRSCHMANN, R. 1994. De-novo design, synthesis and X-ray crystal structures of pyrrolinone-based beta-strand peptidomimetics. *Journal of the American Chemical Society*, 116, 9947-9962.
- SMITH, A. B., KEENAN, T. P., HOLCOMB, R. C., SPRENGELER, P. A., GUZMAN, M. C., WOOD, J. L., CARROLL, P. J. & HIRSCHMANN, R. 1992. Design, synthesis and crystal structure of a pyrrolinone-based peptidomimetic possessing the conformation of a beta-strand - potential application to the design of novel inhibitors of proteolytic-enzymes. *Journal of the American Chemical Society*, 114, 10672-10674.
- SUN, H.-S., DOUCETTE, T. A., LIU, Y., FANG, Y., TEVES, L., AARTS, M., RYAN, C. L., BERNARD, P. B., LAU, A., FORDER, J. P., SALTER, M. W., WANG, Y. T., TASKER, R. A. & TYMIANSKI, M. 2008. Effectiveness of PSD95 inhibitors in permanent and transient focal ischemia in the rat. *Stroke*, 39, 2544-2553.
- SUTHERELL, C. L., THOMPSON, S., SCOTT, R. T. W. & HAMILTON, A. D. 2012. Aryl-linked imidazolidin-2-ones as non-peptidic beta-strand mimetics. *Chemical Communications*, 48, 9834-9836.
- SYRJANEN, S. 2005. Human papillomavirus (HPV) in head and neck cancer. *Journal of Clinical Virology*, 32, S59-S66.
- TAO, Y. X. & RAJA, S. N. 2004. Are synaptic MAGUK proteins involved in chronic pain? *Trends in Pharmacological Sciences*, 25, 397-400.
- THORSEN, T. S., MADSEN, K. L., REBOLA, N., RATHJE, M., ANGGONO, V., BACH, A., MOREIRA, I. S., STUHR-HANSEN, N., DYHRING, T., PETERS, D., BEUMING, T., HUGANIR, R., WEINSTEIN, H., MULLE, C., STROMGAARD, K., RONN, L. C. B. & GETHER, U. 2010. Identification of a small-molecule inhibitor of the PICK1 PDZ domain that inhibits hippocampal LTP and LTD. *Proceedings of the National Academy of Sciences of the United States of America*, 107, 413-418.
- TINA, K. G., BHADRA, R. & SRINIVASAN, N. 2007. PIC: Protein Interactions Calculator. *Nucleic Acids Research*, 35, W473-W476.
- TOCHIO, H., HUNG, F., LI, M., BREDT, D. S. & ZHANG, M. J. 2000. Solution structure and backbone dynamics of the second PDZ domain of postsynaptic density-95. *Journal of Molecular Biology*, 295, 225-237.
- TOOGOOD, P. L. 2002. Inhibition of protein-protein association by small molecules: Approaches and progress. *Journal of Medicinal Chemistry*, 45, 1543-1558.
- TZENG, S.-R. & KALODIMOS, C. G. 2012. Protein activity regulation by conformational entropy. *Nature*, 488, 236-240.
- UCHINO, S., WADA, H., HONDA, S., HIRASAWA, T., YANAI, S., NAKAMURA, Y., ONDO, Y. & KOHSAKA, S. 2003. Slo2 sodium-activated K+

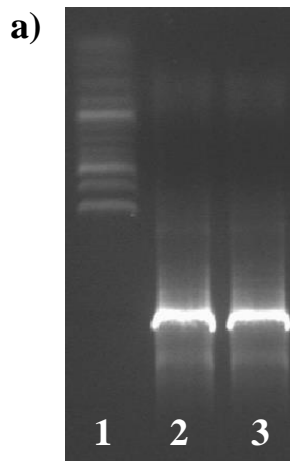
- channels bind to the PDZ domain of PSD-95. *Biochemical and Biophysical Research Communications*, 310, 1140-1147.
- UDUGAMASOORIYA, D. G., SHARMA, S. C. & SPALLER, M. R. 2008. A chemical library approach to organic-modified peptide ligands for PDZ domain proteins: A synthetic, thermodynamic and structural investigation. *Chembiochem*, 9, 1587-1589.
- UDUGAMASOORIYA, G., SARO, D. & SPALLER, M. R. 2005. Bridged peptide macrocycles as ligands for PDZ domain proteins. *Organic Letters*, 7, 1203-1206.
- VAN DIJK, A. D. J., DE VRIES, S. J., DOMINGUEZ, C., CHEN, H., ZHOU, H. X. & BONVIN, A. 2005. Data-driven docking: HADDOCK's adventures in CAPRI. *Proteins-Structure Function and Bioinformatics*, 60, 232-238.
- VAN DIJK, M., VAN DIJK, A. D. J., HSU, V., BOELENS, R. & BONVIN, A. M. J. 2006. Information-driven protein-DNA docking using HADDOCK: it is a matter of flexibility. *Nucleic Acids Research*, 34, 3317-3325.
- VOGRIG, A., BOUCHERLE, B., DEOKAR, H., THOMAS, I., RIPOCHE, I., LIAN, L.-Y. & DUCKI, S. 2011. NMR evaluation of interactions between substituted-indole and PDZ1 domain of PSD-95. *Bioorganic & Medicinal Chemistry Letters*, 21, 3349-3353.
- VOGRIG, A., DORR, L., BOUZIDI, N., BOUCHERLE, B., WATTIEZ, A.-S., CASSIER, E., VALLON, G., RIPOCHE, I., ABRUNHOSA-THOMAS, I., MARIN, P., NAUTON, L., THERY, V., COURTEIX, C., LIAN, L.-Y. & DUCKI, S. 2013. Structure-Based Design of PDZ Ligands as Inhibitors of 5-HT_{2A} Receptor/PSD-95 PDZ1 Domain Interaction Possessing Anti-hyperalgesic Activity. *Acs Chemical Biology*, 8, 2209-16.
- VON OSSOWSKI, I., OKSANEN, E., VON OSSOWSKI, L., CAI, C., SUNDBERG, M., GOLDMAN, A. & KEINANEN, K. 2006. Crystal structure of the second PDZ domain of SAP97 in complex with a GluR-A C-terminal peptide. *Febs Journal*, 273, 5219-5229.
- VRIEND, G. 1990. WHAT IF - A molecular modelling and drug design program. *Journal of Molecular Graphics*, 8, 52-&.
- VUISTER, G. W. & BAX, A. 1992. Resolution enhancement and spectral editing of uniformly C-13-enriched proteins by homonuclear broad-band C-13 decoupling. *Journal of Magnetic Resonance*, 98, 428-435.
- WACKER, D., WANG, C., KATRITCH, V., HAN, G. W., HUANG, X.-P., VARDY, E., MCCORVY, J. D., JIANG, Y., CHU, M., SIU, F. Y., LIU, W., XU, H. E., CHEREZOV, V., ROTH, B. L. & STEVENS, R. C. 2013. Structural Features for Functional Selectivity at Serotonin Receptors. *Science*, 340, 615-619.
- WAITES, C. L., SPECHT, C. G., HAERTEL, K., LEAL-ORTIZ, S., GENOUX, D., LI, D., DRISDEL, R. C., JEYIFOUS, O., CHEYNE, J. E., GREEN, W. N., MONTGOMERY, J. M. & GARNER, C. C. 2009a. Synaptic SAP97 Isoforms Regulate AMPA Receptor Dynamics and Access to Presynaptic Glutamate. *Journal of Neuroscience*, 29, 4332-4345.
- WAITES, C. L., SPECHT, C. G., HARTEL, K., LEAL-ORTIZ, S., GENOUX, D., LI, D., DRISDEL, R. C., JEYIFOUS, O., CHEYNE, J. E., GREEN, W. N., MONTGOMERY, J. M. & GARNER, C. C. 2009b. Synaptic SAP97 isoforms regulate AMPA receptor dynamics and access to presynaptic glutamate. *Journal of Neuroscience*, 29, 4332-45.
- WANG, L., PISERCHIO, A. & MIERKE, D. F. 2005. Structural characterization of the intermolecular interactions of synapse-associated protein-97 with the NR2B

- subunit of N-methyl-D-aspartate receptors. *Journal of Biological Chemistry*, 280, 26992-26996.
- WANG, W., WENG, J., ZHANG, X., LIU, M. & ZHANG, M. 2009. Creating Conformational Entropy by Increasing Interdomain Mobility in Ligand Binding Regulation: A Revisit to N-Terminal Tandem PDZ Domains of PSD-95. *Journal of the American Chemical Society*, 131, 787-796.
- WELLS, J. A. & MCCLENDON, C. L. 2007. Reaching for high-hanging fruit in drug discovery at protein-protein interfaces. *Nature*, 450, 1001-1009.
- WERNESS, B. A., LEVINE, A. J. & HOWLEY, P. M. 1990. Association of human papillomavirus type-16 and type-18 proteins with p53. *Science*, 248, 76-79.
- WITTEKIND, M. & MUELLER, L. 1993. HNCACB, a high-sensitivity 3D NMR experiment to correlate amide-proton and nitrogen resonances with the alpha-carbon and beta-carbon resonances in proteins. *Journal of Magnetic Resonance Series B*, 101, 201-205.
- XIA, Z. Q., GRAY, J. A., COMPTON-TOTH, B. A. & ROTH, B. L. 2003. A direct interaction of PSD-95 with 5-HT_{2A} serotonin receptors regulates receptor trafficking and signal transduction. *Journal of Biological Chemistry*, 278, 21901-21908.
- XU, W., SCHLUETER, O. M., STEINER, P., CZERVIONKE, B. L., SABATINI, B. & MALENKA, R. C. 2008. Molecular dissociation of the role of PSD-95 in regulating synaptic strength and LTD. *Neuron*, 57, 248-262.
- YAMAZAKI, T., FORMANKAY, J. D. & KAY, L. E. 1993. 2-dimensional NMR experiments for correlating C-13-beta and H-1-delta/epsilon chemical-shifts of aromatic residues in C-13-labelled proteins via scalar couplings. *Journal of the American Chemical Society*, 115, 11054-11055.
- YIN, H. & HAMILTON, A. D. 2005. Strategies for targeting protein-protein interactions with synthetic agents. *Angewandte Chemie-International Edition*, 44, 4130-4163.
- ZHANG, W., PENMATSU, H., REN, A., PUNCHIHEWA, C., LEMOFF, A., YAN, B., FUJII, N. & NAREN, A. P. 2011a. Functional regulation of cystic fibrosis transmembrane conductance regulator-containing macromolecular complexes: a small-molecule inhibitor approach. *Biochemical Journal*, 435, 451-462.
- ZHANG, Y., APPLETON, B. A., WIESMANN, C., LAU, T., COSTA, M., HANNOUSH, R. N. & SIDHU, S. S. 2009. Inhibition of Wnt signaling by Dishevelled PDZ peptides. *Nature Chemical Biology*, 5, 217-219.
- ZHANG, Y., DASGUPTA, J., MA, R. Z., BANKS, L., THOMAS, M. & CHEN, X. S. 2007. Structures of a human papillomavirus (HPV) E6 polypeptide bound to MAGUK proteins: Mechanisms of targeting tumor suppressors by a high-risk HPV oncoprotein. *Journal of Virology*, 81, 3618-3626.
- ZHANG, Z., LI, H., CHEN, L., LU, X., ZHANG, J., XU, P., LIN, K. & WU, G. 2011b. Molecular Basis for the Recognition of Adenomatous Polyposis Coli by the Discs Large 1 Protein. *Plos One*, 6.
- ZHOU, L., LI, F., XU, H.-B., LUO, C.-X., WU, H.-Y., ZHU, M.-M., LU, W., JI, X., ZHOU, Q.-G. & ZHU, D.-Y. 2011. Treatment of cerebral ischemia by disrupting ischemia-induced interaction of nNOS with PSD-95 (vol 16, pg 1439, 2010). *Nature Medicine*, 17, 1153-1153.
- ZIFF, E. B. 1997. Enlightening the postsynaptic density. *Neuron*, 19, 1163-1174.

APPENDIX

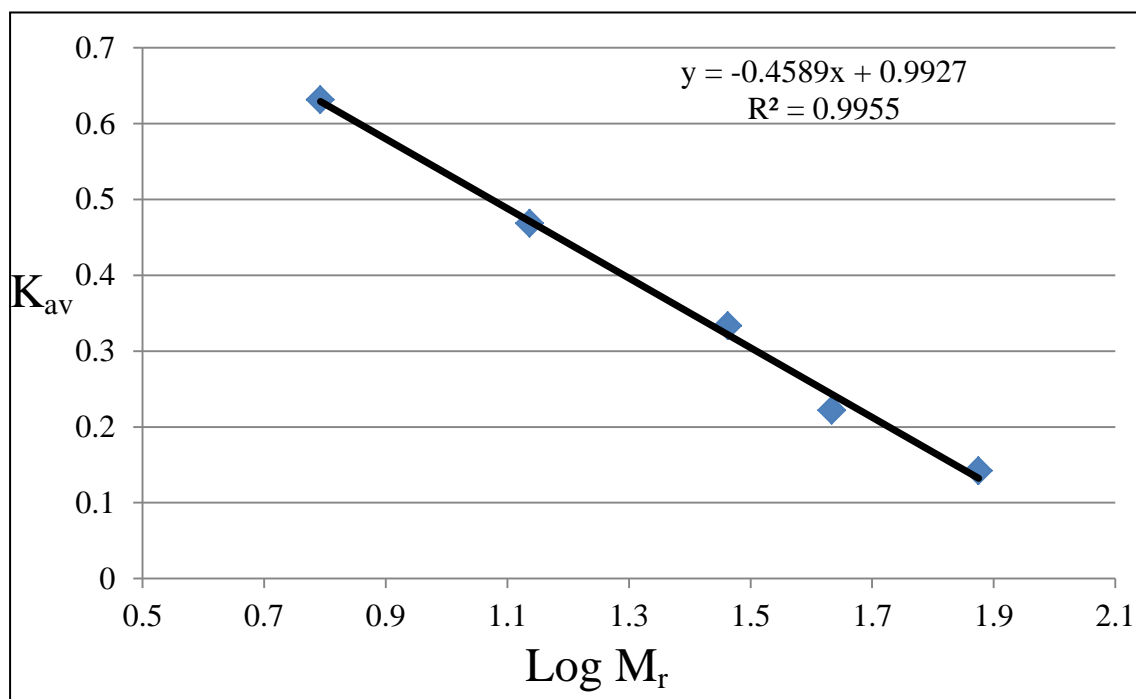
APPENDIX

A.1. a) Agarose gel visualisation under trans UV light of the products from the site-directed ligase-independent mutagenesis (SLIM) procedure on the SAP97 PDZ2 domain; the agarose gel shows that the SLIM methodology resulted in the desired PCR products, indicated by the bright white bands visible: 1 = Marker, 2 = SAP97 PDZ2 H73G and 3 = SAP97 PDZ2 H73T. b) The standard 'generate protons using CNS' protocol implemented to add non-polar hydrogens to the small molecules in the PSD-95 PDZ1 – **3c/4c** complex HADDOCK structures.

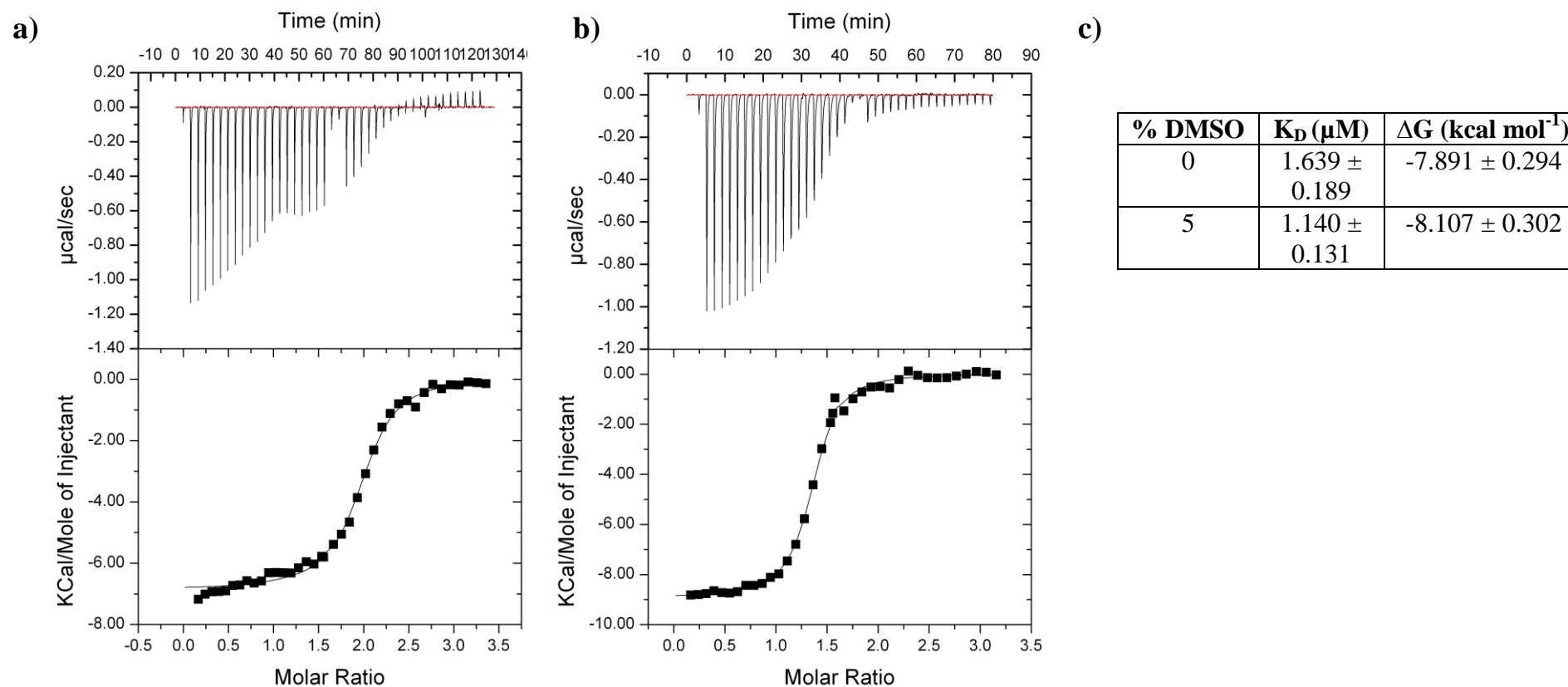


- b)**
1. Split the pdb file of the representative structure into two separate pdb files, where one contains the individual PSD-95 PDZ1 component of the complex and the other contains the small molecule component. Alter the segment ID (SEGID) of the small molecule pdb so that 'SEGID' = 'B' and save accordingly.
 2. Ensure that the mtf file contains the relevant topology (.top) and parameter (.par) files for the small molecule.
 3. Adapt the gen.inp file as necessary for the respective input parameters and output files.
 4. Initiate the process and check that the outputted files contain the desired addition of non-polar hydrogens.

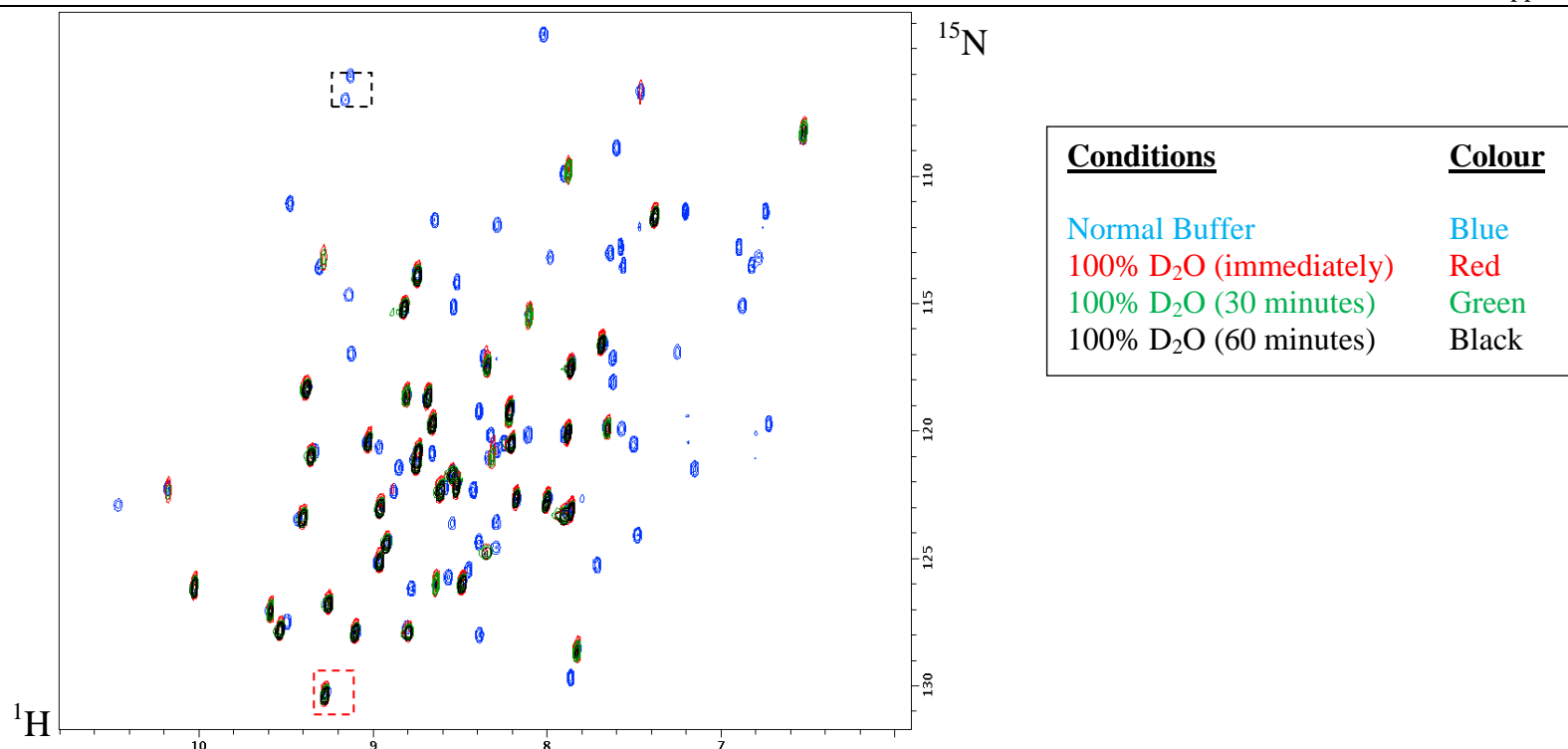
A.2. The calibration process of the HiLoad 26/60 Superdex 75 size exclusion chromatography column carried out by a colleague, where V_o = void volume, V_e = elution volume i.e. retention time, V_c = column volume and $K_{av} = \frac{V_e - V_o}{V_c - V_o}$. Thus, knowledge of the retention time of the protein of interest leads to determination of the $\text{Log } M_r$ value and hence, molecular weight (M_r).



	log M_r	M_r	V_o	V_e	$V_e - V_o$	$V_c - V_o$	K_{av}
Blue Dextran			113				
Conalbumin	1.875	75		142.42	29.42	207	0.142
Ovalbumin	1.633	43		158.97	45.97	207	0.222
Carbonic anhydrase	1.462	29		182.01	69.01	207	0.333
Ribonuclease	1.137	13.7		209.94	96.94	207	0.468
Aprotinin	0.792	6.5		243.65	130.65	207	0.631



A.3. The ITC isotherm (top) and resultant curve (bottom) produced by the ITC binding experiment between $100\mu\text{M}$ SAP97 PDZ2 (cell) and $750\mu\text{M}$ RETQV (syringe) in a) 20mM phosphate, $\text{pH}7.4$ and b) 20mM phosphate, 5% (v/v) DMSO $\text{pH}7.4$, on an iTC_{200} Microcalorimeter (MicroCal) at 298K . c) A table summarising the binding affinity and Gibbs free energy parameters obtained from the respective ITC experiments; fitting of the curve produced by the individual ITC experiment to a single set of sites curve-fitting model, using Origin7, resulted in a binding affinity (K_D) of 1.639 and $1.140\mu\text{M}$ for RETQV to the SAP97 PDZ2 domain, in the absence or presence of 5% (v/v) DMSO respectively. The difference in the obtained binding parameters between the respective ITC binding experiments is small and within experimental error; as the concentration of DMSO present in the ITC competition experiments is 10-fold less than in the experiments shown here, it can be concluded that the presence of DMSO in the samples of the ITC competition experiments will have no or negligible effect on the subsequent results obtained and thus, any conclusions drawn will be valid.



A.4. An overlay of ^1H - ^{15}N HSQC experiments of the ^{13}C , ^{15}N PSD-95 PDZ1 – 5-HT_{2c} complex (P:L = 1:5), acquired at 298K, with a field strength of 600MHz, in either 20mM phosphate 0.1mM EDTA buffer, pH6.3 or 100% D₂O; where the different colour spectra correspond to different buffer and/or time periods and these are detailed in the table to the right. The object of this series of ^1H - ^{15}N HSQC experiments was to determine those residues of the PSD-95 PDZ1 domain forming intramolecular hydrogen bonds, so that they could be used as restraints in the PSD-95 PDZ1 – 5-HT_{2c} NMR solution state structure determination process; this was completed by lyophilising a previously used NMR complex sample, re-suspending in D₂O and then, performing ^1H - ^{15}N HSQC experiments at different time intervals overnight. The overlaid spectra shows that 10Ile (red dashed rectangle) is an example of a PSD-95 PDZ1 residue forming an intramolecular hydrogen bond as the corresponding peak is present in the normal NMR complex (blue), immediately in D₂O (red), 30 minutes in D₂O (green) and 60 minutes D₂O (black) spectra and thus, there is no evidence of backbone NH hydrogen/deuterium exchange occurring to cause attenuation of the peak i.e. an intramolecular hydrogen bond is present which prevents this. The residues that were present in all spectra were then analysed in the PSD-95 PDZ1 crystal structure (PDB ID = 3GSL) and those residues within hydrogen bond formation distance with other residues were taken as hydrogen bond restraints for the PSD-95 PDZ1 domain in the structure determination process. Gly20 (black dashed rectangle) is a PSD-95 PDZ1 residue that does not form an intramolecular hydrogen bond.

A.5. (continues onto next page) The intermolecular distance restraints used in the PSD-95 PDZ1 – 5-HT_{2c} complex NMR solution state structure calculation process; the individual PSD-95 PDZ1 and 5-HT_{2c} residue atoms involved in the given restraint have been detailed, along with the corresponding NOE distance restraint and the allowed upper limit. * denotes where the particular protons were equivalent.

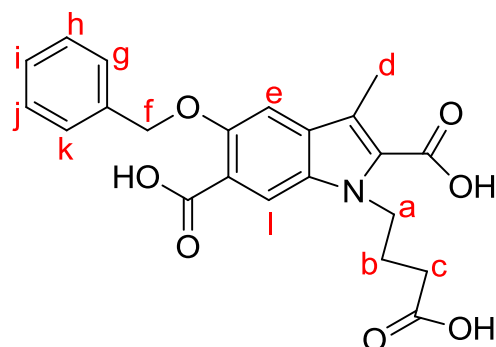
PSD-95 PDZ1 Residue	Atom	5-HT _{2c} Residue	Atom	NOE Distance Restraint (Å)	Upper Limit (Å)
Val78	H γ 1*	Ser8	H β *	2.695	+1.395
Val78	H γ 2*	Val9	H β	2.910	+1.610
Val78	H γ 2*	Ser8	H β *	2.515	+1.215
Leu81	H β 1	Val9	H γ *	3.435	+2.135
Phe21	HN	Val9	H α	3.055	+1.755
Ser22	HN	Ile6	H δ 1*	2.900	+1.600
Ala24	HN	Ile6	H δ 1*	2.760	+1.460
Thr41	HN	Ile6	H δ 1*	2.885	+1.585
Lys42	HN	Ile6	H δ 1*	2.780	+1.480
Leu19	H δ *	Val9	H β	2.750	+1.450
Leu19	H δ *	Val9	H γ *	2.690	+1.390
Ser22	H β *	Ile6	H δ 1*	2.675	+1.375
Ser22	H β *	Ser8	H β *	3.080	+1.780
Ser22	H β *	Val9	H α	3.290	+1.990
Ile23	H γ 1*	Ser8	H β *	3.070	+1.770
Ile32	H δ 1*	Val1	H γ *	3.140	+1.840
Ile32	H δ 1*	Val2	H γ *	3.165	+1.865
Gly33	HN	Val1	H γ *	3.235	+1.935
Gly33	HN	Val2	H γ *	3.260	+1.960
His74	He1	Arg5	H δ *	2.935	+1.635
Leu81	H δ *	Val9	H β	2.525	+1.225
Lys82	H γ *	Val9	H β	2.96	+1.66
Lys82	H γ *	Val9	H γ *	3.41	+2.110
Gly20	HN	Val9	H γ *	3.650	+2.350
Gly18	HN	Val9	H γ *	3.650	+2.350
Ile23	HN	Ser8	H β *	3.265	+1.965
Ile23	HN	Ile6	H δ 1*	2.725	+1.425
Gly25	HN	Ile6	H δ 1*	3.565	+2.265
Ile23	H δ 1*	Ser8	H β	3.390	+2.090
Ser22	H β 2	Ile6	H δ 1*	2.940	+1.640
Ser22	H β 1	Ile6	H δ 1*	2.940	+1.640
Ile23	H α	Ile6	H δ 1*	2.885	+1.585
Ala24	H α	Ile6	H δ 1*	2.950	+1.650
Ala24	H β *	Ile6	H δ 1*	2.68	+1.380
Lys82	H α	Val9	H γ *	2.325	+1.825
Ile23	H β	Ile6	H δ 1*	3.120	+1.820
Ile23	H δ 1*	Val9	H β	2.770	+1.470
Ile23	H γ 2*	Ile6	H δ 1*	2.590	+1.290
Ile23	H γ 2*	Ser8	H β *	2.955	+1.655
Ala24	H β *	Ile6	H γ 1*	2.440	+1.140
Pro30	H β 2	Ser3	H α	3.115	+1.815

PSD-95 PDZ1 Residue	Atom	5-HT _{2c} Residue	Atom	NOE Distance Restraint (Å)	Upper Limit (Å)
Lys42	Hβ2	Ile6	Hδ1*	2.890	+1.590
Lys42	Hβ1	Ile6	Hδ1*	2.890	+1.590
Leu81	Hγ	Val9	Hβ	3.210	+1.910
Val78	Hα	Val9	Hβ	2.89	+1.590
Val78	Hγ1*	Val9	Hβ	2.665	+1.365
Val88	Hγ*	Val9	Hβ	3.355	+2.055

A.6. The intramolecular PSD-95 PDZ1 hydrogen bond restraints used in the PSD-95 PDZ1 – 5-HT_{2c} complex NMR solution state structure calculation process, determined by the process described in A.4. The individual PSD-95 PDZ1 residue atoms involved in the particular restraint have been detailed; the given restraints were set as $1.80\text{Å} \pm 0.20\text{Å}$.

Residue	Atom	Residue	Atom
Glu8	HN	Val92	O
Ile10	HN	Leu90	O
Leu12	HN	Val88	O
Ser22	HN	Lys42	O
Ala24	HN	Phe39	O
Leu55	HN	Ala49	O
Asp59	HN	Arg56	O
Leu62	HN	Tyr91	O
Phe63	HN	Tyr91	O
Val64	HN	Val67	O
Asn65	HN	Arg89	O
Ala77	HN	His74	O
Val78	HN	His74	O
Glu79	HN	Ser75	O
Leu81	HN	Val78	O
Lys82	HN	Val78	O
Val88	HN	Leu12	O
Tyr91	HN	Phe63	O
Val92	HN	Glu8	O
Met93	HN	Asp59	O

A.7. The annotated structure of the small molecule inhibitor **3c**, with tables of the obtained intra- and intermolecular NOE's of the **3c** in the PSD-95 PDZ1-bound form; these NOE distance restraints were used as input parameters in the HADDOCK webserver restraint-driven docking process.



The intramolecular NOE's of **3c** from a two-Dimensional [^{13}C , ^{15}N]-filtered NOE experiment ([PSD-95 PDZ1] : [**3c**] = 1:5) in the PSD-95 PDZ1-bound form.

Assignment	ω_1 (ppm)	ω_2 (ppm)	Relative NOE Intensity ^a
d ↔ h	2.151	7.335	w
d ↔ g	2.154	7.423	m
d ↔ e	2.154	7.197	s
d ↔ f	2.154	5.014	m
l ↔ e	7.448	7.197	m
l ↔ b	7.449	1.756	m
l ↔ c	7.448	1.881	m
b ↔ c	1.757	1.880	s

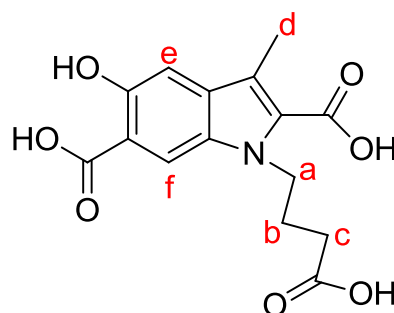
^a. NOE cross-peak intensities were classified as strong (s, 1.8-3.2 Å), medium (m, 1.8-4.5 Å), and weak (w, 1.8-6 Å). Distances were calibrated using the distance between h ↔ g as 2.5Å.

The intermolecular NOE's between the PSD-95 PDZ1 domain and **3c** from 3-D [^{13}C , ^{15}N]-filtered NOE Experiment ([PSD-95 PDZ1] : [**3c**] = 1:5).

Assignment	Relative NOE Intensity ^a	Assignment	Relative NOE Intensity ^a
L12 H δ 1 ↔ i	m	I23 H γ 2 ↔ g	m
L12 H δ 1 ↔ h	w	I23 H δ 1 ↔ g	w
L12 H δ 1 ↔ g	w	I44 H β ↔ d	w
L19 H γ ↔ h	m	I44 H γ 2 ↔ d	m
L19 H γ ↔ g	w	I44 H δ 1 ↔ d	m
L19 H δ 2 ↔ g	w	V78 H α ↔ i	w
L19 H δ 1 ↔ e	w	V78 H γ 1 ↔ i	m
L19 H δ 1 ↔ f	m	V78 H γ 1 ↔ h	m
L19 H δ 2 ↔ f	w	V78 H γ 2 ↔ h	w
I23 H δ 1 ↔ i	w	L81 H δ 1 ↔ g	w
I23 H γ 1 ↔ i	w	L81 H δ 2 ↔ g	m
I23 H γ 1 ↔ h	w	L81 H δ 1 ↔ f	w
I23 H δ 1 ↔ h	m	L81 H δ 2 ↔ f	w

^a. NOE cross-peak intensities were classified as strong (s, 1.8-3.2 Å), medium (m, 1.8-4.5 Å), and weak (w, 1.8-6 Å). Distances were calibrated using the distance between h ↔ g as 2.5Å.

A.8. The annotated structure of the small molecule inhibitor **4c**, with tables of the obtained intra- and intermolecular NOE's of the **4c** in the PSD-95 PDZ1-bound form; these NOE distance restraints were used as input parameters in the HADDOCK webserver restraint-driven docking process.



The intramolecular NOE's of **4c** from two-Dimensional [^{13}C , ^{15}N]-filtered NOE experiment ([PSD-95 PDZ1] : [**4c**] = 1:5) in the PSD-95 PDZ1-bound form.

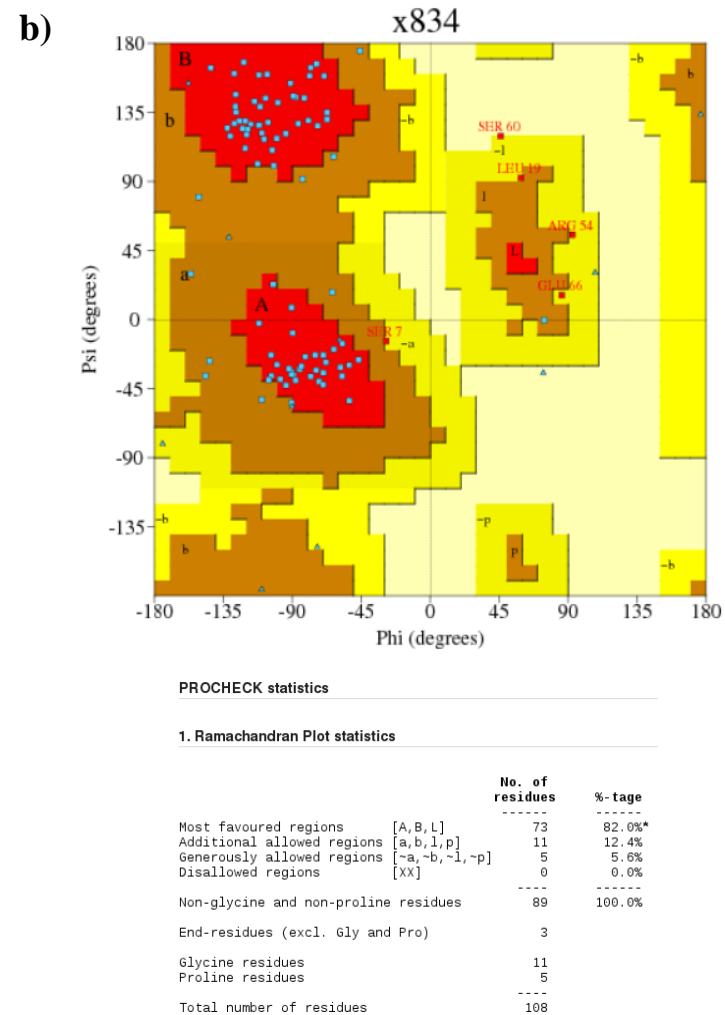
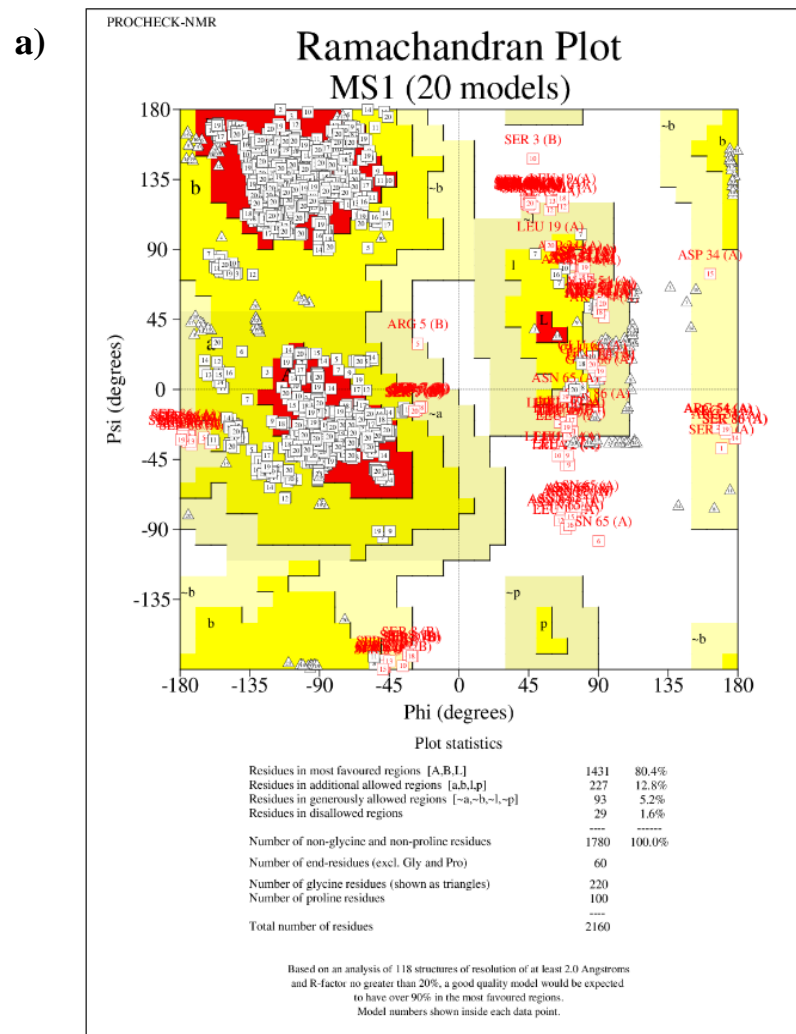
Assignment	ω_1 (ppm)	ω_2 (ppm)	Relative NOE Intensity ^a
e ↔ d	6.942	2.081	s
e ↔ b	6.942	1.787	w
f ↔ d	7.856	2.080	w
f ↔ b	7.859	1.793	m
f ↔ c	7.859	1.935	w
f ↔ a	7.858	4.198	w
a ↔ d	4.222	1.793	w
a ↔ c	4.223	1.937	w
a ↔ b	4.222	2.080	m

^a. NOE cross-peak intensities were classified as strong (s, 1.8-3.2 Å), medium (m, 1.8-4.5 Å), and weak (w, 1.8-6 Å). Distances were calibrated using the distance between d ↔ e as 2.5Å.

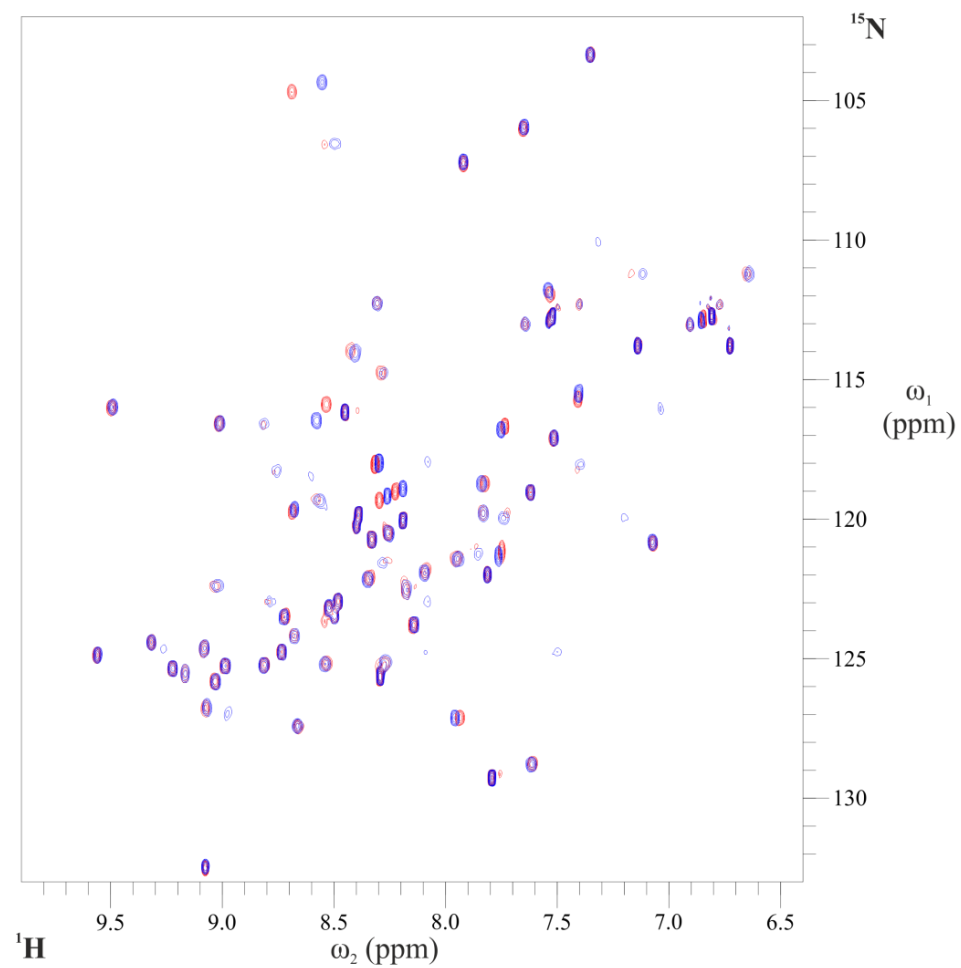
The intermolecular NOE's between the PSD-95 PDZ1 domain and **4c** from 3-D [^{13}C , ^{15}N]-filtered NOE Experiment ([PSD-95 PDZ1] : [**4c**] = 1:5).

Assignment	Relative NOE Intensity ^a	Assignment	Relative NOE Intensity ^a
L19 H δ 1 ↔ d	m	V78 H γ 2 ↔ e	w
L19 H δ 2 ↔ d	w	V78 H γ 1 ↔ f	m
I23 H δ 1 ↔ d	w	V78 H γ 2 ↔ f	w
I23 H γ 2 ↔ e	w	V78 H γ 1 ↔ a	w
I23 H δ 1 ↔ e	w	L81 H δ 1 ↔ d	m
I38 H γ 2 ↔ e	w	L81 H δ 2 ↔ d	m
I41 H γ 2 ↔ e	w	L81 H δ 1 ↔ e	w
V78 H γ 1 ↔ e	w	L81 H δ 2 ↔ e	w

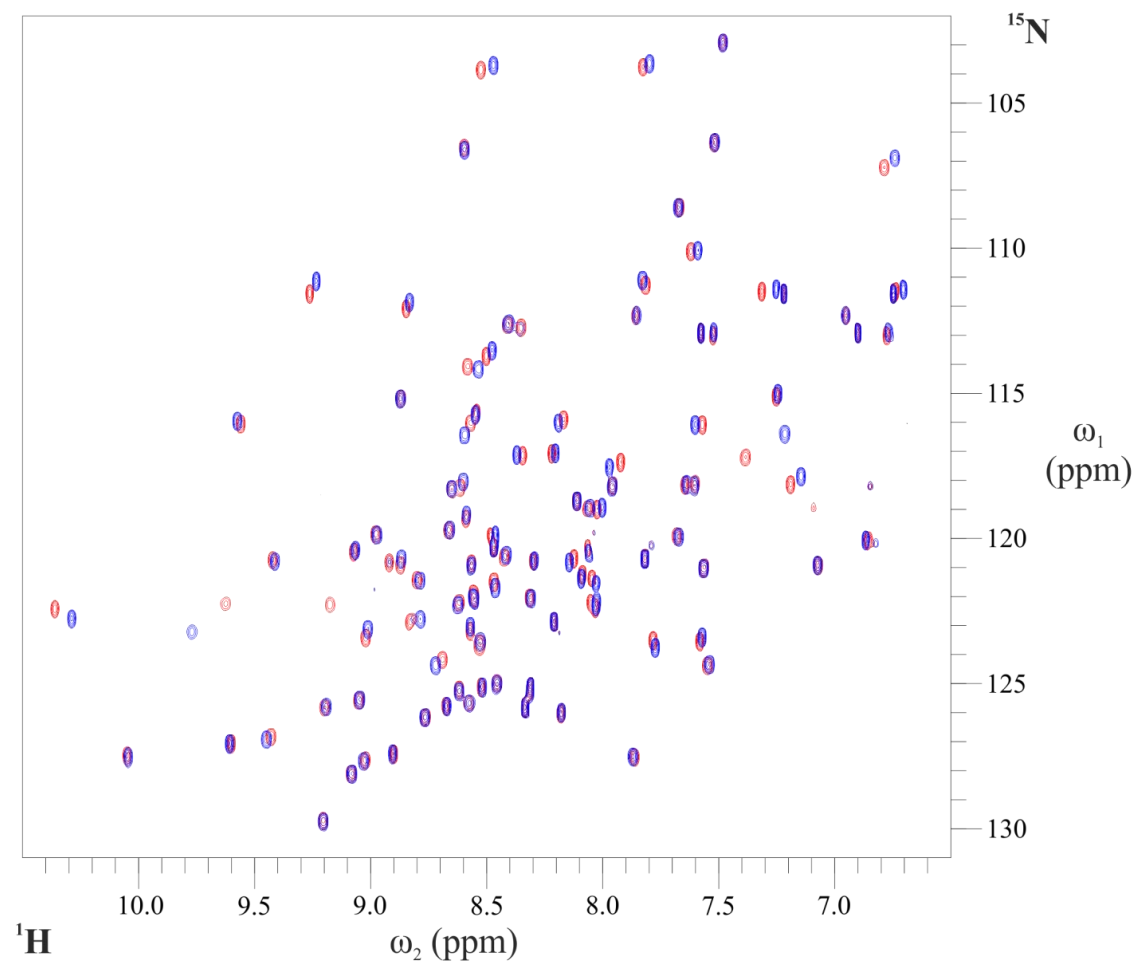
^a. NOE cross-peak intensities were classified as strong (s, 1.8-3.2 Å), medium (m, 1.8-4.5 Å), and weak (w, 1.8-6 Å). Distances were calibrated using the distance between d ↔ e as 2.5Å.



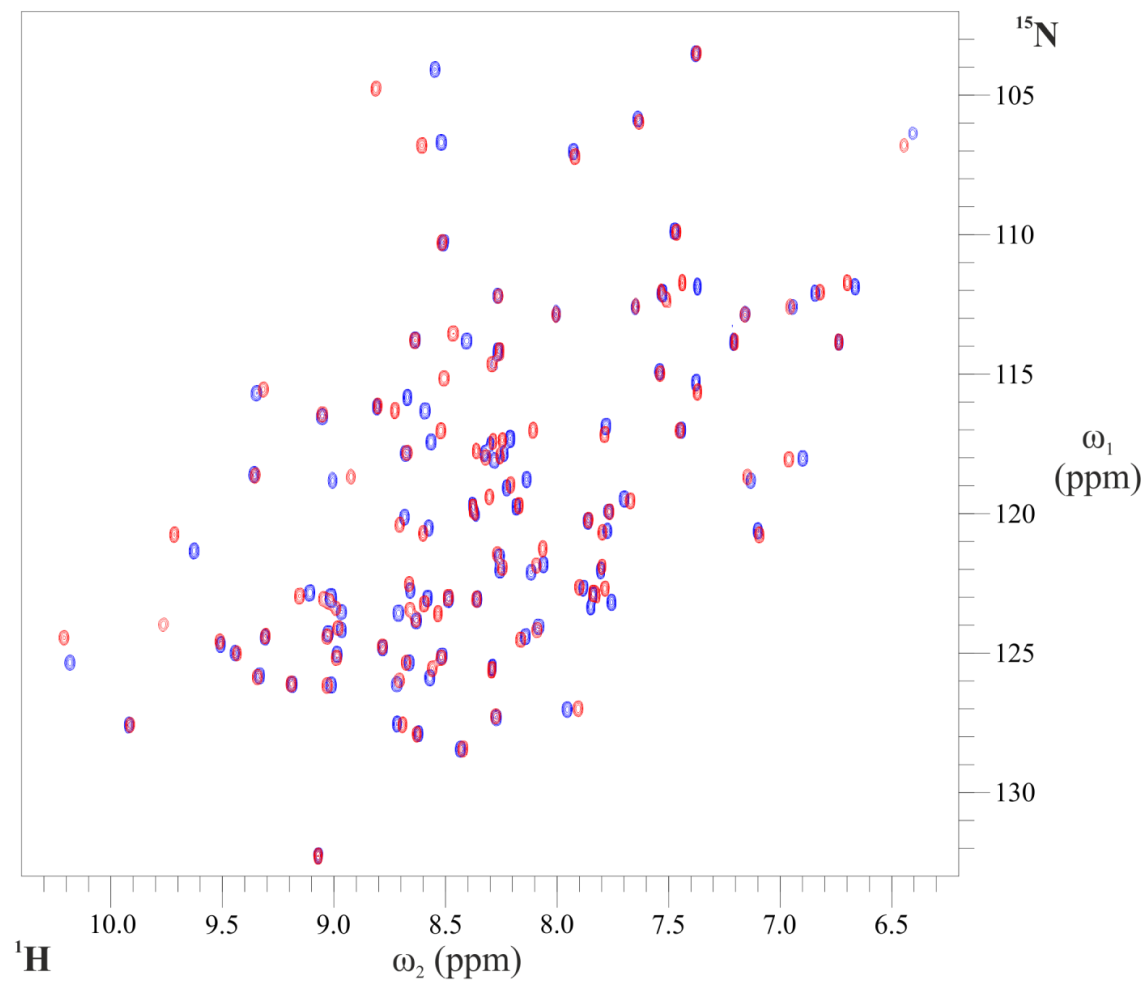
A.9. The Ramachandran analysis of a) the full 20 structure ensemble and b) the representative structure of the PSD-95 PDZ1 – 5-HT_{2c} complex NMR solution state structure, performed by iCING and PDBsum respectively.



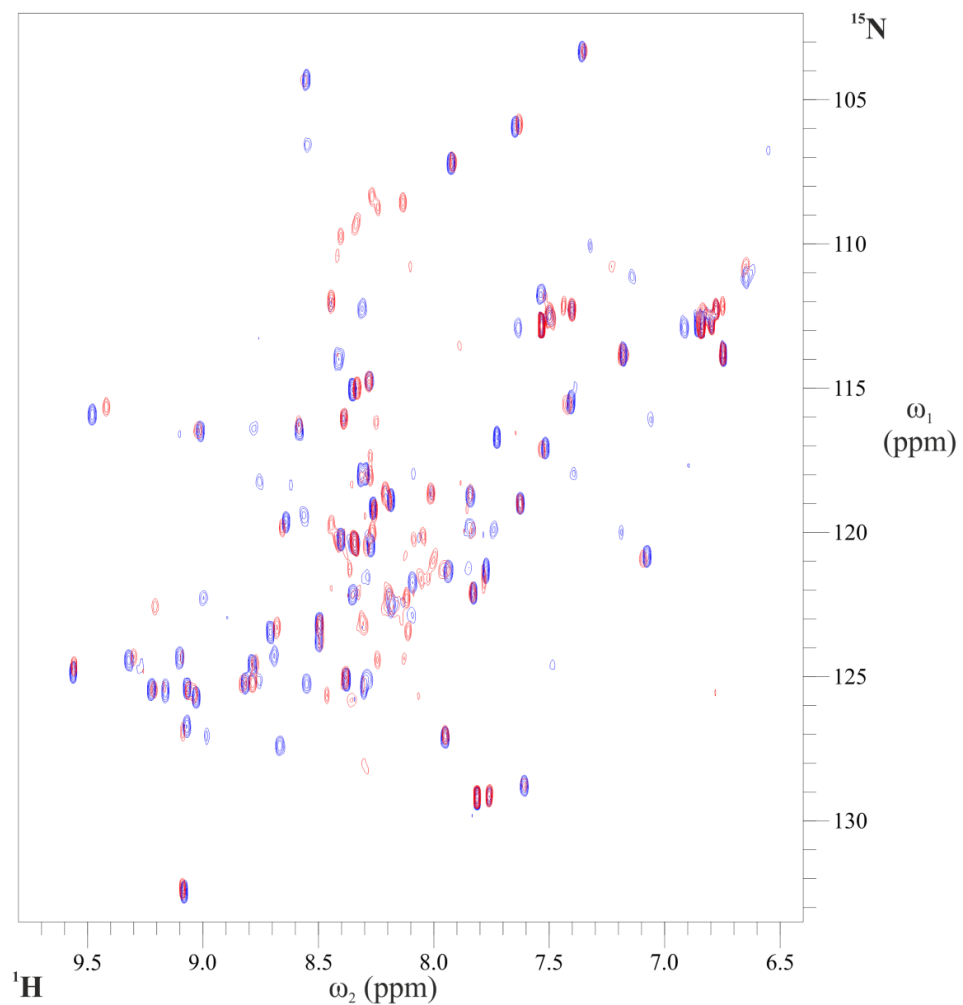
A.10. A 2-D overlay of the $^1\text{H} - ^{15}\text{N}$ HSQC spectra produced of PSD-95 PDZ2 in the free form (blue) and in the presence of **1d** (P:L = 1:10, red), acquired at 298K, with a field strength of 600MHz, in 20mM phosphate buffer, pH6.3.



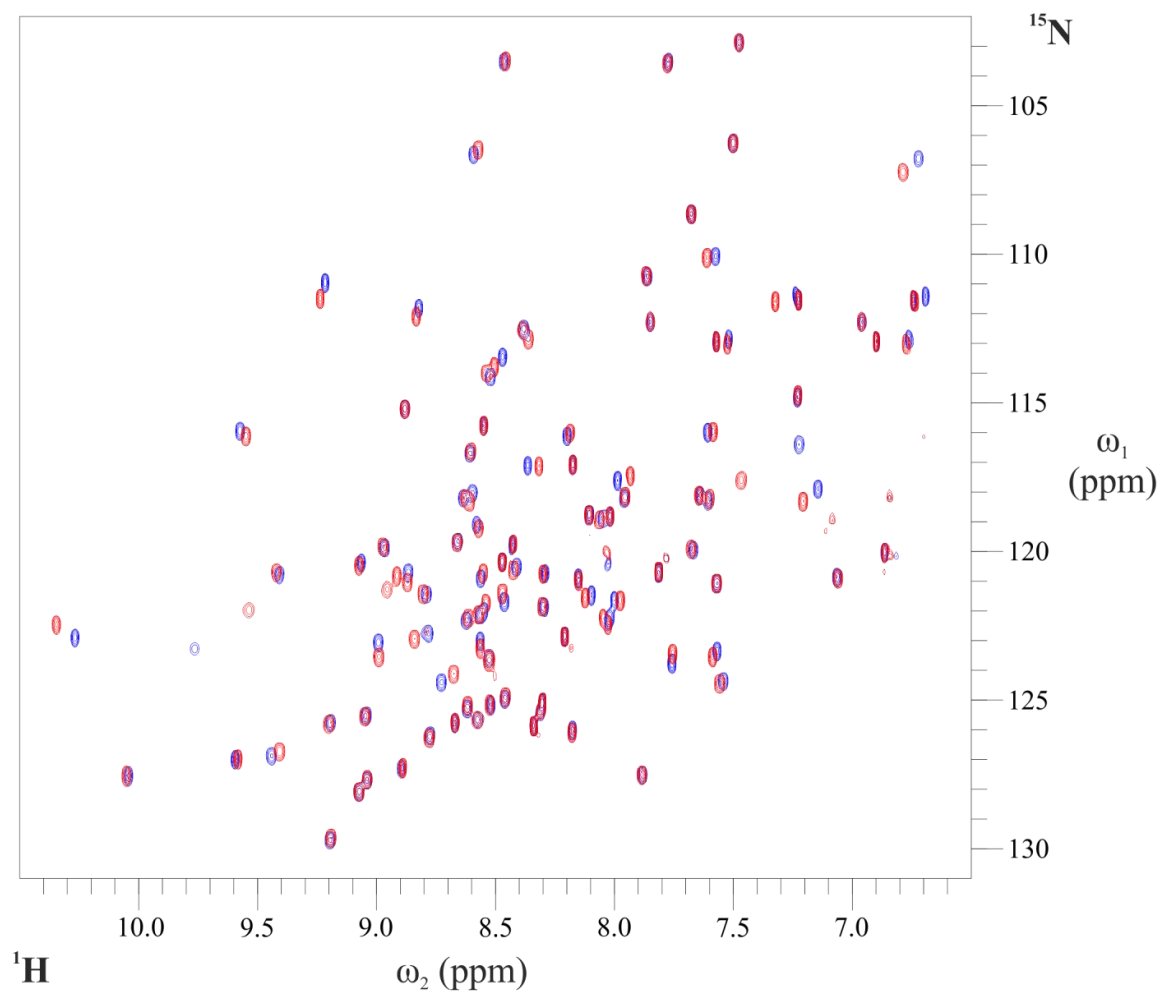
A.11. A 2-D overlay of the $^1\text{H} - ^{15}\text{N}$ HSQC spectra produced of SAP97 PDZ1 in the free form (blue) and in the presence of **1d** (P:L = 1:10, red), acquired at 298K, with a field strength of 600MHz, in 20mM phosphate buffer, pH6.3.



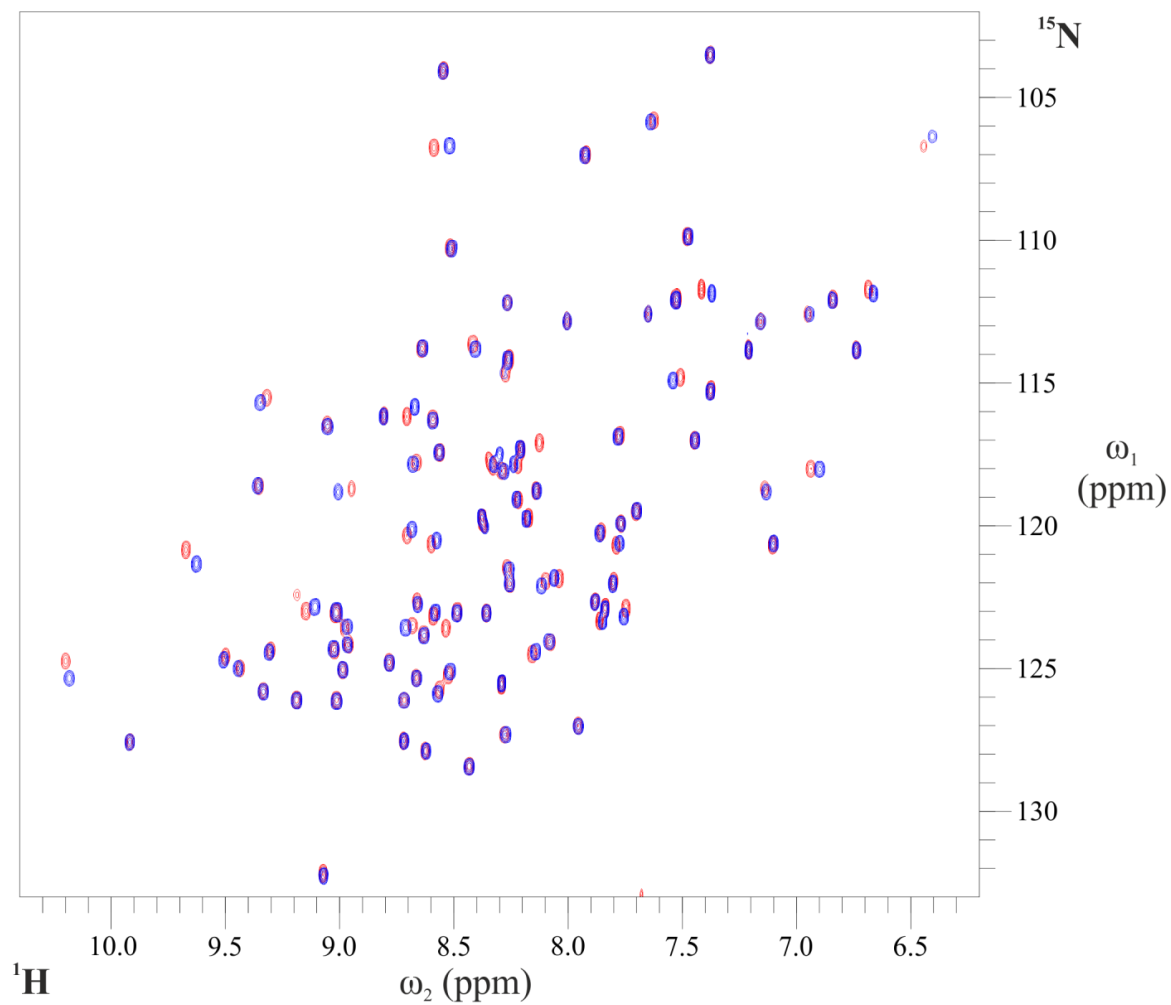
A.12. A 2-D overlay of the $^1\text{H} - ^{15}\text{N}$ HSQC spectra produced of SAP97 PDZ2 in the free form (blue) and in the presence of **1d** (P:L = 1:10, red), acquired at 298K, with a field strength of 600MHz, in 20mM phosphate buffer, pH6.3.



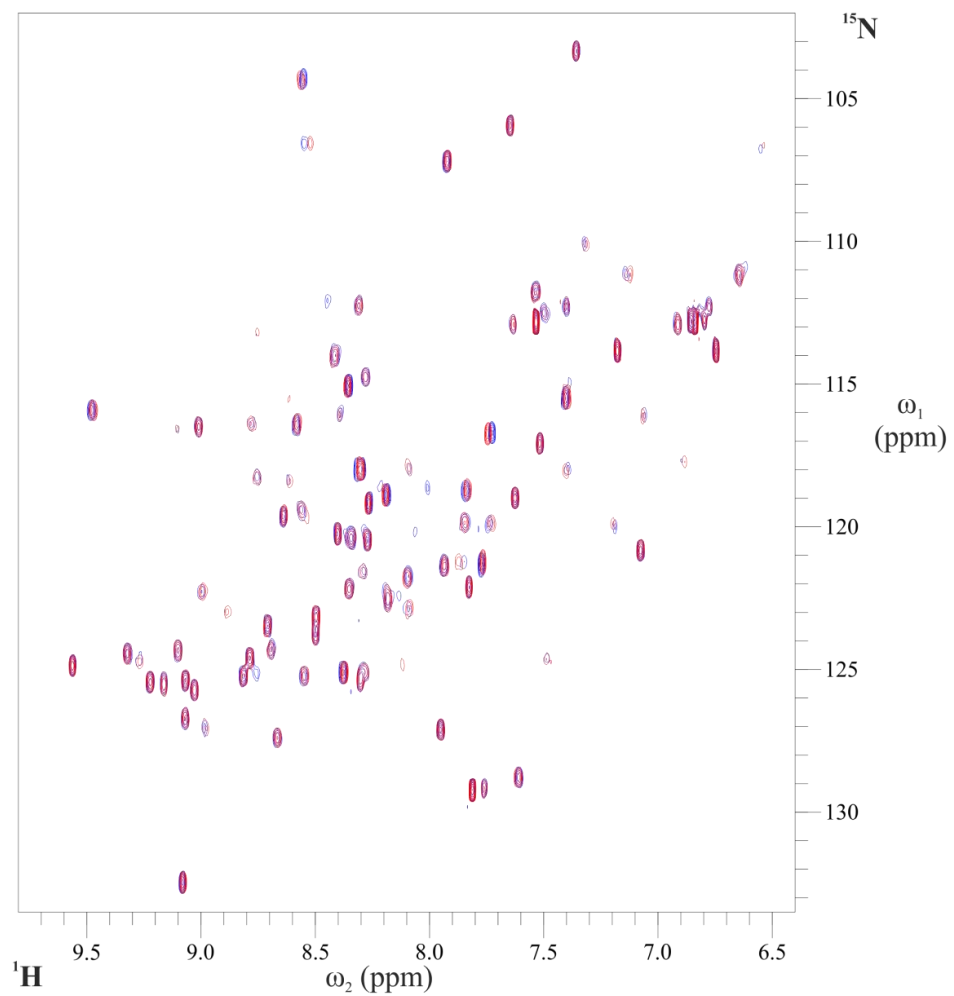
A.13. A 2-D overlay of the $^1\text{H} - ^{15}\text{N}$ HSQC spectra produced of PSD-95 PDZ2 in the free form (blue) and in the presence of **2c** (P:L = 1:10, red), acquired at 298K, with a field strength of 600MHz, in 20mM phosphate buffer, pH6.3.



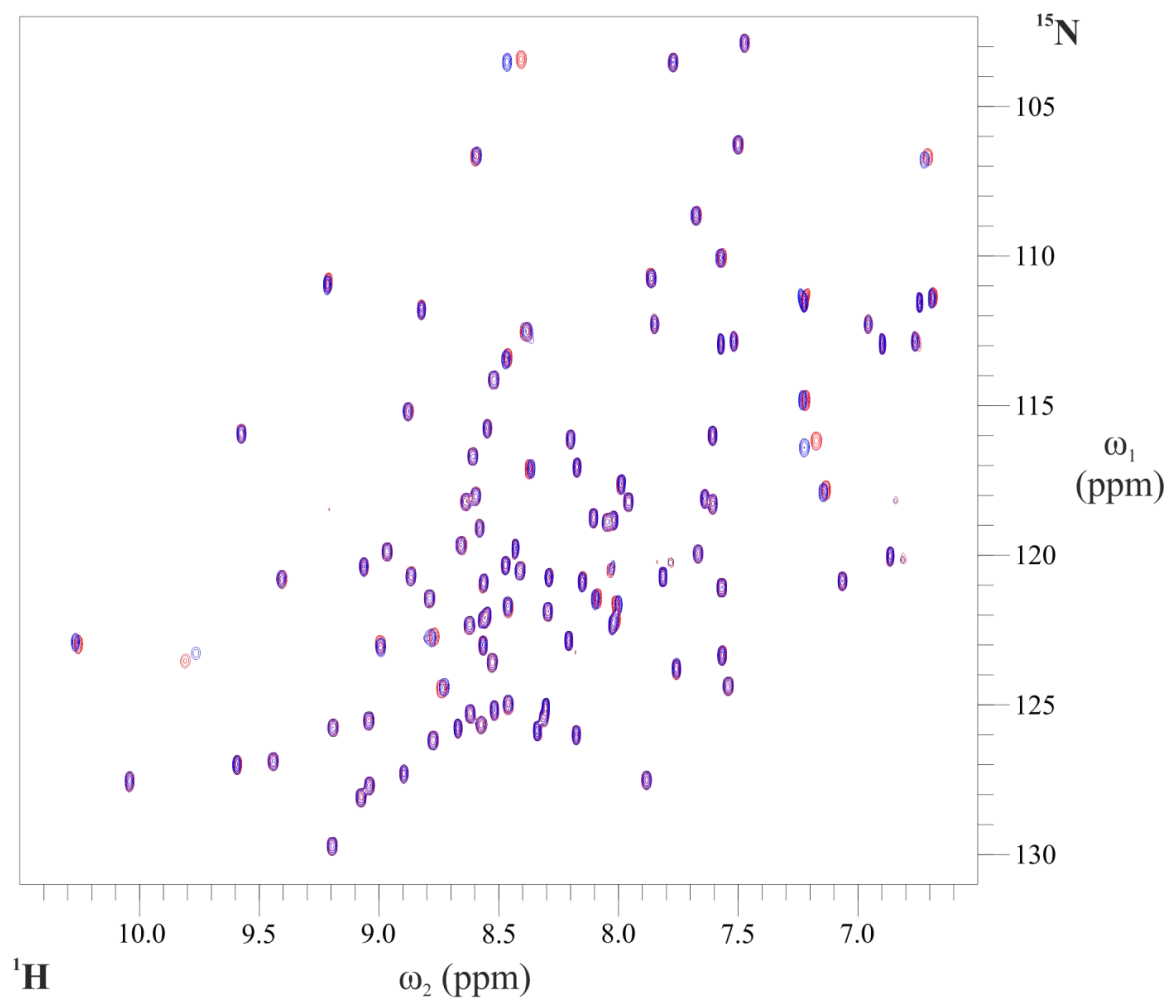
A.14. A 2-D overlay of the $^1\text{H} - ^{15}\text{N}$ HSQC spectra produced of SAP97 PDZ1 in the free form (blue) and in the presence of **2c** (P:L = 1:10, red), acquired at 298K, with a field strength of 600MHz, in 20mM phosphate buffer, pH6.3.



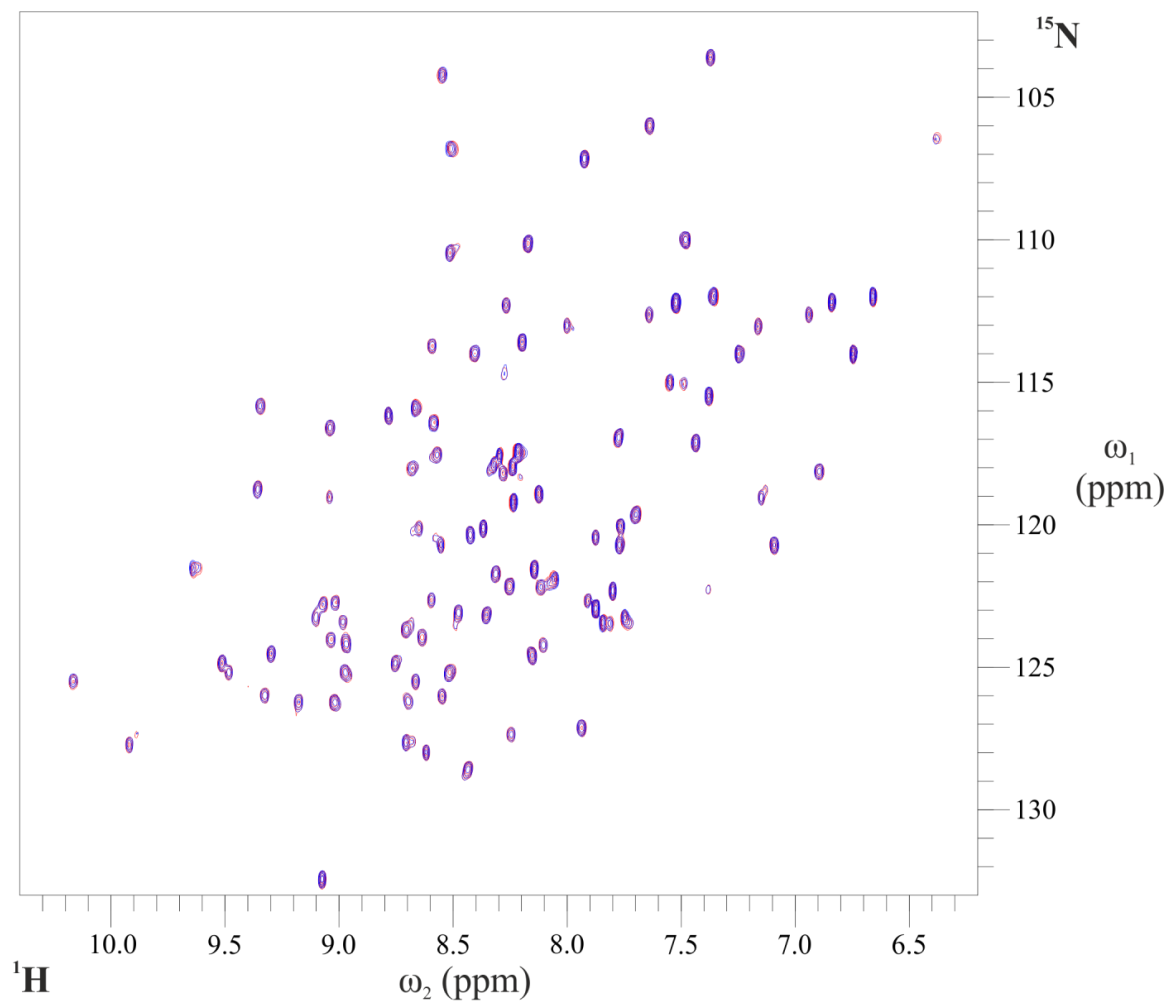
A.15. A 2-D overlay of the $^1\text{H} - ^{15}\text{N}$ HSQC spectra produced of SAP97 PDZ2 in the free form (blue) and in the presence of **2c** (P:L = 1:10, red), acquired at 298K, with a field strength of 600MHz, in 20mM phosphate buffer, pH6.3.



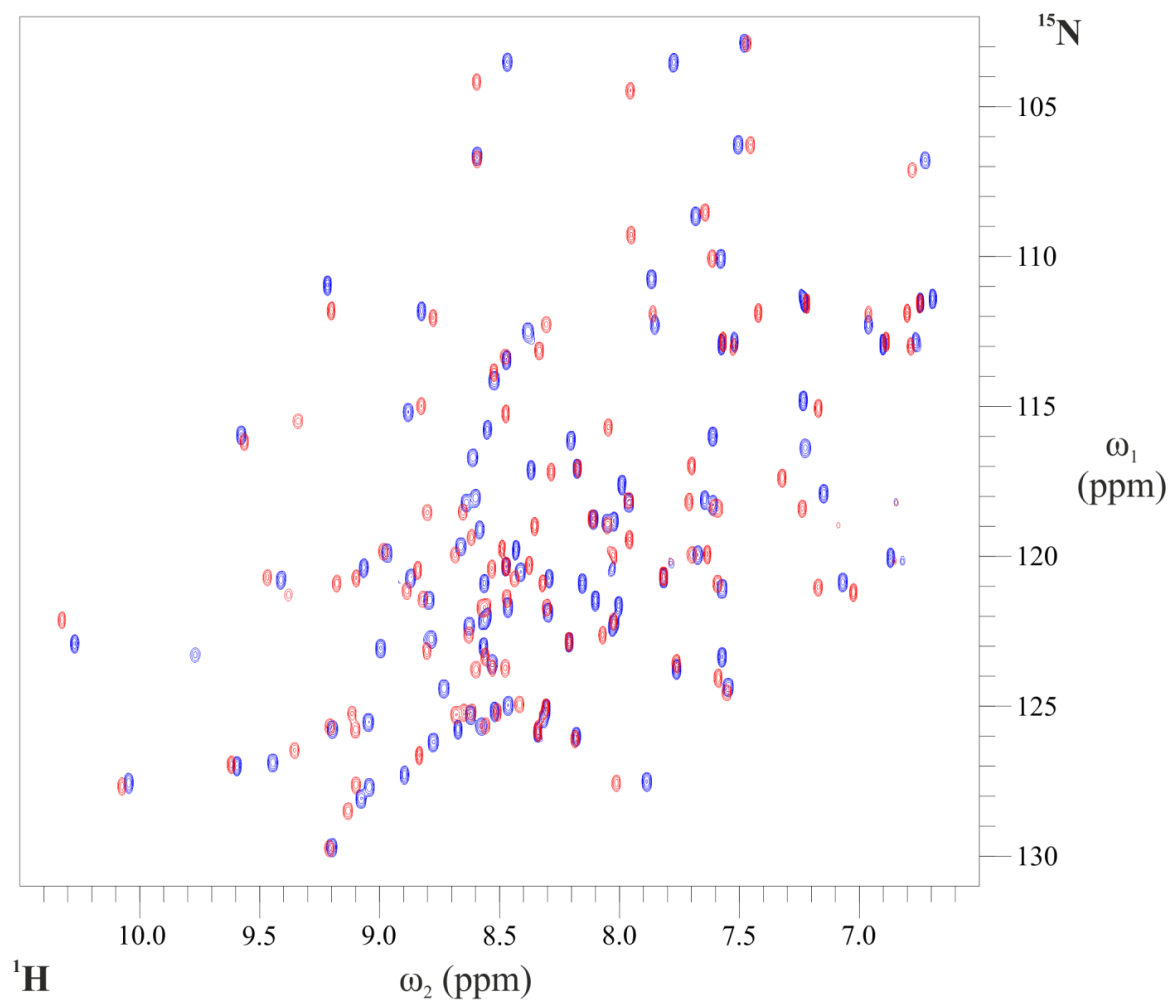
A.16. A 2-D overlay of the $^1\text{H} - ^{15}\text{N}$ HSQC spectra produced of PSD-95 PDZ2 in the free form (blue) and in the presence of **3d** (P:L = 1:10, red), acquired at 298K, with a field strength of 600MHz, in 20mM phosphate buffer, pH6.3.



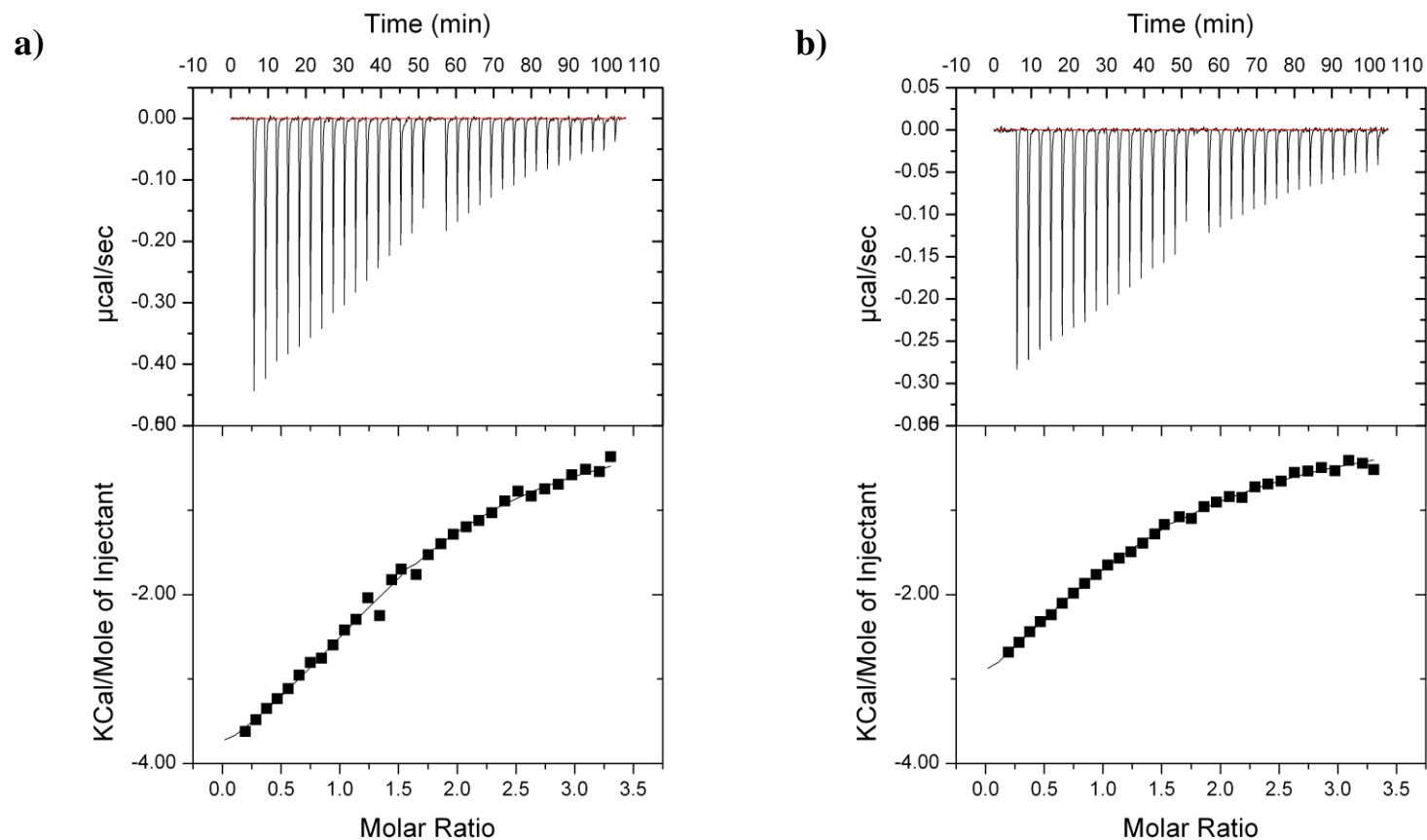
A.17. A 2-D overlay of the $^1\text{H} - ^{15}\text{N}$ HSQC spectra produced of SAP97 PDZ1 in the free form (blue) and in the presence of **3d** (P:L = 1:10, red), acquired at 298K, with a field strength of 600MHz, in 20mM phosphate buffer, pH6.3.



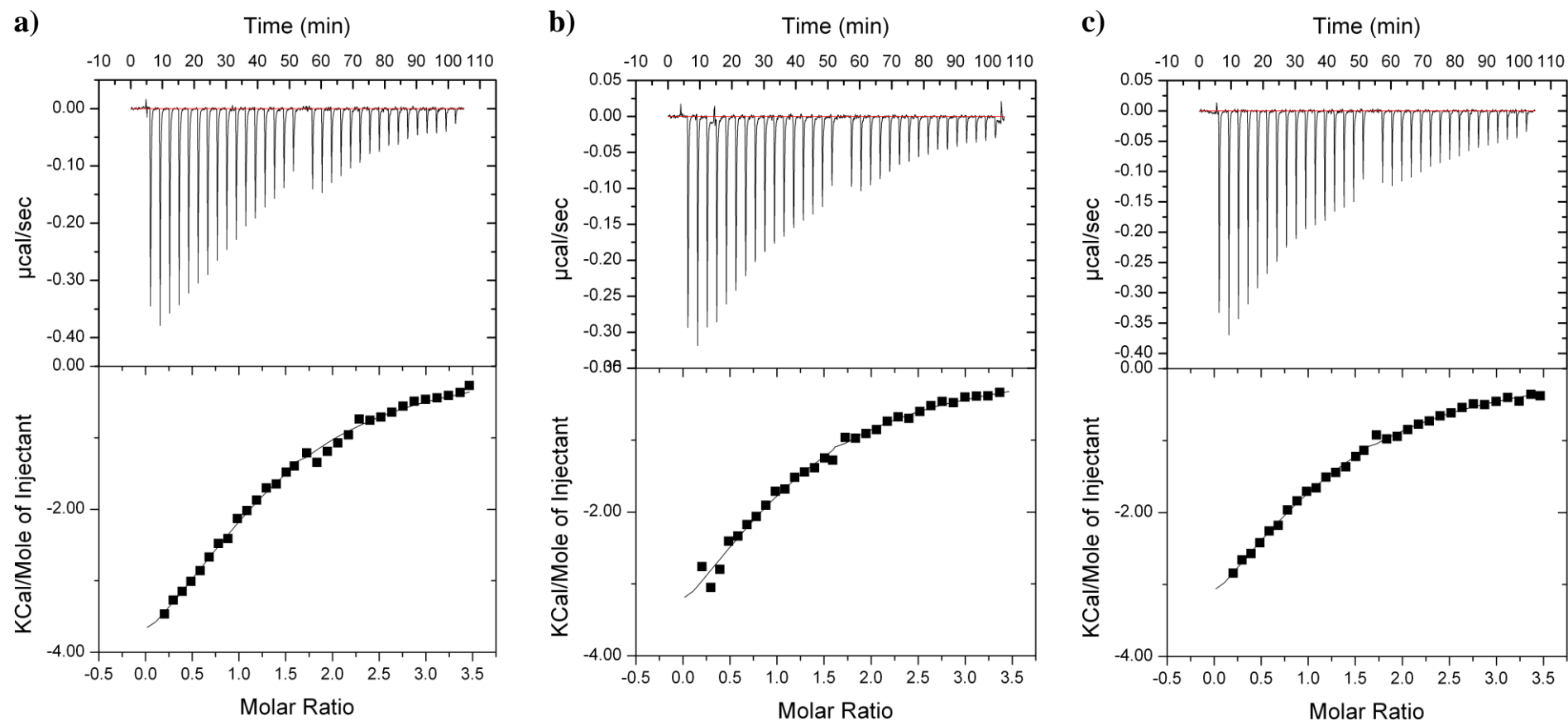
A.18. A 2-D overlay of the ${}^1\text{H} - {}^{15}\text{N}$ HSQC spectra produced of SAP97 PDZ2 in the free form (blue) and in the presence of **3d** (P:L = 1:10, red), acquired at 298K, with a field strength of 600MHz, in 20mM phosphate buffer, pH6.3.



A.19. A 2-D overlay of the $^1\text{H} - ^{15}\text{N}$ HSQC spectra produced of SAP97 PDZ1 in the free form (blue) and in the presence of **4c** (P:L = 1:10, red), acquired at 298K, with a field strength of 600MHz, in 20mM phosphate buffer, pH6.3.



A.20. The ITC isotherm (top) and resultant curve (bottom) produced by the ITC binding experiment between $100\mu\text{M}$ PSD-95 PDZ1 (cell) and $750\mu\text{M}$ 5-HT_{2c} nonapeptide (VVSERISSV, syringe) in 20mM phosphate, pH6.3 with **3c** present in both the cell and syringe solutions at PSD-95 PDZ1 : **3c** ratios of a) 1:10 and b) 1:25, on an iTC₂₀₀ Microcalorimeter (MicroCal) at 298K. Fitting of the curve produced by the individual ITC experiment to a single set of sites curve-fitting model, using Origin7, resulted in an apparent binding affinity (K_D^{app}) of 51.98 and $84.20\mu\text{M}$ for VVSERISSV to the PSD-95 PDZ1 domain, in the presence 10-fold and 25-fold excess of **3c** respectively. These experiments were used to determine the inhibitory constant (K_i) of **3c** for the PSD-95 PDZ1 – 5HT_{2c} interaction.



A.21. The ITC isotherm (top) and resultant curve (bottom) produced by the ITC binding experiment between 100 μM PSD-95 PDZ1 (cell) and 750 μM 5-HT_{2c} nonapeptide (VVSERISSV, syringe) in 20mM phosphate, pH6.3 with **4c** present in both the cell and syringe solutions at PSD-95 PDZ1 : **4c** ratios of: a) 1:2.5, b) 1:5 and c) 1:7.5, on an iTC₂₀₀ Microcalorimeter (MicroCal) at 298K. Fitting of the curve produced by the individual ITC experiment to a single set of sites curve-fitting model, using Origin7, resulted in an apparent binding affinity (K_D^{app}) of 46.51, 54.89 and 73.50 μM for VVSERISSV to the PSD-95 PDZ1 domain, in the presence 2.5-fold, 5-fold and 7.5-fold excess of **4c** respectively. These experiments were used to determine the inhibitory constant (K_i) of **4c** for the PSD-95 PDZ1 – 5HT_{2c} interaction.